Angui Li
Yingxin Zhu
Yuguo Li

Editors

Proceedings of the 8th International Symposium on Heating, Ventilation and Air Conditioning

Volume 1: Indoor and Outdoor Environment

Springer

Lecture Notes in Electrical Engineering

Volume 261

Angui Li · Yingxin Zhu · Yuguo Li
Editors

Proceedings of the 8th International Symposium on Heating, Ventilation and Air Conditioning

Volume 1: Indoor and Outdoor Environment

Editors
Angui Li
Xi'an University of Architecture
    and Technology
Xi'an
People's Republic of China

Yuguo Li
The University of Hong Kong
Hong Kong
People's Republic of China

Yingxin Zhu
Tsinghua University
Beijing
People's Republic of China

Preface

The 8th International Symposium on Heating, Ventilation, and Air Conditioning—ISHVAC2013 is to be held in Xi'an, China from October 19 to 21, 2013, organized by Xi'an University of Architecture and Technology, and co-organized by Tsinghua University and The University of Hong Kong. The proceedings consist of over 220 peer-reviewed papers presented at the ISHVAC2013. We sincerely hope that the 8th International Symposium on Heating, Ventilation, and Air Conditioning will provide a good platform again to HVAC experts and researchers in China and elsewhere to share their latest research findings and new technology development, and looking into the future of HVAC.

Xi'an has more than 3000 years of history as one of the four great ancient capitals of China. Xi'an has now re-emerged as one of the important cultural, industrial, and educational centers in China. History tells us a lot. The history of HVAC is much shorter. Addington (2001) wrote, after the 1918–1919 influenza pandemic, which killed more people than World War I, "*Engineers and manufacturers were quick to capitalize on the public's concern with cleanliness, and pointed out that the air handler could produce 'manufactured weather' that was cleaner and purer than what nature provided (Carrier 1919). In spite of the continued work of open-air enthusiasts such as Winslow and Dr. Leonard Hill during the next several decades to challenge mechanical systems, most of the early ventilation laws remained in place and the air-handler-based system became the standard for conditioning interior environments.*" The new revitalization of natural ventilation and the new development of mixed-mode ventilation in the last 10 years confirms the wisdom of Winslow and Dr. Leonard Hill.

The success of HVAC is and will also be judged in the balance of providing people a comfortable and healthy indoor environment and using the minimum resources and energy. The key to the success of HVAC is in understanding the human physiological needs in thermal comfort and healthy air, and the roles played by human behavior, which is dynamical in nature. We cannot just focus on the HVAC technologies as we have done in the past 100 years.

Urbanization is a huge thing in rapidly developing countries such as in China. More than 50 % of the world's population now lives in cities. The urban population will reach 1 billion by 2030 in China. In the new 10 years, it is expected at least 1 % of the population will become urban dwellers every year. The expectation for better indoor environment is also on the rise in China and other

developing countries as the living standard rises. Building consumes a large proportion of our energy in the world. Efficient HVAC is the key in high performance buildings. Continuing urban warming has been observed and studied in many megacities in the world. Just imagine if you are asked to cool the air in a Mong Kok district in Hong Kong or Wang Fu Jing Street in Beijing by a few degrees, what would you do? When shall we design a city just like designing a building? What can HVAC engineers and researchers do to help?

Xi'an literally means "Peaceful in the West" in Chinese, and it was historically known as Chang An ("Perpetually Peaceful"). We also wish that the world will not only be peaceful, but also sustainable. HVAC engineers and researchers have a great role to play.

Finally, the conference organizing and the high quality of the proceedings are the result of many people's hard work, dedication, and support. The first appreciation goes to the members of the International Scientific Committee. Great appreciation should also go to many people who worked tirelessly on the Organizing Committee. We greatly appreciate the special contributions of all the sponsors and cooperators.

We also express our thanks to the authors who enthusiastically presented their work, ideas, and results.

<div align="right">

Angui Li
Yingxin Zhu
Yuguo Li

</div>

International Scientific Committee

Yi Jiang (China)
Jiaping Liu (China)
Phillip J. Jones (UK)
Hazim B. Awbi (UK)
William Bahnfleth (USA)
Pradeep Bansal (NZ)
Mark Bomberg (USA)
Qingyan Chen (USA)
Zhenqian Chen (China)
Qihong Deng (China)
Shiming Deng (HK, China)
Lei Fang (DK)
Leon R. Glicksman (USA)
Yanling Guan (China)
Per Heiselberg (DK)
Jan Hensen (NL)
Sture Holmberg (SE)
Xiang Huang (China)
Shinsuke Kato (JP)
Angui Li (China)
Baizhan Li (China)
Xianting Li (China)
Yuguo Li (HK, China)
Zhiwei Lian (China)
Martin W. Liddament (UK)
John C. Little (USA)
Weiding Long (China)
Shuzo Murakami (JP)
Vincenzo Naso (IT)
Jianlei Niu (HK, China)
Bjarne W. Olesen (DK)
Saffa Riffat (USA)
Dirk Saelens (BE)
Jan Sundell (China)

Organizing Committee

Angui Li
Yingxin Zhu
Yuguo Li
Lei Zhao
Yi Wang
Yanfeng Liu
Zhiwei Wang
Yuesheng Fan
Qiuhui Yan
Xiaohong Nan
Xiong Liu
Qinghong Zheng

Contents

Part II Climate and Outdoor Environment

Part I
Indoor Environment

Chapter 1
Development of a Building Energy 'Sensitivity' Tool to Inform Early-Stage Design Decisions and its Application in China

Phil Jones, Simon Lannon and Xiaojun Li

Abstract In order to inform the design of a building or a group of buildings in relation to their potential energy efficiency, the main impact will be at the initial concept design stage. Variations and interactions of parameters need to be considered quickly as the design develops. This paper describes the development of a 'sensitivity tool' based around the established building energy model, HTB2. An example case study from China is given to illustrate the process.

Keywords Energy modelling · Early-stage design · Sensitivity tool

1.1 Introduction

Computer simulation is now commonly used to predict the energy performance of buildings. It can range from relatively simple annual energy predictions, such as used in conjunction with building regulations, for example, UK SAP [1], to more advanced numerical models that predict the detailed energy and thermal performance, typically on an hourly time scale over a year, such as Energy +, ESP-r, TRNSYS, and HTB2. HTB2, developed at the Welsh School of Architecture, Cardiff University, is typical of the more advanced numerical models, using as input data, hourly climate for the location, building materials and construction, spatial attributes, system and occupancy profiles, to calculate the energy required to maintain specified internal thermal conditions [2]. HTB2 has advantages of flexibility and ease of modification, which makes it well suited for use in the field of energy efficiency and sustainable design of buildings, which is rapidly evolving. It has been developed over a period of over thirty years and has undergone

P. Jones (✉) · S. Lannon · X. Li
Welsh School of Architecture, Cardiff University, Cardiff, Wales, UK
e-mail: JonesP@cardiff.ac.uk
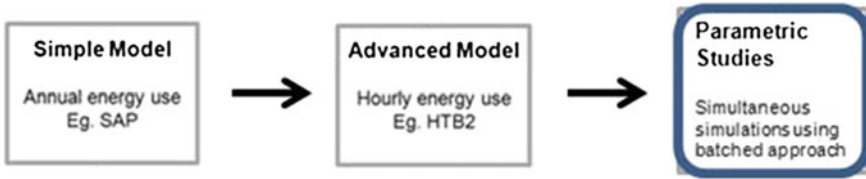
Fig. 1.1 Development of building energy simulation

extensive testing, validation, including the IEA Annex 1 [3], IEA task 12 [4] and the IEA BESTEST [5].

Computer simulation of new buildings should inform the design process. It will therefore have best impact if performed at an early-design stage. At this stage, there are generally many unknowns, and so early-stage simulation will need to include default values and needs to be carried out as simply as possible. There may be a number of iterations in order to optimise energy performance as the design develops. It is generally more common to carry out simulation on a relatively completed building as a check on its performance, maybe related to an environmental assessment process such as LEED or BREAM. However, in such cases, at this relatively late stage, there may be little scope to make major adjustments to the design. It is therefore important to differentiate between 'early-stage' simulation that is carried out to inform the design process and that which is carried out to check the final design.

Figure 1.1 illustrates how building energy simulation has developed from simple modelling to more advanced modelling, and how advanced models can now be used to carry out parametric studies of 1000's of annual hourly simulations simultaneously. Such developments incur large data sets in both the setting up of simulations and analysis of results, which places greater stress on pre- and post-processing.

This paper describes the development of HTB2 within this intensive computational framework, focussing on multi-parameter options for an individual building type. A range of parameter variations can be selected for a specific building type, typically including variations in, facade U-values, glazing ratio's, glazing G-values, HVAC systems, ventilation and internal gains. These are all run within HTB2 as a batch process. The results are interrogated using an on-screen 'sensitivity tool' to quickly evaluate the annual and seasonal heating and cooling energy performance. At an early stage of design, it is often necessary to examine a range of options quickly to determine the most appropriate design options for efficient energy use and reducing carbon dioxide emissions.

1.2 Multi-Parameter Single Building Modelling

HTB2 has been developed to carry out parametric analysis of building types as part of an early-design stage modelling capability. In the case study presented here, over 4,000 hourly annual energy simulations were carried out, generating millions

of data items. A post-processing 'sensitivity tool' is then used to easily interrogate the results.

Using the standard data for office building design in China, together with information on the office case study (provided by Chongqing Academy of Science and Technology, CAST), which was specific to Chongqing, a test model with a symmetrical layout and simple functional zoning (office surrounding central circulation and services zone) was constructed to represent the building for the purpose of early-stage design simulation (Fig. 1.2). At this stage, the detailed design of the building would not be realised. The triangular floor plans illustrated in the figure formed the basis for the simulations. The glazing ratio for each facade was set as 50 %, and the floor height for standard floor was 3.6 m. Simulations were carried out at space/room level (the blue area towards south) with variants including fabric U-value, window G-value, ventilation option, internal gain, orientations, to test the energy performance through different passive design strategies.

The indoor design conditions used for the simulations was taken from the design standards described in Design Standard for Energy Efficiency of Public Building GB 50189-2005, as well as the Design Standard for 50 % Energy Efficiency of Public Building in Chongqing Area DBJ50-052-2006.

The settings for the parameter variations are presented in Table 1.1. The highlighted values are set for the standard case (the base case).

Figure 1.3 summarises the simulation results for all 4,608 runs, regarding the sensitivity of different variants in relation to their annual heating and cooling energy consumption. Overall, the heating energy varies between 0 and 35 kWh/ m^2/annum, and the cooling energy from 29 to 125 kWh/m^2/annum. In each graphs,
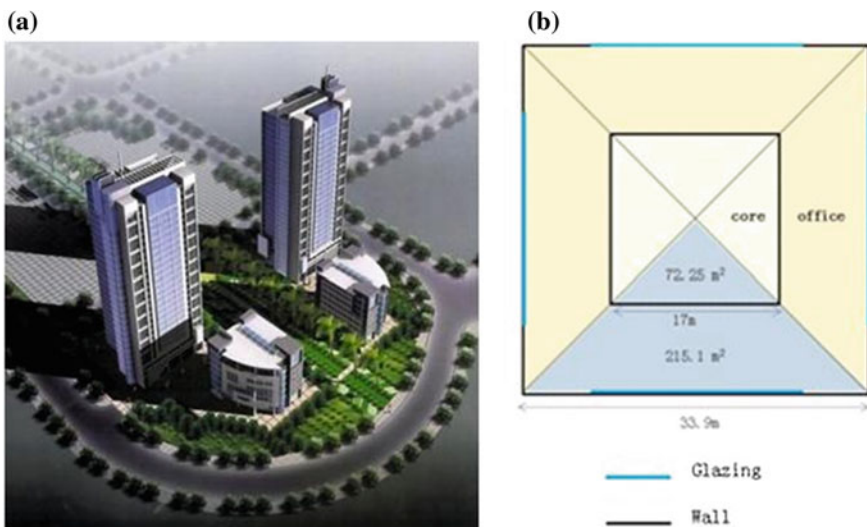
Fig. 1.2 a Example building and **b** simplified form for initial sensitivity analysis

Table 1.1 Different variables and their values

Variables in related to passive design strategies	Values
External wall U-value (W/m^{2}K)	0.3–0.7–**1.1**
External window U-value (W/m^{2}K)	1.0–1.5–**2.5**–3.5
External window G-value	0.1–0.2–0.4–**0.6**
Ventilation (night air change rate for spring, autumn and summer)	0.5–**2.0**–6.0
Internal heat gain (including lighting, equipment and occupants) (W/m^2)	25–35–45–55
Orientation	S–SW–W–NW–N–NE–E–SE

The highlighted values are set for the standard case (the base case)
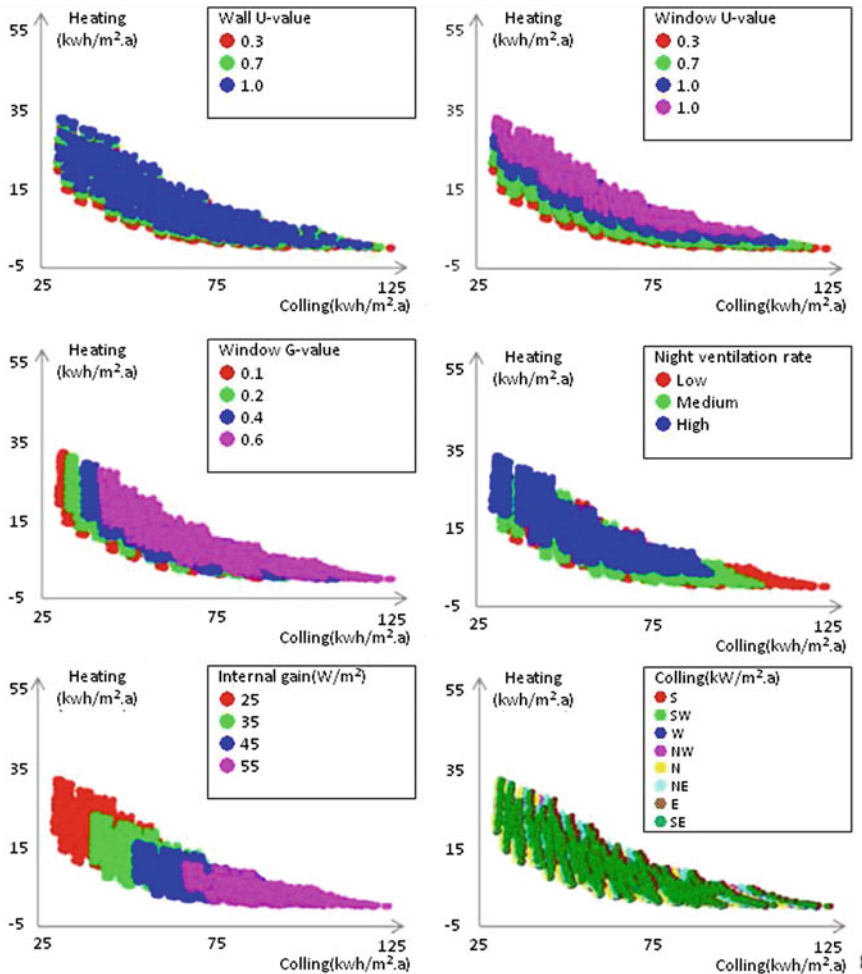
Fig. 1.3 Sensitivity analysis for different variants in GIS (*top-left* wall U-value, *top-right* window U-value, *middle-left* window G-value, *middle-right* night ventilation rate, *bottom-left* internal gains, *bottom-right* orientation)
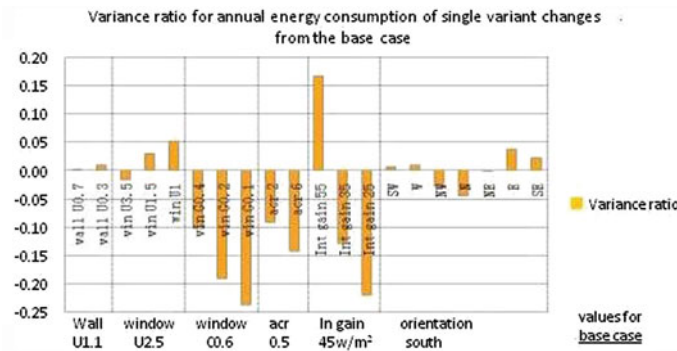
Fig. 1.4 Variance ratios of annual energy consumption of single variant changes from base case

dots colour relates to the variant classification. The graphs indicate the following trends.

- The cases with high wall U-value (blue dots) tend to use more heating energy, but this trend is not strong according to the majority overlapping of different dots, implying not much influence from external wall U-value.
- The cases with high window U-value (purple dots) use more heating energy, but less cooling energy. The trend is stronger than 5a, as there is less overlapping area in this graph, implying a greater impact from window U-value than that from external wall U-value.
- In general, cases with high window G-value (purple dots) use more cooling energy, but less heating energy. The trend is shown clear through the scatter of different colours with little overlapping area, implying great influence from window G-value.
- In general, cases with high night ventilation rate (blue dots) use more heating energy, but less cooling energy. The scatter of different colours shows an influence from night ventilation rate.
- In general, cases with high internal gains (purple dots) use more cooling energy, but less heating energy, vice versa. The trend is strong through the clear scatter of different colours, implying significant influence from internal gains.
- This orientation case shows no distinct trend, implying little impact from orientation. This is a response to the specific climate of Chongqing, which has a high instance of cloud cover.

Figure 1.4 summarises the impact of the variations, indicating that window G-value and the level of internal gains have the main impact for office design in Chongqing.

1.3 The Sensitivity Tool

Based on the simulation results, a sensitivity tool was developed to aid decision making for building design at an early stage. It can access the results from all 4,608 annual simulations on a single computer screen. It describes the annual and monthly energy consumption for different combinations of variants by moving the buttons as required. Besides, by comparing the simulation results, the user can gain a better understanding about the sensitivity of different variants in relation to their impact on building energy performance and identify the most effective design strategies afterwards. Figure 1.5 shows the sensitivity tool set up three cases, 'base case', 'best case' and 'best practical case'. In such a situation, the designer can make a judgement on the viability of different options, and in this case, the 'best case' would represent value for money and the level to which the performance can be achieved in relation to available skills and supply chains. The sensitivity tool allows the user to adjust the values of the variants and obtain data immediately for monthly energy use for heating, cooling and annual energy use (heating, cooling and total). This allows the designer to quickly assess various design options that can then be used to inform the design process. The most appropriate combination of options can then be used to generate the more detailed design stages. The designer can also use the tool to demonstrate, in a simple way to the client and others, the reasoning behind the design decisions in relation to energy and low carbon impacts.

In order to target the level of energy savings appropriate to a specific situation, a range of levels of savings are summarised in Table 1.4. The proposed level of savings suggested from this study fall between levels 1 and 2, which is probably appropriate for the office design situation in Chongqing. The information in Table 1.2 can therefore be used to inform the initial design process (Table 1.3).

1.4 Sensitivity Analysis for Other Chinese Locations

The results from the sensitivity analysis can be summarised in a plot as shown in the top-left of Fig. 1.6, for Chongqing, indicating the impact importance of the different variants. This can be repeated for the same building but in different climate zones, as indicated in the five other plots in Fig. 1.6, corresponding to the locations in Fig. 1.7. This summary of impact of variants indicates that a different approach to low energy design should be adopted according to climate zone. For example, thermal insulation does not have a high impact in warmer zones, where the window G-value is of more importance.
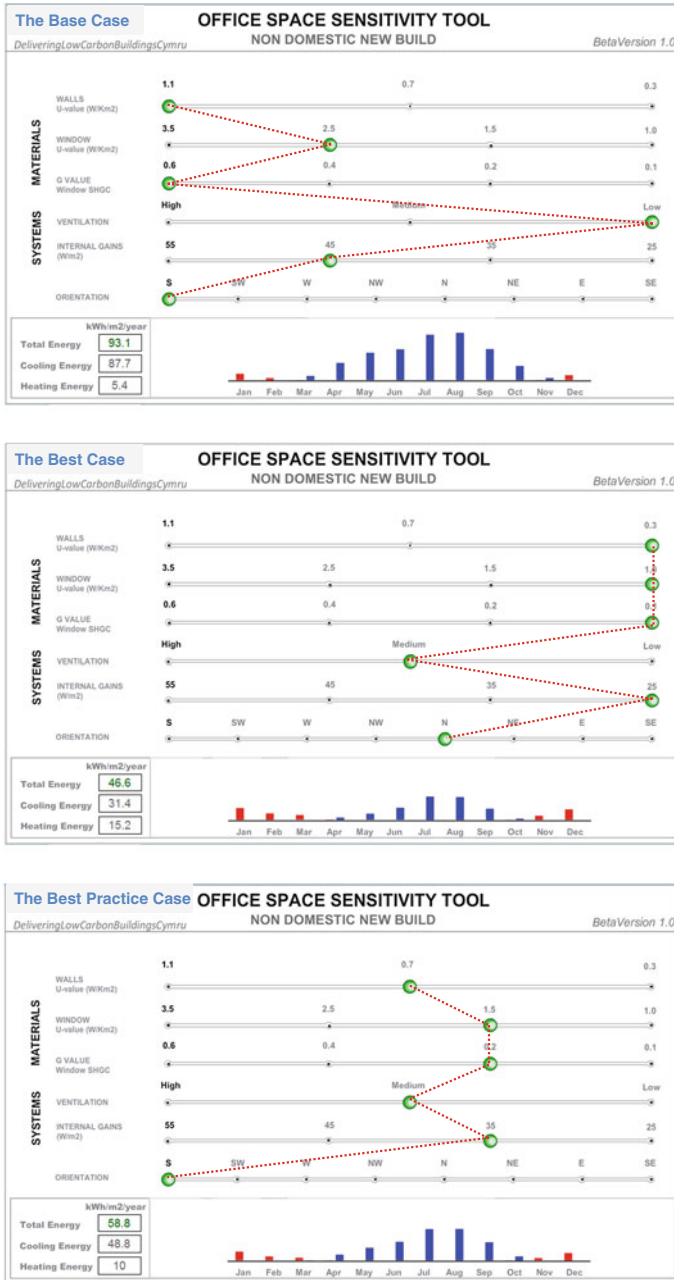
Fig. 1.5 Sensitivity tool set up for the base case (*top*), the best case (*middle*) and the best practice case (*bottom*)

Table 1.2 Example of best practical case

Variants	Standard case	Best case	Best practical case
Wall U-value	1.1 W/m^{2}K	0.3 W/m^{2}K	0.7 W/m^{2}K
Window U-value	2.5 W/m^{2}K	1.0 W/m^{2}K	1.5 W/m^{2}K
Window G-value	0.6	0.1	0.2
Ventilation	0.5 acr	2.0 acr	2.0 acr
Internal heat gain	45 w/m^2	25 w/m^2	35 w/m^2

Table 1.3 Setting targets energy performance for the base case, the best case and the best practical case

	Annual energy consumption (KWH/M^2)	Energy saving rate (%)
Base case	93.1	0
Best case	46.6	50
Best practical case	58.8	36.8

Table 1.4 Target reductions

Standard		Energy reductions (%)	Description
Level 1	Basic level of improvement	25	*General improvements from regulations*
Level 2	Low carbon performance	50	*Environmental assessment methods*
Level 3	Zero carbon performance	75	*Passivhaus/towards zero carbon performance*
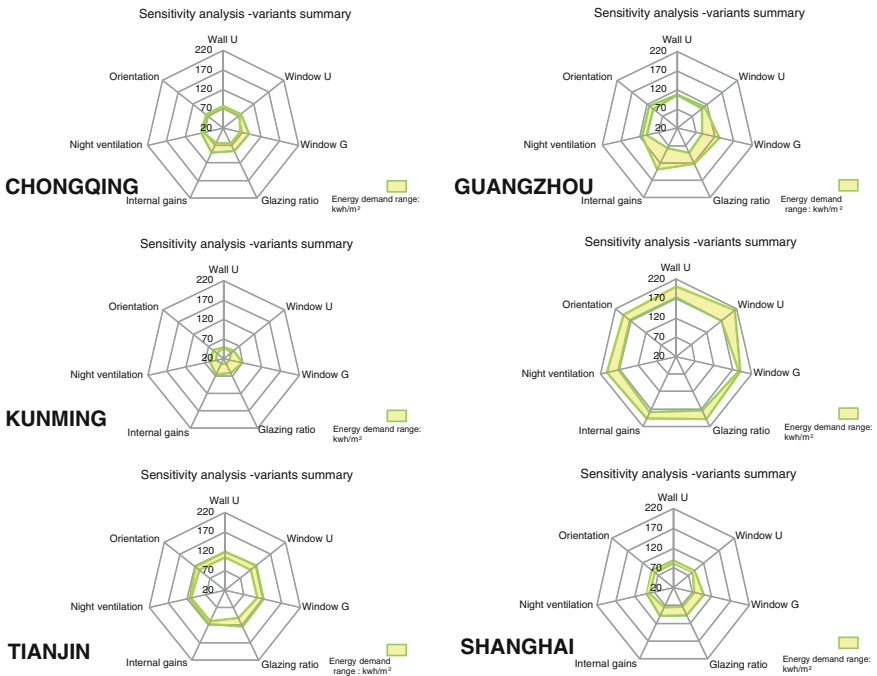
Fig. 1.6 Analysis from 6 locations in China

Fig. 1.7 Locations of sensitivity analysis and climate zones in China

1.5 Conclusions

This paper has described the development and application of a computational intensive energy simulation processes associated with early-stage single building design, using the 'sensitivity tool'.

It illustrates how such simulations can assist in early-stage design decision making providing a relatively speedy method of setting up and analysing large data sets associated with simulating many variants for a single building.

Further work is underway to develop the 'sensitivity' tool to contain more variants and to be operated through a tablet device, such as iPad and Android systems.

References

1. DECC (2012) Standard assessment procedure (SAP), in, DECC
2. Lewis PT, Alexander DK (1990) HTB2: a flexible model for dynamic building simulation. Build Environ 25(1):7–16
3. Oscar Faber and Partners (1980) IEA Annex 1 Computer Modelling of Building Performance: Results and Analyses of Avonbank Simulation. Oscar Faber and Partners, St Albans, UK
4. Lomas KJ, Eppel H, Martin C, Bloomfield D (1994) Empirical validation of detailed thermal programs using test room data, volume 1: final report, international energy agency
5. Neymark J et al (2011) IEA BESTEST multi-zone non-airflow in-depth diagnostic cases, 12th IBPSA, Sydney, 14–16 Nov 2011

Chapter 2
Evaporative Losses from Retail Gasoline Outlets and Their Potential Impact on Ambient and Indoor Air Quality

Laleh Yerushalmi and Soheil Rastan

Abstract Retail gasoline outlets contribute to the emission of volatile organic compounds (VOCs). According to the United States Environmental Protection Agency (US EPA), the concentrations of the common constituents of gasoline such as benzene (a carcinogen), toluene, ethylbenzene, and xylene within 200 m of gas stations are found to be higher than ambient background levels. Many retail gasoline outlets are located in close proximity to populated commercial and residential neighbourhoods. In the light of the above, this paper presents estimates from the survey of industrial processes (SIP), a pilot survey conducted by the Canadian Government, for the overall evaporative emissions from retail gasoline outlets across Canada. The survey suggests that approximately 58 million litres of liquid gasoline is being evaporated each year into the ambient air from the 11,200 retail gasoline outlets across Canada. Such an emission rate is equivalent to the evaporation of the contents of three fully loaded gasoline delivery trucks on each and every day of the year. This silent emission contaminates the ambient air of urban populated neighbourhoods and subsequently the indoor air of buildings that are located in such neighbourhoods. To that end, this paper attempts to raise the awareness of building engineers regarding the locations of gasoline outlets within the vicinity of buildings and the potential short-circuiting of gasoline vapours from the ambient air to the indoor microenvironment.

L. Yerushalmi
Department of Building, Civil, and Environmental Engineering, Concordia University, Montreal, Canada

S. Rastan (✉)
Environment Accounts and Statistics Division, Statistics Canada, Ottawa, Canada
e-mail: Soheil.Rastan@statcan.gc.ca

2.1 Introduction

Many retail gasoline stations are located in populated urban areas adjacent to office buildings, commercial shopping centres, schools, and residential neighbourhoods. Retail gasoline stations contribute to the emissions of volatile organic compounds (VOC) through refuelling activities carried out on daily basis. Gasoline vapour, once released to the atmosphere, combines with nitrogen oxides in the presence of sunlight to form ozone. Ground-level ozone is a component of smog that contributes to respiratory illnesses. Gasoline is being considered for inclusion in the toxic substances list of the Canadian Environmental Protection Act. Volatile organic compounds, the major constituents of gasoline, have adverse impacts on human health, and the estimation of their emissions has been the subject of several studies. For example, the California Energy Commission collects information on all retail gas stations located in California through the California Annual Retail Fuel Establishment Form which needs to be filled out by these facilities as a mandatory report [1]. Environment Australia estimates the aggregated emissions from service stations using information collected in the Australian National Pollutant Inventory (NPI) [2]. According to the European Emission Inventory Guidebook, the contribution of the gasoline distribution sector to the total manmade non-methane volatile organic compounds emissions ranges from 1.5 to 6.7 %. The reported values apply to all 28 European countries that participate in the inventory [3].

Schifter et al. [4] estimated the emissions of volatile organic compounds in the gasoline distribution cycle in the metropolitan area of Mexico City and showed that the contribution of volatile hydrocarbon emissions due to storage, distribution, and sales of gasoline was 6651 t per year. The VOCs concentrations in a service station located in a residential and commercial area in the city of Rio de Janeiro was estimated by de Oliveira et al. [5] who reported a mean concentration of 144.5 μg/m^3 (microgram per cubic metre) for benzene, a potential carcinogenic compound, which is about ten times higher than the concentration in a control location, and about 70 times higher than concentrations in other locations of Rio de Janeiro. Morales Terrés et al. [6] also showed higher VOC concentrations in the air inside and around service stations compared to the background air concentration in the city of Murcia in Spain. They recommended the establishment of a "belt" around service stations where housing or vulnerable populations and activities such as those in schools, hospitals, and community centres should be restricted.

The study of potential contribution of retail gasoline stations to ambient and indoor VOC concentrations and population exposure requires a fundamental understanding of the nature of the source and its emissions. Recently, the Canadian Government carried out a study to identify the sources of evaporative emissions and to estimate the ensuing emissions from retail gasoline stations across Canada. This study was carried out by conducting a pilot survey, called the survey of industrial processes (SIP), which collected data on operational activities and engineering processes of small- and medium-sized enterprises. This survey was

designed as a pilot test of the use of economic and operational data collected through a statistical survey in the estimation of the release of certain criteria air contaminants (CACs) from small-and medium-sized enterprises (SMEs) within a given sector of the Canadian economy. The survey population included retail gasoline stations as well as marinas with gas docks. This study addressed establishments primarily engaged in retailing gasoline fuel whether or not the outlet was operated in conjunction with a convenience store, repair garage, restaurant, or other types of operation. Diesel-only outlets and card locks were excluded from the population. The survey employed standard statistical methods in the collection of data including the design of the survey frame, sample selection, and statistical edits, imputations, and weighting methodologies. Data collected included quantities of gasoline sold, gasoline truck delivery frequencies, number of gasoline storage tanks, number of fuel dispensers, age of site, and other related activities and processes that depict this particular sector of the Canadian economy. Related spatial/temporal climate data such as temperature and solar intensity were obtained from Environment Canada and mapped over the locations of gasoline outlets across Canada.

2.2 Sources of Evaporative Emissions from Your Corner Gas Station

Evaporative losses from retail gasoline outlets can be classified into two categories. The first category includes those attributed to the processes and equipment used by the retail outlet to receive, store, and supply the gasoline. The second category includes losses attributed to the refuelling of vehicles. The following sections summarize some of the important sources of evaporative losses from a typical gas station in Canada.

2.2.1 Working and Breathing Losses

Working loss in gasoline storage tanks is due to the combined effects of gasoline delivery to the storage tanks (the filling of underground storage tanks) and the emptying operation (the pumping of gasoline from storage tanks to the dispensers/gas pumps). During the filling of storage tanks, fuel vapours are released to the atmosphere due to the increased liquid level in the tank pushing up and reducing the vapour space in the tank. The vapour is consequently compressed in the tank, forcing the air–vapour mixture out through vent pipes. These vent pipes are open to the ambient air and are located close to surrounding buildings. If the tank is equipped with a pressure/vacuum (P/V) valve on its vent pipe, vapours are released only when the pressure inside the tank exceeds the valve relief pressure.

In the absence of such valves, as is the case in most of Canada, any increase in tank pressure above atmospheric levels will release the vapours through the open vent pipe. In few areas of Canada such as the Lower Fraser Valley (British Colombia) some parts of Southern Ontario, and the City of Montreal (Quebec), delivery trucks that deliver gasoline to retail gasoline outlets are required by the respective local jurisdiction laws to attach a second hose to each underground storage tank during the refilling operation to capture part of the air–vapour mixture that would have otherwise escaped from the vent pipe. This vapour capturing method is commonly referred to as the "stage one" vapour recovery based on the vapour balancing system. Although some reports claim up to 90 % recovery efficiency, the effectiveness of this particular "second-hose" vapour recovery method (i.e., vapour balancing) in the absence of the aforementioned P/V valve on the vent pipe of an underground storage tank is uncertain [7].

Gasoline pumping activities during the refuelling of vehicles also contribute to the working loss in storage tanks. This occurs due to air being drawn through the vent pipe into the storage tanks as a result of the decrease in storage tank liquid level while pumping out gasoline. The entrained air becomes saturated with gasoline vapours and subsequently expands, expelling air–vapour mixture to the atmosphere through the same vent pipe. Once again, this emission is more pronounced in storage tanks that are not equipped with a P/V valve on their vents as a control measure.

Breathing loss (also known as standing loss) is due to the release of gasoline vapour to the ambient air due to the expansion and contraction of vapour inside storage tanks. The breathing loss results from changes in the temperature and pressure inside and outside of the storage tank, regardless of changes in the liquid level inside the tank. In the absence of a control measure such as a P/V valve, this "breathing process" continues as long as there is some gasoline liquid inside any tank with an open vent.

Since changes in temperature and pressure are less pronounced for underground tanks due to the protective and insulating effects of soil, the US EPA does not associate breathing loss with underground storage tanks. This is, in part, justifiable for several reasons. First, most cities in the USA are in climates where the difference between the ambient air and the underground temperature is less pronounced than in most Canadian cities. Second, underground tanks in the USA are generally equipped with vent pipes that have P/V valves with pre-set pressure and vacuum settings to control the breathing activity. In contrast, the storage tanks in Canada generally employ valve-free vent pipes that are open to the atmosphere. In the light of the above, breathing losses in Canadian underground gasoline tanks were included in the evaporative loss estimates regardless of the partial insulating effects of the underground. In the case of underground tanks, the effect of solar radiation was removed from the calculation and only the impact of temperature was included. The difference between the below ground air temperature of an underground tank and that of the ambient air temperature above was estimated to be 8 degrees Celsius during the cold season and 12 °C during the warm season [8].

2.2.2 Monitoring and Spill Losses (Residual Loss)

The monitoring loss involves inserting a wooden dipstick into the storage tanks to measure the gasoline liquid levels and to check for the presence of water. The measurement of gasoline level is conducted by both the operator of the retail outlet and the gasoline delivery personnel, independently. Monitoring losses from dipsticks occur due to the evaporation of gasoline that has been adsorbed on the wooden surface of the dipsticks. These dipsticks are subsequently placed in the open air, causing the evaporation of adsorbed gasoline on the surfaces of these wooden sticks into the atmosphere. Fixed electronic level-monitoring devices are also available and are commonly used in many retail gasoline outlets across Canada, although the use of dipsticks remains common by gasoline delivery personnel verifying their deliveries. Based on the activity data collected from the SIP and laboratory experiments, the reported evaporative loss estimates have incorporated an empirical model to estimate losses from the use of dipsticks.

A spill loss is any uncontrolled leak/spill that occurs from dispensers. Part of this loss is from nozzle spills. Since absorbents are mainly used by retail gasoline operators to clean up after this particular type of spill, it is assumed that the amount of such spills is correlated with the quantity of absorbents used.

2.2.3 Vehicle Refuelling Loss

Gasoline emissions due to the refuelling of vehicles occur when vapour from the headspace of a vehicle fuel tank is displaced by the liquid gasoline that is dispensed into the said fuel tank. The volume of displaced vapour during the refuelling operation is approximately equal to the volume of gasoline dispensed into the vehicle fuel tank. The quantity of displaced vapours depends on the temperature of gasoline in the fuel tank, vehicle fuel tank temperature, gasoline Reid vapour pressure (RVP), and the dispensed volume of gasoline. The volume of vapour released during refuelling also depends on the vapour recovery method used. In the USA, many dispensers at retail gasoline outlets incorporate vacuum-based nozzles as a vapour recovery method. In the USA, they also rely on the on-board vapour recovery (OBVR) system installed inside vehicles. These two methods are known as "stage two" vapour recovery methods. In Canada, only the OBVR has been applied as the vapour recovery system during vehicle refuelling [9]. In fact, the combined use of the two methods could defeat the purpose since the former method counters the effectiveness of the latter [10]. In Canada, OBVRs have been installed in all newly manufactured vehicles since 1998. OBVRs are up to 98 % efficient in capturing evaporative losses during a refuelling operation [10].

2.3 Data Sources

SIP was the main source of the data presented in this paper. Other sources of data including climate data from hundreds of weather stations across Canada and business registry data to spatially locate retail gasoline outlets across Canada were used as inputs to the evaporative loss algorithm. Details on the SIP are published elsewhere [11].

2.4 Evaporative Loss Algorithm

Gasoline evaporation due to working loss and breathing loss from retail gasoline outlets was estimated based on the models recommended by the US EPA [12]. A set of mass balance and empirical equations were also added to generate the overall estimates of evaporative losses, tank by tank, process by process, for gasoline outlets across Canada. Detail of the methodology, algorithm, and assumptions are reported elsewhere [13].

2.5 Results

The following paragraph highlights some of the basic data obtained from the survey. The ensuing paragraph presents the estimated data from the evaporative loss algorithm applied on the basic data of the survey. The last paragraph presents a range of emission estimates, as a point source, from a typical gasoline station in Canada.

In 2009, over 1.1 million gasoline deliveries were made and 40.7 billion litres of gasoline were sold across Canada. These deliveries corresponded to the capacity of over 700,000 fully loaded trucks, enough trucks to fill two lanes of the Trans-Canada Highway, a highway that connects the Atlantic Ocean with the Pacific Ocean in land, bumper-to-bumper and coast-to-coast. Two decades ago, there were more than 21,000 retail gasoline outlets in Canada. In 2009, there were fewer than 12,000 outlets across the country [14]. Approximately 39 % of retail gasoline outlets identified the age of their sites as being 10 years or younger, 50 % between 11 and 30 years, and 10 % between 31 and 60 years. A handful of outlets reported nearly a century of service at the same location. In 2009, more than 29,000 gasoline storage tanks, both aboveground and underground, were in operation at retail gasoline outlets across Canada. Almost 90 % of these storage tanks were reported as being underground. Close to 41 % of all gasoline tanks at retail gasoline outlets were less than 10 years old; 56 % were between 10 and 25 years old; and 3 % were more than 25 years old. In 2009, over 43,000 fuel pumps or dispensers were in operation at retail gasoline outlets. Newer dispensers with digital

metre displays accounted for almost 87 % of the total. About 60 % of all dispensers were less than 10 years old, 38 % were between 10 and 25 years old, and 2 % were more than 25 years old. Nozzle spills are an issue at most gasoline outlets. Absorbents are used to soak up gasoline spills during refuelling of vehicles. Retail gas stations used about 286 t of absorbents during 2009. With this quantity of absorbents used, the total amount of gasoline spilled while refuelling during 2009 could fill as much as two gasoline delivery trucks [11, 13].

In 2009, approximately 58.3 million litres of liquid gasoline evaporated from 11,200 retail gasoline outlets across Canada. This is equivalent to the evaporation of the contents of one full tanker truck every eight hours. Of all the evaporative losses, almost two-thirds resulted from gasoline storage tanks. The remaining one-third was the result of vehicle refuelling. The resulting estimates of gasoline evaporative losses compare well with Environment Canada's estimates once uncertainties are included. Although the two estimates were produced by using different models in terms of scale and approach, the overlap in the two estimates is promising. The SIP, using a detailed bottom-up approach to estimate evaporative losses, has statistically validated the aggregated top-down approach of Environment Canada. The latter used total national gasoline sales with relevant emission factors and related macrolevel adjustments. On the other hand, the SIP focused on the operational activities and industrial processes used in retail gasoline outlets, tank by tank, outlet by outlet, and process by process. The advantage of the SIP rests on its statistical sampling methodology, with a broad population coverage, statistical weights, and quantifiable uncertainties. The bottom-up approach of using survey data could facilitate the generation of pollution concentration gradients across regions, i.e., those with more stringent gasoline delivery regulations versus those with less stringent regulations to help compare the effects of regulations as they vary from location to location, city to city, or province to province.

Based on the above estimates and related assumptions [11], a typical gasoline station in a Canadian urban neighbourhood tends to lose on average some 5,500 L of liquid gasoline per year. As a point source emission, this corresponds to the evaporation of approximately 15 L of gasoline liquid on a daily basis to the surrounding ambient air. Occupants of buildings adjacent to such a point source would no doubt be in the exposure pathway to gasoline vapour including the carcinogen benzene (0.5 to 2.5 % w/w) [15].

2.6 Implications

The following paragraph places the results of the SIP and its evaporative loss estimates into some perspective. In 2001, a case report published by Environment Canada [16] stated that one particular air quality measuring site in the east end of the city of Montreal, Canada, had the highest mean and maximum levels of benzene ever recorded in Canada during the periods 1989–1993. However, by the year 2000, the benzene values declined in the air samples collected at the same site

by some 60 %. In order to explain this situation, Environment Canada investigated the sources of benzene emissions in that particular location and compared the extent of emissions with the levels measured in ambient air in other air quality measuring sites within the city of Montreal and across Canada. The mean benzene levels measured in the ambient air reflect the magnitude of the releases that occur near the monitoring stations. That particular monitoring station reporting the highest levels is located at some 1.5 km from two refineries and about 200 m from a retail gasoline outlet. A number of factors could explain the drop in the benzene levels observed at the said monitoring site in the year 2000. Noteworthy ones include a number of corrective measures that were put in place to deal with fugitive emissions from the neighbouring refineries, and closure of the gas station that was located about 200 m from the sampling site in January 2000.

The above case report and the estimates of gasoline emissions from a typical gasoline outlet should raise the awareness of building engineers regarding the locations of gasoline outlets within the vicinity of buildings and the potential short-circuiting of gasoline vapours from the ambient air to the indoor microenvironment. A comprehensive research study that would particularly address benzene short-circuiting from a corner gas station into an adjacent building is thus needed.

References

1. California energy commission, California annual retail fuel establishment (2006) Petroleum industry information reporting act (PIIRA) program reporting instructions (CEC-600-2005-032-SF)
2. Environment Australia (1999) Emissions estimation technique manual for aggregated emissions from service stations
3. European emission inventory guidebook (1999) Gasoline distribution (activities 050501-050503)
4. Schifter I, Magdaleno M, Díaz L, Krüger B, León J, Palmerín ME, Casas R, Melgarejo A, López-Salinas E (2002) Contribution of the gasoline distribution cycle to volatile organic compound emissions in the metropolitan area of Mexico City. J Air Waste Manage Assoc 52:535–541
5. de Oliveira KMPG, Martins EM, Arbilla G, Gatti LV (2007) Exposure to volatile organic compounds in an ethanol and gasoline service station. Bull Environ Contam Toxicol 79:237–241
6. Morales Terrés IM, Doval Miñarro M, González Ferradas E, Baeza Caracena A, Barberá Rico J (2010) Assessing the impact of petrol stations on their immediate surroundings. J Environ Manage 91:2754–2762
7. Canadian council of ministers of the environment (1991) Environmental code of practice for vapour recovery in gasoline distribution networks, CCME-EPC-TRE-30E
8. Williams GP, Gold LW (1976) Ground temperatures. National Research Council, Canada
9. Environment Canada (2003) Clean air in Canada, progress report on particulate matter and ozone
10. US EPA, stage II vapour recovery systems issues paper, office of air quality planning and standards emissions monitoring and analysis division emissions factors and policy applications group (document: D243-02)

11. Statistics Canada (2011) Survey of industrial processes (SIP)
12. US EPA (2006) Document AP 42, transportation and marketing of petroleum liquids
13. Statistics Canada (2011) Survey of industrial processes: retail gasoline outlets, the daily, 23 Mar 2011
14. MJ Ervin and associates (2009) National retail petroleum site census
15. Environment Canada (2011) Benzene in gasoline regulations, report SOR/97-493
16. Germain A, Rousseau J, Dann T (2001) Issues related to benzene in Eastern Montreal, environment canada and environmental technology centre, public works and government services Canada, catalogue number: EN40-644/2001E-IN

Chapter 3
Leverage of Behavioural Patterns of Window Opening and Heating Set Point Adjustments on Energy Consumption and Thermal Comfort in Residential Buildings

Stefano Paolo Corgnati, Simona D'Oca, Valentina Fabi and Rune Korsholm Andersen

Abstract The current trend in reduction in energy use in buildings is oriented towards sustainable measures and techniques aimed to energy need restraint. Even so, studies have underlined large differences in energy consumption in similar buildings, suggesting strong influence of occupant behaviour. Variability due to occupants' interactions within buildings is therefore organic. Nevertheless, it is worth noting a lack of knowledge and study of the parameters influencing users' behaviour and their way of life. Existing dynamic energy simulation tools exceed the static size of the simplified methods through a better and more accurate prediction of energy use; however, they are still unable to replicate the actual dynamics that govern energy uses within buildings. Furthermore, occupant behaviour is currently described by static profiles, based on assumptions and average values of typical behaviour, which do not necessarily reflect reality accurately. The pursuit of a comfort condition in indoor environment is a result of complex correlation between different parameters and users' personal sensitivity. As a consequence, a need for always more accurate statistical occupant behaviour models, considering different behavioural patterns and preferences among indoor environmental quality, is arising. Final goal of this research is to simulate, in a more accurate way, the variation in actual energy consumption due to human interaction within buildings. In this effort, the study has highlighted which combination of users' behavioural pattern consists the most energy-saver or energy-waster behaviour in residential buildings.

S. P. Corgnati (✉) · S. D'Oca · V. Fabi
Energy Department, Polytechnic of Turin, Turin, Italy
e-mail: stefano.corgnati@polito.it

S. D'Oca · V. Fabi · R. K. Andersen
ICIEE, Department of Civil Engineering, Technical University of Denmark, Lyngby, Denmark

3.1 Introduction

Several studies [1, 2] have been conducted to investigate the influence of different behavioural pattern and user's level of interaction within building controls on energy consumption in dwellings.

In 1983, Van Raaij and Verhallen [3] carried out a study in 145 Dutch dwellings and defined five patterns of energy behaviour (conservers, spenders, cool, warm and average) in relation to the use of heating systems and ventilation habits. The research highlighted that "warm" behavioural pattern users are generally older than the other four, that the educational level of "conservers" was higher than that of "spenders", and that the household size of the "conservers" cluster was smaller than the rest. They found no difference in users' level of interaction with control systems due to income and employment.

In 2001, Jeeninga et al. [4] showed that the household energy consumptions in completely identical apartments can vary as much as 100 % only considering user actions forced in order to maintain a state of comfort in their homes.

In 2005, a survey conducted by Poortinga and others [5] among households in the Netherlands investigated the acceptability level of different energy-saving measures. They found that different socio-demographic groups and people with different environmental concerns preferred different type of energy-saving measures. Surprisingly, results of the research showed that senior, singles and low-income families were less willing to apply energy-saving measures at home.

Andersen et al. [6] conducted a field survey of occupant behaviour and control of indoor environment in 15 Danish dwellings. Heating set point preferences were monitored and further analysed by means of multiple logistic regressions to infer models of occupants' interactions with building controls. The presented literature confirms that occupant behaviour can invalidate accurate prediction of building energy consumption. In order to get results close to reality, a further step in the research towards the focus on users' level of interaction within building control systems is here presented.

Occupant behaviour is known as the results of an interaction between physical parameters such as indoor and outdoor conditions and psychological, physiological and contextual variables connected to users' preferences and sensitivity [7]. In most building energy performance simulations, this complex frame is inadequately described by fixed and deterministic values, resulting in discrepancies between real and simulated performance indicators. Occupant behaviour could be simulated by probabilistic models based on indoor and outdoor conditions inferred from actual occupant behaviour.

3.2 Method

The purpose of this research was to investigate the influence of different behavioural patterns of window opening and heating set point adjustments on energy consumption and thermal comfort in residential buildings. Models were developed following an incremental philosophy, switching from standardized and deterministic methodologies, towards a probabilistic approach in energy modelling, as synthetically described in the following flow chart (Fig. 3.1) and explained hereafter. Specifically, models considering both occupants interaction as probabilistic input have been developed and implemented in the energy simulation software IDA ICE [8]. Behaviour patterns for active, medium and passive occupant's typologies were combined and subsequently merged in order to simulate the variation in actual energy consumption, due to human interaction within building controls. The aim of the study was to investigate which combination of users' level of interaction represents the most energy-saving or energy-wasting behaviour in residential buildings.

3.2.1 Window Opening and Closing

In the attempt to group behavioural patterns in dwellings, we at first focused on the analysis of the similarity in influential variables only for window opening and
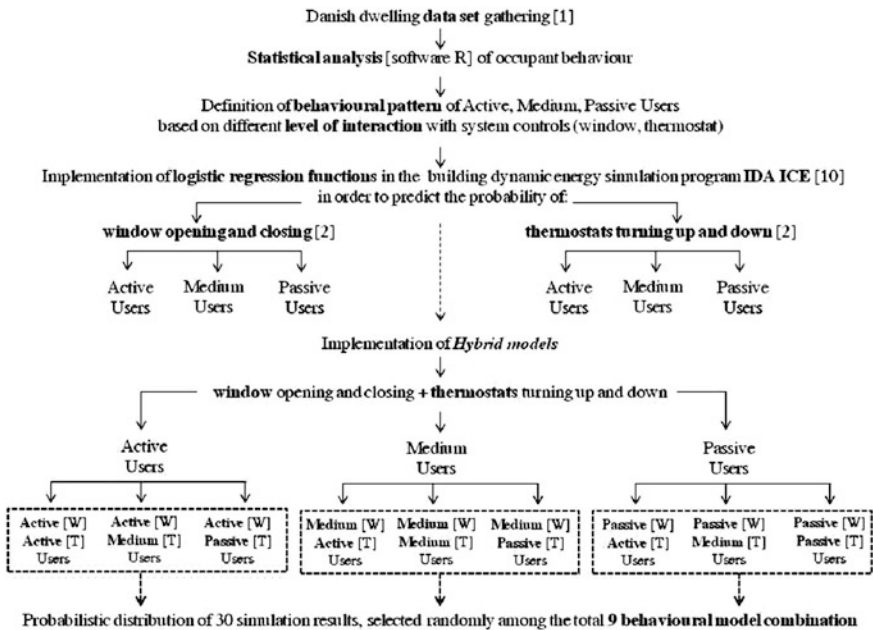
Fig. 3.1 Flow chart explaining the methodology of the study

closing. A first probabilistic model was built in the simulation software IDA ICE, starting from a previous developed model [9]. In this study, Fabi et al. analysed the Danish dwelling data set by means the statistical analysis software R and grouped it on the basis of commons patterns of behaviour emerged. Interestingly, the total number of window opening enormously varies from dwelling to dwelling, in which window has been opened from one time up to 718 times during the whole period of monitoring survey.

3.2.2 Thermostat Adjustments

Following the same methodological approach, the study has further focused on the definition of behavioural patterns for heating set point manipulation. Data proceeded from the same monitoring campaign [10] showed large disparity between individual heating set point settings. Findings can be seen as confirmation of human subjective perception of indoor thermal climate and comfort preferences affecting prevision in controlling indoor temperature. Differences in thermostat set point adjustments from dwelling to dwelling could be a result of variation in occupants' sensitivity to the variables governing their behaviour. In order to overcome the high complexity of the issue, dwellings were grouped after their inhabitants' frequency of thermostats manipulation and then named as active, passive and medium user type. Moreover, the probability of turning up/down the thermostat was inferred for three separated behavioural models.

3.2.3 Hybrid Modelling

The leverage of occupants' level of interaction with personal control on energy consumption in dwellings has been tested by means of *Hybrid models*, accounting as statistical input both the user interaction with window opening and heating set point adjustments. At a first step, starting from the statistical analysis, three models have been developed, by combing the same level of interaction for both window operations and thermostats adjustments for active, medium and passive users.

Some contradictions and simplifications still exist in this modelling approach; thus, users' willingness in reaching a certain level of comfort could be different regarding window operation and heating set point adjustments. Starting from this assumption, a new conceptual methodology was developed. As a matter of fact, occupant behavioural patterns related to active, medium and passive users on windows opening and closing not necessarily comply in the reality with the same level of inhabitant interaction with thermostats. For this reason, each of three behavioural models of window control previously developed has been matched into a macro with the three concerning thermostat adjustments. Accordingly, a

total of nine models were implemented, covering all possible combinations between them.

As a consequence, by selecting randomly (30 times each) different behavioural pattern combinations, it will be feasible to replicate as much as possible the influence of different behavioural pattern of window opening and heating set point adjustments on energy consumption and thermal comfort in residential buildings.

3.3 Results

The most influential variable highlighted for turning up the thermostat is generally the outdoor temperature. As a matter of fact, the probability of turning up the thermostat is a function of outdoor temperature: the probability of turning up the thermostat rises when the outdoor temperature decreases. This finding is specifically related to active users ($p < 0.26$) and also to medium users, even if towards a smaller impact ($p < 0.011$). Moreover, no strong correlation between opening probability for passive users and outdoor parameters has been found from dynamic simulations.

Huge discrepancy in users' level of interaction within thermostats is highlighted in the following graph (Fig. 3.2), both in bedroom and in living room, between active, medium and passive users. Active users adjust heating set point temperatures with highest frequency, also choosing temperatures below a wider range (from 19 to 28 °C). On the contrary, medium and passive users are less interactive and tend to set temperatures in a smaller range (from 20.8 to 23.2 °C). Further, in living room, also passive and medium users chose indoor temperatures standing in a more wide range, but according to a lower frequency.
Heating set point manipulation has no influence on energy consumptions from 15 June to 15 September, since the heating system was not operating. For this reason, thermostat adjustments can only be considered as user preference in case of space heating during this time step.

3.3.1 Window Opening

Results of the research showed a strict correlation between occupant windows' level of interaction and air change rate. This tendency is clearly notable principally in living room, as shown in following graph (Fig. 3.3). Active window user profiles strongly distinguish form medium and passive users, especially during summer period: in June, an increase of +70 % in air change rate has been simulated from passive to active window users.
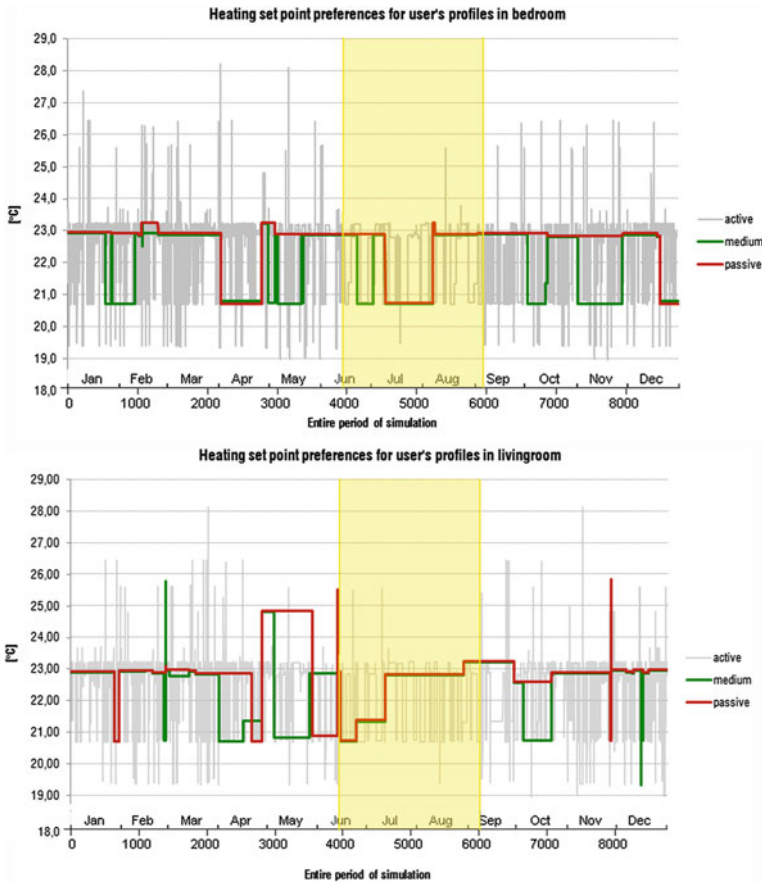
Fig. 3.2 Heating set point preferences for users' profiles in bedroom and living room

3.3.2 Energy-Related User Profiles

Moreover, this research has focused on the definition of the most *energy-waster* and *energy-savers* user profiles, taking into account both users' interactions on windows opening and thermostats adjustments in dwellings. Hybrid behavioural profiles have been selected randomly in order to present an indicator of real variation in energy consumptions in single dwellings, present useful results for the aim of the research. As shown in the following graph (Fig. 3.4), the most energy-waster profile comes out from the combination of active window openers and passive thermostats adjusters (model 3). On the contrary, results underlined that the most energy-saver profile is related to medium windows users combined to passive heating set point users (model 8).
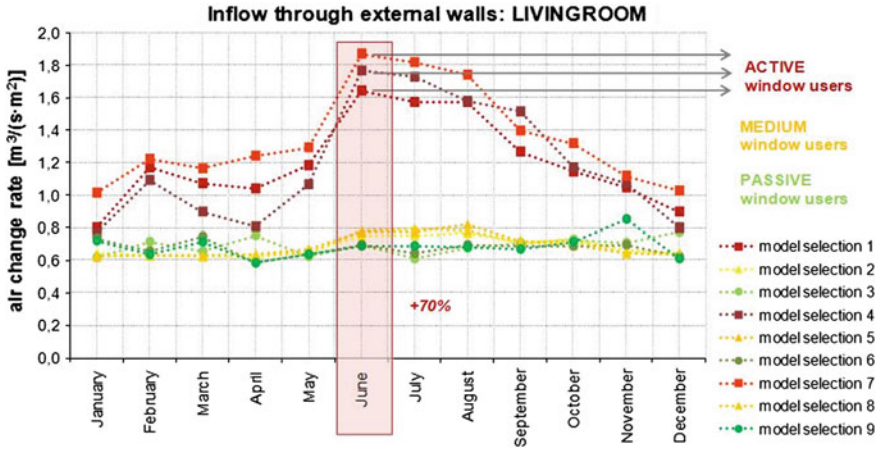
Fig. 3.3 Influence of different users' level of interaction on windows opening
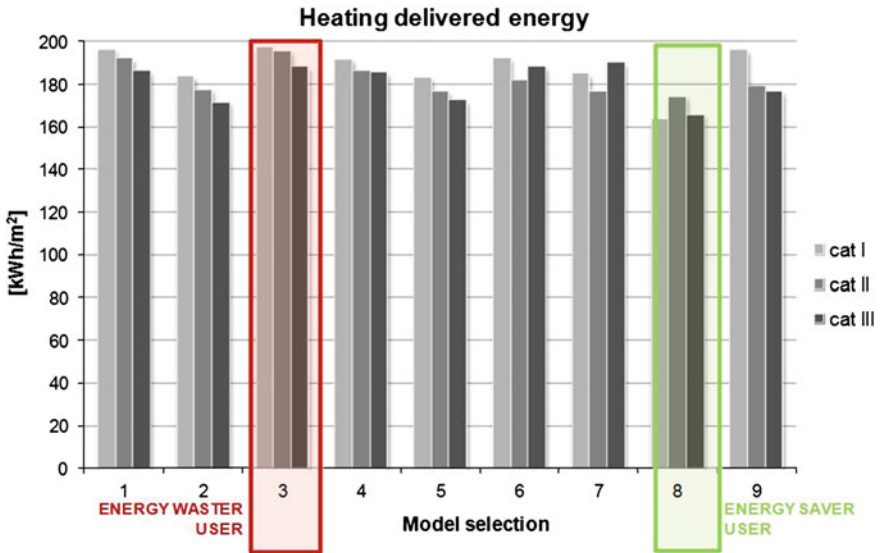
Fig. 3.4 Energy-waster and energy-saver user profiles on the base of heating delivered energy

3.4 Discussion and Conclusion

Active users are the less attentive to energy consumptions in dwellings and literally the most interactive with window opening and closing and heating set point adjustments. For this reason, they could be targeted as "energy-waster". Active users recorded highest frequencies of windows and thermostats interaction, although periods of opening and closing and turning up or down are shorter when compared to passive and medium users. Medium users could be considered as the most "energy-saver" profile in view of the fact that their interaction with building envelope and control system is a coherent and conscious response aiming to restore a condition of comfort. Medium users open window (i.e., bad air quality) and immediately readjust the position once the CO_2 concentration is returned to an acceptable range. Moreover, they turn up the thermostat in case of too cold indoor environment, but they turn it down as soon as the desired temperature has been reached, without letting the room become too warm. Interestingly, passive users' behavioural pattern did not necessarily correspond to an "energy-saver" users profile. Specifically, passive users' behaviour could be defined as *lazy operators*: they open windows driven by a perceived discomfort sensation (i.e., bad air quality) but do not readjust window position once their comfort condition has been restored (air ventilation lowing CO_2 concentration). On the contrary, passive users interact again with system control only because pushed by a new discomfort stimulus (since the window has stayed opened for a long time, the indoor air temperature has decreased, so they turn up the thermostat). Generally, the combination of *medium window users* and *passive thermostats manipulators* resulted as the most energy-saving users' behavioural profile in residential buildings.

References

1. Guerra Santin O (2011) Behavioural patterns and user profile related to energy consumption for heating. Energy Build 43:2662–2672
2. Samarakoon E, Soerbato V (2011) Testing the sensitivity of user patterns in building energy performance simulation. In: Proceeding of building simulation 2011: 12th conference of international performance simulation association, Sydney, 14–16 Nov 2011
3. Van Raaij WF, Verhallen TMM (1983) Patterns of residential energy behaviour. J Econ Psychol 4:85–106
4. Jeeninga H, Uyterlimde M, Uitzinger J (2001) Energy consumption of energy efficient residences, report ECN & IVAM
5. Poortinga W, Steg L, Vlek C, Wiersma G (2005) Household preferences for energy saving measures: a conjoint analysis. J Econ Psychol 29:49–64
6. Andersen RV, Olesen BW, Toftum J (2009) Survey of occupant behaviour and control of indoor environment in Danish dwellings. Energy Build 41(1):11–16
7. Fabi V, Andersen RV, Corgnati SP, Filippi M, Olesen BW (2011) Effect of occupant behaviour in building energy simulation: state of the art and concepts for their improvement. In: Proceeding of Climamed, vol 11. Madrid, 2–3 June 2011, pp 243–258
8. IDA ICE 4.0 (2009) Manual version 4.0 EQUA Simulation AB, 2009

9. Fabi V, Andersen RV, Corgnati SP (2012) Window opening behaviour in residential buildings using models based on field survey. In: Proceeding of 7th Windsor conference: the changing context of comfort in an unpredictable world, Windsor, UK, 12–15 April 2012
10. Andersen RV, Olesen BW, Toftum J (2011) Modeling occupants' heating set point preferences. In: Proceeding of building simulation 2011: 12th conference of international performance simulation association, Sydney, 14–16 Nov 2011

Chapter 4
Influence of Scattering Pattern on the Insulation Performance of VIP Filler Materials

Bongsu Choi, Jongmin Kim and Tae-Ho Song

Abstract Vacuum insulation panel (VIP) is an attractive thermal insulation component to satisfy the needs for high insulation performance. Radiation is a significant heat transfer mode in the VIP. In this study, radiative heat transfer is investigated for each of isotropic and backward-scattering media to evaluate the effect of each scattering pattern on the insulation performance of the VIP. The filler material for practical VIP can be considered as a one-dimensional pure scattering medium between two walls. Both walls are diffuse and have the same emissivity. The resulting insulation performance by each scattering pattern is expressed through the radiative thermal conductivity. A statistical formulation proposed in this paper and a diffusion approximation are used to calculate the radiative thermal conductivity theoretically. Monte Carlo method and discrete ordinate interpolation method (DOIM) are also taken to calculate the radiative transfer numerically. The results of DOIM, Monte Carlo method, and diffusion approximation agree well with those of statistical formulation within 1 % error. The results show that the insulation performance of the VIP can be enhanced by increasing the optical thickness or decreasing the wall emissivity. To decrease the wall emissivity, it is recommended to insert radiation shields or to use an envelope of low emissivity. It is also found that the backward scattering is more effective than the isotropic scattering especially. Therefore, by adding specular metal scales in the filler material, significant improvement in the insulation performance is expected.

Keywords Vacuum insulation panel · Isotropic scattering · Backward scattering · Statistical formulation · Radiative thermal conductivity

B. Choi · J. Kim · T.-H. Song (✉)
School of Mechanical, Aerospace and Systems Engineering, Korea Advanced
Institute of Science and Technology, Daejeon, Korea
e-mail: thsong@kaist.ac.kr

4.1 Introduction

Thermal insulation of building walls is important to reduce the heating and cooling energy consumption and maintain stable thermal environment inside the building. Especially, due to the recent increase in energy cost, there has been a growing interest in thermal insulators. Vacuum insulation panel (VIP) is an attractive thermal insulation component to satisfy the needs for high insulation performance. It has a lower thermal conductivity by a factor of 10 than the conventional insulators such as glass wool and polyurethane foam because it is highly evacuated [1]. To improve the insulation performance of a VIP, it is important to first understand the characteristics of conduction and radiative heat transfer through the filler material. Especially, radiation is a significant heat transfer mode in the VIP since the inner space of the VIP is highly evacuated. Indeed, even for conventional insulators, this heat transfer mode is known to be important at an elevated temperature [2, 3]. For this reason, it has been investigated extensively for various media in the form of powders, foams, and fibers [4, 5]. The previous studies show that the radiative properties such as the absorption and scattering coefficients have an effect on the radiative heat transfer in the insulation materials. Further, Jang et al. [6] predicted the radiative heat transfer in pure isotropic and backward-scattering media using a Monte Carlo method and found that the backward scattering is more desirable in VIPs. The objective of this study is to investigate in detail the scattering effect of filler material on the insulation performance, especially in case of pure isotropic and backward scattering. A Monte Carlo method and the discrete ordinate interpolation method are used for the numerical analysis. A statistical formulation is also proposed to get the exact solutions, and it is validated against the Monte Carlo method. For various optical thicknesses and wall emissivities, the radiative conductivity is calculated and compared to confirm the effect of scattering modes on the insulation performance. From the results, the maximum insulation condition through the scattering phenomena is found.

4.2 Analysis

The filler material of the VIP is considered as a one-dimensional pure scattering medium with height H between two walls. The temperatures of upper and lower walls are T_1 and T_2. Both walls are diffuse and have the same emissivity ε_w. The medium is gray with a constant scattering coefficient σ_s. In this problem, there is only radiative heat transfer and the medium is at a radiative equilibrium.

Monte Carlo method presented earlier by the authors is briefly introduced [6]. In this method, initially, a photon with strength 1 is emitted at the lower wall, and then, the scattering event is simulated with the scattering probability. If a random number is larger than the scattering probability, the photon arrives at the upper wall. Otherwise, it is scattered in the medium.

When scattering occurs, the photon path length l_i is calculated. For the isotropic scattering, to determine the next scattering event, a new height H_{i+1} of the medium is calculated. It is characterized by the polar angle as

$$H_{i+1} = H_i - l_i \text{ for } 0 < \theta_{i+1} < \pi/2, \tag{4.1}$$

$$H_{i+1} = H - (H_i - l_i) \text{ for } \pi/2 < \theta_{i+1} < \pi. \tag{4.2}$$

For the backward scattering, a new height H_{i+1} (Eq. 4.3) is needed to determine whether it is scattered in the next photon direction;

$$H_{i+1} = H - (H_i - l_i). \tag{4.3}$$

If the photon arrives at the upper wall, the absorbed part of the photon strength is accumulated. After tracing of the photon is terminated, a new photon is emitted and a trace for the new photon is performed again. At the end of all calculations, radiative conductivity is calculated.

The discrete ordinate interpolation method (DOIM) is a modification of the discrete ordinate method (DOM) by Cheong and Song [7]. It can be applied to two-dimensional geometries and several multidimensional irregular geometries [8]. In the DOIM, the intensity at a grid point is calculated using the upstream values. From the upstream value at point IN, the intensity at a grid point P in direction $\vec{s}$ can be calculated by

$$I_p = I_{\text{IN}}e^{-\beta s} + S_P(1 - e^{-\beta s}) - \frac{1}{\beta}\frac{dS}{ds}\bigg|_P [1 - e^{-\beta\Delta s}(1 + \beta\Delta s)] \tag{4.4}$$

where I_{IN} is an unknown intensity at a non-grid point, β is the extinction coefficient, and S is the source term. I_{IN} can be obtained by interpolation of neighboring point intensities. This method has been proved to be accurate and numerically stable [7].

Simulations are performed for a two-dimensional rectangular enclosure with pure isotropic or backward-scattering medium using S_8 quadrature. Side walls are specular and have the reflectivity of unity to simulate a symmetric boundary. A 41×11 grid system is used, and the x-direction length is stretched to 10 H.

For a gray medium between parallel gray walls, the radiative conductivity is approximated as Eq. (4.5), using a modified diffusion approximation [9],

$$k_{r,\text{diffusion}} = \frac{4\sigma T_m^3 H}{3\sigma_s H/4 + (2/\varepsilon_w - 1)}. \tag{4.5}$$

The general diffusion approximation is not valid for an optically thin medium since the influence of the temperature jump near the boundaries can be dominant. In this case, the approximation modified with the jump boundary condition is used.

The proposed statistical formulation is based on the probability that the emitted photon at a wall arrives at the opposite wall. Let the probability that a photon emitted from one wall with strength 1 arrives at the opposite wall is R_0, and the

Table 4.1 Probability $G_{2,i}$ that the emitted photon at surface 1 arrives surface 2 for various paths

Case	$G_{2,i}$
$1 \rightarrow 2$	R_0
$1 \rightarrow 1 \rightarrow 2$	$2\rho_w S_0 R_0$
$1 \rightarrow 2 \rightarrow 2$	
$1 \rightarrow 1 \rightarrow 1 \rightarrow 2$	$\rho_w^2 (3S_0^2 R_0 + R_0^3)$
$1 \rightarrow 1 \rightarrow 2 \rightarrow 2$	
$1 \rightarrow 2 \rightarrow 1 \rightarrow 2$	
$1 \rightarrow 2 \rightarrow 2 \rightarrow 2$	
$1 \rightarrow 1 \rightarrow 1 \rightarrow 1 \rightarrow 2$	$\rho_w^3 (4S_0^3 R_0 + 4S_0 R_0^3)$
$1 \rightarrow 1 \rightarrow 1 \rightarrow 2 \rightarrow 2$	
$1 \rightarrow 1 \rightarrow 2 \rightarrow 1 \rightarrow 2$	
$1 \rightarrow 1 \rightarrow 2 \rightarrow 2 \rightarrow 2$	
$1 \rightarrow 2 \rightarrow 1 \rightarrow 1 \rightarrow 2$	
$1 \rightarrow 2 \rightarrow 1 \rightarrow 2 \rightarrow 2$	
$1 \rightarrow 2 \rightarrow 2 \rightarrow 1 \rightarrow 2$	
$1 \rightarrow 2 \rightarrow 2 \rightarrow 2 \rightarrow 2$	
$\vdots$	$\vdots$

probability that the photon comes back to the original wall is S_0 (i.e., $R_0 + S_0 = 1$). Total strength G_2 of photons striking surface 2 can be calculated by considering all the possible sequences until the photon emitted at surface 1 is finally absorbed at surface 2. Some of the sequences are shown in Table 4.1. The total strength G_2 is obtained by summation of $G_{2,i}$ as

$$G_2 = \sum_{i=1}^{\infty} G_{2,i} = \frac{R_0}{(1 - \rho_w)(1 + \rho_w R_0 - \rho_w S_0)}. \tag{4.6}$$

Now, we can obtain the heat flux q_r'' as

$$q_r'' = \varepsilon_w (1 - \rho_w) G_2 (\sigma T_1^4 - \sigma T_2^4). \tag{4.7}$$

If R_0 is known, it is possible to analyze the radiative heat transfer of the pure scattering medium. Certainly, R_0 depends on the polar angle measured from the surface normal vector. It can be written as

$$R_0 = \frac{\int_0^{\pi/2} R_\theta \cos\theta \sin\theta \, d\theta}{\int_0^{\pi/2} \cos\theta \sin\theta \, d\theta}, \tag{4.8}$$

where R_θ is the probability that the photon launched in direction θ at surface 1 arrives at surface 2 and it is expressed as

$$R_\theta = e^{-\tau_L/\cos\theta} + \int_0^{\tau_L} P(\tau) e^{-\tau/\cos\theta} \frac{d\tau}{\cos\theta}, \tag{4.9}$$

where τ is the non-dimensional optical thickness, $\tau_L = \sigma_s H$, and $P(\tau)$ is the probability that the scattered photon at τ arrives at surface 2.

For isotropic scattering, by using the exponential integral function, $P(\tau)$ is given as

$$P(\tau) = \frac{1}{2} E_2(\tau_L - \tau) + \frac{1}{2} \int_0^{\tau_L} P(\tau') E_1\big(|\tau_L' - \tau|\big) \mathrm{d}\tau'. \qquad (4.10)$$

This is a Fredholm integral equation of the second kind. It can be calculated by the Neumann series method [10].

For the backward scattering, P is dependent on the direction cosine μ contrary to the isotropic scattering. The probability $P(\tau)$ that the scattered photon at τ arrives at surface 2 is defined as

$$P(\tau) = \int_0^1 P(\tau, \mu) \mathrm{d}\mu = \int_0^1 \int_0^\tau (1 - P(\tau_L - \tau')) \frac{e^{-(\tau-\tau')/\mu}}{\mu} \mathrm{d}\tau' \mathrm{d}\mu. \qquad (4.11)$$

4.3 Results and Discussion

The insulation performance of a VIP is generally evaluated using the effective thermal conductivity k_{eff} obtained by summation of the solid conductivity k_s and radiative conductivity k_r. It is important to study each of the heat transfer modes separately to improve the insulation performance.

As mentioned before, in this study, only the radiative conductivities of isotropic and backward-scattering media are compared to discuss the scattering effect of filler material in enhancing the insulation performance. Also, the effect of wall emissivity and optical thickness on the radiative conductivities is investigated for each medium.

4.3.1 Isotropic Scattering Medium

To obtain the exact solution using the statistical formulation, firstly, the probability $P(\tau)$ has to be obtained for the isotropic scattering medium. Figure 4.1a shows the probability distribution over a range of optical thickness. When the optical thickness is as small as 0.01, the probability is almost 0.5 everywhere. In other words, when the medium is optically thin, the scattered photon at τ can go to the surface 2 with a 50 % probability, regardless of the location. However, when the medium is optically thick, the closer the location of scattering is to surface 2, the higher is the probability. In this case, the movement of photon is more effectively
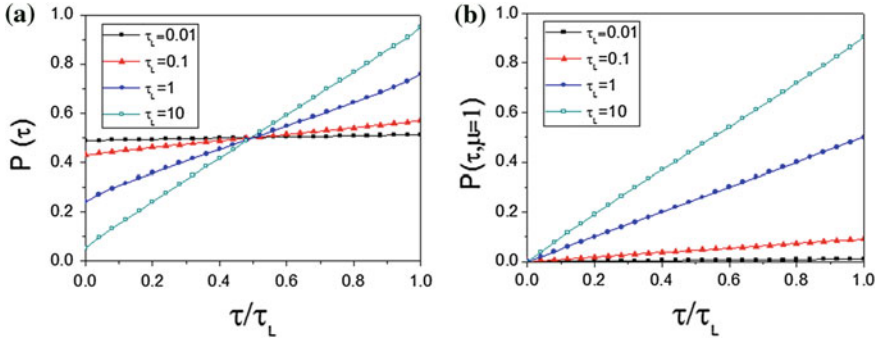
Fig. 4.1 Probability distribution of $P(\tau)$ for the isotropic scattering medium (**a**), and $P(\tau, \mu = 1)$ for the *backward*-scattering medium (**b**), respectively

blocked by the medium. It is confirmed from R_0 for various optical thicknesses as shown in Table 4.2.

Table 4.2 shows the radiative thermal conductivity k_r for various optical thicknesses and wall emissivities for the isotropic scattering medium. The mean temperature T_m is 300 K, and H is 0.01 m. The relative error of the Monte Carlo result to the statistical formulation is less than 1 % here. Since the Monte Carlo solution is widely accepted as "exact," the statistical formulation can be regarded as an exact solution. Table 4.2 also shows that the radiative conductivity decreases with increasing $\sigma_s H$ and decreasing ε_w. It is noteworthy that the radiative conductivity is highly affected by the wall emissivity when the medium is optically thin ($\sigma_s H \ll 1$) since the medium behaves like a non-participating medium. To improve the insulation performance, therefore, it is recommended to insert radiation shields of low emissivity.

Table 4.2 Comparison of radiative thermal conductivities with varying optical thicknesses and emissivities for the isotropic scattering medium ($H = 0.01$ m)

Optical thickness ($\tau = \sigma_s H$)				0.01	0.1	1	10
k_r (mW/m·K)	Statistical formulation	R_0		0.990	0.916	0.553	0.1183
		ε_w	**0.1**	3.22	3.21	3.09	2.31
			0.5	20.3	19.8	16.1	5.86
			0.9	49.7	46.6	30.2	7.06
	Monte Carlo	ε_w	**0.1**	3.22	3.21	3.09	2.30
			0.5	20.3	19.8	16.1	5.82
			0.9	49.7	46.5	30.2	7.00
	DOIM	ε_w	**0.1**	3.22	3.20	3.09	2.32
			0.5	20.3	19.8	16.0	5.80
			0.9	49.7	46.5	30.0	6.96
	Diffusion approx. (Eq. 4.23)	ε_w	**0.1**	3.22	3.21	3.10	2.31
			0.5	20.4	19.9	16.3	5.83
			0.9	49.8	47.2	31.0	7.02

4.3.2 Backward-Scattering Medium

Backward scattering means that the incoming photons return to the direction from which they came. Therefore, it is more difficult for the photon to move forward.

As shown in the statistical formulation, the probability $P(\tau)$ is angle dependent. Figure 4.1b shows the probability distribution for the backward-scattering medium with various optical thicknesses for $\mu = 1$ as an example of $P(\tau, \mu)$. When the optical thickness is small, the probability is almost 0. As the optical thickness gets greater, the probability distribution becomes similar to that of isotropic scattering. Like in isotropic scattering, R_0 decreases as the optical thickness increases, as shown in Table 4.3. For all the cases in Tables 4.2 and 4.3, the predictions are within 1 % error with each other. The difference in R_0 between the isotropic and the backward scatterings becomes greater with the increase in optical thickness since the number of photons that arrive at surface 2 is smaller for a backward-scattering medium than the other one.

Table 4.3 also shows the radiative thermal conductivity in a backward-scattering medium. It is also important to decrease the wall emissivity as well as to increase the optical thickness, which is in common with the isotropic scattering. From the results, it is found that the radiative thermal resistance of the backward-scattering medium is about twice as large as that of the isotropic one when the medium is optically thick. By adding specular metal scales in the filler material, the insulation performance can be improved.

Table 4.3 Comparison of radiative thermal conductivities with varying optical thicknesses and emissivities for the backward-scattering medium ($H = 0.01$ m)

Optical thickness ($\tau = \sigma_s H$)				0.01	0.1	1	10
k_r (mW/m·K)	Statistical formulation	R_0		0.981	0.848	0.387	0.0618
		ε_w	**0.1**	3.22	3.19	2.97	1.79
			0.5	20.3	19.3	13.4	3.37
			0.9	49.3	43.7	21.8	3.73
	Monte Carlo	ε_w	**0.1**	3.22	3.19	2.97	1.79
			0.5	20.3	19.2	13.3	3.39
			0.9	49.3	43.6	21.8	3.71
	DOIM	ε_w	**0.1**	3.22	3.19	2.97	1.80
			0.5	20.3	19.2	13.3	3.38
			0.9	49.3	43.5	21.6	3.74
	Modified diffusion approx. (Eq. 4.25)	ε_w	**0.1**	3.22	3.20	2.99	1.80
			0.5	20.3	19.4	13.6	3.40
			0.9	49.5	44.6	22.5	3.77

4.4 Conclusions

Radiative thermal conductivities of isotropic and backward-scattering media between two diffuse walls are investigated to evaluate the scattering effect of filler material on the insulation performance. A statistical formulation is proposed in this study, based on the probability that the emitted photon at the wall arrives at the opposite wall. An exact solution can be obtained by this formulation. Other numerical solutions are obtained using the Monte Carlo method, DOIM, and diffusion approximation. The results of statistical formulation, Monte Carlo method, and DOIM agree well with each other within 1 % error.

The results show that radiative heat transfer can be reduced by decreasing the surface emissivity or by increasing the optical thickness of the filler material for both isotropic and backward-scattering media. Also, it is found that the backward-scattering medium decreases the radiative heat transfer more effectively than the isotropic scattering one. Especially, when the optical thickness is larger, this advantage of the backward-scattering medium is more distinct.

References

1. Kwon JS, Jang CH, Song TH (2009) Effective thermal conductivity of various filling materials for vacuum insulation. Int J Heat Mass Transfer 52:5525–5532
2. Verschoor JD, Greebler P (1952) Heat transfer by gas conduction and radiation in fibrous insulation. ASME Trams 74:961–968
3. Valenzuela JA, Glicksman LR (1981) Thermal resistance and aging of rigid urethane foam insulation. In: Proceeding of DOE-ORNL workshop on mathematical modeling of roofs Atlanta GA, Conf-811179, pp 261–262
4. Glicksman L, Schuetz M, Sinofsky M (1987) Radiation heat transfer in foam insulation. Int J Heat Mass Transfer 30:187–197
5. Tong TW, Tien CL (1983) Radiative heat transfer in fibrous insulations—Part I: analytical study. J Heat Transfer 105:70–75
6. Jang C, Jung H, Lee JH, Song TH (2012) Radiative heat transfer analysis in pure scattering layers to be used in vacuum insulation panels. Int Conf Appl Energy 2612–2619
7. Cheong KB, Song TH (1997) An alternative discrete ordinates method with interpolation and source differencing for two-dimensional radiative transfer problems. Numer Heat Transfer, Part B 32:107–125
8. Kim K, Lee E, Song TH (2008) Discrete ordinates interpolation method for radiative heat transfer problems in three-dimensional enclosures filled with non-gray or scattering medium. JQSRT 109:2579–2589
9. Howell JR, Siegel R, Menguc MP (2010) Thermal radiation heat transfer, 5th edn. Taylor and Francis/CRC, New York
10. Arfken GB, Weber HJ, Harris FE (2012) Mathematical methods for physicists, 7th edn. Academic Press, Boston

Chapter 5
Analysis of Combined Heat Transfer Through Interstitial Materials of VIPs

Jaehyug Lee, Inseok Yeo, Won Kyeong Kang and Tae-Ho Song

Abstract High-performance thermal insulation material is needed to save the building energy for heating and cooling the indoor space. Vacuum insulation panel (VIP) can achieve a thermal conductivity of about one-tenth of the typical value of conventional insulation materials. Heat transfer in the interstitial materials of VIP occurs by conduction through the solid structure and radiation through the pore. Separate study of those heat transfer modes in porous materials has been carried out widely, but a coupled heat transfer should be taken into the analysis to predict the performance of VIP correctly. This process is analyzed with the discrete ordinates interpolation method (DOIM) incorporated with the commercial code FLUENT®. The interstitial material of VIP is modeled as a 1-D layer with constant properties, and both walls are assumed to be isothermal and diffuse. It is found that the effect of wall emissivity is reduced for a non-scattering medium through the combined analysis. The effective thermal conductivity is significantly larger than that predicted by the simple additive approximation for low emissivity boundaries in an intermediate optical thickness range. When contact resistance between the wall and the filler material is added to the analysis, the effect of conduction–radiation interaction near the wall is compensated with the contact resistance. Therefore, the wall emissivity is more influential than expected in reducing the effective thermal conductivity. The effect of various scattering modes has also been investigated. It is found that backward scattering is more effective in reducing total heat transfer, while isotropic scattering is almost identical with non-scattering case of the same optical thickness. Thus, combined analysis with the modeling of contact resistance should be made in the optimization of insulation performance of VIP with artificial core structure and radiation shields.

Keywords Vacuum insulation panel · Combined conduction and radiation · Discrete ordinates interpolation method · Contact resistance

J. Lee · I. Yeo · W. K. Kang · T.-H. Song (✉)
School of Mechanical, Aerospace and Systems Engineering, Korea Advanced
Institute of Science and Technology, Daejeon, Republic of Korea
e-mail: thsong@kaist.ac.kr

5.1 Introduction

High-performance thermal insulation material is needed to save the building energy for heating and cooling the indoor space. Conventional insulation materials such as expanded polystyrene (EPS) have thermal conductivities of about 30 mW/m–K. Further improvement in thermal performance is limited by the gas conduction inside the porous structure.

VIP is a fascinating insulation component that can achieve a thermal conductivity of about one-tenth of conventional insulation materials' value. VIP is usually composed of an envelope, a core structure, and a desiccant [1].

Heat transfer in the VIP core occurs in three modes: solid conduction through the core structure (responsible for k_s below), residual gas conduction (k_g), and radiation (k_r). The effective conductivity of VIP k_{eff} is often expressed as follows [1]:

$$k_{eff} = k_s + k_g + k_r + k_{cpl}. \tag{5.1}$$

The last term accounts for a coupling effect, if any, between them. Heat transfer of each mode through porous materials has been investigated widely. Solid conductivity in VIP is dependent on the structure and packing density of the porous materials. For common core materials in VIPs, Kwon et al. [2] calculated and reviewed the solid conductivity of various porous materials and artificial structures. The gas conductivity for rarefied gas region can be obtained using a relation suggested by Kwon et al. [2]. The radiative conductivity through porous materials is usually expressed by the diffusion approximation [3].

$$k_r = \frac{16\sigma T_m^3}{3\beta}, \tag{5.2}$$

where the β is the Rosseland mean extinction coefficient.

Conduction and radiation apparently interact with each other in VIPs. However, the combined heat transfer problem is not treated extensively, possibly due to the complexity of the analysis (Fig. 5.1).

Lately, a new type of VIP that uses an artificial core structure has been suggested [4]. In this type of VIP, packing density of the filling materials can be adjusted and radiation shields are employed to reduce the radiation [5]. So, an improved analysis to encounter the effect of combined conduction and radiation is needed.

Fig. 5.1 Structure of 2nd generation VIP [4]
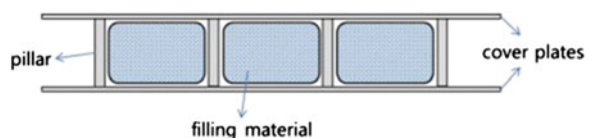
In this study, the effect of coupled conduction and radiation is analyzed with the DOIM incorporated with the commercial code FLUENT®. Typical features of the numerical scheme will be explained in this paper. The effects of optical thickness, emissivity, scattering albedo, scattering phase functions, and contact resistance on the effective thermal conductivity of VIPs are studied.

5.2 Numerical Scheme

Usually, VIP is a thin panel of a few to few tens of millimeters in the thickness. Here, we only consider the heat transfer through the central core material, so the interstitial material in VIPs can be modeled as a 1-D plane-parallel medium.

The filler material is assumed to be gray with constant thermal and radiative properties. Two walls are isothermal at different temperatures T_{B0} and T_{U0}, while a finite contact resistance R_C exists at both sides. Both walls are diffuse and have an emissivity ε_w. The physical model of VIP is depicted in Fig. 5.2.

The energy equation with constant thermal conductivity k_s can be expressed as follows:

$$k_s \nabla^2 T - \nabla \cdot \vec{q}_R = 0. \tag{5.3}$$

Here, the radiative heat source term $\nabla \cdot \vec{q}_R$ is given by [6].

(a)

$$T_{U0} \quad \varepsilon_w \quad R_c$$

$$L \qquad \beta, k_s$$

$$z$$

$$T_{B0} \quad \varepsilon_w \quad R_c$$

(b)

$$q''_{rad}(0^+) = \int_{\hat{n}\cdot\vec{\Omega}<0} I(\Omega)\left|\hat{n}\cdot\vec{\Omega}\right|d\Omega \qquad q''_{cond}(0^+) = -k_s \frac{dT}{dz}$$

$$T_B$$

$$T_{B0}, \varepsilon_w$$

$$q''_{cond}(0^-) = \frac{T_{B0} - T_B}{R_c}$$
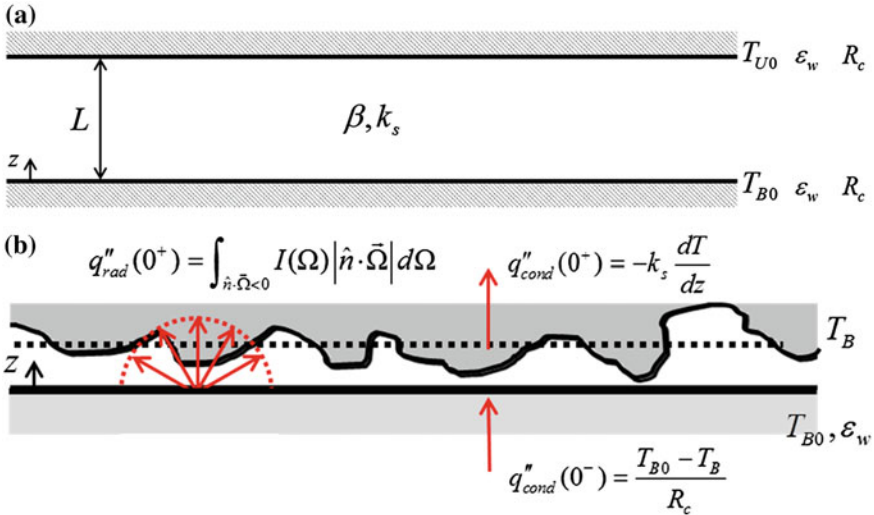
Fig. 5.2 **a** Physical model of VIP used in this study and **b** contact resistance at the boundary

$$\nabla \cdot \vec{q}_R = 4\kappa \left(\sigma T^4 - \frac{1}{4} \int_{4\pi} I d\Omega \right), \tag{5.4}$$

where κ is the absorption coefficient.

Contact resistance is modeled in a way that the temperature at a point infinitesimally away from the wall is determined by conduction boundary conditions:

$$\frac{T_{B0} - T_B}{R_c} = -k_s \frac{dT}{dz}, \text{ and } \frac{T_U - T_{U0}}{R_c} = -k_s \frac{dT}{dz}, \tag{5.5}$$

where T_B and T_U are the temperatures at the points infinitesimally away from the walls, respectively.

The radiative transfer equation (RTE) for gray plane-parallel medium is expressed as follows [6]:

$$\frac{1}{\mu} \frac{dI}{\beta dz} = (1 - \omega)I_b - I + \frac{\omega}{4\pi} \int_{4\pi} I(\Omega\prime)\Phi(\Omega\prime, \Omega)d\Omega\prime. \tag{5.6}$$

where μ is the directional cosine, $\omega = \sigma_s/\beta$ is scattering albedo, and $\Phi(\Omega', \Omega)$ is the scattering phase function of the medium.

For a diffuse wall, the boundary condition for the RTE is given as follows:

$$I_w^+(\Omega) = \varepsilon_w I_{bw} + \frac{1 - \varepsilon_w}{\pi} \int_{\hat{n} \cdot \hat{s}' < 0} I(\Omega')|\hat{n} \cdot \hat{s}\prime| d\Omega\prime. \tag{5.7}$$

Equations 5.3 and 5.6 are nonlinear integro-differential equations and must be solved numerically. The total heat flux q''_{tot} at the centerline is used to determine the effective thermal conductivity of the medium using the relation:

$$k_{\text{eff}} = q''_{\text{tot}} L / (T_{B0} - T_{U0}). \tag{5.8}$$

To solve the problem, the DOIM incorporated into the commercial code FLUENT$^{\circledR}$ is used. The DOIM is a modified version of the discrete ordinates method (DOM) using an interpolation scheme to analyze radiative transfer problems [7]. Recently, the DOIM is incorporated into commercial code FLUENT$^{\circledR}$ and found to be successful in analyzing various combined heat transfer problem [8].

A two-dimensional rectangular enclosure with control volumes of 20×10 (meaning a grid system of 21×11) is used in the simulation. The domain is stretched 10 times in the horizontal direction compared with the vertical direction. Symmetric boundary conditions are given for the side walls.

It is validated with the one-dimensional reference results of Crosbie and Viskanta [9] to find the discrepancy is less than 1 %.

As stated above, conduction and radiation are often considered separately in the analysis of insulation materials. The effective thermal conductivity for an additive solution including the contact resistance is represented as follows [10]:

$$k_{eff} = \frac{k_s}{1 + N_2} + \frac{4\sigma T_m^3 L}{3\tau_L/4 + (2/\varepsilon_w - 1)}, \tag{5.9}$$

where $\tau_L = \beta L$ is the optical thickness of the medium, and $N_2 \equiv \frac{2R_c}{L/k_s}$ is the ratio of contact resistance to the medium conduction resistance.

5.3 Results and Discussion

To see the effect of radiative properties, the effective thermal conductivity is calculated for various cases with a fixed solid conductivity. Solid conductivity of VIP is 1–3 mW/m–K [2]; 1 mW/m–K is taken here for the analysis. The mean temperature is 300 K with $T_{BO} = 310$ K and $T_{U0} = 290$ K. The height L is 0.01 m.

5.3.1 Effects of τ_L and ε_w

Figure 5.3 shows k_{eff} of the medium for various optical thicknesses and wall emissivities. The results are compared with the additive solution calculated from Eq. (5.9). It is noteworthy that k_{eff} increases with the optical thickness when $\varepsilon_w = 0.1$ and τ_L is in the range of 0.01–1, in contrast to the general trends anticipated by the diffusion solution [6]; especially, k_{eff} for combined analysis is up to 2.3 times larger than the additive solution when $\varepsilon_w = 0.1$ and $\tau_L = 1.0$.

When the medium is nearly transparent ($\tau_L \ll 1$), the total amount of conductive and radiative heat fluxes do not depart much from those of additive solution. On the other hand, as optical thickness increases, the variation of k_{eff} with the wall emissivity decreases, possibly due to the conduction–radiation interaction.

Fig. 5.3 The effective thermal conductivities at 300 K by combined analysis and additive solution
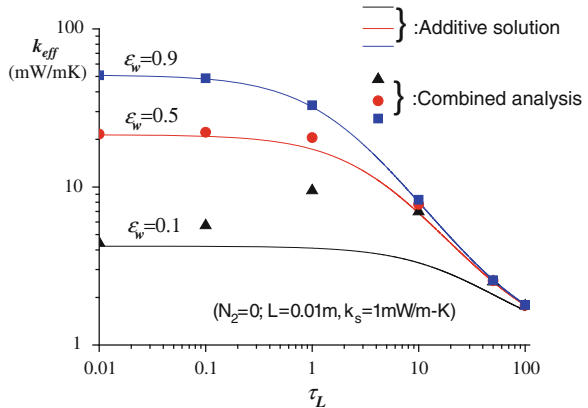
As a result, k_{eff} for combined analysis when $\tau_L > 10$ converges to the values at high emissivity.

For the current VIPs, porous medium with β larger than 3,000 m^{-1} is commonly used without any radiation shield inside. So, the optical thickness of common VIPs is larger than 50, and additive solution (without considering the effect of wall emissivity) can be safely used. However, when optically thin medium such as silica aerogel is considered or many radiation shields are inserted so that the optical thickness is reduced, combined mode of heat transfer considering the effect of wall emissivity should be taken in the analysis.

5.3.2 Effects of Contact Resistance

The effective thermal conductivity of the medium obtained by the combined analysis is shown in Fig. 5.4 for $N_2 = 0.1$ and 1.0. The results are compared with the additive solutions of Eq. (5.9). The effective thermal conductivity decreases for all cases compared to the value calculated without contact resistance. The effect is more pronounced when the emissivity is small and the optical thickness is in the range of 0.1–10. This is where higher value of effective thermal conductivity is observed compared to the additive solution through the influence of interaction with conduction. Also, when the results for $N_2 = 0.1$ are compared to those for $N_2 = 1.0$, the reduction in k_{eff} in the low emissivity boundary is more pronounced when the contact resistance is large. So, it can be deduced that radiative heat transfer decreases as well as conduction with the addition of the contact resistance at the boundaries. Because packing density and pressure load on the interstitial material for a new type of VIP can be adjusted, optimization of performance concerning this factor is desirable.
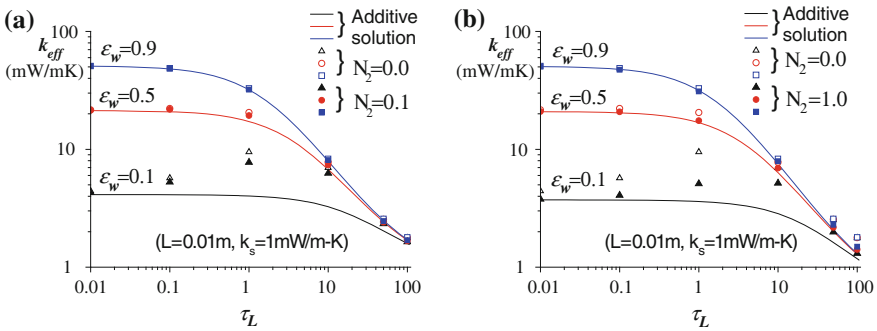
Fig. 5.4 The effective thermal conductivities when ratio of contact resistance to medium conduction resistance N_2 is **a** 0.1 and **b** 1.0
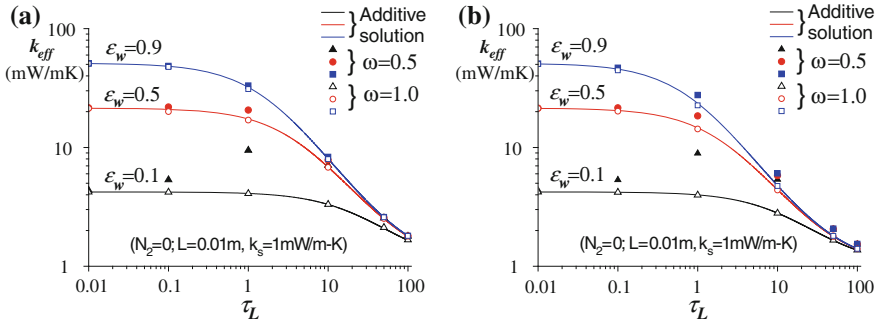
Fig. 5.5 The effective thermal conductivities for **a** isotropic scattering medium and **b** backward scattering medium with $\omega = 0.5$ and $\omega = 1.0$

5.3.3 Effects of Scattering Phase Functions

The effect of isotropic and backward scattering in the pure scattering medium has been studied by using Monte Carlo method [11]. Here, the effects of two scattering modes on the insulation performance of VIP are investigated when combined heat transfer is considered.

Figure 5.5a shows k_{eff} of absorbing, emitting, and isotropic scattering medium, varying the scattering albedo ($N_2 = 0.0$). Compared with the non-scattering case of Fig. 5.3, there is little change in k_{eff} when the scattering albedo ω is 0.5, while the thermal conductivity approaches to the additive solution when $\omega = 1.0$. It can be concluded that isotropic scattering material is analogous to pure absorbing/ emitting medium, unless ω is close to 1. Further investigation is required to predict the behavior of medium with large scattering albedo such as glass fiber.

Figure 5.5b shows k_{eff} for backward scattering medium. Here, scattering phase function is assumed to be purely backward so that the incident radiation is reflected to the opposite direction when scattered. Compared with isotropically scattering case, k_{eff} is significantly smaller and this trend is more obvious when the medium is optically thick. So, adding opacifying materials with highly backward scattering is more effective in reducing k_{eff}. Roughly speaking, backward scattering is twice as much effective as isotropic scattering. Jang et al. [11] have compactly predicted this effect by replacing $3\tau_L/4$ in the denominator of 2nd term in Eq. (5.9) by $3\tau_L/2$. The lines in Fig. 5.5b are drawn with this modification.

5.4 Conclusion

In this study, an analysis on the combined conduction and radiation in the filling materials of VIP is conducted. The effects of various parameters are investigated using the DOIM incorporated into a commercial code FLUENT®.

Analysis of interstitial materials of VIP is conducted for solid conductivity of 1 mW/m–K and various optical thicknesses and wall emissivities. The effect of wall emissivity is significantly reduced in the combined analysis for the optical thickness larger than 0.1 than in the additive solution. So, the effective thermal conductivity is significantly larger for combined heat transfer analysis when the wall emissivity is low. When the optical thickness is large, the results of combined analysis are similar to that of the additive solution with high emissivity. So, combined effect should be considered when installing radiation shields and thus reducing the optical thickness in the VIP. The contact resistance at the wall is found to be effective in reducing heat transfer for low emissivity walls.

The effect of scattering albedo and scattering modes are also investigated. Isotropically scattering medium behaves similarly with non-scattering medium unless the scattering albedo of the medium is about 1.0. On the other hand, the amount of heat transfer is smaller for backward scattering than isotropic scattering. Also, backward scattering medium is effective when scattering albedo is not very large.

Combined analysis developed in this study need be used in the optimization of a new type of VIP with various radiative and conductive properties of porous materials and radiation shields.

References

1. Baetens R, Jelle BP, Thue JV, Tenpierik MJ, Grynning S, Uvsløkk S, Gustavsen A (2010) Vacuum insulation panels for building application: a review and beyond. Energy Buildings 42(2):147–172
2. Kwon JS, Jang CH, Jung H, Song TH (2009) Effective thermal conductivity of various filling materials for vacuum insulation panels. Int J Heat Mass Transfer 52:5525–5532
3. Rosseland S (1936) Theoretical astrophysics atomic theory and the analysis of stellar atmospheres and envelopes. Clarendon Press, Oxford
4. Kim J, Song TH, Yeo I, Choi B (2012) The 2nd Generation vacuum insulation panel. The 4th international conference on applied energy, Suzhou, China
5. Kim J, Jang C, Song TH (2012) Combined heat transfer in multi-layered radiation shields for vacuum insulation panels: theoretical/numerical analyses and experiment. Appl Energy 94:295–302
6. Modest MF (2003) Radiative heat transfer, 2nd edn. Academic Press, New York
7. Cheong KB, Song TH (1997) An alternative discrete ordinates method with interpolation and source differencing for two-dimensional radiative transfer problems. Numer Heat Trans, Part B 32:107–125
8. Kim K, Song TH (2010) Discrete ordinates interpolation method incorporated into a flow and energy solver for solution of combined heat transfer problems. J Quant Spectrosc Radiat Trans 111(14):2070–2083
9. Crosbie AL, Viskanta R (1971) Interaction of heat transfer by conduction and radiation in a nongray planar medium. Wärme Stoffübertragung 4:205–212

10. Tien CL, Cunnington GR (1973) Cryogenic insulation heat transfer. Adv Heat Transfer, vol. 9, Academic Press, New York pp 349–417
11. Jang C, Jung H, Lee J, Song TH (2012) Radiative heat transfer analysis in pure scattering layers to be used in vacuum insulation panels. The 4th international conference on applied energy, Suzhou, China

Chapter 6
Experimental and Theoretical Study on the Thermal Environment Based on Simultaneously Model in a Room

Liugen Lv, Chen Huang, Jianchang Chen, Fei Wang, Zhijun Zou and Xin Wang

Abstract A simultaneously solving model is presented for a small room with single thermal environment, and the model is used to predict inner surface temperature and air temperature. Combined heat transfer consists of thermal conduction, convection, and radiation, which exist on building inner surface temperature and air temperature that are coupled through each other. The construction thought of simultaneously solving model: Based on the principle of energy conservation, heat conservation equations are established for inner surface by considering thermal conduction, convection, and radiation, and air heat conservation equations are also established by using indoor air as control volume. Inner surface temperature and air temperature can be received by simultaneously solving and iterative calculation. Direct radiation absorption model and Gebhart absorption coefficient model are considered, respectively, in heat conservation equations of simultaneously solving model. Taking environmental laboratory ($5 \times 3.5 \times 2.5$ m) as physical model, condition calculation and experimental verification have taken. Under variety of conditions such as different wall heat flow and different air supply volume, inner surface temperature and air temperature are calculated by simultaneously solving model. The simultaneously solving model based on Gebhart absorption coefficient model is more exact than the model based on direct radiation absorption model. The calculation results of two kinds of simultaneously solving model are compared with test date and provide some important information for applying radiation model of simultaneously solving model.

Keywords Thermal environment · Simultaneously solving model · Direct radiation absorption · Gebhart absorption coefficient

L. Lv (✉) · C. Huang · J. Chen · F. Wang ·
Z. Zou · X. Wang
School of Environment and Architecture, University of Shanghai
for Science and Technology, Shanghai, China
e-mail: lvliugen@163.com

6.1 Introduction

Radiation heat transfer cannot be ignored as the temperature of inner surface is different in a large space building with stratified air-conditioning or radiation air-conditioning in a room. Radiation heat transfer calculation is difficult because it is nonlinear relationship between radiation heat and temperature. For long wave radiation in a building, Holman [1] given a radiation heat transfer coefficient, which is expressed by inner surface temperature cube. Refet Karadag [2] described radiation heat transfer coefficient as a function of different temperature between inner surfaces. Morteza [3] established convection heat transfer model and radiation heat transfer model to calculate heat flux for different environment temperature and radiant panel temperature. Many studies have shown that radiation calculation model was considered not only by direct radiation absorption method [4, 5] (first radiation absorption is considered, and first radiation reflection is ignored), but also by Gebhart absorption coefficient method [6, 7] (first radiation reflection absorption is also considered).

In this paper, a simultaneously solving model is presented, and direct radiation absorption model and Gebhart absorption coefficient model are considered, respectively. The calculation results of two kinds of simultaneously solving model are compared with test date and provide some important information for applying radiation model of simultaneously solving model.

6.2 Surface Radiation Heat Transfer Analysis

6.2.1 Surface Heat Transfer Analysis by Direct Radiation Absorption

An inner surface named i received net radiation from other surfaces is as follows:

$$q_{Ri}S_i = -\sigma\varepsilon_i T_i^4 S_i \sum_{j=1}^{N} X_{ij}\varepsilon_j + \sum_{j=1}^{N} X_{ji}\varepsilon_j\sigma T_j^4 S_j\varepsilon_i \tag{6.1}$$

Using interchangeability of angle coefficient $X_{ij}S_i = X_{ji}S_j$, formula (6.1) is expressed as follows:

$$q_{Ri}S_i = -S_i\sigma\varepsilon_i \sum_{j=1}^{N} X_{ij}\varepsilon_j \left(T_i^4 - T_j^4\right) \tag{6.2}$$

As inner surface temperature varies around normal temperature, formula (6.2) is linearized into

$$q_{Ri} = -4T_m^3\sigma\varepsilon_i \sum_{j=1}^{N} X_{ij}\varepsilon_j \left(\theta_i - \theta_j\right) \tag{6.3}$$

where

$$T_m = \sum_{j=1}^{N} S_j T_j \bigg/ \sum_{j=1}^{N} S_j$$

6.2.2 Surface Heat Transfer Analysis by Gebhart Absorption Coefficient

Gebhart absorption coefficient calculation existed in Ref. [7]; an inner surface named i received net radiation from other surface is as follows:

$$q_{Ri} S_i = -\sigma \varepsilon_i T_i^4 S_i + \sum_{j=1}^{N} G_{ji} \sigma \varepsilon_j T_j^4 S_j \tag{6.4}$$

Using interchangeability and integrality of Gebhart absorption coefficient can be gained:

$$\varepsilon_i G_{ij} S_i = \varepsilon_j G_{ji} S_j \sum_{j=1}^{N} G_{ij} = 1$$

By (6.4) can be obtained:

$$q_{Ri} = -\sigma \varepsilon_i \sum_{j=1}^{N} G_{ij} \left(T_i^4 - T_j^4 \right) \tag{6.5}$$

Formula (6.5) is linearized into

$$q_{Ri} = -4 T_m^3 \sigma \varepsilon_i \sum_{j=1}^{N} G_{ij} (\theta_i - \theta_j) \tag{6.6}$$

where

$$T_m = \sum_{j=1}^{N} S_j T_j \bigg/ \sum_{j=1}^{N} S_j$$

6.3 Establish Simultaneously Solving Mode

Heat conservation equations are established for surface i based on law of conservation of energy:

$$q_{di} + q_{ri} + q_{\lambda i} + q_i = 0 \tag{6.7}$$

For simultaneously solving model based on direct radiation absorption method, heat conservation equation is as follows:

$$\alpha_d(t - \theta_i) - 4T_m^3 \varepsilon_i \sigma \sum_{j=1}^{N} X_{ij}\varepsilon_j(\theta_i - \theta_j) + q_{\lambda i} + q_i = 0 \tag{6.8}$$

For simultaneously solving model based on Gebhart absorption coefficient, heat conservation equation is as follows:

$$\alpha_d(t - \theta_i) - 4T_m^3 \varepsilon_i \sigma \sum_{j=1}^{N} G_{ij}(\theta_i - \theta_j) + q_{\lambda i} + q_i = 0 \tag{6.9}$$

Air heat conservation equations are same for two kinds of simultaneously solving model:

$$\sum_{j=1}^{N} \alpha_d(t - \theta_i)f_i + C_p(\rho_2 q_{v2}t_2 - \rho_1 q_{v1}t_1) = 0 \tag{6.10}$$

Two kinds of simultaneously solving model are expressed as array for surface i as 1,2…N

$$\begin{bmatrix} A_1 & B_{11} & \cdots & B_{1N} \\ A_2 & B_{21} & \cdots & B_{2N} \\ \vdots & \vdots & & \vdots \\ A_N & B_{N1} & \cdots & B_{NN} \\ C_1 & D_1 & \cdots & D_N \end{bmatrix} \times \begin{bmatrix} t \\ \theta_1 \\ \vdots \\ \theta_5 \\ \theta_N \end{bmatrix} = \begin{bmatrix} E_1 \\ E_2 \\ \vdots \\ E_N \\ F_1 \end{bmatrix} \tag{6.11}$$

Submatrices as A, C, D, E, F are same in two kinds of simultaneously solving model, and submatrix as B is different.

6.4 Experiment and Analysis of Calculation Example

Taking environmental laboratory (5 × 3.5 × 2.5 m) as physical model, condition calculation and experimental verification have taken. Electrothermal film was pasted to south wall, which can provide heat flux from 0 to 175 W/m²; the rated air flow is 2,000 m³/h, which can be regulated by frequency changer. Two kinds of conditions: case 1, supply air temperature is 20 °C, air volume is 665 m³/h, heat flux of south wall vary—0 W/m², 40 W/m², 80 W/m², 120 W/m², 160 W/m²; case 2, supply air temperature is 20 °C, heat flux of south wall is 40 W/m², air volume vary—6,665 m³/h, 1,056 m³/h, 1,439 m³/h, 1,754 m³/h. The indoor air

temperature and inner surface temperature are recorded. The air temperature sensor is a copper constantan thermocouple, and the date is gathered by data collecting instrument (Agilent 34970A). The inner surface temperature is recorded by infrared video camera (ThermaCAM P20).

6.4.1 Model Calculation and Experimental Verification of Different Heat Fluxes

In case 1, Fig 6.1 shows the result of theoretical calculation and experiment. From 1(a), the calculation result of two kinds of simultaneously solving model agreed well with test date and the calculation result is lower 1.1 °C. Calculation difference between two kinds of simultaneously solving model is below 0.5 °C.

Figure 6.1b–f shows the result of calculation and experiment of inner surface based on two kinds of simultaneously solving model. It can be seen that all inner surface temperatures rise up following heat flux increasing, the south wall temperature is highest and floor temperature is lowest and other inner surface temperatures are near. The difference between Gebhart absorption coefficient model and test date is below 1 °C. The difference between direct radiation absorption model and test date is below 1.5 °C, so the former is more exact 0.5 °C than the latter.

6.4.2 Model Calculation and Experimental Verification of Different Air Volume

In case 2, Fig. 6.2 shows the result of theoretical calculation and experiment. From 2(a), the calculation results of two kinds of simultaneously solving model agree well with test date, and the calculation result is lower 0.6 °C. Calculation difference between two kinds of simultaneously solving model is below 0.3 °C.

Figure 6.2b–f shows the results of calculation and experimental of inner surface based on two kinds of simultaneously solving model. It can be seen that all inner surface temperatures rose up following air volume increasing. The difference between Gebhart absorption coefficient model and test date is below 0.8 °C. The difference between direct radiation absorption model and test date is below 1.2 °C, so the former is more exact 0.4 °C than the latter.
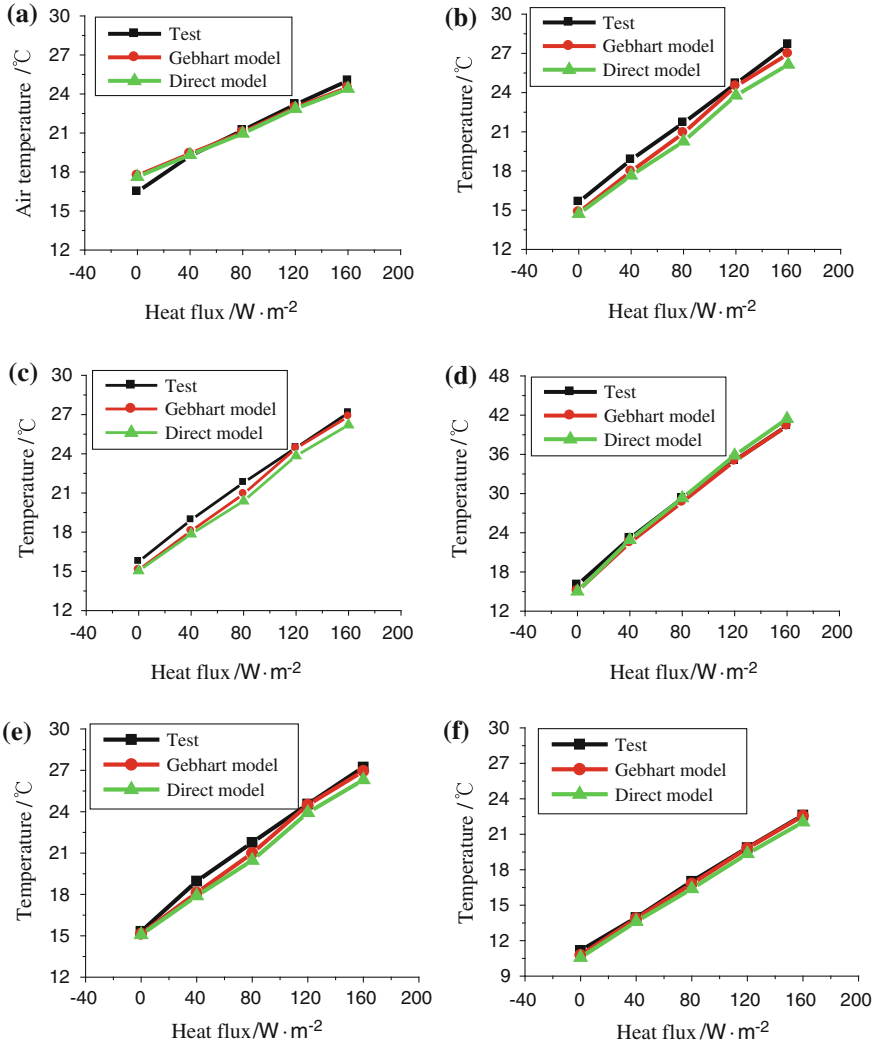
Fig. 6.1 Comparison of model calculation and test date based on case 1. **a** Air, **b** Roof, **c** East wall, **d** South wall, **e** North wall, **f** Floor

6.4.3 Comparison and Analysis Based on Two Kinds of Simultaneously Solving Model

The impacts of the emission rate, air temperature, south wall temperature, and roof temperature are calculated by two kinds of simultaneously solving model. Calculation conditions are the following: supply air temperature is 20 °C, air volume
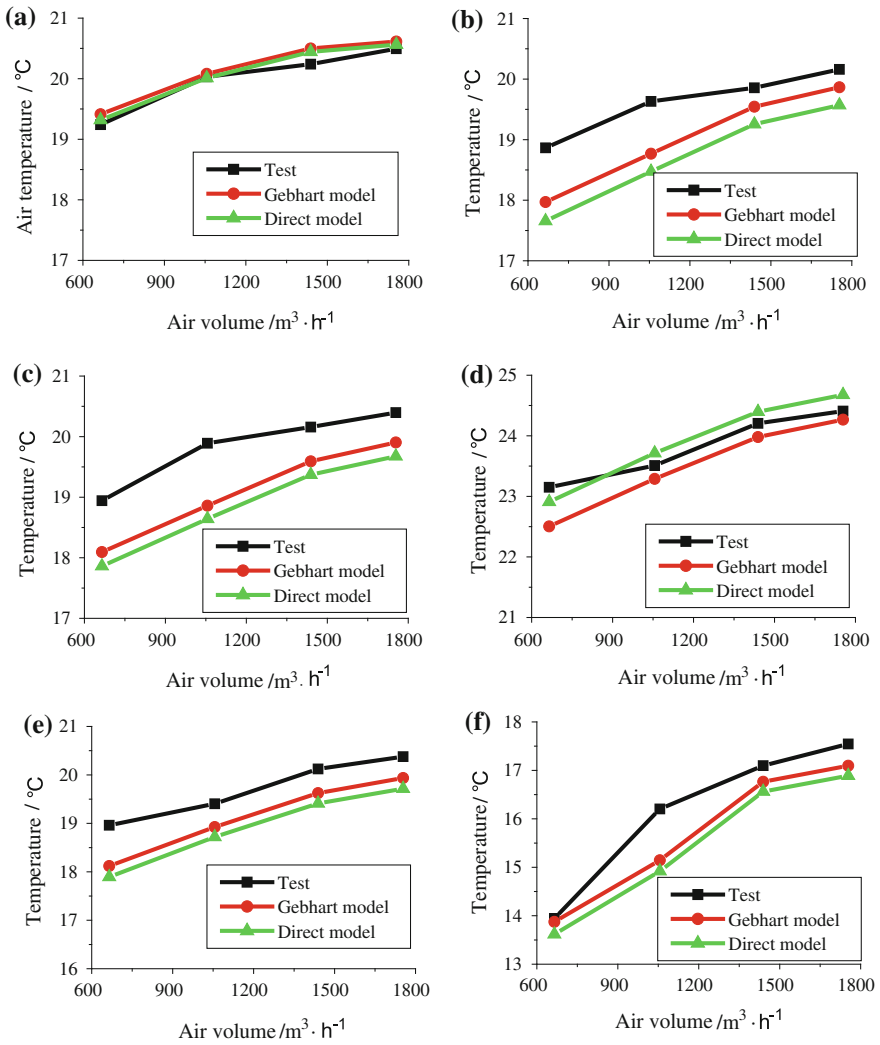
Fig. 6.2 Comparison of model calculation and test date based on case 2. **a** Air, **b** Roof, **c** East wall, **d** South wall, **e** North wall, **f** Floor

is 665 m³/h, heat flux of south wall is 80 W/m². It can be seen that air temperature is same when emission rate changes, south wall temperature (a) is lower and roof temperature (a) is higher than (b) condition when emission rate changes (Fig. 6.3).

Fig. 6.3 Comparison of
model calculation following
changing
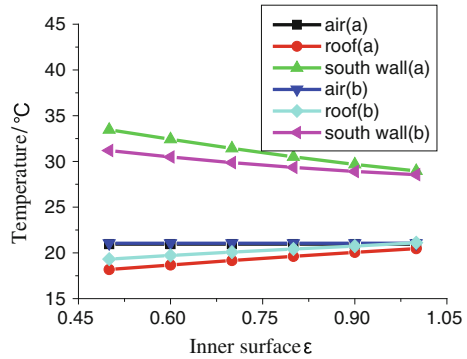
6.5 Conclusions

The simultaneously solving model is presented, and direct radiation absorption
model and Gebhart absorption coefficient model are considered, respectively, in
simultaneously solving model. The calculation results of two kinds of simulta-
neously solving model are agreed well with test date, and the simultaneously
solving model can be used to predict inner surface temperature and air tempera-
ture. The simultaneously solving model based on Gebhart absorption coefficient
radiation model is more exact than the model based on direct radiation model. The
calculation difference between Gebhart absorption coefficient model and direct
radiation model is increasing following emission rate changing.

References

1. Holman J P et al (2002) Heat transfer. McGraw-Hill higher education. A division of the
   McGraw-Hill companies
2. Karadag Refet (2009) New approach relevant to total heat transfer coefficient including the
   effect of radiation and convection at the ceiling in a cooled ceiling room. Appl Therm Eng
   29:1561–1565
3. Ardenali Morteaz M (2004) Proof of concept modeling of energy transfer mechanisms for
   radiant conditioning panels. Energy Convers Manage 45:2005–2017
4. Yaoqing Lu (2008) Practical heating air conditioning design manual. China Building Industry
   Press, Beijing
5. Yan Qishen, Zhao Qingzhu (1986) Building thermal process. China Building Industry Press,
   Beijing
6. Gebhart B (1959) A new method for calculating radiant exchanges. ASHRAE Transactions
   65:321–332
7. Huang C, Li M (2001) A method for calculating surface temperature in the case of coupled
   convective and radiative heat transfer in a large space building. J Univ Shanghai for Sci Tech,
   23(4):322–327

Chapter 7
Air Distribution and Ventilation Effectiveness in a Room with Floor/Ceiling Heating and Mixing/Displacement Ventilation

Xiaozhou Wu, Lei Fang, Bjarne W. Olesen and Jianing Zhao

Abstract The present study investigated different combinations of floor/ceiling heating with mixing/displacement ventilation and their impacts on the indoor air distribution and ventilation effectiveness. Measurements were performed in a room during heating season in December. The results show that indoor vertical air temperature differences and air velocities for different hybrid systems are less than 3 °C and 0.2 m/s when supply air temperature is 19 °C, air change rate is 4.2 h^{-1}, and heated surface temperature of floor/ceiling heating system is 25 °C. Ventilation effectiveness of mixing ventilation system combined with floor/ceiling heating systems is approximately equal to 1.0, and ventilation effectiveness of displacement ventilation system combined with floor/ceiling heating systems ranges from 1.0 to 1.2. The floor/ceiling heating systems combined with mixing ventilation system have more uniform indoor air distribution but smaller ventilation effectiveness compared with the floor/ceiling heating systems combined with displacement ventilation system. With regard to the building heat loss increased by non-uniform indoor air distribution and small ventilation effectiveness, there should be an optimal combination of floor/ceiling heating with mixing/displacement ventilation to have the minimal building heat loss.

Keywords Floor heating (FH) · Ceiling heating (CH) · Mixing ventilation (MV) · Displacement ventilation (DV) · Air distribution · Ventilation effectiveness

X. Wu · J. Zhao (✉)
School of Municipal and Environmental Engineering, Harbin Institute of Technology,
Harbin, People's Republic of China
e-mail: zhaojn@hit.edu.cn

L. Fang · B. W. Olesen
International Centre for Indoor Environment and Energy, Department of Civil Engineering,
Technical University of Denmark, Copenhagen, Denmark

7.1 Introduction

Low-temperature heating systems, such as floor heating systems and ceiling heating systems, are regarded as energy efficient and comfortable heating systems so that they have been extensively used in residential and non-residential buildings [1, 2]. Many energy efficient building technologies involving increased thermal insulation and air tightness have been applied in the low-temperature heating buildings. Unfortunately, these technologies may cause insufficient fresh air to be supplied by infiltration and may thus lead to poor indoor air quality and increased healthy symptom [3]. To avoid this problem, a mechanical ventilation system, such as a mixing ventilation system or a displacement ventilation system, for fresh air supply must be integrated with the low-temperature heating systems.

Compared to the low-temperature heating system, a hybrid system with floor/ceiling heating and mixing/displacement ventilation will create a new situation with regard to air distribution and ventilation effectiveness; i.e., the indoor air distribution in a room with floor/ceiling heating systems may be changed by the integration with mixing/displacement ventilation, and the ventilation effectiveness of mixing/displacement ventilation system may be influenced by the integration with floor/ceiling heating systems.

In order to get the optimal hybrid system with regard to the minimal building heat loss, many measurements have been performed in a room with some combinations of floor/ceiling heating with mixing/displacement ventilation [4–7]. Few studies focus on the air distribution and ventilation effectiveness in a room with all combinations of floor/ceiling heating with mixing/displacement ventilation. Therefore, in this paper, all combinations of floor/ceiling heating with mixing/displacement ventilation and their impacts on the indoor air distribution and ventilation effectiveness were investigated.

7.2 Methodology

7.2.1 Test Room

The room used for the measurements is located on the second floor in building 402 at the International Centre for indoor environment and energy (ICIEE) at Technical University of Denmark (TUD). It is used for regular lectures, occasional meetings, and other events of the ICIEE. In order to simulate the office environment, the room has been rearranged to be an office room for 8 persons in this paper. A schematic outline of the room and the experimental setup is given in Fig. 7.1. The room has an approximate floor area of 72 m^2. The room's usable height is 2.7 m. The outside wall has a total area of 32.4 m^2, including a total window area of 13.2 m^2: four windows with 3.3m^2 each. The dummies are used to simulate office workers in the experiment. There have been a total of 8 dummies of
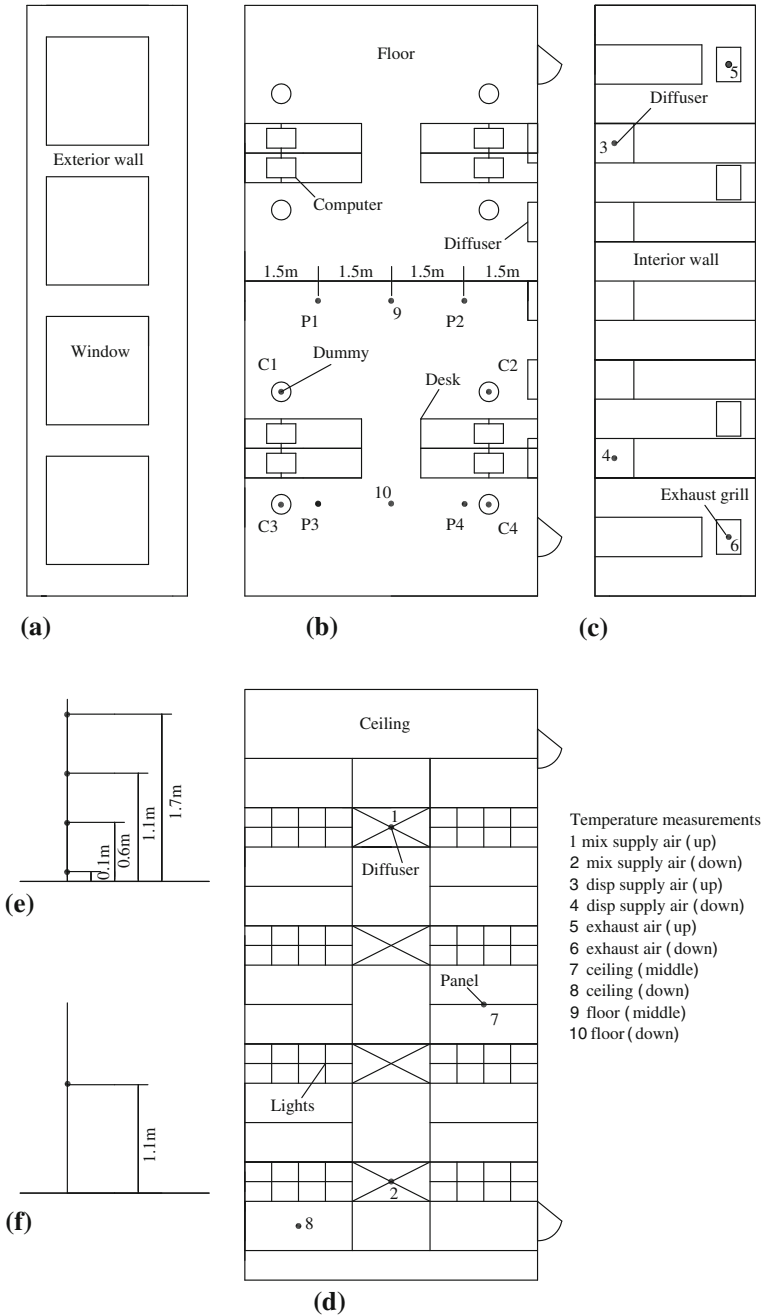
Fig. 7.1 Setup of the test room and location of the sensors. **a** External wall and window. **b** Floor surface. **c** Internal wall surface. **d** Ceiling surface. **e** Vertical air temperature and air velocity measurement point (P1–P4). **f** Contaminant concentration measurement points (C1–C4)

Fig. 7.2 The schematic diagram of test systems
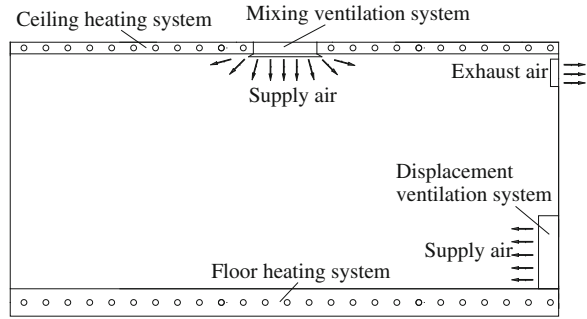
which were equipped with 80 W light bulbs, resulting in a total power of 640 W. Other internal heat sources in a typical office room, such as computers and lights, have a total power of 1010 W. They were placed in the same locations for each of the measurements.

7.2.2 Test Systems

The room is equipped with numerous heating, cooling, and ventilation systems. For this paper, floor heating (FH), ceiling heating (CH), mixing ventilation (MV), and displacement ventilation (DV) were used, as shown in Fig. 7.2.

For displacement ventilation system, air is supplied through supply duct alongside the bottom of the inner wall. For mixing ventilation system, air is supplied through supply duct alongside the ceiling. Air is removed through exhaust ducts below the ceiling in the same wall.

7.2.3 Measurement Parameters

Air velocity and temperature were measured with four spherical probes HT-412 that were connected to transducers HT-428-0. The sensors were used with the measuring station HT-480. This equipment is from the company Sensor Electronic. The minimal velocity that can be measured is 0.05 m/s. From 0.05 to 1 m/s, the accuracy is $\pm$ 0.02 m/s or $\pm$ 1 %. Above 1 m/s, the accuracy is $\pm$ 3 %. The accuracy of the temperature measurement is $\pm$ 0.2 °C.

Air velocity and temperature were measured in four different heights in each of the locations P1 through P4, as shown in Fig. 7.1b. Since only four anemometers were available, measurements had to be done four times. The arrangement of the sensors on the stand is illustrated in Fig. 7.1e. The duration of one measurement was 10 min. After measurements were completed in one location, the sensors were moved to the next location.

Table 7.1 Test conditions for different hybrid systems

Hybrid systems	Supply air temperature (°C)	Reference air temperature (°C)	Ceiling surface temperature (°C)	Floor surface temperature (°C)	Air change rate (h^{-1})
FH + MV	19.0	22.0	–	25.0	4.2
FH + DV	19.0	22.0	–	25.0	4.2
CH + MV	19.0	22.0	25.0	–	4.2
CH + DV	19.0	22.0	25.0	–	4.2

Freon as the tracer gas was used to measure the age of air. Concentration measurement and gas dosing in the room were performed through Innova photoacoustic multi-gas monitor. The instrument was placed outside the room. One dosing point and one sampling point were placed in the supply duct and the exhaust duct of ventilation systems, separately. Other four sampling points (C1–C4) were closed to the four dummies at the height of 1.1 m above floor level, as shown in Fig. 7.1b and f.

7.2.4 Test Conditions

The test conditions for different hybrid systems are shown in Table 7.1, where the reference air temperature and the air change rate refer to the Category I for non-low-polluting building in standard EN 15251 [8].

7.3 Results and Discussions

7.3.1 Vertical Air Temperature Distribution

Vertical air temperature distributions in a room with different hybrid systems are shown in Fig. 7.3.

Figure 7.3 shows the vertical air temperature distribution in a room with floor/ceiling heating and mixing/displacement ventilation. It shows that floor/ceiling heating systems combined with mixing ventilation system have the more uniform vertical air temperature distribution compared with the floor/ceiling heating systems combined with displacement ventilation system. This is mainly due to the "mixing effect" in the mixing ventilation room and the "buoyancy effect" in the displacement ventilation room. Figure 7.3 also shows that vertical air temperature difference between the head level and the foot level is mostly less than 3 °C, which are within the local thermal comfort range according to ISO 7730 [9].
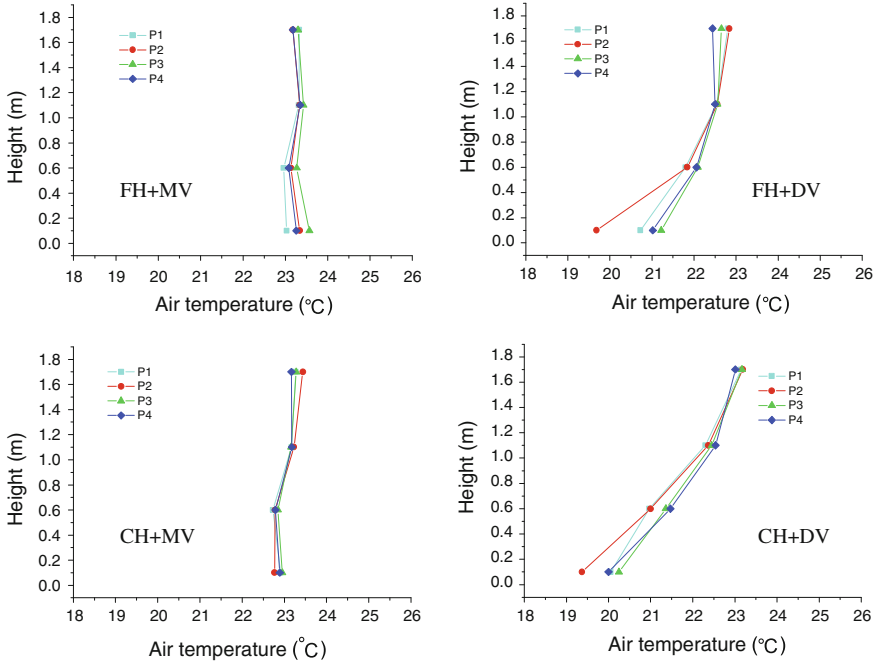
Fig. 7.3 Vertical air temperature distribution in a room with different hybrid systems

7.3.2 Vertical Air Velocity Distribution

Vertical air velocity distributions in a room with different hybrid systems are shown in Fig. 7.4.

Figure 7.4 shows the vertical air velocity distribution in a room with floor/ceiling heating and mixing/displacement ventilation. It shows that the floor/ceiling heating systems combined with mixing ventilation system also have the more uniform vertical air velocity distribution compared with the floor/ceiling heating systems combined with displacement ventilation system. This is also mainly due to the "mixing effect" in the mixing ventilation room and the "buoyancy effect" in the displacement ventilation room. Figure 7.4 also shows that local air velocity are all less than 0.2 m/s, which will not cause any local thermal discomfort in terms of draught when local air temperature are more than 19 °C (as shown in Fig. 7.3).

7.3.3 Ventilation Effectiveness

Ventilation effectiveness includes contaminant removal effectiveness (CRE) and air change efficiency (ACE) [10]. CRE indicates the ability of a ventilation system
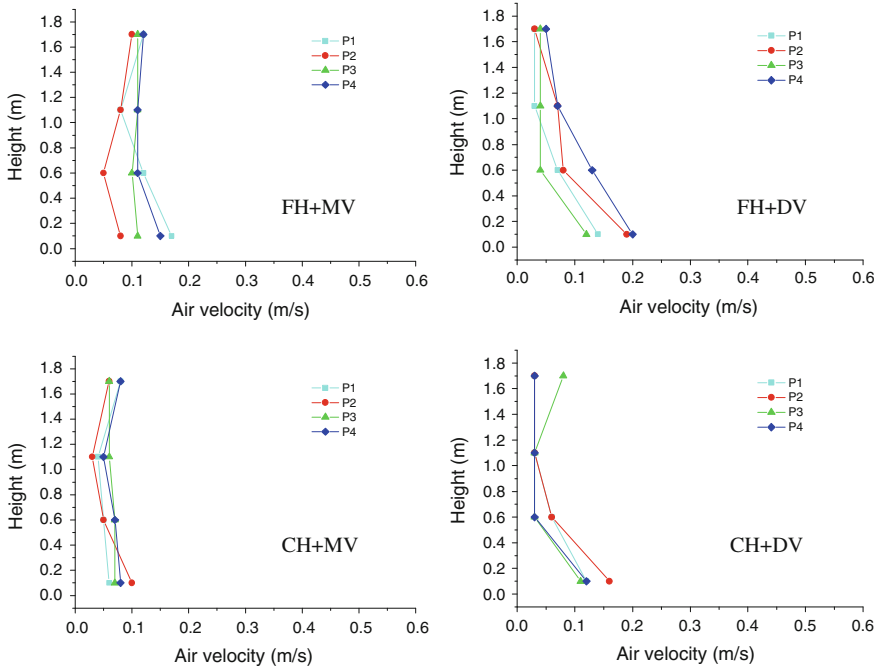
Fig. 7.4 Vertical air velocity distribution in a room with different hybrid systems

to remove airborne contaminants, and ACE indicates the ability of a ventilation system to exchange the air in the room. This study mainly focuses on the fresh air supply, so ACE was used in this paper. ACE can be calculated using Eqs. (1–3):

$$ACE = \frac{\tau_n}{\langle \overline{\tau_p} \rangle} \tag{7.1}$$

$$\tau_n = \int_0^\infty \frac{c_e(t)}{c_e(0)} dt \tag{7.2}$$

$$\overline{\tau_p} = \int_0^\infty \frac{c_p(t)}{c_e(0)} dt \tag{7.3}$$

where τ_n is the time constant, $\overline{\tau_p}$ is the local mean age of room air, $c_p(t)$ is the instantaneous local contaminant concentration in room, and $c_e(t)$ is the instantaneous contaminant concentration in exhaust dust.

Table 7.2 shows the ventilation effectiveness in a room with different hybrid systems. It shows that the mean ventilation effectiveness for mixing ventilation system combined with floor/ceiling heating systems are approximately equal to

Table 7.2 Ventilation effectiveness in a room with different hybrid systems

Hybrid systems	Measurement points				
	S1	S2	S3	S4	Mean
FH + MV	0.99	1.00	1.00	1.00	1.00
FH + DV	1.17	1.12	1.20	1.05	1.14
CH + MV	0.97	0.99	0.96	0.96	0.97
CH + DV	1.02	1.04	1.09	1.08	1.06

1.0, and the mean ventilation effectiveness for displacement ventilation system combined with floor/ceiling heating systems range from 1.0 to 1.2. This means that the ventilation effectiveness of mixing ventilation system combined with floor/ceiling heating system are equal to the recommended value in ASHRAE standard 62.1 [11], and the ventilation effectiveness of displacement ventilation system combined with floor/ceiling heating system is slightly less than the recommended value in ASHRAE standard 62.1. This may be due to the effect of downdraft caused by cold external envelope surface on the vertical air distribution [12].

It seems that it is contradictory to have the most uniform air distribution and the biggest ventilation effectiveness for one combination of the floor/ceiling heating systems with mixing/displacement ventilation systems. Non-uniform air distribution will increase the building envelope heat loss by increasing the room reference temperature, and the small ventilation effectiveness will increase the ventilation heat loss by increasing the required fresh air supply [13]. Although it is impossible to have the most uniform air distribution and the biggest ventilation effectiveness for one hybrid system, there should be an optimal hybrid system with regard to the minimal building heat loss under certain ratio of building envelope heat loss to ventilation heat loss.

7.4 Conclusions

- Air distribution in a room with floor/ceiling heating and mixing/displacement ventilation will not cause any local thermal discomfort in terms of vertical air temperature difference and draught.
- The ventilation effectiveness of mixing ventilation system combined with floor/ceiling heating system are equal to the recommended value in the ASHRAE standard 62.1, and the ventilation effectiveness of displacement ventilation system combined with floor/ceiling heating system are slightly less than the recommended value in the ASHRAE standard 62.1.

References

1. Olesen BW, Mortensen E, Thorshauge J, Berg-munch B (1980) Thermal comfort in a room heated by different methods. ASHRAE transactions 86(1):34–48
2. Babiak J, Olesen BW, Petras D (2007) Low temperature heating and high temperature cooling—rehva guidebook. Brussels, Belgium
3. Daisey JM, Angell WJ, Apte MG (2003) Indoor air quality, ventilation and health symptoms: an analysis of existing information. Indoor Air 13:53–64
4. Skistad H (2003) Floor heating and displacement ventilation. Proceedings of cold climate HVAC, Trondheim, Norway
5. Causone F, Baldin F, Olesen BW, Corgnati SP (2010) Floor heating and cooling combined with displacement ventilation: possibilities and limitations. Energ Build 42:2338–2352
6. Causone F, Olesen BW, Corgnati SP (2010) Floor heating with displacement ventilation: an experimental and numerical analysis. HVAC&R Research 16(2):139–160
7. Olesen BW, Simone A, Krajcik M, Causone F, De Carli M (2011) Experimental study of air distribution and ventilation effectiveness in a room with a combination of different mechanical ventilation and heating/cooling systems. Int J Vent 9(4):371–384
8. EN 15251: 2007-Ventilation for buildings—indoor environmental input parameters for design and assessment of energy performance of buildings addressing indoor air quality, thermal environment, lighting and acoustics
9. ISO 7730-2005, ergonomics of the thermal environment—analytical determination and interpretation of thermal comfort using calculation of the PMV and PPD indices and local thermal comfort criteria, European committee for standardization, Brussels
10. Mundt E, Mathisen HM, Nielsen PV, Moser A (2004) Ventilation effectiveness—rehva guidebook. Brussels, Belgium
11. ASHRAE standard 62.1-2007 (2007) Ventilation for acceptable indoor air quality. American society of heating, refrigerating and air-conditioning engineers
12. Wu X, Olesen BW, Fang L, Zhao J (2013) A nodal model to predict vertical temperature distribution in a room with floor heating and displacement ventilation. Build Environ 59:626–634
13. EN 12831-2003 (2003) Heating systems in buildings—method for calculation of the design heat load, European committee for standardization

Chapter 8
Investigation on Indoor Air Quality at Rural Houses in Winter in Severe Cold Region

Zhaojun Wang, Dongdong Xie, Rui Tang and Xiaohui Sheng

Abstract Chinese Kang is one of the most important heating facilities at rural houses in China. The biomass materials such as wood and straw are the primary fuels, which release many pollutants. Inadequate ventilation prevents the pollutants from discharging out. In this study, we investigated the indoor air quality at rural houses in severe cold region of China. The pollutants including $PM_{2.5}$, PM_{10}, TVOC, CO_2, CO, SO_2, NO_X, and NH_3 were monitored and the subjective questionnaires on indoor air quality were administered simultaneously. The results shows that $PM_{2.5}$, PM_{10}, SO_2, NOx, and CO_2 were the main pollutants at rural houses, with the overproof rates of 97, 79, 99, 63, 71 %, respectively. Nevertheless, the occupants were satisfied with the indoor air quality even the indoor pollutants' concentrations exceeded the limits specified in the indoor air quality standard. It had a strong correlation between the concentrations of PM_{10} and $PM_{2.5}$, and $PM_{2.5}$ also correlated well with the concentration of CO. It is found that the indoor air quality at rural houses improved greatly with the increasing outdoor temperature in March compared to December and January.

Keywords Indoor air quality · Pollutants test · Subjective investigation · Rural houses · Severe cold area

8.1 Introduction

The coal or biomass is often used for heating at rural houses in severe cold area in China. Inferior quality coal and biomass burning releases a lot of smoke. Bad sealing and lack of mechanical ventilation facility make pollutants such as solid

Z. Wang (✉) · D. Xie · R. Tang · X. Sheng
Harbin Institute of Technology, School of Municipal
and Environmental Engineering, 150090 Harbin, China
e-mail: wzjw02@yahoo.com.cn

particulates, CO, NO_x, and SO_2 diffuse into the room, which will have bad effect on indoor air quality.

Bluyssen et al. studied the indoor air quality in 56 European office buildings. The results showed that the concentrations of the mean particulate matter, CO_2, and CO met in general the requirements in standards [1]. Lee and Chang carried out a field study on indoor air quality at five classrooms in Hong Kong; SO_2, CO_2, NO, NO_2, PM_{10}, HCHO, and total bacteria counts were monitored at indoor and outdoor locations simultaneously. It showed that the major problem concerning classroom air quality in Hong Kong was high dust concentrations [2]. Lee et al. tested CO_2, PM_{10}, HCHO, VOC_S, and airborne bacteria at six homes in Hong Kong. The results of this study indicate that the concentrations of CO_2 and PM_{10} in the domestic kitchens investigated were 14 and 67 % higher than those measured in the living rooms [3]. Naeher et al. pointed out CO levels have been demonstrated to correlate well with airborne PM concentrations where there is incomplete combustion of biomass fuels [4].

Liu carried out a field study on indoor air quality at rural houses in the northeast of China. It was found that PM_{10} had the largest overweight [5]. Yang tested air temperature, relative humidity, CO, and CO_2 for 5 days at one rural house. The results showed that CO_2 exceeded the standard requirement seriously and CO was low in bedroom at night [6]. Li et al. investigated indoor air quality at 180 rural houses in western China, and the results showed that the maximum daily mean concentration of CO, SO_2, and $PM_{2.5}$ were 8, 38, and 4 times than the normal standard, respectively [7].

In this study, we launched an investigation on indoor air quality at rural houses in severe cold region of China. The pollutants were monitored and the subjective questionnaires on indoor air quality were administered simultaneously.

8.2 Method

This study was conducted from December 2012 to March 2013. The samples were selected at random in the two villages around Harbin. Ten houses with different heating method including Kang, fire-heated wall, and ground Kang were chosen for the study.

Concentrations of PM_{10}, $PM_{2.5}$, TVOC, CO_2, CO, SO_2, NO_X, and NH_3 were monitored at the rural houses. Measurements were performed at the height of respiratory region according to the indoor air quality standard.

A set of portable instruments including DUSTTRAK II 8532 for dust monitoring, TEL7001 for CO_2 measurement, GT901 for the testing of remaining parameters was used in our field study.

The subjective research covered house envelope features, subject's background, and perceived indoor air quality. Heating modes, fuels, and cleaning habits were included in house information. The subject's background included gender, age,

smoking habit, respiratory diseases, and SBS symptoms. And the perceived indoor air quality included sense of foul, fresh, and odor, the acceptance of indoor air quality is also researched.

8.3 Results

8.3.1 Objective Results

The overproof rate can be derived by dividing the exceeding amount by total amount. As the data were quite discrete with high coefficient of variation (seen in Table 8.1), there would be a large deviation in describing pollutant level by the mean concentration. Therefore, we used the median concentration. The surpassing times of each pollutant can be calculated by comparing median concentration with the standard value.

Table 8.1 shows 97, 79, 99, 63, and 71 % of the samples for $PM_{2.5}$, PM_{10}, SO_2, NO_x, and CO_2 exceeded the limits in the standard. The median concentrations of them were 0.327, 0.350 mg/m^3, 0.62, 0.22, and 1409 ppm, and 3.4, 1.3, 2.5, 0.5, and 0.4 times higher than the values specified in the standard, respectively. It indicates that $PM_{2.5}$, PM_{10}, SO_2, NO_x, and CO_2 in most of the samples exceeded the normal levels seriously. Above all, $PM_{2.5}$, PM_{10}, SO_2, NO_x, and CO_2 are the main pollutants that affect the indoor air quality at rural houses in severe cold area in China.

Table 8.1 Results of pollutants tested

House number	$PM_{2.5}$	PM_{10}	CO	CO_2	NO_X	SO_2	NH_3	TVOC
	mg/m^3	mg/m^3	ppm	ppm	ppm	ppm	ppm	ppm
1	0.294	0.303	3.5	1169	0.01	0.57	0.00	0.14
2	0.824	1.054	75.1	1372	0.41	0.73	0.16	0.55
3	0.393	0.443	6.7	1746	0.19	0.66	0.00	0.41
4	0.223	0.244	3.8	3139	0.25	0.83	0.00	0.16
5	0.398	0.444	12.2	1362	0.29	0.55	0.00	0.33
6	0.482	0.456	6.7	1242	0.23	0.57	0.00	0.20
7	0.200	0.207	1.7	903	0.04	0.50	0.00	0.08
8	0.395	0.464	5.2	1286	0.31	0.72	0.00	0.21
9	0.835	0.936	46.1	2036	0.56	0.81	0.22	0.89
10	0.204	0.219	1.8	881	0.13	0.42	0.00	0.65
Mean value	0.425	0.477	16.3	1514	0.24	0.63	0.04	0.36
Standard	0.075	0.150	8.0	1000	0.15	0.18	0.26	0.50
Standard deviation	0.384	0.505	29.7	732	0.19	0.16	0.105	0.40
Coefficient of variation	90 %	106 %	183 %	48 %	79 %	26 %	270 %	110 %
Median	0.327	0.350	4.6	1409	0.22	0.62	0.00	0.19
Overproof rate	97 %	79 %	28 %	71 %	63 %	99 %	13 %	20 %
Exceeding time	3.4	1.3	−0.4	0.4	0.5	2.5	−1.0	−0.6

From Table 8.1, it is seen that the mean concentrations of PM_{10} and $PM_{2.5}$ were 0.477 and 0.425 mg/m^3, indicating that the particles smaller than 2.5 μm accounted for 89 % of inhalable particles and the particles between 2.5 and 10 μm only accounted for 11 %. As the particles smaller than 2.5 μm can be directly inhaled into bronchus and have greater impact on human health, $PM_{2.5}$ at rural houses should be paid more attention and reduced.

8.3.2 Subjective Results

Figure 8.1 shows the results of perceived indoor air quality. 33, 24, and 43 % of the peasants claimed the indoor air quality "very good," "quite good," and "general," respectively. No one voted "bad" or "very bad." It can be concluded that the subjective results are not consistent with the pollutant test results. It may be explained by the adaptation to the indoor environment and low expectation.

8.4 Discussion

8.4.1 Correlation Analyses

The linear regression equation between the concentrations of PM_{10} and $PM_{2.5}$ is as follows:

$$C_2 = 1.25\,C_1 - 0.05, \quad R = 0.98 \tag{8.1}$$

Fig. 8.1 Perceived indoor air quality
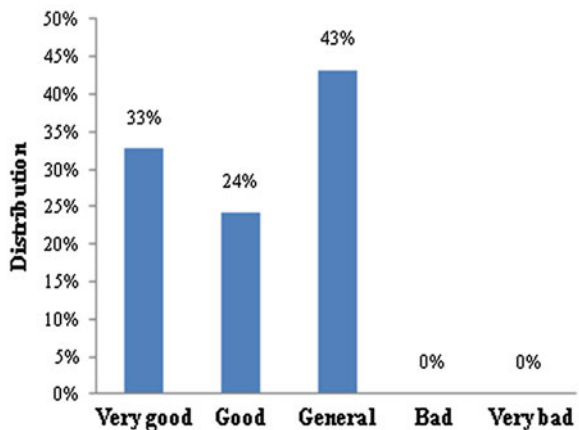
Fig. 8.2 Correlation between concentrations of PM_{10} and $PM_{2.5}$
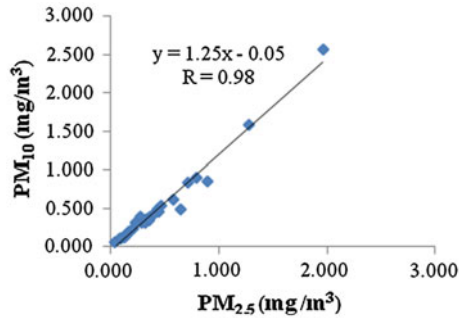
where C_2 is the concentration of PM_{10}, mg/m^3; C_1 is the concentration of $PM_{2.5}$, mg/m^3.

The correlation coefficient of Eq. (8.1) is 0.98, indicating a good correlation between the concentrations of PM_{10} and $PM_{2.5}$.

The curve of the correlation between the concentrations of PM_{10} and $PM_{2.5}$ is shown in Fig. 8.2.

The curve of correlation between the concentrations of $PM_{2.5}$ and CO is shown in Fig. 8.3.

The linear regression equation between the concentrations of $PM_{2.5}$ and CO is as follows:

$$C_1 = 0.0093 + 0.27, R = 0.69 \tag{8.2}$$

where C_1 is the concentration of $PM_{2.5}$, mg/m^3; C_3 is the concentration of CO, ppm.

The correlation coefficient of Eq. (8.2) is 0.69. It shows that there is a good correlation between the concentrations of CO and $PM_{2.5}$, which was consist with the conclusion of Naeher [4].

Fig. 8.3 Regression curve for the concentration of $PM_{2.5}$ and CO
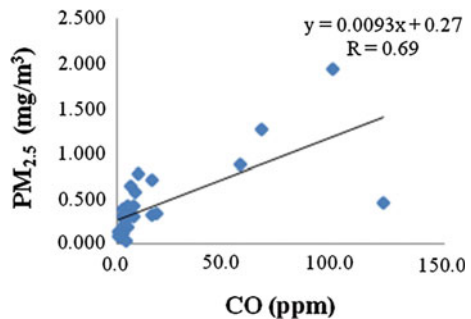
Fig. 8.4 Exceeding times for the main pollutants
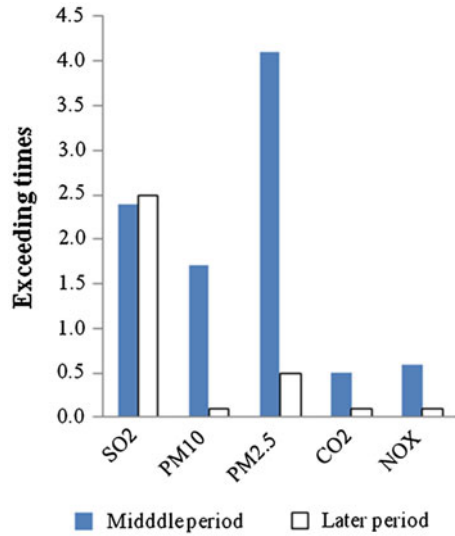
8.4.2 Outdoor Temperature and IAQ

Figure 8.4 compared the surpassing times of the main pollutants between the middle and later period of heating. The middle period of heating lasted from December 2012 to January 2013, and the later period is started from February 2013. It shows that the concentration of most pollutants decreased in the later heating period compared to the middle heating period. The exceeding times of $PM_{2.5}$, PM_{10}, CO_2, and NO_x decreased to 0.5 or less, which shows that the indoor air quality improved greatly with the increasing outdoor temperature.

The mean outdoor temperature is -18.4 °C in the middle period of the heating, which is lower than -13.1 °C in the later period of heating. In the later heating period, the heating load decreased as the outdoor temperature increased. Therefore, less fuel were needed to keep the indoor comfort temperature, which contributed to the improvement of indoor air quality.

8.5 Conclusions

$PM_{2.5}$, PM_{10}, SO_2, NO_x, and CO_2 are the main pollutants at rural houses. 97, 79, 99, 63, and 71 % of the data obtained exceeded the limits in the standard, respectively. The median concentration of $PM_{2.5}$, PM_{10}, SO_2, NO_x, and CO_2 were 3.4, 1.3, 2.5, 0.5, and 0.4 times higher than the standard, respectively.

Because the peasants stay in environment with poor indoor air quality, they may accept the poor indoor air quality. This may be explained by the adaptation to the

indoor environment and low expectation. Therefore, indoor air quality should be paid more attention by the residents in rural areas.

There was a high correlation between the concentrations of PM_{10} and $PM_{2.5}$, and a good correlation between the concentrations of $PM_{2.5}$ and CO.

Indoor air quality at rural houses improved greatly as the outdoor temperature increased.

References

1. Bluyssen PM, Fernandes EO, Groes L et al (1996) European indoor air quality audit project in 56 office buildings. Indoor Air 6:221–238
2. Lee SC, Chang M (1999) Indoor air quality investigations at five classrooms. Indoor Air 9:134–138
3. Lee SC, Li WM, Ao CH (2006) Investigation of indoor air quality at residential homes in Hong Kong. Atmos Environ 36(2):221–238
4. Naeher LP, Smith KR, Leaderer BP et al (2001) Carbon monoxide as a tracer for assessing exposures to particulate matter in wood and gas cookstove households of highland Guatemala. Environ Sci Technol 35:575–581
5. Liu CL (2007) Research on indoor air quality at rural residential house in northeast. Dissertation for the Master Degree. Harbin Engineering University, Harbin (in Chinese)
6. Yang Z (2007) Research on the improvement of indoor air quality and strategies of ventilation for rural houses in cold region. Dissertation for the Master Degree. Harbin Institute of Technology, Harbin (in Chinese)
7. Li X, Wei QY (2000) Status of rural indoor air pollution. Trans CSAE 41:109–113 (in Chinese)

Chapter 9
Field Measurement, Survey and Evaluation on Indoor Thermal Environments in Typical Office Buildings

Pengfei Tao, Angui Li, Guozhi Qiu and Junfu Zhang

Abstract The indoor air environmental conditions of three different typical office buildings were studied with the help of actual measurement and questionnaire survey. The field study was carried out in winter time (heating season, January, 2011) and transition season (October, 2011) in the city of Xi'an. The survey results showed that most workers perceived good thermal environment in the investigated office buildings both the heating season and transition season. However, it was found apparently relative low indoor air humidity at heating season. It was also noticed that there was remarkable difference between predicted mean vote (PMV) index and actual-measurement thermal sensation vote (TSV) in evaluating indoor thermal environments in typical office buildings. Based on the survey, at heating season, the thermal neutral temperature (20.6 °C) of workers is 0.7 °C higher than that at transition season (19.9 °C). From the view of indoor thermal comfort, it is reasonable for Chinese national standard to set the indoor temperature at 20 °C at heating season. The field measurement and survey results showed that the quality of indoor air exerts the greatest impact on the acceptance of environmental quality.

Keywords Office building · Thermal comfort · Indoor air quality · Field survey · Neutral temperature

9.1 Introduction

Sick building syndrome (SBS) is a combination of a syndrome associated with an individual's place of office building or residence. A World Health Organization report into the syndrome suggested up to 30 % of new and remodeled buildings

P. Tao · A. Li (✉) · G. Qiu · J. Zhang
School of Environmental and Municipal Engineering, Xi'an University
of Architecture and Technology, 710055 Xi'an, China
e-mail: liag@xauat.edu.cn

worldwide may be linked to SBS. Most of the SBS is related to poor indoor air quality (IAQ) [1]. However, poor IAQ causes are frequently related to defects in the heating, ventilation, and air conditioning (HVAC) systems. The factors affecting IAQ mainly include temperature, humidity, air exchange rate, air distribution, ventilation, and particle pollutants [2].

P. O. Fanger [3] has taken the view that it is the combined thermal effect of all physical factors which is of prime importance in determining man's thermal state, and he develops the concept into a general comfort equation. Later, P. O. Fanger has proposed the predicted mean vote (PMV) index and the predicted percentage of dissatisfied (PPD) index. PMV predicts the expected comfort vote on the ASHRAE scale of subjective warmth [cold (−3), cool (−2), slightly cool (−1), neutral (0), slightly warm (1), warm (2), hot (3)]. The PMV model has been validated in climate chamber studies with Asian subjects [4, 5] as well as in the field, most recently in ASHRAE's world-wide research in buildings with HVAC systems that were situated in cold, temperate and warm climates and were studied during both summer and winter [6–9].

However, current researches on indoor thermal environment mainly focus on winter and summer with few carried out in transition season. The objective of this study was to compare the indoor air environments of office building under different ventilation modes through field test, analyze the actual thermal comfort of office occupants under real working conditions and compare the test result with PMV index as well as other research achievements. Two seasonal surveys integrating physical measurements with questionnaires were conducted at three office buildings in Xi'an, China. Furthermore, it not only acquired the neutral temperature of office workers in the building under natural ventilation and air-conditioning environment.

9.2 Investigation Content and Method

9.2.1 Test Objects

The test was carried out in three independent office buildings in one plant in Xi'an, whose air-conditioning system apply the primary air and fan-coil units. The air-conditioning system will operate normal in winter and summer, but stop operating in transition season when the windows will be opened for natural ventilation. This provides extremely favorable conditions for the researchers to investigate the indoor air distribution characteristics as well as thermal environment under different air conditioning modes. There are nine floors of the building. The air-conditioning area is 15,210 m^2, the design heat load is 1825.6 kW and the average heat index is 120 W/m^2 with the design air supply temperature of 25 °C. Air-conditioning system adopted the fan coil and fresh air system, each floor is equipped with a variable air volume of fresh air handing units, the outdoor air

filtered by the units and then exchange heat with the refrigerant (hot water or cold water), and finally sent into the room through the fan coil. The fresh air handing units have humidification equipments, which can adjust the humidity of the room.

9.2.2 Investigation Time

Xi'an has a temperate, semi-arid climate influenced by the East Asian monsoon. Since the variation of outdoor temperature as well as relative humidity in transition season is unique compared with that in other seasons, and some researchers had already carried out investigation and analysis on the thermal comfort condition in winter and summer, in this paper, autumn was chosen to be investigated and carried out a comparative analysis by combining the investigation result of heating season (winter). The test was carried out in heating season (January, 2011) and transition season (October, 2011) respectively.

9.2.3 Measuring Parameters and Instruments

In this paper, four measuring points are selected according to the area of the room, The layout of the measuring points is shown in Fig. 9.1, located above the ground 1.2 m (sitting height) and 1.6 m (standing height). The measuring physical parameters mainly include air temperature, relative humidity, air velocity, etc., and the measuring instruments includes Sweden SWEMA multichannel data collection test system. American TSI air quality tester as well as the humiture recorder RR002 developed by China Academy of Building Research Institute. All of the applied instruments were verified for their accuracy. The measurement and measuring point station rules strictly follow the ASHRAE Standard 55-2004 [10].
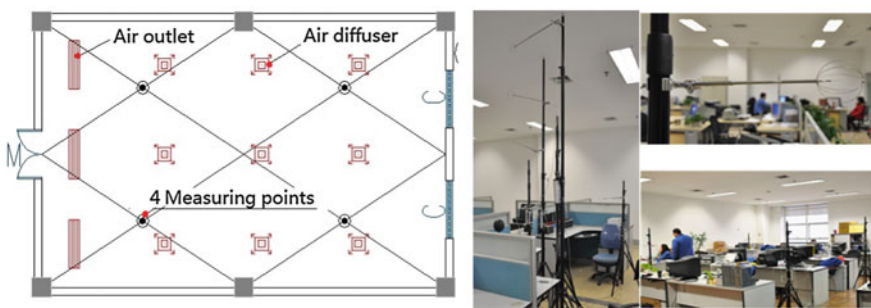
Fig. 9.1 The layout of the measuring points

9.2.4 Subjective Questionnaire Survey

The subjective questionnaire survey was implemented simultaneously when measuring physical parameters. The reliability coefficient of questionnaire reached 0.766, higher than the suggesting 0.7, indicating high reliability of the questionnaire design. As shown in Table 9.1.

There were totally 420 questionnaires issued in this research and 347 questionnaires were returned, achieving the return rate as high as 82.6 %. In addition, there were totally 305 effective questionnaires with an effective rate of 87.9 %,

Table 9.1 Questionnaire for evaluation of the indoor air environmental conditions

Please complete each of the following statements by checking the box that best expresses your personal feelings or preferences (check one)

☐ Male ☐ Female Age: Working age:

(1) I perceive the TEMPERATURE of the area to be: (disregarding the effects of air movement, lighting and humidity)

☐ Cold ☐ Cool ☐ Slightly cool ☐ Neutral ☐ Slightly warm

☐ Warm ☐ Hot

(2) Can you accept the thermal environment in your room?

☐ Acceptable ☐ Unacceptable

(3) I perceive the HUMIDITY of my work area to be: (disregarding the effects of temperature, air movement and lighting)

☐ Very dry ☐ Moderately dry ☐ Slightly dry ☐ Neutral

☐ Slightly humid ☐ Moderately humid ☐ Very humid

(4) Can you accept the humidity in your room?

☐ Acceptable ☐ Unacceptable

(5) I perceive the AIR MOVEMENT of my work area to be: (disregarding the effects of temperature, humidity and lighting)

☐ Very still ☐ Moderately still ☐ Slightly still ☐ Acceptable

☐ Slightly draughty ☐ Moderately draughty ☐ Very draughty

(6) Can you accept the air movement in your room?

☐ Acceptable ☐ Unacceptable

(7) On average, I perceive the thermal environment comfort of my work area to be:

☐ Very Comfortable ☐ Comfortable ☐ Uncomfortable

☐ Slightly uncomfortable ☐ Very uncomfortable

(8) I perceive the indoor air quality of my work area to be:

☐ Very good ☐ Good ☐ Moderately ☐ Bad ☐ Very bad

(9) Can you accept the indoor air quality in your room?

☐ Acceptable ☐ Unacceptable

(10) In conclusion, can you accept the indoor air environment in your room?

☐ Acceptable ☐ Unacceptable

among which 202 were effective questionnaires in heating season while the rest 103 effective questionnaires in transition season.

9.3 Test Result

9.3.1 Physical Parameters of Indoor Air

The distribution frequency of indoor air temperature, relative humidity as well as air velocity in various zoning sections under two different ventilation modes were displayed in Fig. 9.2 respectively. Combined with the chart, the indoor average temperature under air-conditioning environment in heating season is 21.6 °C, and even 12.2 % actual measurement data of indoor air temperature is higher than 25 °C, indicating certain energy waste in air-conditioning application. The average indoor relative humidity only values 19.7 % with the maximum of 27.6 %, far lower than the required 30 % stated in standards. It discovered, through further survey later, that none of the fresh air handling unit of the three investigated office buildings was equipped with humidification function. The indoor air velocity under air-conditioning environment was unable to satisfy the relative requirement of national standard along with non-ideal indoor air flow. However, the office buildings applied natural ventilation in transition season.
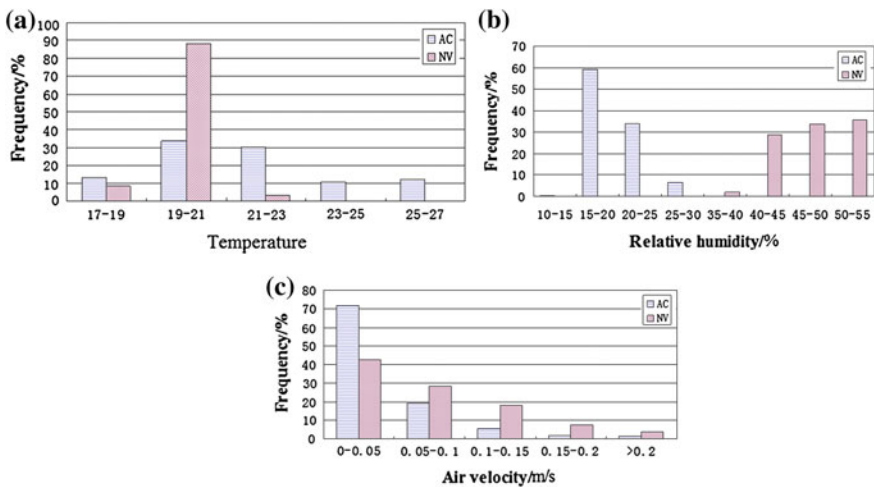
Fig. 9.2 Distribution frequency of physical parameters. **a** Temperature. **b** Humidity. **c** Velocity

9.4 Questionnaire Survey Result

9.4.1 Thermal Sensation Vote

The thermal sensation frequency distributions in heating season and transition season were presented in Fig. 9.3a, from which it can be known that 87.3 % of interviewees' thermal sensation in heating season votes within −1 (slightly cool) ~ + 1 (slightly warm), and 90.3 % of interviewees' thermal sensation in transition season under natural ventilation votes within −1 ~ + 1. Both heating season and transition season achieved over 80 % interviewees' TSV within − 1 ~ + 1, and most interviewees are comfortable with indoor thermal sensation, finding relative good accordance with the objectively measured physical parameter of indoor air.

9.4.2 Humidity Sensation Vote

The humidity sensation vote (HSV) distribution given by interviewees was presented in Fig. 9.3b, from which it can be seen that 83.7 % of interviewees' HSV lies within −1 (slightly dry) ~ + 1 (slightly humid) in heating season, and 16.3 % interviewees vote the current humidity sensation as −2 (dry).
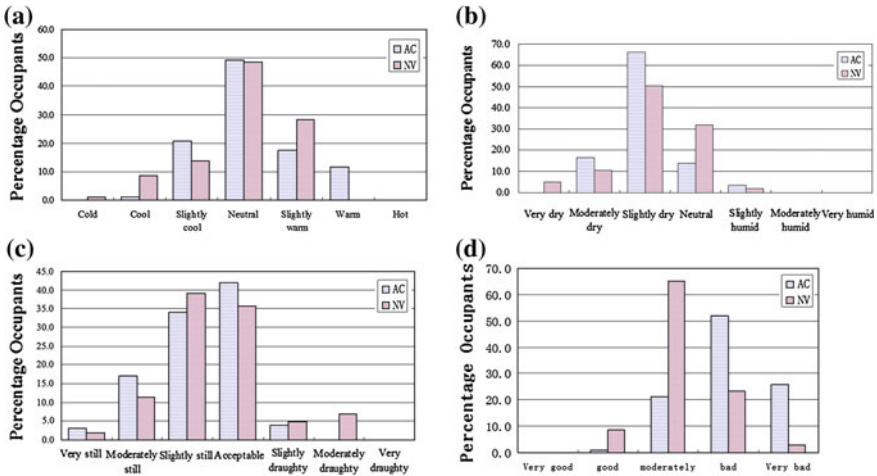
Fig. 9.3 The distribution of the questionnaire survey results. **a** Thermal sensation vote (*TSV*). **b** Humidity sensation vote (*HSV*). **c** Air velocity sensation vote (*DSV*). **d** Indoor air quality vote

9.5 Discussion

9.5.1 Comparison Between Measured TSV and PMV

Draw the PMV obtained in heating season and transition season respectively as well as the actual measured TSV on the coordinate graphs for regression analysis. The coordinate graphs take the operating temperature as x-axis and take thermal sensation scale as y-axis. The results after linear fit were shown in Fig. 9.4.

$$\text{Heating season:} \, \text{PMV} = 0.2275t_{\text{o}} - 5.13634(R = 0.97269) \tag{9.1}$$

$$\text{TSV} = 0.39406t_{\text{o}} - 8.11863(R = 0.93959) \tag{9.2}$$

$$\text{Transition season:} \, \text{PMV} = 0.64037t_{\text{o}} - 13.6404(R = 0.9355) \tag{9.3}$$

$$\text{TSV} = 0.79347t_{\text{o}} - 15.85183(R = 0.82289) \tag{9.4}$$

Based on the above formulas, the thermal neutral temperature (20.6 °C) of office workers in heating season is 0.7 °C higher than that in transition season (19.9 °C), indicating human body's good tolerance to air temperature in transition season. In Fig. 9.4, under heating conditions, the "scissors difference" phenomenon was produced between PMV and TSV at 18 °C. When the indoor temperature was lower than 18 °C, human body's actual thermal sensation will become lower than the prediction gradually. In heating season, staying in warm environment for a long time will restrict human body's adaptability in cold environment to a certain extent, and workers will be easy to complain under over low indoor temperature. This will exert direct impact on people's judgment on actual thermal sensation, thus decreasing interviewees' adaptability after the indoor temperature was set lower than 18 °C, and lowering the actual measurement of thermal sensation than prediction. However, in transition season under natural ventilation, shown in Fig. 9.4b, there's more obvious deviation between PMV and actual investigation result of thermal sensation. This is because PMV deems that no
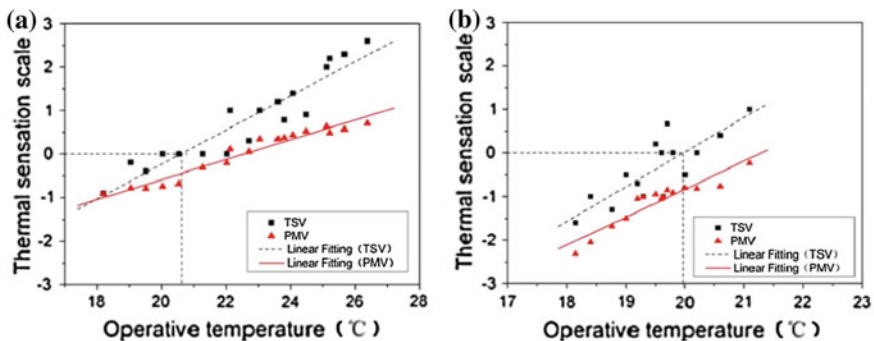
Fig. 9.4 PMV and TSV comparison in heating season (**a**) and transition season (**b**)
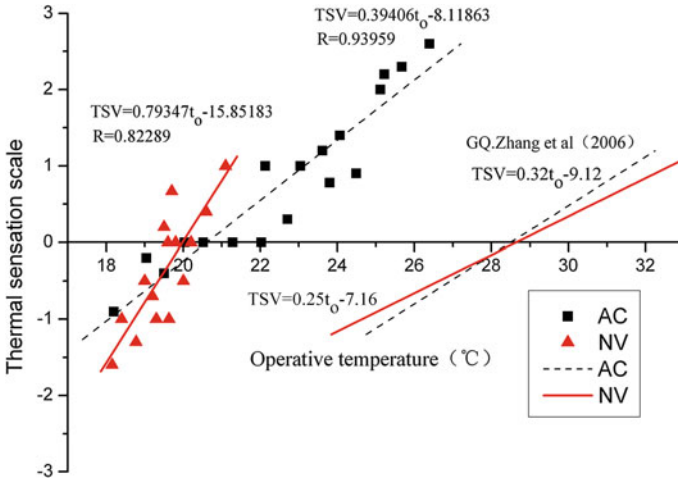
Fig. 9.5 Comparison on the linear relation between TSV and operating temperature

matter which season is concerned, human body produces same physiological and psychological response to thermal environment, and the basis of PMV model establishment-heat balance model is strictly the laboratory product.

9.5.2 Comparison Among Different Ventilation Conditions

According to Fig. 9.5, the equation of linear regression of thermal neutral temperature in the buildings under natural ventilation achieves higher slope than that under air-conditioning environment. The curve slope in transition season under natural ventilation is significantly higher than that obtained by other researchers through the architecture research under natural ventilation, which demonstrates that workers in the office building are more temperature sensitive in transition season under natural ventilation environment than under air-conditioning environment. However, current researches on indoor thermal environment mainly focus on winter and summer with few carried out in transition season, but human body's adaptive adjustment capability of thermal environment and sensation to temperature variation are corresponding to the temperature variation range of local environment.

9.6 Conclusions

In this paper, two seasonal surveys (heating and transition seasons) integrating physical measurements with questionnaires were conducted at three office buildings in Xi'an, China. According to the sorting and analysis of the field

measurements and survey research on the indoor environmental conditions, we could get the following conclusions:

(1) The average value of the indoor air velocity only is 0.04 m/s and there are nearly 90.0 % measured data of indoor air velocity distributed within 0–0.1 m/s, lower than the required air velocity in occupied zone (>0.1 m/s) by "Design Standard for Energy Efficiency of Public Buildings" (GB 50189-2005). Also the change rate of indoor air is not enough, optimize the ventilation system design of office buildings is the effective way to improve the indoor thermal environment and thermal comfort.
(2) The average value of the indoor relative humidity is 19.7 % with the maximum of 27.6 %, far lower than the required 30 % stated in standards. Therefore, it shall attach more attention on the adjustment of indoor air humidity in winter in heating areas.
(3) The thermal neutral temperature (20.6 °C) of office workers in heating season is 0.7 °C higher than that in transition season (19.9 °C), indicating human body's good tolerance to air temperature in transition season. The possibility to lower air-conditioning's set temperature in heating season (below 24 °C) for reducing the energy consumption of air-conditioning system, thus creating more comfortable and energy-efficient green building.

References

1. Redlich CA, Sparer J, Cullen MR (1997) Sick-building syndrome. The Lancet 349(9057):1013–1016
2. Graudenz GS, Oliveira CH, Tribess A, Mendes C, Latorre MRDO, Kalil J (2005) Association of air-conditioning with respiratory symptoms in office workers in tropical climate. Indoor Air 15:62–66
3. Fanger PO (1970) Thermal comfort. Danish Technical Press, CoPenhagen
4. de Dear R, Leow KG, Ameen A (1991) Thermal comfort in the humid tropics. Part I. Climate chamber experiments on temperature preferences in Singapore. ASHRAE Trans 97(1):874–879
5. Tanabe S, Kimura K, Hara T (1987) Thermal comfort requirements during the summer season in Japan. ASHRAE Trans 93(1):564–577
6. Cena KM (1998) In: Cena K, de Dear R (eds) Field study of occupant comfort and office thermal environments in a hot-arid climate, Final report ASHRAE 921-RP. ASHRAE Inc., Atlanta
7. Donini G, Molina J, Martello C, Ho Ching Lai D, Ho Lai K, Yu Chang C, La Flamme M, Nguyen VH, Haghihat F (1996) Field study of occupant comfort and office thermalenvironments in a cold climate, Final report ASHRAE 821 RP, ASHRAE Inc., Atlanta, 1996

8. de Dear R, Fountain M, Popovic S, Watkins S, Brager G, Arens E, Benton C (1996) A field study of occupant comfort and office thermalenvironments in a hot-humid climate, Final report ASHRAE 702 RP. ASHRAE Inc., Atlanta
9. Schiller GE, Arens E, Bauman F, Benton C, Fountain M, Doherty T (1988) A field study of thermal environments and comfort in office buildings, Final report ASHRAE 462 RP. ASHRAE Inc., Atlanta
10. ASHRAE.ASHRAE Standard 55-2004 Thermal environmental conditions for human occupancy[S] .Atlanta, ASHRAE,2004

Chapter 10
Study on Climate Adaptability Design Strategies Based on the Human Body Thermal Comfort: Taking Guanzhong Rural Housing as Example

Cuiyu Ge, Liu Yang, Yi Zhang and Xiaolei Du

Abstract A field survey in Guanzhong plain in China has been done on vernacular dwellings to obtain thermal adaptability model which is expressed as $T_n = 0.691T_{out,m}+12.91(R^2 = 0.915)$. An analysis has been done on local climate data by using climate analysis method combined with psychrometric chart and establishes comfort zones of two seasons of winter and summer in Turpan. In this paper, we defined four controlling potential areas (passive solar heating, the mass effect and night ventilation, natural ventilation, and evaporative cooling) and obtained the number of days when we can apply passive design strategy. Finally, this paper summarized the suitable design strategies which response to climate environment on vernacular dwellings in Guanzhong plain in China.

10.1 Introduction

Climate, which is the key factor influencing architectural style and settlement landscape features of different regions in the world, is paid more and more attention by the architects. But climate is a relatively stable external condition

C. Ge (✉) · L. Yang · Y. Zhang · X. Du
School of Architecture, Xi'an university of Architecture and Technology,
Xi'an 710055, China
e-mail: gcy_3333@163.com

L. Yang
e-mail: yangliu@xauat.edu.cn

C. Ge
School of Architecture Engineering, Nanjing Institute of Technology,
Nanjing 211167, China

compared with other factors such as politics, culture, and economy. Victor Olgyay discussed research results on relationships among architecture design, region, and climate and systematically combined human thermal comfort and regional climate characteristics with architectural design in his book "Design with Climate" in 1963, and then put forward the design concept of bioclimatology.

Climate design involves two questions. Firstly, One is accurate indoor thermal comfort standard. That is to analyze the effects of outdoor climate on thermal sensation by establishing relationship between outdoor climate and indoor comfort requirements and then put forward climate regulation technique to meet human body comfortable requirements and apply it to architecture design. The other is the need to correctly analyze the influence of climate factors on the building and determine the feasibility of climate regulation means for all kinds of buildings. Field study has been conducted on thermal comfort for Guanzhong plain rural house in this paper so as to find indoor comfortable temperature of rural houses. This paper aims to propose reasonable energy saving design strategy and climate control measures and provide guidance basis for energy saving calculation, thermal comfort and passive architectural design through analyzing the relationship between outdoor climatic conditions and human thermal comfort environment and establishing the relationship between the main outdoor climatic conditions and expectations of indoor thermal comfort.

10.2 Method

10.2.1 The Climate of Guanzhong Region

The location investigated in this study is Guanzhong region in Shanxi province. This region is in the subtropical monsoon climate zone, which is characterized by much rainfall and high temperature in summer and little rainfall and mild weather in winter. The annual precipitation ranges from 550 to 650 mm. Except Qinling Mountains, sunshine hours ranges from 2009 to 2528 h and annual average temperature ranges from 11.5 to 13.7 °C. This region belongs to IIA in thermal zone. Extreme highest temperature in summer ranges from 41.4 to 45.2 °C and extreme minimum temperature ranges from -16.9 to -20.8 °C, annual average temperature is ranges from 11.5 to 13.7 °C.

10.2.2 Study Object

Our team has conducted careful study on rural houses in Weinan. The specifics are as follows:

1. Time: Winter (January 2009)

   Location: Rural houses in Weinan, Shanxi
   The number of houses: 36
   The number of subjects: 66 (35 males, 31 females)
   Total number of effective survey data: 198

2. Time: Summer (July and August 2009)

   Location: Guanzhong plain, Shanxi
   The number of houses: 37
   The number of subjects: 64 (23 males, 42 females)

   Total number of effective survey data: 192
   The main research contents include the following:

(a) Background of inhabitants: gender, height, age, etc.
(b) Clothes and activity: recording the amount of clothes the subjects wear and the frequency and intensity of their activities.
(c) Thermal sensation of subjects: applying Fanger's heat feeling scale which is generally accepted in the world [1], namely hot (+ 3); warm (+ 2); little warm (+ 1); zero (0); little cool (1); cool (2); cold (3).
(d) Others: Research on heat accept rate, thermal expectations, humidity, and wind speed feeling, overall thermal comfort of subjects and the adaptability measures on improving indoor thermal environment.

10.2.3 Test Scheme

Subjective thermal comfort data were recorded in a questionnaire, and each subject filled up the questionnaire three times a day, in the morning, at the noon, and in the evening. In the meantime, environment parameters were tested, three times in morning, noon, and evening, respectively, and test environment parameters every day.

Indoor temperature, humidity, wind speed, and black ball temperatures were obtained by temperature and humidity recorder, testo 405-V1 anemometer (wind speed range 0–10 m/s, resolution +0.01 m/s, accuracy + 0.1 m/s + 5 % measured value) and black ball gauge, and the average radiation temperature was calculated.

10.2.4 Survey Purpose

Our survey aims to analyze and research architecture layout, indoor thermal environment, and thermal comfort condition for local rural houses from the angle of architecture design. The relationship between comfort temperature and outdoor

average temperature in Guanzhong plain is established on the basis of survey data. We obtained indoor comfort temperature in winter and in summer, established comfort zone, and determined the boundary of passive design strategies. Combined with regional characteristics, traditional customs, and life habits, we finally get the effectiveness of passive design strategies to provide valuable design ideas for buildings in wide rural areas.

10.3 Data Analysis

Humphreys [2] has conducted field survey for natural ventilation building and established linear relationship between indoor thermal comfort temperature and outdoor monthly average temperature in natural ventilation environment according to survey data, namely Eq. (10.1)

$$T_n = 0.53T_{\text{out},m} + 11.9 \tag{10.1}$$

where T_n is neutral temperature and $T_{\text{out},m}$ is outdoor average temperature.

De Dear and Auliciems [3] had conducted a field study for two cities in Australia and obtained the neutral temperature regression equation for natural ventilation building which has a big difference compared with Humphreys' equation, namely Eq. (10.2).

$$T_n = 0.31T_{\text{out},m} + 17.6 \tag{10.2}$$

According to the above scholars' research methods, the team has conducted survey for indoor and outdoor environment in winter and in summer of rural houses in Guanzhong plain. According to field survey, taking 0.5 °C as step length, we used BIN method [4] to deal with cold and hot sensation and then got the formula,

$\text{MTS} = aT_{\text{op}} + b$. And making

$\text{MTS} = 0$, we obtained neutral temperature T_n of each building. Finally, our team obtained the thermal adaptability model by linear regression between neutral temperature and the corresponding average outdoor temperature of all buildings (Fig. 10.1).

Fig. 10.1 Thermal adaptive model in Guanzhong region

$$y = 0.9564x + 0.7402$$
$$R^2 = 0.8698$$

$$T_n = 0.684T_{\text{out},m} + 8.105$$
$$R^2 = 0.908$$
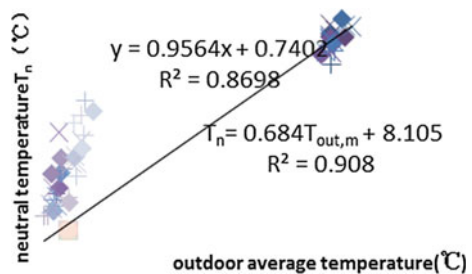
$$T_n = 0.691T_{out,m} + 12.91(R^2 = 0.915) \tag{10.3}$$

where T_n is comfort temperature and $T_{out,m}$ is outdoor average temperature.

Rural houses in Guanzhong region use passive control system, and indoor temperature fluctuates in a certain range. Many studies show that it does not work to predict thermal sensation in natural ventilation by the comfortable standard based on climate chamber [5–11]. In addition to people thermal comfort in different climate, the results are also affected by environment parameters, region, crowd, season, expectations, living habits, economic conditions, etc. For example, there were statistically significant differences in comfort requirements for people in different regions [12].Comfort temperature of English people is 3 °C lower than Americans. The range of comfort temperature of people living in tropical region is from 25 to 27 °C but for people in cold area, it is the opposite case [13]. Therefore, there was a significant difference in calculation results in Eq. (10.3) compared with that in Eqs. (10.1)–(10.2).

10.4 Climate Analysis Method

10.4.1 Drawing Climate Analysis a Diagram

In the study, we chose the typical city, Xi'an, to analyze, collecting climate materials, including air temperature, relative humidity, and so on.

10.4.1.1 Calculating the Local Neutral Temperature

By calculating average temperature of 12 months (To.av) of Xi'an during 30 years (1971–2000) (Table 10.1) [14], we obtained that the annual average temperature of Guanzhong region is 13.6 °C and that thermal neutral temperature is 17.4 °C by Eq. (10.3).

10.4.1.2 Drawing Monthly Meteorological Data on Climate Analysis Chart

The corresponding point produced by the average minimum temperature and the average highest relative humidity is identified as 1. The corresponding point

Table 10.1 Monthly average temperature and neutral temperature in Xi'an

Month	1	2	3	4	5	6	7	8	9	10	11	12
Outdoor average temperature	−0.1	2.9	8.1	14.8	19.8	24.8	26.6	25.3	19.9	13.9	6.9	1.3
Neutral temperature		12.8	14.9	18.5	23.1	26.6	30.1	31.3	30.4	26.7	22.5	17.7	13.8

produced by the average highest temperature, and the average minimum relative humidity is identified as 1'. Connect point 1 with point 1', namely "climate line," and mark 12-months climate lines in the psychrometric chart.

10.4.1.3 Drawing Comfort Zone Based on Neutral Temperature

1. The coldest month and the hottest month is January and July, respectively. 12.84 and 31.29 °C were marked on the curve of the 50 % relative humidity in psychrometric chart to represent the neutral temperature of January and July, respectively. Thermal environment expectations of inhabitants in rural area is below that of people in city, so the utmost and lowest limit of comfort zone is $T_U = T_n + 2.5$ and $T_L = T_n - 2.5$, respectively. Accordingly, the winter neutral temperature limit in winter is from 10.34 to 15.34 °C, and the summer neutral temperature limit in summer is from 28.79 to 33.79 °C which are also marked on the curve of the 50 % relative humidity.
2. Boundary lines on both sides of comfort zone were drawn in psychrometric chart, and horizontal axis intercept of boundary lines (standard effective temperature line) is derived from the following formula [15].

$$T'_U = T_U + 0.023 \times (T_U - 14) \times \text{AHT}_{(50\%)} \tag{10.4}$$

where $\text{AHT}_{(50\%)}$ is absolute humidity in 50 % relative humidity line (g/kg). Horizontal axis intercept of the lower limit value in the coldest month was worked out in the same way.

3. Humidity range is 4–12 g/kg in comfort zone according to ASHRAE55—2004 standard and the relative humidity is not more than 90 %.

10.4.1.4 Climate Control Potential Area

To designers, the ideal solution is that indoor thermal comfort can be achieved easily through the passive control strategies. Whether choosing passive control or not depends on comfort zone, outdoor temperature, and humidity controlled under actual weather conditions. There are 6 thermal control methods: passive solar heating, heat storage, heat storage and night ventilation, natural ventilation, direct evaporative cooling, and indirect evaporative cooling. We established relationship among bioclimatic chart, architectural design, and technology strategy through analyzing potential building passive control area and obtained boundaries of passive design strategies according to relevant Ref. [16–18] (Fig. 10.2).

10.4.1.5 Comfortable days got by Using Passive Compensation Measures

Monthly climate conditions and the distribution of effective days when we need to take improvement measures are calculated according to climate analysis chart (Fig. 10.2).

According to statistics, there are 157 comfortable days in a year in Guanzhong region which accounts for 35.3 % of a year. We can also get more comfortable days by compensation 26 days, accounting for 7.1 % of a year, by using passive solar heating; 15 days, accounting for 4.1 %, by using heat storage of building envelope; 94 days, accounts for 25.2 %, by using active measures; and 15 days, accounts for 4.1 %, by using natural ventilation.

In all passive design measures, passive solar heating which should be considered in design can improve the longest time (7.1 %) for indoor environment, followed by the natural ventilation design and heat storage, respectively 4.1 %. Through the above analysis, we can conclude that if we use reasonable passive technical measures in our design, we can prolong the comfortable days for 67, which accounts for 18.3 % of a year. Plus the original 174 comfort days. The percentage of comfortable days by using passive design measures will be increased to 66 % of all year round. Of course, this study has taken living habits factors of local residents into account.
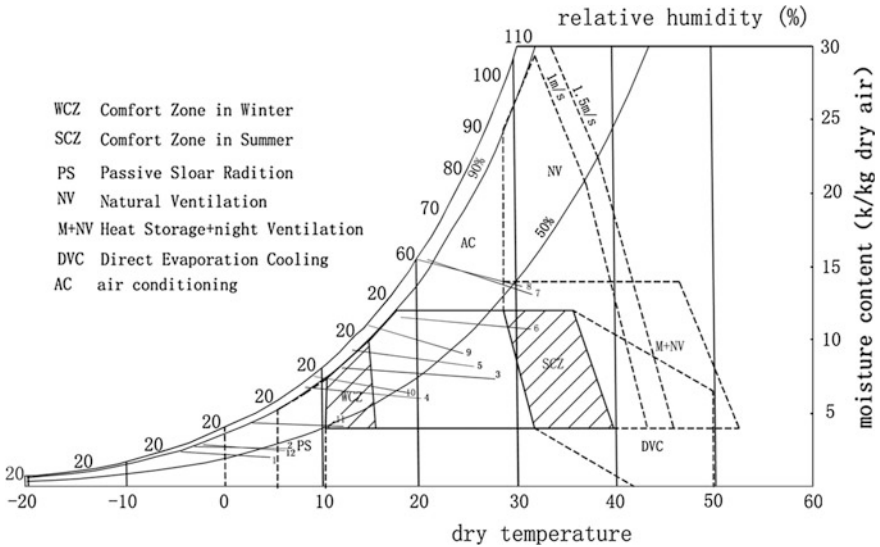
Fig. 10.2 Climate analysis chart in Guanzhong region

10.5 Climate Adaptability Design Strategies

Guanzhong region belongs to cold area IIA in thermal zones. It needs to pay more attention to use solar heating in winter and natural ventilation in summer from the above analysis.

10.5.1 Attention to Air Temperature

In order to ensure indoor suitable temperature, rural houses are adjacent to each other and their wing rooms are also next to their neighbors, so the exposed area to the long side is decreased which reduces the heat loss in winter and save more energy.

In addition to the use of coal, Kang is the main heating facility for local farmers. It is generally placed on the window side of the bedroom in order to effectively use of heat energy, which facilitates the heating and circulation of indoor air and created a very comfortable thermal surroundings centering on Kang. It, therefore, becomes the best place for daily activities. Normally, a temporary stove will be constructed to avoid overheating indoors in summer. Kang, stove chamber, and chimney are connected to form a natural air conditioning system, making the indoor air circulate and cooling.

10.5.2 Attention to Solar Radiation

Guanzhong region is rich in solar energy. Except Qinling Mountains, the annual sunshine duration is 2009–2528.1 h, the annual average air temperature is 11.5–13.6 °C. So we can make full use of passive solar energy technique to achieve heating in winter.

Main activity areas such as room with heated Kang and living room are arranged in the south of the building, and set a climate buffer zone, namely solar room, at the entrance and on the south of the living room, the main purpose of which is to use solar heating to prevent indoor heat loss at night. While auxiliary room, as the north buffer zone, is arranged on the north of the building to prevent heat loss through the wall, wall with big window and the concrete walls and floor makes the room having Kang the solar room.

Meanwhile, there is attic or air layer between the ceiling and roof, forming vertical climate buffer space in order to achieve a purpose of thermal insulation in winter and summer. Kitchen connected with the Kang room in architecture layout, in other words, heat source being centralized in the main activity room, will save more energy by heating Kang while cooking.

10.5.3 Attention to Wind

The dominant wind direction in Guanzhong region is northeast and southwest. Rural houses in Guanzhong region pay great attention to ventilation in summer and windbreak in winter, which are reflected in single building, courtyard arrangement, and settlement combination.

1. Single building usually set wind scoop or hall at the entrance as transition space and hung heavy cotton door curtain to block wind in winter.
2. In order to adapt to the dominant wind direction, the courtyard plane layout is long and narrow from north to south to make courtyard in the shaded area. So, courtyard is very cool in summer to help ventilate the yard. Courtyard design makes full use of space osmosis principle, namely processing technique–gray space, and the wing was designed opening grille to let indoor and outdoor interlinked miscibility.

The story height of most of rural houses in Guanzhong region is from 3.0 to 4.2 m. Because the courtyard is very narrow and long, there are not enough space to do garden greening. The higher story height makes indoor air flow speedup and effectively reduces indoor temperature. The backyard plants tall trees to block out solar radiation, effectively reducing outdoor thermal radiation and making indoor temperature relatively pleasant.

References

1. Fanger PO (1972) Thermal Comfort. McGraw-Hill Book Co., New York
2. Humphreys MA (1978) Outdoor temperature and comfort indoors. Building Res Prac 6(2):92–105
3. De Dear RJ, Auliciems A (1985) Validation of the predicted mean vote model of thermal comfort in six Australian field studies, ASHRAE Transactions, 91(2b):452–468
4. Wang Z (2004) Selection of thermal comfort indexes in the field study. J HV&AC 34(12):39–42
5. Schiller GE (1990) A comparison of measured and predicted comfort in office. Buildings. ASHRAE Trans 96(l):609–622
6. Dedear RJ, Fountain ME (1994) Field experiments on occupant comfort and office thermal environments in a hot-humid climate. ASHRAE Trans 100(2):457–475
7. Donnini G, Molina J, Martello C et al (1996) Field study of occupant comfort and office thermal environments in a cold climate. ASHRAE Trans 102(2):795–802
8. Nicol JF, Raja IA, Allaudin A, Jamy GN (1999) Climatic variation in comfortable temperatures: the Pakistan projects. Energ build 30(2):261–279
9. Oseland NA (1998) Acceptable temperature ranges in naturally ventilated and air-conditioned offices. ASHRAE Trans 104(2):1018–1036

10. Shahin H, Steve S (2002) A comparative analysis of short-term and long-term thermal comfort surveys in Iran. Energ Build 34(2):607–614
11. Feriadi H, Wang NH (2004) Thermal comfort for naturally ventilated houses in Indonesia. Energ Build 36(2):614–627
12. Tao P (1991) The thermal sensation difference between Chinese and American people. Indoor Air 4
13. Liu J, Jilang Z, Liangbin T (2005) Climate responsive architecture—a design handbook for energy efficient building. China Building Industry Press, Beijing (in Chinese)
14. China meteorological information center meteorological reference room (2005) China building thermal environment analysis special meteorological data set. (in Chinese). China Building Industry Press, Beijing
15. Papparelli A, Kurban A, Cunsulo M (1996) Strategies of bioclimatic design in and urban area of an arid zone: San Juan (Argentina). Landscape Urban Plan 34(1996):19–25
16. Liu Y (2003) Climatic analysis techniques and architectural design strategies for bio-climatic design. Dissertation for the Doctoral Degree. Xi'an:Xi'an University of Architecture and Technology, (in Chinese)
17. Tang Y (2010) Bio-climate chart and passive design strategy analysis. Shandong architecture University, Jinan Dissertation for the Doctoral Degree (in Chinese)
18. Xie L (2006) Climate division for passive solar building. Dissertation for the Doctoral Degree. Xi'an University of Architecture and Technology, Xi'an (in Chinese)

Chapter 11
Measurement of Phthalate Concentrations in PVC Wallpapers and Floorings

Mengyan Gong, Lixin Wang and Yinping Zhang

Abstract Certain phthalates may function as endocrine disruptors and have been associated with various adverse health effects. However, information about the indoor phthalate sources is limited, especially in China. This study measured phthalate concentrations in four kinds of PVC wallpapers and four kinds of PVC floorings from Chinese market, and the target chemicals are six commonly used phthalates, i.e., DMP, DEP, DnBP, BBzP, DEHP, and DOP. The phthalate concentrations in different layers of one kind of PVC flooring were semi-quantitatively measured by infrared absorption spectroscopy (Shimadzu IR). The results showed that DEHP was detected, while other five kinds of phthalates were not detected in PVC wallpapers; DEHP concentration was in the range of 0.134–200 mg/g. DBP and DEHP were detected in PVC floorings, while other four kinds of phthalates were not detected; DBP and DEHP concentrations were in the range of nd-14.4 and 69.1–230 mg/g, respectively. The IR analysis showed that PVC flooring was heterogeneous with highest concentrations on the surface and lower concentration in the substrate layer.

Keywords Indoor · Phthalate · Source · DEHP · DBP

11.1 Introduction

Phthalates are ubiquitously detected, sometimes at high concentrations, in human tissues [1–3], urine, blood, breast milk, household air, settled dust, and surface [4–6]. These studies indicate that people are widely exposed to phthalates. Certain

M. Gong (✉) · Y. Zhang
Department of Building Science, Tsinghua University, Beijing, People's Republic of China
e-mail: gongmengyan@gmail.com

L. Wang
School of Environment and Energy Engineering, Beijing University of Civil Engineering and Architecture, Beijing, People's Republic of China

phthalates may function as endocrine disruptors and have been associated with various adverse health effects. Di-2-ethylhexyl phthalate (DEHP) in dust was associated with asthma and wheezing in children [7], teratogenicity [8], pregnancy loss [9] and growth inhibition and estradiol level reduction [10]. The metabolites of dibutyl phthalate (DBP) were associated with the decrease in semen quality [11].

Several studies have measured the emission rates of phthalates from PVC materials [12–14]. However, phthalate concentrations in the source materials have not been measured and information about the indoor phthalate sources is limited, especially in China. This gap is problematic from multiple perspectives. Researchers and regulators rely on phthalate concentration in products for exposure modeling [15, 16]. Researchers need the ingredient information to interpret health studies [17]. Consumers also want the information to make wise choices for product buying.

To develop information about phthalate exposure sources, this paper examined the kinds and concentrations of phthalates in four kinds of PVC wallpapers and four kinds of PVC floorings.

11.2 Materials and Methods

PVC wallpaper 1, 2, 3, and 4 and PVC flooring 1, 2, 3, and 4 were purchased in the local building material market. The materials were delivered as a roll and kept in a clean room.

11.2.1 Sample Preparation and Analysis

The sample preparation process includes three steps. Firstly, Soxhlet extraction: put the sample (2×2 mm, about 1 g) into the extractor; add 120 mL dichloromethane (chromatography reagent, produced in United States) into the 150 mL round flask; extract the samples at 70 °C for 6 h. Secondly, condensation: After cooling, evaporate extraction until about 10.0 mL left in the rotary evaporator and then transfer the sample to 25.0 mL volumetric flask. Lastly, purifying: Filter the concentrated solution with organic microporous membrane (0.45 um).

The samples were determined by GC–MS (DSG, Thermo Fisher) in the selective ion-monitoring (SIM) mode. Chromatographic column is AB-5MS (30 m $\times$ 0.25 mm $\times$ 0.25 um); carrier gas is He, and the flow is 20 mL/min; the base temperature is 250 °C; Splitless, chromatographic conditions: Initial temperature is 60 °C and holds 2 min; the heating-up rate is 10 °C/min; the final temperature is 300 °C and holds 20 min. Mass conditions: The ionization source is EI, and the temperature is 250 °C; the ionization energy is 70 eV; the scan rate is 1,000 cps, and the scan mode is full scan; the first mass is 35 amu, and the last mass is 650 amu.

Quantify the samples by the standard liquid of six kinds of phthalates including dimethyl phthalate (DMP), diethyl phthalate (DEP), dibutyl phthalate (DBP), di-2-ethylhexyl phthalate (DEHP), benzyl butyl phthalate (BBzP), and di-n-octyl phthalate (DOP). The concentrations of standards were 5, 10, 25, 50, and 100 µg/mL. The standard curve equation and correlation coefficient can be seen in Table 11.1. Table 11.1 showed that the correlation coefficients of phthalates were higher than 0.99.

In addition, to know phthalate concentration distribution in the source material which is important to build emission modeling for researchers and regulators, PVC flooring 4 was separated to 7 layers by scraping with a knife and then semi-qualitatively analyzed by infrared absorption spectroscopy (Shimadzu IR); the wavelength is 4000–400 cm^{-1}; the resolution is 4 cm^{-1}.

11.2.2 Quality Assurance and Quality Control

All the containers used in the entire experiment process are made of glass, and these glass apparatuses were baked for 4 h at 300 °C and cleaned with dichloromethane prior to use. The reagent blanks and laboratory blanks were free of phthalates. The recovery rate was measured by adding 10 µg phthalates into the regent blank samples and then the phthalate concentrations are measured. The results showed that it was in the range of 70–112 %.

11.3 Results and Discussion

11.3.1 Phthalate Concentrations in PVC Floorings and Wallpapers

The result of phthalate concentrations in PVC wallpapers (1, 2, 3, and 4) and PVC floorings (1, 2, 3, and 4) can be seen in Table 11.2. The results showed that only DEHP was detected and other five kinds of phthalates have not been

Table 11.1 The standard curve equation and correlation coefficient

Phthalate	Equation	R^2
DMP	$y = 3.88 \times 10^5 x - 1.73 \times 10^6$	0.996
DEP	$y = 6.83 \times 10^5 x - 2.04 \times 10^6$	0.993
DBP	$y = 1.12 \times 10^5 x - 4.80 \times 10^5$	0.994
BBzP	$y = 1.27 \times 10^5 x - 7.45 \times 10^5$	0.992
DEHP	$y = 2.05 \times 10^5 x - 1.01 \times 10^6$	0.994
DOP	$y = 4.16 \times 10^5 x - 2.18 \times 10^6$	0.994

Table 11.2 The phthalate concentrations in the PVC wallpapers and floorings (mg/g)

Materials	DMP	DEP	DBP	BBzP	DEHP	DOP
Wallpaper 1	–	–	–	–	2.35 ± 0.28	–
Wallpaper 2	–	–	–	–	0.134 ± 0.031	–
Wallpaper 3	–	–	–	–	200 ± 15	–
Wallpaper 4	–	–	–	–	44.4 ± 8.7	–
Flooring 1	–	–	6.86 ± 0.53	–	126 ± 21	–
Flooring 2	–	–	14.4 ± 2.1	–	124 ± 18	–
Flooring 3	–	–	–	–	69.1 ± 15.7	–
Flooring 4	–	–	–	–	230 ± 22	–

– no detection

detected in PVC wallpapers. DEHP concentration was in the range of 0.134–200 mg/g, and the relative standard error was from 7.5 to 23 % in PVC wallpapers. DBP and DEHP were detected in PVC flooring, and other four kinds of phthalates have not been detected. DBP and DEHP concentrations were in the range of nd-14.4 and 69.1–230 mg/g, respectively; the relative standard error was lower than 23 %.

Only DEHP was detected in the eight kinds of PVC materials wholly, which showed that DEHP was the main phthalate in these materials. DEHP was the most in the phthalate consumption structure in China [18]; moreover, some studies showed that DEHP concentration in the indoor settled dust was higher than other phthalates [4, 19] in China. Therefore, DEHP may be the most important indoor phthalate in China.

11.3.2 Phthalate Concentration Distribution in PVC Flooring

Figure 11.1a shows the spectra of the 7 layers from top to bottom of PVC flooring 4. Based on the characteristic for DEHP and PVC bands (Fig. 11.1b), it can be seen that lines in Fig. 11.1a have peak in characteristics for DEHP (as pointed by arrow) and for PVC (as marked with arrow and surrounded by an ellipse). It is obvious that the intensity of peak in characteristics for DEHP is the largest on the top layer, while the intensities of peak of substrate layers are smaller. This indicates that DEHP concentration in PVC flooring 4 is heterogeneous with largest value in the top layer and smaller values in substrate layers.

Fig. 11.1 Spectra of the 7 layers of PVC flooring 4 (**a**) and DEHP and PVC (**b**)
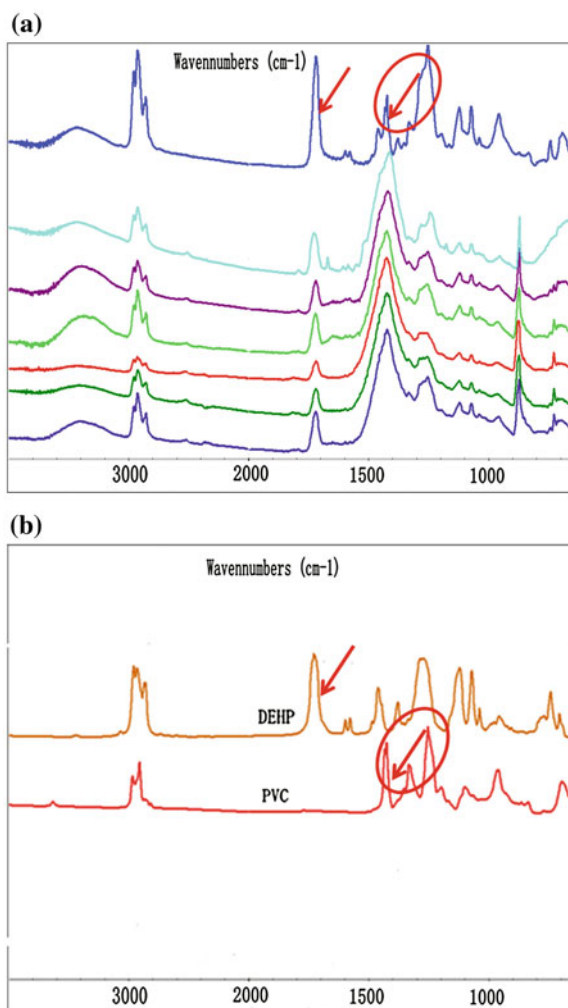
11.4 Conclusions

The concentrations of DEHP in PVC floorings were higher than in PVC wallpapers generally; therefore, PVC floorings can be more important source than PVC wallpapers. DEHP was the most abundant phthalate in these PVC materials and indoor settled dust in China; therefore, DEHP should be paid more attention and be studied much more in China. Phthalate concentration is heterogeneous, which tells that the researchers or regulators should pay attention to the homogenous assumption when developing emission models.

References

1. Guo Y, Alomirah H, Cho H-S, Minh TB, Mohd MA et al (2011) Occurrence of phthalate metabolites in human urine from several Asian countries. Environ Sci Technol 45:3138–3144
2. Durmaz E, Ozmert EN, Erkekoglu P, Giray B, Derman O et al (2010) Plasma phthalate levels in pubertal gynecomastia. Pediatrics 125:E122–E129
3. Hogberg J, Hanberg A, Berglund M, Skerfving S, Remberger M et al (2008) Phthalate diesters and their metabolites in human breast milk, blood or serum, and urine as biomarkers of exposure in vulnerable populations. Environ Health Perspect 116:334–339
4. Guo Y, Kannan K (2011) Comparative assessment of human exposure to phthalate esters from house dust in China and the United States. Environ Sci Technol 45:3788–3794
5. Ctepp-report (2002) A pilot study of children's total exposure to persistent pesticides and other persistent organic pollutants
6. Rudel RA, Perovich LJ (2009) Endocrine disrupting chemicals in indoor and outdoor air. Atmos Environ 43:170–181
7. Bornehag C-G, Sundell J, Weschler CJ, Sigsgaard T, Lundgren B et al (2004) The association between asthma and allergic symptoms in children and phthalates in house dust: a nested case–control study. Environ Health Perspect 112:1393
8. Abdul-Ghani S, Yanai J, Abdul-Ghani R, Pinkas A, Abdeen Z (2012) The teratogenicity and behavioral teratogenicity of di(2-ethylhexyl) phthalate (DEHP) and di-butyl Phthalate (DBP) in a chick model. Neurotoxicol Teratol 34:56–62
9. Toft G, Jonsson BAG, Lindh CH, Jensen TK, Hjollund NH et al (2012) Association between pregnancy loss and urinary phthalate levels around the time of conception. Environ Health Perspect 120:458–463
10. Gupta RK, Singh JM, Leslie TC, Meachum S, Flaws JA et al (2010) Di-(2-ethylhexyl) phthalate and mono-(2-ethylhexyl) phthalate inhibit growth and reduce estradiol levels of antral follicles in vitro. Toxicol Appl Pharmacol 242:224–230
11. Hauser R, Meeker JD, Duty S, Silva MJ, Calafat AM (2006) Altered semen quality in relation to urinary concentrations of phthalate monoester and oxidative metabolites. Epidemiology 17:682–691
12. Afshari A, Gunnarsen L, Clausen PA, Hansen V (2004) Emission of phthalates from PVC and other materials. Indoor Air 14:120–128
13. Clausen PA, Hansen V, Gunnarsen L, Afshari A, Wolkoff P (2004) Emission of Di-2-ethylhexyl phthalate from PVC flooring into air and uptake in dust: Emission and sorption experiments in FLEC and CLIMPAQ. Environ Sci Technol 38:2531–2537
14. Fujii M, Shinohara N, Lim A, Otake T, Kumagai K et al (2003) A study on emission of phthalate esters from plastic materials using a passive flux sampler. Atmos Environ 37:5495–5504
15. Xu Y, Little JC (2006) Predicting emissions of SVOCs from polymeric materials and their interaction with airborne particles. Environ Sci Technol 40:456–461
16. Xu Y, Hubal EAC, Clausen PA, Little JC (2009) Predicting residential exposure to phthalate plasticizer emitted from vinyl flooring: a mechanistic analysis. Environ Sci Technol 43:2374–2380

17. Larsson M, Hagerhed-Engman L, Kolarik B, James P, Lundin F et al (2010) PVC—as flooring material—and its association with incident asthma in a Swedish child cohort study. Indoor Air 20:494–501
18. Yu XX (2002) Analysis of plasticizer market. Advances in Fine Petrochemicals 3(7):24–27 (in Chinese)
19. Lin XT, Shen T, Yu XL, Wang XY (2009) Characteristics of phthalate esters pollution in indoor settled dust. J Environ Health 26:1109–1111 (in Chinese)

Chapter 12
An Exploration of Air-Conditioning System Control Strategies in Beijing-Based on the Results of Field Study

Min Li, Bin Cao, Yingxin Zhu and Qin Ouyang

Abstract The study carried out a long-period survey of indoor environmental parameters, the clothing of occupants, as well as people's voting of their sensation in public buildings and residential buildings in Beijing. Beijing belongs to the cold climate zone, which is cold in winter and hot in summer with short autumn and spring. The study was conducted in 2011 and 2012 and could be divided into four periods: (1) autumn (without HVAC), (2) winter (with heating), (3) spring (without HVAC), and (4) summer (with air-conditioning). The investigated places were classrooms, offices, and student dormitories. The investigated occupants were people who had lived in Beijing for long time and had adapted to the climate of Beijing well. The study was trying to explore people's requirement of indoor thermal environment. Relationships between thermal parameters and people's sensation were found, and some control strategies of indoor thermal environment were suggested. In consideration of occupants' thermal adaptation, the acceptable temperature range should be referred to, instead of the most "comfortable" neutral temperature, when deciding the control aim of indoor temperature.

Keywords Thermal comfort · Field study · Control strategy

12.1 Introduction

Indoor thermal environment quality has a very important impact on the comfort and health of building occupants. From the late twentieth century, the PMV model was widely used for prediction of human thermal sensation. However, in recent years, more and more study found out that the results predicted by the PMV were

M. Li · B. Cao · Y. Zhu (✉) · Q. Ouyang
Department of Building Science, Tsinghua University, Beijing 100084, China
e-mail: zhuyx@tsinghua.edu.cn

often different from those of thermal sensation vote (TSV). In the PMV model, the factors that decide the human thermal comfort include temperature, humidity, wind speed, radiant temperature, clothing insulation, and the metabolic rate [1]. But other field surveys show that there are many other factors which may make the sensation different, such as climate [2], gender, expectations [3]. Scholars have proposed a variety of new models to predict human thermal sensation, but there is no perfect model, which can apply to various conditions. It is necessary to precisely investigate people in certain types of building, to improve the indoor thermal environment quality, and to provide a reference for the energy saving. Therefore, the author investigated people who had adapted to the climate of Beijing in 2011–2012. The surveys were conducted in residential and public buildings. Different building types that may affect thermal sensation were considered.

12.2 Methods

12.2.1 Time, Place, and Instruments

Beijing belongs to the cold climate zone. Winter in Beijing is long and cold. Spring and autumn are short without heating or cooling. Summer is hot and rainy, and buildings in Beijing always have air-conditioning in summer.

The field study was conducted in the period from September 2011 to August 2012. The investigated places were classrooms, offices, and student dormitories. Respondents in classrooms and dormitory buildings were undergraduates, while the office respondents were white-collar workers.

The investigated classrooms and offices were classified as public buildings. The indoor environment parameters including air temperature, mean radiant temperature, relative humidity, and air velocity were measured by the AM-101 PMV and PPD indices meter. The investigated student dormitories were classified as residential buildings, and there was a WSZY-1 self-recording temperature–humidity recorder placed in each dorm to continuously record the indoor air temperature and humidity. The accuracies of AM-101 and WSZY-1 are shown in Tables 12.1 and 12.2.

The investigated classrooms were normally used for 30 students. During each investigation, the environmental parameters were recorded while the respondents filled out all the contents of the questionnaires. Classroom survey was conducted at

Table 12.1 Accuracy of the AM-101 PMV and PPD indices meter

Parameter	Accuracy (valid range)
Temperature	±0.5 °C (15–35 °C)
Relative humidity	±3 % (20–80 %)
Air velocity	±0.1 m/s (0–1 m/s)
	±0.5 m/s (1–5 m/s)

Table 12.2 Accuracy of the WSZY-1 self-recording thermometer and hygrometer

Parameter	Accuracy (valid range)
Temperature	± 0.5 °C (15–35 °C)
Relative humidity	± 3 % (20–80 %)

least once a week. Each time more than 40 questionnaires were retrieved. The investigated offices were in an ordinary office building. The operation of the investigation was almost the same with that in classrooms, which was conducted on weekdays and collected about 20 questionnaires per week.

The places for residential building surveys were 4-person dormitories. Investigators periodically (once or twice a week) reminded the respondents to fill out the online questionnaires (URL: http://www.sojump.com/). And the environmental parameters were recorded by the self-recording instruments.

12.2.2 Respondents

In order to avoid the effect of thermal adaptation caused by different regions, the investigated occupants were all people who had lived in Beijing for long time and had adapted to the climate of Beijing well. The basic information of the respondents is in Table 12.3.

In public building, 82 % of the questionnaires were filled in by 90 respondents whose ages were between 19 and 23, while 18 % were filled in by respondents whose ages were between 24 and 29.

12.3 Results and Discussion

12.3.1 Environment Parameters

The study could be divided into four periods. The investigation of residential buildings lasted for two periods (winter and spring). The distributions of the indoor environment parameters during those periods are shown in Fig. 12.1. And the investigation of public buildings lasted for four periods. The distributions of operative temperature and humidity are shown in Fig. 12.2.

Table 12.3 Basic information of the respondents

Building type	Gender	Age	Height (cm)	Weight (kg)
Public building	Male:female = 1:1.2	24 ± 5	168 ± 14	64 ± 18
Residential building	Male:female = 1:1.1	22 ± 2	168 ± 13	59 ± 11
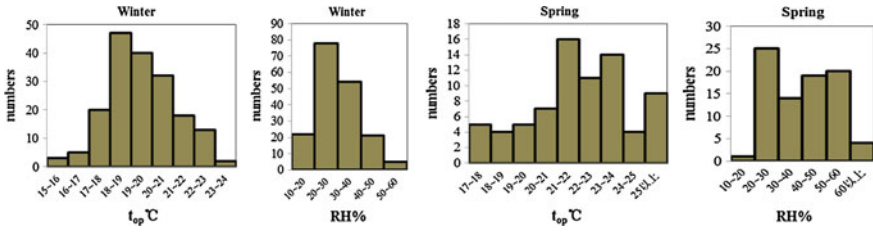
Fig. 12.1 Distributions of indoor environment parameters in residential buildings
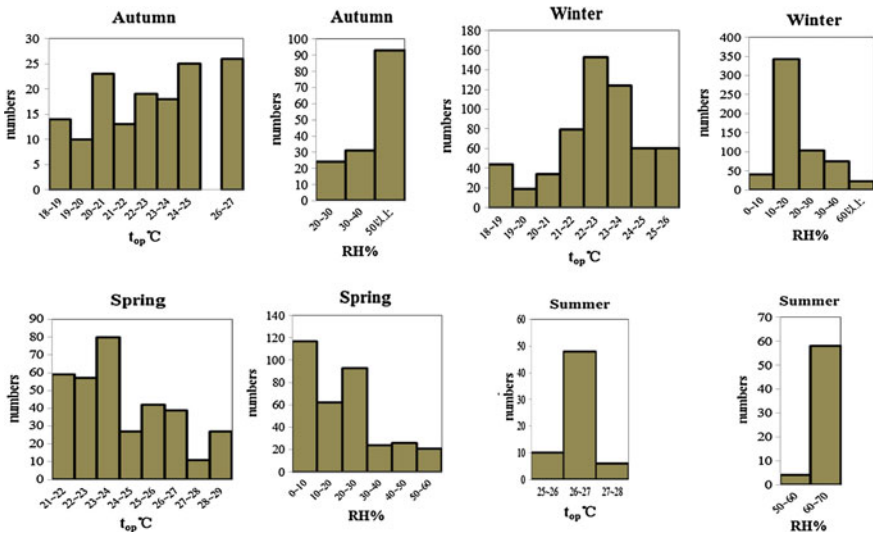
Fig. 12.2 Distributions of indoor environment parameters in public buildings

12.3.2 Clothing Insulation

Changing clothes to make thermal sensation close to neutral is a normal behavioral adjustment. In this study, what the respondents were wearing during the investigation was asked in the questionnaire. The clothing insulations in different seasons were not the same. Even at the same operative temperature, there was a big difference among people.

Figures 12.3 and 12.4 show the maximum and minimum clothing insulation in different seasons. When the operative temperature was the same, respondents dressed less in spring and autumn than in winter.

Adjustment of clothes is an important way by which people can adapt to their surround environments. According to the surveys, the occupants' clothes changed along with the indoor operative temperature. For the same indoor temperature in different seasons, people's clothing amount also showed difference. That was
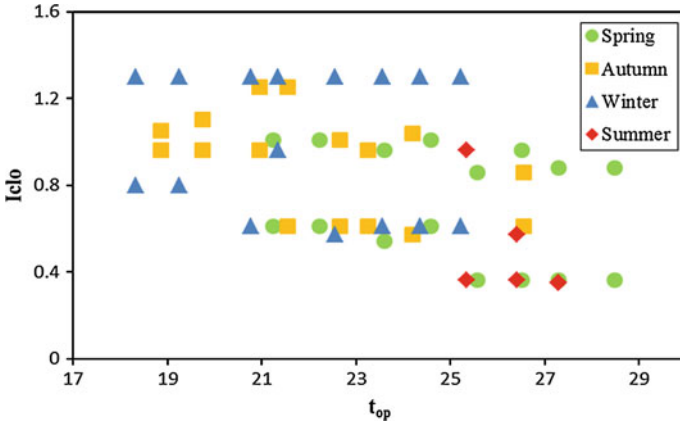
Fig. 12.3 Clothing insulation (clo) in public buildings

caused by thermal adaptation, which had impact on TSV as well. For the same operative temperature in the same season, respondents dress less in residential buildings compared with those in public buildings.

12.3.3 Thermal Sensation Vote

The relationships between operative temperature and Thermal Sensation Vote (TSV) (mean, highest, lowest) are shown in Figs. 12.5 and 12.6. The regression function of the mean TSV is as follows:
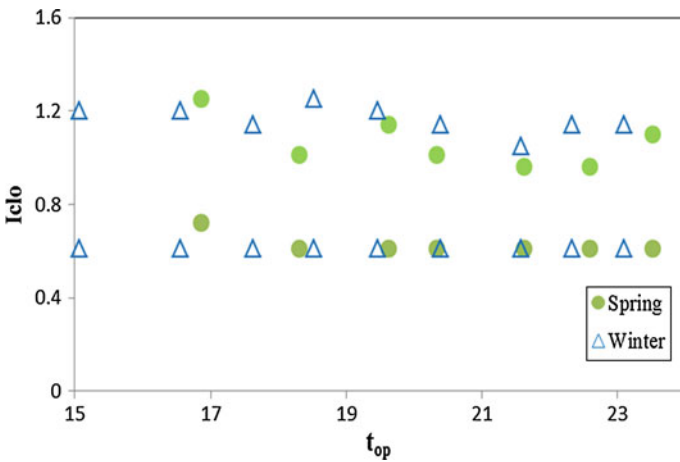
Fig. 12.4 Clothing insulation (clo) in residential buildings
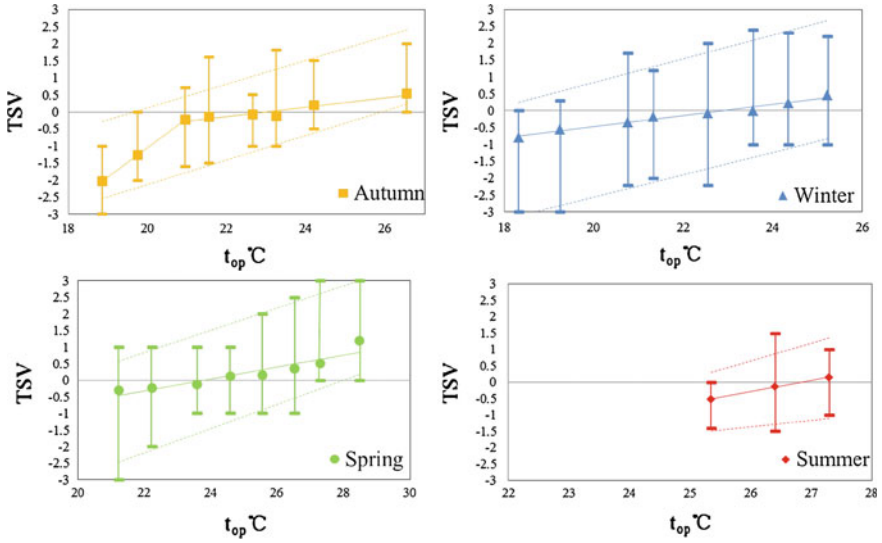
Fig. 12.5 The relationships between operative temperature and TSV in public buildings
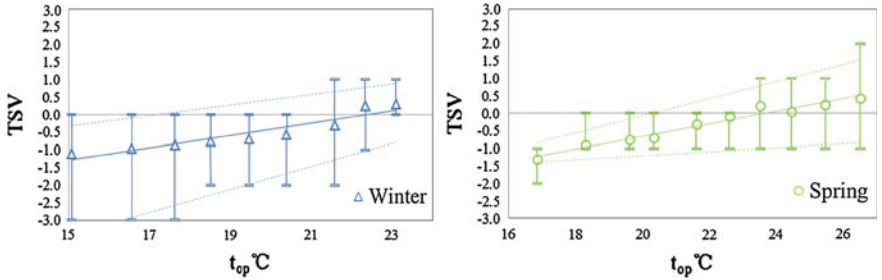
Fig. 12.6 The relationships between operative temperature and TSV in residential buildings

Public buildings		
Autumn	$t_{op} < 21\,^{\circ}\mathrm{C}$: $TSV = 0.8597t_{op} - 18.233(R^2 = 1)$	(1)
	$t_{op} \geq 21\,^{\circ}\mathrm{C}$: $TSV = 0.1361t_{op} - 3.1296(R^2 = 0.9168)$	
Winter	$TSV = 0.1644t_{op} - 3.7663(R^2 = 0.9745)$	(2)
Spring	$TSV = 0.1812t_{op} - 4.3151(R^2 = 0.8686)$	(3)
Summer	$TSV = 0.3416t_{op} - 9.1759(R^2 = 0.999)$	(4)
Residential buildings		
Winter	$TSV = 0.1743t_{op} - 3.8979(R^2 = 0.8828)$	(5)
Spring	$TSV = 0.1793t_{op} - 4.2422(R^2 = 0.9632)$	(6)

Table 12.4 The neutral temperature and the acceptable temperature range

Building type	Season	Neutral temperature (°C)	80 % acceptance (°C) $-0.5 < \mathrm{TSV} < 0.5$	Average clothing (clo)
Public buildings	Autumn	23.0	(20.6, 26.6)	0.85
	Winter	22.9	(19.9, 25.9)	1.15
	Spring	23.7	(21.0, 26.6)	0.79
	Summer	26.9	25.4 (low limit)	0.42
Residential buildings	Winter	22.4	19.5 (low limit)	0.94
	Spring	23.7	(20.6, 26.6)	0.72

Then, we can get the neutral temperature and the acceptable temperature range. This will be the basic for our control strategies. The data are shown in Table 12.4.

The neutral temperatures of people are different among seasons. In summer, the neutral temperature is the highest, while in winter it is the lowest. This means people have stronger adaptation of the cold environment in winter and stronger adaptation of the hot environment in summer. In every case, the acceptable temperature range was very wide, with the contribution of clothing adjustment. People's requirement of indoor temperature does not differ a lot between public buildings and residential buildings. We must take these conditions into account when we make control strategies.

12.4 Control Strategies

12.4.1 Public Buildings

According to the analysis of occupants' thermal sensation, control strategy of indoor environment by HVAC system can be summarized.

In spring and autumn, natural ventilation should be used prior to HVAC, since it can meet occupants' requirements in most conditions and save much energy. Only if when the indoor temperature is higher than 26.6 °C (the high limit of the accepted temperature range) or lower than 20.6 °C (the low limit of the accepted temperature range), cooling or heating may be considered.

In this study, the summer and winter investigations were conducted in air-conditioning or heating buildings. If the indoor environment is required to be kept at a high level, and the occupants' self-adjustments (e.g., changing clothes, moving, using fans) are limited strictly, the HVAC system needs to be controlled according to a strict requirement. The neutral temperature for air-conditioned room in summer is 26.9 °C, while the one for heating space in winter is 22.9 °C, in which conditions 95 % of the indoor occupants are satisfied. If the requirement of indoor environment is not so high and building energy consumption is concerned about, the second control aim is suggested. The acceptable temperature range for air-conditioned room in summer is 25.4–28.3 °C, while the one for heating space

in winter is 19.9–25.9 °C, in which conditions 80 % of the indoor occupants are satisfied. Meanwhile, people should have feasibility to determine their own clothes in order to adapt to the temperature.

12.4.2 Residential Buildings

Compared to public buildings, people's requirement of indoor temperature in residential buildings does not differ a lot. In winter, the neutral temperature was 22.4 °C, and this will be the strict requirement. While the lower limit of 90 % acceptable range is 19.5 °C, this will be the second aim. In spring, the neutral temperature was 23.7 °C, with the 80 % acceptable range of 20.9–26.5 °C. Natural ventilation should be used until the indoor temperature is higher than 26.5 °C or lower than 20.9 °C.

12.5 Conclusions

1. People's thermal comfort reactions differ among seasons. In summer, the neutral temperature of investigated people was 26.9 °C, while in winter the temperature was 22.9 °C. The differences were caused by several adaptive processes such as behavior adjustment (changing clothes, using cooling or heating, etc.), psychological expectation, and physical acclimatization.
2. When discussing control strategies for indoor thermal environment, the most important thing is how to meet the occupants' real requirements, in consideration of individual differences. This is an issue related to thermal adaptation. If the indoor environment is required to be kept at a high level, the HVAC system have to be highly centralized and the control aim of indoor temperature may be the neutral point. If the requirement of indoor environment is not so high and building energy consumption is concerned about, the acceptable temperature range is suggested to be the control aim. Meanwhile, people should have feasibility of self-adjustments (e.g., changing clothes, moving, using fans). In this way, each person can satisfy himself/herself by his/her own approach.

References

1. Fanger PO (1982) Thermal Comfort. Robert E. Krieger Publishing Company, Malabar
2. Cao B, Zhu Y, Ouyang Q, Zhou X, Huang L (2011) Field study of human thermal comfort and thermal adaptability during the summer and winter in Beijing. Energy Buildings 43:1051–1056
3. Fanger PO, Toftum J (2001) Thermal comfort in the future—Excellence and expectation. In: Proceedings of conference: moving thermal standards into the 21st century, Cumberland Lodge, Windsor, UK

Chapter 13
Spatial Distribution of Thermal Environment Parameters and its Impact on Passengers' Comfort in 14 Boeing 737 Aircraft Cabins

Weilin Cui, Qin Ouyang, Yingxin Zhu and Songtao Hu

Abstract Passengers' comfort in air craft cabin is related to many factors. Besides the level of thermal environment parameters, its spatial distribution in aircraft cabin and the place where passengers sit should also matters. In this investigation, a total of 14 Boeing 737 aircrafts including 7 airlines were measured. Each airline had two aircrafts, starting from Qingdao and returning right away after landing. Large-scale subjective questionnaire investigation regarding passengers' comfort was conducted on each flight. As a result, 979 questionnaires were collected. Thermal environment parameters' measurement contained air temperature and relative humidity, wall temperature, radiant temperature, air velocity, noise, illumination, and absolute pressure. The questionnaires collected basic information of passengers (age, height, weight, and clothes level) and their evaluation of the environment (thermal comfort, perceived air quality, and symptoms). The main purpose of this study is to investigate the spatial distribution of thermal environment parameters and find its relationship with passengers' comfort. Thus, different parts in aircraft cabin including both horizontal (front, middle, and back) and vertical (head, knee, and feet) were measured. The passengers' evaluation was also divided according to the place they sat (front, middle and back, window, middle and aisle). The results showed that the uniformity of air pressure and noise in aircraft cabin was quite good. Air velocity was under 0.2 m/s which was imperceptible for passengers. Air temperature was between 24 and 29 °C in all flight, and the deviation in each flight was below 3 °C. The average relative humidity was from 20 to 30 %, and the lowest was between 5 and 20 %. The difference between air temperature and black globe temperature was less than 1.4 °C. Spatial distribution of air temperature, black globe temperature, and relative humidity was relatively small (<3 °C, <10 %) on different cross-sections,

W. Cui · Q. Ouyang · Y. Zhu (✉)
Department of Building Science, Tsinghua University, Beijing 100084, China
e-mail: zhuyx@tsinghua.edu.cn

S. Hu
Department of Environment and municipal engineering, Qingdao Technological University, Qingdao 266033, China

while on the same cross-section, difference was smaller (<1 °C, <2 %). For vertical direction, temperature at the head was higher than the feet but within 2 °C. Wall temperature changed greatly during the flight especially the floor, usually 1–7 °C lower when taking off. Floor temperature near the window seat was generally lower than middle and aisle seat. Passenger was satisfied with cabin environment. Overall evaluation of environment showed no difference among passengers at front, middle, and back. However, passengers at window seat and middle seat showed more comfortable than those at aisle seat.

13.1 Introduction

Passengers' comfort is well related to aircraft cabin environment. In early studies, many researchers investigated cabin environment and its relationship with people. In 1999, Haghighat et al. [1] investigated the thermal environment and air quality on 43 commercial airline flights. Rankin et al. [2] collected data from 3,630 passengers on 71 flights in 1997. Because it is relatively difficult to investigate on real plane, many other researchers conduct their experiments in laboratories to simulate the real cabin environment. Park et al. [3] investigated the relationship between local and overall thermal comfort in a simulated aircraft cabin. Through all these researches, the environment conditions in aircraft cabins are generally well understood. For example, low humidity was considered a serious problem and could cause discomfort and some symptoms especially in long-haul flight [4].

However, some problems still exist. In previous studies, the environment measurement and comfort survey were always separated. Haghighat et al. [1] only measured cabin environment, and no passengers' comfort information was reported, while Rankin et al. [2] collected a large amount of questionnaires without the environment conditions. Besides, for almost all environment parameter measurement, a lumped parameter method was used which meant the environment was uniform in cabin.

In this study, the special distribution of parameters in aircraft cabin was investigated as well as passengers' comfort. The purpose of this paper is to provide more detailed information in aircraft cabin environment.

13.2 Methods

14 B737 aircrafts were included in this investigation. These aircraft belonged to 7 domestic airlines (Qingdao to Harbin, Beijing, Shanghai, Guangzhou, Shenzhen, Chengdu, Kunming), and each airline had 2 aircrafts. Eight environment

Fig. 13.1 Environment measurement devices

parameters were measured including air temperature, relative humidity, black globe temperature, pressure, noise, wall temperature, illumination, and air velocity. The measurement devices used were shown in Fig. 13.1. The parameters were recorded all through the flight. Air temperature, relative humidity, and black globe temperature were recorded automatically every 30 s, and other parameters were recorded manually. For example, pressure was recorded every minute when the plane took off and landed, and every 20 min at cruising period.

Of all these parameters, air temperature and relative humidity were measured at different points. Table 13.1 showed the detailed measure points on each aircraft. Four aircrafts were measured on one section, and ten aircrafts were measured on three sections. Table 13.1 showed the horizontal points. On vertical level, three measure points (head, knee, and foot) were set. For wall temperature, different points (ceiling, sidewall, and floor) were also measured.

The passengers' comfort survey was conducted at cruising period. On each plane, subjective questionnaires were distributed to some passengers. The questionnaires included 9 satisfaction surveys of environment parameters (air temperature, relative humidity, airflow, noise, pressure, vibration, seat comfort, air quality, and overall environment). A broken scale was used for evaluation: −1 (very unsatisfied), −0 (just unsatisfied), +0 (just satisfied), and +1 (very satisfied). Passengers' comfort at different sections in cabin was also investigated. In total, 979 questionnaires were collected.

Table 13.1 Detailed measure points on each aircraft

Measured type	Flight number	Air route	Detailed measure points (seat number)
One section	B1	Beijing to Qingdao	29B/29C (back)
	B2	Guangzhou to Qingdao	13A/13C/13D
	B3	Qingdao to Guangzhou	5D/5F
	B4	Shenzhen to Qingdao	12C/12D/12F
Three sections	B5	Chengdu to Qingdao	2D/15D/25D
	B6	Harbin to Qingdao	02C/16C/27C
	B7	Kunming to Qingdao	02C/02F/12C/24C
	B8	Qingdao to Beijing	07D/15D/25D
	B9	Qingdao to Chengdu	7D/15D/25D
	B10	Qingdao to Harbin	02C/16C/27C
	B11	Qingdao to Kunming	8D/15D/25D
	B12	Qingdao to Shanghai	10D/10F/27D
	B13	Qingdao to Shenzhen	9D/16D/24D
	B14	Shanghai to Qingdao	2D/12A/23B

13.3 Results

Figure 13.2 shows the results of air temperature and relative humidity. Each point was the average of all measured points. Air temperature range was from 24 to 29 °C. The difference between aircrafts was significant. The temperature deviation in one flight was from less than 1–3 °C. The minimum relative humidity in all flights was below 20 %, and some were even below 10 %. This represented the cruising period, and for the whole journey, the relative humidity was about 10 % higher. Figure 13.3 shows that the difference between air temperature and black globe temperature was generally within 1 °C.

Figure 13.4 shows the maximum difference among all measure points in each aircraft. The difference on the same section was minor, with air temperature and black globe temperature less than 1 °C and relative humidity less than 2 %. This means parameter value on one section was relatively uniform. The difference among different sections was larger, with air temperature and black globe temperature less than 3 °C and relative humidity less than 10 %.

Figure 13.5 shows the difference between air temperature and relative humidity between head and foot. It could be concluded that air temperature at head level was generally higher than foot level and the difference was within 3 °C. Most measure points indicated that relative humidity at head level was lower than foot level. But the difference was small, generally less than 4 %.

Figures 13.6 and 13.7 show the results of wall temperature. Figure 13.6 indicated that the floor temperature was generally lower than ceiling and sidewall temperature. During the flight, the change in floor temperature was greater than ceiling and sidewall temperature. For sidewall and floor, the greatest change was about 4 °C. For floor temperature, the greatest change was about 7 °C. Figure 13.7 shows the results of floor temperature at different measure points. The difference among aircrafts was different. For aircraft B6 and B10, the temperature of the window floor was lowest and the temperature of aisle floor was highest, with the temperature of the middle seat floor between. But for B12 and B14, the results were rather close. Yet from Fig. 13.7, it could be seen that the temperature of window floor changed greater than middle and aisle floor.
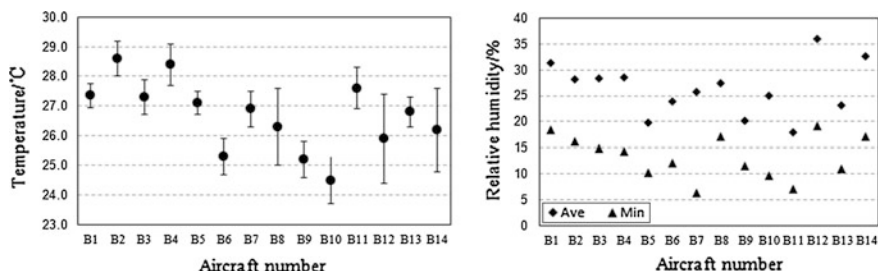
Fig. 13.2 Air temperature and relative humidity
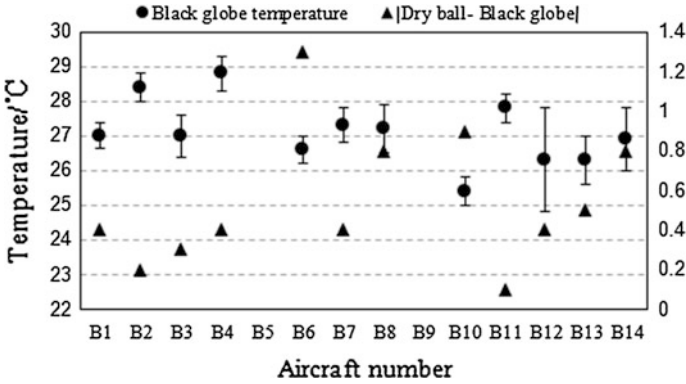
Fig. 13.3 Black globe temperature and its difference with air temperature
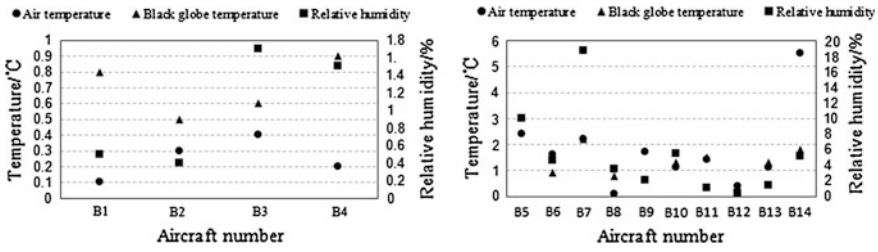
Fig. 13.4 The maximum difference among all measure points in each aircraft
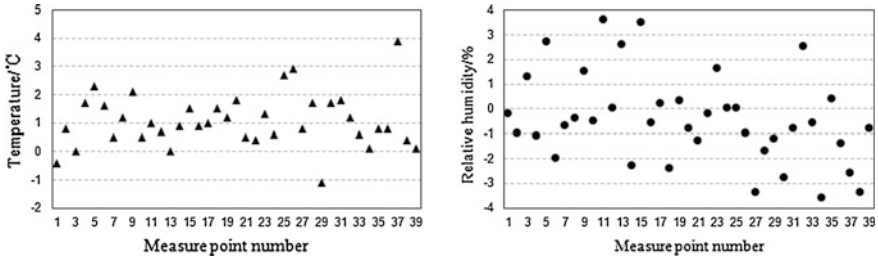
Fig. 13.5 The difference between air temperature and relative humidity between head and foot

Table 13.2 shows the results of the questionnaires. The average values of the vote were above 0, which meant the passengers were generally satisfied with the environment. Yet the values were below 0.4, which meant passengers were not very satisfied with the environment. Of all the parameters, the noise was the most unsatisfying parameter, only 0.06 on average for all aircrafts.

Figure 13.8 shows the results of overall environment evaluation in different parts of the cabin (front, middle, and back) and different seat positions (aisle,
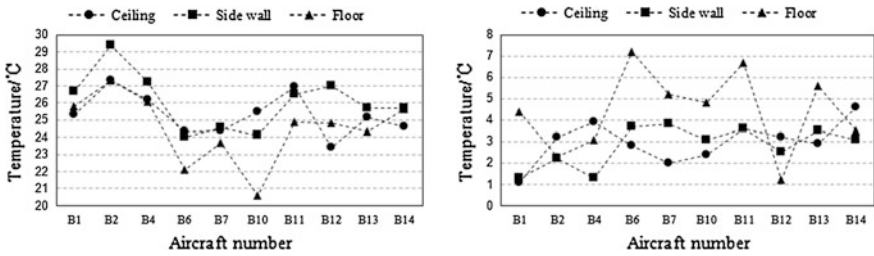
Fig. 13.6 Average wall temperature of ceiling, sidewall, and floor (*left*) and the maximum difference in a whole flight for each measure point (*right*)
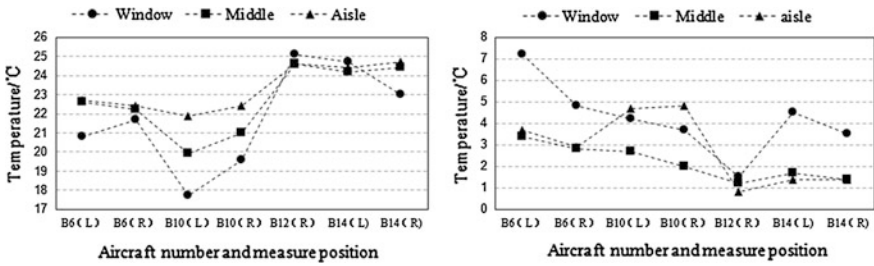
Fig. 13.7 Average temperature floor at different measure points (*left*) and the maximum difference in a whole flight for each measure point (*right*)

Table 13.2 Results of questionnaires (average value)

Flight number	Temperature	Humidity	Airflow	Noise	Pressure	Vibration	Seat comfort	Air quality	Overall envir.
B1	0.1	0.14	0.22	−0.01	0.12	0.19	0.14	0.21	0.17
B2	0.27	0.15	0.13	−0.02	0.22	0.16	0.11	0.21	0.16
B3	0.41	0.24	0.19	0.08	0.17	0.12	0.18	0.28	0.18
B4	0.21	0.18	0.18	0.05	0.16	0.21	0.14	0.17	0.19
B5	0.3	0.22	0.21	0.1	0.2	0.11	0.2	0.23	0.24
B6	0.32	0.35	0.27	0.22	0.29	0.29	0.19	0.36	0.3
B7	0.33	0.19	0.21	0.06	0.23	0.17	0.19	0.27	0.19
B8	0.16	0.14	0.17	0.04	0.07	0.13	0.08	0.17	0.14
B9	0.23	0.16	0.21	0.05	0.17	0.13	0.18	0.23	0.18
B10	0.33	0.25	0.3	0.09	0.18	0.24	0.13	0.23	0.19
B12	0.26	0.19	0.15	0.05	0.12	0.09	0.02	0.19	0.11
B13	0.25	0.21	0.23	0	0.17	0.23	0.16	0.25	0.19
B14	0.22	0.26	0.18	0.09	0.12	0.21	0.26	0.23	0.29
Ave.	0.26	0.21	0.20	0.06	0.17	0.18	0.15	0.23	0.19
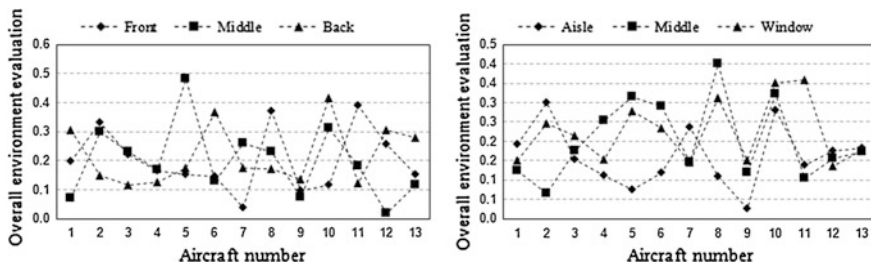
Fig. 13.8 Overall environment evaluation at different positions in each aircraft

middle seat, and window seat). The results indicated that passengers' comfort at front, middle, and back of the cabin was close and it was difficult to tell which part was better for comfort. Passengers' comfort at window seat and middle seat was slightly better than aisle seat.

13.4 Discussions

Many parameters in aircraft cabin affect passengers' comfort, such as air temperature, relative humidity, black globe temperature, wall temperature, pressure, noise, airflow, vibration, and so on. Some parameters are uniform in the cabin, such as pressure, noise, vibration. Passengers feel no difference at different parts in the cabin. But for other parameters like temperature and humidity, it is more likely to show different spatial distributions in the cabin. For example, air temperature may be different at different sections in the cabin, which will cause difference in passengers' comfort.

In this paper, the spatial distribution of air temperature, relative humidity, black globe temperature, and wall temperature was studied. The passengers' evaluation of the environment was also investigated. It was noticeable that although environment was different in different aircrafts, the passengers' comfort was still at the same level. For example, the air temperature of B2 was about 5 °C higher than B10, but the vote for temperature was very close, 0.27 and 0.33, respectively. The factors influencing passengers' comfort were complicated and needed further research.

The aircrafts in this study were all B737. In other aircraft types, the distribution of these parameters is still unknown. In future work, it is necessary to investigate other aircraft types.

13.5 Conclusions

The main results could be concluded as follows:

1. The distribution of air temperature and relative humidity on the same section was relatively uniform, and on different sections, the difference was more significant.
2. Black globe temperature was close to air temperature.
3. The floor temperature was lower than ceiling and sidewall temperature, and the window floor temperature was lower than aisle and middle seat floor.
4. The passengers at front, middle, and back of the cabin showed no big difference in comfort, and passengers at window seat and middle seat were slightly better in comfort than in aisle seat.

References

1. Haghighat F, Allard F, Megri AC et al (1999) Measurement of thermal comfort and indoor air quality aboard 43 flights on commercial airlines. Indoor Built Environ 8:58–66
2. Rankin WL, Space DR, Nagda NL (2000) Passenger comfort and the effect of air quality. American Society for Testing and Materials, West Conshohocken
3. Park S, Helwig RT, Grun G, Holm A (2011) Local and overall thermal comfort in an aircraft and their interrelations. Build Environ 46:1056–1064
4. Nagda NL, Hodgson M (2011) Low relative humidity and aircraft cabin air quality. Indoor Air 11:200–214

Chapter 14
Field Study and Adaptive Equation of Thermal Comfort in University Classrooms in the Subtropics in Winter

Qiuhua Tao and Zhengrong Li

Abstract In order to study the indoor thermal comfort in the winter of subtropics region in which there is no heat supply system, field study of indoor thermal comfort was carried out in classrooms of a university in Xiamen. Data both from field measurements and questionnaire survey were collected and analyzed. Consequently, the neutral and preferred temperatures in the winter of Xiamen were obtained, which show slightly difference with previous studies across China. On the other hand, predicted mean vote (PMV), which was calculated by Thermal Comfort Program software, shows some deviations from the mean thermal sensation (MTS) summarized from questionnaires statistics. Finally, by using multivariate nonlinear regression model based on MATLAB, a new adaptive equation was developed, which could be used to predict the thermal response in classrooms in subtropics region. In addition, it was found that the predicted equation fits very well with the collected data, which reflects variation of thermal sensation in winter. Results from this study provide guidance for the measurement and prediction of thermal comfort in winter of the subtropics region.

Keywords Thermal comfort · Neutral temperature · Preferred temperature · Adaptive equation · Subtropics climate

Q. Tao (✉)
Institute of Energy and Power Engineering, Jimei University, Xiamen, China
e-mail: taojiangshui@163.com

Q. Tao · Z. Li
College of Mechanical Engineering, Tongji University Shanghai, Shanghai, China

14.1 Introduction

With the enhanced awareness of health and comfort, people's demand on the indoor environment is increasing. The outdoor temperature is actually very low in many subtropics regions in winter, such as 5 °C in Hong Kong, Xiamen, and there is no heat supply system in these regions. However, very little attention was paid to the indoor thermal condition in winter. It was suggested, from comparisons of many previous field studies, that people in hot climates might prefer a sensation slightly cooler than neutral, while people in cold climates might prefer a sensation slightly warmer than neutral [1]. Humphreys and Nicol [2] have presented, from extensive field studies conducted in European offices and from the de Dear database, that the desired sensation on the ASHRAE scale depended not only on the prevailing outdoor temperature, but also upon the current indoor temperature. People preferred, on average, sensations on the warm side of neutral if it was cool outdoors and warm indoors, while they preferred sensations cooler than neutral if it was warm outdoors and cool indoors. International standards to describe comfortable indoor thermal environments [3, 4] are based on theoretical analyses of human heat exchange with the environment, which were calibrated using the results from experiments in special climate-controlled laboratories or climate chambers. Fanger's PMV and PPD indices [5] recommended in ISO 7730 [6], and ASHRAE 55-2004 [7] standards predict a numerical value for the mean subjective response to the thermal environment on the ASHRAE scale from six thermal variables. A large number of field studies showed that Fanger's PMV index is applicable in air-conditioned environment [8, 9]. However, the results from naturally ventilated cases [9–11] often failed to support laboratory-based models and thermal comfort standards. Passive methods to achieve thermal comfort in buildings are the ideal solution to provide a healthy and energy efficient indoor environment [12]. In order to investigate the indoor thermal comfort in the winter of the subtropics region, of course without heat supply, field test and questionnaire survey were carried out in university classrooms in Xiamen.

14.2 Methodologies

A field study was conducted within 6 classrooms in a university in Xiamen, from December 2009 to February 2010. About 200 students aged from 18 to 25 were involved in the study. The male-to-female ratio is about 4:1.

Data from both measurements and questionnaires survey were simultaneously collected in each classroom.

14.2.1 Measuring Equipment

In the indoor environment, variables such as air temperature, relative humidity, air velocity, and bubble globe temperature were collected. The air temperature and relative humidity were measured using the multipurpose measuring instrument (Swema Air 3000). The air velocity was measured using a hot-wire anemometer (EY3-2A). Average radiation temperatures are measured using bubble globe temperature thermometer, according to ANSI/ASHRAE Standard 55-2004 [7].

14.2.2 Subjective Questionnaire

In parallel with the field test, a subjective questionnaire survey was also conducted. The content of the questionnaire included clothing thermal resistance, thermal sensation, and local discomfort. The thermal sensation scale was the traditional ASHRAE 7-point scale. In the statistical process, the clothing thermal resistance and thermal sensation vote were collected for each field test.

Totally, 34 field tests were taken and 620 effective questionnaires were obtained.

14.3 Results and Analysis

14.3.1 Outdoor Climates

Figure 14.1 gives the outdoor temperature and relative humidity of each test during the survey period from December 2009 to February 2010. Air temperature (t_o) ranged between 7 and 20.4 °C, with an average of 27 °C. Relative humidity (RH) fell within 40.2 and 90 %. Air velocities ranged from 1 to 5 m/s.
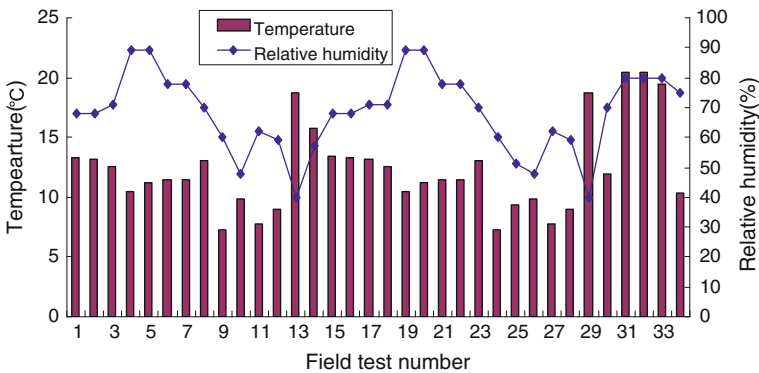
Fig. 14.1 Outdoor temperature and relative humidity of each test

14.3.2 Indoor Environmental Parameters

Figure 14.2 gives the statistical summary of indoor environmental parameters measured during the survey. Air temperature (t_a) ranged between 13.1 and 24.1 °C. Relative humidity (φ) fell within 45 and 80 %. Air velocities ranged from 0.01 to 0.10 m/s. The bubble globe temperature is converted to an average radiation temperature t_r, ranged between 13.1 and 23.5 °C.

14.3.3 Thermal Comfort Responses

The frequency distribution of thermal sensation votes is given in Table 14.1. It is obvious that more than 1/3 of the occupants felt just right (0). And 90.3 % of the votes ranged from "−1" (slightly cool) to "+1" (slightly warm). Only 9 % of the occupants felt cold or very cold. The mean thermal sensation vote is −0.54, between neutral and slightly cool.

14.3.3.1 The Neutral Temperature

The relationship between the mean thermal sensation (MTS) and indoor temperature (t_a) is plotted in Fig. 14.3.

The linear regression equation is fitted for these thermal sensations against air temperature:

$$MTS = 0.0972t_a - 2.0293 \tag{14.1}$$

Fig. 14.2 Indoor temperature and relative humidity of each test
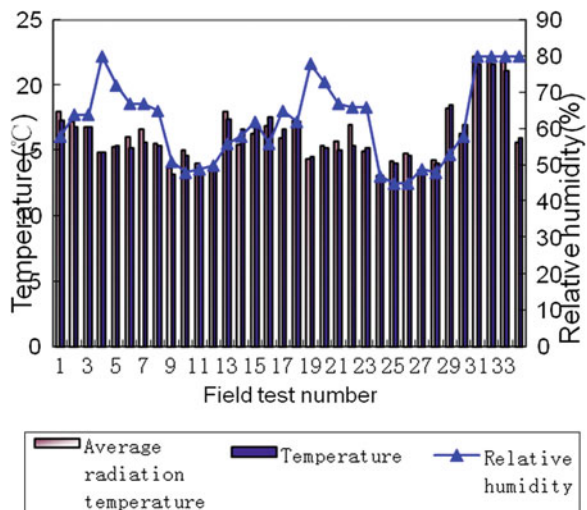
Table 14.1 The distribution of thermal sensation vote

Thermal sensation vote	−3	−2	−1	0	1	2	3
Distribution	1	55	265	261	34	4	0

Fig. 14.3 Relationship between MTS and indoor air temperature
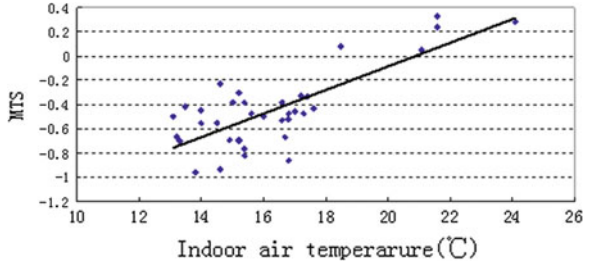
where t_a is the air temperature, and MTS is the mean thermal sensation vote.

The neutral temperature is obtained by solving Eq. (14.1) for a mean thermal sensation vote of zero, and the neutral air temperature $t_n = 20.9$ °C, which is slightly lower than the result of Hong Kong [13] and Chongqing [14]. Results comparison is shown in Table 14.2.

14.3.3.2 The Preferred Temperature

Thermal comfort can also be defined as "a condition where people prefer neither warmer nor cooler" [15]. Further analysis was carried out to find out the preferred temperature based on the result of three scales thermal preference—Mc Intyre scale. According to the answers to the question on the questionnaire: "At present, would you prefer warmer, no change or cooler?" The statistics analysis adopted probit analysis where the survey data were classified into an indoor air temperature bin (0.5 bin). Probit analysis was performed separately for preference vote of "hope to be cooler" and "hope to be warmer." In this separate analysis, the number of preference votes (hope to be warmer or hope to be cooler) was proportionally weighted with the subtotal number of votes in each indoor air temperature bin, shown in Fig. 14.4.

The regression equations were fitted for "hope to be warmer" and "hope to be cooler" against indoor air temperature:

Hope to be warmer: $M_{ww} = 0.1224t_a^2 - 1.1104 + 1.3442t_{a\prime}$, $R^2 = 0.919$;
Hope to be cooler: $M_{wc} = 0.0903t_a^2 - 0.3.8715t_a + 43.127$, $R^2 = 0.913$.

Table 14.2 Contrast of neutral temperature in three subtropics regions in winter

Region	Hong Kong	Xiamen	Chongqing
Neutral temperature	21.4	20.9	21.2

Fig. 14.4 Probit regressive model of preferred temperature
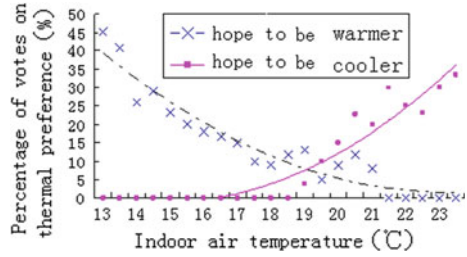
Therefore, the preferred temperature t_p is 19.4, which is 1.5 °C lower than the neutral temperature t_n (20.9 °C). The thermal environment accepted by people may be higher or lower than the neutral temperature, and one living in cold regions would expect slightly warmer, while those living in hot regions may prefer slightly cooler [12]. Results of this study in subtropics region Xiamen show that the preferred temperature is not equal to the neutral temperature and close to cooler side, which is consistent with the conclusion of Ref. [12].

14.3.4 Comparison Between MTS and PMV

Many factors affect human thermal sensation, including objective factors (the ambient air temperature t_a, relative humidity φ, mean radiant temperature t_r, and air velocity v and air quality) and subjective factors (the activities of occupants M, the clothing I_{clo}, living habits, and so on) [16, 17]. A program was developed according to Ref. [4] to calculate predicted mean vote (PMV) of test conditions, and the results are compared with the mean thermal sensation (MTS) obtained from questionnaires statistics, as shown in Fig. 14.5.

It can be seen from Fig. 14.5 that there are some deviations between MTS derived from questionnaires statistics and calculated PMV via measurements,
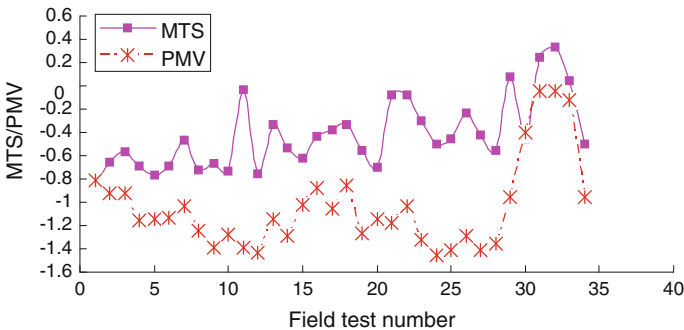
Fig. 14.5 Contrast between PMV and MTS of each test

which underestimate the body's tolerance to cool environment and adaptability. Obviously, it is inappropriate to predict the thermal comfort of non-heating environment in winter by using ISO7730. New thermal comfort prediction equation should be developed for non-heating environment in the subtropics.

14.3.5 Nonlinear Regression of Thermal Comfort Equation

According to references [18], the relationship between influencing factors and PMV was nonlinear. Therefore, multivariate nonlinear regression model was developed to search for functional relationship between the mean thermal sensation (MTS) and influencing factors, namely MTS = $f(t_a, \varphi, t_r, v, M, I_{clo})$. Because students are sitting down, the impact of metabolic ratio (M) is not taken into account, which is set as 69.78 W/m^2. Therefore, above function is simplified to MTS = $f(t_a, \varphi, t_r, v, I_{clo})$.

Using multivariate nonlinear regression model based on MATLAB, MTS as the dependent variable, t_a, φ, v, I_{clo} and as independent variables, the assumption regression equation is as follows:

$$\text{MTS} = b_1 + \frac{b_2 t_a \cdot e^{0.02 t_r}}{I_{clo}} + b_3 \varphi \cdot e^{-0.7 t_a} + \frac{b_4 v \cdot \bar{t}_r}{I_{clo}} \tag{14.2}$$

Empirically, it is assumed that the initial values $b_1 = -3$, $b_2 = 0.1$, $b_3 = 1.0$, $b_4 = 0.5$, and also $b_2 > 0$. After 21 iterations, the optimal solution is obtained, and they are $b_1 = -1.226$, $b_2 = 0.042$, $b_3 = 79.785$, $b_4 = -0.373$, and goodness of fit $R^2 = 0.663$, which indicates that the model can explain 66.3 % of the variation of the dependent variable. Finally, MTS regression equation was developed:

$$\text{MTS} = -1.226 + \frac{0.042 t_a \cdot e^{0.02 t_r}}{I_{clo}} + 79.785 \varphi \cdot e^{-0.7 t_a} - \frac{-0.0373 v \cdot \bar{t}_r}{I_{clo}} \tag{14.3}$$

14.4 Conclusions

1. In classrooms, without heat supply, in the winter of subtropics region, 90.3 % of the recorded votes ranged from "−1" (slightly cool) to "+1" (slightly warm), and only 9 % of the occupants felt cold or very cold. The mean thermal sensation vote is −0.54, which is between neutral and slightly cool.
2. A neutral temperature of 20.9 °C is obtained by regression analyses of TSV on indoor temperature, which is slightly different from results of resent studies in China.

3. The preferred temperature of 19.4 has 1.8 °C lower than the neutral temperature, which is consistent with the conclusions of Humphreys.
4. It is not appropriate to predict the thermal comfort of non-heating environment using the PMV index of ISO7730. A new adaptive Eq. (3) was developed to predict the thermal response in classrooms without heat supply in subtropics region. The new adaptive equation gains goodness of fit, which, to some extent, is able to reflect the variation of thermal sensation in winter of subtropics region.

References

1. de Dear RJ, Brager GS (1998) Developing an adaptive model of thermal comfort and preference. ASHRAE Trans 104(1):145–167
2. Humphreys MA, Nicol JF (2004) Do people like to feel ''Neutral''? Response to the ASHRAE scale of subjective warmth in relation to thermal preference, indoor and outdoor temperature, ASHRAE Transactions 110(2):569–577
3. ISO (1994) International Standard 7730, Moderate thermal environments: determination of PMV and PPD indices and specification of the conditions for thermal comfort. International Organization for Standardization, Geneva
4. Ashrae (1992) Standard 55–92, Thermal environmental conditions for human occupancy, American Society of Heating, Refrigeration and Air-conditioning Engineers, Atlanta, Georgia, USA
5. Fanger PO (1970) Thermal comfort. Danish Technical Press, Copenhagen
6. ISO (2005) International Standard 7730, Ergonomics of the thermal environment— Analytical determination and interpretation of thermal comfort using calculation of the PMV and PPD indices and local thermal comfort criteria. International Standard Organization, Geneva
7. ASHRAE (2004) ANSI/ASHRAE Standard 55 2004. Thermal environmental conditions for human occupancy
8. de Dear RJ, Fountain ME (1994) Field experiments on occupant comfort and office thermal environments in a hot-humid climate. ASHRAE Trans 100(2):457–475
9. Farraj F, Al-ajm DL (2010) Indoor thermal conditions and thermal comfort in air-conditioned domestic buildings in the dry-desert climate of Kuwait. Build Environ 45(3):704–710
10. Nicol F (2004) Adaptive thermal comfort standards in the hot-humid tropics. Energy and Buildings 36(7):628–637
11. Hwang RL, Lin TP, Kuo NJ (2006) Field experiments on thermal comfort in campus classrooms in Taiwan. Energy and Buildings 38(1):53–62
12. Li J (1996) The bioclimatic features of vernacular architecture in China. Renewable Energy 8:629–636
13. Mui KW, Wong LT (2007) Neutral temperature in subtropical climates—A field survey in air-conditioned offices. Build Environ 42:699–706
14. Yao R, Liu J, Li B (2010) Investigation and analysis on classroom thermal environment in winter in Chongqing. Appl Energy 87:1015–1022

15. Fanger PO (1972) Conditions for thermal comfort—a review, In: Proceedings of the Symposium on Thermal Comfort and Moderate Heat Stress (article in CIB W45), Building Research Establishment, UK, pp 3–15
16. Goldman RF (1999) Extrapolating ASHRAE's comfort model. HVAC&R Research 5(3):189–194
17. Fanger PO (1972) Thermal comfort. McGraw-Hill, NY
18. huamei Z (2007) Research on calculate method of PMV under heating in winter through nomograph and equation. Building Energy Environ 26:45–50

Chapter 15
Effects of Airflow on Thermal Comfort Before Sleep Onset in a Warm and Humid Climate

Minlin Zhu, Qin Ouyang, Henggen Shen and Yingxin Zhu

Abstract Fans are widely used in southeast of China to increase heat loss day and night in summer time. However, all-night rotating speed control system, which can produce sleep-friendly airflow, has not been proposed under rigorous human experimental results. Sleeping mode, nowadays, prevailing on the market, are figured out by testing, to be a variant of the simulated natural wind model which is a beta product in the laboratory, thus the so-called sleeping fans are likely to cause rheumatic pain or even temporary paralysis after all-night usage. In this study, customs of using fans during the sleep by Chinese people from different regions and ages are collected through an Internet survey distributed in the summer time. The results of the survey show the necessity of sleep-friendly airflow, customary fan displacement and the preference to the fan type, which partly become the fundamental settings of the human experiment. The human experiment in this study is a preliminary exploration of the airflow preference preceding sleep initiation, which is based on a theoretically possible interaction level in the circadian regulation of sleep that changes in skin temperature rather than core temperature causally affect sleep propensity, for the reason that airflow not only increases heat loss which causes thermal sensation but also stimulates tactile sensation in the skin. In this part, mechanisms and functions of coupling between sleep and body temperature rhythms are given with some physiological and neurobiological findings which can be seen in abundant researches. In the human experiment, subjects were wearing short pyjamas supine on a bed covered by rattan mat with a towel blanket under the following conditions: air temperature(Ta) 30 °C, relative humidity(RH) 60 % and air velocity(V) 0.6, 1.0, 1.5 and 2.0 m/s. Common protocol of subjective evaluation on the effect of airflow is obtained for all subjects. TSV declines with increasing air velocity and arrives at 0.5 when air velocity is

M. Zhu (✉) · H. Shen
School of Environmental and Science Engineering, Donghua University, Shanghai, China
e-mail: Mandy_Zhu@live.com

M. Zhu · Q. Ouyang · Y. Zhu
School of Architecture, Tsinghua University, Beijing, China

around 0.8 m/s, 0.2 m/s lower than that under upright condition. Nearly all subjects prefer the airflow with a constant air velocity to the simulated natural wind with a changeable air velocity. The draft is mainly from too high air velocity and immobile airflow direction.

Keywords Sleep · Skin temperature · Airflow · Supine

15.1 Introduction

Sleep occupies approximately a third of our lives, and despite decades of study on the thermal comfort within indoor environment, we are only just beginning to understand the role that thermal environments play in human sleep. We now know that human sleep is likely to be either disturbed or facilitated by certain thermal environments. Optimal ambient temperatures for different sexes and ages are most studied among researchers [1–13]. In recent years, for the sake of energy saving, airflow has been widely proposed to offset temperature rise in warm and humid climate. It has been shown that thermal sensation during sleep reaches neutral and wakefulness is significantly reduced with proper airflow in a warm and humid sleeping environment (32/80) [14]. Actually, before the birth of mechanical fans and air conditioners, our ancestors have already used natural ventilation to disperse indoor heat and humidity to make a sleep-friendly environment [15]. Nowadays, fans are widely used in southeast of China to increase heat loss during summer night, although air conditioners have been quite popular in urban areas. To meet people's growing needs for thermal comfort in sleep, almost all fans on the market begin to be equipped with sleeping mode and are sold with much higher prices than ordinary ones. The so-called sleep mode, however, is figured out by our testing as a variant of the simulated natural wind mode which is still a beta product in the laboratory, thus those sleeping fans may still cause rheumatic pain or even temporary paralysis after all-night usage. Then, it turns out to be necessary to design an all-night rotating speed control system for the sleep mode of home fans, which can really produce sleep-friendly airflow.

In this study, we only explore the airflow preference preceding sleep initiation by human experiment according to the surveyed results. The mechanisms of sleep are discussed before experimental method being introduced.

15.2 Mechanisms Under Sleep Regulatory Systems

Sleep can be defined as a natural periodic state of immobility where the individual is relatively unaware of the environment and unresponsive to external sensory stimuli. Nearly all voluntary muscles become inactive, and metabolic rate is

reduced. The brain, however, is far from inactive; brain wave display characteristic patterns differ from those displayed during wakefulness or coma [16]. Sleep seems important for humans, despite the desire to be well rested and to make up for lost sleep in order to maintain normal function does not account for the purpose of sleep. Sleep loss has been proved to cause mental and physical disorders [17]. The average amount of sleep that the majority of people actually obtain is between 7 and 7.5 h. Too little or too much sleep over prolonged periods can be detrimental, and both are associated with increased mortality [18]. What we are most concerned about in this study is our regulatory mechanism of sleep timing since thermal comfort depends on whether the rhythm of environmental changes is synchronized with the needs of our body according to the sleep stages. In mammals and birds, sleep is divided into two main types: rapid eye movement (REM) sleep and non-REM (NREM) sleep. In humans, non-REM sleep process is further subdivided into four stages of increasing depth: Stage 1–4, termed S1, S2, S3 and S4, according to sleep scoring criteria [19]. More recently, the American Academy of Sleep Medicine has produced an updated classification where stages N1, N2 and N3 broadly replace stages S1, S2 and S3/S4, respectively [20], but the new system has not yet been adopted by major laboratories and clinics. Different sleep stages do have a distinct preference to thermal environments, but in this study, we tend to look at its higher level of control system inside brain. There are two underlying biological processes controlled by the brain that play a large role in determining our sleep/wake cycle. They are the circadian process (C) and the homeostatic recovery process (S). The circadian and homeostatic processes are separate but interacting and have become known as the two-process model of sleep [21]. The circadian and homeostatic mechanisms determine what time of day we are most likely to fall asleep, how deeply and for how long. The relation between body temperature and sleep has long been discussed, and the change of body temperature is actually driven by the circadian rhythm. The two processes are able to compensate for one another: if, for example, you stay awake all night, the build-up of the S process will be overridden by the C process intervening in the early morning. This means that even if you have gone without sleep for a night, you are still able to function the following day, albeit with reduced performance. Human can manage to stay awake relatively well for periods up to 72 h. After this, our homeostatic drive to sleep is so strong that we can no longer force ourselves to stay awake [3]. This phenomenological result implies that apart from the two-process model, there must have been a third process which is involved in controlling the sleep/wake cycle and can override the circadian and homeostatic propensity for sleep if it is necessary to stay awake. 'Allostatic' process is most recently identified—from the Greek (allo, stasis) meaning 'remaining stable by being variable'. This is the mechanism by which sleep timing and duration can be controlled by external forces such as social and ecological cues [22]. These three processes, corporately determine the vigilance state of human sleep, and all can be controlled for the experimental purpose. Circadian drive is controlled by our 'clock' genes that has its own natural period, 24.3 h in length [23]; homeostatic propensity for sleep is wake-dependent, which can be normalized by developing a regular

routine; allostatic factors can be restricted by providing the same sleeping time, bedding system, environment and subjects being chosen from one societal group.

15.3 Sleep and Temperature Rhythms

The focus has long been on the relation between core body temperature rhythm and sleep, whereas neurobiological findings and modelling studies [24] as well as recent human experimental findings [25] suggest that changes in skin temperature may be more relevant in relation to sleep. This is a good news for studying on the effect of airflow, since airflow not only causes thermal sensation by increasing heat loss but also stimulates tactile sensors in the skin, in other words, airflow has a more prompt effect on the skin than on the core which makes the skin count more in the study of airflow than that of temperature. Thus, changes in distal skin temperature, proximal skin temperature and DPG (the distal minus proximal skin temperature gradient, a reliable indication of possible heat loss) during sleep should be treated more seriously in our following explorations.

15.4 Methods

15.4.1 Conditions

To get the fundamental settings of human experiment, customs of using fans during sleeping are surveyed in the summer time among Chinese people from different regions and ages through a professional network platform (SOJUMP). According to the results of the survey, more than 90 % of 1,055 respondents use fans while sleeping (Fig. 15.1), and most of them let the fan run all night (Fig. 15.2), which reinforced the necessity to add the sleeping mode to fans. Those who do not use fans believe that sleeping with fans on is likely to cause muscle

Fig. 15.1 Frequency of fan usage during summer night
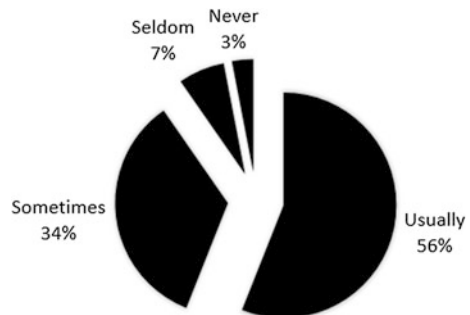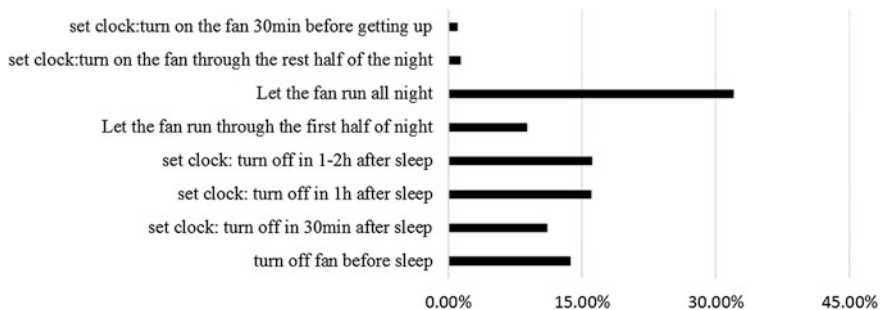
Fig. 15.2 The time when fans are used during summer night
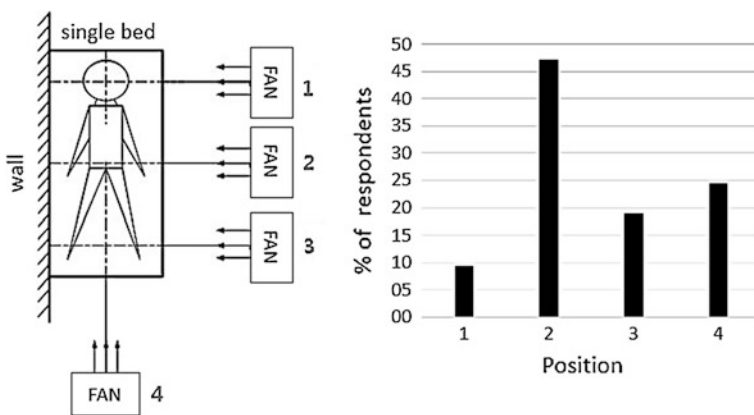
Fig. 15.3 The position where fans are placed during summer night

ache next day and prefer air conditioners. Fan placement at the side of bed and about 1–2 m away from the centre of human body is the most common (Figs. 15.3, 15.4).

In the human experiment, the fan is placed with given wind direction 1.5 m away from the bed, and traditional summer bedding system in southeast of China is applied. In the vast majority of scientific sleep studies to date, sleep has been polysomnographically recorded; simultaneously rectal and skin temperature has been continuously recorded using probes, thermocouples or wireless devices, and sleep quality is usually evaluated before, in the middle of and after the experiments. All the parameters concerned are generally recorded for the different purposes of analysis. However, in this study, three sleep stages—sleep initiation, sleep duration and awakening—which are unprecedentedly proposed, broadly replace the typical classifications. The hallmark of a good sleep in sleep initiation is less time in sleep onset latency (SOL), sleep duration is sleep depth increased and wakefulness reduced, and awakening is no sleep inertia. DPG is expected to
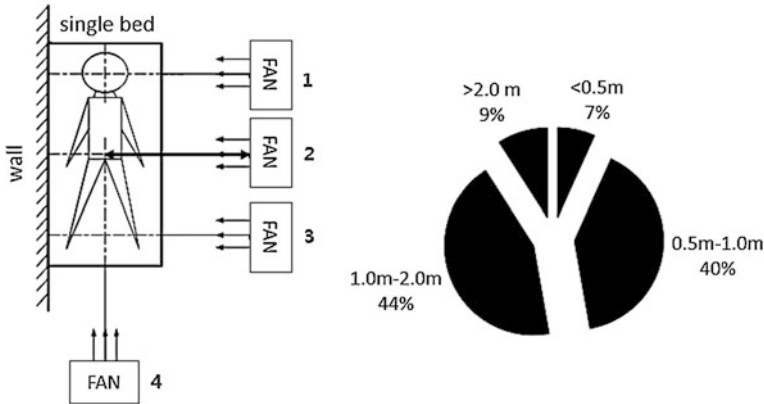
Fig. 15.4 The distance between fans and users during summer night

increase from the negative until it is slightly higher than zero, then decline to the negative, changing with the rhythm of distal and proximal skin temperature (Fig. 15.5).

Before doing any research on the sleeping condition, the airflow preference of fan users preceding sleep initiation should be revealed first, for the higher vigilance state making people more sensitive to the airflow, in which, sensation precedes health. Thirty-two healthy adult volunteers aged 18–22 (mean 20 years) were studied. The experiments were performed under a warm, humid climate with airflow Ta = 30 °C, RH = 60 %, V = 0.6, 1.0, 1.5, 2.0 m/s, respectively. The Ta and RH were stable and never deviated more than ± 0.5 °C and ± 10 %, from the predetermined Ta and RH levels. The airflow was circulated using a stand fan box placed at the side of the bed; V was measured using an anemometer before the subjects laid down on the bed. The average V was measured to be 0.6, 1.0, 1.5 and 2.0 m/s in the middle of the bed, respectively. Subjects were exposed to the airflow

Fig. 15.5 The theoretically possible site of sleep process proposed in this study
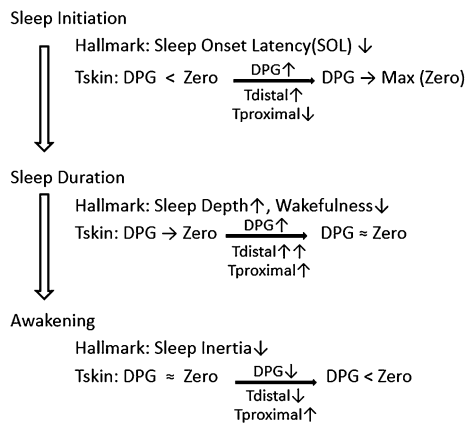
immediately after lying on the bed. The subjects wore briefs or short pyjamas (100 % cotton) and slept on a bed covered with a rattan mat and a towel blanket (100 % cotton) placed on the bedside during the experiment. The subjective evaluation on the thermal comfort was provided in the questionnaires completed by the subjects when the experiment ended.

15.4.2 Procedure

Firstly, the subjects entered the chamber and stayed quietly for 20–30 min before the start of the experiment to calm down and adapt themselves to the environment. The subjects were not informed of the order in which they would be subjected to four airflow conditions. During the resting time, the subjects were told to read experimental notification and questionnaire, and they signed an agreement if they had no objection to the articles. The fan was not allowed to be turned on for the preliminary draft sensation might affect the sensation of the airflow. After the adaptation time, the subjects completed the first vote, including thermal sensation vote (TSV), thermal comfort vote (TCV) and if they were sweating and wanted to turn on the fan. Then, the subjects laid down and the first air velocity condition began. Each condition took 20 min; after that, the fan was turned off and the subjects completed a questionnaire, which included questions regarding TSV, TCV, draft sensation and the acceptance for sleep onset. A total of five sets of answers to the questionnaire were obtained from each subject regarding their subjective experiences in the still air, 0.6, 1.0, 1.5 and 2.0 m/s air velocity. These experiments were carried out during a period of hot and humid weather in July.

15.5 Results and Discussion

Under the supine condition, TSV declines from 1.3 to −0.3 with the air velocity increasing and arrives to 0.5 when air velocity is between 0.6 and 1 m/s (Fig. 15.6). According to ANSI/ASHRAE Standard 55-2010, 90 % people are satisfied with the thermal environment when PMV is 0.5, which implies TSV = 0.5 is an acceptable value in warm and humid climate. Furthermore, TSV under supine condition is a little bit lower than that under the upright condition, and the difference becomes bigger with the air velocity getting higher until it reaches 1.5 m/s. As mentioned above, sleep mode on the market is a variant of simulated natural wind. To figure out whether simulated natural wind is acceptable for sleeping, we compared the effect of simulated natural wind with constant airflow by cutting out a period of simulated natural wind signal, the time average value of which is the same as the air velocity of constant airflow. Nearly all subjects prefer the constant airflow to the simulated natural wind because of the howling and strong draft happening from time to time.

Fig. 15.6 The TSV value
under different air velocities
and conditions
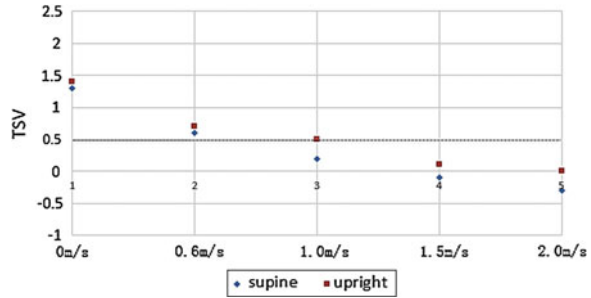
References

1. Miyazawa M (1994) Seasonal changes of sleep environment at bedtime and on arising. The proceeding of the 18th symposium on human-environment system [In Japanese]
2. Rohles FH (1983) New directions in comfort research. ASHRARE Trans 89:634–645
3. Haskell EH, Palca JW, Walker JM, Berger RJ, Heller HC (1981) The effects of high and low ambient temperatures on human sleep stages. Electroencephalogr Clin Neurophysiol 51:494–501
4. Mckenna JJ, Thoman EB, Anders TF, Sadeh A, Schechtman VL, Glotzbach SF (1993) Infant-parent co-sleeping in an evolutionary perspective implication for understanding infant sleep development and the sudden infant death syndrome. Sleep 16(3):263–282
5. Nelson EAS, Taylor BJ (2001) International child care practices study: infant sleeping environment. Early Human Dev 62(1):43–55
6. Telliez F (1997) Skin derivative control of thermal environment in a closed incubator. Med Biol Eng Compu 35(5):521–526
7. Candas V, Libert JP, Muzet A (1982) Heating and cooling stimulations during SWS and REM sleep in man. J Therm Biol 7:155–158
8. Macpherson RK (1973) Thermal stress and thermal comfort. Ergonomics 16(5):611–622
9. Karacan I, Thornby JI, Anch AM, Williams RL, Perkins HM (1978) Effects of high ambient temperature on sleep in young men. Aviation, Space, and Environment Medicine, July:855–860
10. Sewitch DE, Kittrell EMW, Kupfer DJ, Reynolds CF (1986) Body temperature and sleep architecture in response to a mild cold stress in women. Physiol Behav 36:951–957
11. Palca JW (1986) Thermoregulation, metabolism, and stages of sleep in cold-exposed men. J Appl Physiol 61:940–947
12. Dewasmes G, Telliez F, Muzet A (2000) Effects of a nocturnal environment perceived as warm on subsequent daytime sleep in humans. Sleep 23(3):409–413
13. Di Nisi J, Ehrhart J, Galeou M, Libert JP (1989) Influence of repeated passive body heating on subsequent night sleep in humans. Eur J Appl Physiol 59:138–145
14. Tsuzuki K, Okamoto-Mizuno K, Mizuno K, Iwaki T (2008) Effects of airflow on body temperatures and sleep stages in a warm humid climate. Int J Biometeorol 52:261–270
15. Awbi HB (2003) Ventilation of buildings, 2nd edn. Spon Press, London and New York
16. Paterson LM (2012) The science of sleep. In: Andrew G, Alex W (eds) Sleep: multi-professional perspectives, 1st edn. Jessica Kingsley Publishers, London and Philadelphia
17. Jane H, Andrew G (2012) Broken sleep. In: Andrew G, Alex W (eds) Sleep: multi-professional perspectives, 1st edn. Jessica Kingsley Publishers, London and Philadelphia
18. Kripke DF, Garfinkel L, Wingard DL, Klauber MR, Marler MR (2002) Mortality associated with sleep duration and insomnia. Arch Gen Psychiatry 59(2):131–136

19. Rechtschaffen A, Kales AA (1968) Manual of standardized terminology, techniques and scoring system for sleep stages of human subjects, University of California, Brain Information Service/Brain Research Institute, Los Angeles, CA
20. Iber C, Ancoli-Israel S, Chesson A, Quan SF (2007) The AASM manual for the scoring of sleep and associated events: rules, terminology and technical specification. American Academy of Sleep Medicine, Westchester
21. Borbély AA (1982) A two process model of sleep regulation. Hum Neurobiol 1(3):195–204
22. Saper CB, Scammell TE, Lu J (2005) Hypothalamic regulation of sleep and circadian rhythms. Trends Neurosci 28(3):152–157
23. Czeisler CA, Duffy JF, Shanahan TL, Brown EM et al (1999) Stability, precision, and near-24-hour period of the human circadian pacemaker. Science 284(5423):2177–2181
24. Van Someren EJW (2000) More than a marker: interaction between the circadian regulation of temperature and sleep, age-related changes, and treatment possibilities. Chronobiol Int 17:313–354
25. Raymann RJEM, Swaab DF, Van Someren EJW (2005) Cutaneous warming promotes sleep onset. Am J Physiol 288:R1589–R1597

Chapter 16
Research on Thermal Comfort for Teachers' Residential Buildings in Cold Region

Huifen Zou, Yu Rong, Xiaozhen Cao and Sheng Ye

Abstract This paper mainly discusses the field test of the thermal and humid environment in closed bedrooms in a university teachers' residential building in Shenyang Province during heating period in winter. The research in this study focuses on three aspects: indoor temperature and humidity changes at nights, the effects of indoor humidity at different humidification locations, and indoor thermal comfort. Results showed that the average indoor temperature at night is 22.2 °C and the relative humidity is 47.56 % also that the three methods of room humidification came up with a conclusion that clarified the role of the effects of humidification, based on contrast and analysis. The third method evaluated thermal comfort of the room using PMV and PPD, which gave the conclusion that the study room was the most comfortable one. Furthermore, this paper analyzes how to improve the indoor thermal comfort.

Keywords Temperature · Humidity · PMV–PPD · Thermal comfort

H. Zou · Y. Rong (✉) · X. Cao
School of Municipal and Environment Engineering,
Shenyang Jianzhu University, Shenyang, China
e-mail: rongyu@sjzu.edu.cn

H. Zou
e-mail: hj_zhf@sjzu.edu.cn

X. Cao
e-mail: hj_cxz@sjzu.edu.cn

S. Ye
School of Management, Shenyang Jianzhu University, Shenyang, China

16.1 Introduction

With tremendous developments in 'education strategy' of China, the emphasis on improvement in university teaching quality seems to have weighed more than ever. Indoor air quality of the university teachers' residential building can affect the psychological factors, physical health, and teaching quality of those staying in them [1]. According to statistics, since there are 34 general universities in Shenyang Province (which is an important higher education base) as of August 2009, a large number of universities residential buildings for teachers are constructed. However, studies on thermal comfort and humidity in this area are rare [2, 3]. For the purpose of studying thermal comfort, this paper presents the discussion of the topics related to it.

Shenyang is located in the south of Northeast China, at the center of Liaoning Province. The main terrain is plain, and mountains and hills are in the southeast. Liao River, Hun River, and Xiushui River flow through the city. Shenyang has a temperate monsoon climate, annual average temperature of 6.2–9.7 °C, and annual average relative humidity of 63 %, with hot summers and cold dry winters.

16.2 The Arrangement of Measuring Points and Experimental Instrument

The schematic diagram of the experiment and the arrangement of the five measuring points are shown in Fig. 16.1. The room has an area 12.6 m^2 and height 2.7 m. The outer brick wall is 490 mm and the inner brick wall 240 mm. The window faces the north and the door is closed.

Fig. 16.1 Simplified plan
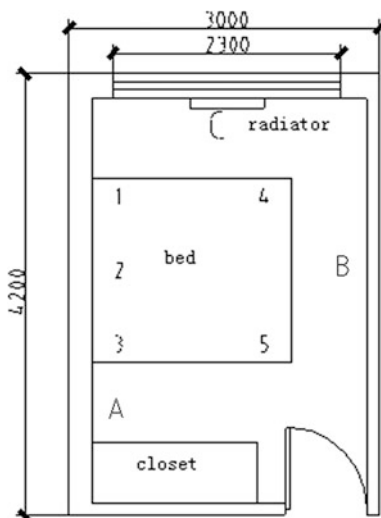
Fig. 16.2 Infrared
thermometer

The arrangement of measuring points: 5 points (numbered 1–5 shown in Fig. 16.1), they have a common height of 0.7 m (The height of the person lying).

RR002 temperature self-recorder was used to measure the temperature and humidity of the room. Temperature ranged from −10 to 50 °C, with precision ±0.5 °C. Humidity ranged from 0 to 95 %RH, with precision ±3 % RH. The surface temperature of the walls was measured using an infrared thermometer (shown in Fig. 16.2), the precision being ±1 °C. The following parameters were measured using a common household humidifier: rated voltage 220 V, rated power 50 Hz, tank capacity 3.0–4.0 ml/h, and noise ≤36 dB (A).

16.3 The Experimental Scheme and Results

Several types of factors affect indoor thermal comfort and humidity, such as climate factors, construction factors, and human factors. The paper mainly studies the changes in temperature and humidity in the bedroom (from 23:00 to 6:00) in airtight conditions during winter heating period and then analyzes whether the comfort index of the room meets the requirements.

Most of the buildings in the district which the test room belongs to are using centralized heating. In Shenyang, the heating period starts on 1 October. The experiment was conducted from October 4 to October 13, 2011. Temperature and humidity were measured at five points in the closed condition as mentioned above, and their averages were taken [4].

The hourly mean temperature inside the bedroom at night is shown in Fig. 16.3. Very little fluctuations in temperature can be seen (remains at about 22.2 °C) during testing period. The indoor hourly mean humidity value is shown in
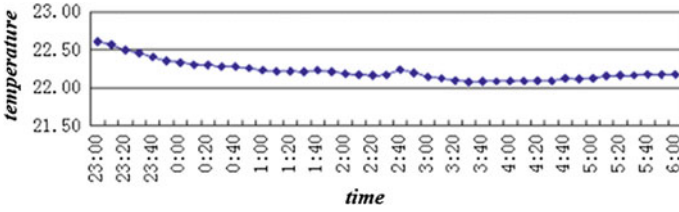
Fig. 16.3 Hourly mean temperature
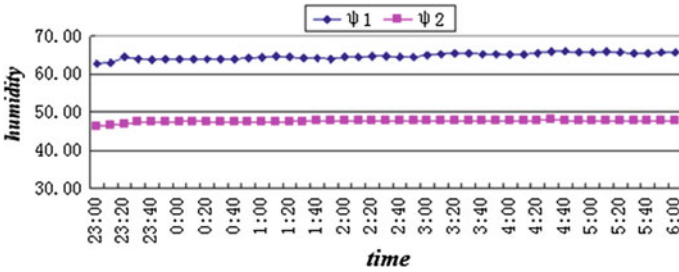
Fig. 16.4 Hourly mean humidity

Fig. 16.4, in which $\psi 1$ represents the trend in indoor humidity change in case of using humidifier for two hours before testing (after which humidifier was stopped) and $\psi 2$ represents the trend in indoor humidity change in case of no humidifier. It can be seen that humidity values tend to be constant under both operating conditions.

To study how different locations of humidifier affect indoor humidity under unchanged temperature conditions at night, the humidifier is placed at three test points (A, B, and C, as shown in Fig. 16.1), respectively. The humidifying direction in case A is parallel to the edge of the bed toward the door. The humidifying direction in case B is toward the radiator. Cases A and B both are at the same height from the bed. The humidifying direction in case C is toward the radiator located on the ground. Humidifier was run using three methods mentioned above from 20:30 to 23:00, and changes in humidity $\psi(\%)$ with respect to time $\triangle t$(min) were observed. Results were analyzed using a linear fitting software (as shown in Figs. 16.5, 16.6 and 16.7) and are presented in Table 16.1.

R^2 represents fitting degree, and its values closer to 1 indicate that the fitting effect is better. All of the three fitting degrees are very close to 1, so curve fitting is good, which can reflect the changes under different humidification modes accurately. The rates of humidity changes with time are 0.069, 0.083, and 0.079, respectively, for cases A, B, and C. The required humidity can be achieved in case B in a relatively short period of time, so its humidifying effect is the best.

Fig. 16.5 Case A
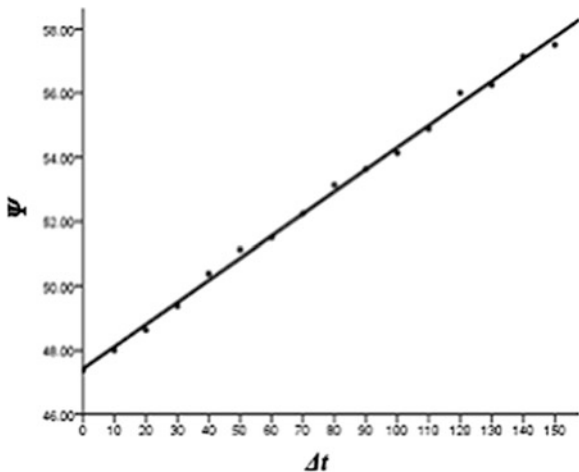
Fig. 16.6 Case B
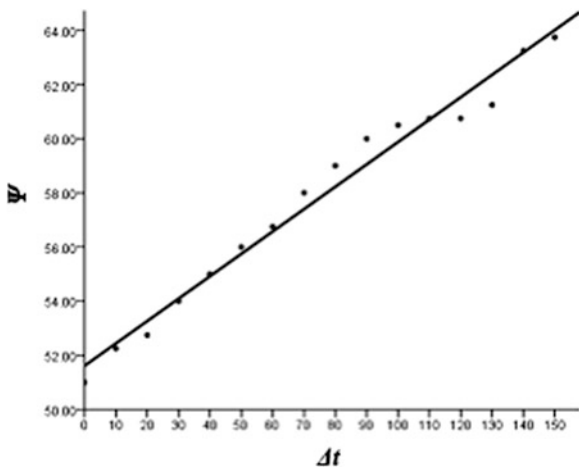
16.4 Thermal Environment Evaluations

A total of 1396 American and Danish subjects had participated in the test, and P.O. Fanger had collected their hot and cold feeling data, and then he put forward PMV and PPD [5, 6]. The PMV represents the Predicted Mean Vote in the same environment and the value of PPD represents the percentage of dissatisfied with thermal environment. ISO7730-recommended values of PMV and PPD are, respectively, between +5 and –5 and <less than 10%.

From 23:00 to 06:00, the temperature of bedroom 22 °C, with nearly no changes. This paper has calculated the values of PMV and PPD under different humidity conditions. The thermal resistance of the quilt is 2.0clo, the sleep

Fig. 16.7 Case C
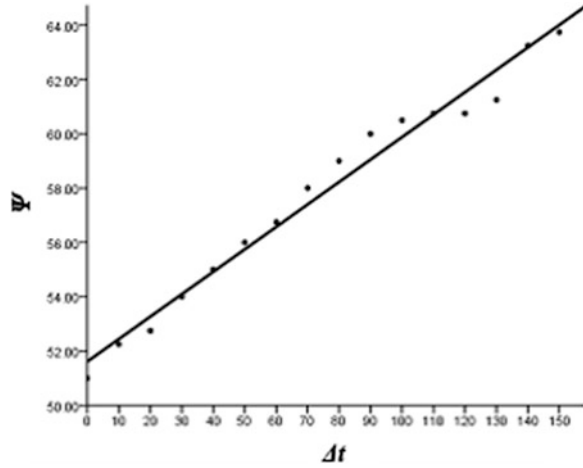
Table 16.1 Curve fitting

Case	Equation	R^2
A	$\varphi = 0.069\Delta t + 47.423$	0.997
B	$\varphi = 0.083\Delta t + 51.614$	0.979
C	$\varphi = 0.079\Delta t + 45.999$	0.964

metabolic rate 46.4 W/m², and indoor average wind speed 0.5 m/s [7]. As shown in Fig. 16.8, when humidity is within the range of 45–65 %, the PMV ranges from −0.10 to 0.08 and PPD ranges from 5 to 5.2 %. In the case of no humidification (as shown in Fig. 16.4), humidity changes little and remains at about 47.56 %, the corresponding PMV value is about -0.8, and the PPD value is about 5.1 %. According to the ISO7730 standard, these values have met the thermal comfort requirements.

In order to further improve teachers' quality of sleep, from Fig. 16.8, it can be summarized that PMV approximately linearly increases with the humidity. When the humidity is closer to 56.5 %, PMV is 0 and PPD is 5 %, which represent the
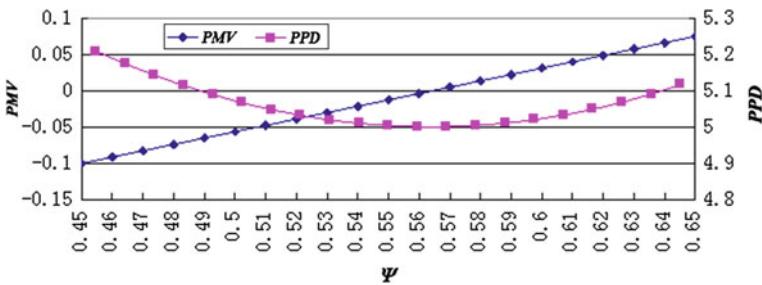
Fig. 16.8 PMV and PPD curves

best thermal comfort. Therefore, an appropriate increase in humidity can improve indoor thermal comfort. The thermal environment can be improved by humidification way before going to sleep. As mentioned above, using case B for room humidification, the fitting curve is $\varphi = 0.083\Delta t + 51.614$, where $\varphi = 56.5\%$ and $\Delta t = 58.9$ min. In other words, using case B for bedroom humidification for about an hour can ensure the best thermal comfort all night.

16.5 Conclusions

The following conclusions can be made:

1. The average temperature of the bedroom is 22.2 °C and the average relative humidity 47.56 %.Both temperature and relative humidity change slightly during the whole night.
2. In this experiment, the humidifier has been placed in three different locations, among which the best method is placing the humidifier beside the end of the bed (toward the radiator).
3. The calculated PMV and PPD values show that the thermal comfort is the best in case B.
4. In order to enhance thermal comfort, the humidifier has to be run about 1 h before we going to sleep, which can ensure the best thermal comfort.

References

1. Wang L, Wang F, Liu J et al (2010) Research on indoor thermal environment of house hotel in Heshun village. J Civil Eng 1(43):426–429
2. Xu X, Li B (2005) Influence of indoor thermal environment on thermal comfort of human body. J Chongqing Univ 4(23):102–105
3. Ding X, Hu Q, Li K (2007) The research progress of human thermal comfort. J DongGuan Technol Univ 1(14):43–47
4. Wang Z, Zhang Z, Lian Y (2002) Discussion of thermal comfort indices and design indoor temperature for winter heating. HVAC HV&AC 2(32):26–28
5. Zhang Y, Zhao R (2010) Literature review and discussion on human thermal adaptation in built environment. HVAC HV&AC 9(40):38–48
6. He H (2007) Study on the indoor thermal environment of university in Harbin. Harbin Engineering University, Harbin
7. Yang Q (2010) Study on the indoor thermal comfort in the cold zone. Xi'an Architecture and Technology University, Xi'an

Chapter 17
Field Research on the Rural House Thermal Environment in Southwest Region of Shandong Province

Lili Zhang, Enshen Long and Jun Wang

Abstract In this present study, the indoor thermal environment of current rural house located in the southwest region of Shandong Province was tested and analyzed; the measured parameters include air temperature and relative humidity. The results show that the indoor air environment temperatures of all rural houses are below 2.6 °C, which are far away from the comfortable temperature. Meanwhile, their absolute humidity is relatively low. The inner wall surface temperature varies in the range from 0.4–2.0 °C. Accordingly, the cold radiations of west and north surface walls are much severe. The analysis and results in this paper provide useful technical support for sustainable development of agricultural house and the new rural construction.

Keywords Rural house · Indoor thermal environment · Temperature · Humidity

17.1 Introduction

The southwest area of Shandong Province is in cold region of China, which has outdoor air average temperature range from 0 to 10 °C in coldest month and 70-day period of the temperature below 0 °C. With the extreme weather appearing, this period becomes longer. Meanwhile, simple rural residence has building envelope without insulation and poor indoor thermal environment for a long term, as a result of the influence of economy and regional characteristics. Villagers spontaneously adopt various ways to resist the cold climate in winter, which have no obvious

L. Zhang · E. Long (✉) · J. Wang
College of Architecture and Environment, Sichuan University, Chengdu 610065, China
e-mail: 1onges2@163.com

L. Zhang
Jincheng Institute of Sichuan University, Chengdu 611731, China

heating effect and high energy consumption. Some previous researches have investigated the indoor thermal environment of the countryside residence in different areas of cold region, China [1–3]. But there is not specific analysis and research on the living thermal environment of present rural residence. Especially China folk habits and climate characteristics are diverse in different regions, the existing studies cannot provide effective guide for thermal environment improvement of the farming cartilage [4]. Therefore, the indoor thermal environment of current rural residence is analyzed in this present study, based on measuring indoor thermal environment of a typical rural residence in Jining city, southwestern region of Shandong Province. Moreover, some suggestions for improving indoor thermal environment of rural house are proposed and guidance for the new rural construction and sustainable development of the rural house is provided.

17.2 Typical Residence and Test Conditions

17.2.1 Description of Typical Residence and Test Points

The measured residence is located in a village of Jining city in southwest region of Shandong Province, which has area of 237.6 m^2 and independent garden. The prototype and test point arrangement are shown in the plan and elevation forms, seeing in Fig. 17.1. The bedroom and sitting room are main test objects.

Fig. 17.1 Arrangement of test points in the typical house (mark size unit: mm)
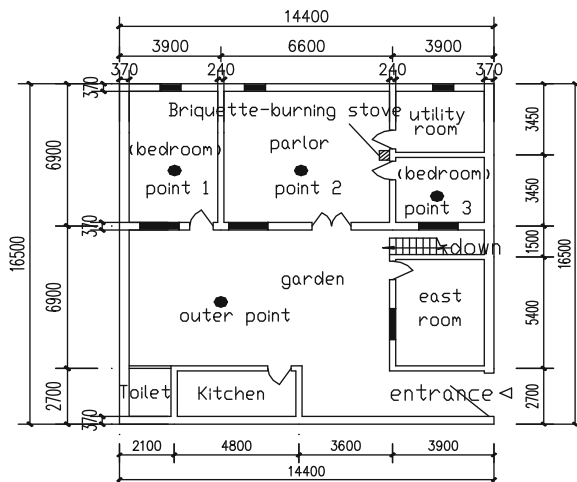
17.2.2 Construction and Physical Parameters of Building Envelope

In order to facilitate analysis of the thermal performance of typical residence, construction and physical parameters of building envelope are given in Table 17.1. Meanwhile, the limiting values of heat transfer coefficient are chosen according to "Design Standard for Energy Efficiency of Residential buildings in Sever Cold and Cold Zones JGJ26-2010."

It can be seen from Table 17.1 that the thermal performance of the existing rural residences is generally poor, which have a big gap with the national norms.

17.2.3 Test Methods

The measurement points of indoor temperature and relative humidity are located at 1.5 m high above the ground in the middle of a room and those of outdoor temperature and relative humidity are placed at 1.5 m high above the ground in the open space. Meanwhile, the test results are prevented from adverse influence of direct sunlight through effective shade. Indoor and outdoor wall surface temperatures were obtained by calculating the mean value of many test points at each wall. The test day is a representative day in winter, which has rest snow. The test time is from 9:00 a.m. to 17:00 p.m., and the interval is 1 h. Instruments have been calibrated before testing, in order to ensure the accuracy of test results.

Table 17.1 Typical building envelope construction and building physical parameters

Building envelope and parameters			
Name of building envelope	Building envelope construction	Heat transmission coefficient $W/(m^2 \cdot K)$	Heat transmission coefficient limit $W/(m^2 \cdot K)$
North wall	Bean green washed granolithic + 20 mm cement mortar + 240 mm brick wall + 20 mm cement mortar	2.13	0.45
The rest wall of building	bean green washed granolithic + 20 mm cement mortar + 370 mm brick wall + 20 mm cement mortar	1.55	
Roof	20 mm cement mortar + 60 mm hollow + 20 mm cement mortar	3.53	0.35
Ground	Terrazzo floor + 20 mm cement mortar + 200 mm gravel cushion	4.24	1.2
Windows	Single-frame wood + 6 mm glass	6.4	2.5

17.3 Test Results and Discussion

17.3.1 Indoor Air Temperature of the Typical Residences

Figure 17.2 shows the comparison of indoor air temperature in three typical rooms, which is the mean temperature of the indoor test points in the corresponding typical rural residence. The temperature in room 1 covers a range from 0 to 1 °C, room 2 from 1 to 2.2 °C, and room 3 from 1.5 to 2.6 °C. The mean temperature during the test period is 1.7 °C. Temperature rises in room 2 and room 3 after 12:00 a.m.

The reason for the above phenomenon is that room 2 and room 3 are in the middle and east of building with farmhouse cooking and persons staying at noon, respectively, which cause indoor air temperature to rise. Moreover, building envelope heat storage and the sun radiation at noon also makes indoor air temperature rise. However, the room 1 is in the west and temporarily has no one living. In addition, according to the thermal comfort model, the best indoor comfortable temperature should be 12–14 °C. For obvious difference between room temperature and comfortable temperature (see in Fig. 17.3), it can be found that the indoor temperature of three represented rooms is much lower than the comfortable temperature, namely indoor thermal environment is poor. Actually, the occupants feel very cold in the rooms during the test process, and their bodies behave a state of tension, cervical spine, and heart uncomfortable. Therefore, raising indoor air temperature in winter is one critical issue for improving the indoor thermal environment.

17.3.2 Indoor Relative Humidity of Three Typical Residences

Figure 17.4 shows the comparison of indoor relative humidity of three typical rooms. The indoor air relative humidity in room 1 covers a range from 60 to 95 % and has a large amplitude variation, room 2 from 68 to 78 %, and room 3 from 80 to 89 %.

Fig. 17.2 Comparison of indoor temperature
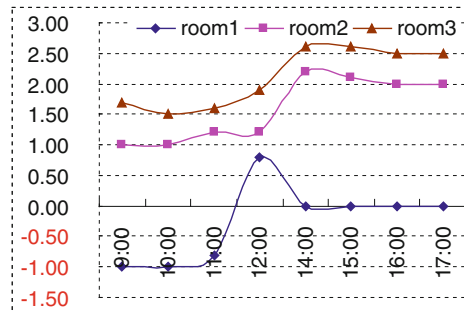
Fig. 17.3 Comparison of
indoor and comfortable
temperature
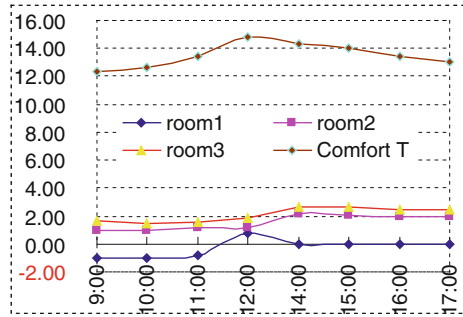
Fig. 17.4 Comparison of
indoor relative humidity
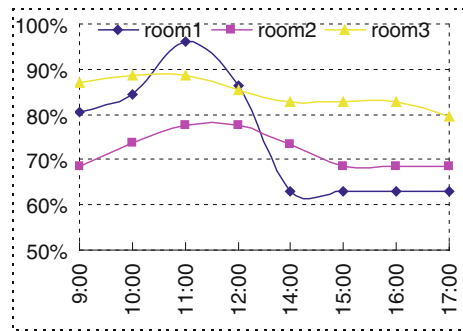
The relative humidity of these three rooms is more than 60 %. Combined with
Fig. 17.2, we can find that the indoor thermal environment shows the characteristics
of low temperature and high humidity. Correspondingly, the absolute humidity is
very low and far less than the amount of relative comfort moisture, as shown in
Fig. 17.5, which leads the people in the room to feel very dry, nose bleeding phe-
nomenon. Therefore, improvement in the air absolute humidity also should be
considered.

17.3.3 Mean Inner Wall Surface Temperature
of Typical Residence

Figure 17.6 shows the comparison among inner wall surface temperature of the
typical house. The mean ground surface temperature is between 0.4 and 2.0 °C,
from −0.7 to 2.6 °C for inner roof surface temperature, variation of −2.1 to 0.5 °C
for west wall surface temperature, those of −0.4 to 1.1 °C, 0.15 to 1.35 °C, −0.3
to 0.9 °C for south wall surface temperature, east wall surface temperature, north
wall surface temperature, respectively. The inner roof surface temperature
increases after 12:00, owing to the sun radiation at 10:00 a.m.

Fig. 17.5 Comparison of
indoor and comfort absolute
moisture content
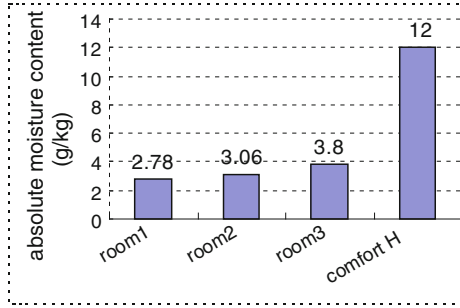
Fig. 17.6 Comparison of
inner wall surface
temperature
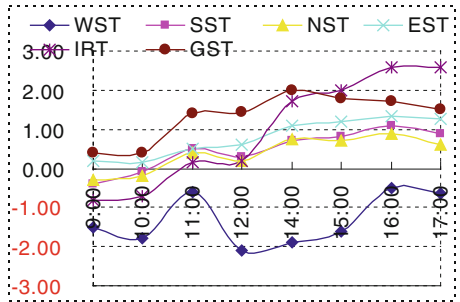
Changing the trend of east, south wall surface temperature and north wall surface temperature remain consistent. As the west wall is basically in shadow all day and the rain and snow wall leakage phenomenon have strengthened the cold radiation of the inner west wall, inner west wall surface radiation temperature changes obviously and is much lower than that of the other surfaces. In addition, Fig. 17.7 presents the comparison among inner wall surface average radiation temperature. It can be seen that the north and west inner wall surface radiation temperatures are very low, cold radiation is the most serious and all the wall radiation temperature is far less than comfortable temperature, and there are different degrees of cold radiation. It should be noted that WST means west inner surface temperature, SST means south inner surface temperature, NST means north inner surface temperature, EST means east inner surface temperature, IRT means inner roof surface temperature, and GST means ground inner surface temperature, which are shown in Figs. 17.6 and 17.7.

17.3.4 Outer Wall Temperature and Outdoor Air Temperature

Figure 17.8 shows variation in outer wall temperature and outdoor air temperature with time.

Fig. 17.7 Comparison of
inner wall surface average
radiation temperature
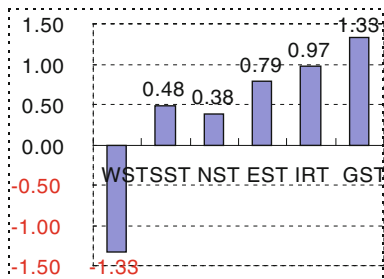
Fig. 17.8 Comparison of
outdoor air temperature and
outer wall surface
temperature
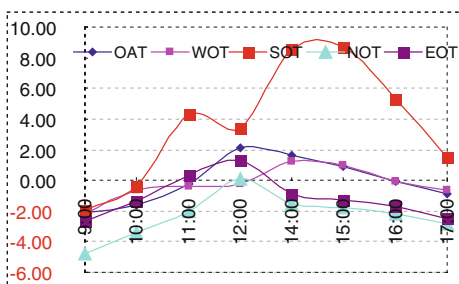
As a result of the solar radiation effect, the south outer wall surface temperature has a great rise after 10:00 a.m. North outer wall temperature is relatively low and affected marginally by solar radiation. The west and east outer wall surface temperatures change in line with the intensity of solar radiation, namely east outer wall surface temperature is impacted by solar radiation before 13:00 p.m., after 13:00 p.m. for that of west outer wall. Meanwhile, west outside wall surface temperature is slightly higher than that of the east outside wall after 13:00 p.m. West outside wall surface temperature drops to below 0 °C after 16:00 p.m. As for rich solar energy in this area, the south outer wall surface temperature is affected obviously by the solar radiation. Therefore, the solar energy should be collected and applied by the passive way. The east outer wall may also be appropriated for using solar energy. Moreover, furniture regenerative energy or heat accumulator is one possible choice for improving the indoor thermal environment. To clarify, OAT means outdoor air temperature, WOT means west outer surface temperature, SOT means south outer surface temperature, NST means north outer surface temperature, and EST means east outer surface temperature, which are shown in Fig. 17.8.

17.4 Conclusions

According to the field research on the rural house thermal environment, the following conclusions can be obtained:

1. The indoor air temperature is far below the comfortable temperature in winter, which affects the farmers' normal daily life and needs to be improved.
2. The indoor cold radiation is serious in the region, which can be reduced by selecting inner wall with thermal storage material and rational design functional partition to determine human activities space.
3. The building envelope heat transfer coefficient is much higher than the reference architecture limit in the region. Heat loss should be reduced to maintain the stability of indoor air temperature. The indoor thermal environment may be improved by using solar radiation on the south wall or east wall.
4. Due to the abundant solar energy resource in the region, passive solar houses and solar water heaters can be used to provide winter heating and domestic hot water and improve the thermal environment of residents.

References

1. Guo H (2004) Indoor thermal environment of rural residence in Guanzhong region. Xi'an University of Architecture and Technology
2. Yan ZF (2004) Dynamic modeling of the indoor thermal and humidity environment in the adobe buildings. Xi'an University of Architecture and Technology
3. Jin H, Zhao H, Wang X (2006) Research on the indoor thermal comfort environment of rural housing in winter in super-cold region. J Harbin Inst Technol 38:2108–2111
4. Zhao Y, Zhu J, Zongshan W, Mulin D, Haiwen S (2010) Research and analysis on comfortable and energy-saving firewall-type structure and characteristics of heated kang. Tech Exch:60–64

Chapter 18
Theoretical and Experimental Investigations on the Evaporative Cooling Characteristics of the Lightweight Planting Soil Module

Zhangyuan Wang, Wansheng Yang, Junjie Lv and Xudong Zhao

Abstract The evaporative cooling effect of the lightweight planting soil module on the building roof could reduce the heat to the top building rooms and improve indoor thermal comfort. Until now, the researches, domestic and overseas, have concentrated on the thermal insulation properties of the actual buildings. However, the investigations on the evaporative cooling characteristics under different controlled environments have not been found yet. In this paper, experiments will be conducted on the evaporative cooling effect of the roof module with planting soil under different moisture contents and environmental controls by using the guarded hot box testing method. From the experimental results, the relationship between the evaporation capacity and moisture content could be obtained, and the influence of the environmental parameters, e.g., relative humidity and ambient temperature, to the evaporation capacity will be analyzed. Based on the variation patterns of the accumulative evaporation capacity with time, a theoretical model for the evaporative cooling effect of the roof module under uneven water supply conditions will be proposed, which will provide basic data for the practical engineering projects and thermal insulation analysis.

Z. Wang (✉) · W. Yang · J. Lv
School of Civil and Transportation Engineering, Guangdong University of Technology, Guangzhou 510006, China
e-mail: zwang@gdut.edu.cn

X. Zhao
Department of Engineering, University of Hull, Hull HU6 7RX, UK

18.1 Introduction

With the increase in urbanization, the urban thermal island effect has been more serious in recent years. Eco-roof has a significant effect to improve the building indoor and outdoor environment. Researches indicated that the thermal insulation effect of the planting module depends primarily on the passive evaporative cooling of the module. The main factors that affect the evaporative cooling effect of the insulation module include atmospheric evaporation force (i.e., meteorological environmental conditions, including temperature, relative humidity, wind speed, solar radiation) and water supply capacity of the module (i.e., moisture content) [1–7]. About the surface soil dehydration model, researchers, domestic and overseas, proposed different evaporative water loss models [8–16]. Researchers also studied the factors affecting soil evaporation and their impacts and methods of computation [17–20]. However, these studies have not involved the evaporative water loss model of the lightweight planting soil under shallow and uneven water supply conditions. In this paper, experiments will be conducted to investigate the characteristics of evaporation of the lightweight planting soil module under different moisture contents and controlled environmental conditions, and the evaporative water loss model of the module will be proposed under shallow and uneven water supply conditions. This research will provide basic experimental basis for the practical engineering applications of lightweight planting soil module in the passive evaporative cooling of buildings.

18.2 Experimental Methods and Equipments

18.2.1 Experimental Methods

Three thermal insulation modules with different moisture contents will be involved in this experiment as given in Table 18.1. During testing, the modules will be located in a sealed environmental control box, and the temperature will be set at 35 °C. The module will be weighted every one hour. The testing will be run from 9 a.m. to 5 p.m. in 6 days.

Table 18.1 Initial moisture content of different experimental modules

Module	Module 1	Module 2	Module 3
Initial moisture content (%)	8.6	16.5	23.2

18.2.2 Construction of the Module and Introduction of Testing Equipments

18.2.2.1 Construction of the Module

The experimental module was composed of PVC module board, water storage and drainage board, geotextile and lightweight soil. The size of the module was at $42 \times 36 \times 20$ cm. The water storage and drainage board will be located at the bottom of the module and covered with the geotextile. Lightweight soil with the thickness of 6.5 cm will be placed above the geotextile. During testing, the module will be placed in a PVC board with the size of $48 \times 42 \times 20$ cm for the purpose of reducing heat transfer from the module to the surroundings. Mineral wool will be used to seal the cracks of the module for thermal insulation. The detailed structure of the module and positions of the measuring points are shown in Fig. 18.1.

18.2.2.2 Environmental Control Box

Environmental control box is the forced draft drying cabinet in the type of HN101-2A, and the basic performance data are shown in Table 18.2.

18.2.2.3 Temperature Measuring Set

The temperature data of the module were collected in every 1 h by using the multi-channel temperature inspecting instrument in the type of JK-8/JK-16. The performance data are presented in Table 18.3.
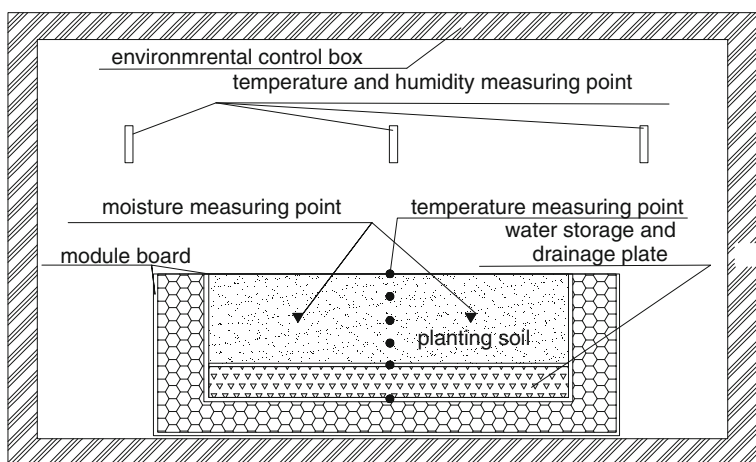
Fig. 18.1 Testing device and module structure

Table 18.2 Performance data of environmental control box

Voltage	Input power	Temperature accuracy	Temperature range	Safety classification	Size (cm^3)
220 V	2.2 kW	±1 °C	0–300 °C	Class I, level B	550 × 550 × 450

Table 18.3 Performance data of multi-channel temperature inspecting instrument

Channel no.	Temperature range	Measuring accuracy	Supply power	Experimental environmental temperature
JK-16:16	−50–300 °C	±(50 % + 1) °C	220 V ± 10 %	0–50 °C

18.2.2.4 Measurement of Evaporation Capacity

The evaporation capacity of the module will be measured in every 1 h by using a high-accuracy electronic scale in the type of XK3100-TC. The maximum weight of the scale was 80 kg, and the minimum accuracy was 2 g.

18.3 Experimental Results and Analyses

18.3.1 Experimental Results

The experimental results of the three modules are summarized in Table 18.4.

18.3.2 Discussion and Analysis

18.3.2.1 Influence of Initial Moisture Content to Evaporation Capacity

From Table 18.4, it can be concluded that the average evaporation capacity of the module presented a gradually decrease relation with time under the same initial moisture content as shown in Fig. 18.2. The first-day average evaporation capacity was higher than the last-day one at 0.039 kg/(h·m²) for module 1, 0.086 kg/(h·m²) for module 2, and 0.066 kg/(h·m²) for module 3. This was mainly due to the decrease in the module soil moisture content, leading to the reduction in the moisture into the environmental control box, and the gradual decrease in the water vapor pressure between the module surface and environmental control box, which resulted in the module average evaporation decreasing.

From Fig. 18.2, it can be seen that the lower the module initial moisture content, the smaller the average evaporation capacity. During the first two days, the average evaporation capacity of module 1 was far larger than that of modules 2 and 3. After that, the average evaporation capacity of the three modules tended to be the same.

Table 18.4 Testing results of three modules

Days	Relative humidity (%)			Environmental temperature (^{o}C)			Average evaporation capacity (kg/(h·m^2))			Accumulative evaporation capacity (kg/m^2)		
	1	2	3	1	2	3	1	2	3	1	2	3
1	54.8	47.9	76.3	31.1	31.4	33.0	0.079	0.139	0.132	0.635	1.124	1.032
2	53.1	42.1	76.9	31.7	32.8	33.5	0.060	0.119	0.106	1.098	2.077	1.892
3	49.6	50.7	75.5	32.8	33.2	34.2	0.053	0.073	0.099	1.495	2.672	2.672
4	47.7	53.6	71.1	32.7	33.8	35.4	0.046	0.060	0.099	1.865	3.175	3.426
5	48.1	50.4	74.1	33.1	34.2	34.9	0.040	0.060	0.073	2.196	3.651	3.981
6	44.1	53.8	69.0	33.4	33.8	35.3	0.040	0.053	0.066	2.487	4.061	4.511

Note Average evaporation capacity is the average of the evaporation capacity during 8 h testing period from 9 a.m. to 5 p.m.; accumulative evaporation capacity is the total evaporation capacity during the testing period
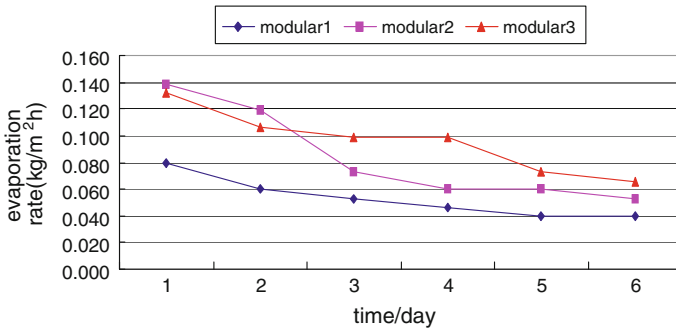
Fig. 18.2 Relation between average evaporation capacity and testing time

Under different initial moisture content conditions, the average evaporation capacity of module 3 was lower than that of module 2 at 0.007 kg/(h·m^2) during the first day and 0.013 kg/(h·m^2) in the second day. This can be explained from that the module evaporation capacity was significantly influenced by environmental factors due to the sufficient water content in modules 2 and 3. In the closed environment, the higher the initial moisture content of the module, the larger the relative humidity of the environment. That was why the environmental relative humidity of module 3 was higher than that of module 2, and the evaporability of module 3 was weaker than that of module 2. After that, the evaporation capacity of module 3 was larger than that of module 2, and the maximum difference of these two was at 0.039 kg/(h·m^2) in the fourth day. This was because the module surface tended to dry, and the water supply ability of the module was the main control factor for water evaporation. The module with higher initial water content had a strong sustainable capacity of water supply and slow water evaporation ability during the later period.

18.3.2.2 Influences of Environmental Factors to Evaporation Capacity

1. **Relative Humidity**

Under the same initial moisture content conditions, the environmental relative humidity of modules 1 and 3 decreased gradually. Theoretically, the atmospheric evaporation capacity should be gradually strengthened. However, the test results showed that the average evaporation capacity decreased. This was because that the moisture content of the module was the main factor limiting the module evaporation. Although the relative humidity inside the environmental control box and the moisture content of the module were reduced, the vapor pressure ratio in the module surface and environmental control box was smaller with the extension of time. That was why the module average evaporation capacity showed a trend of decrease.

2. **Environmental Temperature**

Under the same initial moisture content conditions, the environmental temperature increased gradually. This was because the heat supply for water evaporation in the environmental control box was reduced with the decrease in the module evaporation capacity, leading to the sensible heat and air temperature increasing. However, the average evaporation capacity of each module still presented a reducing pattern, meaning that the moisture content was still the main factor controlling the evaporation of the module.

18.4 Improvement of Evaporation Model

18.4.1 Model for the Relation of the Accumulative Evaporation Capacity and Time

In 1969, Black [7] proposed a relation between the accumulative evaporation capacity and time under no underground water supply by conducting experiments as in:

$$E = A + Bt^{1/2} \tag{18.1}$$

where E was the accumulative evaporation capacity of soil, A and B were the evaporation parameters from experiments, and t was the evaporation period.

Equation (18.1) could be simplified as in Eq. (18.2), which followed a regression method.

$$E = AX + B \tag{18.2}$$

Based on the test results of the three modules, the mathematical models of the accumulative evaporation capacity are shown in Fig. 18.3 and Table 18.5.

From Table 18.5, it can be seen that with the increase in the module initial moisture content, the gradient of the equation increased, meaning that the module evaporation rate increased with the increase in the initial moisture content.

18.4.2 Relation of Average Evaporation Capacity with Initial Moisture Content

18.4.2.1 Gardner Model

Gardner [7] indicated that the average evaporation capacity of the soil showed a linear relation with the moisture content of surface soil as in Eq. (18.3).

$$Y = AX + B \tag{18.3}$$

The regression relations of the average evaporation capacity with the initial moisture content of the three modules are shown in Fig. 18.4 and Table 18.6.

From Table 18.6, it can been that the gradient of the equation increased with the increase in the module initial moisture content, meaning that the module evaporation rate increased with the increase in the initial moisture content. However, there were differences between the test results and the regression lines, especially for module 2.

18.4.2.2 Improvement of the Model

For the improvement of the above models, Eq. (18.4) was used to describe the relation between the average evaporation capacity and initial moisture content. Figure 18.5 and Table 18.7 show the regression curve line of the three modules. The coefficient of determination (R^2) was larger than 0.91, which could accurately
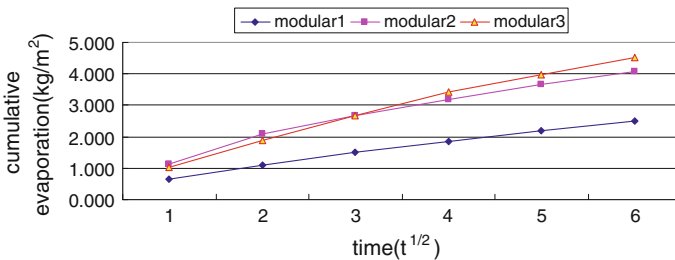
Fig. 18.3 Relation of accumulative evaporation capacity with time (X)

Table 18.5 Relation of accumulative evaporation capacity with time (X)

Module	Equations	Coefficient of determination (R^2)	Initial relative humidity (%)
Module 1	$E = 0.4552X - 0.6949$	0.9978	8.6
Module 2	$E = 0.7077X - 0.8205$	0.9985	16.5
Module 3	$E = 0.8614X - 1.4793$	0.9979	23.2
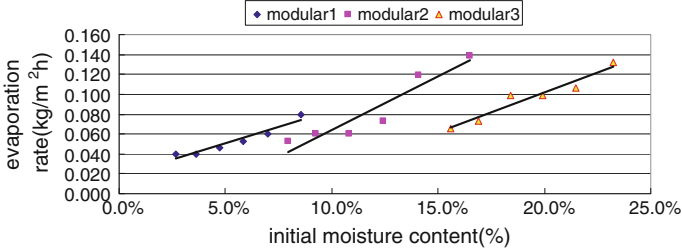
Fig. 18.4 Relation of average evaporation capacity with initial moisture content

Table 18.6 Relation of average evaporation capacity with initial moisture content

Module	Equations	Coefficient of determination (R^2)	Initial relative humidity (%)
Module 1	$E = 0.6635X - 0.0171$	0.9237	8.6
Module 2	$E = 1.0732X - 0.0433$	0.8832	16.5
Module 3	$E = 0.8056X - 0.0592$	0.9264	23.2
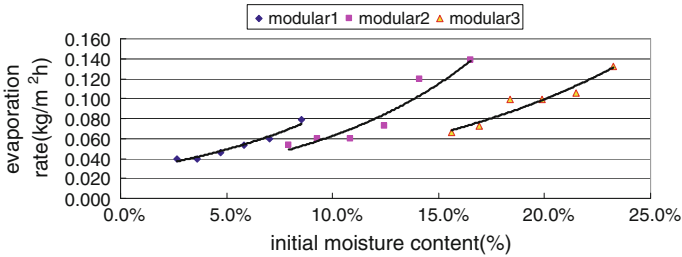
Fig. 18.5 Relation of average evaporation capacity with the initial moisture content for the improved model

indicate the relation between the module evaporation rate and initial moisture content.

$$Y = Ae^{BX} \tag{18.4}$$

Table 18.7 Relation of average evaporation capacity with the initial moisture content for the improved model

Module	Equations	Coefficient of determination (R^2)	Initial moisture content (%)
Module 1	$Y = 0.0269e^{11.979X}$	0.9621	8.6
Module 2	$Y = 0.0185e^{12.156X}$	0.91	16.5
Module 3	$Y = 0.018e^{8.5584X}$	0.9203	23.2

18.5 Conclusions

The conclusions could be summarized as follows:

1. Under the same initial moisture content conditions, the main control factor for the evaporation of the module was the initial moisture content, and the average evaporation capacity reduced with the moisture content decreasing.
2. Under different initial moisture content conditions, the initial moisture content of the module was small, and the average evaporation capacity was low. Evaporation process had been controlled by the water supply capacity of the module (i.e., the initial moisture content). The variation of the environmental parameters influenced less than the initial moisture content.
3. The model reflecting the relation between the accumulative evaporation capacity and time under uneven water supply conditions was constructed through experiments. The coefficient of determination reached 0.999, showing a good correlation between them.
4. An improved regression curve model was proposed to reveal the accurate relation between the average evaporation capacity and initial moisture content, and the coefficient of determination was higher than 0.91.

References

1. Wang Z (2003) Influencing factor analysis of the soil moisture evaporation. J Shanxi Water Conservancy 26(2):26–28
2. Wang K (2010) Water flow and solute migration in unsaturated soil. Beijing Science Press, Beijing

3. Van Genucheten MT (1980) A closed form equation predicting the hydraulic conductivity of unsaturated soil. Soil Sci Soc Am J 44:892–898
4. Liang C, Zhang F, Shi X (2009) Mathematical model for a thin-layer soil water evaporation. Chin Water 9(4):181–183
5. Shi X, Zhang F, Wang G (2006) Dynamic experimental study of soil water dehydration. J Appl Found Eng Sci 14(3):333–338
6. Bernard K, Vanclin M, Vidal-Majar D (1981) Possible use of active microwave remote sensing data for prediction regional evaporation by numerical simulation of soil water movement, the unsaturated zone. Water Resour Res 17:1603–1610
7. Ma J, Sun X, Guo X, Wang Z (2010) Soil water evaporation experimental study under the water storage pit irrigation condition. Mod Agric Water Free Efficient Use Theor Pract 2:266–269
8. Gardner WR (1959) Solutions of the flow equation for the drying of soil and other porous medial. Soil Sci Soc Am J 23:183–187
9. Zhao H, Liu X, Wu Q (1992) Soil water evaporation mathematical mode for the leave covering conditions. Soil Water Conserv Bull 19(2):61–64
10. Xie X, Zuo D (1991) Farmland evaporation. China Meteorological Press, Beijing
11. Jiang J (1995) Research on the soil water evaporation model. Sichuan Forestry Sci Technol 15(4):20–25
12. Lu W, Bai K (1987) New method for calculating evaporation value. Hydraul Eng 26(3):12–15
13. Lei S (1984) Theoretical analysis on one-order soil water evaporation model. J Chengdu Univ Sci Technol 4:135–138
14. Zhang Y, Cai S, Cai M (1991) Uneven soil water evaporation research under the conditions of low water content of surface soil. J Wuhan Hydraul Power 24(2):157–164
15. Jin D, Yang S (1981) Method to calculate soil water evaporation capacity based on ordinary meteorological data. People's Yangtze River 4:47–52
16. Li H, Cai H, Wang J, Zhao W (2008) Soil water evaporation mathematical model in the reference of water evaporation capacity. J Agric Eng 24(3):1–4
17. Fan A, Liu W, Wang C (2004) Influence of environmental factors to soil water evaporation. Sol Energy 25(1):1–5
18. Kang S, Liu X, Gao X (1992) Computational simulation for the soil-crop-atmosphere continuum moisture transmission. J Hydraul Eng 3:1–12
19. Choudhury B (1983) Modeling the effect of weather condition and soil water potential on canopy temperature for corn. Agric Meteorol 29:169–182
20. Wang J, Cai H, Liu H (2002) Research on the farmland water evaporation capacity by using Penman-Monteith model and evaporating dish methods. Arid Region Agric Res 20(4):67–71

Chapter 19
Study on the Characteristics of Flow Field Affected by Obstacle with Push–Pull Ventilation

Yu Zhou, Yi Wang, Kai Zheng and Xiaojing Meng

Abstract Push–pull ventilation system has an advantage over local ventilation system in being more applicable to large working areas. In the ventilated room, there are always varieties of obstacles, such as operator, work piece, and work table. The presence of the obstacles can disrupt the predicted airflow or change its predicted direction. The uniform flow of push–pull ventilation system has advantages over common push–pull ventilation system. The air originated from push hood moves toward the pull hood keeping the same velocity as well as the same air vector. Then, invisible air layers are formed in the midst of the open air. The air flow velocity is very low as 0.2–1.0 m/s, while the recommend air flow velocity of ACGIH is greater than 5 m/s, and with such a very low velocity, the operators cannot feel it even in the center of air flow. In addition, the uniform flow of a push–pull ventilation system has a character that it is not easy to be disturbed relative to the common push–pull ventilation system. In this study, smoke visualization was used in preliminary studies to observe the effects of a uniform flow velocity and the presence of an obstacle in the ventilation zone. On the basis of the results, the positions of the obstacle were selected to test by experimental measurements. From the experiment, conclusions were obtained as follows. The uniform push–pull ventilation has high capture efficiency even under the low velocity. Its law is different from the general push–pull ventilation, that is, in the region of jet, the velocity reduced slowly. And the uniform push–pull ventilation has a character of flow recovery that means the air flow can detour the obstacle in its path and the flow field can return into the original shape.

Y. Zhou · Y. Wang (✉) · K. Zheng · X. Meng
School of Environmental and Municipal Engineering, Xi'an University of Architecture and Technology, Xi'an 710055 Shaanxi, China
e-mail: wangyi@xauat.edu.cn

Y. Zhou
e-mail: zhouyu@xauat.edu.cn

Keywords Push–pull ventilation · Uniform velocity · Obstacle · Smoke visualization · Experiment · Aerodynamic characteristics

19.1 Introduction

Adequate ventilation in any workplace is essential for good health and productivity. Local ventilation systems have been the main method to remove the contaminants in factories. However, it is well known that suction power decreases exponentially as distance increases and the control distance of an exhaust hood is very limited. The distance between the source of the contamination and the exhaust hood must not be more than one meter. Push–pull ventilation system has an advantage over local ventilation system in being more applicable to large working areas. The push–pull ventilation system consists of a push unit and a pull unit. A jet of air is blown from the push unit and air is sucked by a hood of the pull unit on the opposite side. Along the path of the air, pollutants are induced by the air jet and carried into the exhaust hood.

In ventilated room, there are always varieties of obstacles, such as operator, work piece, and work table. The presence of the obstacles can disrupt the predicted airflow or change its predicted direction. Experiments and predictions of Nielsen [1] show that obstacles such as desk, computer, and chair redistribute the velocity field in the occupied zone of the room. Nielsen [2], Awbi [3], and Christensen [4] presented the results describing the influence of ceiling-mounted obstacles by experiments and numerical simulations. The study of Welling [5] has shown that the presence of the worker affects the air flow pattern strongly, and workers arm movements influence contaminant dispersion.

Ojima [6] establishes a measurement of the capture efficiency of a push–pull ventilation system by means of a tracer gas method. The capture efficiency was 95.1–97.9 % when a blockage material, a manikin, was set in the ventilation zone. The results suggest that the uniform flow of a push–pull ventilation system will detour a blockage, and the performance of the system will not be reduced.

While the obstacles in ventilated room were thoroughly investigated in previous study, most of the previous studies have dealt with the effect of obstacles in conditioning room by general ventilation not by push–pull ventilation. The present guidelines for push–pull ventilation systems have been given by the American Conference of Governmental Industrial Hygienists. The recommended push velocity is greater than 5 m/s, and the push–pull systems are not suitable in cases where there are obstacles in the path of the air flow.

The uniform flow of push–pull ventilation system has advantages over common push–pull ventilation system. The air originated from push hood moves toward the pull hood keeping the same velocity and the same air vector. Then, invisible air layers are formed in the midst of the open air. The air flow velocity is very low as 0.2–1.0 m/s, while the recommended air flow velocity of ACGIH is greater than

5 m/s, and with such a very low velocity, the operators cannot feel it even in the center of air flow. In addition, the uniform flow of a push–pull ventilation system can save energy. Moreover, it has a character that it is not easy to be disturbed relative to the common push–pull ventilation system.

While the present guidelines are useful for the uniform flow push–pull ventilation systems, they may not be accurate for considering the presence of an obstacle in the ventilation zone. This chapter describes the effects of uniform flow of push–pull ventilation system and the presence of an obstacle in the ventilation zone on the flow characters of the push–pull ventilation system.

In this study, smoke visualization was used in preliminary studies to observe the effects of a uniform flow velocity and the presence of an obstacle in the ventilation zone. On the basis of the results, the positions of the obstacle were selected to test by experimental measurements.

19.2 Experimental Methods

19.2.1 Apparatus

The installation of the push–pull ventilation system is shown in Fig. 19.1. The test room's dimensions were $5{,}850 \times 5{,}450 \times 3{,}000$ mm. The experimental equipment consisted of push unit and pull unit. The open faces of the push unit and the pull unit were 1,000 mm (H) $\times$ 1,000 mm (b), respectively, and the distance between these unit was 3,800 mm. A pull hood flange with a height $F_3 = 1{,}500$ mm is installed, while the push hood is not equipped with a flange.

The push unit and the pull unit were set opposite to create horizontal, uniform flow between them. Determination of the velocity of the push unit and pull unit is made according to the guideline of the flow rate ratio method 7, and the velocities of the push unit and pull unit were $V_1 = 0.63$ m/s and $V_2 = 3.60$ m/s, respectively.

The most important aspects for the uniform flow push–pull ventilation system are the uniformity of air flow from the push hood which produces a highly stable air velocity and direction and good performance that does not disperse
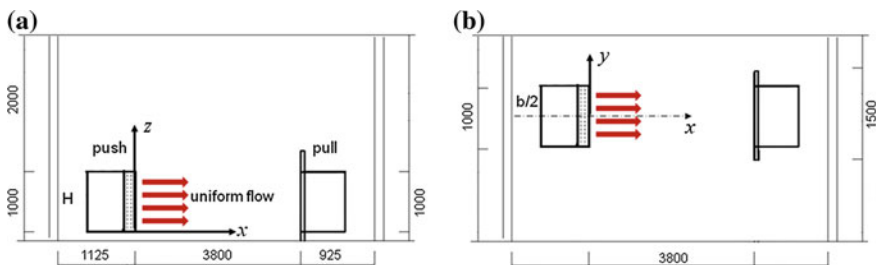
Fig. 19.1 Overview of the push–pull system. **a** *Front* view. **b** *Top* view
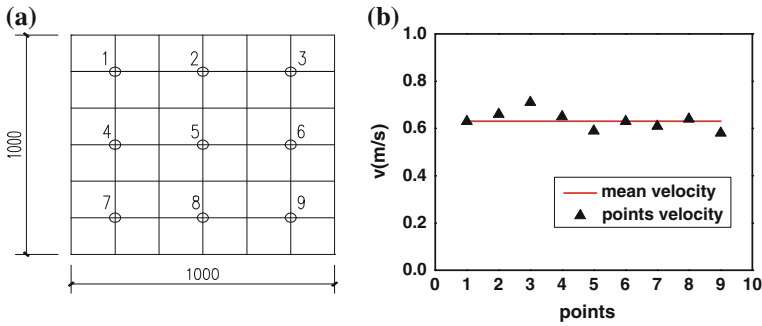
Fig. 19.2 Sampling points and deviation of the push hood. **a** Sampling points. **b** Deviation

contaminant. However, it is very difficult to create uniform flow having same vector of the air. Orifice plate and honeycomb were used in push hood to create the uniform flow. Uniform flow velocity was measured by swema 3,000. The sampling points of the push hood are shown in Fig. 19.2. There were 9 sampling points, the mean velocity was 0.63 m/s, and the maximum deviation and minimum deviation were 18 and 1.8 %. The results meet the performance of uniform flow.

19.2.2 Position of Obstacle

In ventilated room, there are always varieties of obstacles, such as operator, work piece, and work table. Operator is always in the ventilated area and affects the ventilation performance. In this study, a mock-up mannequin in a seated pose which simulated an operator at work was used as an obstacle. The dummy was about 1.2 m in height as it seated and 0.4 m in width. The area occupied by the obstacle in the ventilation zone of cross-sectional area was 40 %. Among the push unit and the pull unit, obstacle was placed and the positions of obstacle are shown in Fig. 19.3. Positions 1, 2, 3, and 4 are at the centerline of the uniform flow. Position 5 is beside position 2, and the distance between position 2 and position 5 is 0.6 m.

Fig. 19.3 Positions of obstacle
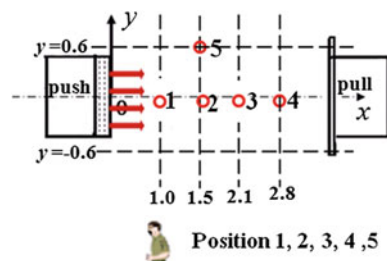
Fig. 19.4 Measurement
location
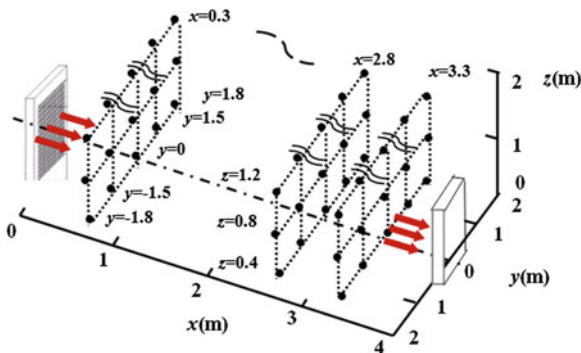
Figure 19.4 is the measurement location. The origin of the coordinates is the center of the push hood. The x-axis is the horizontal coordinate from the push hood to the pull hood, and it is the same direction with the push jet. Toward x direction, at every 0.3 m, there is a sample point; toward y direction, at every 0.3 m, there is a sample point, and there are 3 planes in z direction, and the coordinates are $z = 0.4$, 0.8, 1.2 m.

19.2.3 Smoke Generator

The current study made the flow visible by using a smoke generator SZ550. The smoke was emitted in front of the push hood. The smoke visualization technique helped to understand the uniform push–pull flow without obstacle and with obstacle.

19.3 Results and Discussion

19.3.1 Smoke Visualization

Using the smoke visualization technique, the flow field is observed. Figure 19.5 shows smoke visualization with obstacle at different positions. In order to examine the performance of the uniform push–pull ventilation with obstacle, the push–pull ventilation without obstacle was first to be tested to compare with it.

Figure 19.5a shows the flow field of the push–pull ventilation without obstacle. The trajectory of the jet remains almost horizontal toward the pull hood. Under this circumstance, the smoke is all drawn into the pull hood and the air is not dispersion.

In Fig. 19.5b, the obstacle is at position 1 where the manikin was placed 1.0 m from the push hood. It shows a small part of the smoke is drawn into the pull hood,
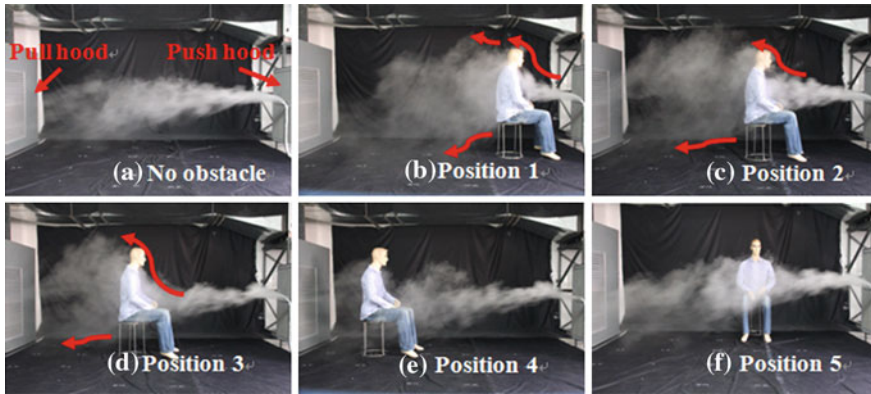
Fig. 19.5 Smoke visualization of obstacle at different positions

and that represents a large part of the jet fluids is dispersed into the atmosphere. At the location of $x/L = 0.26$, it is too close to the push hood and the obstacle obviously has a huge effect on push jet. The performance of the push–pull ventilation system was lowered by the obstacle which interrupted the uniform flow of the system. In Fig. 19.5c and d, the obstacle is at position 2 and 3 where the manikin was placed 1.5 and 2.1 m from the push hood, as $x/L = 0.40$, 0.55, respectively. The two positions are approximately in the middle of the push unit and pull unit. This circumstance is often encountered in work place, so position 2 and 3 are the typical cases. Figure 19.5b–d shows the uniform flow of a push–pull ventilation system all detours the obstacle in front of it, and the separation of the boundary layer occurs at the obstacle's back. It is recognized that the air flow is not dispersed and reversed when the push jet come across the obstacle. The air flow goes along the profile of the obstacle and separated at the back of the obstacle and then moves on. The performance of the uniform push–pull ventilation is better with the increase in distance from the push hood. In Fig. 19.5e, the obstacle is at position 4 where the manikin was placed 2.8 m from the push hood. It shows most of the smoke is drawn into the pull hood. The position 4 is close to the pull hood, so it is not necessary to have the push hood; the pull hood only is needed.

In Fig. 19.5f the obstacle is at position 5 where the manikin was placed 1.5 m from the push hood and 0.6 m from the y axis, as $x/L = 0.40$, $2y/b = 1.2$. The picture shows that although the manikin was positioned in the uniform flow field, it hardly affected the push–pull flow field.

19.3.2 Experiment Results

From Fig. 19.5, the smoke visualization, obstacle at position 1 is too close to the push hood, and the capture efficiency is low. Obstacle at position 4 is close to the pull hood, though the capture efficiency is high; the push hood is no useless.
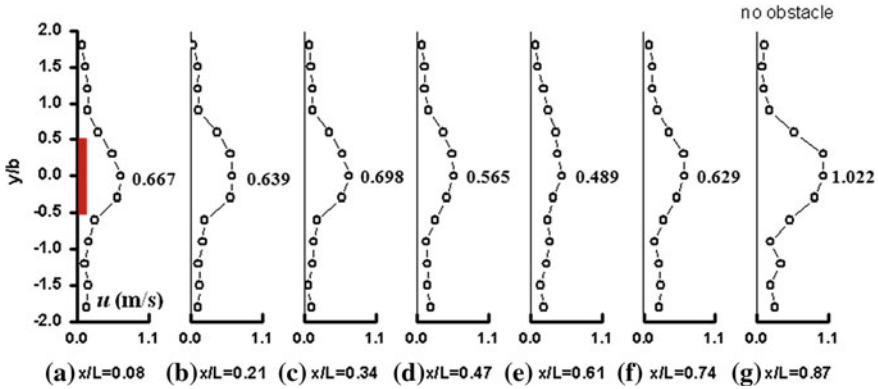
Fig. 19.6 Variations of velocity without obstacle ($z = 0.4$ m)

Obstacle at position 5 is hardly affected by the push–pull flow field. From the above, obstacle at positions 1, 4, and 5 was not studied, obstacle at positions 2 and 3 was studied.

Figure 19.6 shows the velocity field with no obstacle. The velocity of axis reduced slowly, it is in the region of jet field. The velocity accelerated, and it is in the region of confluence flow field. The velocity in $-0.5 < y/b < 0.5$ was maintained, and in the region of $y/b > 0.9$ or $y/b < -0.9$, the velocity is nearly to zero.

Figures 19.7 and 19.8 show the velocity field with obstacle at positions 2 and 3. In the region of obstacle, the velocity field reduced close to zero, and the velocity laws in the region without obstacle were the same, that is, in the jet field, the velocity reduced slowly, and in the region of Confluence flow field, the velocity gradually recovered.
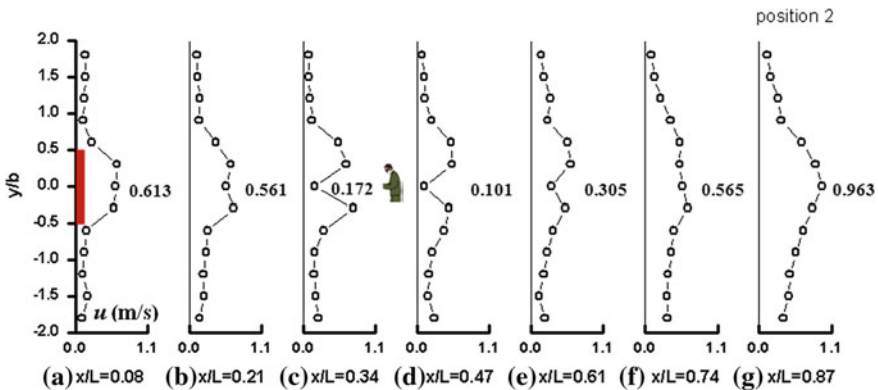
Fig. 19.7 Variations of velocity with obstacle at position 2 ($z = 0.4$ m)
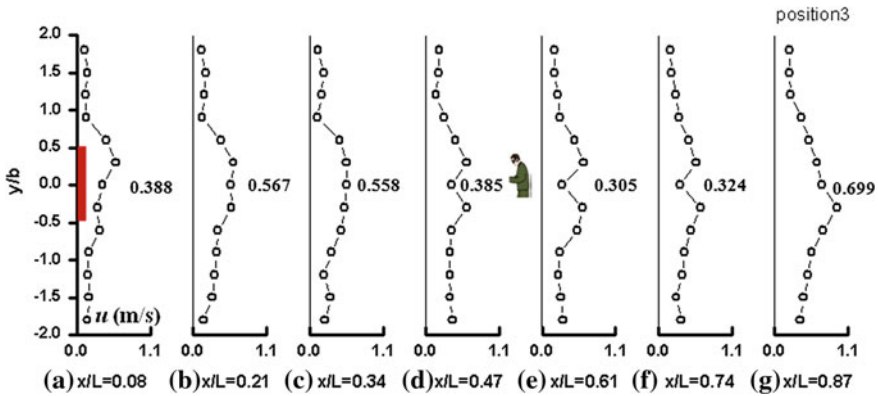
Fig. 19.8 Variations of velocity with obstacle at position 3 ($z = 0.4$ m)

19.4 Conclusions

The uniform push–pull ventilation has high capture efficiency even under the low velocity. Its law is different from the general push–pull ventilation, that is, in the region of jet, the velocity reduced slowly. And the uniform push–pull ventilation has a character of flow recovery that means the air flow can detour the obstacle in its path, and the flow field can return into the original shape.

References

1. Nielsen PV (2004) Computational fluid dynamics and room air movement. Indoor Air 14:134–143
2. Nielsen PV (1983) Air diffusion in rooms with ceiling-mounted obstacles and two dimensional isothermal flow. In: 16th International congress of refrigeration, Paris, 1983
3. Awbi HB, Setrak AA (1987) Air jet interference due to ceiling-mounted obstacles. Proceedings of the international conference on air distribution in ventilated spaces, Stockholm, pp 431–437
4. Christensen KS (1992) Numerical prediction of airflow in a room with ceiling-mounted obstacles. Instituttet for Bygningsteknik, Aalborg Universitetscenter, 1992
5. Welling I, Andersson M, Rosen G, Räisänen J, Mielo T, Marttinen K, Niemelä R (2000) Contaminant dispersion in the vicinity of a worker in a uniform velocity field. Ann Occup Hygiene 44(3):219–225
6. Ojima J (2009) Tracer gas evaluations of push-pull ventilation system performance. Ind Health 47(1):94–96

Chapter 20
Study on Indoor Air Quality in the Education Building Teaching Space

Xiaokun Xu and Zengfeng Yan

Abstract Maintaining good indoor air quality (IAQ) aimed at meeting human requirements on health and comfort of a space. This study takes the IAQ of the construction square of Xi'an University of Architecture and Technology before winter heating as an example. Four basic parameters: indoor air temperature, CO_2 concentration, relative humidity and wind speed were tested to evaluate the basic condition of IAQ in the construction square. Through the analysis of the basic parameters of indoor air changes with time and the influence to the human body, this study will point out the existing problems in this space and give some improving suggestions.

Keywords Education space · IAQ · Human thermal comfort

20.1 Foreword

The concept of the IAQ was raised by some Western countries in the 1970s first. China learns from the introduction of the concept based on foreign standards. The first IAQ standards (GBT 18883-2002) has formulated, promulgated, and implemented by the State Administration of Quality Supervision, Inspection and Administration, State Environmental Protection Administration (SEPA), and the Ministry of Health on March 1, 2003, in China [1]. With the continuous development in industrial enterprises, the air picks up all kinds of pollutants in different degrees. Usually, in the natural ventilation of open outdoor, air pollutants have little impact on people's health [2]. But with the change in the mode of living as well as the improvement in the living conditions, people more than 70 % of the

X. Xu (✉) · Z. Yan
Institute of Arch., Xi'an University of Architecture and Technology, 710055 Xi'an, China
e-mail: xxkxxk2008@163.com.cn

time were in the indoor environment [3]. So building IAQ problems is increasingly being taken seriously, and detection and research in this regard continue to be strengthened.

In recent years, with the rapid development in China's economy, increasing urban architecture and architectural decoration grade level escalating makes the source of indoor air pollution and the factors that affect the quality of indoor air become more and more. For example, some closed indoor space, the poor indoor microclimate, and the use of air conditioning expose population likely to cause unreasonable adverse building syndrome [4]. On the other hand, as people's living standards improved steadily and the overall quality of life also constantly improved, people want a clean, comfortable and warm work, study, and living space and thus have good IAQ and a healthy desire to become even more urgent and serious. The research on evaluating the IAQ can not help the government to make policy to protect the indoor environment [3]. Therefore, monitoring and research on IAQ in China are continued to strengthen. However, most of the research focuses on the living environment, while there are few concerns about the quality of the indoor environment in public places. In this paper, through experimental testing and data analysis, the indoor air quality of the education space is explored.

20.2 Experimental Section

The study site is located in East Building Construction Square of Xi'an University of Architecture and Technology, which is mainly based on the following reasons: ① The square is set for visiting, reading, having lectures and so on. It is a typical indoor public space. ② The square is ready to be rebuilt. So this test has important practical significance to study indoor air conditions for public space.

Xi'an is a cold region, and the annual collective heating start time is November 15th. This test is selected in a period of time before the heating. During this time, as the outdoor temperature decreased, the interior generally not performs the heating. Construction square of Xi'an University of Architecture and Technology, as the object of the study, belongs to a typical indoor public places. And the construction of the fourth floor is steel construction and large-span, so this monitoring can learn more about the indoor microenvironment status.

20.2.1 Parameter Selection

The parameters of this test and research objectives are selected parameters as follows: (1) temperature; (2) humidity; (3) CO_2 volume fraction; (4) wind. The first three monitoring is done by Q-Trak 7565 indoor air quality monitoring of U.S. TSI and the fourth by wind speed measurement instrument.

These parameters are the basic parameters of the IAQ assessment indicators affecting the work of the people in the room, learning efficiency as well as the people in the room comfort. In addition to the above four indicators, national standard provisions need to be measured by indicators such as number of concentrations of particulate matter, formaldehyde concentration, the concentration of radioactive elements in the air, and so on.

20.2.2 Research Methods

1. Place instruments in the selected position to monitor and set test period in accordance with the actual situation and requirements. Target parameters were measured at a fixed period of time and then processed by analysis and mapping software Origin, to derive parameter trends.
2. Compare the test results with the current specification and evaluate the IAQ in the public places tested. Finally, discuss the existing problems based on the evaluation status.

20.2.3 Monitoring Point Location

1. The position of Q-Trak test sampling points is set in construction square as shown in Fig. 20.1, according to the function of construction square; the space is divided into five research areas, namely print room, reading room, exhibition and learning space, learning space, cafe space.

   The probe needs to be set at 1.5 m height from the ground when the instrument detector arranged [4].

2. The position of wind speed meter test points is set in the construction square as shown in Fig. 20.2. According to the characteristics of construction square plane, a total of 22 testing points are set.

20.2.4 Monitoring Time

The experiment is to select a period of time before heating starts in cold regions. Q-Trak test time is from November 7 to 12 in 2011 and sampled five areas in 6 days, each regional tested 24 h. Wind speed measuring instrument test time is November 7, November 9, and November 11 in 2011 and sampled 22 points in 3 days.
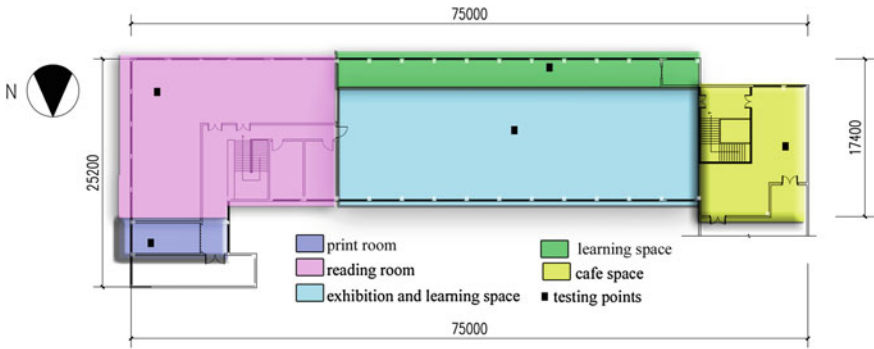
Fig. 20.1 Q-Trak test sample point distribution
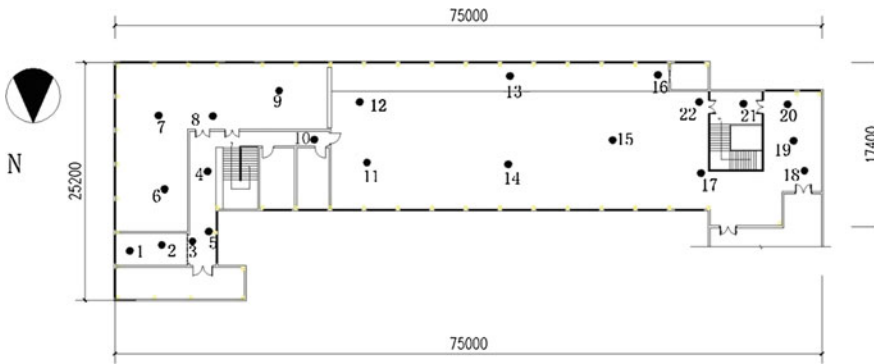
Fig. 20.2 Wind speed measuring instrument test sampling point distribution

20.3 Test Results and Analysis

20.3.1 Instrument Q-Trak Measured Data Analysis

Instrument Q-Trak has measured three basic parameters of the IAQ as follows: the indoor temperature T (°C); air relative humidity (%); CO_2 volume fraction (%). The data will be analyzed through the mapping software Origin changing over time.

1. Temperature

The resultant data are plotted in Fig. 20.3, and Table 20.1 describes variation in temperature. Figure 20.3 shows the overall similarity of the temperature change tendency of the five partitions. The highest value of the temperature appears within the time period 13:30–18:30, while the minimum value appears within the time

period 06:00–08:00 in the next morning. This also indicates that the activities of the people in the room have some impact on the indoor temperature.

The print room and reading room inside have air-conditioned heating, while the other three regions had no heating, so the average temperature is higher than that of the other three regions. Comparing the various district's average daily temperature with winter heating standard values of IAQ standards (GBT 18883-2002), we concluded that the indoor temperature in these regions is in line with regulatory requirements.

2. Relative humidity

Indoor relative humidity is an important parameter to affect the thermal comfort. Indoor health conditions directly related to the domestic and foreign construction air quality standards are clearly defined on the indoor relative humidity indicators. As shown in Fig. 20.4 and Table 20.2, five star region changes in relative humidity curves show different trends in the construction square. During 10 a.m. on November 7 to 10:30 a.m. on November 8, print room indoor relative humidity generally showed a downward trend. A maximum value of 66.5 % appears at 13:21 on November 7th, while the lowest value 52.5% appears at 10:08 on November 8. The average relative humidity of reading room is 49.2 %, lower than the other districts. The highest value 59.9% comes at 11:54 a.m. on November 8, while the lowest value 37.0% comes at 16:13 on November 8. The highest value of learning and exhibition space comes at 7:52 am on November 10, and the highest value is 57.4 %. The highest value of the learning space is 59.2 %, and the time is at 18:01 on November 11; the lowest value is 50.8 %, and the time is at 10:50 on November 12. The Café space highest value is 60.1 %, and the time is at 06:28 on November 11.

3. CO_2 volume fraction

CO_2 is one of the major sources of pollution of indoor air; the CO_2 itself generally does not produce toxic effects to the human body, but when its

Table 20.1 Sampling point measured temperature data statistics list

Partition	Date/time	Mean (°C)	Max (°C)	Min (°C)
Print room	10:50:47/11/07/2011–10:13:43/11/08/2011	18.2	19.6	16.9
Reading room	11:54:45/11/08/2011–00:44:43/11/09/2011	18.9	20.9	16.7
Exhibition and learning space	10:29:18/11/09/2011–10:11:14/11/10/2011	17.3	20.1	15.0
Cafe space	10:19:46/11/10/2011–10:18:42/11/11/2011	16.4	17.5	15.5
Learning space	12:14:34/11/11/2011–10:59:30/11/12/2011	16.6	18.0	15.1
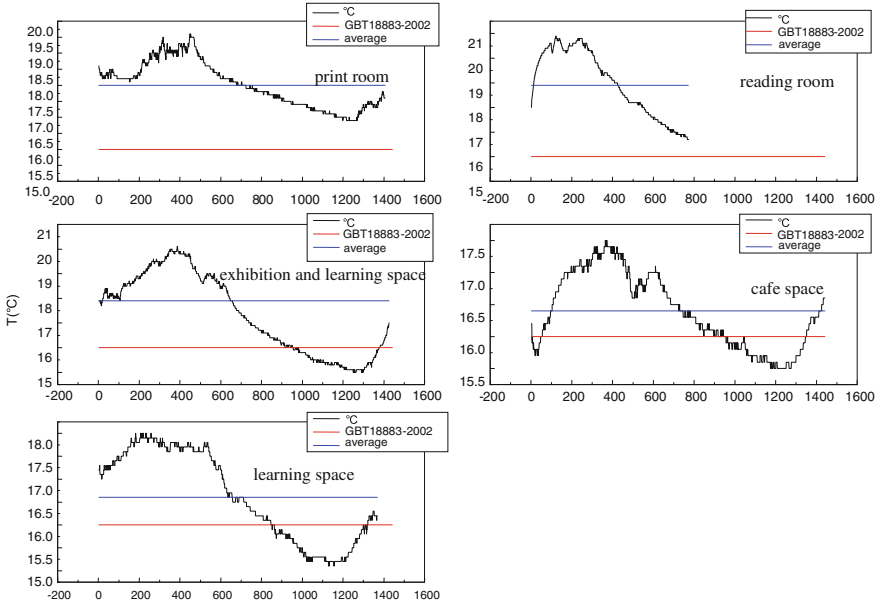
Fig. 20.3 Transform statistical graph of temperature with time

Table 20.2 Sampling points measured relative humidity statistics list

Partition	Date/time	Mean (%)	Max (%)	Min (%)
Print room	10:50:47/11/07/2011–10:13:43/11/08/2011	60.1	66.5	52.5
Reading room	11:54:45/11/08/2011–00:44:43/11/09/2011	49.2	59.9	37.0
Exhibition and learning space	10:29:18/11/09/2011–10:11:14/11/10/2011	52.3	57.4	46.0
Cafe space	10:19:46/11/10/2011–10:18:42/11/11/2011	57.4	60.1	52.8
Learning space	12:14:34/11/11/2011–10:59:30/11/12/2011	56.6	59.2	50.8

concentration exceeds a certain range, the toxic effects affect the human body. When the CO_2 concentration reaches from 0.3 % to 0.4 %, the person will realize the following symptoms: increased depth of breathing, headache, tinnitus stagnant pulse, blood pressure, etc.

As shown in Fig. 20.5 and Table 20.3, the changes in the CO_2 concentration of the five subregion of the construction square with similar trend. CO_2 volume fraction and the indoor human activity changes in relationship can be clearly seen in the curve shown in Fig. 20.5. In work time on November 7 of print room, due to the constant flow of personnel, CO_2 volume fraction presents strong changes. After work, CO_2 volume fraction decreased, and the curve flattens. After the second start
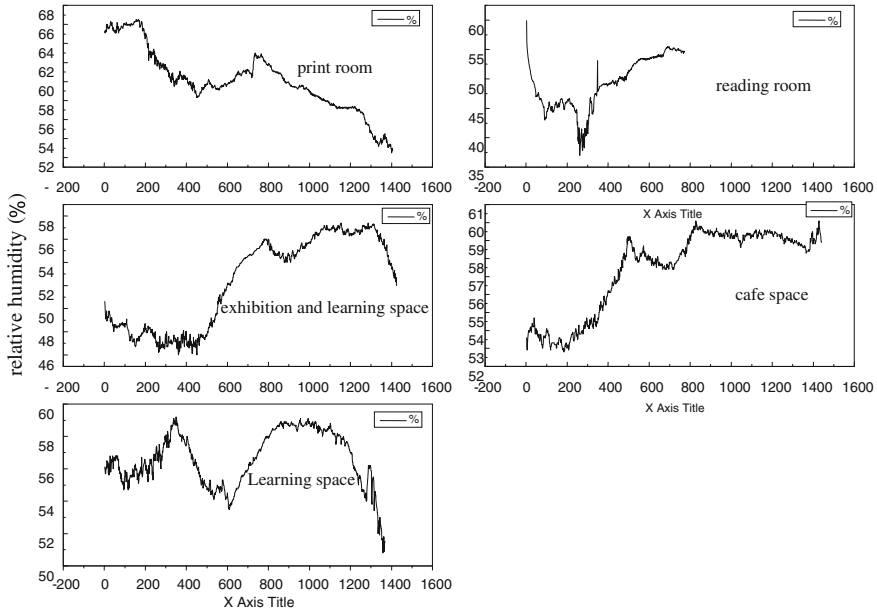
Fig. 20.4 The relative humidity over time transform statistical graph

work in the morning, the CO_2 volume fraction is beginning to show an upward trend. CO_2 volume fraction of the average of reading room is 635, which is due to the detection equipment installed between the places near the library staff, so higher than other partitions. The exhibition learning space are often occupied with students, so the average CO_2 concentration also showed a higher value. While in the rest of the two sub-regions, the mean CO_2 concentration is relatively small. As shown in Fig. 20.5, compared with national indoor air quality standard value, CO_2 volume concentrations are within the range specified in the standard.

20.3.2 Wind Speed Measuring Instrument Measured Data Analysis

Indoor wind speed will produce two effects on the human body: First, it enhances the heat exchange between the human body and the surrounding environment; second, hair may have a sense of the wind speed increased. These two effects affect the thermal comfort of the human body, and in different seasons, the wind affecting the human body is not the same. With the change in wind speed, the body will follow a series of physiological regulation in order to adapt to different environments of wind speed. China's indoor air quality standards (GBT 18883-2002) also

Table 20.3 Sampling points measured CO_2 statistics list

Partition	Date/time	Mean (ppm)	Max (ppm)	Min (ppm)
Print room	10:50:47/11/07/2011–10:13:43/11/08/2011	578	870	441
Reading room	11:54:45/11/08/2011–00:44:43/11/09/2011	635	1077	438
Exhibition and learning space	10:29:18/11/09/2011–10:11:14/11/10/2011	604	915	451
Cafe space	10:19:46/11/10/2011–10:18:42/11/11/2011	558	776	442
Learning space	12:14:34/11/11/2011–10:59:30/11/12/2011	542	1070	436
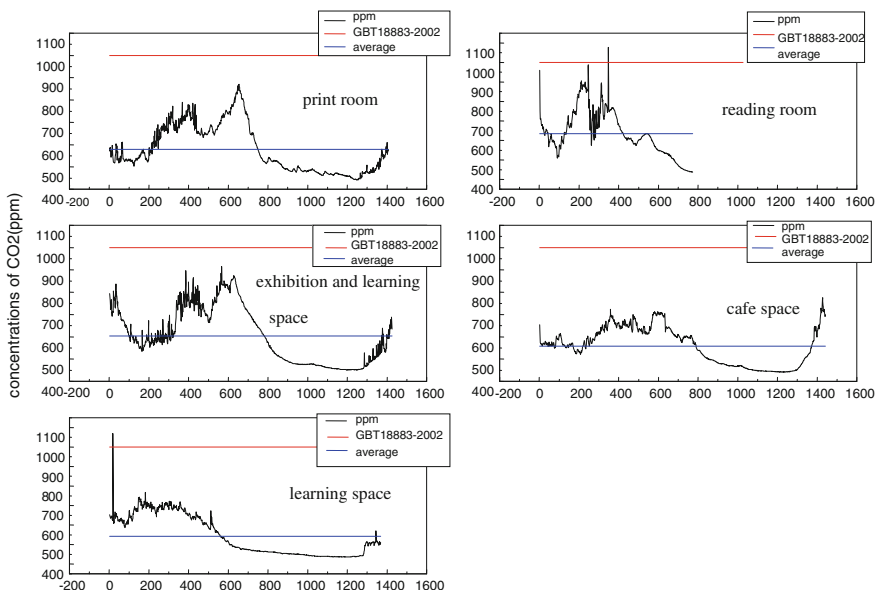
Fig. 20.5 CO_2 over time transform statistical graph

make provision for air velocity. And with winter heating air flow rate standard as a reference, this test will analyze wind speed of construction square.

The tests monitored 22 points in the Plaza of the building in day 7, 9, 11 November, 2011, a total of three measurements for 3 days. The test sampling point distribution is shown in Fig. 20.2, each point is measured from three groups of data each time. Then, the three groups of data were averaged, using Origin software. And the data are compared with the air quality standards, as shown in Fig. 20.6.

The wind speed is relatively large at the point of 20, 21, 22. It is due to the three points are near the stairs, and the door is always open.

20.3.3 IAQ Assessment

IAQ standard (GBT 18883-2002) for the parameters of the physical and chemical parameters predetermined as shown in Tables 20.4 and 20.5 [1].

1. Since the relevant physical parameters, experimental monitoring were done in the winter heating season, the winter heating standards is chosen a reference. Five partitions in the construction square temperature daily averages were as follows: 18.2, 18.9, 17.3, 16.6, and 16.4 °C, within the limits prescribed in the standard. Daily average of relative humidity were 60.1 %, 49.2 %, 57.4 %, 52.3 %, 56.6 %. The average relative humidity in the print room is relative humidity slightly higher than the standard value. The values of relative humidity in the rest four partitions are within the scope of the standard requirements. The wind speed of point 20, 21 and 22 which are near the stairwell is relatively large, while the wind speed of the rest points is within the range of the standard.
2. On the chemical nature of the parameters, the CO_2 concentration of the five district building plaza's daily averages were: 0.0578, 0.0635, 0.0604, 0.0542, 0.0558 %, are less than 0.1 %, and compliance with the standard values.
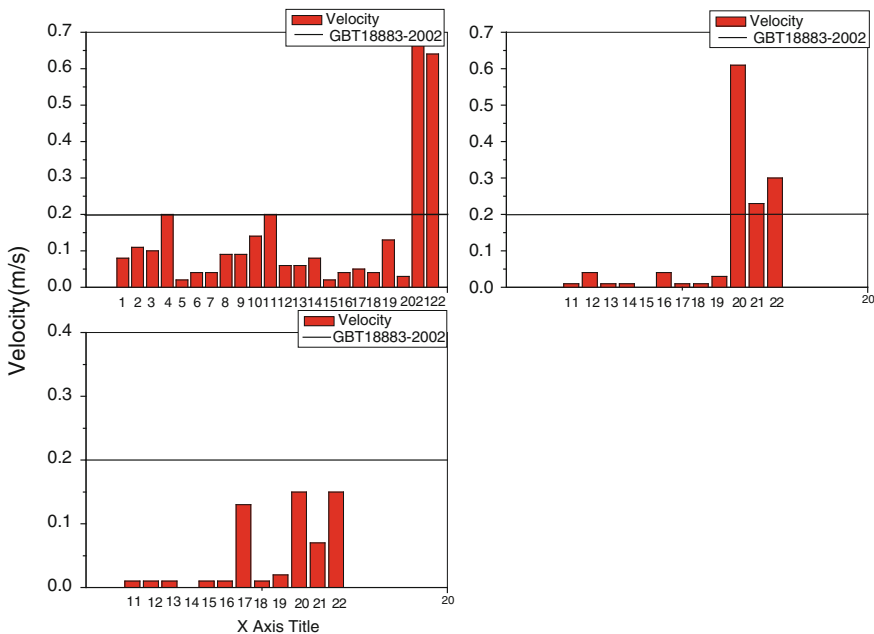
Fig. 20.6 Wind speed at each point of the contrast histogram

Table 20.4 Physical indicators

Parameter	T (°C)	Relative humidity (%)	Wind velocity (m/s)
Standard values	16–24	30–60	0.2
Note	Winter heating	Winter heating	Winter heating

Table 20.5 Chemical indicators

Parameter	CO_2 (%)
Standard values	0.10
Note	Daily mean

20.4 Conclusion

Seen from the results of the test, the air in the reading room is relatively dry, this may be the cause of indoor air conditioning and closed relative to the remaining four partitions. Cafe space near the stairs, and frequent personnel access, the temperature is relatively low, the wind speed is larger than the other partitions and slightly cold in this period before the heating time. On the whole, temperature, relative humidity, CO_2 concentration, wind speed are normal and the period of time before the heating, IAQ is relatively good of construction square.

References

1. (GB50325-2002) Code for indoor environmental pollution control of civil building engineering. China Planning Press, Beijing, China
2. Zhang Y, Wang Y (2004) Analysis of university library indoor air quality. Work Study Libr (3):81–84
3. Deng D, Cai J (2007) Carbon dioxide pollution in the classroom and the measure of fresh air. Environ Sci Technol (9):45–47
4. Wei Z, Dong J (2010) A case study on building indoor air quality—take 44 m² small dwelling residential of Wanda Plaza, Yanta Road as an example. Ningxia Eng Technol 9(3):259–263

Chapter 21
Discussion on Indoor Design Parameters of Air-Conditioning in the Large Space Building with Considering Comfort and Energy Consumption Based on Nomograms

Chen Huang, Ning Cai and Li Shen

Abstract Nowadays, the trade-off among comfort, health, and energy consumption in deciding indoor design parameters of air-conditioning becomes more and more concerned. In the large space buildings with stratified air-conditioning, human comfort is different from common buildings, and each wall temperature is usually different. Thus, the settings of indoor design parameter for air-conditioning in these buildings are different from common building. In this paper, we provided a series of figures where design temperature and humidity were determined on the difference of black globe temperature and air temperature under certain PMV conditions. Because the fresh air volume is one of the healthy indicators for indoor air environment, we provided a nomogram which can be used to determine the fresh air volume with considering the indoor and outdoor environment, situation of room staff activities, occupant density, and building characteristics. Furthermore, the larger the fresh air volume, the better the indoor air quality, but the larger the energy consumption. We also showed a nomogram that can be used to determine the energy consumption of fresh air and the PMV value under certain design temperature and humidity.

C. Huang (✉) · L. Shen
School of Environment and Architecture, University of Shanghai
for Science and Technology, Shanghai, China
e-mail: huangc@usst.edu.cnhcyhyywj@163.com

N. Cai
College of Energy and Power Engineering, Nanjing Institute of Technology, Nanjing, China

21.1 Introduction

With in-depth development of building energy efficiency, the balance between comfort, health, and energy consumption in indoor design parameters of air-conditioning becomes more and more concerned, especially in the large space. Design parameters in occupied zone have a large impact on energy consumption of the air-conditioning system.

Becker [1] has brought up that the model's curve of predicted percentage of dissatisfied (PPD) substantially overestimated the actual percentage of dissatisfied within the partial group of respondents who voted TS (thermal sensation) >0 in winter, as well as within the partial group of respondents who voted TS <0 in summer. Toftum [2] has found out that determining acceptable indoor thermal environments with the adaptive comfort model may result in significant energy savings and having no large influence in the occupants' mental performance. Moreover, Wan [3] has also suggested that larger relative humidity and lower indoor temperature can be chose in order to reducing energy consumption in an air-conditioning building. However, Jang [4] has focused his study on the evaluation of the optimal temperature in each cabin of the Korean maritime patrol vessels. Much energy would be saved if the air-conditioning based on PMV/PPD. Hwang [5] has found out that an energy-saving approach with sacrificing occupants' thermal comfort is difficult to set into action, but those methods, which can ensure the occupants' comfort, are more acceptable and easier in popularizing.

Based on the results in above researches and Professor Fanger's indoor comfort theory [6], we described a series of nomograms for the indoor design parameters, which related to comfort, health, and energy consumption and focused on the large exhibition hall, discussed problems of human required indoor environment in different clothes in eastern and western countries, and provided a scientific theory for designing the indoor thermal environment.

21.2 Relationship Between Design Air Parameters and Comfort in the Air-Conditioning Zone of the Large Space Building

The difference between indoor air temperature and mean radiant temperature is significant in the large space building. The radiant temperature that people in occupied zone felt was caused by integrated radiant effect in upper non-air-conditioning zone and in lower air-conditioning zone. In order to evaluating conveniently, only the cases, which environment black globe temperature was 1–3 °C higher than air temperature, were taken into account to judgment of indoor human comfort.

Figure 21.1 shows the relationship between the comfort predicted mean vote (PMV) index and design air temperature or humidity under cases of M (1.6 met

and 1.2 met), I_{cl} (0.5clo and 0.8clo), Δt (0, 1, 2, and 3 °C), where M means metabolism rate; I_{cl} means clothing thermal resistance; Δt means difference between black globe temperature and air temperature. PMV index increased by the increase in Δt. Taking Fig. 21.1a, for example, under the same indoor air temperature and relative humidity, the PMV index arose about 0.24 when Δt was increased by 1 °C, and moreover, the PMV increased by increase in I_{cl} and M. It was illuminated that if the impact of radiant temperature was considered, the range of design indoor air temperature reduced under a certain PMV. Also, when black globe temperature increased by each 1 °C, in order to gaining the same indoor thermal comfort, the design air temperature had to be decreased by 0.85 °C. Figure 21.1 also shows the impact of relative humidity, human activity, and clothes on design indoor comfortable parameters. The scope of design indoor comfortable parameters was decreased by increasing these factors. Each parameter scope can be seen in Fig. 21.1 clearly under the same comfort condition.

The proper design indoor air temperature can be chosen according to the different Δt in real buildings. For exhibition constructions, when human activity intensity was large ($M = 1.6$ met) and I_{cl} was 0.5clo (suitable for dressing habit of eastern people in summer), if air temperature was 24 °C (meet the standard of ISO7730), the limit value of Δt was 2.5 °C; if air temperature and relative
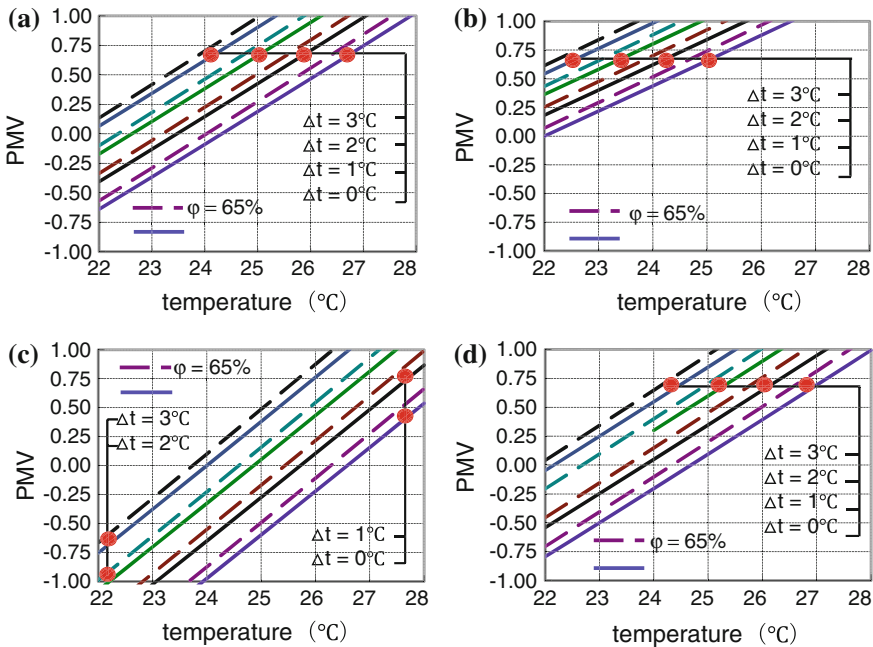
Fig. 21.1 Relationship between design indoor air temperature, humidity, and PMV in different Δt **a** $M = 1.6$ met, $I_{cl} = 0.5$clo, **b** $M = 1.6$ met, $I_{cl} = 0.8$clo, **c** $M = 1.2$ met, $I_{cl} = 0.5$clo, **d** $M = 1.2$ met, $I_{cl} = 0.8$clo

humidity were 26 °C and 50 %, the limit value of Δt was 0.1 °C. The thermal comfort can be hardly met under a stratified air-conditioning system in a large space. When I_{cl} was 0.8clo (suitable for dressing habit of western people in summer), even if indoor air temperature was 24 °C, the 0.3 °C of limit value of Δt was also unrealizable, and this was the main reason of lower design indoor air temperature in international constructions.

21.3 Relationship Between Design Parameters and Health in the Air-Conditioning Zone

Nowadays, one of the most effective ways, which were used to improve the indoor air quality, is to increase the fresh air volume in the room. With the more attention people are paying to the indoor air quality, the interior decoration materials are also to be considered for the fresh air volume besides considering the exhaust quantity of CO_2 by people. In 1996, ASHRAE proposed the new basis of calculation of the fresh air volume that considered both the two factors [7]:

$$L_{f,\min} = L_p \frac{P}{A} + L_b \qquad (21.1)$$

where $L_{f,\min}$ means the minimum fresh air volume per area; L_p and L_b mean the fresh air volume needed by one person per hour ($m^3/(p \ h)$) and by building ($m^3/(m^2 \ h)$), respectively, which can be obtained by ASHRAE Standard [7]; P/A means the occupant density in room (p/m^2).

The CO_2 pollution in room was considered only in formula (21.1). If the outdoor concentration of CO_2 was 0.035–0.04 %, and the indoor personnel work with standing in slight activity intensity [8], the required fresh air volume (RFAV) is to be 35–38 $m^3/(h \ p)$ according to the standard of indoor air quality [9]. If the interior decorating was considered simultaneously, the RFAV need per people would be much more.

Figure 21.2 shows the nomogram to determine the RFAV. It can be defined according to five parameters, namely the concentration of CO_2 in atmosphere, the limit of concentration indoor, person in room work with activity intensity, the occupant density, and fresh air for building.

Assuming that the density of architectural personnel was 0.22 p/m^2 [10] in the exhibition hall of World Expo Shanghai 2010, the concentration of the atmosphere outdoor is 0.035 %, the concentration permitted indoor is 0.1 %, slight activity intensity of people (stand), the fresh air volume needed by the structure itself per hour is 5 $m^3/(m^2 \ h)$, then the RFAV per square meter is 12.8 $m^3/(h.m^2)$. The excess of RFAV is about 39–37 % over that of considering person only. From the nomogram Fig. 21.2, the RFAV can be obtained simply and conveniently by different conditions.

Fig. 21.2 Required fresh air
volume per sq.m
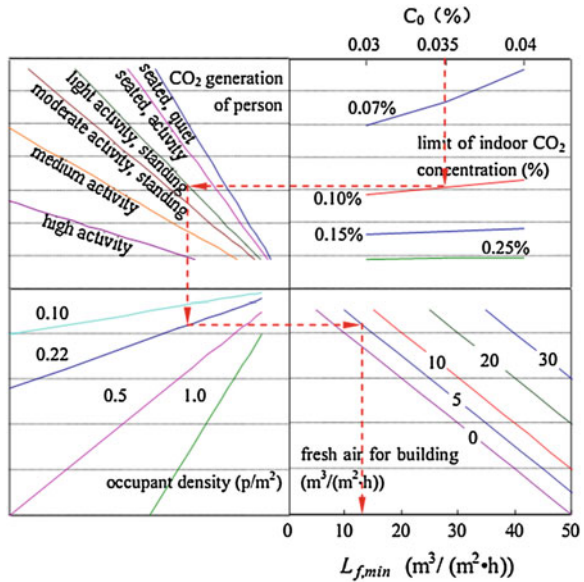
21.4 Discussion on Energy Consumption of Fresh Air and Comfort Under an Indoor Air-Conditioning

The design indoor parameters can influence the human comfort and the energy consumption of air-conditioning. In which the fresh air consumption has a greater impact. The influence of indoor parameters to fresh air cooling load can be calculated as formula below:

$$q_{fr} = L_{fr}\rho(i_w - i_n)/3600 \text{ kW/m}^2 \tag{21.2}$$

where L_{fr} means fresh air volume in unit covered area (m³/(m² h)), and it can be obtained from Fig. 21.2; ρ is air density; i_n means indoor air enthalpy based on design parameters; i_w means enthalpy outdoor. In a typical year for analyzing building thermal environment, outdoor air enthalpy is the single-valued function of outdoor air temperature [11]. The fresh air cooling load and PMV index can be calculated under different outdoor and indoor parameters (the indoor air velocity was 0.5 m/s) and are shown in Fig. 21.3.

Figure 21.3 also shows that the temperature had great influence in both enthalpy and PMV index. Under the condition of the same relative humidity, the enthalpy increased about 2.1–2.3 kJ/kg when indoor air temperature was increased by each 1 °C and, while the PMV index increased about 0.22–0.39 (0.32 of average). Indoor humidity had a great impact on enthalpy, but less impact on PMV index. Under the same temperature, when humidity increases each 5 %, the increased amount of enthalpy is equivalent when temperature increases each 1 °C under the same humidity. The temperature had a great influence in the enthalpy
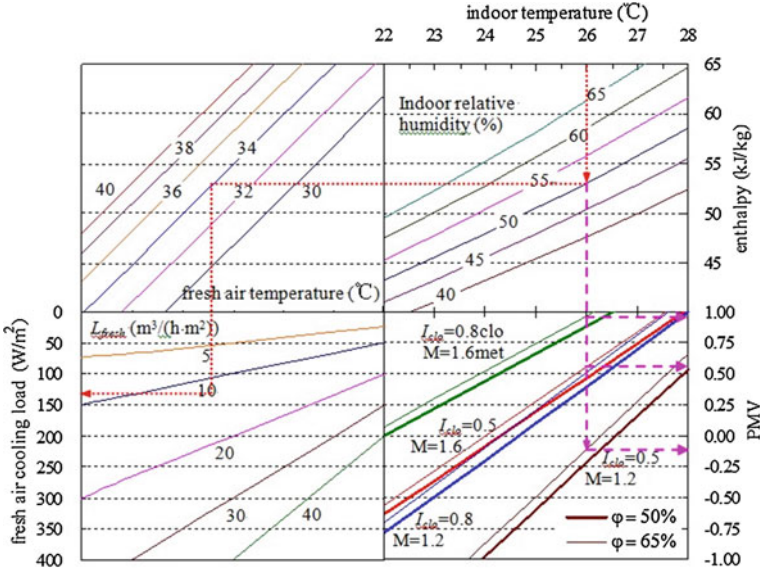
Fig. 21.3 Comfort and fresh air energy consumption under different design indoor parameters

which was closely linked with the amenity indoor and the energy consumption. Therefore, in order to decrease the energy consumption, the design air humidity should be as high as possible. In Fig. 21.3, the design air parameters are related to energy saving and comfort.

World Expo of Shanghai 2010 was held from 1 May to 31 October. During these days, the meteorological parameters changed a lot, and the Bin method was induced to calculate the energy consumption as follows:

$$Q_{\text{fr}} = \sum_{i=1}^{i=N} \tau_i L_{\text{fr}} \rho (i_{wi} - i_n)/3,600 \, \text{kWh/m}^2 \qquad (21.3)$$

where Q_{fr} is the energy consumption (kW h/m^2); N and τ_i are the number of subsection of outdoor dry-bulb temperature during World Expo and the hours (h).If the exhibition halls' opening time is from 9:30 to 22:30, according to the data of typical year and extreme high temperature year in "The meteorological

Table 21.1 BIN data during 2010 Word Expo (outdoor dry-bulb temperature at 9:00 ~ 22:00)

BIN (°C)	8	10	12	14	16	18	20	22
Hours in typical meteorological year (h)	1	7	12	38	62	185	323	417
Hours in extreme high temperature year (h)			17	31	107	166	271	287
BIN (°C)	24	26	28	30	32	34	36	38
Hours in typical meteorological year (h)	390	358	331	173	66	23	6	
Hours in extreme high temperature year (h)	336	324	257	217	191	114	61	13
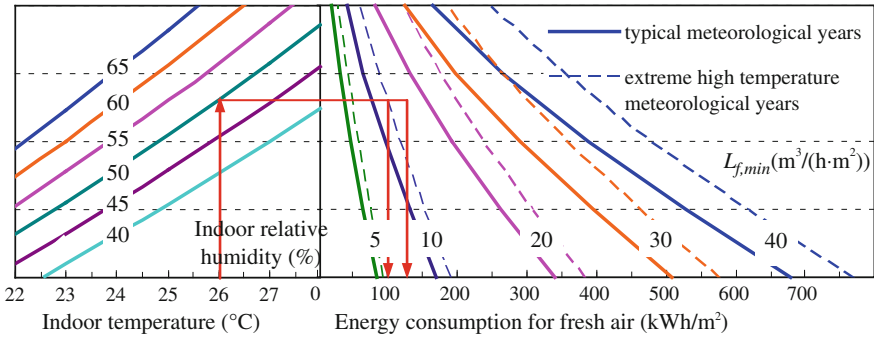
Fig. 21.4 Total energy consumption of fresh air during 2010 World Expo

data of Chinese thermal environment analysis" [12], the BIN data during World Expo are listed in Table 21.1.

Figure 21.4 shows the fresh air energy consumption during Shanghai 2010 World Expo. Based on design indoor parameters and fresh air volume (per area) L_{fr}, the total energy consumption of fresh air can be acquired. For example, L_{fr} was 12.8 $m^3/(m^2 h)$ in the case above, then the energy consumption of fresh air per area was 100–125 kWh/m^2, if L_{fr} was doubled, and the energy consumption of fresh air per area was reached to 200–250 kWh/m^2, and then the value was huge.

21.5 Conclusions

When Δt is increased by each 1 °C, PMV index is increased by approximately 0.24. In large space building, affected by radiant heat exchange from roof, the scope of design air temperature in stratified air-conditioning system is reduced under the certain PMV. When black globe temperature is increased by 1 °C, the air temperature will be decreased by 0.85 °C under the same comfort condition.

If people and construction surface are taken into account, the RFAV per sq.m of construction can be acquired from Fig. 21.2. For example, the person density in exhibition hall of Shanghai 2010 World Expo is 0.22 p/m^2 and the fresh air volume per sq.m of construction is 12.8 $m^3/(h.m^2)$, according to the nomogram in this paper.

The indoor design air temperature shall be chosen wisely, because it has great influence on the enthalpy which is closely linked with the human comfort and the energy consumption. Humidity has less impact on PMV. In order to reduce the energy consumption, the design air humidity shall be as high as possible.

References

1. Becker R, Paciuk M (2009) Thermal comfort in residential buildings—failure to predict by standard model. Build Environ 44:948–960
2. Toftum J (2009) Occupant performance and building energy consumption with different philosophies of determining acceptable thermal conditions. Build Environ 44:2009–2016
3. Wan JW, Yang K, Zhang WJ et al (2009) A new method of determination of indoor temperature and relative humidity with consideration of human thermal comfort. Build Environ 44:411–417
4. Jang MS, Koh CD, Moon IS (2007) Review of thermal comfort design based on PMV/PPD in cabins of Korean maritime patrol vessels. Build Environ 42:55–61
5. Hwang RL, Cheng MJ, Lin TP et al (2009) Thermal perceptions, general adaptation methods and occupant's idea about the trade-off between thermal comfort and energy saving in hot–humid regions. Build Environ 44:1128–1134
6. Fanger PO (1989) The new comfort equation for indoor air quality. ASHRAE (Am Soc Heating, Refrig Air-Conditioning Eng) J 31(10):33–38
7. ANSI/ASHRAE (2007) Standard 62.1-2007, Ventilation for acceptable indoor air quality. ASHRAE Inc
8. Huang C, Jiang P, Lou YY et al (2005) Built environment. China Machine Press, Beijing
9. Ministry of Health of the People's Republic of China (2002) Indoor air quality standard (GB/T18883-2002). China Environment Science Press, Beijing
10. Zhou ZY, Chen Y (2007) Study on the scale of grounds and pavilions for world exposition. Architectural J 1:67–69
11. Huang C, Liu S, Luo X (2007) Study on the running of a hybrid ventilation system. J Harbin Inst Technol (New Ser) 14:295–298
12. Meteorological Phenomena Information Centre of China Meteorological Administration (2005) The meteorological data of Chinese thermal environment analysis. China Architecture and Building Press, Beijing

Chapter 22
Measurement of the Pollutants from Cooking Chinese Dishes

Yujiao Zhao, Angui Li, Ran Gao and Pengfei Tao

Abstract An assessment of a current situation of the actual pollution process of cooking oil fumes during Chinese cooking was carried out in this study. Parameters were measured during cooking mode, and idle mode included the continuous measurements of air temperature, air relative humidity, and generations of CO, CO_2, and TVOC during cooking process of the breathing zone. From the data available, we could find that without using an exhaust hood, the concentrations of the breathing were far more than the acceptable level. In addition, the generation of CO and CO_2 had little to do with the cooking time and occurred largely as a result of the burning of the gas. The high emission of TVOC concentration was related to the use of the seasonings and ingredients. There was a significantly higher value of temperature during cooking the eight case-study dishes, because the wasted heat cannot be removed effectively. The influence factor of relative humidity is complicated. After we turned on the exhaust hood, the concentrations of CO, CO_2, and TVOC exhibited an exponential decay with respect to the measuring time.

Keywords Indoor air quality · Chinese residential kitchen · Cooking oil fumes · Indoor thermal environment · Measurement

22.1 Introduction

China has the maximum population, nearly 1.3 billion in the world, and consumes numerous foods cooked by various ways everyday. In China, a wide range of seasoning is applied during cooking process [1]. Therefore, the emissions from

Y. Zhao (✉) · A. Li · R. Gao · P. Tao
School of Environmental and Municipal Engineering, Xi'an University
of Architecture and Technology, Xi'an, 710055 Shaanxi, China
e-mail: zhaoyujiaobaobao@163.com

different styles of cooking operation might make a quite significant contribution to indoor air pollution in China.

Chinese's housewives spend 3.4–4 h in the kitchen, and it is about 1/4 of their everyday life [2]. By analyzing the samples of cooking oil fumes, Weng et al. [3] found out that a high concentration of carcinogens was in the cooking oil fumes. The risk of contracting cancer for non-smoking women was reported by Ko et al. [4]. He found that it was associated with the efficiency of the exhaust hood. Seow et al. [5] found that inhalation of carcinogens generated during frying of meat may increase the risk of lung cancer among non-smokers. Li et al. [6] measured particle size distribution from scrambling eggs, frying chicken, and cooking soup. Based on measurements, the concentrations of submicrometer particles increased ten times during cooking.

Chinese kitchen environment was reported only in a few literatures. Chao's measurements showed that carbon monoxide (CO) concentration is at highest level during cooking hours in Taiwanese [7]. Individual exposure to NO_2 in residences was tested in Hong Kong by Chao and Law [8]. The study showed that one's exposure to NO_2 has a lot to do with cooking behavior. Chiang et al. [9] and Li et al. [10] investigated indoor air environment in traditional, residential, and commercial kitchens. Lai [11] discovered that the generation of CO_2 occurs largely as a result of the burning of the gas and has been little to do with the cooking behavior.

The previous studies highlight the importance of good indoor air quality in the kitchen. However, the actual pollution process of cooking oil fumes during Chinese cooking is still unknown. In order to improve the indoor thermal environment of typical Chinese-style kitchen and fully understand the emission process of cooking oil fumes, a study was undertaken in a traditional residential kitchen of Xi'an, China, to investigate the pollution process during cooking the typical dishes of China.

22.2 Experimental Methods

Xi'an is one of the most famous Chinese metropolises with more than 7 million populations. So it is a perfect place to investigate the indoor environment in Chinese residential kitchens during cooking. A typical Chinese residential kitchen was selected in May 2012. The residential kitchen is part of a typical middle-sized family apartment building. The apartment building is sited in a street with little traffic where some other apartment buildings are found. No open chimney or other sources of air pollution were noted nearby. The studied hood, range, and appliances are the typical type used in Chinese residential kitchens. The geometric data of this case-study kitchen are listed in Table 22.1. Schematic diagram of the case-study kitchen is presented in Fig. 22.1. In this study, it was assumed that the primary air would flow from the crack under the interior doors, with a height of 0.02 m from the floor. The front lower edge of the hood of the case-study kitchen overhang is set to the 1.8 m as measured vertically from the finished floor. The face velocity of the exhaust hood is 4 m/s.

Table 22.1 Geometric specifications of the model kitchen (*unit* m)

Case-study kitchen	$3 \times 2.5 \times 2.8$
Cooking bench	$1 \times 2.5 \times 0.8$
Gas fire	$0.7 \times 0.2 \times 0.2$
Exterior window	2×0.9
Interior door	2×0.9
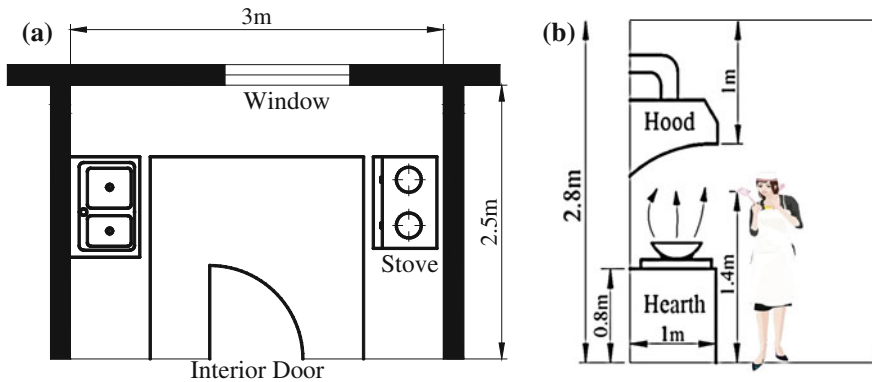
Fig. 22.1 Schematic diagram of the case-study kitchen. **a** Space diagram. **b** Side view

22.2.1 Procedures

The experimental process was as follows: First, the interior door and exterior window are closed. Then, we placed the measuring sensors at the breathing zone of Chinese women (140 cm) and measured the background levels of the kitchen indoor environment for a period of 600 s. After that, we started cooking one of the case-study dishes and continuously measured the air temperature, air relative humidity, and concentrations of CO, CO_2, and TVOC. A sample was collected outdoor. When the cooking process was finished, the exhaust hood was turned on until the concentrations in the kitchen restabilized at an acceptable level. The consumed quantity of gas during cooking each dish is presented in Table 22.2.

22.3 Results

22.3.1 Spring Rolls

In cooking spring rolls, after ensuring the background values, the cooking process was as follows: Step 1: Turn on the stove; Step 2: Enough cooking oil was poured in a deep skillet; Step 3: When the oil was heated, we fried the spring rolls until

Table 22.2 The consumed quantity of gas during cooking each dish

Dishes	Consumed quantity of gas (m^3)
Spring rolls	0.023
Fish head en casserole	0.101
Tofu soup, Monk Wen Si Style	0.074
Sautéed minced shrimps with mixed vegetables	0.034

golden brown; Step 4: Dished out the spring rolls; Step 5: Turn off the stove; Step 6: Turn on the exhaust hood.

The results of test parameter's measurement are presented in Fig. 22.2. From the test results of Step 1 and Step 2, we could find that "turn on the stove" was the main reason that caused the increase in CO, CO_2, and TVOC concentrations. After turning on the stove (Step 1), CO concentration increased dramatically and achieved the "peak values": 15.8 ppm. Temperature and relative humidity would be increased because of heating the oil (Step 2). In this process, relative humidity achieved the "peak values": 79 %, and it was 13 % (19.7 %) higher than the outdoor value, while other test parameter's values increased slightly. When we put spring rolls in hot oil and deep-fried them until golden brown (Step 3), TVOC concentration rose shapely and achieved the "peak values": 4.39 mg/m^3. At the same time, CO_2 accumulation concentration achieved the peak level: 1,746 ppm. The test parameters except temperature all decreased after turning off the stove (Step 5). When the exhaust hood was turned on, temperature value achieved the "peak values": 29.94 °C, and it was 7.94 °C (36.1 %) higher than the outdoor value. Then, all the other test parameters were reduced.

Fig. 22.2 Variations in test parameters over cooking spring rolls in the experiment without using an exhaust hood. Spring rolls. **a** Temperature. **b** Relative humidity. **c** CO concentration. **d** CO2 concentration. **e** Total volatile organic compound

22.3.2 Fish Head en Casserole

In cooking fish head en casserole, after ensuring the background values, the cooking process was as follows: Step 1: Turn on the stove with a high heat; Step 2: As soon as the crackling sound is heard, pour 30 ml liquor in the pottery pot and stir gently. At the same time, reduce heat to low; Step 3: Cover the pot; Step 4: The high TVOC concentration triggered the gas alarm; Step 5: Turn off the gas; Step 6: Open the window and turn on the canopy hood; Step 7: Turn on the stove again; Step 8: Remove from heat and simmer it for 1 min.

The results of test parameter's measurement are shown in Fig. 22.3. After we turned on the stove (Step 1), temperature, relative humidity, and concentrations of CO, CO_2, and TVOC all increased. As soon as we poured 30 ml liquor in the casserole and reduced heat to low (Step 2), relative humidity value decreased, while all the other parameters rose. Among them, TVOC concentration rose to 5.04 mg/m^3. Then, we covered the pot (Step 3), TVOC concentration initially decreased, reached a minimum value at 3.67 mg/m^3, and then increased to 25 mg/m^3. The value exceeded the high alarm of the ppbRAE volatile organic compound monitor (Model PGM-7240), and a loud buzzer and red flashing LED were activated immediately. At the same time, the high TVOC concentration triggered the gas alarm. When the TVOC concentration reached 30.5 mg/m^3, we have to temporarily stop the experiment. After we turned off the gas (Step 5), concentrations of TVOC and CO_2 rose sharply and achieved the "peak values" 36.8 mg/m^3 and 4,144 ppm, respectively. Then, CO concentration and temperature values achieved the peak level 20.9 ppm and 37.44 °C, respectively. As soon as we opened the window and turned on the canopy hood (Step 6), all the test parameter values went down. In this process, relative humidity achieved the "minimum values": 29 % and it was 36 % (55.4 %)
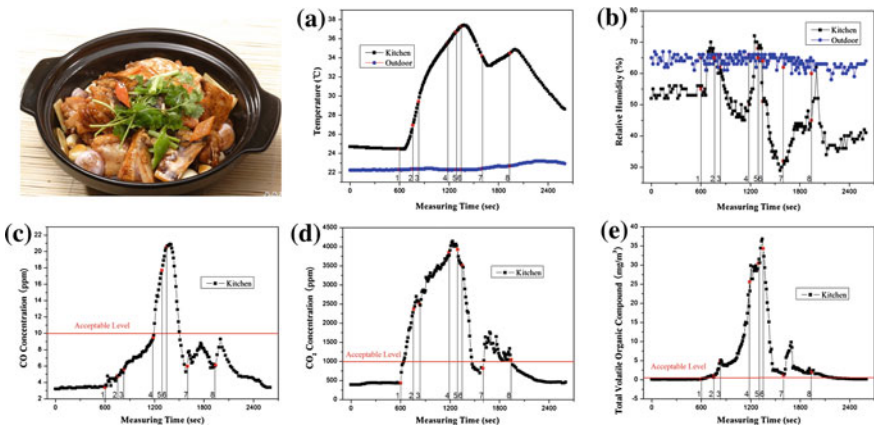
Fig. 22.3 Variations in test parameters over cooking fish head en casserole in the experiment without using an exhaust hood. Fish head en casserole. **a** Temperature. **b** Relative humidity. **c** CO concentration. **d** CO2 concentration. **e** Total volatile organic compound

lower than the outdoor value. When all clear, we turned on the stove again (Step 7) and the test parameter values all increased slightly.

22.3.3 Tofu Soup, Monk Wen Si Style

In cooking Wensi tofu soup, after ensuring the background values, the cooking process was as follows: Step 1: Turn on the stove to high and brought a pot of water to the boil; Step 2: Blanch soft tofu over boiling water; Step 3: Turn off the stove; Step 4: Turn on the stove to high. Put the chicken broth into the pot and brought it to the boil; Step 5: Added the vegetables in the chicken broth. Reduced the heat and simmered for five minutes; Step 6: Turn off the stove and then serve it hot; Step 7: Turn on the exhaust hood. Figure 22.4 described the results of test parameter's measurement. During the process of bringing a pot of water to the boil (Step 1), all the test parameter values increased. When blanched soft tofu over boiling water (Step 2), TVOC concentration increased sharply. As soon as we turned off the stove (Step 3), concentrations of CO, CO_2, and TVOC decreased, while temperature and relative humidity increased. When we put the chicken broth into the pot and brought it to the boil (Step 4), all the test parameter values except relative humidity increased. After we added the food materials in the chicken broth (Step 5), the concentrations of CO, CO_2, and TVOC all rose sharply and achieved the "peak values" 31.3 ppm, 4,897 ppm, and 7.25 mg/m^3, respectively. As soon as we turned off the stove (Step 6), relative humidity, concentrations of CO, CO_2, and TVOC decreased. At the same time, temperature value achieved the "peak values": 41.5 °C, and it was 10.5 °C (33.9 %) higher than the outdoor value.
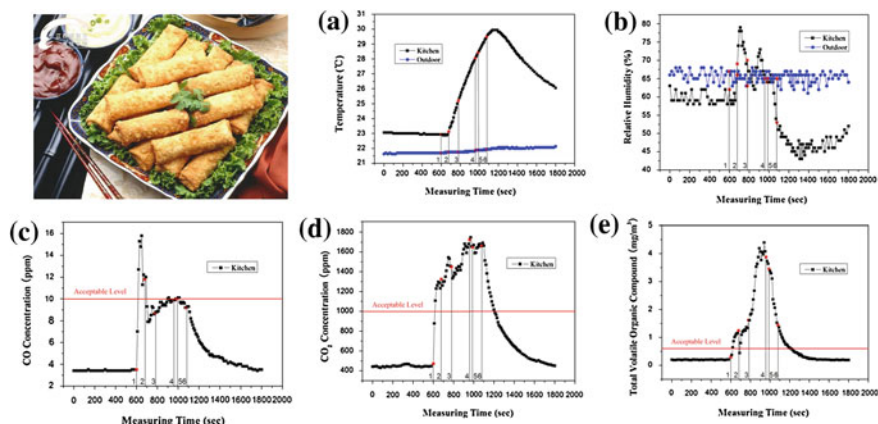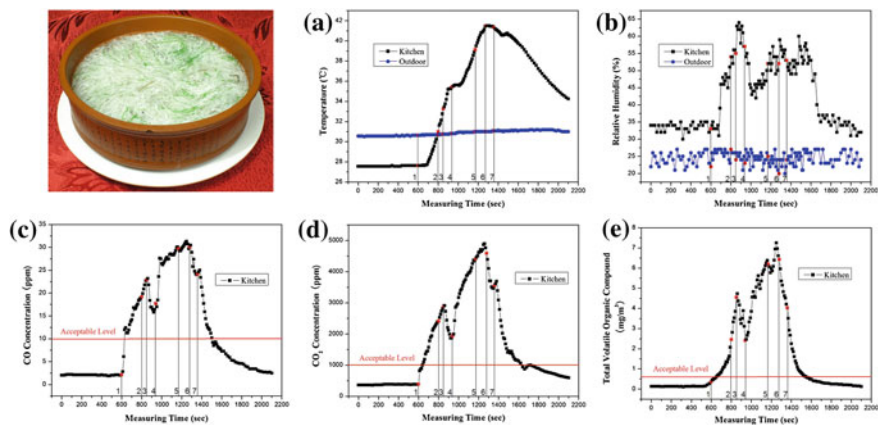

Fig. 22.4 Variations in test parameters over cooking Wensi tofu soup in the experiment without using an exhaust hood. Wensi tofu soup. **a** Temperature. **b** Relative humidity. **c** CO concentration. **d** CO2 concentration. **e** Total volatile organic compound

22.3.4 Sautéed Minced Shrimps with Mixed Vegetables

In cooking sautéed minced shrimps with mixed vegetables, after ensuring the background values, the cooking process was as follows: Step 1: Turn on the stove and add one tablespoon cooking oil. Step 2: When the oil was heated, add all the ingredients and stir-fry until it is really heated up; Step 3: As soon as shrimps turned white, add the sauce and stir it for a few minutes with the high heat; Step 4: When the sauce thickens, turn off the stove, take the dish out and serve it hot; Step 5: Turn on the range hood.

The results of test is depicted in Fig. 22.5. During the process of "heat the oil" (Step 1) and "added all the ingredients with stir-fry" (Step 2), temperature, relative humidity and TVOC concentration increased slightly. As soon as we added the sauce (Step 3), all the test parameter values increased dramatically. The concentrations of CO and CO_2 achieved the "peak values" 22.4 and 2,962 ppm, respectively, while they were 10.4 ppm (104 %) and 1,962 ppm (196.2 %) higher than the acceptable values. When we turned off the stove (Step 4), temperature continuously rose. Besides, relative humidity and TVOC concentration achieved the "peak values" 91 % and 8.28 mg/m^3, respectively, while they were 39 % (75 %) and 7.68 mg/m^3 (1,280 %) higher than the outdoor and acceptable values. After turning on the canopy hood (Step 5), temperature value initially increased, reached the "peak values": 32.88 °C, which was 11.75 °C (55.6 %) higher than the outdoor value, and then decreased.
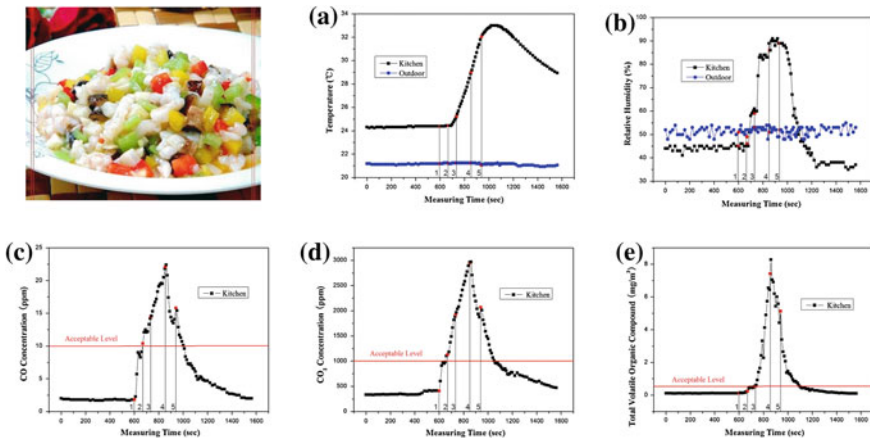
Fig. 22.5 Variations in test parameters over cooking sautéed minced shrimps with mixed vegetables in the experiment without using an exhaust hood. Sautéed minced shrimps with mixed vegetables. **a** Temperature. **b** Relative humidity. **c** CO concentration. **d** CO2 concentration. **e** Total volatile organic compound

22.4 Conclusions

This paper presents an experimental study on the actual pollution process of cooking oil fumes during cooking eight typical dishes of China. From the general view, the generation of CO and CO_2 had little to do with the cooking time and occurred largely as a result of the burning of the gas. The lower of the heat is used in cooking; the larger of CO concentration generates. The higher of the heat is used in cooking; the larger of CO_2 is generated. In the experiment, the extremely high emission of TVOC concentration, 36.2 mg/m^3 (6,033.3 %), was due to the use of high-purity liquor during cooking fish head en casserole.

There was a significantly higher value of temperature in cooking the eight case-study dishes. Even the smallest growth in temperature was 10.5 °C (33.9 %) higher than the outdoor values. Because without an exhaust hood, the wasted heat cannot be removed effectively, this significantly affected the productivity. The influence factor for relative humidity is complicated.

References

1. Ishige N (1992). In: Nakayama T (ed) Chinese dietary culture. Chinese Social Science Press, Beijing, pp 6–13 (in Chinese)
2. Lai C (2005) Assessment of side exhaust system for residential kitchens in Taiwan. Build Serv Eng Res Technol 26(2):157–166
3. Weng M, Zhu L, Yang K, Chen S (2009) Levels and health risks of carbonyl compounds in selected public places in Hangzhou, China. J Hazardous Mater 164(2–3):30
4. Ko Y-C, Lee C-H, Chen M-J, Huang C–C, Chang W-Y, Lin H-J, Wang H-Z, Chang P-Y (1997) Risk factors for primary lung cancer among non-smoking women in Taiwan. Int J Epidemiol 26(1):24–31
5. Seow A, Poh W-T, The M, Eng P, Wang Y-T, Tan W-C, Yu MC, Lee H-P (2000) Fumes from meat cooking and lung cancer risk in Chinese women. Cancer Epidemiol Biomark Prev 9(11):1215–1221
6. Li C-S, Lin W-H, Jeng F-T (1993) Size distributions of submicrometer aerosols from cooking. Environ Int 19(2):147–154
7. Chao NT, Chiang CM, Wang WA, Chou PC (1996) A study on the control strategies to improve indoor sir quality with outdoor air demonstrated by bathroom design. In: Proceedings of the 7th international conference on indoor air quality and climate, Nagoya, Japan
8. Chao YH, Law A (2000) A study of personal exposure to nitrogen dioxide using passive samplers. Build Environ 35:545–553

9. Chiang CM, Lai CM, Chou PC, Li YY (2000) The influence of an architectural design alternative (transoms) on indoor air environment in conventional kitchens in Taiwan. Build Environ 35:579–585
10. Li AG, Zhao YJ, Jiang DH, Hou XT (2012) Measurement of temperature, relative humidity, concentration distribution and flow field in four typical Chinese commercial kitchens. Build Environ 56:139–150
11. Lai C (2005) Assessment of side exhaust systems for residential kitchens in Taiwan. Build Serv Eng Res Technol 26(2):157–166

Chapter 23
Ventilation System Type and the Resulting Classroom Temperature and Air Quality During Heating Season

Jie Gao, Pawel Wargocki and Yi Wang

Abstract The present study investigated how different ventilation system types influence classroom temperature and air quality. Five classrooms were selected in the same school. They were ventilated by manually operable windows, manually operable windows with exhaust fan, automatically operable windows with and without exhaust fan and by mechanical ventilation system. Temperature, relative humidity, carbon dioxide (CO_2) concentration and opening of windows were continuously monitored for one month during heating season in 2012. Classroom with manually operable windows had the highest carbon dioxide concentration levels so that the estimated ventilation rate was the lowest compared with the classrooms ventilated with other systems. Temperatures were slightly lower in classroom ventilated by manually operable windows with exhaust fan. Windows were opened seldom even in the classroom ventilated by manually operable windows. Classrooms with automatically operable windows and exhaust fan and with mechanical ventilation systems achieved the best thermal environment and air quality during heating season among all classrooms examined.

J. Gao (✉) · P. Wargocki
International Centre for Indoor Environment and Energy, Department of Civil Engineering, Technical University of Denmark, Kongens Lyngby, Denmark
e-mail: yourjane20307@gmail.com

J. Gao · Y. Wang
Xi'an University of Architecture and Technonlogy, Xi'an, 710055 Shaanxi, China

23.1 Introduction

In more than 60 % of Danish schools, air quality does not meet the requirements of Danish Building Regulations [1] because the measured CO_2 concentration levels are frequently above 1,000 ppm [2]. High level of CO_2 indicates inadequate classroom ventilation and implies that air quality in the classrooms may not be acceptable. Poor air quality results usually in high prevalence of acute health symptoms, known as sick building syndrome (SBS) symptoms [3] and in decreased ability to perform typical school work which may affect proper progress in learning [4–7]. Consequently, many Danish classrooms/schools should be retrofitted with the systems, providing adequate ventilation. It is important to examine the performance of potential ventilation solutions.

Classroom ventilation can be obtained in different ways; some of which are very simple allowing pupils and teachers to merely open windows manually, and some are much more sophisticated as, for example fully balanced mechanical ventilation systems with or without cooling and heat recovery. Mumovic et al. carried out measurements in three new secondary schools in the UK with different ventilation systems including classrooms with automatically operable windows, with exhaust fan and with balanced mechanical system [8]. They found that the use of these systems in classrooms satisfied the recommended ventilation performance according to Building Bulletin 101 [9]. However, with regards to the thermal comfort, many classrooms did not meet the relevant levels required by CIBSE Guide [10].

When systems utilizing natural forces are used to achieve classroom ventilation, the ventilation rates and air quality are to a high degree dependent on outdoor conditions including the location of a school (urban and/or rural) and climatic conditions (wind speed and direction, outdoor temperatures), as well as window-opening behaviour by pupils and teachers. Wargocki and Silva investigated to which extent the system informing pupils when the windows should be opened in classrooms ventilated by manually operable windows can influence classroom temperature and air quality [11]. They showed that providing indication that the classroom air quality is poor by measuring classroom CO_2 concentration level improves classroom ventilation in the heating season as the pupils open the windows more frequently. They showed also that providing cooling system in the classroom will restrict window opening resulting in aggravated air quality. They concluded that it is the classroom temperature not a poor air quality that is probably the main cause why the windows are being opened.

Gao et al. investigated how different ventilation systems in classrooms influence classroom temperatures and air quality during non-heating season in a school in Denmark [12]. The results showed that classroom temperatures were controlled better when they were ventilated by mechanical system and/or by automatically operable window with exhaust fan, allowing to achieve cross-ventilation compared to classrooms ventilated with manually operable windows. In the former classrooms, CO_2 concentration levels were also lower, suggesting that the ventilation rates were higher and that classroom air quality was better.

The results of Gao et al. need to be extended for heating season to provide full information on the performance of different ventilation systems in classrooms and consequently to be able to advice which ventilation systems can be recommended for Danish schools to achieve adequate control of air quality and thermal environment. The present study was carried out to provide such an extension.

23.2 Methodology

The study was performed in an elementary school built in the early 1970s, made of bricks and concrete [12]. The school is situated in a suburban area with low-rise buildings (Fig. 23.1). The classrooms are located in three buildings in Wing A, Wing B and the Main building (Fig. 23.2). The ventilation in classrooms in Wing A and Wing B is achieved by automatically operable windows with exhaust fan supporting cross-ventilation; the classrooms were retrofitted with this system during major renovation of the school in the last decade. Each classroom in these Wings has got three automatically operable windows at upper level, two manually operable windows at lower part of a window section and one garden door which can be manually opened directly to the school yard area. The classrooms in the Main building are equipped with the balanced mechanical ventilation system and have two narrow, manually operable windows and one garden door also opened manually and facing school yards.

The classrooms with automatic windows have control system especially developed to provide adequate ventilation and taking into account numerous factors including schedule of the classrooms and location of the school. Opening of

Fig. 23.1 Satellite image of the school (*source* from Google Earth)

Fig. 23.2 Plan view of the school; indicated classrooms selected for the measurements
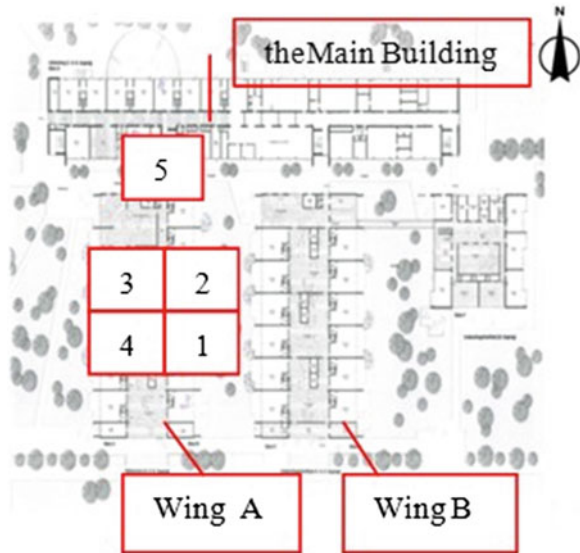
automatic windows is mainly controlled by the sensor measuring classroom temperature and CO_2 concentration; the sensor is located centrally in the classroom. This strategy is overruled if weather conditions are unfavourable, e.g. during stormy weather. The speed of exhaust fan is controlled by the CO_2 concentration in the classroom and increased gradually from the lowest speed when the CO_2 concentration level in the classroom is increasing. Mechanical ventilation system in the main building is operating between 6 am and 4 pm. It provides ventilation rate of 120 L/s per class. This rate was measured during experiments using Hood method.

For the purpose of the present experiments, four classrooms in Wing A and one classroom in the Main building were selected (Fig. 23.2); their typology is presented in Table 23.1. Ventilation systems in classrooms located in Wing A were modified to achieve different modes of ventilation: in one classroom, the automatically operable windows and exhaust fan were idled and thus the classroom could only be ventilated by manual opening of windows; in one classroom, the exhaust fan was idled, but the automatic opening of windows remained unchanged; in one classroom, automatically operable windows were idled, while the operation of the exhaust fan remained unchanged; and in one classroom, no changes to the ventilation strategy were made, i.e. the classroom was ventilated by the automatically operable windows and exhaust fan. No changes to classroom ventilation achieved by the mechanical system in the Main building were made. Besides the indicated methods of ventilation of classrooms, all classrooms participating in the experiments could be ventilated by manually operable windows and garden doors. The pupils and the teachers were not informed about the changes to ventilation, and they were not asked or instructed to change the school and class routines including window-opening behaviour; no restrictions were imposed on the opening of windows and garden doors.

Table 23.1 Typology of classroom ventilation

Classroom	Ventilation type (classrooms with * had the ventilation system modified for the purpose of the present experiment)	Average occupancy during experiments (pupil +teacher)	Class volume (m^3)	Coding
1*	Natural ventilation with manually operable windows	18 + 1	123.5	NV
2*	Natural ventilation with exhaust fan	22 + 1	123.5	NV + EF
3*	Natural ventilation with automatically operable window	21 + 1	123.5	NV + AW
4	Natural ventilation with automatically operable window and exhaust fan	23 + 1	123.5	NV + AW + EF
5	Balanced mechanical ventilation	15 + 1	180	MV

In each classroom, the following measurements were carried out: CO_2 concentration using VAISALA GM20D sensor (accuracy: $\pm$ 30 ppm + 2 % of the reading) connected to HOBO U12 logger collecting additionally data on air temperature and relative humidity (RH) (accuracy: $\pm$ 0.7 °C and $\pm$ 5 % RH); opening of windows and garden doors registered by HOBO State loggers. Outdoor temperature and RH were measured in parallel to indoor measurements using weather station used to control automatic opening of windows. In the middle of the measuring period, the pupils were asked to fill the questionnaire collecting information on their immediate perceptions of environment (e.g. quality of air, noise, thermal environment) and their health symptoms experienced at the time of answering the questionnaire (e.g. headache, irritation of mucous membranes, dryness of nose). Classroom ventilation rate was estimated using the peak values of CO_2 concentration for each day during the measuring period (assuming that they are indicative of the steady-state CO_2 concentration levels) and using non-linear curve fitting with mass balance model [13]. The CO_2 generation rate per pupil was assumed to be 0.004 L/s and per teacher to be 0.0054 L/s [14]. The outdoor CO_2 was not monitored and was assumed to be 380 ppm.

The measurements were performed in November and December of 2012 when the outdoor temperatures ranging from -7.3 to 10.9 °C and being on average 1.9 °C $\pm$ 4.2.

23.3 Results

Time-weighted average temperature in classrooms with different ventilation systems is shown in Fig. 23.3. Temperature was mostly above 20 °C. At the start of school day, the temperature differed as much as 3 °C between different classrooms. The classrooms with exhaust fan (NV + EF) and mechanical system (MV)

had the lowest indoor temperatures which increased in the course of the school day, respectively, by nearly 2 °C and 4 °C. In other classrooms, the temperature was fairly stable; the fluctuations were within ± 1 °C.

Time-weighted average CO_2 concentration levels in the classrooms with different ventilation systems are shown in Fig. 23.4. The highest CO_2 concentration reaching about 2,200 ppm was registered in the classroom where ventilation was achieved by manually operable windows (NV). The CO_2 concentration levels in the classrooms with automatically operable window (NV + AW) and with exhaust fan (NV + EF) were slightly higher than these measured in the classrooms with automatically operable window and exhaust fan (NV + AW + EF) and with mechanical ventilation system (MV), but the differences were not substantial. Fluctuations in CO_2 concentration levels reflect well elementary school routines in Denmark with major breaks in the early and late morning. Besides classroom with manually operable windows, all other classrooms had CO_2 concentrations below 1,500 ppm while the classroom with mechanical ventilation below 1,000 ppm.

Table 23.2 shows the average length of window and garden door opening in the classrooms with different ventilation systems during the periods of experiments. Manually operable windows were opened seldom or not at all in classrooms with automatic windows and mechanical ventilation system. In classrooms ventilated by manually operable windows with and without exhaust fan windows were opened more frequently but still generally for quite short period considering up to a 6.5-hour school day. In classrooms with automatic windows, the total opening time of the three automatic windows was longer as their opening was controlled by the automated control strategy. Generally, the length of opening of windows and
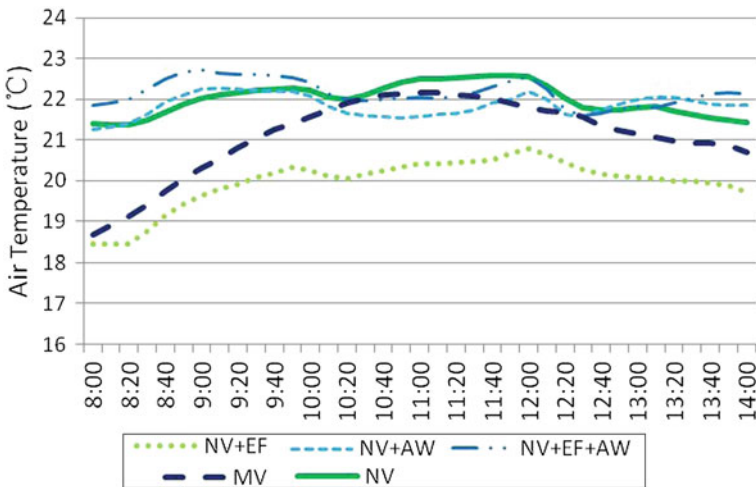
Fig. 23.3 Time-weighted average temperature in classrooms with different ventilation systems
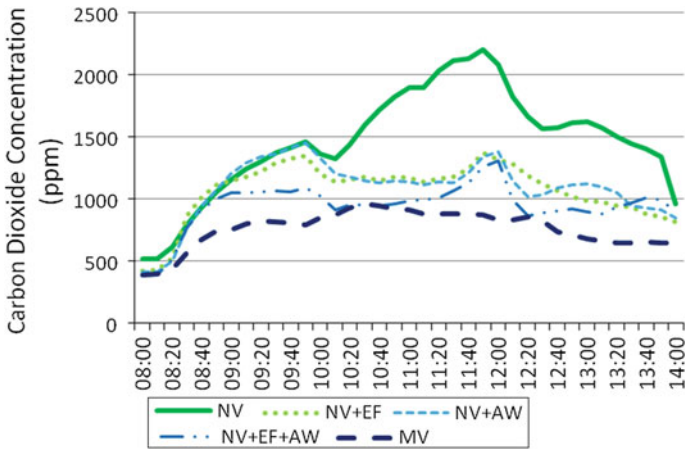
Fig. 23.4 Time-weighted average CO_2 concentration in classrooms with different ventilation systems

Table 23.2 Average opening hour of windows per day in classrooms with different ventilation systems

Ventilation type	Manually operable window #1 (h/day)	Manually operable window #2 (h/day)	Garden door (h/day)	Automatically operable window (h/day)	Total opening time for all windows (h/day)
NV	0,5	0,1	0,0	N/A	0,6
NV + EF	0,3	0,0	0,2	N/A	0,5
NV + AW	0,1	0,0	0,1	1,3	4,1
NV + AW + EF	0,0	0,0	0,1	0,3	1,0
MV	0,0	0,0	0,0	N/A	0,0

doors correlates well with the measured CO_2 concentration levels in the classrooms.

23.4 Discussion

According to the European Standard EN15251, the range of operative temperatures should be between 20 and 24 °C in the classroom during heating season in the building with Class II indoor environmental quality [15]. Assuming that air temperature equalled operative temperature, the cumulative frequency chart presented in Fig. 23.5 shows that the temperature in classrooms ventilated only with exhaust fan (NV + EF) did not meet this requirement for more than 50 % of school time during the measuring period. The temperatures in the classrooms with
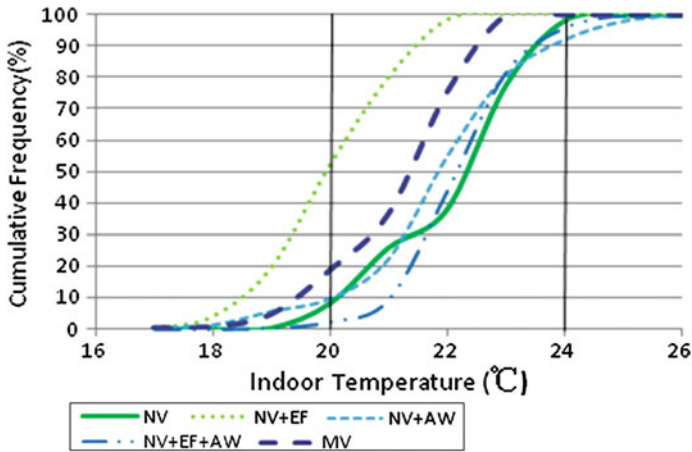
Fig. 23.5 Cumulative frequency curve of temperatures during school hours in classrooms with different ventilation systems

automatically operable window and exhaust fan (NV + EF + AW) and with balanced mechanical ventilation system (MV) exceeded the above criterion only for less than 20 % of school hours. Classroom with manually operable windows (NV) had too low temperatures of about 10 % of school day. Thus, from the aspect of controlling thermal environment, classrooms with mechanical ventilation and with automatically operable windows with exhaust fan would be recommended, though classrooms with no dedicated ventilation system, where airing is achieved by window opening, can also be considered.

The heating in the classroom was achieved by water radiators with thermostatic valves. Thus, the differences in temperatures presented in Fig. 23.5 could occur due to different set points of thermostatic valves in the classrooms. These set points were not registered. Consequently, the conclusions regarding the control of thermal environment in the classrooms with different ventilation systems should only be considered as provisional.

According to the Danish Building Regulations, classroom CO_2 concentration should not be higher than 1,000 ppm [1]. Figure 23.6 shows that this level was exceeded in classroom where ventilation was obtained by manually operable windows (NV) for about 70 % of school hours, while in the classrooms with other systems for less than 50 % of school hours, except the classroom with mechanical ventilation (MV) where 1,000 ppm was exceeded for less than 15 % during measuring period. Based on these results, mechanical ventilation system can be recommended for keeping low levels of CO_2. Among the remaining systems, ventilation with automatically operable windows and exhaust fan was performing the best.

CO_2 concentration in the classroom is the result of outdoor air supply rate and the metabolically generated CO_2 by pupils and the teacher and is often simply used
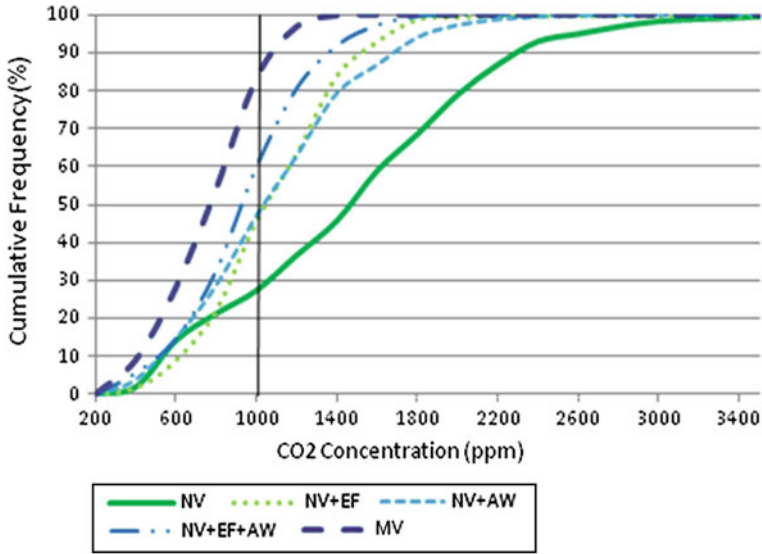
Fig. 23.6 Cumulative frequency curve for CO_2 concentration during school hours in classrooms with different ventilation systems

as a proxy for estimating ventilation rate. Table 23.1 shows that the average number of persons varied in classroom with different ventilation systems. Thus, using purely CO_2 concentration levels may somewhat misrepresent the actual ventilation rate in the classrooms. The actual ventilation rates were consequently estimated taking number of persons into account. They are presented in Table 23.3. Ventilation rates estimated using peak concentration was slightly lower than these estimated using non-linear curve fitting. As both methods may be prone to some source of errors, the average of the two estimated rates were used.

According to the Danish Building Regulations [1], outdoor air supply to and extraction from normal teaching rooms must be no less than 5 l/s/person plus 0.35 l/s/m² floor area. The results presented in Table 23.2 show that only the classroom with mechanical ventilation meet the requirements of Danish Building Regulations, being about 6 L/s per pupil considering size of the class [1]. The classroom with manually operable windows had the lowest ventilation rate, while the other classrooms were basically below the requirement except the classroom with automatically operable window (NV + AW) which was just below the requirement if the average of the two estimated rates is taken into account. It should be noted that the typical number of pupils in the classrooms is 24 and except the classroom with automatically operable windows and exhaust fan (NV + AW + EF), the number of pupils in the classroom was below this limit especially in the mechanically ventilated classroom. Thus, the actual ventilation rates per person would be lower than those observed during present experiments if these classrooms had had the nominal number of pupils. Measured ventilation rate

Table 23.3 Estimated ventilation rates in classrooms with different ventilation systems

Ventilation system types	Ventilation rate estimated by non-linear curve fitting		Peak CO_2 concentration	Ventilation rate estimated using peak CO_2 concentration		Average estimated ventilation rate	Ventilation rates required by [1]
	L/s per person	h^{-1}	ppm	L/s per person	h^{-1}	L/s per person	L/s per person
NV*	2.2	1.2	2,200	2.3	1.3	2.3	5.5
NV + EF	5.1	3.4	1,368	4.2	2.8	4.7	5.5
NV + AW	4.7	3.0	1,447	3.9	2.5	3.3	5.5
NV + AW + EF	5.6	3.9	1,303	4.5	3.2	5.1	5.5
MV*	9.5	3.1	954	7.3	2.3	8.4	5.9

* According to the difference in ventilation rates, pupils in classroom with mechanical ventilation would perform their school work better (by about 20 %) compared with children in the naturally ventilated classroom [5]

in the mechanically ventilated classroom using hood method was 120 L/s thus about 7.5 L/s per person (including teacher) which is close to the rate estimated from peak CO_2 measurements. With 24 pupils, the classroom would have ventilation rate similar to this estimated in the classroom with automatically operable windows and exhaust fan namely about 5 L/s per person. A small readjustment would then be needed.

The estimated rates in classrooms in Wing A without mechanical ventilation system are expected to be mostly outdoor air supply rates considering configuration of the classrooms. Still it cannot be ruled out that some dilution of CO_2 concentration was due to the air drawn from the halls especially in the case of classroom with exhaust ventilation only (NV + EF) considering general low level of manual window opening (Table 23.2), being most likely the result of low outdoor temperatures.

The limitation of the present results is that to achieve different ventilation strategies in the classrooms in Wing A, either the automatic operation of windows or the exhaust fan were idled. In case if the exhaust fan was switched off, the one-sided natural ventilation with automatically operable windows was modelled. However, the classrooms were not designed for such a system as no special slots or openings were designed to promote cross-ventilation, which is an usual approach in such a case. Thus, the estimated ventilation rates for this case could be slightly lower than those in the classrooms especially designed for one-sided natural ventilation. When the automatic opening of windows was idled and exhaust fan was kept running, the estimated ventilation rate could contain both the air drawn from the hall as well as from outdoors; no special slots were designed above windows to allow outdoor air supply to the classroom, which is typical for the buildings with exhaust ventilation. The slots above window or in facade are also sometimes designed for buildings where ventilation is achieved only by manually

operable windows to achieve some minimum level of ventilation. Finally, the teacher and the pupils could be accustomed to automatic opening of windows, which could somewhat influence their window-opening behaviour—they could open the windows less frequently compared with the classroom where airing is normally achieved only by manually opened windows. Present results thus require confirmation in other schools which by design, not by intervention as in the present study, have different ventilation systems.

23.5 Conclusions

- Present results suggest that classrooms with mechanical ventilation system and where ventilation is obtained by automatically operable windows with exhaust fan can achieve fairly acceptable thermal environment and air quality during heating season.
- Opening of windows in classrooms during heating season was observed to be very modest regardless of the type of ventilation system in classrooms.

References

1. Building Regulations (2010) Danish Ministry of Housing. Copenhagen
2. Menå HM, Larsen EM (2010) Indoor environment in schools. MSc thesis v
3. Myhrvold AN, Olsen E, Lauridsen O (1996) Indoor environment in schools pupils health and performance in regard to CO_2 concentrations. In: Proceedings of seventh international conference on indoor air quality and climate, Nagoya, Japan, 4: 369–74
4. Daisey JM, Angell WJ, Apte MG (2003) Indoor air quality, ventilation and health symptoms: an analysis of existing information. Indoor Air 13:53–64
5. Wargocki P, Wyon DP (2013) Providing better thermal and air quality conditions in school classrooms would be cost-effective. Build Environ 59:581–589
6. Shaughnessy RJ, Haverinen-Shaughnessy U, Nevalainen A, Moschandreas D (2006) A preliminary study on the association between ventilation rates in classrooms and student performance. Indoor Air 16(6):465–468
7. Bakó-Biró Zs et al (2012) Ventilation rates in schools and pupils' performance. Build Environ 48:215–223
8. Mumovic D et al (2007) A comparative analysis of the indoor air quality and thermal comfort in schools with natural, hybrid and mechanical ventilation strategies. In: Proceedings of Clima WellBeing Indoors

9. ODPM (2005) Building bulletin 101 ventilation of school buildings, Office of the Deputy Prime Minister
10. CIBSE (2002) CIBSE guide A1 environmental design, London
11. Wargocki P, Da Silva N (2012) Use of CO2 feedback as a retrofit solution for improving air quality in naturally ventilated classrooms. In: Proceeding of Healthy Buildings 2012. Brisbane, Australia
12. Gao J, Wargocki P, Wang Y (2013) Ventilation system type and the resulting classroom temperature and air quality during non-heating season. In: Proceeding of Clima 2013. Prague, Czech
13. Persily AK (1997) Evaluating building IAQ and ventilation with indoor carbon dioxide. ASHRAE Trans 103(2):193–204
14. Coley DA, Beisteiner A (2002) Carbon dioxide levels and ventilation rates in schools. Int J Vent 1:45–52
15. EN15251-2007. European Standard on Indoor environmental input parameters for design and assessment of energy performance of buildings- addressing indoor air quality, thermal environment, lighting and acoustics

Chapter 24
Experimental Research on Indoor Secondary Pollution and Control Technology of Public Buildings

Huixing Li, Geng Geng, Guohui Feng, Wei Wang and Huiyu Guo

Abstract This paper gives a brief introduction on secondary pollution caused by central air-conditioning system of public buildings in cold region. Then, the feasibility analysis of humidity control of central air-conditioning system is conducted, which finds out that central air-conditioning system implementing humidity control can handle secondary pollution to some extent; but due to factors like the inadequate fresh air rate and restricted chilled water temperature, it cannot realize efficient control. The author proposes using activated carbon–nano-TiO$_2$ photocatalytic composite purification technology to control secondary pollution caused by the system, and related tests are conducted. The results show that the compound purification unit can effectively purify VOCs and microbial pollution in sealed environment under certain conditions, and conditions including environmental temperature, ultraviolet intensity, air velocity, and initial pollutant concentration will influence the purifying performance.

Keywords Indoor air quality · Secondary pollution · Humidity control · Activated carbon · Nano-photocatalysis

24.1 Introduction

In recent years, an increasing number of public buildings have been using central air-conditioning systems for heating and cooling. Modern air-conditioning system is effective conditioning indoor air humiture and creating comfortable indoor environment. However, the IAQ has been deteriorating, and the problem of secondary pollution of indoor air is protruding due to worldwide energy shortage,

H. Li · G. Geng · G. Feng (✉) · W. Wang · H. Guo
Municiple and Environmental Engineering College,
Shenyang Jianzhu University, Shenyang, China
e-mail: fengguohui888@163.com

the implementation of energy saving and emission reduction, the sustainable development policy, immature air-conditioning system, and inactive energy-saving measures [1–5].

This paper gives a brief introduction on the secondary pollution caused by central air-conditioning system of public buildings in cold area, and the feasibility of controlling secondary pollution caused by central air-conditioning system implementing humidity control technology is also analyzed. Based on the analysis, this research proposes activated carbon–nano-TiO_2 photocatalytic composite purification technology to handle secondary pollution and related tests are conducted.

24.2 Secondary Pollution

The central air-conditioning system is mainly composed of wind system, aqueous system, and terminal devices. The humid condition under which heat exchanger, filter unit, and condensate system operate will supply an ideal environment for microbes passing through the primary filter to grow and reproduce. When the unit starts again, the microbes and its metabolite flow into the room in the form of aerosols, producing secondary pollution and harming human health. Cooling water can be polluted when meeting ambient air during cycling, which causes microbes and molds growing and reproducing in the cooling tower. For public buildings, the cooling towers are often installed on the rooftop, where the pollutants inside the water spread into the air around the cooling tower as aerosols to aggregate. Then, the polluted air flows into the room through fresh air system or natural draft, which can also pollute the indoor air [6].

24.3 Feasibility of Humidity Control

Winters are cold and dry in Shenyang, so central air-conditioning system adds wet to the room in heating season. And in summer, the system of humidity control ensures there is enough amount of fresh air to eliminate moisture load by controlling the humidity of fresh air actively; the terminal only needs to eliminate heat load. The system of humidity control decouples the humidity and temperature control of the conditioning room during operating, which can avoid generating interior wet surface. Central air-conditioning system implementing humidity control technology can effectively prevent return air probably with pathogenic bacteria from touching wet surface, and supplying a favorable growing condition for microbes. It can ensure the cleanness of fresh air flowing into the conditioning room, reducing the risk of generating secondary pollution. Eq. (24.1) shows the required moisture content of supply air [7]:

$$W_s = W_p - \frac{Q}{0.75\,V_s} \tag{24.1}$$

where W_s is the moisture content of supply air (g/kg); W_p is the set moisture content of the indoor air (g/kg); Q is the interior moisture load (W); V_s is the fresh air rate (m^3/h).

Moisture content of fresh air is influenced by the temperature of chilled water. According to construction regulations, the inlet and outlet temperatures are 7 and 12 °C. The temperature of chilled water cannot be too low, so W_s has its minimum value $W_{s\,min}$, and the dehumidifying capacity of the system has its maximum value. Besides, according to (24.1), the fresh air rate is the key factor to the dehumidifying capacity of the system. But central air-conditioning systems of public buildings usually reduce the fresh air rate in order to reduce energy use, which can hardly satisfy the requirement of dehumidifying capacity of fresh air, resulting in inefficient dehumidification.

In conclusion, the author proposes using activated carbon–nano-TiO$_2$ photocatalytic composite purification technology to control secondary pollution caused by the central air-conditioning system, and few tests on its purification performance are conducted.

24.4 Experimental Systems and Scheme

Activated carbon–nano-TiO$_2$ photocatalytic composite purification technology can almost handle all types of gaseous pollutants. Because the collision probability of molecules of pollutants in low concentrations and TiO$_2$ molecules is very low, the photocatalytic reaction rate is not high enough. Activated carbon–TiO$_2$ composite can effectively improve the volatile organic compounds (VOCs) degradation rate as well as the sterilization efficiency. Activated carbon is non-polar adsorbent, which can provide higher adsorption affinity potential to VOCs, and with the activated carbon as the adsorption center, its strong adsorption can make the low concentration of VOCs effectively enriched and concentrated, providing higher concentration reaction environment for the photocatalytic in order to accelerate the photocatalytic reaction. Photocatalytic bactericidal mechanism is mainly causing damage to microbial cell walls and cell membranes, resulting in the loss of semipermeability, and then the leakage or inactivation of intracellular substances, which can cause cell death [8].

The experimental facility is a sealed chamber with an air duct, and the purification unit is composed of domestic activated carbon–nano-TiO$_2$ photocatalytic composite purification nets and UV lamps. There is a conversion fan equipped at the entrance of the return air duct, supplying dynamic for inner air flow. Figures 24.1 and 24.2 show the experimental facility and the purification unit, respectively.

Aim at the two main types of pollutants: microbes and harmful gases, the dirt (with microbes in) inside central air-conditioning system is chosen as the microbe

Fig. 24.1 Experimental facility
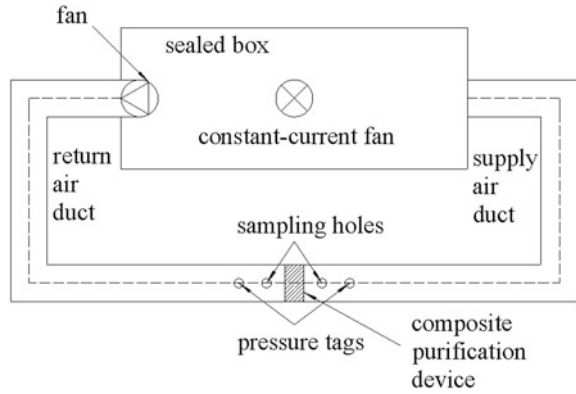
Fig. 24.2 Purification unit
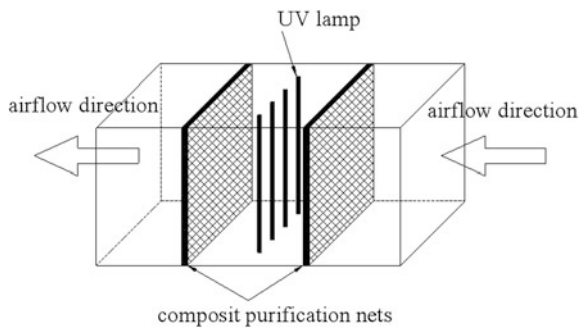
pollution source, simulating the microbial pollution; and emulsion paint (organic glass as carrier) as the VOCs pollution source, simulating the VOCs pollution. The microbe concentration is tested by domestic microbial air sampler LWC-I; the total volatile organic compound (TVOC) concentration is tested by import hand-held VOC detector PGM-7240.

Test analysis on the control of harmful gas pollution is mainly from the per-spective of the emission characteristics of the pollution source. While the microbial pollution caused by the central air-conditioning system can be influ-enced by many interior environmental factors, and microbes are both the pollutants itself and pollution sources generating metabolites and other harmful gases, so this study chooses the experimental research on the control of microbial pollution as key analytical content.

24.5 Results and Discussions

24.5.1 Influence of Ambient Temperature on VOCs Purification

Research finds out that when emulsion paint emits VOCs in confined spaces, the environmental temperature has great influence on its volatilization: the higher the temperature is, the faster the volatilization rate gets. As it is shown in Fig. 24.3, when the environmental temperature is 15 °C, the highest TVOC concentration is 2.295 mg/m^3, while when the environmental temperature rises to 50 °C, the highest TVOC concentration is 17.43 mg/m^3, which is almost seven times more than the concentration of 15 °C.

Under experimental conditions below, relative humidity is (63 ± 5) %, ultraviolet intensity is 250 μw/cm^2, air velocity is 0.8 m/s, environmental temperature rises gradually from 15 to 30 °C, the test on the influence of environmental temperature on the effect of purifying VOCs of the composite purification unit is conducted. Analyzed test results are shown in Fig. 24.4, which shows that the purifying efficiency increases as the environmental temperature rises, but the efficiency begins to decrease when the environmental temperature reaches to 22 °C, indicating that the purification unit achieves the best purifying results at 22 °C.

24.5.2 Influence of Ultraviolet Intensity on Microbes Purification

The test on the influence of ultraviolet intensity on the effect of purifying microbes of the composite purification unit is conducted under experimental conditions

Fig. 24.3 Relation between TVOC concentration and temperature
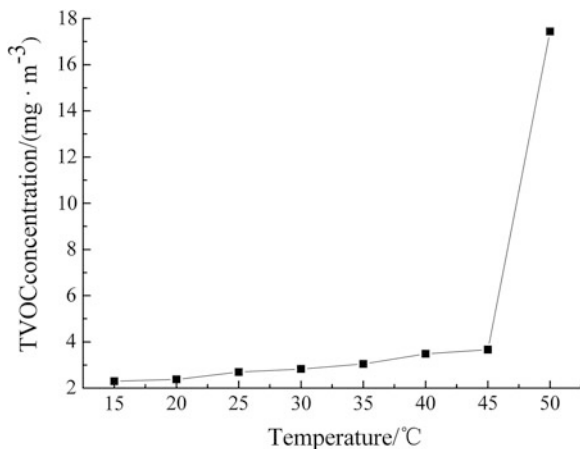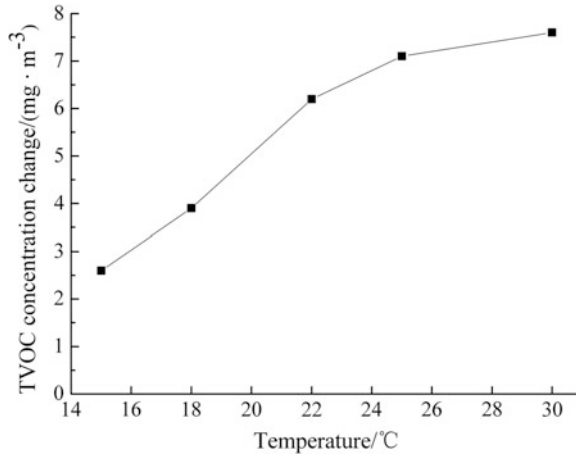
Fig. 24.4 Relation between TVOC concentration change and temperature

below: Environmental temperature is (22 ± 1) °C, relative humidity is (60 ± 5) %, air velocity is 0.8 m/s, initial microbe concentrations are 4560, 4320, 4290, and 4200 cfu/m^3, corresponding to the ultraviolet intensity of 30, 60, 120, and 240 μw/cm^2. Test results are shown in Fig. 24.5, and it can be figured out that the photocatalytic reaction efficiency increases as the ultraviolet intensifies. In the principle of photocatalytic purification, the electron and hole concentrations created by TiO$_2$ increase as the ultraviolet intensifies, which creates a larger number of photons and electrons; in turn, more active oxygen and radicals are created, improving photocatalytic reaction efficiency.
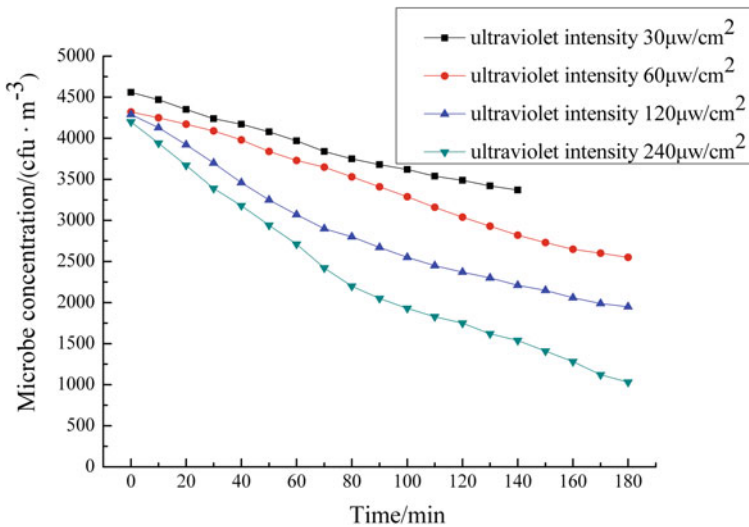
Fig. 24.5 Influence of different ultraviolet intensity on microbes purification

24.5.3 Influence of Air Velocity on Microbes Purification

Under experimental conditions below, environmental temperature is (22 ± 1) °C, relative humidity is (58 ± 5) %, ultraviolet intensity is 250 μw/cm^2, initial microbe concentrations are 4510, 4450, and 4390 cfu/m^3, corresponding to the air velocity of 3.5, 2.5, and 0.8 m/s, the test on the influence of air velocity on the effect of purifying microbes of the composite purification unit is conducted. Analyzed test results are shown in Fig. 24.6, which shows that the purifying effect is reversely related to the air velocity. In the principle of photocatalytic purification, reaction time length directly affects the depth of photocatalytic reaction, so that good purifying effect only can be achieved when the pollutant and the purification nets are fully contacted with each other. Therefore, lower air velocity can help to increase photocatalytic reaction time, improving the reaction efficiency.

24.5.4 Influence of Initial Concentration on Microbes Purification

The test on the influence of initial pollutant concentration on the effect of purifying microbes of the composite purification unit is conducted under experimental conditions below: Environmental temperature is (22 ± 1) °C, relative humidity is (58 ± 5) %, ultraviolet intensity is 250 μw/cm^2, air velocity is 0.8 m/s, and initial microbe concentrations are 12370, 8650, and 4390 cfu/m^3. Test results are shown in Fig. 24.7, and it can be figured out that the higher the initial pollutant
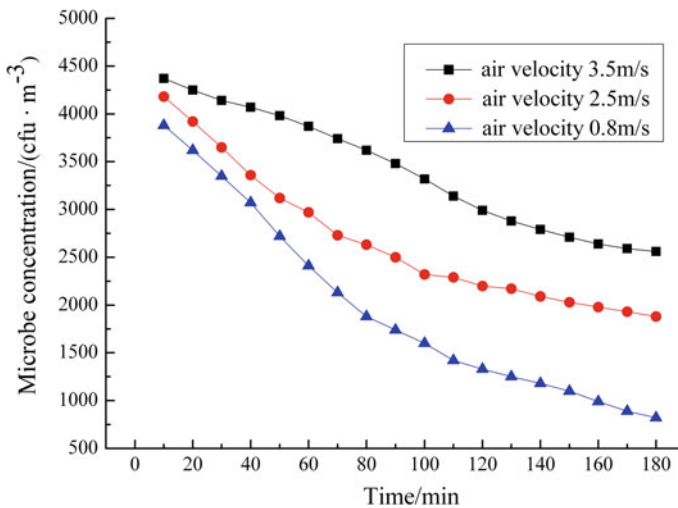
Fig. 24.6 Influence of different air velocity on microbe's purification
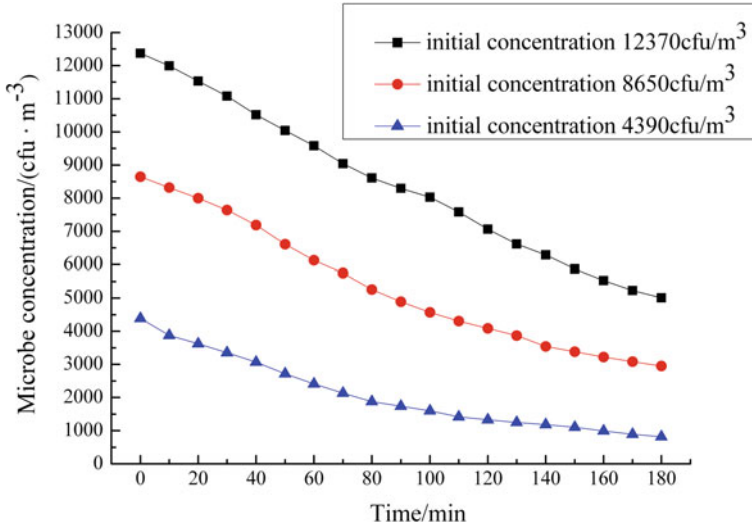
Fig. 24.7 Influence of different initial concentration on microbe's purification

concentration is, the greater the purifying effect will be. This result can be explained by the law of mass action.

24.5.5 Project Case

An active carbon–nano-TiO_2 composite photocatalytic purification unit is installed in the filter section of the central air-conditioning system of Liaoning Provincial Hospital of Traditional Chinese Medicine. One operating room is chosen as the test subject, and the tests on microbe and TVOC concentration before and after purification are conducted with microbial air sampler LWC-I and handheld VOC detector PGM-7240. The results show that 120 min after starting the central air-conditioning system installed with composite purification unit, the total number of bacterial colonies sharply reduces from 1780 to 210 cfu/m^3; the TVOC concentration is 0.1 mg/m^3, both well below the requirement of the National Standards-Indoor Air Quality Standards.

24.6 Conclusions

(1) Central air-conditioning system implementing humidity control can handle secondary pollution caused by microbes to some extent; but due to factors like the inadequate fresh air rate and restricted chilled water temperature, it cannot realize efficient control.

(2) The author proposes using activated carbon–nano-TiO$_2$ photocatalytic composite purification technology to control secondary pollution caused by the central air-conditioning system. The results of experimental research on activated carbon–nano-TiO$_2$ photocatalytic composite purification purifying VOCs and microbes show that the compound purification unit can effectively purify VOCs and microbial pollution in sealed environment under certain conditions. The conditions including environmental temperature, ultraviolet intensity, air velocity and initial pollutant concentration will influence the purifying performance.

(3) Activated carbon–nano-TiO$_2$ photocatalytic composite purification unit can effectively purify VOCs and microbes in real central air-conditioning systems.

References

1. Shen JM (1997) Indoor air quality evaluation. J HV AC 4(1):22–25
2. Li Y, Leung GM, Tang JW (2007) Role of ventilation in airborne transmission of infectious agents in the built environment—a multidisciplinary systematic review. Indoor Air 27(3):2–18
3. Li YF, Zhao YH, Chen P (2008) Preparation of the immobilized TiO$_2$ activator and the experimental study on its photo activity. J Shenyang Jianzhu Univ Nat Sci 24(2):123–128
4. Daisey JM, Angell WJ, Apte MJ (2003) Indoor air quality, ventilation and health symptoms in schools: an analysis of existing information. Indoor Air 2(13):53–64
5. Yu M (2007) Study on indoor pollution caused by central air conditioning and controlling. Master's thesis, Shandong University, Shandong, China
6. Xu Q L (2007) The strategy to improve indoor air quality and eliminate secondly contamination of HVAC system. Master's thesis, Tongji University, Shanghai, China
7. Yang XD, Xu FF (2006) Research and application of photocatalytic bactericidal effect in the air conditioning field. Build Energ Environ 5(1):11–16
8. Bluyssen PM, Oliverira FE, Groes L (1996) European audit project to optimize indoor air quality and energy consumption in office buildings. Indoor Air J 6(2):221–223

Chapter 25
Research on the Effect of Angles of Airflow to form Displacement Ventilation Air Distribution in Winter

Can Li, Miaoshu Li, Hanqing Wang, Yi Li and Shuxiang Cui

Abstract As heat pollutant and dust pollutant sources both exist, large workshop of welding and grinding are specially fittable to adopt displacement ventilation system. Displacement ventilation system has been developed based on summer condition. In order to research the effect of air distribution in winter, numerical simulation and experiment method are taken to study flow field in a large displacement ventilation workshop. Effects of air distribution in winter condition is changed by adjusting air angle of cylindrical ventilators and brought in ventilation efficiency η to estimate air distribution of angles 0°, 15°, 30°, 30°, 45°, 60°, 75° to horizontal direction separately. Based on these studies, the following conclusions can be obtained: (1) the thermal buoyancy lift effect of hot stream can be reduced by adjusting the angle of air supply downward, and air distribution of displacement ventilation can be improved in winter. (2) With the angle of 45°, the ventilation efficiency η is better than the others.

Keywords Angles of airflow · Winter · Displacement ventilation

25.1 Introduction

With the development of mechanical manufacturing technology, according to the survey, mechanical manufacturing technology keeps a high speed to develop for five years during the period of the Tenth Five-Year Plan, and the output value and production are about 2.5 times as great as that of the last, which make the welding technology promoted. As most equipments have strict standard on the process of production, large integral industrial workshop is being promoted in the field of

C. Li · M. Li · H. Wang (✉) · Y. Li · S. Cui
Hunan University of Technology, TaiShanWestRoad88, Zhuzhou 412007, China
e-mail: 499384474@qq.com

welding technology to provide a good and health environment. For some characteristics in large integral industrial workshop, such as heat and pollution source with no fixed location, pollutant generated with heat and made it fittable to apply displacement ventilation system [1].

Displacement ventilation mode is come up with summer condition. Based on the power of thermal buoyancy, fresh cold air is sent to indoor with low speed, formed a fresh air lake near the ground and influenced by heat source in the indoors. As the power of density difference, airflow moves from bottom to top and discharges in the top of the room [2]. In winter, as the temperature of supply air is higher than indoor, supply air has a tendency to rising, so it is a disadvantage to form displacement ventilation air distribution. Currently, most of air-condition changes angles of airflow by guide vanes in market, so it has realistic significant to study the relationship between angle of airflow and air distribution.

25.2 Model and Boundary Condition

The prototype of model is large integral industrial welding workshop. As seen in Fig. 25.1, the length × width × height = $L(x) \times W(y) \times H(z) = 22 \times 12 \times 6$ m. There are 6 cylindrical ventilators in every side in the direction of length, and the cylindrical ventilators have a symmetrical distribution; the distance between the bottom of cylindrical ventilator and the ground is 1.5 m. There are 3 welding posts in the workshop on ground in front of cylindrical ventilator, and its length × width × height = $0.7 \times 0.55 \times 0.7$ m. At the height of 12 m, there are 4 square outlets, its length × width = 0.5×0.5 m. In the direction of length, 4 square outlets are distributed homogeneously in each side, and the distance between the middle of square outlets and sidewall is 8 m. As shown in Fig. 25.2, the height of each cylindrical ventilator is 885 mm, and the diameter φ is 450 mm. The horizontal distance from external wall to center of cylindrical ventilator is 0.7 m. According to the equipments location and air distribution have symmetrical characteristic, 1/6 of physical model is established to simulate.

In the study, the boundary condition inlet is set as velocity inlet, the speed magnitude is 3 m/s, and the temperature of supply air is 292 k. The boundary

Fig. 25.1 Geometry model
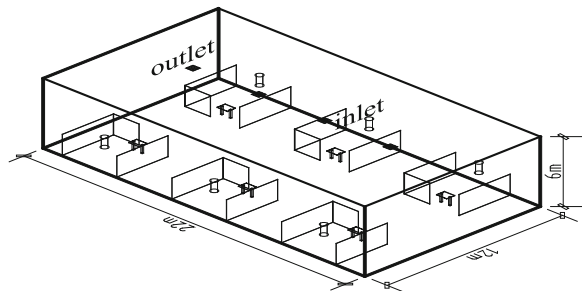
Fig. 25.2 Front view of cylindrical ventilator
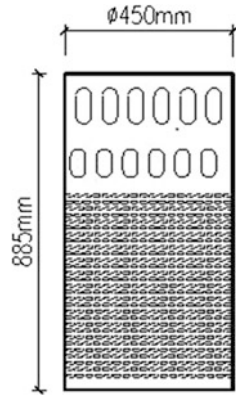
condition of outlets is set as outflow. The heat flow of welding manipulator is 100 w/m^2. In winter condition, the surrounding walls and ceiling have lower temperature, both 278 k. Ansys14.0 is used to simulate all conditions in the study. Three-dimensional model is established and adopted standard k - ε turbulence model. As a lot of heat is generated during the welding process, density is adopted Boussinesq equation. Simplec arithmetic is used to solve process. Governing equation could be found in Ref [3].

25.3 Simulation Result and Analysis

25.3.1 Simulation Conditions

In the study, CFD is used to simulate displacement ventilation system's temperature field and velocity field with different angles of airflow in winter condition (Table 25.1).

25.3.2 Simulation Result

25.3.2.1 Temperature Field

From the Figs. 25.3, 25.4, 25.5, 25.6, 25.7, and 25.8, some conclusions can be obtained as follows:

Table 25.1 Simulation conditions

Supply air		Cool wall	Angles of airflow					
Temperature (K)	Velocity (m/s)	Temperature (K)						
292	3	278	0°	15°	30°	45°	60°	75°

Fig. 25.3 Angle = 0°
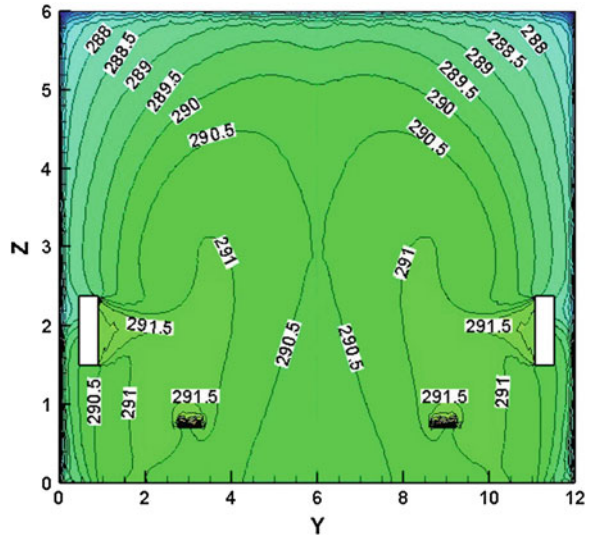
Fig. 25.4 Angle = 15°
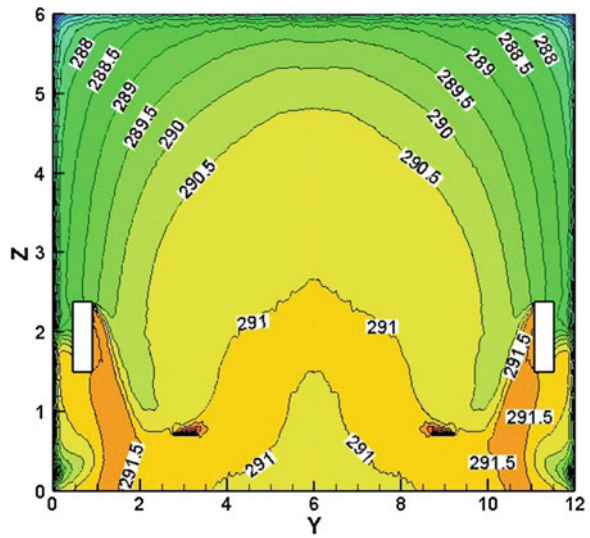
1. As seen in Fig. 25.3, when supply air temperature is higher than indoor's temperature, the air has a tendency to rising with the angle of 0, and the air is more obvious rising while going through welding post. The phenomena can be explained: as the air is heated up, its density is decreased, and density difference between cold and heat air becomes larger, so buoyancy lift increases that makes airflow rising.

2. Compared Figs. 25.3, 25.4, 25.5, 25.6, 25.7, and 25.8 with the angle of airflow becoming larger, the same isotherm has lower height. The phenomena can be

Fig. 25.5 Angle = 30°
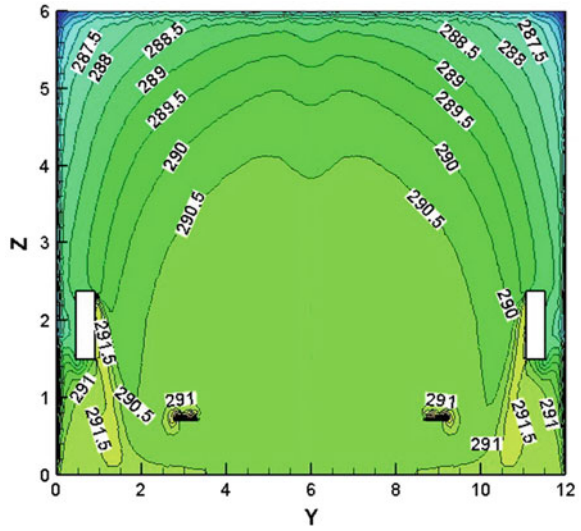
Fig. 25.6 Angle = 45°
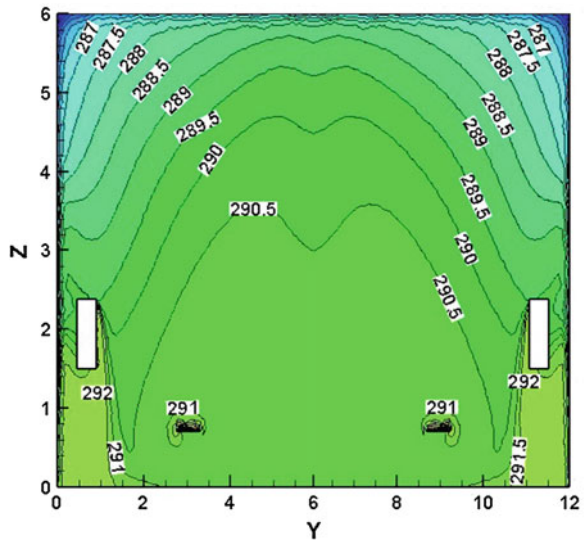
explained: angles of airflow have influence on throw of air stream. When the angle of airflow is 0°, as the workshop is large, airflow of cylindrical ventilators can be considered to free space jet. While angles of airflow have impact on air distribution for impeding diffusive motion of jet flow, so the power of convolution is decreased, which make the energy of air supply lower.

Fig. 25.7 Angle = 60°
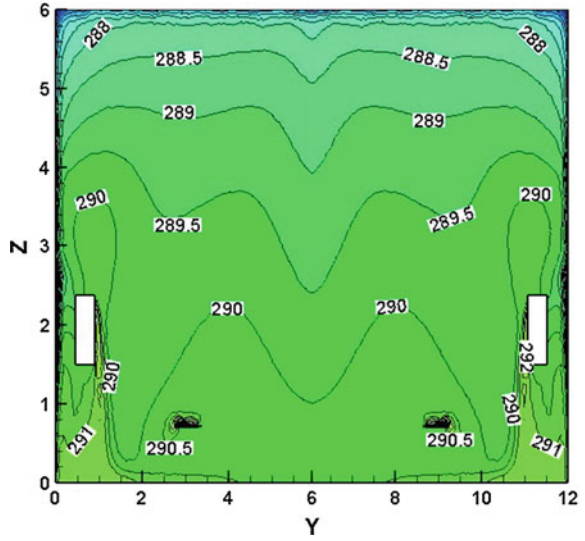
Fig. 25.8 Angle = 75°
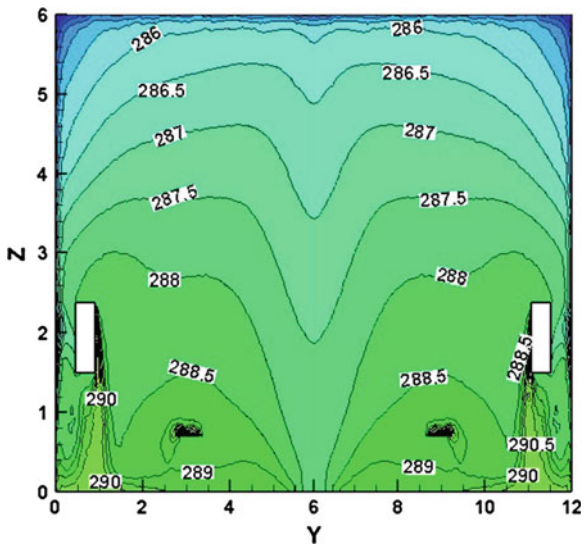
25.3.2.2 Velocity Field

From the Figs. 25.9, 25.10, 25.11, 25.12, 25.13, and 25.14, some conclusions can be obtained as follows:

1. As seen in Fig. 25.9, with angle of 0°, a vortex is formed above the welding post, and velocity in the bottom of workshop is smaller than the top. The phenomena can be explained: air is heated while going through welding post,

Fig. 25.9 Angle = 0°
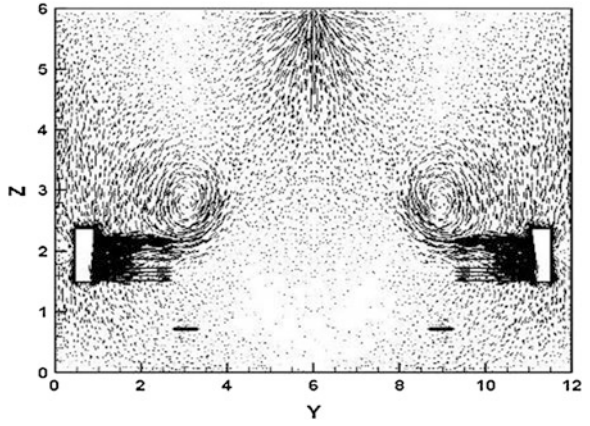
Fig. 25.10 Angle = 15°
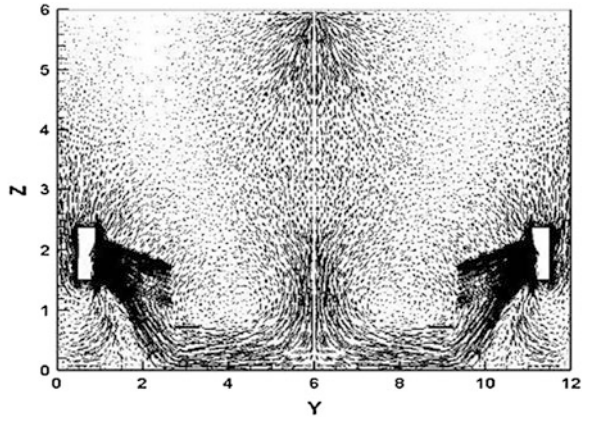
Fig. 25.11 Angle = 30°
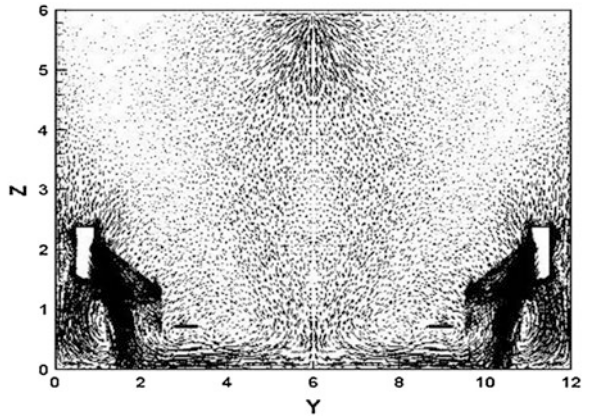
Fig. 25.12 Angle = 45°
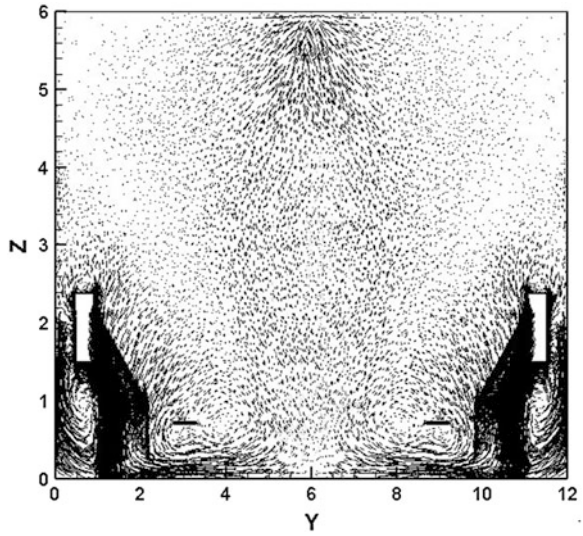
Fig. 25.13 Angle = 60°
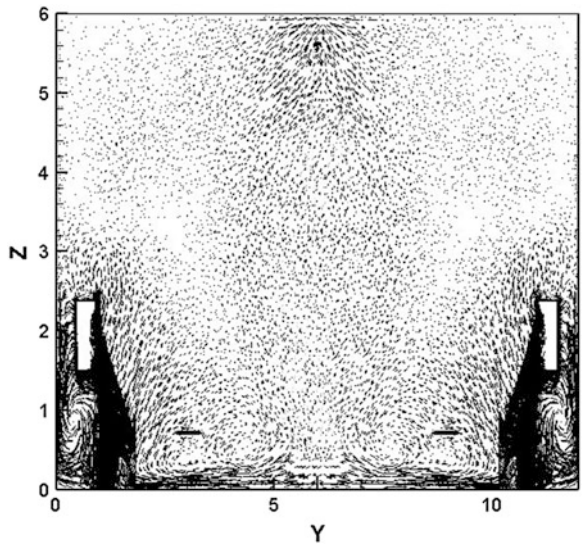
and the surrounding air is rising with the density decreased, and negative pressure is formed which led to emerging vortex. As the airflow cannot reach the bottom of workshop, air distribution of displacement ventilation cannot be obtained.

2. Compared Figs. 25.9, 25.10, 25.11, 25.12, 25.13, and 25.14 with the angles of airflow becoming larger, the speed magnitude of outlet is smaller, and the bottom of velocity has a decreasing tendency except for angle of 0°. The

Fig. 25.14 Angle $= 75°$
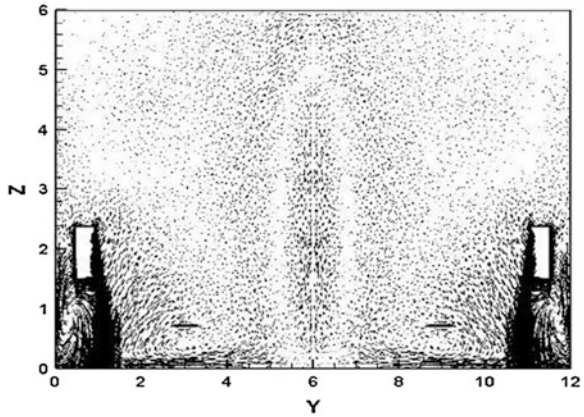
Table 25.2 Ventilation efficiency of different angles in simulation process

Angles of airflow	0°	15°	30°	45°	60°	75°
Ventilation efficiency η	1.314	1.396	1.519	1.943	1.502	1.564

phenomena can be explained: as the airflow reaches the bottom of workshop, the ground could reduce the energy of supply air, so with the angles of airflow becoming larger, the energy is dropped faster, and the velocity of bottom and outlet is smaller.

25.3.3 Result Analysis

In order to estimate air distribution and energy use efficiency, ventilation efficiency η is used to judgment in the study.

$$\eta = \frac{t_p - t_0}{t_n - t_0} \tag{25.1}$$

and

t_p Air exhaust temperature (°C)
t_0 Supply air temperature (°C)
t_n Workspace temperature (°C).

Table 25.3 Ventilation efficiency of different angles in simulation process

Angles of airflow	0°	15°	30°	45°	60°	75°
Average temperature of 1.5 m height (K)	290.443	290.490	290.233	290.126	289.576	288.026
Ventilation efficiency	1.417	1.358	1.432	1.509	1.367	1.465

The average temperature of z = 1.5 m is taken to be the workspace temperature. According to the formula 25.1, as shown in Table 25.2, the ventilation efficiency η of different angles of airflow could be acquired.

25.4 Experimental Verification

Considering the symmetrical characteristic of workshop structure and distribution of airflow, 12 measure points are set at 0–6 m in the direction of width, and the interval of two measure points is 0.5 m. Testo multifunctional testing instrument is adopted to test temperature of height 1.5 m. Supply air temperature is 19 °C, and air exhaust temperature is 19 °C. The 24 values are taken to be the average temperature of height of 1.5 m. The ventilation efficiency of different angles in simulation process is shown in Table 25.3 with different angles.

According to the formula 25.1, ventilation efficiency with different angles in experiment can be obtained as shown in Table 25.4.

Compared ventilation efficiency in simulation process within the experiment, the trend graphs of ventilation efficiency can be described in Fig. 25.15 .

Table 25.4 Ventilation efficiency of different angles in experiment

Angles of airflow	0°	15°	30°	45°	60°	75°
Ventilation efficiency η	1.547	1.573	1.655	1.829	1.535	1.420

Fig. 25.15 Trend graphs of ventilation efficiency
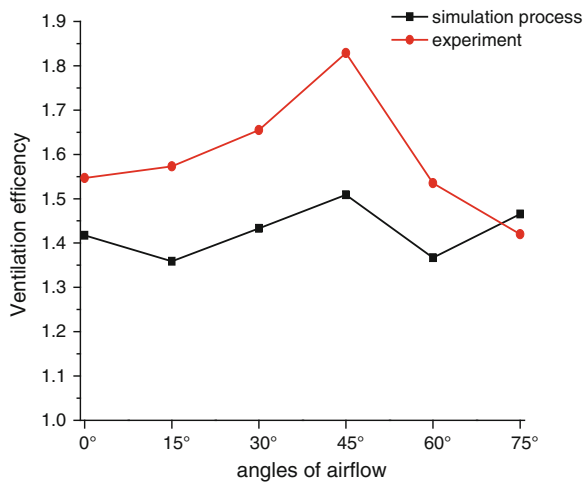
25.5 Conclusions

Compared the simulation result and experiment are as follows:

1. The thermal buoyancy lift effect of hot stream can be reduced by adjusting the angle of air supply downward, and air distribution of displacement ventilation can be improved in winter.
2. The ventilation efficiency in simulation process and experiment is better than the others with the angle of 45.

References

1. Ma X, Li C (2010) Experiment study on displacement ventilation in welding workshop. Technol Refrig 4:1–2
2. Chen J, Wang X et al (2002) Application and energy-saving on displacement ventilation of pollution sources. Energ Saving 6:21–22
3. Ma G, Mao Q, Chen B (2005) The effect of heat source location to air distribution of displacement ventilation. Technol Clean Air Condition 3:2

Chapter 26
Passengers' Exposure to $PM_{2.5}$, PM_{10}, and CO_2 in Typical Underground Subway Platforms in Shanghai

Huan Ma, Henggen Shen, Zhen Liang, Liuchuang Zhang and Chan Xia

Abstract Based on the statistics of Shanghai metro corporation, currently, above 7 million commuters travel on the Shanghai metro system each day. However, information related to the characteristics of indoor air particulate matter (PM) level in underground stations of this system is limited. The concentrations of $PM_{2.5}$, PM_{10}, and CO_2 were measured in this study with portable monitors at two typical underground subway platforms of Shanghai Metro Line 9 during 19 January to 22 January. Experimental results showed that: (1) The anthropogenic activity had a significant impact on the contaminant concentration. Pronounced diurnal variations were observed in the underground subway platforms, and the concentrations of $PM_{2.5}$, PM_{10}, and CO_2 displayed a bimodal pattern, with peaks between 7:00 and 10:00 and between 16:00 and 19:00 during the rush hour of workdays. Meanwhile, the $PM_{2.5}/PM_{10}$ ratio indicated that the human activities contribute the most course particles. (2) The pollutant density had a slightly reduction just a few seconds before the subway train came. It could be explained by the dilution of piston effect on the subway station through tunnel and passageway. (3) The contaminant samples of different station layer were also collected during off-peak hours with the same stable passengers. Correlation between pollutant concentration and station depth has been confirmed.

Keywords Underground subway platforms in Shanghai · $PM_{2.5}$ · PM_{10} · $PM_{2.5}/PM_{10}$ ratio · CO_2

H. Ma · H. Shen (✉) · Z. Liang · L. Zhang · C. Xia
School of Environmental Science and Engineering, Donghua University,
2999#, North Renmin Road, Songjiang, Shanghai, China
e-mail: shenhg@126.com

26.1 Introduction

Climate, environment, and health have been affected greatly by atmospheric particulate matter (PM) through a great variety of processes [1]. And PM can be divided into PM_{10} and $PM_{2.5}$ by size which means particles with mass median aerodynamic diameter smaller than 10 and 2.5 μm, respectively [2].

Many epidemiological studies have conducted over the past decades, which have proved that exposure to small short-term increases in PM levels has a strong association with the increases in daily mortality and symptoms of certain illnesses [3]. It reported that 4 % in all cause, 6 % in cardiopulmonary, and 8 % in lung cancer mortality increase was aroused by each 10 μg/m^3 increase in $PM_{2.5}$ [1], while each 10 μg/m^3 rise in PM_{10} concentration will lead to total daily mortality rate increase by approximately 1 % [4]. As the particle size determines the deposition site in the respiratory tract, the health problems brought about by PM is closely related to particle size. Even now the major property of PM to account for the majority of health effects is not clear. But several reported triggers might be particle levels, total surface area, electrostatic factors, and the chemical and biological composition [5].

Subway systems are a very high frequency service established mainly in underground tunnels or on elevated tracks compared with other traffic, and this kind of transportation modes serves billions of commuters annually in metropolitan areas worldwide. The underground portion of a metro system is a confined space that may accumulate the concentration of contaminants either from the outside environment or generated by pollutants internally [6]. The mechanical ventilation system is vital to this situation; otherwise, the contaminants may accumulate to a severe harmful level [7]. Furthermore, Karlsson et al. [8] stated that metro PM inducing oxidative stress in cultured human lung cells, so it was more genotoxic than street PM.

The metropolitan area of Shanghai is the biggest and most important developing urban areas in China. The transportation system is well developed in Shanghai, especially the metro system; 13 metro lines have been constructed, and other 3 metro lines are building. So, metro lines are becoming the most popular and congest place for commuters in Shanghai. But epidemiological studies have shown that commuting in traffic is associated with adverse health effects. So, it is vital to investigate commuters' exposure to traffic-related air pollutants before considering potential health risks [9]. Previously reported measurements have mostly focused on chemical compositions or source appointment of $PM_{2.5}$, while the diurnal variations of $PM_{2.5}$ concentration are rarely conducted [10]. The aim of this paper is to investigate the diurnal mass concentration levels of $PM_{2.5}$, PM_{10}, and CO_2 in typical underground metro platforms: Yishan Road Station and Lujiabang Road Station (as shown in Fig. 26.1). Meanwhile, pronounced seasonal variation in the urban area has been observed, with the highest concentrations typically observed in the winter and the lowest concentrations generally found in the summer [2]. So, this study was conducted in winter on 19 January to 22 January.
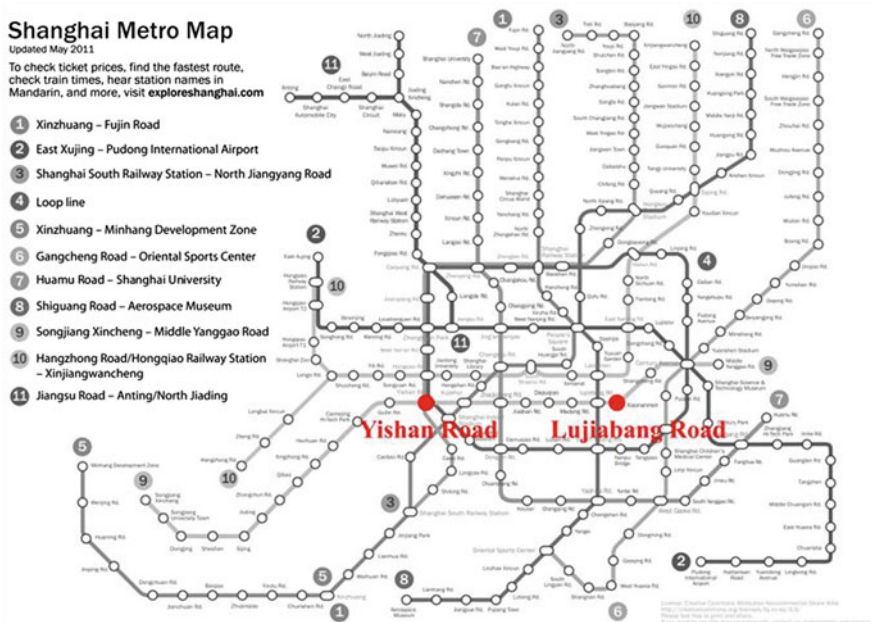
Fig. 26.1 Measurement locations: Yishan Road Station and Lujiabang Road Station

26.2 Measurement

26.2.1 Site Description

The platforms identified for detailed study are selected in an attempt to minimize variability in environmental factors, platform configurations, and passenger volumes to ensure greater homogeneity across all underground station platforms. These two typical underground metro platforms selected for monitoring are within the elevated inner beltway of Shanghai. They both can serve as stations for transformation. Also, their passenger volume is relatively large and stable in workdays compared with other stations.

Yishan Road Station is located on the Kaixuan Road in Xuhui District. Passengers from line 3, line 4, and line 9 can transfer from one to another in this station. Measurements were taken in passengers' floor of line 9 which is located in the −2 floor. Lujiabang Road Station is located in Lujiangbang Road in Huangpu District. There are 2 metro lines cross here: line 8 and line 9. The platform of line 8 is on the −2 floor, and the platform of line 9 is on the −3 floor. Measurements were conducted in passengers' floor of both line 8 and line 9. The platform of each measured station is quite similar with each other (as shown in Fig. 26.2).

The time table of line 9 below is from the metro operation Web site (as shown in Table 26.1).

Fig. 26.2 Typical
measurement metro platform
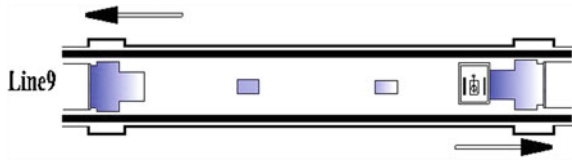
26.2.2 Instruments and Observation

In the test, the gravimetric concentration of $PM_{2.5}$ and PM_{10} samples were collected with two Grimm Aerosol Spectrometers, and the CO_2 concentration were measured using a TESTO 435-4 multi-function measuring instrument and a TSI 7545 indoor air quality meter. Statistical analyses were also carried out to estimate the possible sources of the pollutants. Additionally, the instruments are calibrated daily to re-zero the units and ensure reading accuracy. To collect samples, the instrument was placed at the measure point, and the probe was in the breathing zone about 1.5 m high from the ground.

The measurement of diurnal variation and short-term variation in $PM_{2.5}$, PM_{10}, and CO_2 concentration was conducted in Yishan Road at points A and B in Fig. 26.3. Zone A was supposed to be the busiest zone with large amounts of passengers in this layer. So, the results could reveal the connection between passenger volume and $PM_{2.5}$, PM_{10}, and CO_2 concentration. The passenger volume at point B is relatively small and more stable. So, the reason for short-term variation in $PM_{2.5}$, PM_{10}, and CO_2 concentration might be easy to discover at point B.

The measurement of floor-depth variation in $PM_{2.5}$, PM_{10}, and CO_2 concentration was take in Lujianbang Road at points C and D in Fig. 26.4 It is quite similar and more stable for passengers' volume at points C and D. Thus, the relation between floor-depth variation and $PM_{2.5}$, PM_{10}, and CO_2 concentration could get with less interference. It has been demonstrated that the Grimm OPC overestimated PM values through tests at a highway toll station conducted by Cheng and Li [11].

Table 26.1 The time table of line 9

Monday to Friday			Saturday and Sunday		
Name	Time	Train headway	Name	Time	Train headway
Morning peak	07:25–08:35	About 3 min	Peak time	08:00–20:00	About 6 min
The other time	08:35–16:30	6 min 40 s to 10 min			
Evening peak	16:30–19:30	About 4 min			

Fig. 26.3 The location of
points A and B
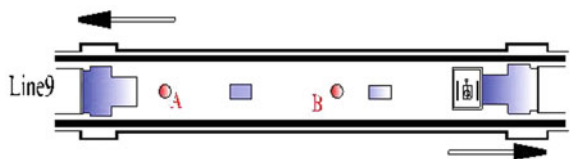
So, in order to avoid the measured deviation, the real values collected from the tests were non-dimensionalized by the corresponding average value.

The instruments operated approximately 5 h and average data points were logged. The first and last several minutes of data are discarded to ensure that start and stop times are synchronized. As the buttery of instruments can only afford as long as 6–7 h, so point A was visited triple in two days, once during the morning peak (between 7:00 and 12:00 a.m.), once during the afternoon peak (between 3:00 and 8:00 p.m.), and once during 11:00 a.m. to 4:00 p.m. While points B, C, and D were visited once in another two days, during 10:00 a.m. to 4:00 p.m. Points C and D are measured at the same time. In total, the study includes 1,600 min readings.

26.3 Results and Discussion

26.3.1 Diurnal Variation in $PM_{2.5}$, PM_{10}, and CO_2 Concentration

The diurnal variations in $PM_{2.5}$, PM_{10}, $PM_{2.5}/PM_{10}$ ratios, and CO_2 concentration at Yishan Road on 21–22 January are shown in Fig. 26.5(a–d). The data were averaged as follows: $PM_{2.5}$real/$PM_{2.5}$ave., PM_{10}real/PM_{10}ave, CO_2real/CO_2ave, and it was collected in two days: morning peak (between 7:00 and 12:00 a.m.) and afternoon peak (between 3:00 and 8:00 p.m.) were collected on 21 January, while the data of 11:00 a.m. to 4:00 p.m. was gathered on 22 January. The CO_2 concentration is assessed in relationship to the passenger volume. So, the concentration curve of CO_2 could be regarded as the variation tendency of passenger
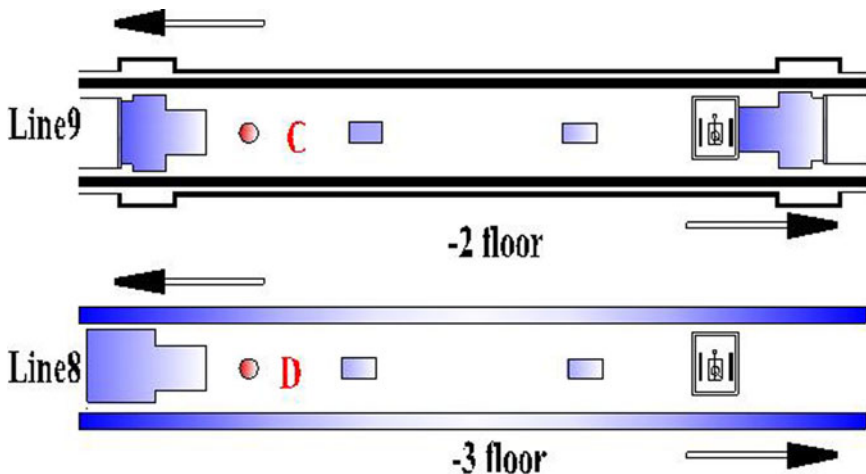
Fig. 26.4 The location of points C and D

(a)

(b)

(c)

(d)
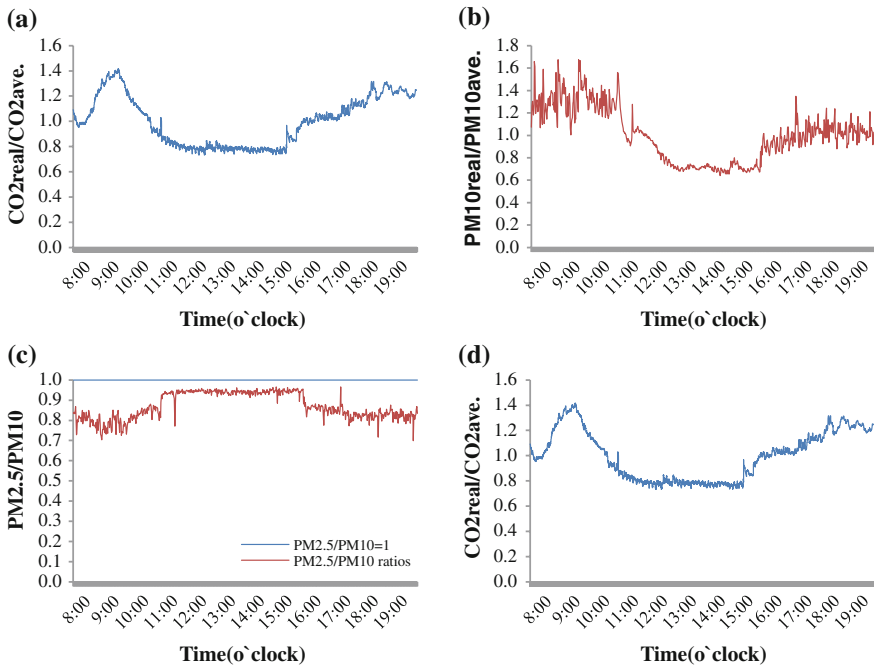
Fig. 26.5 The diurnal variation in $PM_{2.5}$, PM_{10}, and CO_2 concentration, (**a**) $PM_{2.5}$real/$PM_{2.5}$ave, (**b**) PM_{10}real/PM_{10}ave, (**c**) $PM_{2.5}$/PM_{10} ratio values, (**d**) CO_2real/CO_2ave

volume. Pronounced diurnal variations are observed in the figures. Compared Fig. 26.5a, b, and d, the curves of the three figures are quite similar with each other. In Fig. 26.5, the concentrations are generally low from 10:00 to 16:00, after a morning peak around 7:00 and 10:00 a.m., then they reach to another peak from 16:00 to 19:00. The concentrations therefore display a bimodal pattern which is similar to that observed in New York City [12]. During rush hours, both $PM_{2.5}$ and PM_{10} measurements are much higher than non-rush hours.

Figure 26.5c shows the ratio ranges of $PM_{2.5}$/PM_{10} during the time from 7:30 to 19:00. The value is lower at rush hour than that at non-rush hour. It indicates that the particle matter caused by human has larger diameter than that generated by mechanical friction.

26.3.2 Short-term Variation in $PM_{2.5}$, PM_{10}, and CO_2 Concentration

Figure 26.6e and f show that the short-term variation of $PM_{2.5}$, PM_{10}, and CO_2. And this measurement was conducted on 20 January. The contaminant levels plotted in the figures are divided by their corresponding mean values. The
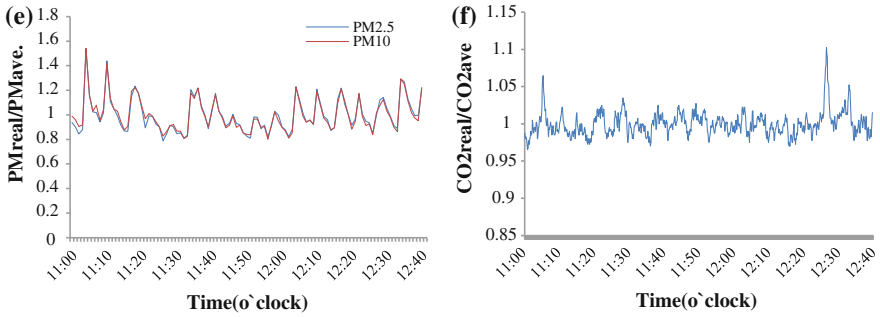
Fig. 26.6 The short-term variation in $PM_{2.5}$, PM_{10}, and CO_2 concentration, (**e**) short-term values of $PM_{2.5}$ and PM_{10}, (**f**) short-term values of CO_2

contaminant curves present fluctuation in the figures below. The range of PM2.5 and PM10 are quite familiar with each other and more notable, while the CO_2 is relatively more stable. So, besides the influence of passenger volume, piston wind caused by the train movement was found to be an important factor influencing the
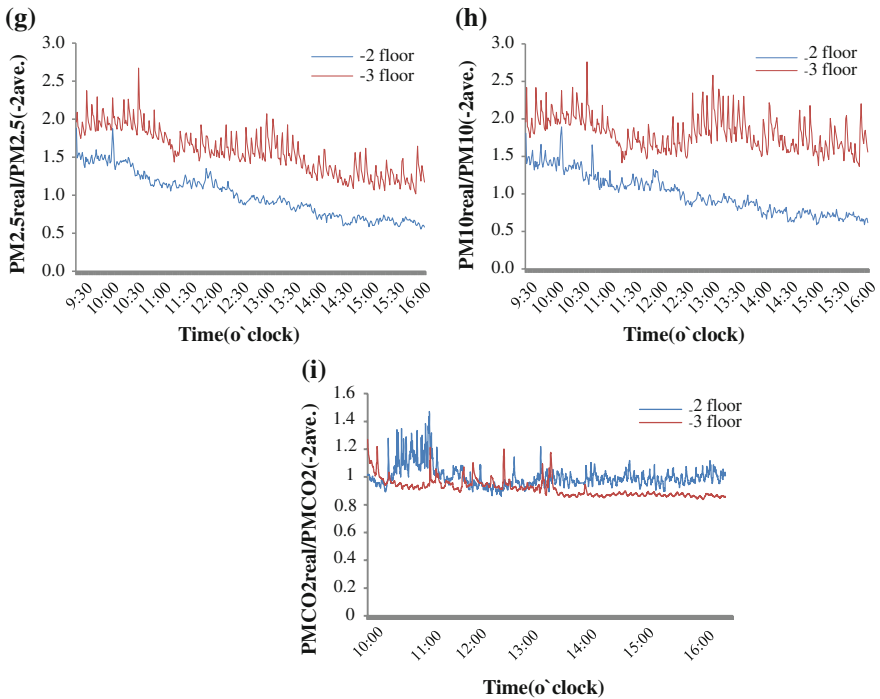
Fig. 26.7 The floor-depth variation in $PM_{2.5}$, PM_{10}, and CO_2 concentration, (**g**) the $PM_{2.5}$ value of -3 floor and -2 floor, (**h**) the PM_{10} value of -3 floor and -2 floor, (**i**) the CO_2 value of -3 floor and -2 floor

PM value in underground platforms. The contaminants could be diluted by the flow generated when the train comes and leaves. The theory of PM levels in underground subway stations has great relation to the frequency at which trains run was reported by Johansson and Johansson [13] and Salma et al. [14]. Their results indicate that re-suspension owe to the movement of trains can lower PM levels. The results were demonstrated in this study.

26.3.3 Floor-depth Variation in $PM_{2.5}$, PM_{10}, and CO_2 Concentration

Figure 26.7i illustrates the CO_2 relative value of different floors in Lujiabang Road on 19 January. The values are quite similar in the two different floors. It indicates that the passenger volumes in these floors are similar too. Without the interference of passenger volume, the PM value of different floor-depths is shown in Fig. 26.7g and h much apparently. The data plotted in the figures were averaged by the mean value of floor -2. The figures indicated that the PM value would get greater when the depths get lower. The reason of this phenomenon might be the influence of outdoor contaminants through corridors or stairway shafts. The deeper the floor is, the greater the outdoor contaminants of influence. This conclusion is quite similar with that of Branis [15] achieved in 2006.

26.4 Conclusion

Information related to the characteristics and variations of indoor air quality in the underground stations in Shanghai subway system is limited. This study measures the $PM_{2.5}$, PM_{10}, and CO_2 levels at two underground stations on the same rapid transit line. The results reveal that: (1) PM levels in underground environments display a bimodal pattern. Two peak regions both appeared at rush hour. Meanwhile, the $PM_{2.5}/PM_{10}$ ratios presented that the particles result from human activities are mainly course particles, and the mechanical friction produces the majority of fine particles. Effective measures and some improvements should be taken to control the contaminants to prevent people from being harmed during rush hours. (2) Piston wind generated by the train movement can affect the PM levels. The indoor air quality can be improved if the air quantity and diffusers are well designed. (3) The PM level might be relevant to the depth of the floor of the underground metro platforms. The data show that the PM values increase with the decrease in the floor-depth. It probably results from the influence of outdoor PM pollutants.

References

1. Pope CR, Burnett R, Calle MJT, Krewski E, Ito K, Thurston G (2002) Lung cancer, cardiopulmonary mortality, and long-term exposure to fine particulate air pollution. J Am Med Assoc 287:1132–1141
2. Zhao X, Zhang X, Xu X, Xu J, Meng W, Pu W(2009) Seasonal and diurnal variations of ambient $PM_{2.5}$ concentration in urban and rural environments in Beijing. Atmos Environ 43:2893–2900
3. Harrison RM, Yin J (2000) Particulate matter in the atmosphere: which particle properties are important for its effects on health. Sci Total Environ 249:85–101
4. Lippmann M (1998) The 1997 US EPA standards for particulate matter and ozone. In: Hester RE, Harrison RM (eds) Issues in environmental science and technology 10: Royal Society of Chemistry, pp 75–99
5. Monn C (2001) Exposure assessment of air pollutants: a review on spatial heterogeneity and indoor/outdoor/personal exposure to suspended particulate matter, NO2, and O3. Atmos Environ 35:1–32
6. Cheng YH, Yan JW (2011) Comparisons of particulate matter, CO, and CO2 levels in underground and ground-level stations in the Taipei mass rapid transit system. Atmos Environ 45:4882–4891
7. Nieuwenhuijsen MJ, Gómez-Perales JE, Colvile RN (2007) Levels of particulate air pollution, its elemental composition, determinants and health effects in metro systems. Atmos Environ 41:7995–8006
8. Karlsson HL, Nilsson L, Möller L (2005) Subway particles are more genotoxic than street particles and induce oxidative stress in cultured human lung cells. Chem Res Toxicol 18:19–23
9. Huang J, Deng F, Wu S, Guo X (2012) Comparisons of personal exposure to PM2.5 and CO by different commuting modes in Beijing, China. Sci Total Environ 425:52–59
10. Wang J, Xie Z, Zhang Y, Shao M, Zeng L, Cheng C, Xu X, Zhao X, Meng Y (2004) Study on the characteristics of mass concentration of atmospheric fine particles in Beijing. Acta Meteorologic Sinica 62 (1):104–111 (in Chinese)
11. Cheng YH, Li YS (2010) Influence of traffic emissions and meteorological conditions on ambient PM10 and PM2.5 levels at a highway toll station. Aerosol Air Qual Res 10:456–462
12. DeGaetano AT, Doherty OM (2004) Temporal, spatial and meteorological variations in hourly $PM_{2.5}$ concentration extremes in New York City. Atmos Environ 38:1547–1558
13. Johansson C, Johansson PA (2003) Particulate matter in the underground of Stockholm. Atmos Environ 37:3–9
14. Salma I, Weidinger T, Maenhaut W (2007) Time-resolved mass concentration, composition and sources of aerosol particles in a metropolitan underground railway station. Atmos Environ 41:8391–8405
15. Branis M (2006) The contribution of ambient sources to particulate pollution in spaces and trains of the Prague underground transport system. Atmos Environ 40:348–356

Chapter 27
Thermal Comfort with Floor Heating

Zhaojun Wang, Juan Hou, Chengzu Kang and Haoran Ning

Abstract This study aimed at investigating the thermal comfort and thermal sensation of subjects in an asymmetric radiant thermal environment; 16 healthy subjects were participated in the experiments. According to the results in non-uniform environments with the cold radiation of outer window and floor heating, the local thermal sensations of body parts were different and were the local thermal comfort and skin temperature. The difference would be reduced as the air temperature increasing. In different conditions, forehead and back skin temperature differed not greatly; the difference of hand skin temperature was large due to hand exposed. Women were more sensitive than men to ambient temperature. In the experiment, women's thermal sensations were colder under the same environment.

Keywords Thermal sensation · Thermal comfort · Skin temperature · Floor heating · Asymmetric radiant thermal environment

27.1 Introduction

The outside average temperature in severe cold area in China is very low. Hence, indoor heating is necessary. Radiant heating as a mean of energy saving, convenient adjustment, and comfort is widely used. In severe cold area, the cold radiant of outer wall and window and radiant heating form an asymmetric radiant thermal environment. Under non-uniform conditions, the thermal sensation and thermal comfort of each part of human body are various because of the different temperature. The local parts influence each other; furthermore, the local parts affect the whole body [1]. Nevin et al. analyzed the effect of heated floor temperatures on

Z. Wang (✉) · J. Hou · C. Kang · H. Ning
Harbin Institute of Technology, School of Municipal and Environmental Engineering,
Harbin 150090, China
e-mail: wzjw02@yahoo.com.cn

thermal comfort [2]. Olesen et al. investigated thermal comfort requirements for floors occupied by people with bare feet [3]. This study focused on the thermal comfort and thermal sensation of subjects in an asymmetric radiant thermal environment.

27.2 Method

The experiment is carried out in an artificial chamber, which consists of Room A and Room B. Heating floor is used in Room A, which can be used to simulate indoor radiant heating. An evaporator is placed in Room B, which can be used to simulate outdoor climate in severe cold area in China. The wall and window between Room A and Room B can be treated as the exterior wall and window of Room A. Thus, an asymmetric radiant thermal environment is created in Room A.

A total of 16 healthy subjects (8 males, 8 females) were participated in the experiments. They lived in Harbin for more than two years and have adapted to the Harbin cold climate. The subjects were requested to wear the uniform clothes. A male student and a female student attended each experiment at the same time.

This experiment includes two experimental conditions. One is the colder condition 1, and the other is the neutral condition 2. The air temperature of Room B was kept at -15 °C in both conditions. In condition 1, the air temperature of Room A was kept at 19 °C. And in condition 2, the air temperature of Room A was kept at 22 °C. Under the both conditions, an asymmetric radiant thermal environment was created in Room A.

The measurement point 1 was placed in the middle of the Room A, and the measurement point 2 was placed near the subjects. At point 1, air temperature was measured at the height of 0.6, 1.1 m, and the other parameters like black ball temperature, air velocity, and relative humidity were recorded at the height of 0.6 m. At point 2, air temperature was measured at 0.1, 0.6, and 1.1 m heights. At 0.1, 0.6, and 1.1 m heights, the ankle, waist, and head of a seated subject were presented, respectively.

The experiment lasted 90 min and was divided into two stages. The first 30 min was the preparation stage, and the other 60 min was the experimental stage. During the experimental period, skin temperatures, air temperature, relative humidity, black ball temperature, the surface temperatures of chamber and floor were recorded every 5 min. The air velocity was measured every 10 min. At the experimental stage, the subjects reported their feeling every 10 min.

The subjective questionnaires include local and overall thermal sensation, local and overall thermal comfort. The local body parts include head, back, hand, arm, and lower leg whose skin temperatures were recorded. Local and overall thermal sensations were reported on ASHRAE 7-point continuous scale [4], and thermal comfort was reported on Hui Zhang's discontinuous scale [5].

27.3 Results and Analysis

27.3.1 Environmental Parameters

The air temperature of point 1 and point 2 is shown in Table 27.1. In both conditions, the air temperature of point 2 is lower than that of point 1 caused by the cold radiant of outer wall and window. In condition 2, the average air temperature of point 1 is 2.4 °C higher than that of condition 1; the average air temperature of point 2 is 2.1 °C higher than that of condition 1. The air temperature of point 2 increases as the height increasing.

In both conditions, each of the mean air velocities is 0.01 m/s, which meets the requirement of the ASHRE55-2004. The relative humidity is almost 30 %, which is within the range of thermal comfort.

In Fange's PMV index [6], the environmental parameters, which affect thermal comfort, are air temperature, air velocity, relative humidity, and mean radiation temperature. In two conditions, the mean radiation temperature at the height of 0.6 m of point 1 were 19.1 and 21.4 °C, both were lower than the air temperature (19.5 and 21.9 °C). Consequently, the thermal environment of Room A is an asymmetric radiant thermal environment.

27.3.2 Thermal Sensation

In the non-uniform thermal environment, the human overall thermal reaction is a result of integrated effects of local thermal responses. Thus, the effects of local sensations on overall sensation are described here. Figure 27.1 illustrates local and overall thermal sensation votes in two conditions. Every point in this figure represents the mean vote of all subjects' thermal sensation. It is obvious that the head thermal sensation vote is the highest and the lower leg thermal sensation vote is the lowest. Because the air temperature around head is higher than the other parts, the air temperature around lower leg is lower than other parts [7].

Table 27.1 Air temperature in two conditions

Location	Height/m	Air temperature/°C	
		Condition 1	Condition 2
Point 1	0.6	19.5	21.9
	1.1	18.4	20.9
	Mean	19.0	21.4
Point 2	0.1	17.2	19.3
	0.6	17.5	19.4
	1.1	18.4	20.6
	Mean	17.7	19.8

Fig. 27.1 Local and overall thermal sensation votes
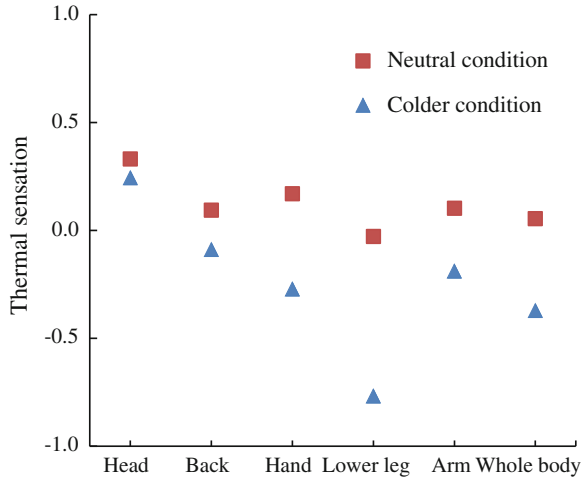
In condition 1, local and overall thermal comforts are below 0 except the head; the lower leg thermal sensation is the lowest, about −0.77; the difference of local thermal sensation is rather obvious. In condition 2, the local and overall thermal comfort are above 0 except the lower leg; the overall thermal sensation is 0.05, close to neutral; the difference of local thermal sensations in condition 2 is definitely less than that in condition 1.

27.3.3 Thermal Comfort

Figure 27.2 indicates local and overall thermal comfort in two conditions. In condition 1, overall thermal comfort is 0.08, near slightly comfort; the lower leg thermal comfort is the lowest, around −0.07, between slightly discomfort and discomfort; while the other local body parts and overall thermal comfort are above 0, between slightly comfort and comfort, the head thermal comfort is the highest, about 0.45; the difference of local thermal comfort is obvious.

In condition 2, local and overall thermal comfort are above 0, between slightly comfort and comfort; the lower leg thermal comfort is the lowest, about 0.30; the head thermal comfort is the highest, close to 0.63; the difference of local thermal comfort in condition 2 is significantly less than that in condition 1.

27.3.4 Skin Temperature

Figure 27.3 shows the local skin temperature curve in two conditions. In condition 1, the skin temperatures for the forehead and back are the highest of the body

Fig. 27.2 Local and overall
thermal comfort votes
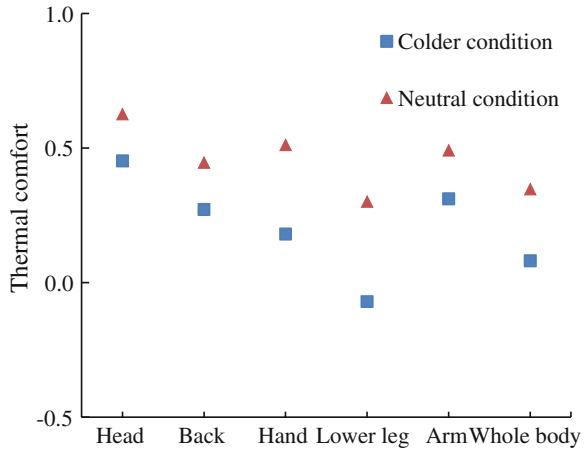
Fig. 27.3 Local skin
temperatures
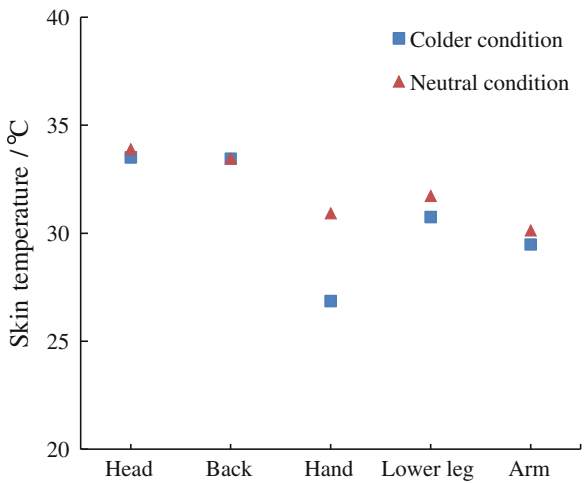
parts, almost 33.5 °C; the arm skin temperature is lower than that of forehead and
back, practically 30.8 °C; the hand skin temperature is the lowest, only 26.9 °C;
the difference of local skin temperatures is relatively obvious.

In condition 2, the skin temperatures for the forehead and back are also the
highest of all body parts, respectively, 33.9 and 33.4 °C. The lower leg skin
temperature is the lowest, only 30.1 °C. The difference of local skin temperatures
in condition 2 is less conspicuous than that of condition 1.

In both conditions, the forehead skin temperature is very close to the back skin
temperature; the differences of arm skin temperatures and lower leg skin tem-
peratures are 0.9 and 0.6 °C, respectively. The difference of hand skin temperature
is largest, almost 4 °C. It may be caused by the hand exposed, and the hand skin
temperature is closely related to the air temperature.

Fig. 27.4 Thermal sensation votes in condition 1
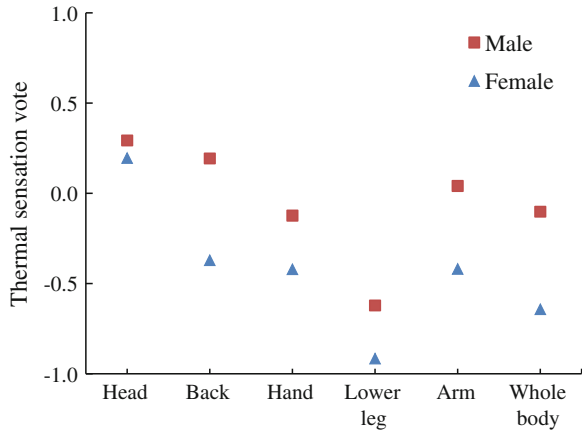
27.4 Discussion

A large number of studies have shown that women are more sensitive than men to environmental temperature [8]. Figure 27.4 describes men and women' thermal sensation votes in condition 1. The male and female subjects' forehead votes are the highest, respectively, 0.29 and 0.19. The lower leg votes are the lowest, respectively, −0.62 and −0.92. The difference is 0.3 scales, which shows that females are more likely to feel cold around leg. The female subjects' local and overall thermal sensation votes are significantly lower than the male subjects.

Figure 27.5 illustrates that the male and female subjects' forehead thermal sensation votes are the largest in condition 2, respectively, 0.38 and 0.28. The lower leg votes are the lowest, respectively, 0.13 and −0.19. The difference is 0.32 scales, which shows that females are more likely to feel cold around leg. Male subjects' thermal sensation votes are all above 0; female subjects' local and overall

Fig. 27.5 Thermal sensation votes in condition 2
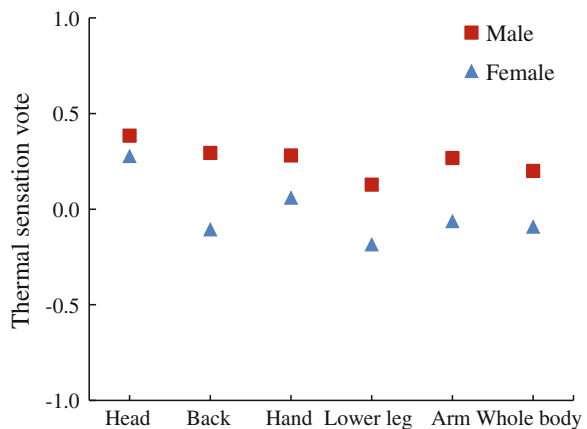
thermal sensation votes are significantly lower than male subjects. In conclusion, women will feel colder under the same environment.

27.5 Conclusions

In non-uniform environments with the cold radiation of outer window and floor heating, the local thermal sensations of body parts were different and were the local thermal comfort and skin temperatures. The differences would be reduced as the air temperature increasing.

In different conditions, the forehead and back skin temperature differed not greatly; the difference of the hand skin temperature was large due to hand exposed.

Women were more sensitive than men to ambient temperature. In the experiment, women's thermal sensations were colder under the same environment.

References

1. Cheong KWD, Yu WJ, Sekhar SC et al (2007) Local thermal sensation and comfort study in a field environment chamber served by displacement ventilation system in the tropics. Build Environ 42(2):525–533
2. Nevins RG, Michaels KB, Feyerherm AM (1964) The effect of floor surface temperature on comfort: Part I, college age males. ASHRAE Trans 70:29–36
3. Olesen BW (1977) Thermal comfort requirements for floors occupied by people with bare feet. ASHRAE Trans 83(2):41–57
4. ASHRAE (2004) ANSI/ASHRAE Standard 55-2004, Thermal environmental conditions for human occupancy. American Society of Heating, Refrigerating, and Air-Conditioning Engineers, Inc, Atlanta
5. Arens E, Zhang H, Huizenga C (2006) Partial- and whole-body thermal sensation and comfort, Part I: uniform environmental conditions. J Therm Biol 31(1–2):53–59
6. Fanger PO (1970) Thermal comfort. Danish Technical Press, Copenhagen
7. Wang ZJ, He YN, Hou J et al (2012) The effect of cold radiation on human thermal sensation and thermal comfort in Harbin winter. In: Proceedings of the second international conference on building energy and environment (COBEE), US, Colorado, 1–4 Aug 2012
8. Schellen L, Loomans MGLC, de Wit MH et al (2012) The influence of local effects on thermal sensation under non-uniform environmental conditions—Gender differences in thermophysiology, thermal comfort and productivity during convective and radiant cooling. Physiol Behav 107:252–261

Chapter 28
The Characters of the Nozzle's Jet and Design Method of the Secondary Airflow-Relay Equipment in the Large-Space Building

Yezan Cui and Chen Huang

Abstract When the nozzle is used to form the stratified air-conditioning system in the large-space and large-span building, the nozzle air supply does not meet the requirements of the air-conditioning zone in the stratified air-conditioning system because the nozzle's jet range is limited. To solve this problem, we have taken an actual large-space building as an example and adopted the secondary airflow-relay equipment to relay the nozzle's air supply. In this paper, basing on the results of the field experiments, we described the design method of the secondary airflow-relay equipment, studied the characters of the nozzle's jet, and provided the size and fixed form of the secondary airflow-relay equipment in the large-space and large-span building.

Keywords Large space · Jet track · Secondary airflow-relay equipment · Design method · Jet range

The Symbol Table

X	The nozzle's jet range (m)
Y	The jet vertical drop (m)
D_0	The nozzle's diameter (m)
α	The angel of the nozzle's axis airflow to the horizontal direction
K	Correction factor
A	The nozzle's turbulence factor
T_0	The thermodynamic temperature of export airflow (K)
T_n	The thermodynamic temperature of the indoor air (K)
ΔT	The temperature difference between the nozzle's axis airflow and the indoor air (K)
V_0	The axis speed of the nozzle's jet (m/s)

Y. Cui · C. Huang (✉)
School of Environment and Architecture, University of Shanghai
for Science and Technology, Shanghai, China
e-mail: huangc@usst.edu.cn; hcyhyywj@163.com

g	Free-fall acceleration (m/s^2)
Ar	Archimede's number
$H_{0,1}/H_{0,2}$	The axis's height in Case 1 and Case 2 (m)
Vr	The speed of the point at the distance r to the axis on the cross section of the jet (m/s)
R	The cross-sectional diameter in the nozzle's jet range X (m)
r	The distance to the jet axis (m)
Vx	The axis's velocity in the nozzle's jet range X (m/s)
Tx	The axis's temperature in the nozzle's jet range X (K)
ΔTx	The axis and the indoor air design temperature difference along the nozzle's jet (K)
Q_0	The secondary airflow equipment's volume (m^3/h).

28.1 Introduction

Presently, the nozzle air supply is widely adopted in the stratified air-conditioning system in the large-space building. Higher the installed nozzles, higher the level interface of the stratified air-conditioning system and more energy consumption. At the same time, the jet range, the indoor air distribution of thermal environment, and the occupants' comfort are affected by the installed height of the nozzles.

The secondary airflow equipment can relay the nozzle's jet in the large-space or large-span building. Thereby, it can improve the nozzle's limited in jet range. However, this method is rarely used in the large-span building. The secondary airflow equipment has been used in the ventilation system of the underground garages [1], tunnels, large-space buildings [2] as well as the air-conditioning system of some large-space buildings [3]. The secondary airflow-relay equipment could relay that the nozzle's low-temperature air supply, which depends on the track of the nozzle's jet, is the key to apply this technology in the air-conditioning systems of the large-span and large-space building. Abramovich's and Alfred Koestel's formulas, which are determined by experiments on the basis of the theoretical derivation, are the main formulas [4–6] to calculate the track of the nozzle's jet in the large-space building. These formulas have different forms but the same essence. However, they are not suitable to calculate the nozzle's jet track of the large-space building.

This paper aims to get the nozzle's jet theoretical track by the experiments and put forward the design method of the secondary airflow-relay equipment's parameters and installed location with basing on the nozzle's jet characters at the point of the equipment's location and the requirements of the building's span and installed location.

28.2 The Experimental Overview of the Nozzle's Jet

28.2.1 The Research Object's Overview

An engineering center is adopted to be the research object which has a gable structure, the top height 14.4 m, the total area 500 m^2, the east–west direction length 27.7 m, the south–north direction length 17.7 m, and a south–north direction beam which clear height is 6 and 10 m to the east wall.

The energy source of this center is made up of the ground source heat pump and the air source heat pump, and the design total air volume of the frequency fan is 30,000 m^3/h. The main forms of air supply are the nozzles which are installed at two different heights, 5.5 and 8.2 m, 8 nozzles of each height, and air return on the east wall.

28.2.2 The Experiment of the Nozzle's Jet Track

28.2.2.1 The Test Condition

The experiment of the nozzle's jet track was undertaken without indoor heat source and the indoor thermal environment was stable as the air-conditioning system runs from 9:00 to 17:00. The air's velocity of nozzle's jet was measured by Vientiane anemometer and hot-wire anemometer. Table 28.1 demonstrated the tested cases of the 5.5-m-high nozzle.

28.2.2.2 The Measured Points and Testing Method

The Abramovich's calculative system was selected to calculate the theoretical jet track through analysis, as follows:

$$\frac{Y}{D_0} = k\left[\frac{X}{D_0}\tan\alpha + A_r\left(\frac{X}{D_0\cos\alpha}\right)^2\left(0.51\frac{ax}{D_0\cos\alpha} + 0.35\right)\right] \qquad (28.1)$$

Table 28.1 The tested cases

Case	The temperature of air supply (°C)	The temperature of air return (°C)	The temperature difference of air supply (°C)	The velocity of air supply (m/s)	The volume of air supply (m^3/h)
Case 1	15.8	20.3	4.5	9.4	30,000
Case 2	13.8	19.4	5.6	5.1	15,000

Fig. 28.1 The velocity's measured points of the nozzle's jet track
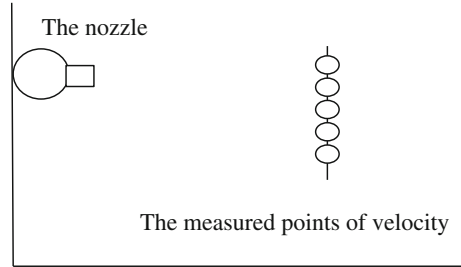
According to Abramovich's formula as shown in Eq. 28.2 about the velocity distribution in the cross section of the nozzle's jet, it is found that the air's velocity of the cross section distributes symmetrically along the axis. Thus, the velocity's measured points (Fig. 28.1) were arranged in the cross section and vertical direction of the nozzle's jet to reflect the characters of the non-isotheral jet drop. As the axis of the track is the point which has the most velocity, the nozzle's jet track is based on the vertical height of the point which has the most velocity in the cross section.

$$\frac{V_r}{V_0} = \left[1 - \left(\frac{r}{R}\right)^{1.5}\right]^2 \tag{28.2}$$

28.3 The Analysis of the Experimental Results and the Characters of the Nozzle's Jet Range

28.3.1 The Experimental Results and the Correction on the Jet Track

Since this experiment does not have the same experimental conditions as the Eq. 28.1 demonstrating, a corrective factor k is used to correct the experimental results. When the corrective factor $k = 3.3$, the nozzle's theoretical jet track of the conditions in Table 28.1 and the jet track corrected by Eq. 28.1 has been drawn in Fig. 28.2, as well as the experimental points. The maximum difference of Case 1 between the corrective calculation results and the experimental results is 0.2 m when $X = 10$ m, the variance 0.14. And the maximum difference of case 2 is 0.37 m, when $X = 7.5$ m, the variance 0.17. Thus, the corrective equation can be applied to calculate the nozzle's jet track of this large-space building.
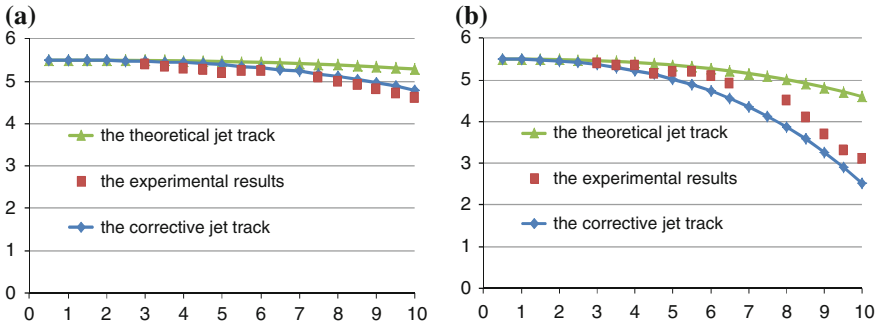
Fig. 28.2 The comparison between the experimental results of the nozzle's jet track and the calculation of the corrective equation and Eq. 28.1. **a** Case 1. **b** Case 2

28.3.2 The Analysis of the Nozzle's Range in the Large-Space and Large-Span Building

When the end of the nozzle's jet track reaches to the air-conditioned zone which is 2 m high, the nozzle's jet range is defined as the horizontal distance from the nozzle to the end of the jet track. This engineering center's span is 23 m from the nozzle along the direction of the nozzle's jet. The nozzle's jet tracks are demonstrated on the conditions of the different heights of the nozzles and different fan volumes. It can be found that: (1) the nozzle's jet range would be more if the fan's volume increases on the same conditions, but the jet track's downward trend slows down. (2) the air's velocity at the end of the 5.5- and 8.2-m-high nozzles' jet track in the design volume of the fan is 1.1 m/s and this might cause draft sensation. (3) the 5.5- and 8.2-m-high nozzles' jet range in the fan's design volume cannot meet the requirement of the building's span, so the air's velocity and temperature's uniform distribution could not be achieved in the form of the stratified air-conditioned system either. Above all, the secondary airflow equipment is fixed up to optimize the indoor air's thermal environment (Fig. 28.3).

28.4 The Design of the Secondary Airflow-Relay Equipment

28.4.1 The Principle of the Secondary Airflow-Relay Equipment

The secondary airflow-relay equipment is used to relay the nozzle's jet range which cannot meet the span of the large-space building. The cool or heat energy is transported to another end of the building by the fan's induction and entrainment.
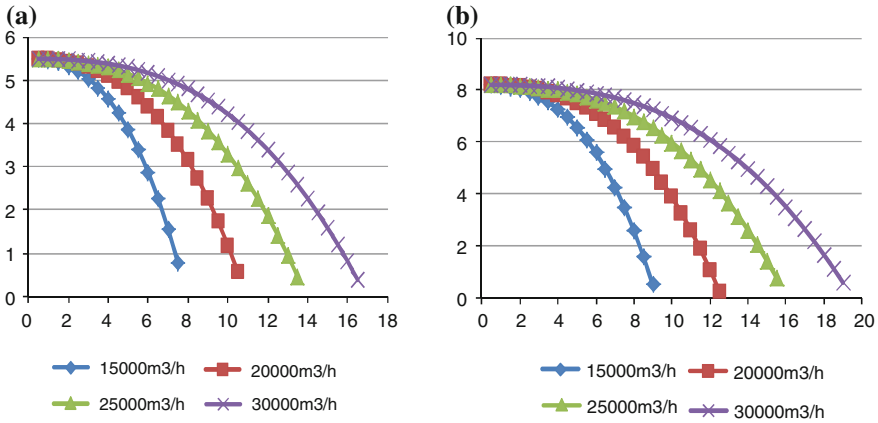
Fig. 28.3 The nozzle's jet track of different installed heights and different fan volumes. **a** 5.5-m-high nozzle. **b** 8.2-m-high nozzle

The air's velocity and temperature in the work area's distribution would be uniform. The main idea of the application of the secondary airflow-relay equipment in the underground garage is to relay the fresh air and remove the pollutant air. The application of the secondary airflow-relay equipment involved in this paper is to relay the low-temperature air of the nozzle's jet and meets the requirements of the air-conditioned zone in the large-space and large-span building.

28.4.2 The Reduction in the Air's Velocity and Temperature of the Nozzle's Jet

Vx and ΔTx of the Abramovich's calculative system at X can be determined as Eqs. 28.3 and 28.4. Thus, the reduction in the air's velocity and temperature of the nozzle's jet is gained.

$$\frac{V_x}{V_0} = \frac{0.48}{\frac{aX}{D_0} + 0.145} \tag{28.3}$$

$$\frac{\Delta T_X}{\Delta T_0} = 0.73 \frac{v_x}{v_0} \tag{28.4}$$

Table 28.2 Four different groups of the secondary airflow-relay equipment's characters

Group	V_0 (m/s)	D_0 (m)	Q_0 (m³/h)	X = 23 m, ΔTx(°C)	X = 23 m, Hx (m)	X = 23 m, Vx (m/s)
1	6.50	0.40	2,939.04	0.6	0.58	0.93
2	8.00	0.40	3,617.28	0.6	2.14	1.14
3	6.50	0.50	4,592.25	0.9	1.32	1.16
4	8.00	0.50	5,652	0.9	2.62	1.43

28.4.3 The Design of the Secondary Airflow-Relay Equipment

The parameters of the secondary airflow-relay equipment include the nozzle's diameter, the fan's volume, and the noise level. The equipment are installed on the beam at the horizontal distance of 6 m to the nozzle with $\Delta Tx = 3.5$ °C. The air supply's velocity and the nozzle's diameter of the equipment are adjusted, $0.2 \text{ m} \le D_0 \le 0.8 \text{ m}$, $V_0 \le 12$ m/s [7]. The superposition range of the nozzle's jet and the secondary airflow-relay equipment's jet is 23 m. The temperature difference of the jet track's end is $\Delta Tx \le 0.5$ °C, and the air's velocity of the jet track's end is $Vx \le 1$ m/s [6]. Thus, the air supply's velocity and the nozzle's diameter of
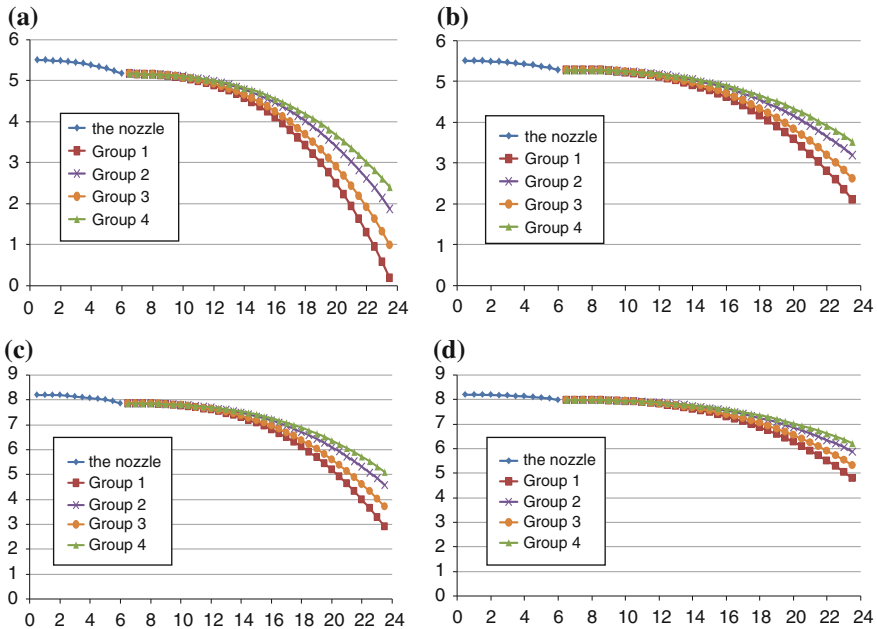
Fig. 28.4 The jet superposition of the nozzle and the secondary airflow-relay equipment. **a** 5.5-m-high nozzle and full cooling load. **b** 5.5-m-high nozzle and partial cooling load. **c** 8.2-m-high nozzle and full cooling load. **d** 8.2-m-high nozzle and partial cooling load

the equipment would meet the standard if the above targets are achieved. Four different groups of the secondary airflow-relay equipment's characters are compared to the condition of case 1 in Table 28.2.

The group 1, $V_0 = 6.5$ m/s, $D_0 = 0.4$ m, $Q_0 = 2939$ m^3/h, which has been analyzed and compared to other groups, can be used as the design parameters of the secondary airflow-relay equipment. The installed height of the secondary airflow-relay equipment will change as the alterative cooling load of this building that causes the nozzle's jet track changing at the point of the equipment's location. And every nozzle has had secondary airflow-relay equipment, which could relay the nozzle's jet range to the end of the building. The jet superposition of the nozzle and the secondary airflow-relay equipment on the condition of different cooling load and different installed height of the nozzles is shown in Fig. 28.4.

28.5 Conclusions

The theoretical jet track formula which has been corrected by the corrective factor can be applied to calculate different large-space and large-span buildings' jet track.

The secondary airflow-relay equipment can be used in the large-space buildings of which the nozzle's jet range is less than the span. And the cooling energy can be transported to the building's end to make the air's velocity and temperature of the air-conditioned zone uniform.

The design of the secondary airflow-relay equipment's parameters in the large-space building should be calculated on the basis of the inner structure of the building and compared with other parameters. The requirements of the nozzle's jet range and the air's velocity at the end of the jet track should be achieved.

The secondary airflow-relay equipment's air supply form can be confirmed by the first air supply form. The first nozzle's jet track formula can be applied to calculate the secondary airflow-relay equipment's jet track, so the equipment chooses nozzle as the air supply form.

References

1. Zhang JY (2003) The feasibility discussion on application of jet fan for smoke control in underground garage. J Saf Sci Technol 05:71–73
2. Giesen BJM, Penders SHA (2011) Modelling and simulation of a jet fan for controlled air flow in large enclosures. Environ Model Softw 26(2):191–200
3. Dai TR, Wu MZ (2005) Application of some air conditioning and ventilating technologies to Guangzhou International Conference and Exhibition Center. HV&AC 8:99–101

4. Zivov A (1993) Theory and practice of air distribution with inclined jets. ASHRAE Trans 99(1):1152–1158
5. Koestel A (1955) Paths of horizontally projected heated and chilled air jets. ASHRAE Trans 61:213–232
6. Gu XL, Han WP, Zhao JN et al (2009) Calculation method of nozzle jets in large space. HV&AC 10:128–137
7. Lu YQ (2008) Practical heat and air conditioned design manual, second version. China building industry press, Beijing, pp 1915–1921

Chapter 29
Study on an Unsteady and Synchronous Solving Model for Low Sidewall Air Supply System in the Large-Space Building

Weimin Rong, Chen Huang and Xianyan Zhang

Abstract In large-space building, the distribution of vertical temperature has obvious difference. According to this feature, the energy consumption in air-conditioning would be greatly reduced if the designs of airflow are preferable in these buildings. The low sidewall air supply system is widely installed in the large-space buildings since it can directly sent the handled air to the personnel activity area, thereby has lower energy consumption than other systems. In this paper, a Gebhart-Block synchronous solving model is built to solve the vertical temperature distribution of an actual large-space building with low sidewall air supply system. The simulative physical model is divided into eight blocks in the vertical direction. According to the mechanism of heat transfer, unsteady-state heat balance equation is established for indoor air and wall in each block. The unsteady and synchronous solving model is established with integrating these balance equations. Furthermore, to predict the temperature distribution of indoor air and inner wall surface, the theoretical values of this model are calculated with programming by Visual Basic.

W. Rong · C. Huang (✉)
School of Environment and Architecture, University of Shanghai for Science and Technology, Shanghai, China
e-mail: huangc@usst.edu.cn; hcyhyywj@163.com

X. Zhang
Textile Architecture Design Institute of Shanghai, Shanghai 200060, China

Abbreviations

$q_{d,w,I}^{p}$	Convection transfer heat from outdoor air to outside wall per area at time p, W/m^2
$q_{r,I}^{p}$	Radiation heat transfer from inside wall surface to other internal surface per area at time p, W/m^2
$q_{d,n,I}^{p}$	Convection transfer heat from the indoor air to the wall internal surface per area at time p, W/m^2
$V_{w,I}$	Wall volume of the I layer, m^3
$(\rho C)_W$	Unit heat capacity of the wall, $kJ/(m^3 \cdot K)$
$\theta_{w,pj,I}^{p}$	Average temperature of the I layer at time p, K
$A_{w,I}$	Internal surface area of the I layer, m^2
$\alpha_{h,w,I}$	Coefficient of convection heat transfer from outdoor air to the outside surface of I layer wall, $W/(m^2 \cdot K)$
T_m^{p}	Area-weighted average temperature of all the inner wall temperature at time p, K
t_{zw}^{p}	Comprehensive temperature of the outdoor air at time p, K
$\theta_{w,w,I}^{p}$	Temperature of the I layer outside wall at time p, K
ε_I	Surface radiation rate of Wall I
σ	Stefan–Boltzmann constant, $5.67 \times 10^{-8} W/(m^2 \cdot K^4)$
F_{Ij}	Radiation angle coefficient of Wall I to wall j
F_{Ic}	Radiation angle coefficient of wall I to the roof
F_{If}	Radiation angle coefficient of wall I to the floor
$\theta_{w,n,I}^{p}$	Temperature of internal face of the wall in the I layer at time p, K
$\theta_{w,n,j}^{p}$	Temperature of the j layer internal face of the wall at time p, K
$\alpha_{h,n,I}^{p}$	Coefficient of convection heat transfer of indoor air and the inner surface of I layer wall at time p, $W/(m^2 \cdot K)$
$T^{p}(I)$	Air temperature of Block(I) at time p, K
$m_{in}^{p}(I,K)$	Air mass flow from interior wall surface K into Block(I) at time p, kg/s
$m_{out}^{p}(I,K)$	Air mass flow from Block(I) into interior wall surface at time p, kg/s
$m_c^{p}(I+1)$	Air mass flow from Block($I+1$) into Block(I) at time p, kg/s
$m_c^{p}(I)$	Air mass flow from Block(I) at time p, kg/s
m_s	Air supply of Block(I), kg/s
m_h	The amount of return air of Block(I), kg/s
$T_m^{p}(I,K)$	Mean temperature of inner wall surface at time p, K
$\alpha_{h(I)}$	Coefficient of inner wall surface heat transfer, $W/(m^2 \cdot K)$
θ_{wI}^{p}	Over temperature of wall surface, K
$\alpha_w(I)$	Heat transfer coefficient from the side of the outdoor to the inner wall surface, $W/(m^2 \cdot K)$
$t_z(\tau)$	Wave function of the outdoor temperature.

29.1 Introduction

The characteristic of vertical temperature distribution is one of the main indicators to evaluate the indoor thermal environment in large-space building. For investigating this characteristic, many scholars have done notable works in theory, for example, vertical multi-zone model was proposed by a Japanese scholar, K. Miura. The main idea of this model is area heat and mass balance theory. The space was divided into several zones in the vertical direction. Heat and mass balance equations were established in each zone. These theoretical calculated values were good agreement with the experimental data [1]. According to the difference of indoor air flow and heat transfer characteristics in large-space building, C. Huang divided the space into isothermal air-conditioning area, convection main area, and top heat retention area in the vertical direction. Differential equations were established in different areas to solve air and interior wall vertical temperatures [2]. Y. G. Li combined the multi-node model and experiment to research the vertical temperature distribution of a displacement ventilation room and found that indoor air vertical temperature distributions were heavily influenced by the wall heat conduction and the radiation heat transfer between the interior surfaces. He proposed a method that using node model to predict the indoor air vertical temperature distribution [3]. X. Wang referenced the thought of Block model and took the complicated indoor airflow organization under composite ventilation as the result of joint action of five strands of airflow. She established the compound ventilation model to predict vertical distribution of indoor air temperature under composite ventilation of large-space building [4]. Basing on the Block model, Y. Song proposed a Gebhart-Block model and used the Gebhart model and the Block error correction model to research the indoor thermal environment under the natural ventilation in the large-space building [5]. Considering the mutual coupling effect of the indoor air and the wall temperature, N. Cai established a kind of steady and synchronous mathematical model of indoor air temperature and wall temperature. The theoretical calculated values were perfectly agreement with the experimental data [6]. On the basis of the steady and synchronous solving model, an unsteady and synchronous solving model (USSM) under low sidewall air supply system is studied. The storage and release heat of indoor air and cycle changes of outdoor comprehensive temperature are considered in the model. This study provides a basis for describing the indoor thermal environment under stratified air-conditioning in large-space building and calculating the unstable air-conditioning load subsequently.

29.2 Unsteady and Synchronous Solving Model with Low Sidewall Air Supply System

29.2.1 Main Idea of the Model

The USSM is based on steady and synchronous solving model. Storage characteristic of the mainstream air and periodic variation of the outdoor temperature are considered in the model (Fig. 29.1). Unsteady air and wall heat balance equations are established. Wall heat transfer coefficient, thermoelectric heat transfer coefficient, and other coefficients are also introduced. A certain period of the outdoor temperature is fitted using the least squares method. Single value in the steady and synchronous model is replaced by fitting formula. Then, multiple linear equations of layers of wall and air temperature at every moment are established.
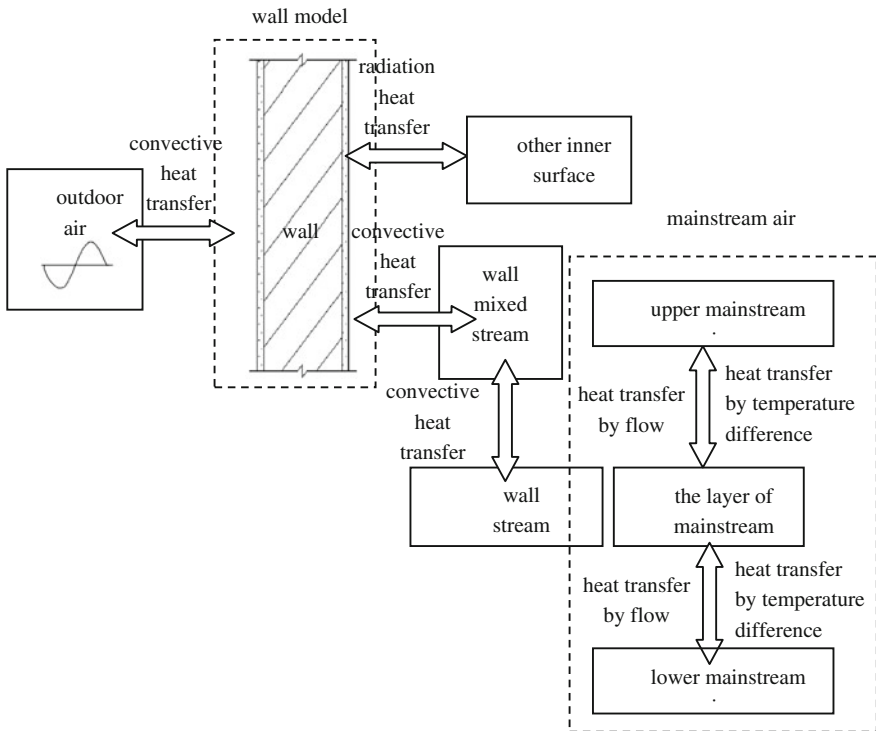
Fig. 29.1 Flow chart of the unsteady and synchronous solving model

Fig. 29.2 The diagram for wall heat transfer model
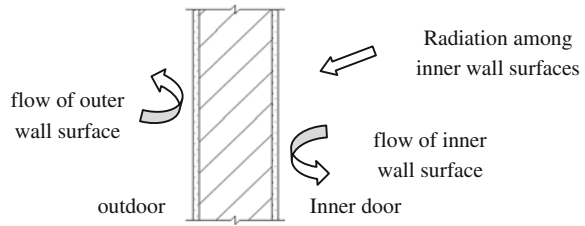
29.2.2 Model Established

29.2.2.1 Wall Model

Convection heat transfers from the outside surface of the wall to outdoor air. Simultaneously, convection heat transfers from the inner surface to indoor air. Among inner surfaces, reciprocal radiation heat transfer exists (Fig. 29.2).

The unsteady heat balance equation of the first layer wall column at time p is

$$q_{d,w,I}^p + q_{r,I}^p + q_{d,n,I}^p = V_{w,I}(\rho c)_w \frac{\theta_{w,pj,I}^p - \theta_{w,pj,I}^{p-1}}{3.6 \times \Delta\tau \times A_{w,I}} \tag{29.1}$$

The convection heat transfer from outdoor air to the outside wall surface at time p is

$$q_{d,w,I}^p = \alpha_{h,w,I}\left(t_{zw}^p - \theta_{w,w,I}^p\right) \tag{29.2}$$

The radiation heat transfer between the internal wall surface and other internal surface j at time p is

$$q_{r,I}^p = -4\left(T_m^p\right)^3 \cdot \varepsilon_I \cdot \sigma \left(\sum_{j=1}^N F_{Ij} + F_{Ic} + F_{If}\right)\left(\theta_{w,n,I}^p - \theta_{w,n,j}^p\right) \tag{29.3}$$

The quantity of heat convection from the internal face to the wall and indoor air at time p is

$$q_{d,n,I}^p = \alpha_{h,n,I}^p\left(T^p(I) - \theta_{w,n,I}^p\right) \tag{29.4}$$

The above formulas (29.2)–(29.4) are substituted into the wall unsteady heat balance equation of I layer at time p is

$$\begin{aligned}
&\alpha_{h,w,I}\left(t_{zw}^p - \theta_{w,w,I}^p\right) 4\left(T_m^p\right)^3 \varepsilon_I \sigma \left(\sum_{j=1}^N F_{Ij} + F_{Ic} + F_{If}\right)\left(\theta_{w,n,I}^p - \theta_{w,n,j}^p\right) \\
&\quad + \alpha_{h,n,I}\left[T^p(I) - \theta_{w,n,I}^p\right] = V_{w,I}(\rho c)_w \frac{\theta_{w,pj,I}^p - \theta_{w,pj,I}^{p-1}}{3.6 \times \Delta\tau \times A_{w,I}}
\end{aligned} \tag{29.5}$$

29.2.2.2 Near-Wall Stream Model

Influenced by outdoor environmental conditions, the inner surface temperature of wall is lower or higher than the indoor air temperature. Thus, a downward or upward direction of airflow near the wall would be formed (Fig. 29.3). A stream flows out from Block (I). Its temperature and mass are $T_d(I,K)$ and $m_{out}(I,K)$, respectively. It mixed with the upward stream (the temperature and mass are $T_m(I-1,K)$ and $m_{md}(I-1,K)$, respectively). The temperature and mass of the mixed stream are $T_m(I,K)$ and $m_m(I,K)$, respectively. If $T_m(I,K)$ is smaller than the temperature of mainstream air in the same layer, then the mixed stream will flow into the mainstream air absolutely. If $T_m(I,K)$ is higher than the temperature of the same layer mainstream air and is smaller than the temperature of the next mainstream air, some of the mixed stream will flow into the mainstream air in the same layer, the other will flow into the next layer and take part in the next mixing and distribution. If $T_m(I,K)$ is higher than the temperature of the next mainstream air, the mixed stream will flow into the next layer absolutely.

Mass and temperature solving equations of wall surface mixed stream are as formulas (29.6) and (29.7) show

$$m_m(I,K) = m_{md}(I-1,K) + m_{out}(I,K) \tag{29.6}$$

$$T_m(I,K) = [m_{md}(I-1,K) \cdot T_m(I-1,K) + m_{out}(I,K) \cdot T_D(I,K)/m_m(I,K)] \tag{29.7}$$

29.2.2.3 Mainstream Air Model

Figure 29.4 shows the large-space building which is divided into eight layers in vertical direction. Mainstream air flow mainly includes two parts: near-wall flow region and mainstream air flow region. Because of temperature difference, the mass flows are caused between different layers (Fig. 29.5).
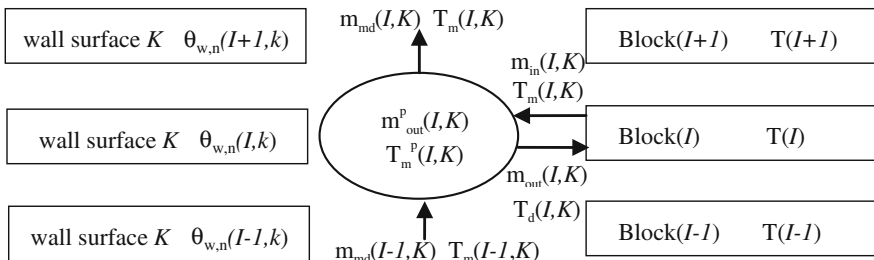
Fig. 29.3 The diagram for upward near-wall stream model

Fig. 29.4 The diagram for
physical model
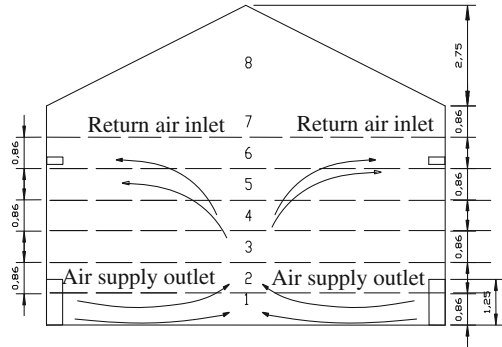
Fig. 29.5 The diagram for
mainstream air model
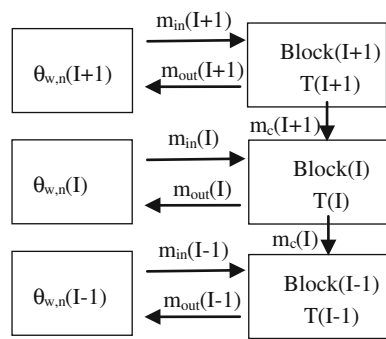
The flow of heat transmission created by the air flow between adjacent layers at time p is

$$q_m^p(I) = c_p m_c^p(I+1)[T^p(I+1) - T^p(I)] - c_p m_c^p(I)[T^p(I) - T^p(I-1)] \quad (29.8)$$

Heat transfer because of temperature difference between the adjacent layers is

$$q_c^p(I) = C_B(I)A_B(I)[T^p(I+1) - T^p(I)] - C_B(I-1)A_B(I-1)[T^p(I) - T^p(I-1)] \quad (29.9)$$

According to the above formula (29.6), formula (29.7), formula (29.8), and formula (29.9), the unsteady heat balance equation of mainstream air in the I layer at time p is

$$
\begin{aligned}
\sum_{k=1}^{m} & C_p m_{in}^p(I,K)[T_M^p(I,K) - T^p(I)] + C_B(I+1)A_B(I)[T^p(I+1) - T^p(I)] \\
& + C_p m_c^p(I+1)[T^p(I+1) - T^p(I)] + C_B(I)A_B(I)[T^p(I-1) - T^p(I)] \\
& + C_p m_c^p(I)[T^p(I) - T^p(I-1)] + C_p m_s[T_s - T^p(I)] + C_p m_h[T^p(I) - T_h] \\
& = \rho_I V_I C_p \frac{\partial T(I)}{\partial \tau} \\
& = \rho_I V_I C_p \frac{T^p(I) - T^{p-1}(I)}{\Delta \tau}
\end{aligned}
$$

$$(29.10)$$
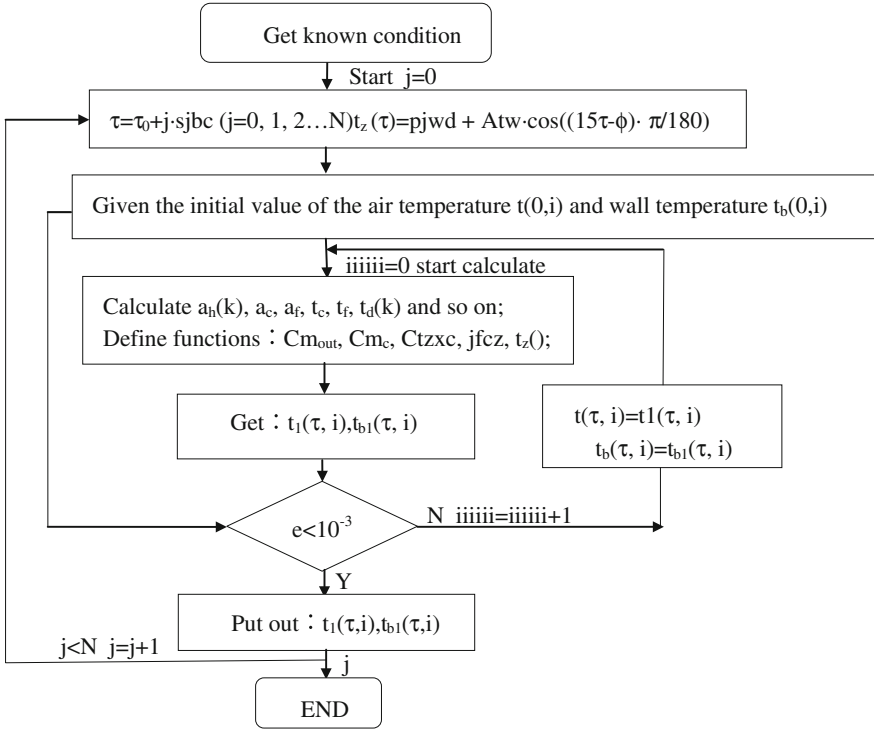
Fig. 29.6 The diagram for the process of calculation

Unsteady heat balance equation of air and wall in different block at time p is established by using the mainstream air model and wall radiation model, then 2N linear equations about θ_{wI}^p and $T^p(I)$ are obtained at the same time. The 2N linear equations are sorted into matrix form such as formula (29.11).

$$
\begin{pmatrix}
A_{11} & A_{12} & \cdots & A_{1N} & B_{11} & B_{12} & \cdots & B_{1N} \\
A_{21} & A_{22} & \cdots & A_{2N} & B_{21} & B_{22} & \cdots & B_{2N} \\
& & \vdots & & & & \vdots & \\
A_{N1} & A_{N2} & \cdots & A_{NN} & B_{N1} & B_{N2} & \cdots & B_{NN} \\
\alpha_h(1) & 0 & \cdots & 0 & C_{11} & C_{12} & \cdots & C_{1N} \\
0 & \alpha_h(2) & \cdots & 0 & C_{21} & C_{22} & \cdots & C_{2N} \\
& & \vdots & & & & \vdots & \\
0 & & \cdots & 0 & \alpha_h(N) & C_{N1} & C_{N2} & \cdots & C_{NN}
\end{pmatrix}
\begin{pmatrix}
T^p(1) \\
T^p(2) \\
\vdots \\
T^p(N) \\
\theta_{w1}^p \\
\theta_{w2}^p \\
\vdots \\
\theta_{wN}^p
\end{pmatrix}
=
\begin{pmatrix}
D_1 \\
D_2 \\
\vdots \\
D_N \\
E_1 \\
E_2 \\
\vdots \\
E_N
\end{pmatrix}
$$

$$(29.11)$$

29.3 Process of Calculation

Figure 29.6 is the whole calculation process of the USSM, which can be calculated through the programming of Visual Basic. Calculated process mainly includes two iterative cycles: (1) calculating the air and wall temperature values until the results meet the error precision requirements; (2) the time cycle of temperature calculation goes into the next time. At the end of the cycle, we can get the temperature distribution of the air and wall at any time.

References

1. Togari S, Arai Y, Miura K (1993) A simplified model for predicting vertical temperature distribution in a large space. ASHRAE Trans 99(1):84–90
2. Huang C, Li ML (1999) Study of vertical temperature distribution in a large space building. Doctoral thesis. University of Shanghai for Science and Technology, Shanghai
3. Li YG, Sandberg M, Fuchs L (1992) Vertical temperature profiles in rooms ventilated by displacement: full-scall measurement and nodal modelling. Indoor Air 2:225–243
4. Wang X (2008) Study of motion mechanism and theoretical models of complex ventilation in large space building. Doctoral thesis, University of Shanghai for Science and Technology, Shanghai
5. Song Y, Huang C, Wang X (2008) Application of the Gebhart-Block model for predicting vertical temperature distribution in a large space building with natural ventilation. HV&AC 38(12):22–25
6. Cai N, Huang C, Cao WV (2001) Study on a synchronous solving model for stratified air conditioning under low sidewall air supply system in a large space building. J Refrig 32(3):42–47

Chapter 30
Experimental Research on Thermal Performance of Lightweight Envelope Integrated with Phase Change Material

Jun Wang, Long Xu and Enshen Long

Abstract Present relief camp built with lightweight envelope has obvious cold-house effect and poor indoor thermal environment. Advantage of phase change material provides one possible way to improve thermal performance of lightweight envelope. This study analyzed the thermal performance of lightweight envelope with and without PCM and presented their difference by establishing one experimental system, including one special model with PCM and one ordinary model without PCM. The results show that the lightweight envelope integrated with PCM has better thermal performance and thermal inertia than those of lightweight envelope without PCM. Meanwhile, PCM applied in lightweight envelope can make indoor air temperature fluctuation be weak. This study provides some guides for structure design and optimization of relief camp, in order to acquiring favorable indoor thermal environment.

Keywords Lightweight envelope · Phase change material · Thermal performance

30.1 Introduction

Relief camp, e.g., prefab house, is usually built with lightweight envelope, the thickness of which is 50–75 mm. Owing to thin wall and roof, indoor thermal environment of the relief camp is very poor in most cases [1]. Some surveys show

J. Wang (✉) · L. Xu · E. Long
College of Architecture and Environment, Sichuan University, Chengdu 610065, China
e-mail: wangjunhvac@163.com

L. Xu
e-mail: 767328898@qq.com

E. Long
e-mail: Longes2@163.com

that indoor air temperature of prefab house is less than 18 °C and its lowest value reaches to 13 °C in daytime of winter. For night of winter, it may be less than 10 °C and below the outdoor air temperature [2, 3]. Therefore, cold-house effect exists in the prefab house, as a result of poor thermal insulation property of lightweight envelope. In order to improve its thermal performance, the lightweight envelope integrated with phase change material (PCM) [4–6] may be one possible method. This study analyzes the thermal performance of lightweight envelope with and without PCM based on experiment and provides the difference between them.

30.2 Experimental System

The experimental system used in this study is established in college of architecture and environment, Sichuan University, including one special model with PCM and one ordinary model without PCM, shown in Fig. 30.1. They have length of 1,000 mm, width of 800 mm, and height of 1,300 mm. The special model has lightweight envelope of two-layer color sheet (2 mm), one-layer polystyrene foam board (40 mm), one-layer PCM (23 mm) with phase-transition temperature 18–26 °C and one-layer plasterboard (8 mm). The structure of lightweight envelope applied in the ordinary model does not have the layer of PCM, but its other layers are the same with those of the special model.
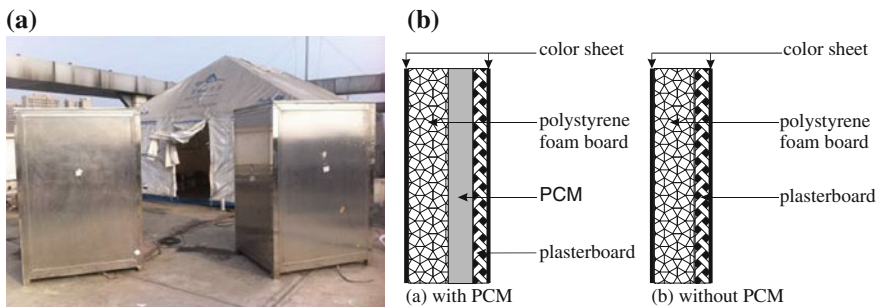
Fig. 30.1 Experimental system, **a** Model for experiment, **b** Lightweight envelope structure

Table 30.1 Physical properties of each layer material

	Density kg/m^3	Specific heat capacity J/kg.K	Thermal conductivity W/(m.K)
Color sheet	7,966	470	13.31
Polystyrene foam board	20	1,330	0.037
PCM	1,300	1,785	0.25 (phase change), 0.5
Plasterboard	580	870	0.18

For another hand, the physical properties of each layer material are given in Table 30.1.

The test parameters in this experiment include outdoor and indoor air temperature of the two models, internal surface temperature of lightweight envelope. The time for this experiment proceeding is from Nov 2 to Nov 13, 2013, totally 11 days.

30.3 Results and Discussion

According to the experiment results, variations of outdoor air temperature and indoor air temperature with time are shown in Fig. 30.2. When outdoor air fluctuates in the range of 7.7–20.1 °C, it can be found that indoor air temperature of the ordinary model varies in the range of 6.9–31.8 °C and that of the special model rises and falls in the range of 9.4–23.3 °C. Therefore, ups and downs of outdoor air temperature may induce obvious fluctuation of indoor air temperature for the ordinary model, owing to weak thermal inertia of its lightweight envelope without PCM. Meanwhile, PCM applied in lightweight envelope can reduce indoor air temperature fluctuation and strengthen its thermal inertia.

Figures 30.3, 30.4, 30.5, 30.6, and 30.7 present variation of outdoor air temperature, internal surface temperature of east wall, south wall, west wall, and north wall and roof with time, respectively.

As to the peak point, it can be seen that internal surface temperatures of lightweight envelope integrated with PCM are 30.1, 28.5, 30.1, 28.8, and 25.1 % lower than those of lightweight envelope without PCM for east wall, south wall, west wall, north wall, and roof, respectively. Furthermore, for the valley point, the internal surface temperatures of lightweight envelope integrated with PCM are 42.0, 42.6, 40.0, 42.6, and 34.4 % higher than those of the lightweight envelope without PCM at east wall, south wall, west wall, north wall, and roof,
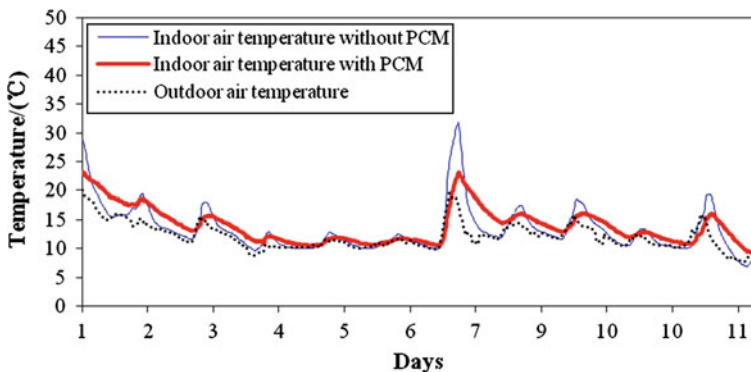
Fig. 30.2   Variations of outdoor air temperature and indoor air temperature with time
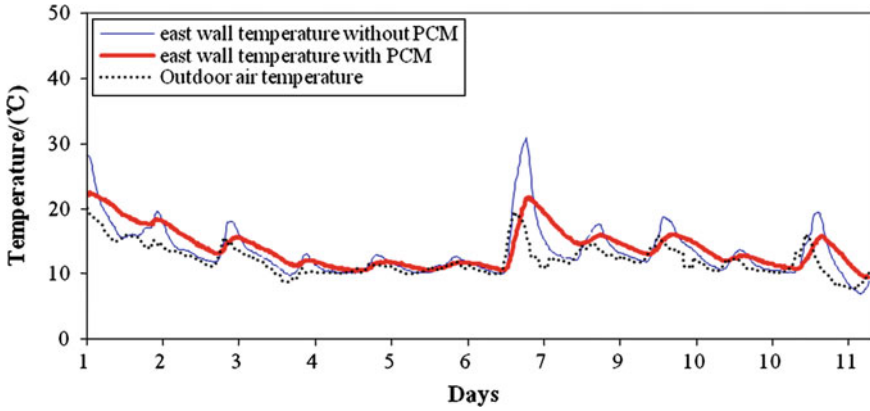
Fig. 30.3 Variation of outdoor air temperature and east wall temperature with time
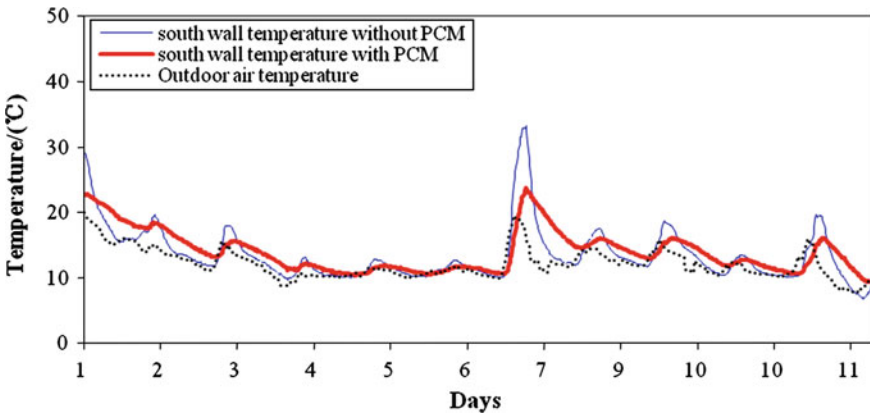
Fig. 30.4 Variation of outdoor air temperature and south wall temperature with time
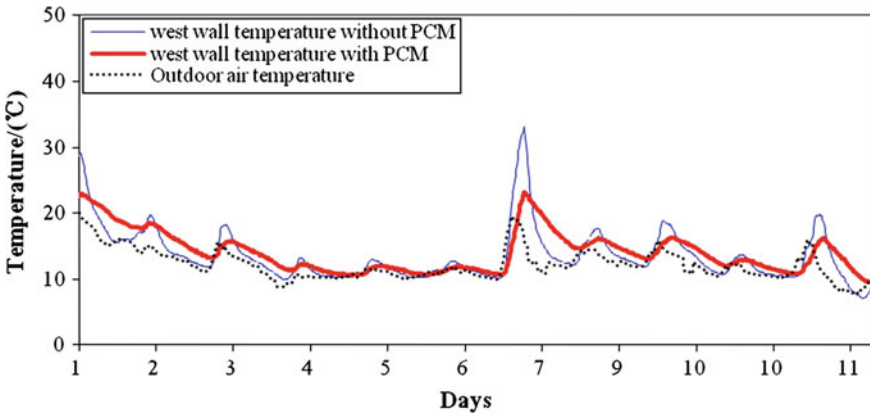
Fig. 30.5 Variation of outdoor air temperature and west wall temperature with time
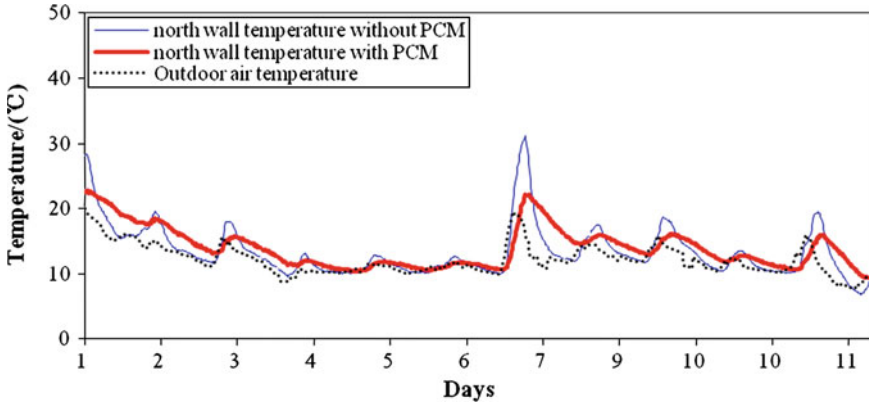
Fig. 30.6 Variation of outdoor air temperature and north wall temperature with time
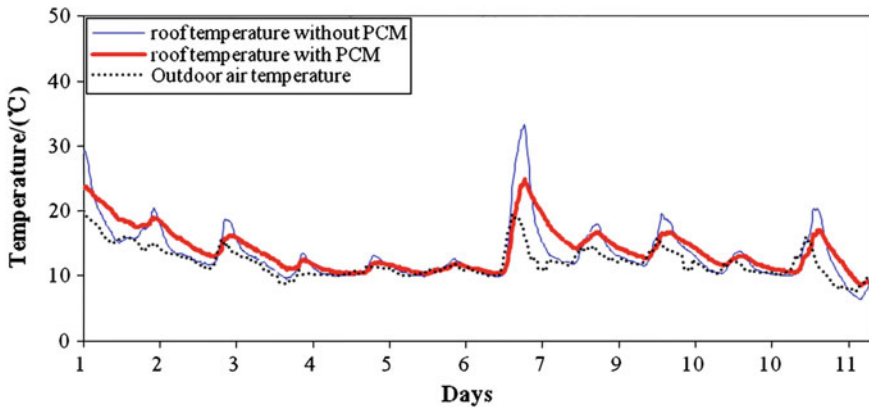
Fig. 30.7 Variation of outdoor air temperature and roof temperature with time

correspondingly. These results indicate that lightweight envelope integrated with PCM behaves better thermal performance than that of lightweight envelope without PCM, which can weak the influence of outdoor air temperature fluctuation obviously.

On the other hand, the PCM applied in lightweight envelope can make the emergence of internal surface temperature peak point be delayed, compared the time of lightweight envelope without PCM internal surface temperature peak point appearing. The reason for this phenomenon is that the envelope integrated with PCM has better thermal inertia.

30.4 Conclusions

Thermal performances of lightweight envelope integrated with and without PCM were analyzed with experiment, and their difference was obtained in this study. PCM applied in lightweight envelope can improve its thermal performance and strengthen the thermal inertia. Meanwhile, indoor air temperature fluctuation becomes weak, as a result of lightweight envelope integrated with PCM. These findings in this present study provide some meaningful guidance for structure design and optimization of relief camp.

References

1. Liang ZT, Zhang XY (2009) Computation of thermal environment of light weight steel temporary house under natural ventilation condition. New Build Mater 9:44–48
2. Chen HQ, Long ES, Huang LH, Wang T (2011) Discussion of the indoor thermal environment of prefab house in winter of Chengdu. Refrig Air Conditioning 25(1):60–64
3. Chen HQ (2011) Research on indoor thermal and humidity environment and simulation of improvement measures for prefab houses. Chongqing University, Chongqing
4. Baetens R, Jelle BP, Gustavsen A (2010) Phase change materials for building applications: a state-of-the-art review. Energ Buildings 42:1361–1368
5. Frédéric K, Damien D, Kevyn J, Jean-Jacques R (2011) A review on phase change material integrated in building walls. Renew Sust Enery Rev 15:379–391
6. Dutil Y, Rousse DR, Salah NB, Lassue S, Zalewski L (2011) A review on phase-change materials: mathematical modeling and simulations. Renew Sust Energ Rev 15:112–130

Chapter 31
Field Study on PM1 Air Pollution in a Residential Underground Parking Lot

Yu Zhao and Jianing Zhao

Abstract PM1 (fine particles with a diameter smaller than 1 μm) number concentrations are more straightforward compared with particle mass concentrations for air quality assessment in underground parking lots. PM1 number concentrations, hourly vehicle passages, real-time temperature, relative humidity, and real-time velocity in the entrance and exit cross sections were measured over the course of one week in May at a residential underground parking lot in Harbin. The daily peak and total number of vehicle passages are much less than those in a commercial underground parking lot. PM1 concentrations were found to be higher in the morning and evening and lower at both weekends and nonpeak traffic times, such as outside of rush hour. During weekdays, the peak-to-trough deviation and daily average value of PM1 concentrations were, respectively, 1.4 and 1.5 times higher than the concentrations during weekends. The vehicle passages per hour and the velocity and temperature per hour in the entrance and exit cross sections had the greatest impact on the PM1 concentration. These findings indicate that PM1 pollution in residential underground parking lots can reach serious levels.

Keywords Residential underground parking lot · Particulate matter · Number concentrations · Field study

Y. Zhao · J. Zhao (✉)
School of Municipal and Environmental Engineering, Harbin Institute of Technology, Harbin, China
e-mail: zhaojn@hit.edu.cn

Y. Zhao
e-mail: zy19870104@163.com

31.1 Introduction

The number of vehicles has increased rapidly in the last decade in China. To accommodate this trend, most new buildings are equipped with parking lots, and the majority of these are underground due to limitations of ground space. This underground microenvironment is potentially a hazard zone for human health because of its semi-enclosed structure and the high number of vehicle passages. Motor vehicle emissions constitute the main source of air pollutants in underground parking lots. A major constituent of vehicle emissions is fine and ultrafine particulate matter [1–4]. Several studies have focused on the relationship between human health and traffic-related particulate matter. Klot et al. reported asthma medication use and symptoms increase in association with particulate air pollution [5]. Similar conclusions have been found in some other researches [6–8]. An association was also found between exposure to traffic and the onset of chronic diseases such as myocardial infarction and lung cancer [9–11]. In these studies, traffic volume and particle concentration are considered as indicators of mortality. As car traffic and air pollution levels have undergone large increases in China because of rapid spread of urbanization [12], mortality from respiratory and cardiovascular diseases is anticipated to also increase due to traffic-related particle pollutants. For this reason, research into traffic-related pollution control should be of major importance.

Studies on air pollution in underground parking lots have thus far been very limited. CO has been used as an indicator of air pollution levels in parking lots at the early stage of research [13, 14]. There are few published reports describing particle pollution levels in underground parking lots. Sung et al. measured concentrations of vehicle-related air pollutants in an urban parking lot [15]. The results showed that particle-bound polycyclic aromatic hydrocarbons exhibited the highest (1.08 %) increase in vehicle count pollutant coefficients among the pollutants found in the lot. Chen and Jiang investigated exhaust gas pollution in an underground parking lot in Shanghai, China, and found that the biggest exceeding criterion multiple of lead is equal to 4.64 times of China national limit of daily safe exposure per adult [16]. Due to the severe health hazards posed by particulate matter pollution and growing traffic intensity in underground spaces, research on particulate matter pollution in underground parking lots warrants greater attention.

In the present study, we employed a condensation particle counter and a multi-function measuring instrument in order to evaluate PM1 concentrations along with wind velocity, temperature, and the relative humidity per hour of both entrance and exit cross sections in the parking lot. Hourly vehicle passages were also counted and compared with the variation of PM1 concentrations by the author.

31.2 Methodology

This study provides a single case study of PM1 concentrations in a residential underground parking lot in Harbin. The residential underground parking lot stands

Table 31.1 Detailed information on parking lot

Location	Length (m)	Width (m)	Height (m)	Number of parking places (entrances/exits)
Basement 1	109	36	3.5	82
Basement 2	109	36	4	102
Entrance driveway	–	2.2	2.9	(2)
Exit driveway	–	2.2	2.9	(1)

below the middle of the residential area. The parking lot covers 4,000 m^2 and is a two-story structure. Detailed information on the parking lot is given in Table 31.1.

During the measurement, both the entrance and exit were open at all times. The mechanical ventilation system in the parking lot was turned off. As a result, the parking lot only received natural ventilation. Measurements were performed between 7th May and 13th May. The test time was from 7:00 a.m.to 7:00 p.m. for weekdays and from 8:00 a.m.to 8:00 p.m. during weekends.

First, we tracked the number of vehicles passing through per hour. The number of vehicles passages in the parking lot per hour was recorded by the author over the course of the study. Next, PM1 number concentrations were measured. 12 stations were set up to measure PM1 number concentrations. These were located throughout the parking lot, from entrance driveway to exit driveway. Each measuring station stood 1.5 m above the parking lot ground. The location of each station is shown in Fig. 31.1. The interval between adjacent stations in Fig. 31.1 was 5 min. The condensation particle counter (TSI, Model 3007) was used in this study to measure particle number concentrations in real time. Finally, temperature, relative humidity, and real-time wind velocity in the entrance and exit cross sections were recorded. For the purpose of continuous measurement and so as not to impede vehicular traffic, one station near the top of the fire shutter door was set
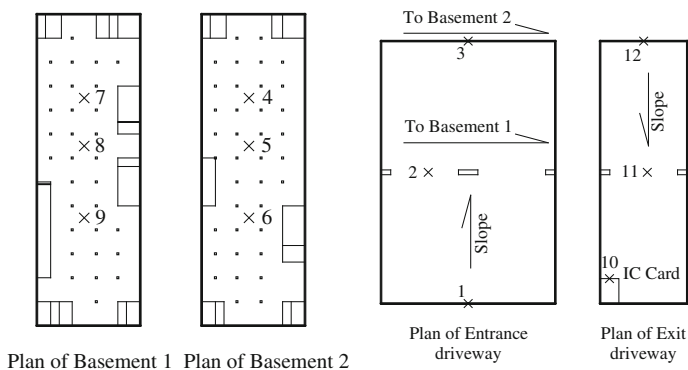
Fig. 31.1 PM1 number concentrations measurement stations in the parking lot. The *left* figure shows measurement stations in basement *1* and *2* and the *right* figure shows measurement stations in entrance/exit driveway

Fig. 31.2 Measurement station in entrance and exit cross section
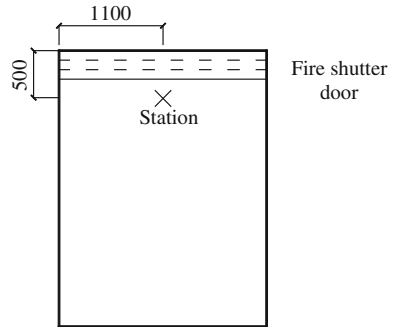
Elevation plan of Entrance and Exit

up in between the entrance and exit (Fig. 31.2). The inter-record gap of measurement station in Fig. 31.2 was 1 min. Two multifunction measuring instruments (Testo, Model 435) were used in this study to measure temperature, relative humidity, and real-time wind velocity in the entrance and exit cross sections.

31.3 Results and Discussion

Vehicle passages in the parking lot, the variation in PM1 number concentrations, and the factors influencing PM1 number concentrations are discussed in the following subsections.

31.3.1 Vehicle Passages in the Residential Uunderground Parking Lot

Vehicle passages in the parking lot showed a regular U-shaped diurnal variation with maxima in the morning (7–9 a.m. on weekdays and 8–10 a.m. on weekends) and evening, with minimum occurring during mid-day (12 p.m. on weekdays and 2 p.m. at the weekend) (Fig. 31.3). The peak-to-trough deviations on weekdays was 29 vehicles, which is almost 2.5 times higher than that of the weekend (12 vehicles). The regular variation coincides with the regular diurnal schedule of residents on weekdays and weekends.

Ding reports the hourly peak vehicle passages in a commercial underground parking lot in Shenzhen, China [17]. Figure 31.3 shows the difference between average vehicle passages per day in the residential underground parking lot and those in the commercial underground parking lot.

This comparison suggests that the variation in hourly average vehicle passages in a residential underground parking lot, with two maxima during the morning and
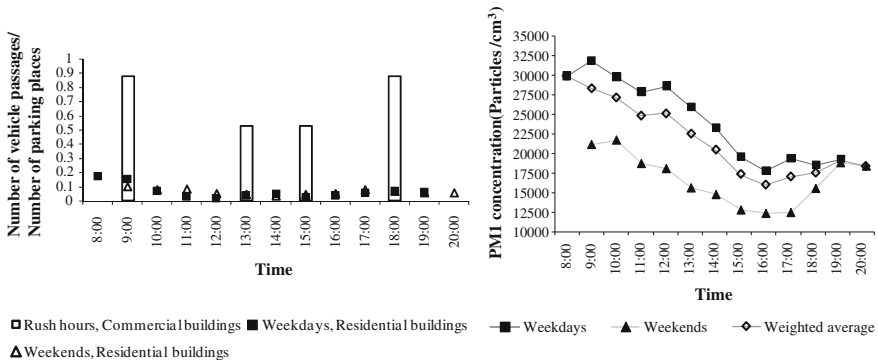
Fig. 31.3 Hourly peak vehicle passages per parking place and hourly average PM1 number concentrations on the weekdays and weekends. The *left* figure shows the comparison of hourly peak vehicle passages per parking place between this study and a commercial underground parking lot and the *right* figure shows hourly average PM1 number concentrations on the weekdays and weekends

the evening, is different from that in a commercial underground parking lot with four maxima during the day. The hourly peak vehicle passages per parking place in a commercial underground parking lot is nearly 5 times (on weekdays) and 9 times (on weekends) higher than in a residential underground parking lot. The daily average vehicle passages parking place in a commercial underground parking lot was 6.6 times higher than that in the residential underground parking lot. Both vehicle traffic intensity and number in a commercial underground parking lot is much higher than that in a residential underground parking lot.

31.3.2 PM1 Number Concentrations

The hourly average PM1 number concentrations for both weekdays and weekends are also shown in Fig. 31.3. The concentrations show a regular variation, which follows closely the pattern of vehicle passages. During weekdays, there was one maximum (7:00–10:00 a.m.) while weekends showed two maxima (8:00–10:00 a.m. and 6:00–8:00 p.m.). In contrast, PM1 number concentrations almost present a symmetric distribution with minimum at 4:00 p.m. during weekends. The hourly average concentrations in the afternoon and evening on weekdays are much lower than in the morning, and minimum appears at 4:00 p.m. During weekdays, the average concentrations and average peak-to-trough difference were 24,384 and 13,855 particles/cm^3, respectively. Somewhat lower levels and peak-to-trough deviations were found during weekends—16,897 and 9,175 particles/cm^3, respectively. The ratio of the weekdays and weekends PM1 levels and peak-to-trough deviations is 1.4 and 1.5, respectively. This finding indicates that the variation in PM1 concentrations on the weekdays is more drastic than that on the

Table 31.2 Correlation coefficients between each independent variable and dependent variable

Serial number	Independent variable	Dependent variable	Correlation coefficient
1	Vehicle passages per hour	Hourly average PM1 number concentrations	0.43
2	Hourly average velocities in the entrance and exit cross sections		−0.23
3	Hourly average temperatures in the entrance and exit cross sections		−0.36
4	Hourly average values of relative humidity in the entrance and exit cross sections		0.19

weekends. Hourly weighted average PM1 concentrations show a regular variation with maximum in the morning (8:00 a.m.) and minimum in the afternoon (4:00 p.m.).

The variation of PM1 concentrations between weekdays and weekends can be attributed to the difference of daily vehicle passages and hourly vehicle traffic intensity on weekdays and weekends. The daily average PM1 concentrations on weekdays are higher than on weekends due to higher vehicle passages during weekdays. The vehicle traffic intensity in the morning of weekdays is very high due to limits of office time. The hourly peak concentrations on weekdays appear in the morning because of the massive discharge of vehicle exhaust. The concentrations in other periods of the weekdays are not as high as the morning due to lower vehicle traffic intensity and dilution of natural ventilation. The symmetric distribution of PM1 concentrations follows closely the U-shaped variation in vehicle passages on weekends. The peak-to-trough deviations of vehicle passages on weekdays are 2.4 times higher than on weekends (Fig. 31.3), which leads to higher peak-to-trough deviations of PM1 number concentrations on weekdays.

31.3.3 Factors Influencing PM1 Number Concentrations

The correlation coefficients between each independent variable and dependent variable are given in Table 31.2.

The factor having the greatest impact on PM1 number concentration variation is the number of vehicle passages per hour and the correlation is positive with PM1 number concentration. Hourly average wind velocities and temperatures in the entrance and exit cross sections are two other predominant factors in PM1 concentration variation. This relationship is negative because as hourly average wind velocities and temperatures increase, the movement of particles is faster, which facilitates the deposition of particles. The hourly average values of relative humidity in the entrance and exit cross sections have a positive impact on PM1 concentration variation. The inexact synchronization of the relative humidity's hourly average values in the entrance and exit with those from inside the parking

lot and combined influence of vehicle passages per hour, hourly average wind velocities and hourly average temperatures in the entrance and exit cross sections on hourly average values of relative humidity may account for the positive relationship between hourly average values of relative humidity in the entrance and exit cross sections and PM1 number concentrations.

31.4 Conclusion

Vehicle passages in a representative underground residential parking lot show a regular U-shaped diurnal variation with maxima in the morning and evening and minimum during the noon. The daily average vehicle passages parking place in a commercial underground parking lot is 6.6 times higher than that in a residential underground parking lot.

The hourly average PM1 number concentrations on weekdays and weekends also show a regular variation, which closely follows the variation in vehicle passages. The ratio of the weekdays and weekends daily average levels and peak-to-trough deviations is 1.4 and 1.5, respectively.

The factor having the greatest influence on PM1 number concentration is vehicle passages per hour. The hourly average wind velocities and temperatures in the entrance and exit cross sections are two other predominant factors on PM1 concentration variation and the relationships are both negative.

References

1. Fruin SA, Winer AM, Rodes CE (2004) Black carbon concentrations in California vehicles and estimation of in-vehicle diesel exhaust particulate matter exposures. Atmos Environ 38:4123–4133
2. Canagaratna MR, Jayne JT, Ghertner DA, Herndon S, Shi Q, Jimenez JL, Silva PJ, Williams P, Lanni T, Drewnick F, Demerjian KL, Kolb CE, Worsnop DR (2004) Chase studies of particulate emissions from in-use New York City vehicles. Aerosol Sci Technol 38:555–573
3. Maricq MM, Podsiadlik DH, Chase RE (1999) Gasoline vehicle particle size distributions: comparison of steady state, FTP, and US06 measurements. Environ Sci Technol 33:2007–2015
4. Wong CP, Chan TL, Leung CW (2003) Gasoline vehicle particle size distributions: characterisation of diesel exhaust particle number and size distributions using mini-dilution tunnel and ejector–diluter measurement techniques. Atmos Environ 37:4435–4446
5. Von Klot S, Wölke G, Tuch T, Heinrich J, Dockery DW, Schwartz J, Kreyling WG, Wichmann HE, Peters A (2002) Increased asthma medication use in association with ambient fine and ultrafine particles. Eur Respir J 20:691–702
6. Pekkanen J, Timonen KL, Ruuskanen J, Reponen A, Mirme A (1997) Effects of ultrafine and fine particles in urban air on peak expiratory flow among children with asthmatic symptoms. Environ Res 74:24–33

7. Nicolai T, Carr D, Weiland SK, Duhme H, Von Ehrenstein O, Wagner C, Von Mutius E (2003) Urban traffic and pollutant exposure related to respiratory outcomes and atopy in a large sample of children. Eur Respir J 21:956–963

8. Penttinen P, Timonen KL, Tiittanen P, Mirme A, Ruuskanen J, Pekkanen J (2001) Ultrafine particles in urban air and respiratory health among adult asthmatics. Eur Respir J 17:428–435

9. Peters A, von Klot S, Heier M, Trentinaglia I, Hörmann A, Erich WH, Löwel H (2004) Exposure to traffic and the onset of myocardial infarction. New England J Med 351:1721–1730

10. Hoek G, Brunekreef B, Goldbohm S, Fischer P, van den Brandt PA (2002) Association between mortality and indicators of traffic-related air pollution in the Netherlands: a cohort study. The Lancet 360:1203–1209

11. Sunyer J, Schwartz J, Tobias A, Macfariane D, Garcia J, Antó JM (2000) Patients with chronic obstructive pulmonary disease are at increased risk of death associated with urban particle air pollution: a case-crossover analysis. Am J Epidemiol 151:50–56

12. Du X, Wu Y, Fu LX, Wang SX, Zhang SJ, Hao JM (2012) Intake fraction of $PM_{2.5}$ and NO_X from vehicle emissions in Beijing based on personal exposure data. Atmos Environ 57:233–243

13. Chaloulakou A, Duci A, Spyrellis N (2002) Exposure to carbon monoxide in enclosed multi-level parking garages in the central Athens urban area. Indoor Built Environ 11:191–201

14. Fadel MEI, Alameddine I, Kazopoulo M, Hamdan M, Nasrallah R (2001) Carbon monoxide and volatile organic compounds as indicators of indoor air quality in underground parking facilities. Indoor Built Environ 10:70–82

15. Kim SR, Dominici F, Buckley TJ (2007) Concentrations of vehicle-related air pollutants in an urban parking garage. Environ Res 107:291–299

16. Chen G, Jiang S (1999) Investigation on exhaust gas pollution of underground garage. Shanghai Environ Sci 18:374–375

17. Ding J (2009) Analysis on ventilation of an underground parking-area of commercial building. Constr Conserves Energy 37:23–26

Chapter 32
Experiment and Thermal Sensation Estimating Model at Different Active Levels Under Hypobaric Condition Based on Principal Component Analysis

Guodan Liu, Feng Qi, Songtao Hu, Angui Li, Haiying Wang, Meinan Wang and Li Tong

Abstract The factors dramatically influencing thermal comfort usually involve air temperature, radiant temperature, air humidity, air velocity, clothes insulation, and metabolic rate. However, under some special conditions, e.g., altitude environment, the air pressure should be taken into account. Exposure to altitude tends to produce deterioration in human heat diffusion performance, rate of convective heat transfer decreases, and rate of convective heat transfer increases with altitude, energy balance between human body and environment is different from in the normal conditions. In the experiments, thermal perception of 20 test persons (240 person-times) was observed by subjective questionnaire in a simulated hypobaric chamber where the air parameters were controllable. The temperature was set at 22 °C, and the barometric conditions were set at 1, 0.95, 0.9, 0.8 atm of simulated hypobaric conditions, corresponding altitude of 0, 400, 800, 2,000 m, respectively. Experiments solved the metabolic rate raised with pressure drop, and the measured PMV differed from actual thermal sensation votes in hypobaric conditions. Moreover, the falling barometric pressure leads to decline in alveolar oxygen, a variety of adaptive physiological processes for oxygen delivery, human metabolism, and thermoregulatory responses as well as thermal perception change. However, the present thermal sensation models were built in the normal environment and there were many divergences in conclusions. Combined with the experiments, this article builds the thermal sensation estimating model under the hypobaric conditions by principal component analysis. The purpose of this study was to make clear whether hypobaric exposure will affect people's thermal sensation and maybe helpful to establish the indoor thermal comfort criterion in the hypobaric environment.

G. Liu (✉) · F. Qi · S. Hu · H. Wang · M. Wang · L. Tong
Qingdao Technological University, No. 11 Fushun Road, Qingdao, China
e-mail: lguodan@163.com

A. Li (✉)
Xi'an University of Architecture and Technology, Xi'an 710000, China
e-mail: visitli@aliyun.com

32.1 Introductions

In order to evaluate the indoor thermal environments, Fanger P. O. built the PMV model in 1970s [1], which involved four environmental factors (air temperature, radiant temperature, humidity, and wind velocity) with two human body factors (intrinsic clothing insulation and metabolic rate) together.

The prediction of PMV model at the thermal environment is accurately, but under the naturally ventilate condition which deviate from the actual human body heat sensation [2]. Expressly, under the normal pressure condition, the characteristic of heat dissipation and physiology change are different from the normal pressure conditions, and there is a deviation between PMV model and the actual human thermal sensation in the hypobaric environments [3–7]. On the other side, when calculating PMV model, the metabolic rate is confirmed by checking table, but even when people are at the same activity level, the metabolic rate is different.

So we did a series of experiments at different active levels under the hypobaric environment within 0.8–1.0 atm. The thermal perception was observed by subjective questionnaire in a simulated hypobaric chamber. Then, the thermal sensation prediction models were established by the principal component analysis.

32.2 Experimental Methods

The experiments were held in decompression chamber to simulate different altitudes in the HVAC laboratory of Qingdao Technological University. The pressure of cabin was monitored and controlled by the automatic pressure control system, which could real-time change and display the cabin pressure value. Pressure control range was 0.20–1 atm, and control accuracy was ±5 kPa.

The decompression chamber was set in the room, fan coils were equipped to control the air temperature and relative humidity effectively, and the temperature control accuracy was ±0.5 °C. Layout of the chamber was shown as follows (Fig. 32.1).

The experiments were made in the summer, air temperature was set at 22 °C, and the barometric conditions were set stepwise at 1.0, 0.95, 0.9, and 0.8 atm of simulated hypobaric conditions. People were, respectively, in sitting position, running at speed of 1.5 and 3.5 m/s.

All subjects were college students who were healthy. Before experiment, we removed people who were extremely sensitive to the cold and hot after preliminary experiment. After screening, there were twenty people (twelve men and eight women) participated in the experiment and finally, four people a group;
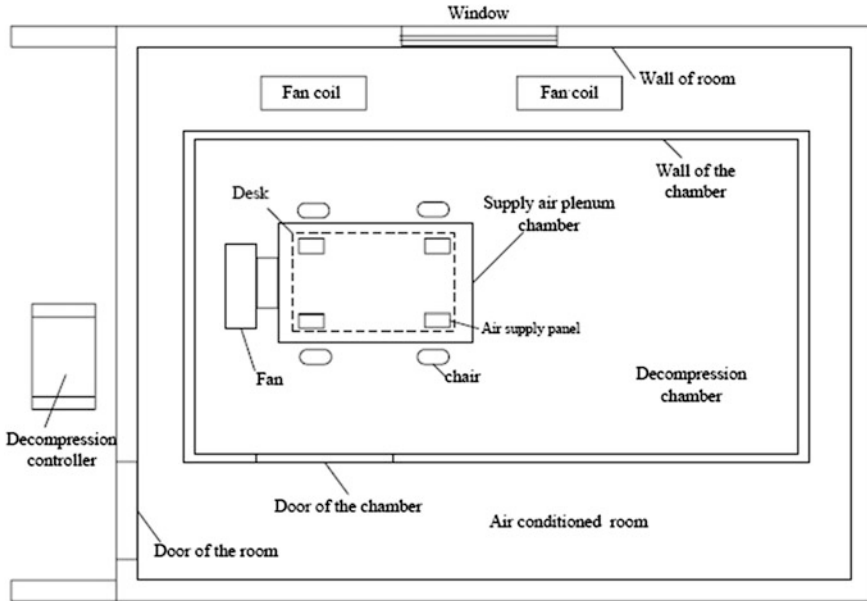
Fig. 32.1 Layout of the experiment chamber and room

experiments were total of 240 person-times. Participants worn uniform clothing; the total thermal resistance of clothing was 1.02 clo when participants seat quietly; 0.92 clo when participants were running at speed of 1.5 m/s; 0.81 clo when participants were running with speed 3.5 m/s [8, 9]. During the period of the experiment, participants did normal work and rest, normal diet, not drink.

In the experiment, the participants' hot feeling, thermal comfort, and sweating feeling were surveyed by questionnaire; we measured air temperature, relative humidity, air velocity, and pressure inside and outside of chamber; and we measured the subjects' metabolic rate, skin temperature, blood pressure, and heart rate.

The experiment lasted 3 h, and each pressure condition was maintained about 50 min and filled out two questionnaires at each condition. At the same time, we measured the environmental parameters and physiological parameters. When the experiment finished, the experimental personnel checked the questionnaire, and the participants left.

32.3 The Experimental Results and Analysis

32.3.1 The Metabolic Rate of Different Activity Level

We measured metabolic rate by the Vmax Encore System during experiments, shown in Fig. 32.2.
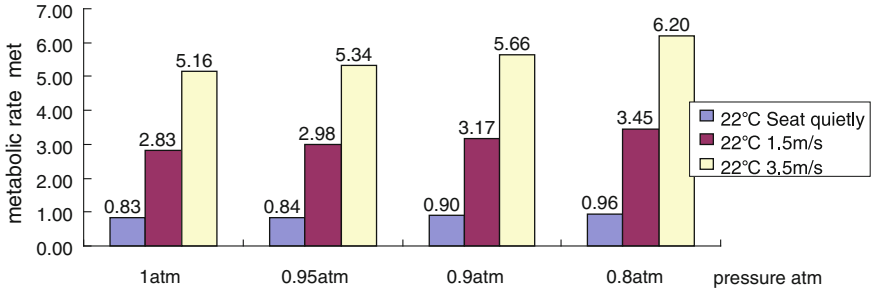
Fig. 32.2 The metabolic rate of different activity level

From Fig. 32.2, at the same activity level, the metabolic rate rises with pressure drop, which is same to the experiments' conclusions of Haiying [4] and Liu [10]: the human metabolic rate under hypobaric condition is higher than under the normal pressure condition at the same activity level. This indicates that the change of pressure may have affect on the consumption of human energy, which should be confirmed and analyzed by physiology.

The average value of metabolism at the above three kinds of activity level were 0.88 met, 3.11 met, 5.59 met, respectively. Because 2–5 met is within the scope of the metabolic activity belong to medium activity level [4], so the three kinds of activity levels, respectively, belong to sitting, moderate, and severe activities.

32.3.2 The Contrast of MTS and PMV

According to the calculation method of PMV in ASHRAE Handbook 2005 [11], and combining with the experiment data, we can obtain the curve of measured thermal sensation (MTS) and PMV changes with the pressure, shown in Fig. 32.3.
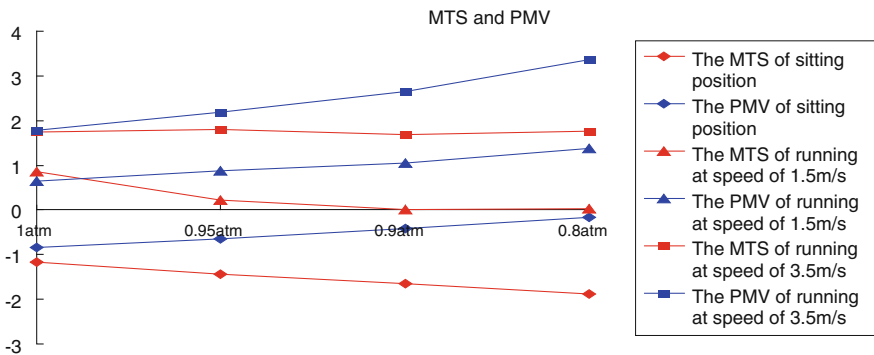
Fig. 32.3 The curve of the measured thermal sensation *MTS* and the *PMV*

We can see from the above figure that PMV perception value and the measured average thermal sensation value have deviation. At the same activity level, MTS votes decrease with pressure drop, but the prediction results of PMV reverse, so both tendencies are different.

While the pressure reduces from 1.0 to 0.8 atm, people at sitting position, the MTS vote reduces by 0.71 scale and the PMV value increases by 0.68 scale; when people run at the speed of 1.5 m/s, MTS reduces by 0.84 scale and PMV value increases by 0.74 scale; At the speed of 3.5 m/s, the MTS vote reduces by 0.015 scale and the PMV value increases by 1.58 scale. The reason is that human metabolic and human body heat dissipation changes follow with pressure drop, it is necessary to study the thermal sensation prediction models under hypobaric condition.

32.4 The Establishment of Thermal Sensation Model

32.4.1 The Principle of Principal Component Analysis

Principal component analysis is a kind of statistical analysis method that turn the original multiple variable into a few comprehensive index. From the mathematical view, this is a kind of dimension reduction processing technology [3].

Principle: Suppose there are n samples, each sample has p a variable, constitute a $n \times p$ order data matrix.

$$X = \begin{bmatrix} x_{11} & x_{12} & \cdots & x_{1p} \\ x_{21} & x_{22} & \cdots & x_{2p} \\ \vdots & \vdots & & \vdots \\ x_{n1} & x_{n2} & \cdots & x_{np} \end{bmatrix} \tag{32.1}$$

The original variable indicators for x_1, $x_2...x_p$, they dimension reduction process after the comprehensive index, namely the new variable for z_1, $z_2...z_m$ (m or less p), then

$$\begin{cases} z_1 = l_{11}x_1 + l_{12}x_2 + \cdots + l_{1p}x_p \\ z_2 = l_{21}x_1 + l_{22}x_2 + \cdots + l_{2p}x_p \\ \quad\quad\cdots\cdots\cdots\cdots \\ z_m = l_{m1}x_1 + l_{m2}x_2 + \cdots + l_{mp}x_p \end{cases} \tag{32.2}$$

The principle to determine the coefficient of l_{ij}:

1. z_i and z_j ($i \neq j$; $i, j = 1, 2 ...m$) is independent to each other.
2. z_1 is the biggest variance of all the linear combination of x_1, $x_2...x_P$; z_2 is the biggest variance of all the linear combination of z_1 irrelevant to x_1, $x_2... x_P$; z_m

is the biggest variance of all the linear combination of $z_1, z_2...z_{m-1}$ irrelevant to $x_1, x_2...x_P$.

The new variable index $z_1, z_2...z_m$ are, respectively, called the original variable index $x_1, x_2... x_P$'s the first, second...principal components.

From the above analysis, we can see that the essence of the principal component analysis is to make sure that the original variable x_j ($j = 1, 2... p$) in the principal component z_i ($I = 1, 2... m$) load l_{ij} ($I = 1, 2...m; j = 1, 2... p$).

32.4.2 The Establishment of the Thermal Sensation Model by Principal Component Analysis

Wang Haiying has built the thermal sensation prediction models (TSV models) under the normal pressure condition at moderate activity level by principal component analysis [4]. But when we study the thermal sensation under hypobaric condition, the models of TSV has a big deviation from MTS. This is mainly because the human metabolic rate, the body dissipation, and the change of physiology under hypobaric condition are different under the normal condition. It is necessary to establish the thermal sensation prediction model by principal component analysis under hypobaric condition.

Atmospheric pressure influences average skin temperature $T_{sk}(°C)$, metabolic rate M(met), sweating feeling SFI, and skin moisture W_{sk}, so we select T_{sk}, M, SFI, and W_{sk} as main elements. Table 32.1 shows the correlation coefficient matrix after standardizing of data treatment.

According to the Tables 32.2 and 32.3, whose total value is greater than 1.0 or the cumulative is greater than 85 %, the element is selected as the principal components, with the expression of the element 1, 2 as follows:

$$Z_1 = 0.603515^*T_{sk} + 0.955621^*W_{sk} + 0.986007^*M + 0.974961^*SFI \quad (33.3)$$

$$Z_2 = 0.797164^*T_{sk} - 0.28129^*W_{sk} - 0.10666^*M - 0.19304^*SFI \quad (33.4)$$

The comprehensive principal component is written as

$$Z = 0.639806^*T_{sk} + 0.723818^*W_{sk} + 0.781237^*M + 0.771657^*SFI \quad (33.5)$$

Table 32.1 Correlation matrix

Factor	$T_{sk}(°C)$	W_{sk}	M(met)	SFI
$T_{sk}(°C)$	1.000	0.354	0.511	0.498
W_{sk}	0.354	1.000	0.977	0.949
M(met)	0.511	0.977	1.000	0.951
SFI	0.498	0.949	0.951	1.000

Table 32.2 Total variance explained

Component	Initial eigenvalues			Extraction sums of squared loadings		
	Total	Variance (%)	Cumulative (%)	Total	Variance (%)	Cumulative (%)
1	3.200	80.005	80.005	3.200	80.005	80.005
2	0.738	18.451	98.456	0.738	18.451	98.456
3	0.056	1.396	99.852			
4	0.006	0.148	100.000			

Table 32.3 Component load list

	Component			
	1	2	3	4
$T_{sk}(°C)$	0.603515	0.797164	0.012911	0.011472
W_{sk}	0.955621	−0.28129	0.067378	0.05587
M(met)	0.986007	−0.10666	0.117677	−0.05067
SFI	0.974961	−0.10988	−0.19304	−0.01062

By the linear regression, relationship of the comprehensive principal component Z and the MTS is obtained, shown in Fig. 32.4, expressed as

$$MTS = 0.6382^*Z - 14.502 (R^{\wedge}2 = 0.9664) \tag{33.6}$$

32.4.3 The Specific Expression of the Thermal Sensation Model by Principal Component Analysis

Taking the Z into the above relationship between MTS and Z, we establish the thermal model by main principal component analysis.

$$MTS = 0.408324^*T_{sk} + 0.46194^*W_{sk} + 0.49858^*M + 0.49247^*SFI - 14.502 \tag{33.7}$$
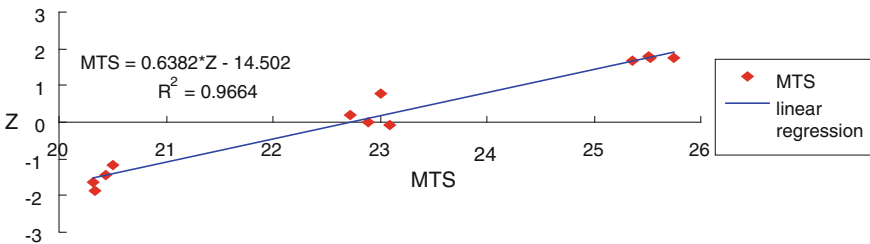
Fig. 32.4 The relationship of *MTS* and principal component Z

The correlation coefficient is 0.9664 and shows that they have well linearly dependence.

32.5 Conclusions

The studies in this article find, at the same activity level, as other environmental factors are kept constant, the metabolic rate rises with pressure drop; MTS votes decrease as atmospheric pressure drop, and hypobaric environment tends to make people feel cooler. But the prediction results of PMV reverse. So we select average skin temperature T_{sk}, metabolic rate M, sweating feeling SFI, and skin moisture W_{sk} as main elements, and by main principal component analysis, establish thermal sensation model; it can match to the people's thermal sensation. This model needs to be verified by a large number of experiments, but the physical meaning of this method is clear and feasible.

References

1. Wang H, Hu S (2009) The applicability analysis of thermal comfort model of PMV. Build Sci 25(6):108–114
2. Ouyang Q (2005) The thermal comfort analyzes under naturally ventilates condition. HV& AC 35(8)
3. Liu G (2008) Human thermal comfort research in domain of no symptoms plateau reaction under hypobaric condition. Ph.D. thesis of Xi'an university of architecture and technology
4. Wang H (2012) Human thermal comfort research under medium activity level and hypobaric condition. Ph.D. thesis of Xi'an university of architecture and technology
5. Xin Y (2008) Initial Human thermal comfort research in domain of medium-elevation plateau under hypobaric condition. Master Thesis of Qingdao Technological University
6. Fan Q (2009) The affect of the velocity of airflow on human thermal comfort under hypobaric condition. Master Thesis of Qingdao Technological University
7. Zhou J (2010) Human thermal comfort research based on manual nerve network under hypobaric condition. Master Thesis of Qingdao Technological University
8. Zhu Y (2008) The experimental research of the operating temperature, clothing thermal resistance and season of partial thermal environment effect on human thermal sensation. HV&AC 38(2):112–117
9. Zhou X (2010) The experimental research of the environmental control ability effect on human thermal sensation. Build Sci 26(10):177–180
10. Liu R (2010) Human thermal comfort research based on the human metabolic rate and the average skin temperature. Master Thesis of Qingdao Technological University
11. ASHRAE Handbook 2005

Chapter 33
Brief Analysis on Energy Consumption and Indoor Environment of Inner Mongolia Grassland Dwellings

Guoming Dong, Jiaping Liu and Liu Yang

Abstract Since the middle of the twentieth century, with the development of production and urbanization, many problems such as environmental pollution, energy shortages, and ecological degradation, and atmospheric warming, have become increasingly serious. Paying attention to the living environment has become a trend of the international community, which is also the focus of attention paid by governments and the whole society. A good living environment should reflect the characteristics of the three aspects: ecology, economy, and culture. These features are closely related to the building physical environment [1]. Based on the grassland typical living form—Mongolia yurt, this paper analyzes the physical environment of such living type, according to the natural environment of grassland and climate characteristics, drawing a conclusion that the energy consumption of traditional grassland dwellings is rather large, and the indoor environment, especially the indoor thermal environment, is far from the pleasant living environment.

Keywords Inner Mongolia · Grassland dwellings · Energy consumption · Indoor environment

33.1 Introduction

In the wave of national sustainable development, Inner Mongolia Autonomous Region has come up with certain sustainable development policies since 2001, roundly discussing questions in terms of Inner Mongolia economy, society, resources, and environment. The grassland living environment and ecological

G. Dong (✉) · J. Liu · L. Yang
Institute of Architecture, Xi'an University of Architecture
and Technology, Xi'an 710055, China
e-mail: 405230436@qq.com

construction are also included. With the purpose to provide valuable references for the sustainable development of grassland in the future, this article points out some present problems and puts forward the corresponding measures to improve the indoor environment of Inner Mongolia grassland dwellings.

33.2 The Community Characteristics of Grassland

33.2.1 Population Characteristics of Grassland

From the point of view of the geographical population, There are more than 30 thousand herdsmen living on about 788 thousand square kilometers of grassland, which means that each herdsman occupies about 2 km^2. For example, SiZiWangQi, attached to the city Wulanchabu of Inner Mongolia, has a total area of 25,000 km^2, where there is 20,843 km^2 grassland, of which more than 20,000 km^2 are natural grass pasture. And its population of animal husbandry is 20 thousand. Therefore, each person can occupy about 1 km^2 grassland. At present, the population size is shown in the Table 33.1.

It is usually that the distance between households is 3–6 km, and 15 km above between settlements, 30–50 km between administrative villages. The distance between townships is much more. According to the research of grassland ecological animal husbandry and the suitable size of grassland habitat, we can predict the appropriate size of the central Inner Mongolia prairie residential area in the future as shown in the Table 33.2.

The central SuMu refers to places where people are relatively concentration, the public service facilities are completed, and the grassland model economy develops rapidly.

Such a living form with much land and few people is decided by the style of animal husbandry production, the environmental bearing capacity, and the gathering benefits of grassland habitat. In the future development of grassland ecological animal husbandry process, the average residential density of grassland will

Table 33.1 Present population size of grassland

Living level	HaoTe (settlements)	GaZha (village)	SuMu (township)
Population size	6–12	30–100	100–1,500
Household number	1–3	5–20	20–300

Table 33.2 Ideal population size of grassland

Living level	HaoTe	GaZha	General SuMu	central SuMu
Population size	30–100	100–1,000	1,000–2,000	2,000–3,000
Household number	8–30	20–200	200–400	400–600

be more stringent control, with the construction and development of ecological immigration area.

33.2.2 Basic Forms of Grassland Dwellings

On grassland, it can be said that almost one hundred percent of the housing is a one-story building. According to the history of all national residential buildings, the main forms of grassland dwellings can be concluded as follows: the folding tent and Mongolian yurt mainly used by herdsmen; Cuoluozi, Mukeleng, and barrack used by the Ewenki nationality and Daur nationality in the early time; the cave dwelling and raw-soil house constructed by the Hui nationality, the Han nationality, and other minorities; the adobe house, red-brick house and tile-roofed house built by all ethnic groups in the late time.

33.3 Grassland Resources

For thousands of years, the main energy used by steppe nomads is cattle and sheep droppings, which is conveniently obtained. But such energy cannot provide more warming benefits. In long winter, because of lack of energy, people have to tolerate lower indoor temperature, and it is hard for animals to get a warm condition of bring young animals into the world.

Recently, some researches have proved that Inner Mongolia is rich in coal resources and power. However, because of some disadvantages such as the unique pattern of scattered scale, bigger community public service radius, and the less-developed highway network, the price of the coal material stays at a high level, which results that the coal supply cannot be ensured, and the coal power supply network is difficult to fully cover the whole areas. Although the use of coal resource has become increasingly developing, this situation is also difficult to change in quite a long period of time.

The use of solar and wind energy in pastoral areas has been strongly pushed by the government. This is because grassland areas are extremely rich in solar and wind energy resources.

33.3.1 Wind Energy Resource

The wind energy resource in Inner Mongolia ranks first in our country. The average cumulative time of wind whose speed is greater than or equal to 3 m/s each year is 4,000–6,500 h, and the wind energy available area occupies 80 % of the total area, and the majority of which is grassland. In the area of places which is

Fig. 33.1 Energy utilization
ratio of buildings in different
times
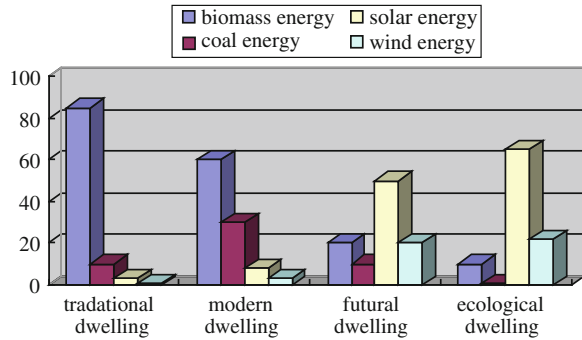
abundant in wind energy resource, the annual average effective wind energy
density is 2,480–1,000 KW h/m^2, and wind power generators in this area can work
normally 325–220 days in a year's time. According to statistics, presently, there
have been more than 200 thousand sets of small wind generators in pastoral areas.

33.3.2 Solar Energy Resource

Inner Mongolia ranks second in solar energy resources. Its solar annual sunshine
time is 3,400–2,600 h, and the annual total solar radiation is 6,400–4,800 MJ/m^2. In
the area of places which is abundant in solar energy resource, the annual total amount
of radiation is 6,439–5,550 MJ/m^2, the annual sunshine time is 3,452–2,870 h, and
the days of effectively using solar energy is about 330–270 a year. Since last century,
such areas have been equipped with solar battery 579 KW [2].

In recent years, the state has determined the strategy of the ecological animal
husbandry and utilization of new energy development. About 150 thousand fam-
ilies have solved the problem of living electricity and part of production power
with small wind turbines and solar panels. The government of Inner Mongolia
decides to improve the proportion of new energy from current 30–40 % in 2020.

According to the research, in future, as long as we make full use of the natural
resources, and comprehensively utilize building energy-saving technology, passive
solar heating technology, photoelectric conversion of solar energy technology, as
well as wind power and geothermal heat pump technology, such renewable
energies will not only meet the need of residential heating and daily life, but also
help us achieve sustainable development with one hundred percent in the use of
housing.

The energy utilization ratio of Inner Mongolia grassland dwellings in the past,
now, and in the future can be represented in Fig. 33.1.

Table 33.3 Energy consumption in January [2]

Energy demand	Cooking	Life electricity	Production power	Heating	Water warming
Consumption (KW·h/d)	4.6	2.5	1.8	138.8	2.0
Proportion (%)	3.1	1.7	1.2	92.7	1.3

Table 33.4 The range of index of heating consumption [2]

Style	Mongolian yurt	Adobe house	Brick house	Energy-saving building	Passive solar house
E-C (W/m^2)	100–200	120–140	80–100	35–45	15–20
C–C (W/m^2)	90.7–108.8	108.6–127.0	72.6–90.7	31.7–40.8	13.6–18.0

Notes E-C Energy consumption, *C–C* Coal consumption

33.4 The Energy Consumption of Steppe Dwellers

In the production and life of steppe nomads, there are many main factors on energy consumption: life cooking heat in four seasons of a year, lighting and TV requiring electricity, drinking water requiring water kinetic energy, indoor heating for 5–6 months in winter, lambing production requiring heat for 40–60 days per year, and so on. This research selects a separate brick-concrete structure house whose construction area is 96.4 m^2 with height 2.8 m, indoor temperature 18 °C, and the index of heat loss 59.7 W/m^2, to analyze its energy consumption proportion. The result of energy consumption calculation in winter of January shows as Table 33.3.

In the energy consumption proportion, cooking heat is mainly dependent on the combustion of cattle and sheep manure and coal; life electricity and production power is mainly provided by wind power generators (each household installing a 300–500 W wind power generator can meet life energy need); the largest proportion of total energy consumption is the heating.

However, in real life, the actual indoor temperature is lower than the calculated temperature during most of time in a day, and the poor thermal stability makes the indoor temperature fluctuate at about 12 °C. Therefore, the actual residential energy consumption is far lower than the energy consumption calculation. So, in the future, how to provide herdsmen ideal indoor thermal comfort environment and reduce energy consumption of heating in winter will become the important problem to be solved.

Through the research on different forms of residential building materials, construction, doors and windows insulation, and living habits, it can be concluded that under the interior calculation temperature 18 °C, in Inner Mongolia SiZiWangQi area, the index of heating consumption range of residential housing in winter shows as Table 33.4.

33.5 Residential Thermal Environment of Grassland Dwellings

According to the investigation on grassland residential thermal comfort in different period of a year, the views of young knowledgeable nomads for their basic living conditions, the analysis of herdsmen's dressing case all the year round, and the relationship between their thermal comfort and the corresponding temperature data, this paper approximately describes the indoor thermal environment as follows:

In the past, in winter, indoor temperature can reach 22 °C in a relatively short period of time, but the minimum temperature below 0 °C is also very common; in summer, indoor temperature is usually below 25 °C and the night temperature below 10 °C is not relatively rare.

In the existing houses during the day in winter, indoor temperature is between 22–14 °C in general, and the temperature at night can be maintained at 18–10 °C; in summer, indoor temperature is often below 25 °C while the temperature at night is 16 °C.

In the ecological residence in future, herdsmen hope that during the day in winter, indoor temperature will be controlled at 22–18 °C, and at night, indoor temperature will maintain at 16–18 °C; in summer, indoor temperature will be below 26 °C, and the temperature at night will be generally above 18 °C.

33.6 Ecological Design Strategies

In the design of ecological residential areas, we should as far as possible make sure that households are connected, the residential buildings and production buildings are in combination, the main room is located at the south side of the house while the secondary room at the west and north, as well as that doors and windows occupy a proper proportion of walls. However, according to the actual situation, the grassland dwelling housing is built without the north windows, and both west and east sides are also rarely put windows, only opening large doors and windows on the south wall.

In the construction of ecological grassland dwellings, the use of energy-saving technology, which concludes the use of appropriate building exterior insulation materials, roof insulation materials, and the ground insulation materials, can make the heating energy consumption drop to below 40 W/m². In grassland dwelling houses, the use of energy-saving doors and windows should be widely promoted, while thick walls and thin roof must be removed.

33.7 Conclusion

In the premise of using building energy-saving technologies, we should make full use of passive solar energy application technology and set up the attached sunspace, solar walls, and regenerators at the south side of the room [3].

During the design, we must persist to use firewall, fire bed and other traditional beneficial measures to improve the thermal stability of the building. At the same time, we should strongly promote the development and utilization of wind turbines; make full use of solar energy technology, and set up solar panels on the roof of the building so as to collect solar energy to heat the room in winter.

Wind-sunshine complementary system also should be promoted to support the living energy when there is small wind or cloudy day. Though the use of geothermal resource heat pump is scientific, feasible in theory, its economy and promotion of technology need further improvement.

References

1. Liu J (2000) Architectural physics. China Architecture and Building Press
2. Yang L (2010) Bioclimatic architecture. China Architecture and Building Press
3. Liu Z (2006) Analysis on inner Mongolia grassland residential energy consumption and thermal environment

Chapter 34
Case Comparison of Chinese and Finnish District Heating Substations

Meng Wang and Jianjun Xia

Abstract District heating is developing very fast in China. At the same time, energy consumption for heating is increasing rapidly. To reduce the level of energy consumption, energy conservation measures should be put in place. In Finland, district heating is well established. Both district heating companies and consumers are encouraged to save energy consumption by effective control methods and management measures. From the view of two typical substations in China and Finland, the differences between Chinese and Finnish district heating systems are revealed. The difference in the design and the control method shows the technological shortages. The difference in the pricing system shows the imperfect management system. The Finnish substation gives an example of the modernization substation. The automatic control of the heat substation is the development tendency. Also the Finnish pricing system and management is worth learning to push forward the heat reform in China.

Keywords Comparison · Heating substation · Design · Operation · Pricing system

34.1 Background

In North China, district heating has developed very fast since the 1980s. The total district heating area in North China increased from 1.07 billion m^2 to 9.22 billion m^2 from 1996 to 2010 [1]. The annual rate of the district heating area is increased about 17 %. With the fast development of urbanization, the district heating area in North China will continue to increase rapidly in the future. What is more, some residents in

M. Wang (✉) · J. Xia
Department of Building Science, Tsinghua University, Beijing 100084, China
e-mail: wangmenghere@sina.com

South China are claiming district heating to improve their life quality. So district heating has an expansive market in China. It also means more energy consumption in the future. In 2010, the total heating energy consumption is 163 million tons of standard coal equivalents. It is expected that heating energy consumption will increase to 0.3 billion tons of standard coal by 2020 at the current rate of development without energy conservation measures put in place.

In Finland, district heating is the most common form of heating, which has been produced since the 1950s. The number of district heating customers in 2011 was 133,500 with 1.3 million dwellings and 2.7 million inhabitants. The market share of district heating in 2011 was 46 % [2]. District heating is well established in Finland. Both district heating companies and consumers are encouraged to save energy consumption by effective technological methods and management measures.

This article made comparison of two typical substations in China and Finland from design parameters and measured data, as well as the management and heat pricing system, pointing out experiences worthy of being applied into Chinese heat substations. At the end of this article, improvement suggestions were put forward for the Chinese district heating system.

34.2 Case Introductions

The two substations in this comparison are named as A and B which are in China and Finland, respectively. Information collected from the two district heating companies and data measured in the two substations supported the comparison and analysis in this article.

Substation A is located in Chifeng, which is in southeast of Inner Mongolia. The substation supplies heat to 20 buildings. The buildings are constructed in different years, 7 in 2001, 9 in 2010, the rest before 2000. Buildings built before 2000 have no insulation. Figure 34.1 shows the schematic of substation A. There are heat exchangers, pumps, strainers, thermometers, and manometers in the substation. The central monitoring center reads the measurements in real time. In the secondary side, the water separator divides supply water into six branches, and each branch supplies hot water to several buildings.

Substation B is located in Espoo, which is 20 km west from the center of Helsinki. The substation supplies heat to 2 separate buildings that are 4-story buildings constructed in 1974 with 51 flats totally. The total summarized volume is 14,810 m^3. The buildings are made of prefabricated concrete units having insulation between the interior and the external wall. The buildings have double windows in each flat and in general areas such as corridors and saunas located in the basements of the buildings. Figure 34.2 shows the schematic of substation B. There are two heat exchangers, for space heating and domestic hot water, respectively. The domestic hot water system circulates all the time to ensure a hot water supply at any time.
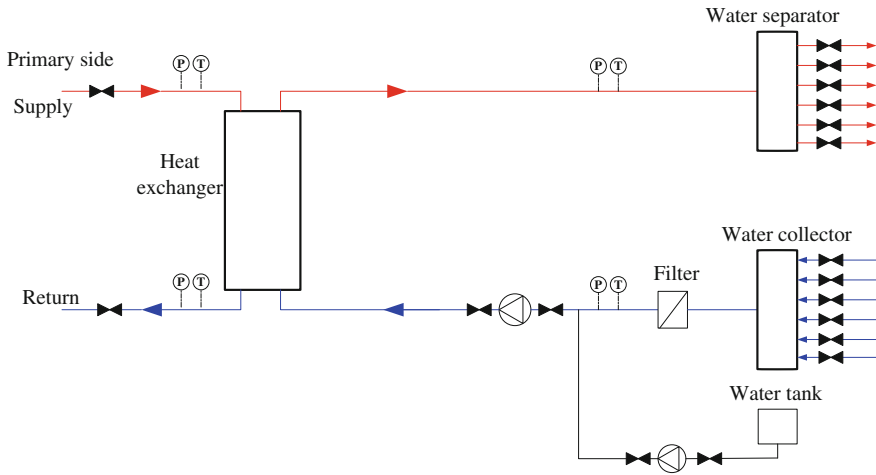
Fig. 34.1   Substation A schematic
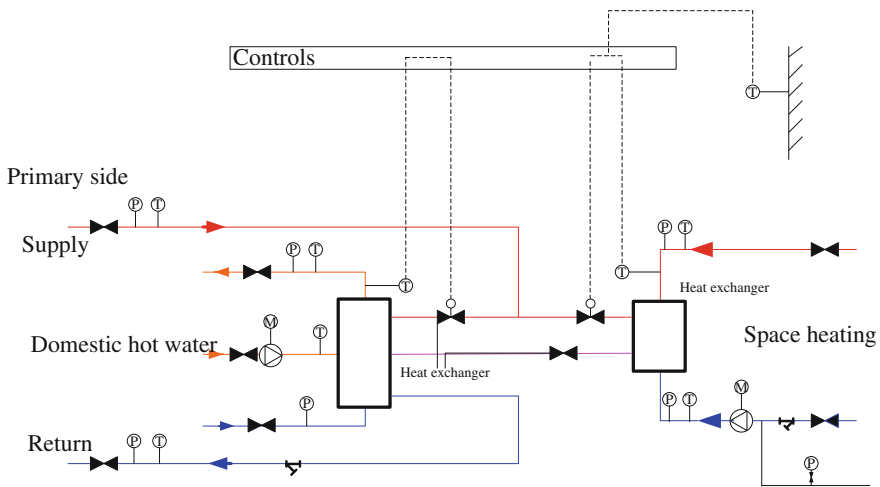
Fig. 34.2   Substation B schematic

34.3 Design Parameters Comparison

According to different national codes and principles for hydronic heating systems in buildings, the design temperature of district heating is different. In substation A, the design temperature for radiator heating is 95/70 °C. The design heat capacity is 6 MW. District heating lasts from November to March. In summer time, the district heating systems do not work. Domestic hot water is generated separately in each household by gas boilers, solar collectors or electric heating.

In substation B, the design temperature for radiator heating is 70/40 °C [3]. Domestic hot water temperature is 55 °C. The design radiator heating capacity is 276 kW, heating capacity for domestic hot water is 314 kW. During summer time, the radiator heating systems in buildings do not work, while the domestic hot water system continues to work. So the district heating system supplies heat to consumers all year around.

34.4 Operation Comparisons

34.4.1 Control Method

Substation A is owned and operated by a district heating company. The main control principle of the district heating company is to meet the minimum room temperature criterion (usually 18 °C) in heating season. The substation is controlled manually. In the primary side, the water supply temperature varies with the outdoor temperature; the water flow is constant or stage-adjusted. In the secondary side, the water supply temperature varies with the primary side; the water flow is constant or stage-adjusted. In residents' houses, there are no control valves to adjust room temperature. The heat fee is charged according to house area.

Substation B is owned by a house company and automatically controlled. The district heating and the house company made a contract about max heat capacity and primary side water supply temperature. The district heating company is responsible for contracted water supply temperature. The substation follows the variable flow scheme and has automatic control valves. In the primary side, the water supply temperature varies with the outdoor temperature. In the secondary side, the radiator supply water temperature is linear with outdoor temperature and controlled by primary side water valves, while the domestic hot water temperature is constant and controlled by primary side water valves. There are thermostatic valves in residents' homes. Heat fee is charged according to metered heat in the substation and divided between residents according to building area.

34.4.2 Measured Data Analysis

34.4.2.1 Substation A

In Fig. 34.3, the left picture is hourly primary side supply and return temperature from 18 December 2011 to 14 February 2012; the right picture is the secondary side. It has been shown that both the supply and return water temperature were stable during the 2 months. In the primary side, the supply water temperature was 90 °C, and the return water temperature was 40 °C. In the secondary side, the
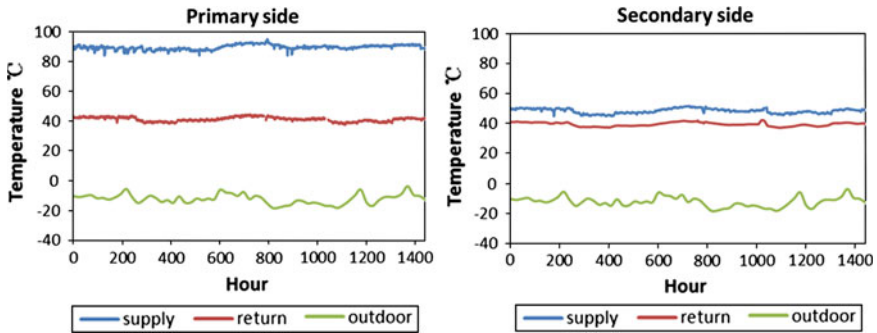
Fig. 34.3 Hourly water temperature and outdoor temperature of substation A
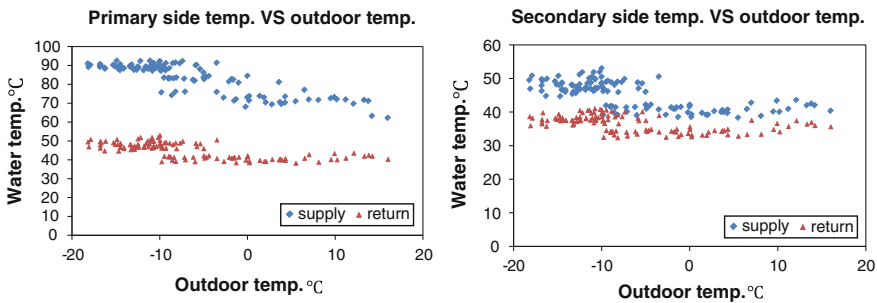
Fig. 34.4 Relationship between water temperature and outdoor temperature of substation A

supply water temperature was 50 °C, and the return water temperature was 40 °C. The cooling temperature of the primary side was 50 °C, and the secondary side was 10 °C. The average daily outdoor temperature varied between −18 and −3 °C.

In Fig. 34.4, the left picture is a scatter diagram of daily average primary supply and return water temperatures with the average outdoor temperature of substation A; the right picture is a scatter diagram of the average daily secondary supply and return water temperature with the average outdoor temperature. In the primary side, the supply temperature was stage changed with outdoor temperature. In the secondary side, the supply water temperature was also stage changed with the outdoor temperature. The relationship between water temperature and outdoor temperature is corresponding to the control method that primary supply water temperature is manually changed according to outdoor temperature. In Fig. 34.5, the heat load of substation A is in week linear correlation with the outdoor temperature. The R-squared value is 0.63.
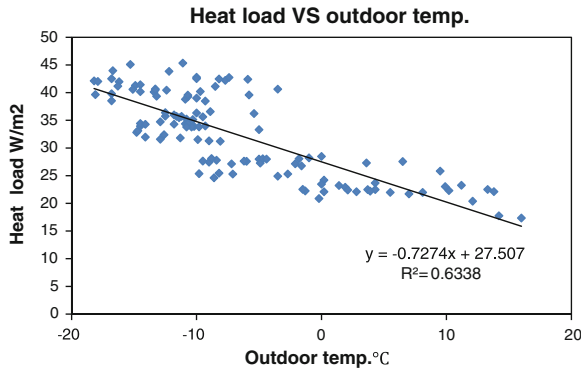
Fig. 34.5 Heat load and outdoor temperature of substation A
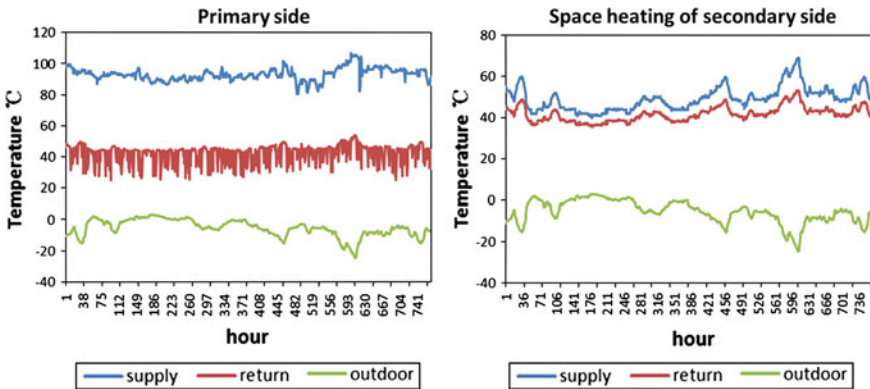
Fig. 34.6 Hourly water temperature and outdoor temperature of substation B

34.4.2.2 Substation B

In Fig. 34.6, the left picture shows hourly data of the primary side supply and the
return temperature from 25 December 2012 to 25 January 2013; the right picture is
hourly data of space heating side. In the primary side, the supply water temper-
ature varied from 80 to 105 °C; the return water varied from 25 to 50 °C. The
primary return water temperature fluctuated frequently in one day because of
domestic hot water usage. In the space heating side, the supply water temperature
varied from 40 to 68 °C; the return water temperature varied from 30 to 52 °C.
The cooling of the secondary side varied from 5 to 16 °C.

In Fig. 34.7, the left picture is a scatter diagram of primary side supply and return
temperature with outdoor temperature of substation B; the right picture is the radiator
side. The data were measured every 5 min from 25 December 2012 to 25 January
2013. It has been shown that the primary supply temperature was approximately
linear with the outdoor temperature. The supply water temperature drops from the
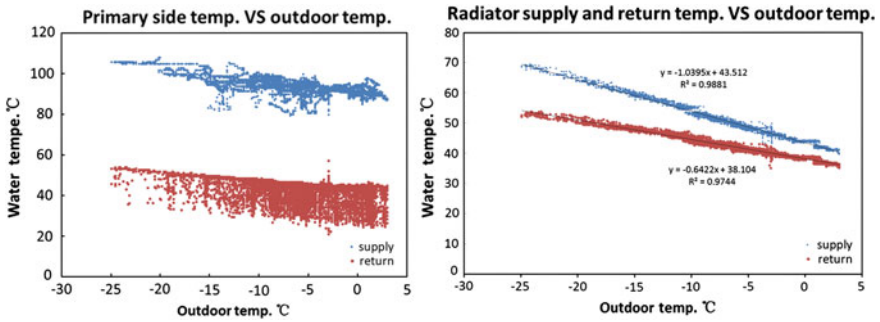
Fig. 34.7 Relationship between water temperature and outdoor temperature of Substation B

heat source to the substation because of heat loss. The return water temperature is as low as 25 °C, because domestic hot water is heated from 5 to 55 °C. In the space heating side, both the supply and the return temperature were linear with the outdoor temperature. The relationship between the radiator supply temperature and the outdoor temperature is corresponding to the control method so that the radiator supply temperature is automatically controlled according to the outdoor temperature by the primary water flow. In Fig. 34.8, the substation B heat load is in linear correlation with the outdoor temperature. The R-squared value is 0.85, higher than that of substation A. This is because substation B has a water supply temperature control and thermostatic valves in radiators to achieve stable room temperature.

34.5 Comparison Summaries

The design parameters and the control method are different between substation A and substation B. The Chinese design parameter for space heating is 95/70 °C, while the Finnish one is 70/40 °C. Domestic hot water is heated by district heating in

Fig. 34.8 Heat load and outdoor temperature of substation B
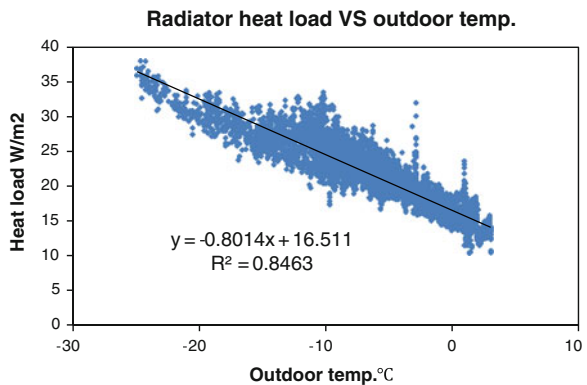
Finland. Substation A is manually controlled. Primary side supply water temperature varied with the outdoor temperature; secondary side supply water temperature varied with the primary side. Substation B is automatically controlled. The radiator supply water temperature varied with the outdoor temperature; the domestic hot water temperature was constant. The measured supply and return water temperature of substation A is more stable. The radiator side supply and return water temperature of substation B is linear with the outdoor temperature. The correlation of the space heating load and the outdoor temperature of substation B is higher than that of substation A.

The substation management is different. In China, the substation is owned and operated by a district heating company, who is responsible to supply heat from a heat source to residents' houses. The district heating company purchases heat from heating plants and sells heat to residents. In Finland, the substation is owned by a house company and automatically operated. The district heating company and the house company make a contract about the max heat capacity. The district heating company produces heat and sells heat to the house company.

The pricing system is different. The heat fee in China is charged according to building area. In Finland, the heat pricing system divides into: connection fee, power charge, and energy charge. The customer pays a connection fee for joining the district heating network. The fee varies according to location and the size of the house. The power charge conforms to the contracted capacity and covers mainly the fixed cost of heat procurement. The energy charge depends on the heat consumption and covers the variable cost of heat procurement. The heat consumption of the building is metered. The heating cost is divided between residents, according to living space. The district heating supplier provides their customers with a follow-up report on heat consumption at least once a year. In many locations, customers can monitor their consumption directly on the heat supplier's website.

34.6 Conclusions

The Chinese heat substation is short in automatic control. The Finnish heat substation gives an example of an automatically controlled substation. The automatic control of the heat substation is the development tendency, which can improve the management level and save energy consumption. Room temperature control is also useful to achieve a stable room temperature and dismiss overheating.

Heat metering is a way to encourage consumers to save energy. The Chinese government has implemented heat meter reform for years, but most consumers are still charged according to area. The reason is the lack of relevant consumer actions and a pricing system, as well as legal constraints. The Finnish experience of metering in the substation and dividing according to area is an easy way to be used in practice. More study on the relationship between heat consumers and suppliers should be carried out.

References

1. Tsinghua Building Energy Research Center (2011) China building energy research report 2011. Press of Chinese Building Industry, Beijing
2. Finnish Energy Industries (2012) District heating in Finland 2011
3. Skagestad B, Mildenstein P (2002) Programme of research, development and demonstration on district heating and cooling

Chapter 35
The Applicable Research of Predicted Mean Vote Evaluation Index in Ceiling Radiant Cooling Panels

Jinying Sheng and Nianping Li

Abstract The purpose of this study was to investigate whether the PMV index can evaluate the thermal comfort in ceiling radiant panel systems. In a previous experimental investigation using an office equipped with radiant cooling panel, it was found that the indoor relative humidity and indoor air velocity kept at 61.5 % and 0.01 m/s, respectively, could help to reduce condensation on the chilled surface and increase thermal comfort. The value of PMV and predicted percentage of dissatisfied (PPD) were calculated with the data measured and recorded in the test room, and they would be validated with the result of 85 thermal comfort questionnaires. By comparing the conclusion, it was concluded that there were some residuals when using the PMV calculation formula to calculate the value of PMV in ceiling radiant cooling panel system compared with the realistic, and a correction coefficient was needed in the PMV' equation.

Keywords Ceiling radiant cooling panels · Thermal comfort · PMV-PPD · Application

35.1 Introduction

Well known as comfort, energy efficiency in Scandinavian countries, Switzerland, and Germany, the ceiling radiant cooling panel systems have been getting prevalent recently. After solving the problems related to condensing, dripping, first cost and cooling capacity, the using of this system has increased in North America and Asia.

J. Sheng · N. Li (✉)
College of Civil Engineering, Hunan University, Changsha, 410082 Hunan, China
e-mail: linianping@126.com

Many studies were carried out on the ceiling radiant cooling panel systems in the literature. For thermal comfort, J. Miriel et al. [1] used GRES test protocol to characterize the thermal comfort of a room equipped with ceiling heating panel and assessed its comfort with predicted percent dissatisfied (PPD) by using 5 criteria, finding that the thermal comfort was very good with for the global feeling a percentage of dissatisfied close to 5 %, but few parts was beyond 10 %. Tiberiu Catalina et al. [2] evaluated the thermal comfort of this system by using combined CFD and experimentation study in a test room equipped with a cooling ceiling and concluded that a local discomfort at feet/ankle zone was observed, but it vertical temperature is less than 1 °C and its PMV distribution plots showed that thermal comfort is achieved and is uniformly distributed no matter the position in the room for the different panels in the test room. Takehito Imanari et al. [3] compared the ceiling radiant cooling panel system with conventional all-air system and found that CPCR system could provide a more superior thermal environment for its officer.

The PMV index was put forward on the basis of convective condition system and has been successful used in evaluating its thermal comfort for a long time, but as we all know that the mechanism of heat transfer between radiation and convection was different, and scholars commonly ignore this difference and seldom to investigate the application of PMV index in radiant condition system, so the objective of this paper was to solve this problem and offered help for the further study on thermal comfort in the ceiling radiant panel systems.

35.2 Experimentation

35.2.1 Test Chamber and Ceiling

Thermal environments, along with human responses, were introduced to use a big office equipped with radiant ceiling panels. The office, which was adjacent to the flourish street and no window facing outside, was on the 9th floor of Zhuhai Yantong company, in the south of China and has a surface of 72 m^2. The main structure of the test chamber was reinforced concrete, and the floor, wall, and ceiling were all white. The climatic parameters were average during the whole experiment and recorded in Table 35.1.

The ceiling radiant cooling panel used in this experiment, which would provide a large heat capacity and make the ceiling surface temperature more asymmetry,

Table 35.1 Climatic conditions

	Temperature (°C)	Relative humidity (%)	Velocity (m/s)
Indoor	24	61.5	0.01
Outdoor	26.5	67.1	0.67
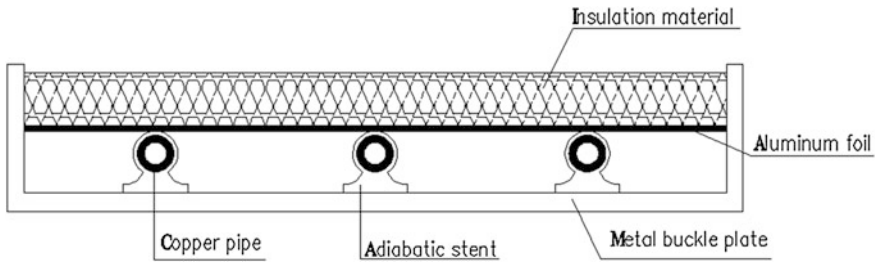
Fig. 35.1 The structure of patent radiant cooling panel

was invented by Yantong company itself, the patent number is ZL 2007 2 0060407.9 (Fig. 35.1). In order to guarantee the indoor air quality and keep the indoor relative humidity at a level where no condensation was detected, a small volume of outdoor air was introduced into the test room and delivered by double chilled coin fan, new patent (ZL 2008 2 0050512.9) [4] which was invented to match this cooling panel by Yantong company.

35.2.2 The Measurement of Indoor Parameters

The indoor air temperature was measured by thermometer, which was placed in different position of the room, at different heights starting from 0.1 to 1.8 m. The walls and floor were all equipped with two thermocouples to calculate their capacity of heat transmission, and it's measurement error was ±0.5 °C. The indoor humidity was measured by the hygrometer with a precision of ±2 % for measurements of relative humidity between 10 and 90 %. As the volume of air sent into the indoor was so small that there is nearly no wind speed shown in anemometer.

35.2.3 Questionnaires

The questionnaires were used to validate the theoretical value of PMV-PPD. This experiment will provide 85 questionnaires and be filled in by all participants. The participants were divided into 5 groups, and there was only one group went into the test chamber, stayed for one hour and then filled in the questionnaires before they went out the room every time. The questionnaires conclude their clothing situation, activity, their satisfaction and dissatisfaction to ceiling, heat environment, acoustics of the room and thermal comfort sensation.

All data and the questionnaires were measured and filled in the stable state.

35.3 The Calculation of PMV

35.3.1 The Introduction of PMV

PMV was on the basis of man's heat load which reflects the deviation to man's heat balance. It adopted seven-class scale index (seen in Table 35.2) considered man and environment factor and represented the sensation of most people in the same environment, but it ignores the individual difference between human beings. In order to remove this influence, Fanger put forward PPD. According to the criteria ISSO7730, when the PMV is 0, the value of PPD is 5 %, that means even if the indoor environment was in the best state of thermal comfort, there were 5 % of persons still felt dissatisfaction. So the recommended value of PMV in ISSO7730 criteria was from −0.5 [5–7].

35.3.2 The Calculated Method of PMV

PMV was a heat environment index based on thermal balance equation that put forward by professor P. O. Fanger.

$$PMV = f(M) \cdot S \tag{35.1}$$

Among which

$$f(M) = 0.303\exp(-0.306\,M) + 0.028 \tag{35.2}$$

$$S = M - (C + R + E) - (C_{res} + R_{res}) \tag{35.3}$$

where M is metabolic rate, W/m^2; C is convective heat transfer, W/m^2; R is radiant heat transfer, W/m^2; E is evaporation loss of human, W/m^2; C_{res} and R_{res} are apparent heat and latent through respiration, W/m^2.

When perspiration and heat reaction are not apparent, the parameters in Eq. (35.1) can be concluded simply.

$$C = f_{cl}h_c(t_{cl} - t_a) \tag{35.4}$$

$$R = 3.96 \times 10 - 8f_{cl}(t_{cl} + 273.15)4 - (t_r + 273.15) \tag{35.5}$$

$$C_{res} = 0.0014\,M(34 - t_a) \tag{35.7}$$

$$E_{res} = 0.0173\,M(5.87 - P_a \cdot M) \tag{35.8}$$

Table 35.2 PMV thermal sensation value

Thermal sensation	Hot	Warm	A bit warm	Thermal neutrality	A bit cool	Cool	Cold
The value of PMV	+3	+2	+1	0	−1	−2	−3

$$t_{cl} = t_{sk} - 0.155\,I(C + R) \tag{35.9}$$

$$t_{sk} = 35.7 - 0.0275\,M \tag{35.10}$$

$$(t_r + 273.15)^4 = (t_g + 273.15)^4 + 2.47 \times 10^8 \sqrt{V}(t_g - t_a) \tag{35.11}$$

where f_{c1} is the coefficient of clothing area, $f_{cl} = 1.0 + 0.3\,I_{cl}$; h_c is the coefficient of convective heat transfer, W/m^2 °C; t_a is the air temperature, °C; P_a is the part pressure of vapor, mm Hg; t_r is the mean radiant temperature, °C; t_{cl} is the temperature of clothing, °C; t_{sk} is the temperature of skin, °C; I is the clothing insulation, clo; t_g is the globe temperature, °C; v is the velocity of air, m/s [8].

Due to the difference between t_a and t_g would not exceed 2–3 °C, so the Eq. 35.11 can be simplified as Eq. 35.12.

$$t_r = t_g + 273.15\sqrt{V}(t_g - t_a) \tag{35.12}$$

Combined the equation above, we can get the value of PMV, and then according to the relationship between PMV and PPD (Eq. 35.13), we could easily get the dissatisfaction of people in this environment.

$$PPD = 100 - 95\exp\left[-\left(0.03353\,PMV^4 + 0.2719\,PMV^2\right)\right] \tag{35.13}$$

In this paper, all participants in the test room were in a sedentary state (70 W/m^2) and in a light suit, the clothing insulation is 0.5 clo and the coefficient of clothing area is 1.1. The globe temperature is 24 °C, measured by globe thermometer. Because the fresh air delivered into the indoor environment was very small and the air velocity was very slow (seen in Table 35.1), the indoor convection was belong to natural convection. According to Rapp, when a person was in sedentary state, the convective coefficient was 4.0 W/(m^2 °C). The part pressure of vapor, which can be looked over in the psychrometric chart, is 13 mm Hg. The mean skin temperature is 25.5 °C.

35.3.3 Result and Discussion

Using the formula above, we could easily get the value of PMV and PPD, 4 and 20 %, respectively, by computer which are against the ASHRAE rules seriously [9]. But for the solution to the questionnaires, we find that only two participants feel a little cool, which means that nearly 98 percent of the occupants are satisfied with the thermal environment and feel comfortable. Apparently, there is a confliction between the theoretic value and experimental value, among which we could find that the formula of PMV may not apply under the radiation condition. Due to the limited condition, we adopt a correction coefficient method to correct the equation of PMV in this study and get the correction coefficient 0.2 [7, 10].

The result obtained in this study would offer some references for the further study of the thermal comfort under the radiation condition.

References

1. Miriel J, Serres L, Trombe A (2002) Radiant ceiling panel heating-cooling systems: experimental and simulated study of the performances, thermal comfort and energy consumptions. Appl Therm Eng 22:1861–1873
2. Tiberiu C, Joeshp V, Frederic K (2009) Evaluation of thermal comfort using combined CFD and experimentation study in a test room equipped with a cooling ceiling. Build Environ 44:1740–1750
3. Takehito I, Toshiaki O, Kazuaki B (1999) Thermal comfort and energy consumption of the radiant ceiling panel system. Comparison with the conventional all-air system. Energy Build 30:167–175
4. Xuhan Z, Nianping L, Jiguang Y (2012) Adaptability analysis of new ceiling radiant cooling panels with dedicated outdoor air systems used in summer moist region. Key Eng Mater 517:864–869
5. Choi JK, Miki K, Sagawa S, Shiraki K (1997) Evaluation of mean skin temperature formulas by infrared thermography. Int J Biometeorol (2):68–75
6. Feustel HE, Stetiu C (1995) Hydronic radiant cooling-preliminary assessment. Energy Build 22:193–205
7. Refet K (2009) The investigation of relation between radiative and convective heat transfer coefficients at the ceiling in a cooled ceiling room. Energy Convers Manage 50:1–5
8. ASHRAE ANSI/ASHRAE Standard 55-2004 (2004) Thermal environmental conditions for human occupancy, Atlanta: American Society of Heating Refrigerating and Air-Conditioning Engineers Inc.
9. Prapapong V, Surapong C (2007) Application of radiant cooling as a passive cooling option in hot humid climate. Build Environ 42:543–556
10. Wilikins CK, Kosonen R (1992) Cool ceiling systems: a European air conditioning alternative. ASHRAE J 34(8):41–45

Chapter 36
Thermal Environment and Passengers' Comfort in Aircraft Cabin

Weilin Cui, Qin Ouyang, Yingxin Zhu and Songtao Hu

Abstract Passengers' comfort is becoming more and more important in aircraft cabins. In this study, thermal environment parameters on 10 airlines (1 international and 9 domestic) including 23 aircrafts and 6 different aircraft types were measured with 155 subjective questionnaires regarding passengers' comfort collected. Thermal environment parameters contained air temperature and relative humidity, wall temperature, radiant temperature, air velocity, noise, illumination, and absolute pressure. The questionnaires collected basic information of passengers (age, height, weight, and clothes level) and their evaluation of the environment (thermal comfort, perceived air quality, and symptoms). The results showed that air temperature was between 23 and 27 °C and average level of humidity was 26.3 %. Wall temperature was slightly lower than air temperature, but radiant temperature was very close. Air velocity was generally below 0.2 m/s, which was imperceptible for passengers. Average noise level was 82.5 dB (A weighted sound pressure level). The illumination changed greatly, and air pressure dropped when taking off and rose when landing and at cruise period; low pressure between 77 and 90 kPa was maintained. Subjective questionnaire assessment showed passengers were satisfied with the environment, and they believed noise and air pressure contributed most to their comfort level. More than 15 % of the passengers reported drowsiness and symptoms related to humidity (dry eye, nose, and throat). Deep analysis indicated that the longer the fight, the less comfortable passengers felt. Seasonal factor showed no significant influence on comfort level.

Keywords Aircraft cabin · Thermal environment · Passengers' comfort

W. Cui · Q. Ouyang · Y. Zhu (✉)
Department of Building Science, Tsinghua University, Beijing 100084, China
e-mail: zhuyx@tsinghua.edu.cn

S. Hu
Department of Environment and Municipal Engineering, Qingdao Technological University, Qingdao 266033, China

36.1 Introduction

Researchers have studied the aircraft cabin environment for decades. In 1999, Haghighat et al. [1] investigated the thermal environment and air quality on 43 commercial airline flights. Air temperature and relative humidity were used as indicators for thermal comfort, and the concentration of carbon dioxide was measured to evaluate the air quality. It was found that the air temperature was often below the recommended range of 23–26 °C, and the relative humidity was always too low compared with the recommended level of minimum 30 % in ASHRAE Standard 55–92 [2]. The US Federal Aviation Administration [3] proposed that the allowable carbon dioxide concentration in aircraft cabin should be lower than 5,000 ppm, and in real aircraft, the concentration seldom exceeded 1,500 ppm. Rankin et al. [4] collected data from 3,630 passengers on 71 flights in 1997. Conclusions from the study were that seat comfort, flight smoothness, and air quality were the important determinants of passengers' comfort. The most frequent symptoms experienced by passengers included back/joint/muscle pain, dry/irritated/itchy eyes, and dry/stuffy nose.

In China, little information is available on cabin environment research. In 1996, Li et al. [5] investigated cabin environment of 24 aircrafts of six types (B737, B757, B767, MD82, A300, and Y7), and the results indicated the cabin basically met the environmental hygienic requirements for protecting aircrew and passenger's health and ensured the aircrew's work efficiency. In 1999, Liang et al. [6] measured cabin environment of 10 A320 aircrafts, and the results were almost the same as Li et al. [5].

In early researches, the environment in aircraft cabins and passengers' health were well concerned. Only little information was available on passengers' comfort especially in China. Now, airplane is becoming more and more important in transportation, and the comfort of passengers needs more attention. In this research, 23 aircrafts including 6 different types were investigated. The environment parameters and passengers' comfort were measured.

36.2 Methods

Nine domestic airlines (Beijing to Chengdu, Guangzhou, Fuzhou, Shanghai, Qingdao, Wuhan, Guiyang, Kunming, and Shanghai to Guangzhou) and one international airline (HongKong to Brisbane) were included. Eight environment parameters were measured including air temperature, relative humidity, black globe temperature, pressure, noise, wall temperature, illumination, and air velocity. The measurement devices used are shown in Fig. 36.1. The measurement position for each aircraft was in the middle part of the cabin, and it was assumed that the environment in the cabin was uniform.

The parameters were recorded all through the flight. Air temperature, relative humidity, and black globe temperature were recorded automatically every 30 s,

Fig. 36.1 Environment measurement devices

and other parameters were recorded manually. For example, pressure was recorded every minute when the plane took off and landed and every 20 min at cruising period. Although in China, researchers have investigated the cabin environment, the passengers' comfort conditions are not concerned, which is also studied in this research.

The passengers' comfort survey was conducted at cruising period. On each plane, subjective questionnaires were distributed to some passengers. The survey mainly contained three parts: thermal comfort, air quality, and some symptoms. Passengers needed to evaluate the environment parameters on scales: thermal sensation (7-point scale, −3 to +3, very cold–very hot), thermal comfort (4-point scale, 0 to 3, comfortable–very uncomfortable), relative humidity (5-point scale, −2 to +2, very humid–very dry), draught (5-point scale, 0 to 4, imperceptible–too strong), noise (5-point scale, 0 to 4, quiet–too strong), seat comfort (5-point scale, 0 to 4, comfortable–very uncomfortable), odor (5-point scale, 0 to 4, no–very strong), satisfaction of pressure, noise, illumination, air quality, and overall environment (broken scale, −1 to −0, very unsatisfied–just unsatisfied, +0 to +1, just satisfied–very satisfied).

36.3 Results

36.3.1 Environment Parameters Measurement

Table 36.1 shows the overall results of the environment parameters measurement. The data are the average value in the whole flight.

The range of air temperature was from 23.1 to 27.4 °C, and the average value of all flight was 25.7 °C. The average value of relative humidity was among the range of 16.6–50.4 %. Because in cruising period, passengers would experience an environment of very low humidity, and from the above table, the minimum relative humidity was from 9 to 43.3 %. For most flight, the humidity at cruising was below 25 %, which was below the recommended 30 % in ASHRAE Standard 55–92 and 40–60 % in GB9673. The black globe temperature was relatively close to air temperature, and for most flight, the difference was 1 °C. For most flight, the wall temperature was lower than air temperature and black globe temperature, and the difference was at most 4 °C. The pressure at cruising period was all below the standard atmospheric pressure, and for long-haul flight, the pressure could be 77–80 kPa, while for short-haul flight pressure was higher, 88–91 kPa generally.

Table 36.1 Overall results of environment parameters measurement in the aircraft cabin

Airline	Aircraft type	Flight time/min	T_d/°C	RH/%	RH_{min}/%	T_b/°C	P_{cabin}/kPa	N_{cabin}/dB	T_{wall}/°C	I_{cabin}/lux	v_{cabin}/m/s
Chengdu, Kangding	B737	35	26.6	35.7	26.7		82	64	27.4	80	0.15
Qingdao, Beijing	A321	70	23.8	21.5	18	23.7					0.3
Qingdao, Beijing	B737	70	25.8	18.7	14.3	25.8					
Qingdao, Beijing	B737	70	27.1	31.5	22.3	27.2	88	72.1	26.6	534.7	0.2
Qingdao, Beijing	B737	70	24.4	27.7	20.8	26.8					
Wuhan, Beijing	B737	120	27.1	23.2	17.4		84.9	74	25.6	126.2	0.1
Wuhan, Beijing	B737	120	25.5	23.9	18.2		90.9				
Shanghai, Shenzhen	B737	120					77.3				
Shanghai, Beijing	A330	120					83.4				
Beijing, Chengdu	A321	130	27	26.5	11.4	26.4	82.7	73.9	26.1	170	0.1
Beijing, Guiyang	B737	150	26.7	18.2	8.9	23.9					
Quanzhou, Beijing	B737	150	27.1	35.2	23.6	27.3	81.6		24	336	
Beijing, Quanzhou	B737	150	27.1	23.6	16.7	26.6	81.6		27	143	
Shenzhen, Beijing	A321	180	24.7	19.1	28.9	24.5					
Beijing, Shenzhen	A330	180	24.4	21.5	12.2	24.2	82.9				
Shenzhen, Beijing	A321	180	27.4	21.6	14.8	26.8	82	75.6	23	621.8	0.1
Shenzhen, Beijing	B737	180					79.8				
Beijing, HongKong	A330	210	24	50.4	43.3		77.6	69.1	19.7	30	0.13
HongKong, Beijing	B747	210	26.4	30.8	15.3						
HongKong, Brisbane	A340	510	23.1	27	10.5	22.1	80.2	69.5	19.3	57	0.09
Brisbane, HongKong	A340	510	23.7	16.6	9			64	27.4		

The noise level was between 60 and 80 dB. The illumination variation was very large due to the climate conditions and the use of lights and the sun shield in the cabins. For air velocity, all measured data were below 0.3 m/s, which means that in cabin environment, the airflow was imperceptible for passengers.

36.3.2 Subjective Results for Passengers' Comfort

One hundred and fifty-five subjective questionnaires were collected, and the results were shown in Figs. 36.2 and 36.3. Figure 36.2 shows the evaluation of passengers on environmental parameters. The upper and lower limits of the grey box in each graph were the upper and lower quartile of all votes, and the endpoints of the black line through the grey box were the maximum and minimum values of the votes.

The thermal sensation vote was between −2 (cold) and 2 (hot); 50 % of the passengers voted between −1 (slightly cold) and 1 (slightly warm). Most
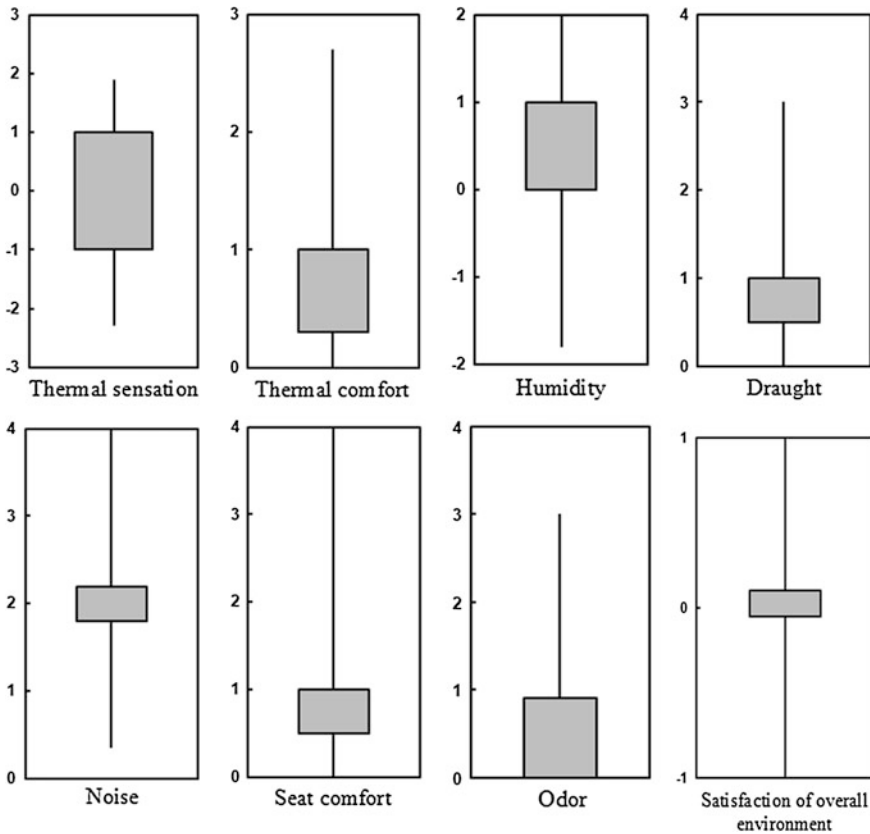
Fig. 36.2 Subjective questionnaire results (Part 1)
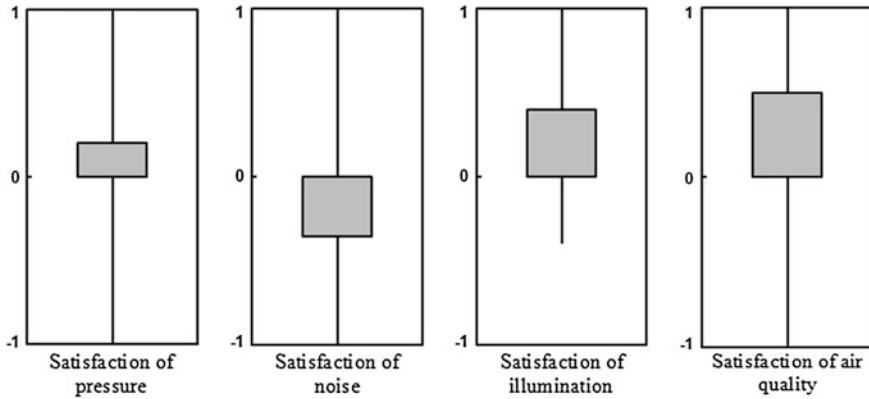
Fig. 36.3 Subjective questionnaire results (Part 2)

passengers voted their thermal comfort level between 0 (comfortable) and 1 (slightly uncomfortable). Passengers felt the cabin environment was little dry (0–1), and the draught was slight, which accorded with the environment parameters measurement. The evaluation of noise was medium (2), and most passengers were relatively satisfied with seat comfort. As for air quality, passengers reported no odor (0) to slight odor (1).

According to Fig. 36.3, most passengers were satisfied with pressure, illumination, and air quality. Yet for noise, passengers showed dissatisfaction. The overall environment satisfaction vote was around 0 (just unsatisfied and just satisfied).

Figures 36.4 and 36.5 showed that passengers were satisfied with the environment, and they believed noise and air pressure contributed most to their comfort level, and more than 15 % of the passengers reported drowsiness and symptoms related to humidity (dry eye, nose, and throat).
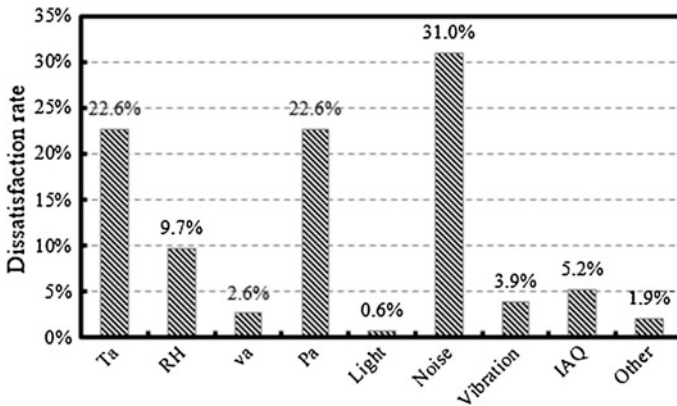
Fig. 36.4 Dissatisfaction rate of the environment parameters
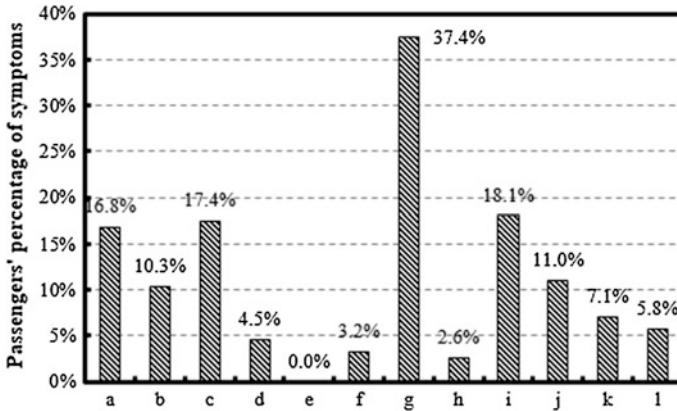
Fig. 36.5 Passengers' percentage of the symptoms

36.4 Discussions

The environment in cabin is very important to passengers' comfort and health. But the existing standards have different recommended values for the same parameters. Besides, some recommended parameter values do not meet with real conditions. For example, the recommended values for relative humidity are 30 % in ASHRAE Standard and 40–60 % in GB9673. In real cabin environment, humidity is usually below 30 % and even lower in long-haul flight. So, it is necessary to revise the standards to meet the real needs.

From this study, it could be concluded that most measured parameters satisfied the existing standards except for humidity. And from the questionnaire results, it was also clear that passengers felt that the cabin environment was generally acceptable. They were satisfied with most parameters like pressure and air quality. Most passengers complained the noise in cabin was too loud, and noise was the only parameter that passengers were dissatisfied with (Table 36.2).

Table 36.2 The symptoms

Serial number	Symptoms
a	Eye dryness
b	Nose dryness
c	Throat dryness
d	Chest suppression
e	Asthma
f	Skin dryness
g	Drowsiness
h	Dysphoria
i	Dizziness
j	Nausea
k	Distraction
l	Others

This study is only a preliminary research with many problems to solve. The measurement of parameters was rather rough, and more detailed data are needed. The number of collected questionnaires was not enough to present a comprehensive picture of passengers' comfort. The measurement was conducted mainly in spring and summer. Data from other seasons are necessary.

36.5 Conclusions

The main results could be concluded as follows:

1. Environment parameters among different aircraft were different, but generally, most parameter values were close to or satisfied the recommended values in existing standards.
2. Humidity in real aircraft cabin was very low especially in cruising period. The recommended values in existing standard do not conform to reality.
3. Passengers were generally satisfied with cabin environment, but from the questionnaires, it could also been seen that there is still plenty room for improvement in comfort.

References

1. Haghighat F, Allard F, Megri AC et al (1999) Measurement of thermal comfort and indoor air quality aboard 43 flights on commercial airlines. Indoor Built Environ 8:58–66
2. ASHRAE (1992) ANSI/ASHRAE Standard 55-1992, thermal environmental conditions for human occupancy. Atlanta, American Society of Heating, Refrigerating and Air-Conditioning Engineers, Inc. USA
3. Federal Aviation Administration (1993) 'Federal Aviation Regulation'. Washington DC, 25.831
4. Rankin WL, Space DR, Nagda NL (2000) Passenger comfort and the effect of air quality. Am Soc Test Mater, West Conshohocken
5. Li LY, Ge SQ, Jin LJ (1996) Hygienic investigation of passenger aircraft cabin in China. Space Med Med Eng 9(2):130–133
6. Liang ZH, Sun WP, Feng CY (1999) Hygienic investigation of microclimate in 10 A320 aircraft cabins. Guangdong Health Epidemic Prev 25(2):74–76

Chapter 37
Prediction Model of Human Thermal Sensation Under Low-Air-Pressure Environment

Weilin Cui, Qin Ouyang, Yingxin Zhu and Songtao Hu

Abstract Passengers in aircraft cabins experience a low-air-pressure environment in most time of the flying period. So the influence of low air pressure on passengers' comfort needs further research. The most commonly used model to predict human comfort is predicted mean vote (PMV) model. But PMV is designed for standard atmospheric environment, not for low-pressure environment. Researchers have confirmed that under low-pressure environment, human body heat loss through convection will decrease while through evaporation will increase. Thus, PMV model is not suitable for prediction under low-pressure environment and needed to be revised. The main purpose of this study was to investigate human body heat loss under low-pressure environment through both theoretical derivation and experimental validation, thus the model to predict human thermal comfort under low-air-pressure environment could be promoted. The heat loss was divided into four parts: convection heat loss, skin evaporation heat loss, radiation heat loss, and respiration heat loss. From theoretical derivation, following conclusion could be obtained. Radiation heat loss is more related to temperature, and the influence of air pressure is not significant. The convection heat loss will decrease and skin evaporation heat loss will increase under low pressure environment. Heat loss through respiration increases under low-pressure environment. The total heat loss will increase under low-pressure environment. Experimental validation was conducted with six experiment conditions: 22 and 27 °C (1.0/0.9/0.8 atm). Thirty subjects were recruited, and thermal sensation was significantly lower under low-pressure environment than standard pressure environment. Linear regression was analyzed between the value of thermal sensation vote and human thermal storage rate. Instead of the value PMV model predicted

W. Cui · Q. Ouyang · Y. Zhu (✉)
Department of Building Science, Tsinghua University, Beijing 100084, China
e-mail: zhuyx@tsinghua.edu.cn

S. Hu
Department of Environment and Municipal Engineering,
Qingdao Technological University, Qingdao 266033, China

which was significantly higher than thermal sensation vote, the new model developed was more effective in predicting human thermal comfort under low-pressure environment.

Keywords Low-pressure environment · Prediction model · Human body heat loss

37.1 Introduction

The air pressure in aircraft cabin is lower than standard atmospheric pressure at cruising period. The planes are designed to maintain an air pressure that is at least equivalent to the air pressure at 2,500 m above sea level (around 75 kPa) [1]. In recent years, the comfort in aircraft cabin is more and more important. To evaluate the comfort level, it is necessary to know the thermal environment conditions and the passengers' reaction. The most common method used is to evaluate thermal sensation by questionnaire. The ASHRAE/ISO 7-point thermal sensation scale is based on Fanger's PMV model. The PMV model was originally designed for standard atmospheric pressure environment. Whether this model could be used under low-pressure environment is not clear. Li et al. [2] investigated convection and evaporation heat dissipation under low-pressure environment and found that convection heat dissipation would decrease and evaporation heat dissipation would increase in low-pressure environment. In PMV model, other heat dissipation factors are also included such as radiation and heat release through breathing. In this study, an experiment was conducted in a chamber where low-pressure environment could be simulated to evaluate thermal sensation. Theoretically, the heat dissipation was calculated using real experiment conditions. With these two results, the preliminary model which could predict thermal sensation was proposed.

37.2 Methods

The experiment was conducted in low-pressure environment chamber in Qingdao Technological University. Six conditions were designed: 22 and 27 °C (1.0/0.9/0.8 atm). Thirty subjects were recruited including 20 males and 10 females (university students). They were divided into 6 groups and participated in all environment conditions. Latin-square method was used to decide the order. Subjects wore uniform clothes (around 1.11clo), and the metabolic rate of 1.0 was met when sat still. Each experiment lasted 90 min, and the procedure is shown in Table 37.1. The 7-point thermal sensation scale was used.

The heat dissipation was divided into four parts: convection heat loss through the skin, evaporation heat loss through the skin, radiation heat loss, and heat loss

Table 37.1 Experiment procedure

Time/min	0–10	10–40	40	50	60	70	70–90
Event	Depressurize	Adaption	Vote	Vote	Vote	Vote	Pressurize

through breathing. With these four parts, the heat storage of the human body could be calculated. The PMV model gives the relationship between heat storage and vote results. In this study, unary linear regression was applied between thermal sensation vote and heat storage rate. In this way, the model to predict human thermal sensation under low-pressure environment could be proposed.

37.3 Results

37.3.1 Experiment Results

Figure 37.1 shows the results of thermal sensation vote under different air pressure and temperature. The trend in both temperatures was the same. As air pressure decreased, TSV value also decreased. Significant difference was found between 1.0 atm and other two low-pressure environments. Between 0.8 and 0.9 atm, no significant difference was found. But under 27 °C, the difference in TSV values between 0.9 and 0.8 atm was larger than 22 °C.

37.3.2 Numerical Calculation

The heat dissipation was divided into four parts: convection heat loss through the skin, evaporation heat loss through the skin, radiation heat loss, and heat loss through breathing. The values of real experiment condition parameters used in calculating are shown in Table 37.2.
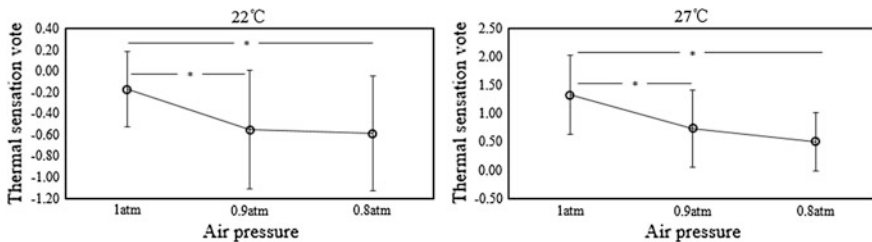
Fig. 37.1 Thermal sensation vote under different temperature and air pressure

Table 37.2 Parameters used in the calculation

Parameters	Symbol	Value
Clothing thermal resistance	I_{cl} (clo)	1.11
Clothing area coefficient	f_{cl}	1.33
Skin surface temperature	t_{sk} (°)	34.1
Skin surface saturated vapor pressure	P_{sk} (kPa)	5.3
Skin moist degree	W	0.14 (22 °C), 0.24 (24 °C)
Metabolic rate	M (W/m^2)	58.2
Vapor osmotic coefficient	i_{cl}	0.41

According to the study of Li et al. [2], the equation to calculate convection heat dissipation through skin is as follows:

$$C_p = \frac{f_{cl}h_{c,p}(t_{sk} - t_a)}{f_{cl}h_{c,p}I_{cl} + 1} = \frac{f_{cl}h_{c,0}\left(\frac{P_p}{P_0}\right)^{2n}(t_{sk} - t_a)}{f_{cl}h_{c,0}\left(\frac{P_p}{P_0}\right)^{2n}(I_{cl} - t_a)} \qquad (37.1)$$

In this equation, $n = 0.33$. The heat dissipation was calculated from 22 to 27 °C, which is shown in Fig. 37.2. The figure on the left indicated that convection heat dissipation decreased rapidly as temperature rose, and when pressure decreased, heat dissipation also decreased, but the scale was rather smaller. The right figure showed the heat dissipation with different pressure under 22 and 27 °C. At higher temperature, the decreasing speed of heat dissipation was slower than low temperature.

The radiation heat dissipation would not be affected by air pressure change, and the following Eq. (37.2) was used.

$$R = 3.96 \times 10^{-8} f_{cl} \times [(t_{cl} + 273)^4 - (\bar{t}_r + 273)^4] \qquad (37.2)$$

The clothes' surface temperature t_{cl} would change with air temperature. In this study, it was assumed that the human skin temperature would not change with air
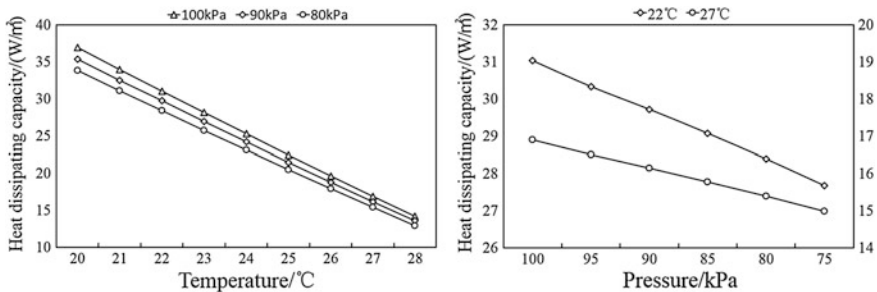
Fig. 37.2 Convection heat dissipation under different pressure and temperature

temperature, and the change in convection heat dissipation under different pressure levels could be neglected. So t_{cl} could be calculated with Eq. (37.3).

$$t_{cl} = t_{sk} - I_{cl}(R + C) \tag{37.3}$$

Figure 37.3 shows the results of t_{cl} and radiation heat dissipation R. It was clear that the clothes' surface temperature t_{cl} increased when air temperature rose. And due to the rise in t_{cl}, the radiation heat dissipation decreased when air temperature rose.

Evaporation heat dissipation through skin was calculated according to Eq. (37.4). The results showed that the change in evaporation heat dissipation was just opposite to that of convection heat dissipation. As temperature rose or pressure decreased, the heat loss increased. At higher temperature, the change in heat loss was more obvious with pressure change (Fig. 37.4).

$$E_{sk,p,n} = \frac{\omega f_{cl} \times 39.27(t_{cl} - t_a)^{0.25} \left(\left(\frac{P_0}{P_p} \right) P_{sk} - P_{a,0} \right)}{f_{cl} \times 39.27(t_{cl} - t_a)^{0.25} \frac{I_{cl}}{16.5 \times i_{cl}} + \left(\frac{P_0}{P_p} \right)^{2n}} \tag{37.4}$$

Heat dissipation through breathing was divided into two parts: sensible heat dissipation C_{res} and latent heat dissipation E_{res}, and the equations were as follows [3].
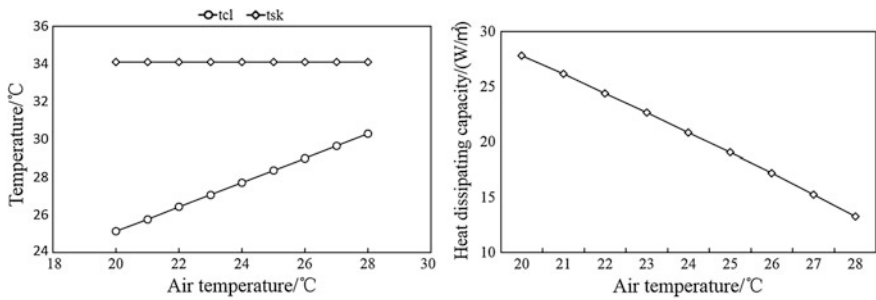
Fig. 37.3 Clothes' surface temperature and radiation heat dissipation
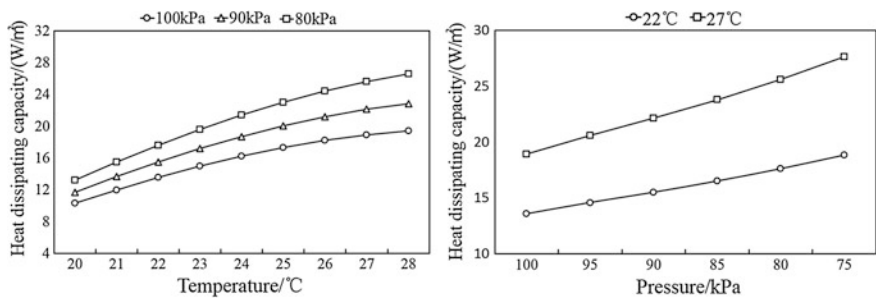
Fig. 37.4 Evaporation heat dissipation under different pressure and temperature

$$C_{\text{res}} = 0.0014\,\text{M}(34 - t_{\text{a}}) \tag{37.5}$$

$$E_{\text{res}} = 0.0173\,\text{M}(5.867 - P_{a,0}(P_p/P_0)) \tag{37.6}$$

The results were shown in Fig. 37.5. As temperature rose, the heat dissipation decreased, and under low-pressure environment, the heat loss would increase. It was also clear that the heat loss through breathing was much smaller than through convection and evaporation.

The total heat dissipation is shown in Fig. 37.6. At 22 °C, heat loss was significantly higher than at 27 °C. Under low-pressure environment, total heat loss increased. But the increasing level was quite different under different temperature. According to the results, under hotter environment, more heat would be lost when pressure decreased. Then the heat storage could be calculated using Eq. (37.7).

$$\text{HS} = M - W - C_p - R - E_{\text{sk},p} - C_{\text{res},p} - E_{\text{res},p} \tag{37.7}$$

The thermal sensation vote and heat storage are shown in Table 37.3. Unary linear regression was done between TSV and HS. The new parameter to predict thermal sensation under low-pressure environment is defined as PMVp, and the regression result was as Eq. (37.8) shows.
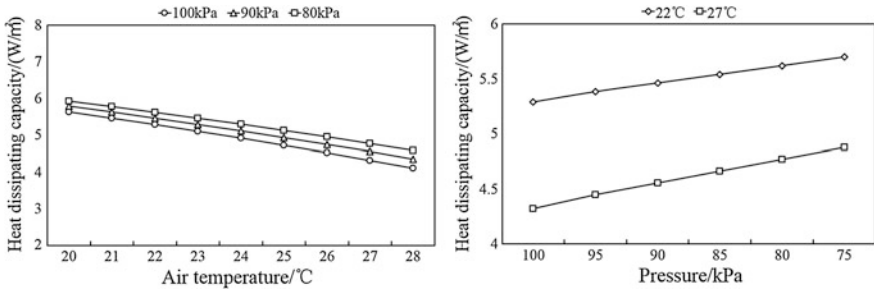
Fig. 37.5 Heat dissipation through breathing under different pressure and temperature

Fig. 37.6 Total heat dissipation under different pressure and temperature
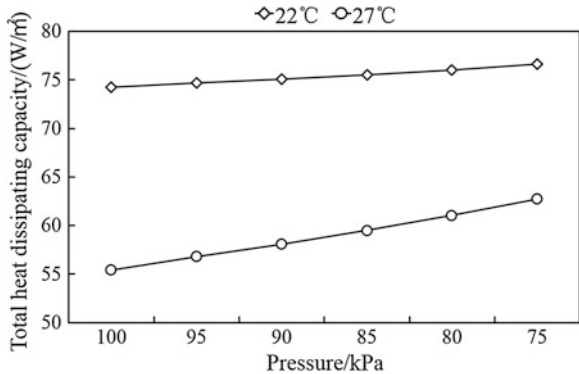
Table 37.3 Thermal sensation vote and heat storage

Temperature/°C	Pressure/atm	HS/ (W/m^2)	TSV
22	0.9	−16.9	−0.55
	0.8	−17.8	−0.59
27	0.9	0.1	0.73
	0.8	−2.8	0.50

$$PMV_{0.8} = 0.074HS + 0.715, R^2 = 0.999 \qquad (37.8)$$

37.4 Discussion

Both the TSV values and the calculation results confirm that under low-pressure environment, heat dissipation will increase compared with standard atmospheric environment. So, it is necessary to revise the existing PMV model which could not predict thermal sensation under low-pressure environment well. This study is a preliminary investigation and many results need to improve. For example, there were actually two important assumptions in calculating. One was that the metabolic rate would not change under different pressure level, and the other was skin surface temperature maintained stable under all conditions. The aim of the two assumptions was to make the calculation simple. Whether these two assumptions are reliable needs further validation. The data used to establish the new model are still not enough. In Fanger's PMV model, the coefficient before the heat storage is a function related with metabolic rate. But in the new model, the coefficient is a constant. So the data under different metabolic rate should be included.

37.5 Conclusion

The main results could be concluded as follows:

1. Thermal sensation vote value decreases under low-pressure environment compared with standard atmospheric environment.
2. As pressure goes down, convection heat dissipation decreases and evaporation heat dissipation increases.
3. Total heat dissipation increases when pressure decreases, and when temperature is higher, the decrease is more significant.

References

1. Haghighat F, Allard F, Megri AC et al (1999) Measurement of thermal comfort and indoor air quality aboard 43 flights on commercial airlines. Indoor Built Environ 8:58–66
2. Li XQ, Sheng XY, Xin YZ, Liu GD (2009) A primary study on human heat release characteristics under low-pressure environment. J Qingdao Technol Univ 30(5):8–13
3. Fanger PO (1982) Thermal comfort. Robert E. Krieger Publishing Company, Malabar

Chapter 38
Comparative Study on the Insulation Performance of a Lightweight Planted Roof Module Based on Outdoor Guarded Hot-box Testing Method

Wansheng Yang, Zhangyuan Wang, Xuejun He and Xudong Zhao

Abstract Green roof has the advantages of energy-saving and ecological environmental protection effects with, however, insufficient investigations quantitatively, which will keep it from practical engineering projects. In this paper, based on the guarded hot-box testing method, the energy-saving and thermal insulation properties of two lightweight roofing insulation modules with *Sedum lineare* and light planting soil will be studied and compared in the outdoor climate. The experiments involved two operating conditions, i.e., with the air conditioning on and off, that both maintained the moisture content of the two modules the same. It was found that the air temperature within the guarded hot-box was lower than the outdoor air temperature by 5.4 °C for the roof module with *S. lineare*, and the temperature drop of 5.4 °C was 0.8 °C lower than that of the roof module with lightweight planting soil. The average cumulative power consumption of the module with *S. lineare* was about 0.27 kWh/m^2, which was 0.05 kWh/m^2 lower than that of the module with lightweight planting soil. The electrical saving rate of the module with *S. lineare* was at 15.6 % compared with that of the module with the lightweight planting soil.

W. Yang (✉) · Z. Wang · X. He
School of Civil and Transportation Engineering, Guangdong University
of Technology, Guangzhou 510006, China
e-mail: gdyangwansh@126.com

X. Zhao
Department of Engineering, University of Hull, Hull HU6 7RX, UK

38.1 Introduction

In recent years, with the improvement of urban thermal environment and development of building energy-saving requirement, the insulation technology of the eco-roof/green roof has been focused on by many governments and researchers. Green roof, due to its favorable insulation property and ecological environment effect, has been utilized broadly [1–4]. However, compared with the mature green roof systems in the foreign countries, the domestic research was mainly in the area of construction technology [5–13], while the energy-saving property of the green roof has only been performed a few times [14, 15]. In this paper, the comparative study on two roof modules, i.e., one with *Sedum lineare* and another with lightweight planting soil, has been conducted experimentally under real weather conditions using an outdoor guarded hot-box device to obtain the guiding results beneficial to the actual engineering projects.

38.2 Descriptions of the Experimental Equipment and Method

38.2.1 Construction of the Guarded Hot-Box and Positions of the Measuring Points

As shown in Fig. 38.1, the experimental guarded hot-box was composed of inner and outer parts. The inner box was constructed by fly ash bricks in sides, and its bottom was cement mortar of 5 cm thickness and polythene foam board with thickness above 10 cm for thermal insulation. The top of the inner box was installed with lightweight thermal insulation roof module. The outer box was extruding polystyrene board with a thickness of 5 cm. Air-conditioning systems were positioned between the inner and outer boxes as well as inside the inner box for the regulation of the environmental temperatures.

38.2.2 Construction of the Experimental Module

The size of the module was 1,100 × 1,100 × 130 mm with PVC board external wall of 5 mm thickness. The module constituted water-retaining/drainage board, geotechnical fabric, lightweight planting soil, and vegetation layer from bottom to top, as shown in Fig. 38.2.
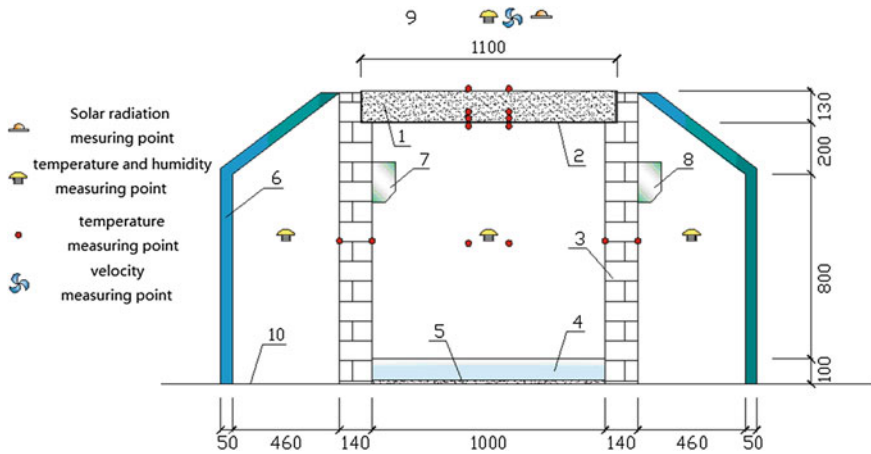
Fig. 38.1 Construction of guarded hot-box and positions of measuring points *1* lightweight planted roof module, *2* supporting board, *3* inner box, *4* polythene foam board, *5* cement mortar, *6* outer box, *7* air conditioning inside the inner box, and *8* air conditioning between inner and outer boxes
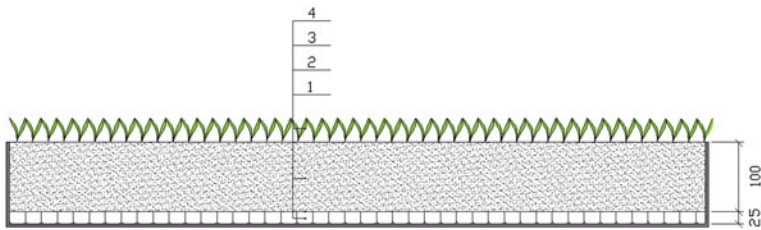
Fig. 38.2 Construction of the experimental module *1* water-retaining/drainage board (25 mm), *2* geotechnical fabric (1 mm), *3* lightweight planting soil (100 mm), and *4* *Sedum lineare* (40 mm)

38.2.3 Testing Equipment and Instrumentations

The main performance parameters of the experimental equipment and instrumentations are shown in Table 38.1.

38.2.4 Testing Principle and Method

In this testing, two identical guarded hot-boxes were used for the comparison of the thermal insulation and energy-saving properties of two lightweight roof modules. One was put with lightweight planting soil module on the top of the inner

Table 38.1 Main performance parameters of the experimental equipment and instrumentations

Testing equipment/ instrumentations	Model	Main performance parameters
Multi-channel temperature inspecting instrument	JK-64U	Temperature range −100–1,000 °C; accuracy ±1 °C
Multi-channel temperature/humidity monitoring system	JTDWS-1	Temperature range −50–300 °C; accuracy ±0.1 °C; relative humidity (RH) range 0–100 %; RH accuracy ±2 %
Soil moisture content monitoring recorder	HC-TSY	RH range 0–100 %; RH accuracy ±3 %
Pyranometer	JTBQ-S2	Spectrum measuring range 280–3,000 nm; accuracy <5 %; radiation measuring range −2,000–2,000 W/m^2
PROVA anemometer	AVM-07	Speed range 0–45 m/s; accuracy ±3 % (±0.1 m/s)
Electrical power monitoring instrument	PowerBay	Power range 5–2,200 W; accuracy ±1 %
GREE split cold air wall-hung air conditioning	KF-26GW/(26,556)	Cooling capacity 2,600 W; rated power 742 W; EER 3.50; recirculating air rate 520 m^3/h
Kelon split wall-hung air conditioning	KF-26GW/N2	Cooling capacity 2,600 W; rated power 930 W; EER 2.80; recirculating air rate 440 m^3/h

box and another one was with *S. lineare* module on the top of the inner box. The thickness, structure, and materials of the planting soil were the same for both modules. The environment temperature of the space between the inner and outer boxes was regulated to the same by the air-conditioning system. When the temperature difference between the internal and external surfaces of the wall of the inner box was small, the heat transfer through the sidewalls could be ignored. That is, the temperature variation inside the inner box was caused only by the heat transfer through the top insulation module.

The testing was conduced from June 15, 2012 to July 28, 2012, with the time period of 8 a.m. to 6 p.m. The location of the testing was at the Outdoor Testing Field, Structural Laboratory, School of Civil and Transportation Engineering, Guangdong University of Technology, Guangzhou, China. Two operating modes were considered for both modules. One was that all the air-conditioning systems were turned on and set at 26 °C and the testing period was from June 15 to July 7. Another one was that all the air-conditioning systems were turned off and the testing period was from July 8 to July 28 under natural climate conditions. The electrical consumption of the air-conditioning system, solar radiation, and wind speed were recorded every hour, and the temperature and humidity were recorded every 10 min.

38.3 Testing Results and Analyses

38.3.1 Air-conditioning ON Mode

38.3.1.1 Cumulative Electrical Consumption

During the testing, the cumulative power consumption of the air-conditioning system and environmental parameters are shown in Table 38.2.

From Table 38.2, it can be seen that the cumulative electrical power consumption of the air-conditioning system was influenced greatly by the outdoor environmental parameters. The average cumulative power consumption was at 0.32 kWh for the module with lightweight planting soil and 0.27 kWh for the module with *S. lineare*, respectively. The daily cumulative power consumptions of the two modules are shown in Fig. 38.3.

According to the volume of the hot-box at 1 m^3 and the effective area of the module at 1 m^2, the module with *S. lineare* could save energy at 0.05 kWh/m^2 compared with module with lightweight planting soil, and the energy-saving rate was at 15.6 %.

38.3.1.2 Relationship Between the Power Consumption and Outdoor Environmental Parameters

Based on the data in Table 38.2, the influence of the environmental parameters on the cumulative power consumption could be analyzed using linear regression method as in Table 38.3.

From Table 38.3, it can been seen that the influence of the environmental parameters on the power consumption was in the intensity sequence of outdoor air temperature, solar radiation, wind speed, outdoor air humidity and soil water content for the module with lightweight planting soil, outdoor air temperature,

Table 38.2 Cumulative power consumption of the air-conditioning system and environmental parameters

Parameters	July 1		July 2		July 3		July 4		July 5	
	(1)	(2)	(1)	(2)	(1)	(2)	(1)	(2)	(1)	(2)
Cumulative power consumption (kWh)	0.18	0.14	0.16	0.12	0.45	0.4	0.56	0.49	0.25	0.21
Soil water content (%)	1.1	11.8	1.2	9.1	1.3	6.9	1.1	4.0	1.1	4.3
Solar radiation (W/m^2)	694.0		694.0		766.0		782.0		594.0	
Outdoor air temperature (°C)	32.6		33.1		33.9		36.1		31.3	
Outdoor air humidity (%)	67.7		68.8		69.6		67.6		70.7	
Wind speed (m/s)	0.51		0.68		0.47		0.26		0.08	

Note (1) for roof module with lightweight planting soil; (2) for roof module with *Sedum lineare*
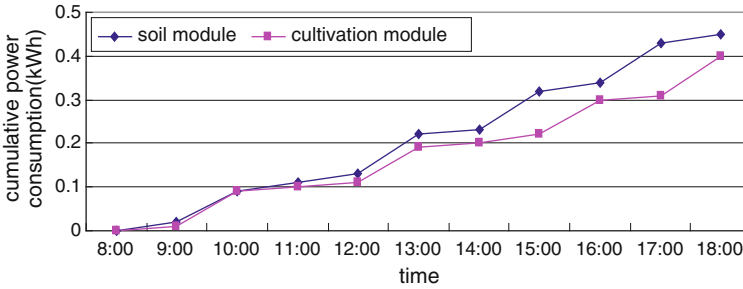
Fig. 38.3 Cumulative power consumptions of the two modules on July 3

solar radiation, soil water content, wind speed, and outdoor air humidity for the module with *S. lineare*, respectively. The two modules were exposed to sunlight under the same climate conditions before testing, leading to the closely constant initial water content of soil. The difference between the power consumptions of the two modules was caused from that the *S. lineare* reduced the water evaporation from the soil, resulting in the property of thermal insulation and decrease in solar radiation absorption.

The relationship between the energy-saving amount of the module with *S. lineare* and outdoor air temperature is shown in Eq. (38.1) and Fig. 38.4.

$$\Delta Q = 0.0068X - 0.1785, R^2 = 0.8578 \tag{38.1}$$

38.3.2 Air-conditioning OFF Mode

38.3.2.1 Effect of Thermal Insulation

Under the air-conditioning OFF (natural climate condition) mode, the testing results of the temperatures in the hot-box, outdoor air temperature, and solar radiation are presented in Table 38.4.

From Table 38.4, it can be seen that under the same climate conditions, both modules had favorable thermal insulation properties (as in Fig. 38.5). By comparing the air temperature in the hot-box and outdoor air temperature, the average temperature difference was 4.6 °C for the module with lightweight planting soil and 5.4 °C for the module with *S. lineare*, which meant that the thermal insulation performance of the module with *S. lineare* was better than that of the module with lightweight planting soil.

Table 38.3 Relationship between the power consumption and outdoor environmental parameters

Module		Outdoor air temperature	Solar radiation	Wind speed	Soil water content	Outdoor air humidity
(1)	Equation	$Q_1 = 0.08X - 2.3$	$Q_1 = 0.002X - 0.87$	$Q_1 = 0.29X + 0.43$	$Q_1 = 0.31X - 0.04$	$Q_1 = 0.02X + 1.95$
	R^2	0.6585	0.4978	0.1433	0.0251	0.0310
(2)	Equation	$Q_2 = 0.07X - 2.2$	$Q_1 = 0.002X - 0.83$	$Q_1 = -0.27X + 0.38$	$Q_1 = -0.03X + 0.51$	$Q_1 = 0.02X + 1.60$
	R^2	0.6354	0.5077	0.1469	0.45	0.0234

Note (1) for roof module with lightweight planting soil; (2) for roof module with *Sedum lineare*
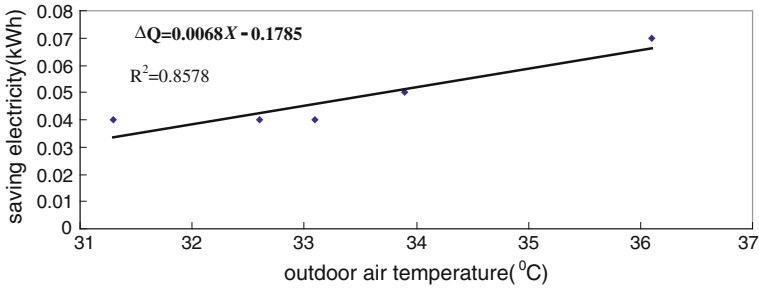
Fig. 38.4 Relationship between the energy-saving amount of the module with *Sedum lineare* and outdoor air temperature

Table 38.4 Testing results of the temperatures in the hot-box, outdoor air temperature, and solar radiation

Parameters	July 8		July 9		July 10		July 11		July 12	
	(1)	(2)	(1)	(2)	(1)	(2)	(1)	(2)	(1)	(2)
Air temperature in the hot-box (°C)	28.9	28.2	29.8	29.0	30.4	29.6	30.8	30.1	31.4	30.6
Outer surface temperature of the inner hot-box wall (°C)	29.0	29.1	29.8	30.1	30.5	30.7	31.0	31.2	31.6	31.7
Inner surface temperature of the inner hot-box wall (°C)	28.3	28.4	29.2	29.3	29.8	29.9	30.3	30.4	30.8	30.9
Outdoor air temperature (°C)	33.5		34.4		35.1		35.6		35.7	
Solar radiation (W/m^2)	248.0		522.0		716.0		597.0		729.0	

Note (1) for roof module with lightweight planting soil; (2) for roof module with *Sedum lineare*
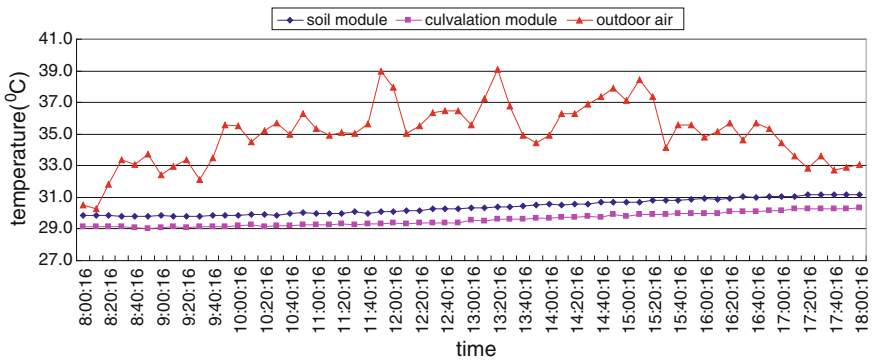
Fig. 38.5 Comparison of the air temperature in the hot-box and outdoor air temperature for the two modules on July 10

Table 38.5 Relationship of the temperature drop effect to the outdoor air temperature and solar radiation

Modules	Outdoor air temperature (°C)		Solar radiation (W/m^2)	
	Equation	R^2	Equation	R^2
Lightweight planting soil module	$\Delta t = 0.96T - 29.0$	0.9371	$\Delta t = 0.003S + 2.5$	0.3405
Sedum lineare module	$\Delta t = 0.97T - 28.7$	0.9544	$\Delta t = 0.003S + 3.4$	0.3858

38.3.2.2 Relationship of the Thermal Insulation Effect and Outdoor Air Temperature/Solar Radiation

In order to further analyze the influence of the outdoor air temperature and solar radiation on the thermal insulation properties of the two modules, the relationship of these three parameters, based on the testing data, are shown in Table 38.5.

From Table 38.5, it can be seen that under natural climate conditions, the thermal insulation effect of the modules were mainly influenced by the outdoor air temperature. The higher the outdoor air temperature was, the better the temperature drop effect of the modules was. Due to the existence of the vegetation layer, the thermal insulation property of the module with *S. lineare*, influenced by the outdoor air temperature and solar radiation, was more obvious than that of the module with lightweight planting soil. The height and concentration of the vegetation layer will be one of the significant factors for the cooling effect of the lightweight modular green roof, in addition to the structure of the module.

38.4 Conclusions

In this paper, an outdoor guarded hot-box method was used for the comparative investigations on the thermal insulation and energy-saving performance of two types of lightweight roof insulation module. Outdoor guarded hot-box method could avoid the violent temperature variation from summer outdoor heat and adverse effect due to the unsteady indoor/outdoor heat transfer in conventional measurement. Therefore, it was widely applied in a large number of thermotechnical performance testing of most kinds of thermal insulation modules. The testing results indicated that the thermal insulation and energy-saving properties of the module with *S. lineare* were better than that of the module with lightweight planting soil under the same climate conditions, which provided solid evidence for the application and promotion of the lightweight modular green roof.

References

1. Feng C, Zhang Y, Meng Q (2010) Current situation of the thermotechnical performance of the vegetation roof. Huazhong Build 28:91–94
2. Zhao D, Tan Y, Tang M (2011) Energy-saving effect of lightweight green roof technology. Constr Technol 2:82–84
3. Yang W, Guo K (2011) Performance testing analysis on the thermal insulation layer of a modular vegetation roof. New Build Mater 38:40–48
4. Zhao D, Xue W (2008) Electricity saving effect of lightweight green roof. Shanghai Agric Acad J 24:99–101
5. Gardner WR (1959) Solutions of the flow equation for the drying of soil and other porous medial. Soil Sci Soc Am J 23:183–187
6. Zhao H, Liu X, Wu Q (1992) Soil water evaporation mathematical mode for the leave covering conditions. Soil Water Conserv Bull 19(2):61–64
7. Xie X, Zuo D (1991) Farmland evaporation. China Meteorological Press
8. Jiang J (1995) Research on the soil water evaporation model. Sichuan For Sci Technol 15(4):20–25
9. Lu W, Bai K (1987) New method for calculating evaporation value. Hydraul Eng 26(3):12–15
10. Lei S (1984) Theoretical analysis on one-order soil water evaporation model. J Chengdu Univ Sci Technol 4:135–138
11. Zhang Y, Cai S, Cai M (1991) Uneven soil water evaporation research under the conditions of low water content of surface soil. J Wuhan Hydraul Power 24(2):157–164
12. Jin D, Yang S (1981) Method to calculate soil water evaporation capacity based on ordinary meteorological data. People's Yangtze River 4:47–52
13. Li H, Cai H, Wang J, Zhao W (2008) Soil water evaporation mathematical model in the reference of water evaporation capacity. J Agric Eng 24(3):1–4
14. Ren G (2011) Comparative study on the overseas mature green roof systems. China Build Waterproof 23:24–28
15. Li L, Li X (2007) Analysis on the planted roof system technology in Weida, Germany. New Build Mater 34:13–15

Chapter 39
Indoor Formaldehyde Concentration Increase and Decay Pattern in a Real Residential Unit

Weihui Liang and Xudong Yang

Abstract Formaldehyde is commonly observed in indoor air, and it is proved that it has significant effect on human health. Natural ventilation is an effective way for pollutant removal. One of the most directly usage way is to open and close the window, but the indoor pollutant concentration decreases with window open. The decayed pattern under different window opening angles has not been studied well. In this article, the formaldehyde concentration increase pattern when external windows and doors were closed and the decay patterns under different window opening angles were studied. The increasing tendency is fast at the beginning 2 h and then slower for the following 2 h. The concentration decay pattern under different window open angles was different, and the larger the window open angle, the faster is the decay of the indoor concentration. Indoor formaldehyde concentration can be removed in several minutes if we open the window at 90°. The timescale of formaldehyde concentration increase pattern is much longer than the decay pattern which takes hours. It implies that to control indoor formaldehyde concentration, we should open the window more frequently other than keeping it open and close for a long time.

Keywords Real building · Concentration increase · Concentration decay · Window open and close

39.1 Introduction

Formaldehyde is a common indoor air contaminant and has been widely studied and proved that it is associated with adverse health effects [1]. Symptoms related to low-level exposure of formaldehyde are eye and throat irritation, chest tightness,

W. Liang · X. Yang (✉)
Department of Building Science, Tsinghua University, Beijing 10084, China
e-mail: xyang@tsinghua.edu.cn

and breath shortness [2]. High-dose exposure increases the risk of acute poisoning, while prolonged exposure can lead to chronic toxicity and even cancer [3]. To avoid the harmful health effects on sensitive people, the World Health Organization [4] has recommended that the formaldehyde concentration in air should be below 0.1 mg/m^3 as a 30-min average. This value is also recommended by Chinese National Standard [5] for 1 h exposure limit.

An effective indoor contaminant control strategy is to use natural ventilation. Increased ventilation can decrease indoor contaminant concentration [6, 7]. However, windows cannot be always open in cold winter or hot summer, due to thermal comfort or energy consumption constraints. In China as well as many developing countries, occupants open the windows intermittently in order to remove contaminant and save energy. To understand how the indoor contaminant concentrations change by opening or closing windows could help to develop guidelines of effective ventilation strategies.

In this article, concentration increase pattern when external windows and doors were closed and decay patterns under different window opening angles were measured and analyzed in a real residential building.

39.2 Methods

39.2.1 Room Configuration

Figure 39.1 presents the layout of the two-story apartment unit. The areas of the first and second floors were 124.2 m^2 and 57 m^2, respectively, and the room height for both floors is 2.46 m. The position of each piece of furniture is presented in the
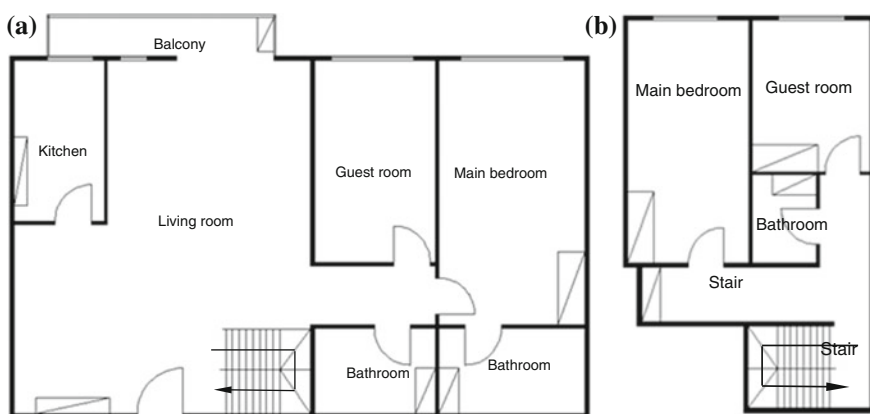
Fig. 39.1 Configuration and furniture position of the tested house, "▱" represents the furniture. **a** First floor. **b** Second floor

figure. It is a non-smoking family with four adults and one child. Construction was completed on June 9, 2007.

39.2.2 Field Measurement Method

An Interscan 4160 digital electrochemical analyzer (made in USA) was used to measure the concentrations of formaldehyde. It is a portable online formaldehyde instrument and has been used in gaseous formaldehyde concentration monitoring [8, 9]. The online instrument is very useful in rapid indoor measurements compared to the sampling method which needs tens of minutes for taking the air sample without instantaneous reading. To ensure the measurement accuracy, the instrument was calibrated by the ultraviolet spectrophotometry formaldehyde concentration measurement method.

On July 17, 2007, we measured the indoor formaldehyde concentration increase over time in first-floor guest room. We first ventilated the house by opening the windows for a few hours to remove the indoor formaldehyde and then closed the external windows and doors. The internal door between each room was left opened to benefit the mixing level of the house. While the doors and drawers of all the furniture were opened, it represent the worst or the largest amount of indoor formaldehyde emitting. From the room measurement conducted before, it implied that the air in each room is well mixed, so the increasing concentration curve in the first-floor guest room can roughly be treated as the curve in the whole house.

To obtain the formaldehyde concentration decay pattern under different window open angles, the external windows and doors should be closed for several hours, while the door of the furniture is kept opened to quickly increase the indoor formaldehyde concentration to a relatively high level, the internal doors connecting each room remain closed. Then, we open the window of the room and remain it at a constant open angle and measure the concentration decay profile. Because the concentration needs to increase before the decay pattern measurement, so the concentration decay pattern in a room under different open angles cannot be measured in a day, but can be measured in different rooms. So we get different case scenarios to observe the concentration decay pattern under different window open angles and different outdoor climate conditions. Table 39.1 gives the detailed information of the measurement case scenario.

39.3 Results and Discussion

39.3.1 Concentration Increase Profile

Figure 39.2 is the concentration increase profile of the apartment after the external windows and doors were closed from open status. The increasing tendency was

Table 39.1 Measurement scenarios information of concentration decay pattern under different window open angles

Floor No.	Room name	Case No.	Window open angle	Test date
First floor	Main bedroom	Case 1	90°	June 10, 2007
		Case 2	<10°	July 21, 2007
	Living room	Case 3	90°	June 10, 2007
		Case 4	90°	June 10, 2007
	Guest room	Case 5	30°	June 10, 2007
		Case 6	90°	July 19, 2007
		Case 7	90°	July 21, 2007
Second floor	Guest room	Case 8	60°	June 10, 2007
		Case 9	45°	July 21, 2007

Note Case 3 was conducted at 11 a.m. and Case 4 was conducted at 7 p.m. on June 10, 2007

fast at the beginning, with indoor formaldehyde concentration increased from 0.05 to 0.27 ppm within the first two hours. It then became slower in the following hours. This phenomenon should be taken into consideration in measuring indoor concentrations, i.e., more frequent measurements should be taken during the early increase period.

39.3.2 Formaldehyde Concentration Decay Pattern

The concentration decay pattern of different case scenarios is presented in Fig. 39.3. The subfigures of Fig. 39.3 were classified by room name.

All the measurement results indicated that when the window is opened, indoor formaldehyde concentration will decay. The decay profiles of most cases are near linearity, which means that the decay rate is almost constant within the measurement time. Based on this conclusion, the decay rate of each case can be calculated which is presented on Table 39.2. From Table 39.2, the decay patterns are different between each window open angle and each test date, which represent the different weather conditions.

Fig. 39.2 Indoor formaldehyde concentration increase profile with external windows and doors closed, while internal doors and furniture doors opened
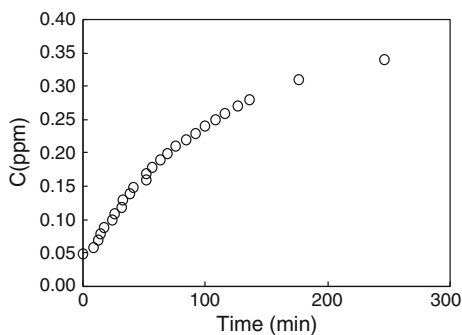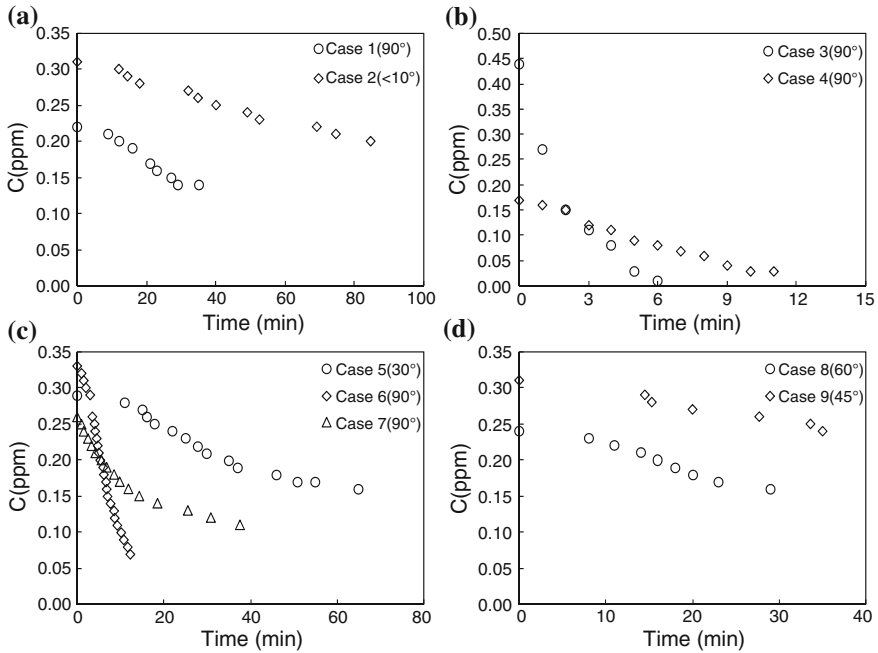
Fig. 39.3 Indoor formaldehyde concentration decay pattern under different window open angles, number in the brackets represents the window open angle. **a** First-floor main bedroom. **b** Living room. **c** First-floor guest room. **d** Second-floor guest room

Generally speaking, the concentration decay patterns were faster with window opened at 90° than the other window open angle. The average decay rate of Case 9 (45°) and Case 5 (30°) is almost the same and slightly faster than Case 2 (<10°) while lower than Case 8 (60°). Case 3 (90°) and Case 4 (90°) were conducted in the same day with the same window open angle, and the date rate difference between these two cases may result in the changed weather condition, where the

Table 39.2 The concentration decay range and decay rate of each window open cases

Case No. (window open angle)	Concentration range (max/min) (ppm)	Decay time (min)	Decay rate (ppm/h)
Case 1 (90°)	0.22/0.14	35	0.137
Case 2 (<10°)	0.31/0.2	84.5	0.078
Case 3 (90°)	0.44/0.01	6	4.300
Case 4 (90°)	0.17/0.03	11	0.764
Case 5 (30°)	0.29/0.16	65	0.120
Case 6 (90°)	0.33/0.07	16	0.900
Case 7 (90°)	0.26/0.11	37.5	0.224
Case 8 (60°)	0.22/0.16	33	0.145
Case 9 (45°)	0.31/0.24	35	0.120

Fig. 39.4 Indoor
formaldehyde concentration
decay and increase pattern
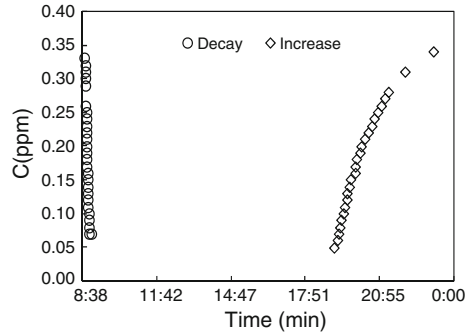
temperature difference between indoor and outdoor or wind velocity is larger in Case 3 than Case 4. The influence of weather condition is also reflected by Case 6 (90°) and Case 7 (90°). The influence of weather condition is more significant than window open angle.

From contaminant removal point of view, it is sufficient to open the window at 90° and left it open tens minutes. The window open time could be prolonged as the window open angle decreased.

39.3.3 Concentration Decay and Increase Pattern Comparison

On July 17, 2007, we measured indoor formaldehyde concentration decay and increase profile of first-floor guest room. It is the increase profile measurement and the decay pattern of Case 6. The concentration decay and increase profile of each room were presented in Fig. 39.4.

The indoor formaldehyde concentrations of guest room decay from 0.33 to 0.07 ppm in 16 min, while it increases from 0.05 to 0.34 ppm in 4 h. The concentration scale of the decay and increase profile are almost the same, but the timescale of increase pattern is over 12 times longer than the decay profile. These measurements indicated that the indoor concentration decay pattern is much faster than increase pattern. If the occupants want to control indoor concentration by opening and closing the window, it only needs to open the window for tens of even several minutes, but the total window close time can be prolonged.

39.4 Conclusion

Concentration decay pattern depends on window open angle and weather condition. Generally speaking, the larger the window open angle, the faster is the decay of indoor concentration. The influence of weather condition on indoor concentration decay pattern is more significant than window open angle.

Indoor concentration decay pattern is much faster than increase pattern. From the measurement of Case 3 and Case 6, pollutant removed in tens of even several minutes, while the increase profile with same concentration range will be prolonged to several hours. To control indoor contaminant concentration by open and close window, we only need to open the window at 90° and left it opened for tens of minutes, while the window close time should within a certain hours. This phenomenon suggests that we should open and close the window more frequently other than keeping it open or closed for a long time.

References

1. Tang XJ, Bai Y, Duong A et al (2009) Formaldehyde in China: production, consumption, exposure levels, and health effects. Environ Int 35:1210–1224
2. Main DM, Hogan TJ (1983) Health effects of low-level exposure to formaldehyde. Official Publication of the Industrial Medical Association 25:896–900
3. IARC (2006) IARC monographs on the evaluation of carcinogenic risk to humans. Formaldehyde, 2-butoxyethanol and 1-tert-butoxypropan-2-ol, vol 88. World Health Organization, International Agency for Research on Cancer, p 478
4. WHO-ROE (2000) Air quality guidelines for Europe. World Health Organization Regional Office for Europe
5. Indoor Air Quality Management Group of China (2002) Indoor Air Quality Standard; GB/T 18883-2002. Ministry of Health, Beijing
6. Salthammer T, Fuhrmann F, Kaufhold S et al (1995) Effects of climatic parameters on formaldehyde concentrations in indoor air. Indoor Air 5:120–128
7. Gilbert NL, Gauvin D, Guay M et al (2006) Housing characteristics and indoor concentrations of nitrogen dioxide and formaldehyde in Quebec City Canada. Environ Res 102:1–8
8. Lu Z, Li CM, Qiao Y et al (2008) Effect of inhaled formaldehyde on learning and memory of mice. Indoor Air 18:77–83
9. Wang F, Li C, Liu W et al (2012) Modulation of microrna expression by volatile organic compounds in mouse lung. Environ Toxicol 1–11

Chapter 40
The Influence of Particle Size Distribution on DEHP Concentrations

Yuanyuan Lu, Xinke Wang and Yanyu Zhang

Abstract It is well recognized that particles would enhance SVOC flux between surfaces and bulk air and contribute to inhalation exposure to SVOCs. DEHP are ubiquitous in indoor environment and can be accumulated in indoor particles. It has become widely recognized as a major indoor pollutant. Our objectives are to clarify the further mechanism of the influence of particulate size distribution on DEHP phase distribution and to estimate indoor exposure. A lumped model for predicting instantaneous DEHP concentrations in gas phase, particle phase, dust phase, and surface phase is proposed. In the model, ventilation, penetration, deposition, and resuspension are considered to simulate particle concentrations with different size distributions including dust. A relationship between particle/air partition coefficient and particulate diameters is defined by the model. Five typical size distributions of particles in the literature are adopted for particle concentration simulation. The simulated results show an obvious difference of indoor concentrations in various phases for the different particle size distributions. The results imply a possible strategy to control various phase DEHP concentrations and exposures.

Keywords: Indoor air quality (IAQ) · Particle · Semi-volatile organic compounds (SVOCs) · Health exposure · Phthalate

40.1 Introduction

Since the 1950s, there have been great changes in the materials used by the indoor decoration materials and daily necessities. Semi-volatile organic compounds (SVOCs), such as plasticizers, flame retardants, and biocides, are present in many

Y. Lu · X. Wang (✉) · Y. Zhang
Department of Building Environment and Services Engineering, Xi'an Jiaotong University, Xi'an 710049, China
e-mail: wangxinke@mail.xjtu.edu.cn

building materials and household products. Because of their substantial and widespread use, SVOCs have become ubiquitous environmental contaminants [1]. The plasticizer di-(2-ethylhexyl) phthalate (DEHP) is frequently used as a softener in polyvinyl chloride (PVC) products and building materials, such as vinyl flooring, food packaging materials, and personal care products [2]. Exposure to DEHP has been associated with allergies and asthma, and researches have suggested that exposure may also affect reproductive development in humans [3]. Wang et al. [4] studied pollution problem indoors from PAEs in China. They conclude that PAEs exist in most of the indoor environment in China and DEHP is the most common.

DEHP is emitted slowly into the surrounding environment and has become widely recognized as a major indoor pollutant. It can be easily sorbed to particles and interior surfaces, so its emission may be affected by the characteristics of adsorbent. It is well recognized that particles enhance SVOC flux between surfaces and bulk air [5]. Because the particle size distributions of indoor particles are distinct for different particle sources, the concentrations of DEHP in various phases and exposures to human are different even for the same source, which is seldom taken into account in previous studies.

Our objectives are to clarify the further mechanism of the influence of particle size distribution on phase distributions of DEHP and to estimate its indoor exposure. A lumped model for predicting instantaneous DEHP concentration in gas phase, particle phase, dust phase, and surface phase will be proposed. In the model, ventilation, particle penetrating from outdoor air into indoor air through building envelop and filter, deposition onto indoor surfaces, and resuspension from indoor surfaces are considered for simulating indoor particle concentration with different size distributions including dust.

40.2 Method

40.2.1 The Model

To better estimate the further mechanism of the influence of particle size distribution on DEHP phase distribution and indoor exposure, a schematic representation of a residential room is shown in Fig. 40.1. Vinyl flooring is the only source of DEHP, and there is no particle source in this room. Its conditions are provided in Table 40.1. Here, the room size is the same as that used in Xu and Hubal [6], so that the measured parameters for the particle could be applied in this study.

With reference to Fig. 40.1, the accumulation of particle in the room obeys the following mass balance:

$$V \frac{\mathrm{d}C_p}{\mathrm{d}t} = P_p Q C_{p,o} - Q C_p + \mathrm{RMA}_f - v_d C_p A_s \qquad (40.1)$$

Fig. 40.1 Schematic representation of a life-size residential room
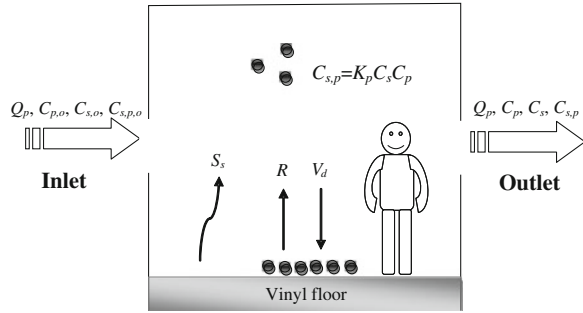
Table 40.1 Conditions for the model room

Parameters	Values
Volume, V (m $\times$ m $\times$ m)	$3 \times 3 \times 3$
Ventilation rate, Q (m^3/h)	13.3
Area of vinyl flooring, A_f (m^2)	9
Area of surface, A_s (m^2)	41[a]

[a] Including ceiling and wall

where C_p (μg/m^3) is the indoor particle concentration, P_p is the particle penetration coefficient, Q (m^3/h) is the natural ventilation rate, $C_{p,o}$ (μg/m^3) is the outdoor particle concentration, R (h^{-1}) is the particle resuspension rate, M (μg/m^2) is the particle mass loading on the surface (ceiling and wall), and v_d (m/h) is the particle deposition velocity. The accumulation of SVOC is given by

$$
V \frac{dC_s}{dt} + V \frac{dC_{s,p}}{dt} + A_s \frac{dC_{s,\text{surf}}}{dt} + A_f \frac{dC_{s,\text{dust}}}{dt} \\
= P_s Q C_{s,o} - Q C_s + P_p Q C_{s,p.o} - Q C_{s,p} + S_s \tag{40.2}
$$

where C_s (μg/m^3) is the gas-phase concentration of DEHP, $C_{s,p}$ (μg/m^3) is the particle-phase concentration, $C_{s,\text{surf}}$ (μg/m^2) is the DEHP concentration on surface, $C_{s,\text{dust}}$ (μg/m^2) is the settled dust-phase concentration, P_s is the penetration of gas, $C_{s,o}$ (μg/m^3) is the outdoor gas-phase concentration, $C_{s,p,o}$ (μg/m^3) is the outdoor particle-phase concentration, and S_s (μg/h) is the emission rate of the DEHP source.

40.2.2 Partition Coefficient

For airborne particles, there is an equation that has been used successfully to parameterize particle/air partition coefficient, or

$$
C_{s,p} = K_p C_s C_p \tag{40.3}
$$

where K_p (m^3/µg) is the particle/air partition coefficient. In a similar way, the fractional concentration of DEHP in dust and the partition coefficient between surface and air are given.

Liu et al. [5] predicted that particles would enhance SVOC flux between surfaces and bulk air, and the extent depended on the particle/air partition coefficient, particle size, and the concentration of particles. Here, we firstly define the adsorbed capacity per particle. It solely depends on the type of particle. Thus, its value will be a constant due to the hypothesis of the single type of spherical particle indoors. Assuming a linear relationship for it, the ratio of the DEHP concentration on a particulate surface to its concentration in the gas phase is equal to the adsorbed capacity coefficient, or

$$K_c = \frac{C_{s,p,s}}{C_s} \tag{40.4}$$

Based on Eq. (40.3), the relationship between particulate size and particle/air partition coefficient is

$$K_p = \frac{6}{D_p \rho_p} K_c \tag{40.5}$$

In Eqs. (40.4) and (40.5), K_c (m) is the sorption capacity coefficient for a type of particles, $C_{s,p,s}$ (µg/m^2) is the particle surface concentration of DEHP, D_p (µm) is the particulate diameter, and ρ_p (g/m^3) is the density of particle.

40.2.3 Estimation of Parameters

As shown in Eq. (40.1), the key parameters of particle fate indoors include the particle penetration coefficient, particle deposition velocity, particle resuspension rate together with the particle mass loading on the surfaces, and the particle emission rate. Particles larger than 10 µm are assumed not to break into rooms by penetration. Here, particles are divided into five groups. All the parameters mentioned above are listed in Table 40.2.

Table 40.2 Parameters for indoor particle accumulation [7]

Size fraction (µm)	Mass fraction (%)	P_p	$R \times 10^6$(1/h)	v_d (m/h)	M^a (mg/m2)
0–0.5	1.4	0.91	0.99	0.18	2,200
0.5–1	2.8	0.74	0.44	0.09	
1–3	8.3	0.83	18	0.51	
3–5	15.3	0.53	18	1.98	
5–10	72.2	0.12	83	6.12	

[a] The mass loading of dust (M) listed in the column is the sum of all size fraction

Fig. 40.2 Relationship of article/air partition coefficient, gas-phase concentration, and particle-phase concentration versus particulate diameter
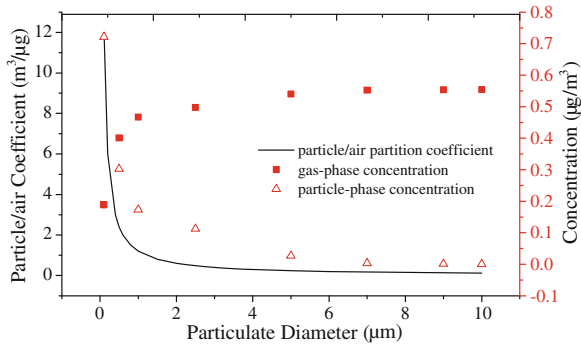
A detailed description of the process of DEHP emission from vinyl flooring is given by Xu and Little [8]. The DEHP emission rate can be expressed by

$$S_s = h_m A_f (C_0 - C_s) \qquad (40.6)$$

where h_m (m/h) is the convective mass transfer coefficient and C_O ($\mu g/m^3$) is the concentration in the air immediately adjacent to the vinyl floor surface.

40.3 Results and Discussion

40.3.1 Comparison with Previous Results that Treat Particle/Air Partition Coefficient as a Constant

The baseline conditions used for the calculation are listed in Table 40.1. The results show that there is an affinity between the DEHP concentration and particle size distribution. Through Eq. (40.5), partition coefficient is inversely proportional to particle diameter. Figure 40.2 illustrates that both particle/air partition coefficient and particle-phase concentration of DEHP decreased significantly with increasing diameter and that gas-phase concentration increased simultaneously.

Table 40.3 Steady-state airborne DEHP concentration for previous models compared against the present model

Parameters ($\mu g/m^3$)	Xu et al.		Liu et al.		Our study	
	$D_p = 0.1\ \mu m$	$D_p = 1\ \mu m$	$D_p = 0.1\ \mu m$	$D_p = 1\ \mu m$	$D_p = 0.1\ \mu m$	$D_p = 1\ \mu m$
C_s	0.019	0.17	0.074	0.36	0.19	0.47
$C_{s,p}$	0.92	0.63	3.57	1.38	0.72	0.18
$C_{airborne}^a$	0.94	0.80	3.64	1.74	0.91	0.65

[a] $C_{airborne} = C_s + C_{s,p}$

As shown in Table 40.3, the gas-phase concentration of DEHP increases and the particle-phase concentration decreases as a result of the increase in particulate diameter. However, we find that for 0.1 μm-diameter particles, gas-phase concentration is dominant in airborne concentration predicted by three studies and that for 1 μm, the contribution of particle-phase concentration in airborne concentration in our study is 27.7 %, which are not as much as predicted by Xu et al. [6]. and Liu et al. [5]. A sufficient large and permanent value of the particle/air partition coefficient could result in particle-phase contributions that are both higher than 75 % in Xu et al. and Liu et al.

40.3.2 Phase Distribution of DEHP

Phase distribution of DEHP in residence is studied to further assess the effects of DEHP on human exposure in more detail. As shown in Table 40.4, the concentration data are particularly interesting and illuminating. Significant compositional differences are observed between airborne DEHP concentration and surface-phase and dust-phase concentrations. DEHP indoors mainly exist on interior surfaces and in settled dust. Compared with Wang et al. [9], the particle-phase concentration in our study is obviously less. One possible explanation is that in our study, the particle/air partition coefficient is treated as a parameter related to particulate diameter.

It should be noted that the different size distributions may lead to a variation in airborne DEHP due to the different contribution of particulate sizes. Figure 40.3 shows the relationship between size fractions and different phase concentrations. Particle phase and dust phase are dominant in the size fraction of 0–0.5 μm due to the high penetration rate and the maximum particle/air partition coefficient. With the increase in particulate size, deposition and resuspension both have an obvious effect. As a result, gas phase is dominant, while particulate diameter is greater than 1 μm. Therefore, controlling gas-phase concentrations of DEHP is the key point for controlling airborne concentrations.

Table 40.4 Concentrations of DEHP in gas, particle, surface, and dust phases

Parameters	Wang et al.	References (max)	Our study
C_s (μg/m^3)	0.012–0.3	0.4 [10]	0.19–0.55
$C_{s,p}$ (μg/m^3)	0.19–4.8	2.18[b]	0.0076–0.73
$C_{s,\text{surf}}$ (μg/m^2)	NA[a]	1,300 [11]	472–1,385
$C_{s,\text{dust}}$ (μg/m^2)	202–5,190	3,392[b]	146–4,980

[a] NA indicates not available
[b] Detected value not published by us
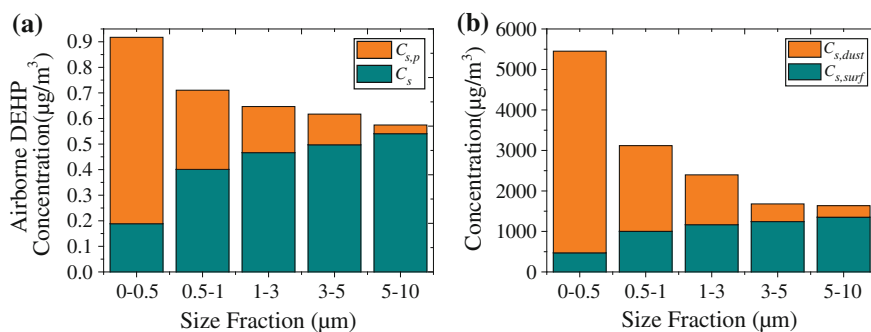
Fig. 40.3 Relationship between size fraction and various phase concentrations

40.4 Conclusions

This model defined a relationship between particle/air partition coefficient and particulate diameter. Results suggest that airborne DEHP is dominated by the particle phase for fine particles (smaller than 0.5 μm in this study) and by the gas phase for coarse particles (larger than 1 μm in this study). Particle penetration and resuspension of coarse particles have an obvious effect on the exposure to airborne DEHP. The above results imply a possible strategy to control various phase DEHP concentrations and exposures.

References

1. Weschler CJ, Nazaroff WW (2008) Semivolatile organic compounds in indoor environments. Atmos Environ 42(40):9018–9040
2. Rudel RA, Camann DE, Spengler JD, Korn LR, Brody JG (2003) Phthalates, Alkylphenols, Pesticides, Polybrominated Diphenyl Ethers, and Other Endocrine-disrupting compounds in indoor air and dust. Environ Sci Technol 37(20):4543–4553
3. Bornehag CG, Nanberg E (2010) Phthalate exposure and asthma in children. Int J Androl 33(2):333–345
4. Wang LX, Zhao B, Liu C, Lin H, Yang X, Zhang YP (2010) Indoor SVOC pollution in China: a review. Chin Sci Bull 55(15):1469–1478
5. Liu C, Morrison GC, Zhang Y (2012) Role of aerosols in enhancing SVOC flux between air and indoor surfaces and its influence on exposure. Atmos Environ 55:347–356
6. Xu Y, Cohen Hubal EA, Clausen PA, Little JC (2009) Predicting residential exposure to phthalate plasticizer emitted from vinyl flooring: a mechanistic analysis. Environ Sci Technol 43(7):2374–2380
7. Liu C, Zhao B, Zhang Y (2010) The influence of aerosol dynamics on indoor exposure to airborne DEHP. Atmos Environ 44(16):1952–1959

8. Xu Y, Little JC (2006) Predicting emissions of SVOCs from polymeric materials and their interaction with airborne particles. Environ Sci Technol 40(2):456–461

9. Wang LX, Zhao B, Liu C, Lin H, Zhang YP (2010) Analysis on exposure of indoor phthalate acid esters. Build Sci

10. Fromme H, Lahrz T, Piloty M, Gebhart H, Oddoy A, Rüden H (2004) Occurrence of phthalates and musk fragrances in indoor air and dust from apartments and kindergartens in Berlin (Germany). Indoor Air 14(3):188–195

11. Clausen PA, Hansen V, Gunnarsen L, Afshari A, Wolkoff P (2004) Emission of Di-2-ethylhexyl phthalate from PVC flooring into air and uptake in dust: Emission and sorption experiments in FLEC and CLIMPAQ. Environ Sci Technol 38(9):2531–2537

Chapter 41
The Measurement and Simulation of Thermal Environment in Heritage Nanjing Tulou Buildings, China: A Comparative Study

Xiao Sun, Qindi Li and Xudong Yang

Abstract *Introduction* World Heritage Site—Nanjing Tulou buildings, which were composed of thick (about one meter) rammed earth walls and wooden frameworks, are large-scale civilian residential buildings distributed across the southeastern China. The characteristics of indoor thermal environment in Tulou buildings are, however, unavailable in the literature. *Method* In this study, the measurement of indoor thermal environment along with a survey of both thermal comfort and energy consumption in Nanjing Tulou buildings was taken, both in summer and in winter. *Results* Based on the measurement data obtained, in a typical summer day, when the maximum outdoor temperature reached 35.0 °C, the maximum indoor temperatures of three Tulou buildings were 28.0, 28.6, and 28.9 °C, respectively, lower than the maximum indoor temperature of a normal rural building in that region. In a typical winter day, when the minimum outdoor temperature reached 9.9 °C, the minimum indoor temperatures of three Tulou buildings were 15.8, 14.4, and 13.8 °C, respectively, higher than the minimum indoor temperature of a normal rural building. Meanwhile, through the survey, the results showed that the thermal comfort satisfaction was higher and average energy consumption per household was lower in Tulou buildings than in normal rural buildings, respectively. *Discussion and conclusions* A model was set up using DeST-h to simulate the indoor temperature trends under different circumstances. It could be concluded that the better indoor thermal environment of Tulou buildings benefited from walls of substantial thickness, large ventilation rates in summer, and better airtightness in winter. Inspired by this study, the potential implications for future low-energy rural housing construction were discussed.

Keywords Tulou buildings · Thermal environment · Measurement · DeST-h

X. Sun · Q. Li · X. Yang (✉)
Department of Building Science, School of Architecture,
Tsinghua University, Beijing, China
e-mail: xyang@mails.tsinghua.edu.cn

41.1 Introduction

In China, the total rural housing floor area reached approximately 60 % of the total building floor area in 2006 [1]. With the severe energy situation and people's demand of higher living standards, the comfort and energy saving of rural residential buildings should be given attention [2].

Tulou ("earthen house" or "earthen towers") is a kind of large-scale civilian residential buildings built mainly of rammed earth and in a wooden framework, distributed across the mountainous region of southeastern China such as Fujian, Jiangxi, and Guangdong provinces. Tulou buildings in Fujian Province have been designated by UNESCO designation as a world heritage site [3]. The structures of Tulou buildings not only facilitate environmental sustainability, but also endow the inhabitants with material, social, and spiritual sustainability [4]. The usual Tulou building is an enclosed communal house with three or more story to meet the needs of the whole clan living together and a sound defensive function (Fig. 41.1) [5]. Each household owns one room in each story vertically, first story as kitchen and sitting room, second story as larder, and the higher story rooms as bedrooms.

The existence of Tulou buildings may give us some enlightenment on the designing of future rural housing. Through extensive literature survey, it was found that Tulou buildings were comfortable to live, warm in winter, and cool in summer [3]. However, the studies of Tulou buildings were mainly focused on architecture or civil engineering. Wang's work, using a simulation program, showed that the thermal performance of the earthen tower is "excellent" [6]. But it was indistinct to say "excellent" because no comparison was made in their study. Yuan et. al. have done measurements and CFD simulations to prove that Tulou buildings had better thermal environment than normal rural buildings in that area [7, 8], but the studies were limited in analysis. There was still a need for reliable measurement data and systematic thermal analysis of the thermal environment.

Fig. 41.1 The aero view (*left*) and inside (*right*) of Tulou buildings

In this study, the measurement of indoor thermal environment along with a survey of both thermal comfort and energy consumption in Nanjing Tulou buildings and normal rural buildings (Fig. 41.2) was taken. Based on the data obtained from the measurement, the characteristics of thermal environment in Tulou buildings, including the indoor temperature and the ventilation rates on each story, were obtained. A model was set up using DeST-h, and the effect of wall thickness was investigated. The results of energy consumption and thermal comfort have been discussed in another article [9]. Through comparing with the normal rural buildings in the same region, the possible reasons for the characteristics of thermal environment in Tulou buildings were analyzed. Furthermore, implications for future rural housing construction were discussed.

41.2 Method

41.2.1 Building Types and Envelope Characteristics

The studied Tulou buildings included Tianluokeng Tulou Cluster, Hekeng Tulou Cluster, and Huaiyuan Tulou, which are on the World Heritage List. The studied normal rural buildings belong to Kanxia village near the Tulou buildings. Tulou buildings are characterized by thick walls (Table 41.1).

Fig. 41.2 The photograph of normal rural buildings built of rammed earth (*left*) and brick (*right*)

Table 41.1 Basic information of studied Tulou and normal rural buildings

Type	Name of the building	Thickness of envelope (m)	Height (m)	Number of storys
Tulou cluster	Ruiyun	1.2	11.2	3
Tulou cluster	Chaoshui	1.7	11.3	3
Tulou cluster	Huaiyuan	1.2	13.5	4
Normal rural buildings	Jian's House	0.4	7–8	2

41.2.2 Measurement of Indoor Thermal Environment

August 4, 2011, and February 15, 2012, were, respectively, chosen as the typical summer day and winter day. We chose the south room in the studied Tulou and normal rural buildings and put the temperature and humidity data logger (Fig. 41.3a WSZY-1, Tian Jianhuayi Technology Development Co., Ltd) in the middle of each room at the height of 1.2 m. The temperature and humidity data logger for outdoor environment had extra shielding to prevent solar radiation. The temperature and humidity data were recorded every minute.

For the selected winter day, natural ventilation rates of rooms on each floor in Huaiyuan Tulou building were measured, with doors and windows open or close, respectively. Ventilation rates were obtained by the tracer gas decay method (Fig. 41.3b carbon dioxide source & (c) Telaire 7001 CO_2 sensor). Carbon dioxide extinguisher was used as the tracer gas source. Using the same method, the ventilation rates of one representative normal rural building were also measured.

41.2.3 Simulation in DeST-h

DeST-h is simulation software for building thermal environment, especially for residential buildings, developed by Tsinghua University through more than 10 years' effort. The load simulation used by DeST-h is the state space method [10]. A 34-room model was set up in DeST-h to explore the relationship between natural room temperature and some factors, such as ventilation and wall thickness. The parameter values were set as presented in Table 41.2. Household appliances load had been investigated in our previous study [9] (Fig. 41.4).
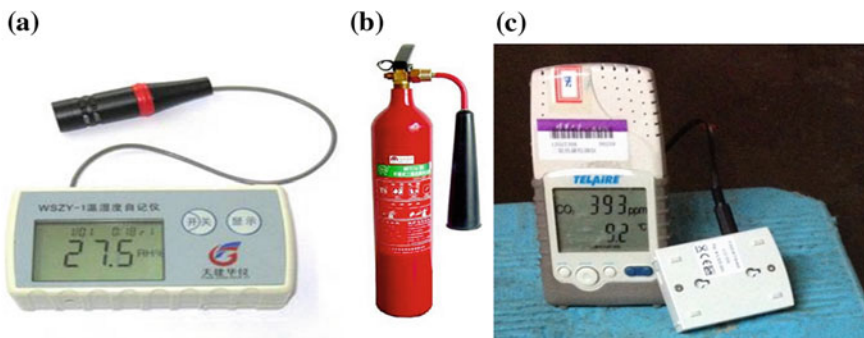
Fig. 41.3 Instruments used for measuring thermal environment: **a** temperature and humidity data logger; **b** carbon dioxide extinguisher; **c** carbon dioxide sensor

Table 41.2 Tulou input parameters set in DeST-h	Geometric parameters	
	Roof height	1.7 m
	Room height	2.7 m
	External diameter	39 m
	Building materials	
	Floor	120-mm cedar board
	External wall	1,200-mm adobe wall (controlled variable)
	Internal wall	700-mm adobe wall
	Roof	160-mm cedar board +10 mm tile
	Door	25-mm pine board
	Window	6-mm single-layer glass
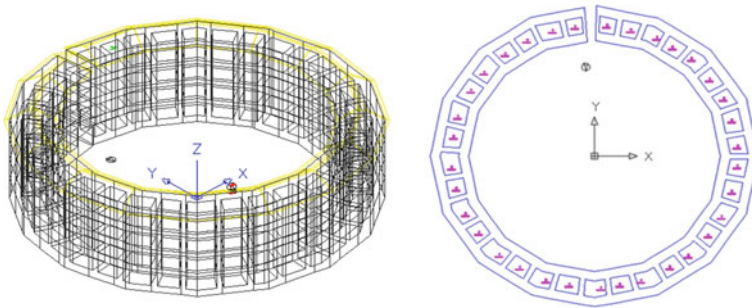
Fig. 41.4 The model setup in DeST-h: 3D view and plane graph

41.3 Results

41.3.1 Comparison of Indoor Temperature

From Figs. 41.5 and 41.6, when the maximum outdoor temperature reached 35.0 °C, the maximum indoor temperatures of three Tulou buildings were 28.0, 28.6, and 28.9 °C, respectively, lower than 29.2 °C, the maximum indoor temperature of a normal rural building in that region. In a typical winter day, when the minimum outdoor temperature reached 9.9 °C, the minimum indoor temperatures of three Tulou buildings were 15.8, 14.4, and 13.8 °C, respectively, higher than that in the normal rural building counterpart (11.2 °C).

41.3.2 Comparison of Indoor Humidity

From Fig. 41.7, there were no obvious differences in the humidity level between Tulou buildings and normal rural building.
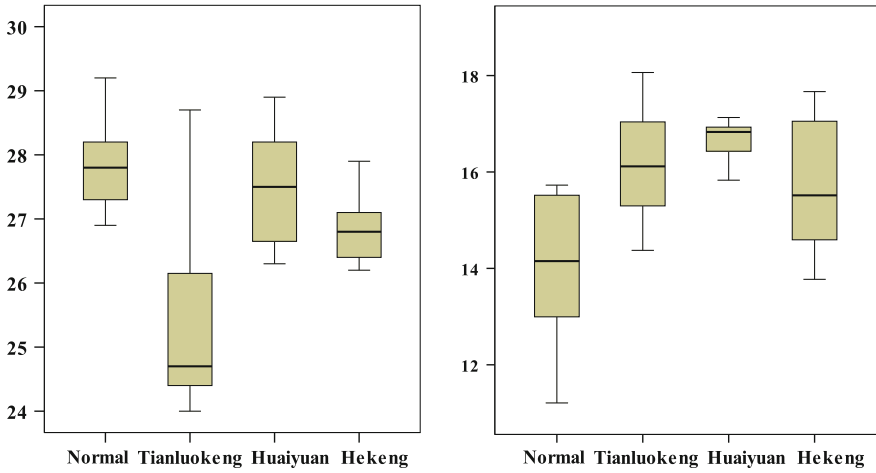
Fig. 41.5 Temperature comparison between normal rural building and Tulou buildings, in summer (*left*) and winter (*right*). The gage uses Celsius
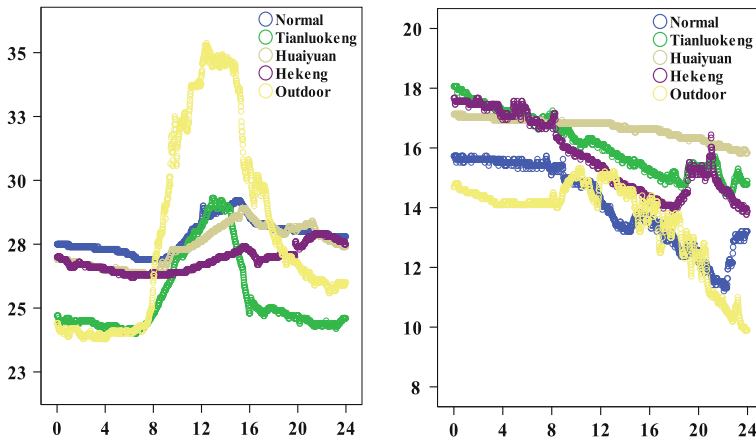
Fig. 41.6 Variations in outdoor and indoor temperatures of normal rural building and Tulou buildings, in summer (*left*) and winter (*right*). The gage uses Celsius and hour

41.3.3 Comparison of Indoor Ventilation Rates

Table 41.3 showed the results of natural ventilation rates in Huaiyuan Tulou building and normal rural building. The ventilation rates in Tulou were significantly higher. However, the normal rural buildings had better airtightness.
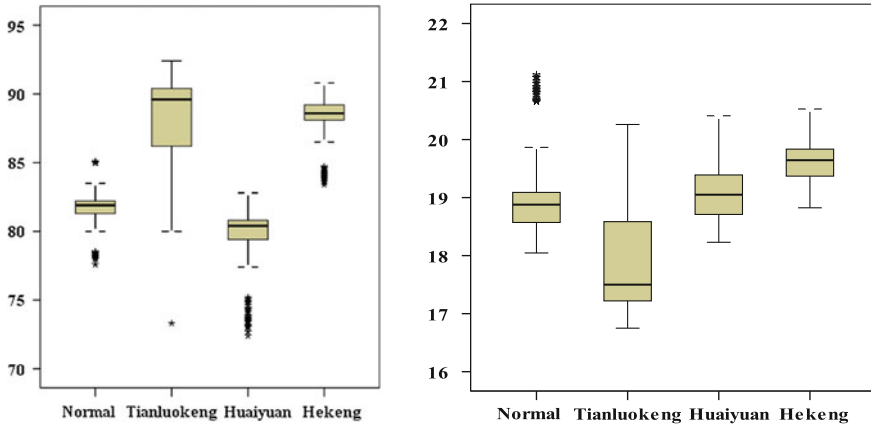
Fig. 41.7 Humidity in normal rural building and Tulou buildings in summer, relative humidity (*left*, %), and absolute humidity (*right*, g/kg)

Table 41.3 Natural ventilation rates (h^{-1}) in Huaiyuan Tulou and normal rural buildings

Normal rural building				Huaiyuan Tulou buildings							
Bedroom (second floor)		Kitchen (first floor)		Kitchen (first floor)		Storage (third floor)		Bedroom (third floor)		Bedroom (fourth floor)	
WO[a]	S	DO	S	DO	S	WO	S	WO	S	WO	S
7.336	0.180	10.38	7.982	12.51	10.22	16.43	0.835	20.78	1.242	19.24	1.148

[a] *WO* means window open; *DO* means door open; *S* means sealed

41.4 Discussion and Conclusions

41.4.1 Simulation in DeST-h

Simulation results (Fig. 41.8) show that with the increasing thickness of rammed earth wall, the room temperature tended to be flat in both summer and winter. Larger thermal mass due to thick wall could store much heat against short-term temperature variations in the outdoor. Buildings with thicker walls had lower room temperature in summer and higher room temperature in winter.

41.4.2 Thermal Comfort Satisfaction and Energy Consumption

The survey results [9] showed that the energy consumption of summer cooling in Tulou buildings was lower than that in normal rural buildings. In Tulou buildings,
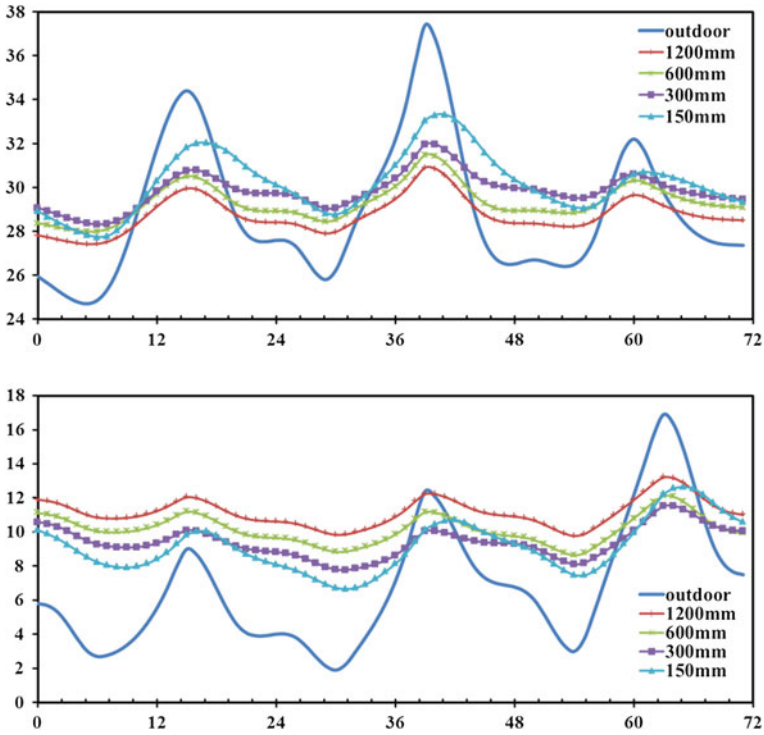
Fig. 41.8 DeST-h simulation results: natural temperature in the bedroom of Huaiyuan Tulou building: 8.3–8.5 in typical summer days; 2.14–2.16 in typical winter days. The gage uses Celsius and hour

the percentages of households that use electric fans and air conditioners for cooling were 74.8 and 0.0 %, respectively, which were lower than that in normal rural buildings (96.9 and 11.3 %, respectively). Thermal comfort survey results indicated better indoor thermal comfort in Tulou than in normal rural buildings: satisfaction vote: 0.64 versus 0.50; thermal sensation vote (TSV): 0.29 versus 0.71; thermal comfort vote (TCV): 0.12 versus 0.54.

In winter, the energy consumption for heating in both Tulou and normal rural buildings was quite low. The results of thermal comfort survey indicated better indoor thermal comfort in Tulou than in normal rural buildings: satisfaction vote: 0.48 versus 0.30; TSV: −0.50 versus −0.78; TCV: 0.34 versus 0.65.

41.4.3 Low-Energy Rural Housing

The results indicated that the residents in Tulou buildings were able to achieve better indoor thermal comfort with lower energy consumption than those in normal

rural buildings. Low heat transfer coefficient and high thermal mass and reasonable ventilation could benefit indoor thermal environment in southeast China. In the future, with the development of economy in rural China, the residents may consume more energy to achieve better indoor thermal comfort. In that case, it is important to learn the internal discipline of traditional local-style dwelling houses, to construct real sustainable buildings.

References

 1. Thuberc (2008) Annual report on China building energy efficiency. China Architecture & Building Press, Beijing
 2. Sun JW (1996) Real rural residential energy consumption in China, 1990. Energ Policy 24:827–839
 3. United Nations Educational, Scientific and Cultural Organization (UNESCO) (2008) Nomination File of Fujian Tulou
 4. Lowe KD (2012) Heaven and earth—sustaining elements in Hakka Tulou sustainability 4:2795–2802
 5. Qi W (2011) http://www.nipic.com/
 6. Wang F (1992) A study on the thermal performance of the earthen tower in summer. Build Environ 27:413–421
 7. Yuan J, Ran R (2008) Tulou rural house of indoor thermal environment test. J Huaqiao Univ (Nat Sci) 1:91–93 (in Chinese)
 8. Yuan J, Ran R, Huang Y (2011) Simulation of wind environment of Tulou buildings in Fujian residential space. J Xiamen Inst Technol 2:45–48 (in Chinese)
 9. Li QD, Sun X, Chen C, Yang XD (2012) Characterizing the household energy consumption in heritage Nanjing Tulou buildings, China: A comparative field survey study. Energ Build 49:317–326
10. Zou Y, Shen TX (2011) Research on simulation method of subdividing spaces based on DeST-h. 2011 Int Conf Mach Intell (ICMI 2011) 24: 81–86

Chapter 42
Effects of Test Methods on Human Axillary Temperature

Lijuan Wang, Yanfeng Liu, Jiaping Liu, Yuhui Di and Hao Zhou

Abstract The objective of this paper is to study the effects of test methods on axillary temperature. Three test methods were that the mercury thermometer was only in the left armpit, alternately in left and right armpits, and alternatively passed from one subject to another. The results show that the effects of the three test methods on axillary temperature are obvious. Besides, the axillary temperature is obviously affected by handedness. For right-handed people, the axillary temperature in the right armpit is higher than that in the left armpit, while for left-handed people, it is the opposite. The maximum difference between right and left axillary temperatures is 0.60 °C in this research.

Keywords Axillary temperature · Test method · Handedness

42.1 Introduction

In building environment, human thermal comfort and thermal adaptiveness are studied extensively. Before these researches, human body must be in normal core temperature. In Professor Fanger's experiment [1], oral temperature was taken after entering the pre-test room and no subject whose temperature was above

L. Wang · Y. Di
School of Environmental and Chemical Engineering, Xi'an Polytechnic University, Xi'an 710048 Shaanxi, China

Y. Liu (✉) · H. Zhou
School of Environmental and Municipal Engineering, Xi'an University of Architecture and Technology, Xi'an, 710055 Shaanxi, China
e-mail: lyfxjd@163.com

J. Liu
School of Architecture, Xi'an, University of Architecture and Technology, Xi'an 710055 Shaanxi, China

37.2 °C was permitted to participate. Core temperature was also tested by many researchers about human thermal sensation or thermal comfort. Huizenga et al. [2] studied skin and core temperature responses to partial—and whole-body heating and cooling. Kilic et al. [3] studied the required core temperature for thermal comfort by theoretical formulas and experiment. Professor Yuan [4] also tested core temperature in his research about the mathematical model of human thermoregulation system with extra-vehicular activity suits. So core temperature is very important in the research of human thermal response.

Core temperature also is studied by many medical scholars. The temperatures that reflect the core temperature are rectal temperature, oral temperature, and axillary temperature. Giuffre [5] studied the accuracy of the axillary site as an indicator of core temperature. Barringer [6] provided the agreement between temporal artery, oral, and axillary temperature measurements in the perioperative period. Ahmadnia [7] proved the use of intravesical temperature as core temperature following kidney transplantation and compared it with rectal, axillary, and oral measurement. Wilshaw [8] compared the use of tympanic, axillary, and rectal thermometers in infants. Many researchers studied the accuracy of the three approaches to reflect the core temperature. In this paper, the effects of test methods will be supplied.

Rectal temperature is not easily tested for sedentary subjects. Oral temperature test impacts questionnaire. The axillary temperature was proved clinically meaningful to reflect the core temperature [5, 9]. So the axillary temperature is selected in this experiment.

42.2 Method

42.2.1 Laboratory

The laboratory dimension was $4.2 \times 3.0 \times 3.3$ m, as shown in Fig. 42.1. The filled circle represented the mercury thermometer, while the hollow circle represented the subjects. The subjects were numbered by capital letters in each test. A, C, E, G, I, K, and M represented men, while B, D, F, H, J, L, and N represented women. The left or right in Fig. 42.1 was subjects' left or right side.

The axillary temperature was measured by mercury thermometers under the armpit. Their measuring errors were +0.10 °C and −0.15 °C. The measuring time for each test should be 10–15 min. It was 12 min in this research.

42.2.2 Requirements of Subjects

This research involved 70 Chinese subjects, 35 men and 35 women. For men, the age, weight, and height were 24 ± 2 years old, 69.40 ± 8.30 kg, and

Fig. 42.1 Laboratory
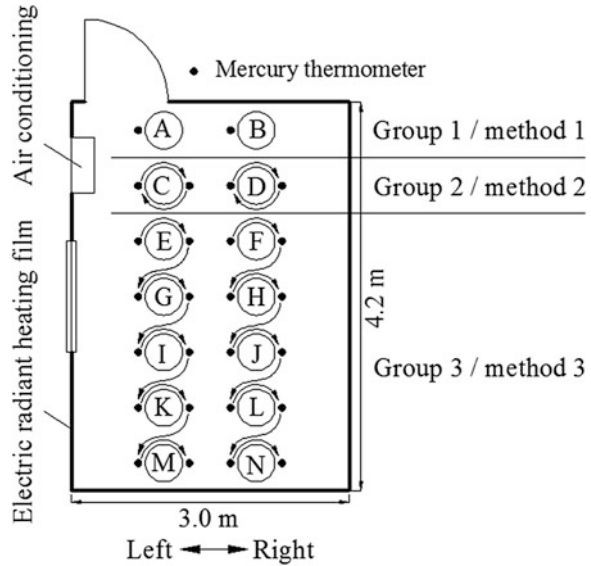
1.729 ± 0.08 m, respectively, while for women, they were 24 ± 2 years old, 54.56 ± 8.60 kg, and 1.629 ± 0.051 m. The somatotype of all the subjects was moderate. The body mass index (BMI) was 20–25 for male subjects and 19–24 for female subjects.

Before entering the laboratory, the subjects were asked to previously have a normal night's sleep and a normal meal. After entering the laboratory, it was made sure that the subjects stayed awake 40 min before being tested. It is well known that the axillary temperature is affected by strenuous activity, boiled or cold drinking, and alcohol drinking. So prior to the experiment, these activities were prohibited. Before each test, if there was sweat in the armpit, it was blot with a dry towel.

42.2.3 Experimental Procedure

The subjects were divided into three groups according to three test methods. There were 5 men and 5 women in group 1/method 1, 5 men and 5 women in group 2/method 2, and 25 men and 25 women in group 3/method 3. The subjects were sedentary. They were uniformly distributed in the laboratory, and the distance between subjects was about 0.2 m, shown in Fig. 42.1.

For the method 1, the mercury thermometers were used only in the left armpit of subjects A and B, as shown in Fig. 42.1. For the method 2, the mercury thermometers were used alternately in the left and right armpits of subjects C and D. For the method 3, the mercury thermometers were used alternatively from one to

another of subjects E, F, G, H, I, J, K, L, M, and N. After testing both in left and right armpits, the subjects E and F would pass the mercury thermometers to G and H, then to I and J, K and L, and at last to M and N in turn. Method 3 is the common method to measure axillary temperature. In this experiment, all the subjects were tested in the evening, the clothing thermal resistance was 0.87 clo, and environment temperature was 22 °C. The three methods were measured 5 times. For each time, the subjects were different.

For each condition, the mercury thermometer kept for 12 min in the armpit, while it needed 3 min to read temperature value, change clothes, or dry sweat. So it needed about 15 min to obtain each axillary temperature. During the whole test, the axillary temperature was tested 10 times in the left armpit of subjects A or B, 5 times in the left or right armpit of subjects C or D, and only once in the left or right armpit of subjects E, F, G, H, I, J, K, L, M, or N.

42.3 Results

The tested results are shown in Figs. 42.2 and 42.3. In those figures, subjects J and M are left-handed people, while other subjects are right-handed people. The axillary temperature of subjects A and B was tested by method 1, the axillary temperature of subjects C and D was alternately tested by method 2, and the axillary temperature of subjects E, F, G, H, I, J, K, L, M, and N was tested by method 3. In Figs. 42.2 and 42.3, L means the axillary temperature in the left armpit, R means the axillary temperature in the right armpit, X/L means the axillary temperature of subject X in the left armpit, and X/R means the axillary temperature of subject X in the right armpit. The short dotted line shows the variation tendency of axillary temperature in the ipsilateral armpit for right-handed subjects and in the opposite armpit for left-handed people. The time in horizontal axis is the moment of taking out the mercury thermometer.

Figure 42.2 shows the axillary temperature of subjects A, B, C, and D in the environment temperature of 22 °C and with the clothing thermal resistance of 0.87 clo. At 0, all the axillary temperature of subjects A, B, C, and D was tested in the left armpit. The axillary temperature of women is about 0.17 °C higher than men. At 15 min, the axillary temperature of subjects A and B was still tested in the left armpit, but the axillary temperature of subjects C and D was tested in the right armpit. The axillary temperature of subjects A and B is higher than that of subjects C and D, and from 30 min to 135 min, this phenomenon always exists. For subjects A and B, the mercury thermometer was always in the left armpit, and the left arm always pressed the trunk. So there was a sealed microenvironment in the left armpit. For subjects C and D, the axillary temperature was alternately tested in left and right armpits. When the left arm pressed the trunk, the right arm was relaxed, while when the right arm pressed the trunk, the left arm was relaxed. The microenvironment in the left or right armpit was open for outside environment. Therefore, the axillary temperature of subjects A and B is higher than that of

Fig. 42.2 Axillary temperature of subjects A and B for method 1 and C and D for method 2
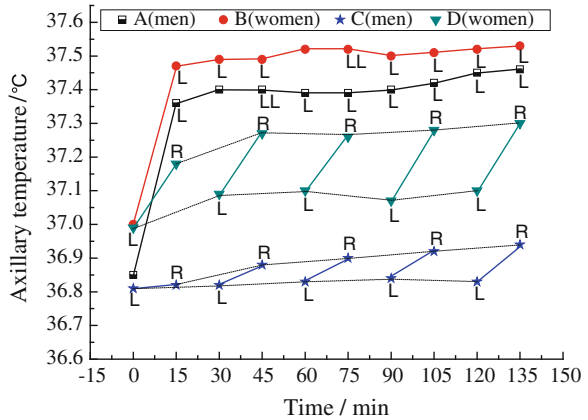
Fig. 42.3 Axillary temperature of subjects E, F, G, H, I, J, K, L, M, and N for method 3
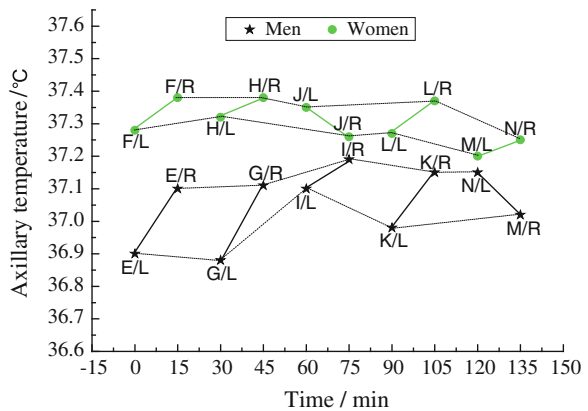
subjects C and D. From 0 to 135 min, whatever tested only in the left armpit or alternately in left and right armpits, the axillary temperature of women is higher than that of men.

For subjects A and B in Fig. 42.2, the axillary temperature increases with time. Since the time in horizontal axis is the moment of taking out the mercury thermometer, the axillary temperature increased faster in the first 30 min. The axillary temperature of A and B can maximally increase by 0.61 and 0.53 °C, respectively. For subjects C and D in Fig. 42.2, the axillary temperature in the right armpit is higher than that in the left armpit. The difference between right and left axillary temperature is 0.21 °C maximally and 0.13 °C averagely.

Figure 42.3 shows the axillary temperature of subjects E, F, G, H, I, J, K, L, M, and N in the same environment temperature 22 °C and with the same clothing thermal resistance 0.87 clo. The axillary temperature in Fig. 42.3 was tested only once in the left or right armpit and was not affected by sealed microenvironment. So, the axillary temperature in the ipsilateral armpit is almost the same for each

right-handed subject. For subjects J and M who are left-handed people, the axillary temperature in the left armpit is higher than that in the right armpit. For other subjects who are right-handed people, the axillary temperature in the right armpit is higher than that in the left armpit. The difference between right and left axillary temperature is 0.23 °C maximally and 0.12 °C averagely. That proved again that the axillary temperature is related to handedness.

Figures 42.2 and 42.3 show that from method 1, 2, and 3, the effect of sealed microenvironment on axillary temperature weakens gradually, and the increase of axillary temperature with time diminishes gradually. So the test methods affect the axillary temperature.

42.4 Conclusions

From test method 3 (alternatively from one subject to another), test method 2 (alternately in left and right armpits), and test method 1 (only in the left armpit), the axillary temperature increases gradually because it is affected by sealed microenvironment of the armpit. To evaluate core temperature in a climate chamber, repeated test in the same armpit can produce errors. In that case, oral temperature or anal temperature should be considered.

The data tested by method 2 and 3 indicate that the axillary temperature is affected by handedness. For the right-handed people, the axillary temperature in the right armpit is higher than that in the left armpit, while for left-handed people, it is opposite. From all the data, the maximum difference between right and left axillary temperature is 0.23 °C, and the average difference is 0.13 °C.

The findings are helpful to analyze core temperature of human body in a climate chamber. All the data of axillary temperature are tested in Chinese laboratory. Whether all the results in this paper apply to people of other nations or other experiment conditions? It needs to be proved.

References

1. Fanger PO (1982) Thermal comfort. Krieger Publishing Company Malabar, Florida
2. Huizenga C, Zhang H, Arens E et al (2004) Skin and core temperature response to partial-and whole-body heating and cooling. J Therm Biol 29:549–558
3. Kilic M, Kaynakli O, Yamankaradeniz R (2006) Determination of required core temperature for thermal comfort with steady-state energy balance method. Int Commun Heat Mass 33:199–210

4. Yuan XG (2005) Mathematical model of human thermoregulation system. University of Aeronautics and Astronautics Press, Beijing
5. Giuffre M, Heidenreich T, Carney-Gersten P et al (1990) The relationship between axillary and core body temperature measurements. Appl Nurs Res 3(2):52–55
6. Barringer L, Evans C, Ingram L et al (2012) Agreement between temporal artery, oral, and axillary temperature measurements in the perioperative period. J Peroanes Nur 27(3):45–46
7. Ahmadnia H, Khaje Daluee M, Mojahedi M et al (2006) Use of intravesical temperature as core body temperature following kidney transplantation and comparison with rectal, axillary and oral measurement. Urology 68:259
8. Wilshaw R, Beckstrand R, Waid D et al (1999) A comparison of the use of tympanic, axillary, and rectal thermometers in infants. J Pediatr Nurs 14(2):88–93
9. Fulbrook P (1993) Core temperature measurement: a comparison of rectal, axillary and pulmonary artery blood temperature. Intens crit care nurs 9(4):217–225

Chapter 43
Using Natural Ventilation in Office Buildings Under Subtropical Climate: A case Study in Shenzhen

Jérôme Damiens, Min Li, Zufeng Pei, Yimin Liu and Yingxin Zhu

Abstract Although thermal comfort standards indicate that in hot climates natural ventilation can offset the temperature above which air conditioning becomes necessary, actual applications remain scarce. This paper details the results of the post-occupancy evaluation of an office building in the subtropical Chinese city of Shenzhen, which uses natural ventilation through user-controlled windows to reduce yearly air-conditioning time by 35 %. Investigation of the indoor environment and thermal comfort of occupants showed overall satisfaction. Electricity consumption of the office part of the building was found to be 60.2 kWh/m^2.a, which is below the standard deviation band of a statistical sample of 57 Shenzhen office buildings. These results support the feasibility of using natural ventilation in mixed-mode buildings in subtropical climates for increased energy efficiency.

Keywords Natural ventilation · Mixed-mode building · Subtropical climate · Building energy consumption · Indoor environment · Occupant satisfaction · Case study

43.1 Introduction

The traditional comfort standard for office building design uses the predicted mean vote (PMV) index, which estimates occupants' satisfaction based on 6 physical parameters. Because this approach does not apply properly to free running spaces

J. Damiens · M. Li · Z. Pei · Y. Liu
Shenzhen Institute of Building Research Co. Ltd, 29, Meiao 3rd Rd.,
Upper Meilin, Futian District, Shenzhen, China
e-mail: liuym@ibrcn.com

Y. Zhu (✉)
Department of Building Science, Tsinghua University, Beijing 100084, China
e-mail: zhuyx@tsinghua.edu.cn

such as naturally ventilated (NV) rooms, alternative standards were developed for such spaces based on worldwide field studies. They link the acceptable indoor temperature range to an average of the mean temperature over the preceding few days; other parameters are either deemed marginally relevant (humidity) or will be controlled by occupants (clothing and wind speed) [1–3].

Although there are standards, natural ventilation is seldom used in office buildings in warm climates: the smaller number of parameters they deal with might increase perceived risk for professionals unaccustomed to this kind of buildings, especially as there is a lack of documented cases of offices using either NV or a mixed-mode system (NV part of the year, AC the rest of the time). Another issue is that current NV standards have no special focus on the upper limit of their applicability range; therefore, NV might not be envisioned as a potential solution if humidity is high and/or indoor temperatures surpass 26 °C.

In the decades to come, significant numbers of new offices will be built in places with warm and humid climates such as China and Brazil, and higher expected levels of comfort will lead to a huge increase in energy demand if traditional designs are employed [4]. Vernacular architecture in Chinese sub-tropical areas makes effective use of natural ventilation [5, 6], and a number of results show that air circulation can be very effective in offsetting the maximum acceptable temperature in a work space [7–11]. Therefore, there is a need to further assess the potential of natural ventilation for offices in subtropical and tropical areas.

In this paper, we present the results of a study on the energy and comfort performances of the Shenzhen Institute of Building Research (iBR) headquarters, a mixed-mode office building with a bioclimatic design.

43.2 Presentation of the Studied Building

43.2.1 Climate and Geography

The building is located in Shenzhen, South China, on the border with Hong Kong.

Shenzhen has a hot, humid, subtropical climate (Köppen *Cwa*). Average outdoor temperatures range from 32 to 26 °C in July and 20–12 °C in January. Summer is damp with precipitations up to 638 mm in August, causing high humidity. There-fore, the average office building needs AC 10 months a year. The low latitude (22°33'N) results in significant radiation levels year round, with even north facades receiving direct radiation during the summer day if not properly shaded.

The building is located in a recently developed district located on the southern side of a mountain chain, surrounded by forested slopes on its eastern, western, and northern sides. Dominant wind directions are from the north in winter and from the southeast in summer. Traffic around the building is low; there is a highway at mid-slope on the eastern hillside.

43.2.2 Description of the Building

The appearance and schematic plan of the building can be seen on Fig. 43.1. It has been in use since mid-2008, and electricity use has been stable since 2010, making it suitable for analysis. The building also uses some natural gas for the kitchens.

43.2.2.1 Building Design

The 15-floor building contains spaces with various functions: offices, laboratories, exhibition areas, hanging gardens, conference and meeting rooms and accommodations for visiting experts, and a canteen. Design features relevant to this study include the following:

- Mixed-mode building: AC is used during summertime and NV during the rest of the year (no space heating in winter),
- Natural ventilation through operable windows: occupants can use them at discretion during the NV period. The conference room can also be naturally ventilated and lit thanks to the exterior wall, which can be opened,

Fig. 43.1 *Left*: picture of the building's *southeast* side. *Top right*: view on the central corridor platforms in the upper part of the building. *Bottom right*: schematic view of the floor plan of the *upper* part of the building; 1 (*orange*): working areas equipped with AC; 2 (*light green*): outside corridor and stairs; 3 (*dark green*): outside functional areas (for meeting, hot water, printers); 4 (*gray*): bathrooms, indoor stairs, elevators, and technical rooms

- The building has a U shape to enhance natural ventilation and limit room depth (north and south areas have a depth of 17.5 and 15 m, respectively),
- Exposed windows are equipped with horizontal light shelves, providing shading, and the building is topped by a ventilated roof that shades the center void,
- The main lobby and staircase, each floor's corridor, hot-water room, and smoking area are all outside spaces,
- Energy-saving lighting controlled by occupants through switches,
- Solar energy systems on the roof and west facade provide hot water and electricity.

43.2.2.2 Air-Conditioning System

The building is equipped with an AC system with independent temperature and humidity control.

Humidity is controlled with a liquid desiccant dehumidifier, which treats fresh air sent to the rooms. Humidity values measured during work hours in the AC period were about 10 % RH under night-time values.

Each of the two rooms on each floor has its own small chiller unit for temperature control. Cold water at about 16 °C is provided to fan coil units in the room. Any of the chillers can be turned down independently from the rest of the system.

All these systems are linked to two shared cooling towers.

The AC system is typically used for 6 months per year from mid-April to mid-October, similar to the average office building in Beijing. During usage periods, space cooling runs from 8:30 to 18:00 on workdays.

Lastly, some additional split units are installed in a few specific rooms (elevators, IT rooms, the control room, direction offices, and apartments).

43.3 Indoor Environment and Comfort

The core question about this building is the kind of environment—especially from a thermal point of view—it provides and whether it is judged to be comfortable.

Starting from August 2012, ten humidity and temperature data loggers were installed in the tenth floor southern open working area. A temperature data logger was also installed on the floor's outside platform. Hourly data series were obtained from nine of the indoor loggers. Outdoor data had to be corrected manually for aberrant values linked to direct sunshine on the captor in the morning.

Occupants in this area were asked to fill a questionnaire on thermal sensation and comfort once to twice a week. Questions included thermal sensation and expectation. This study on indoor environment and comfort is still ongoing, and more complete results will be provided in further work.

Current results cover the end of the AC period (August 24–October 19, 360 working hours, 209 valid questionnaires) and the beginning of the NV period (October 22–November 13, 169 working hours, 117 valid questionnaires).

43.3.1 Indoor Environment During Work Hours

Figure 43.2 shows the relationship between the average of the nine indoor temperature measurement points and outdoor temperature during work hours. The regression shows that the AC system maintains room temperature in the range of 26–27 °C (249/360 h, 69.2 %). Average indoor temperature was over 28 °C during 15 of the total 360 h (4.2 %) of the AC period, and during 25 of the total 169 h (20.8 %) of the NV period.

43.3.2 Reported Comfort

Figure 43.3 shows the distribution of thermal expectation votes in function of the average indoor temperature during working hours. The percentage of working hours spent at each temperature is also given. Results show that in both AC and NV modes, a majority of participants (typically 70 %) wish temperature to remain constant under the most frequent temperature levels in the room. Further study will focus on obtaining more data regarding temperatures above 28 °C during the NV period.

The repartition of thermal sensation votes can be found in Fig. 43.4. It shows overall satisfaction of occupants in both periods.
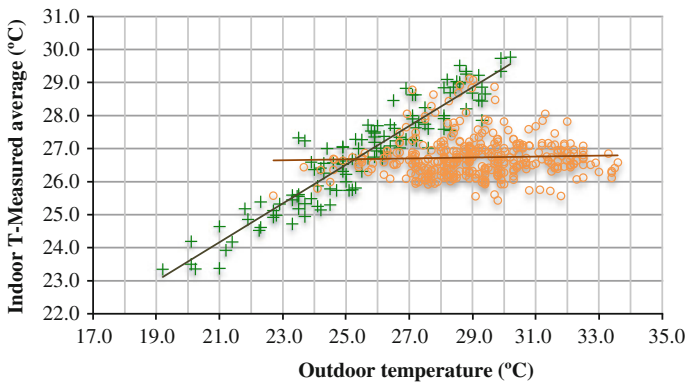
Fig. 43.2 Relationship between outdoor temperature and the spatial average of indoor temperature, both during the AC period (orange data) and the NV period (*green* data)
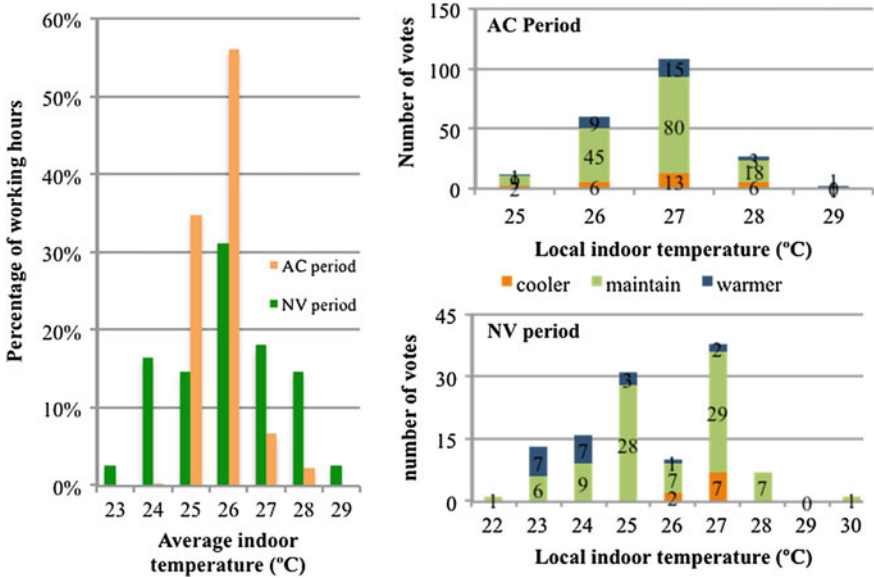
Fig. 43.3 *Left*: percentage of working hours at a given room temperature; *right*: expectation votes of occupants at each temperature during AC and NV working hours
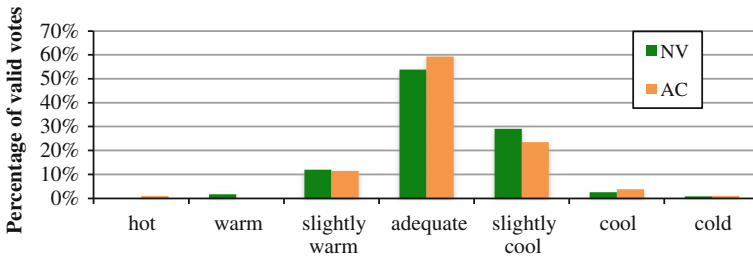
Fig. 43.4 Repartition of thermal sensation votes—total number of valid votes: NV period, 117; AC Period, 209

43.4 Energy Consumption

Monthly electricity use data compiled from the on-site automated monitoring system from January 2010 to October 2012 were provided by iBR. This set of data was checked for errors using electricity use data from power bills and monthly manual handmade records provided by the property management. After corrections, a coherent composite data set was built ensuring a total error level (global meter value—sum of value from all the branches) of less than 5 % of total.
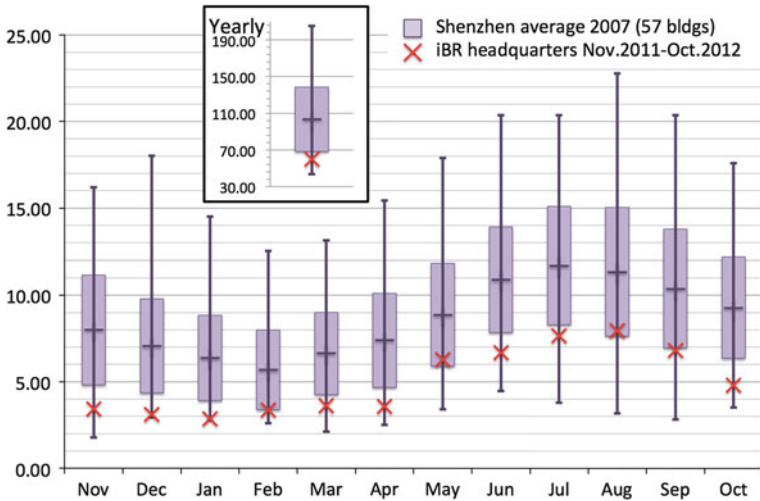
Fig. 43.5 Energy intensity of the office building equivalent of iBR from November 2011 to October 2012 and the statistical distribution of a 2007 sample of 57 office buildings located in Shenzhen. The box is the standard deviation zone and bars represent max and min values. Unit is kWh/m^2

From November 2011 to October 2012, total electricity use was 1,155,722 kWh or 57.8 kWh/m^2 for the entire building.

To make comparisons with other office buildings more relevant, we subtracted the energy consumption and area corresponding to exhibition spaces, gardens, labs, and the apartments for visiting experts from the total; the office building equivalent obtained consumed 60.2 kWh/m^2, of which AC accounted for 19.6 kWh/m^2 (33 %) and lighting & plugs for 20.8 kWh/m^2 (34 %).

As the photovoltaic panels produced 66,585 kWh over the period, the office building equivalent consumed 56 kWh/m^2 from the power grid.

Figure 43.5 shows a comparison of the electricity use of the office building equivalent with the 2007 monthly electricity consumption of a sample of 57 office buildings located in Shenzhen. From November 2011 to October 2012, iBR headquarters office's equivalent energy consumption was lower than the standard deviation lower limit of the 2007 group. Only two buildings in the 2007 sample consumed less electricity, which could be due to low occupancy or service levels.

43.5 Conclusion

A post-occupancy evaluation was conducted on a mixed-mode office building in Shenzhen, South China, featuring a bioclimatic design with user-controlled operable windows and use of natural ventilation to reduce the AC period to half a

year instead of the 10 months typical to the area. The office part of the building consumes about 60 kWh/m^2. Electricity, making it one of the most energy efficient in the city. From mid-August to mid-November 2012, indoor temperatures during work hours mainly ranged between 25 and 27 °C during the AC period and between 24 and 28.5 °C during the NV period. Answers to comfort questionnaires showed that, overall, occupants were satisfied with their thermal environment.

The study is still going on and more complete results will be presented in future work. However, current results already strongly advocate the combined use of natural ventilation and air conditioning to achieve a comfortable and energy-saving working environment in humid and warm subtropical climates.

References

1. Nicol JF, Humphreys MA (2002) Adaptive thermal comfort and sustainable thermal standards for buildings. Energ Build 34:563–572
2. de Dear RJ, Brager GS (2002) Thermal comfort in naturally ventilated buildings: revisions to ASHRAE standard 55. Energ Build 34:549–561
3. Olesen BW (2007) The philosophy behind EN15251: Indoor environmental criteria for design and calculation of energy performance of buildings. Energ Build 39:740–749
4. Xiao H, Wei Q, Jiang Y (2012) The reality and statistical distribution of energy consumption in office buildings in China. Energ Build 50:259–265
5. Lin B, Tan G, Wang P, Song L, Zhu Y, Zhai G (2004) Study on the thermal performance of the Chinese traditional vernacular dwellings in Summer. Energ Build 36:73–79
6. Song L, Lin B, Zhu Y (2003) Simulation of the summer indoor thermal condition of a traditional Chinese residential building in Anhui. J Tsinghua Univ (Sci Tech) 43(6):826–828, 843 (in Chinese)
7. Fountain ME, Arens EA (1993) Air movement and thermal comfort. ASHRAE J 35(8):26–30
8. Nicol F, Roaf S (1996) Pioneering new indoor temperature standards: the Pakistan study. Build Environ 23:169–174
9. Khedari J, Yamtraipat N, Pratintong N, Hirunlabh J (2000) Thailand ventilation comfort chart. Energ Build 32:245–249
10. Huang L, Ouyang Q, Zhu Y (2012) Perceptible airflow fluctuation frequency and human thermal response. Build Environ 54:14–19
11. Cândido C, de Dear R, Lamberts R (2011) Combined thermal acceptability and air movement assessments in a hot humid climate. Build Environ 46:379–385

Chapter 44
Temperature Impact on the Emissions from VOC and Formaldehyde Reference Sources

Wenjuan Wei, Jianyin Xiong and Yinping Zhang

Abstract In order to improve the measurement accuracy for indoor volatile organic compounds (VOCs) and formaldehyde emissions, the polymethyl pentene (PMP) reference material and the liquid-inner tube diffusion-film-emission (LIFE) reference source were developed as two qualified tools to evaluate the performance of a chamber system for furniture/building material VOCs/formaldehyde emission tests. The temperature effect on the emission of PMP reference loaded with toluene and LIFE reference loaded with formaldehyde was measured in some pioneer researches. In this paper, the correlations of temperature and the emission parameters (diffusion coefficient of VOCs/formaldehyde in the material, material/gas partition coefficient) of both references were investigated. The correlations were fixed for each reference at the temperature of 10, 23, and 30 °C with the target VOCs of toluene for PMP and formaldehyde for LIFE. The results show that there are exponential relationships between the emission parameters and the temperature which are similar to the correlations developed for emissions from building materials. This phenomenon expends the usage of the original correlations addressing the temperature effect on building material's emission parameters to general correlations of temperature effect on the parameters of indoor VOCs/formaldehyde emissions from building materials and reference sources.

Keywords VOCs · Formaldehyde · Reference source · Temperature

44.1 Introduction

Volatile organic compounds (VOCs) and formaldehyde are recognized as harmful air pollutants for human health [1], which are emitted indoors from furniture/building materials. In previous studies of building material emissions, people have

W. Wei · J. Xiong · Y. Zhang (✉)
Department of Building Science, Tsinghua University, Beijing 100084, China
e-mail: zhangyp@mail.tsinghua.edu.cn

found that temperature was an important environmental factor which affects the emission parameters (the diffusion coefficient of VOCs/formaldehyde in the building material, D_m, and the material/gas partition coefficient, K) of target building materials which can be described by experimental correlations [2, 3].

The measurement of VOCs/formaldehyde emissions from furniture/building materials are commonly tested in environmental chamber systems [4]. However, questions exist regarding the performances of environmental chamber testing systems and the errors associated with the measurements of VOCs/formaldehyde emissions from building materials. The polymethyl pentene (PMP) film references and the liquid-inner tube diffusion-film-emission (LIFE) references have been developed that emit VOCs/formaldehyde at a predictable rate [5–9], which can be useful tools to evaluate the performance of a chamber system for measuring the emission of VOCs/formaldehyde from furniture/building materials.

The emission profiles of PMP and LIFE are controlled by the diffusion films that are carefully chosen for different species of VOCs/formaldehyde. In the factorial studies of toluene PMP reference and formaldehyde LIFE reference, temperature was found to be the dominant environmental factor that resulted in the changes in the emission parameters of PMP reference and LIFE reference [10]. However, the correlations of the emission parameters and temperature for both of PMP reference and LIFE reference are not clear. The purpose of this study is to address the temperature effect on the emission parameters of toluene PMP reference and formaldehyde LIFE reference.

44.2 Materials and Methods

44.2.1 Correlations Between Emission Parameters and Temperature for Building Material

Correlations between emission parameters and temperature for building material have been studied [2, 3], which can be described for diffusion coefficient and partition coefficient, respectively, as:

$$\frac{D_m}{T^{1.25}} = A \exp\left(\frac{B}{T}\right) \tag{44.1}$$

$$\frac{K}{T^{0.5}} = A \exp\left(\frac{B}{T}\right) \tag{44.2}$$

Equations (44.1) and (44.2) are general equations to describe and predict the emission parameters of building materials at different temperature environments. For each different species of building material and the target VOC, A and B are its relevant coefficients which are needed to be determined.

44.2.2 Correlations Between Temperature and Emission Parameters of Toluene PMP Reference and Formaldehyde LIFE Reference

The PMP reference is a piece of PMP film loaded with toluene gas generated from permeation tubes. The film adsorbs the toluene during the loading process at a stable concentration and then emits toluene like a building material in a target chamber. The emission parameters of the PMP film can be measured, and its emission rate can be predicted by mass transfer model [5, 11]. The emission parameters of the reference (the diffusion coefficient of toluene in PMP film, D_m, and the material/gas partition coefficient, K) were measured at the temperature of 10, 23, and 30 °C. D_m was found to be $(1.0 \pm 0.2) \times 10^{-14}$, $(3.3 \pm 0.3) \times 10^{-14}$, and $(6.4 \pm 0.3) \times 10^{-14}$ m^2/s, while K was found to be $1{,}150 \pm 80$, 500 ± 30, and 370 ± 20 at 10, 23, and 30 °C, respectively [10].

The LIFE source consists of a polytetrafluoroethene (PTFE) tube that holds formaldehyde–water solution with a thin polydimethylsiloxane (PDMS) film cover to control its emission property and profile. The emission parameters (the diffusion

Fig. 44.1 Temperature effects on the emission parameters of the toluene PMP reference

(a)

y-axis: $D_m/T^{1.25}$

Legend:
● Experimental data
— $y = 8.99\text{E-}06\exp(-7849x)$, $R^2 = 1.00$

x-axis: $1/T$

(b)

y-axis: $K/T^{0.5}$

Legend:
● Experimental data
— $y = 6.18\text{E-}07\exp(5420x)$, $R^2 = 1.00$

x-axis: $1/T$
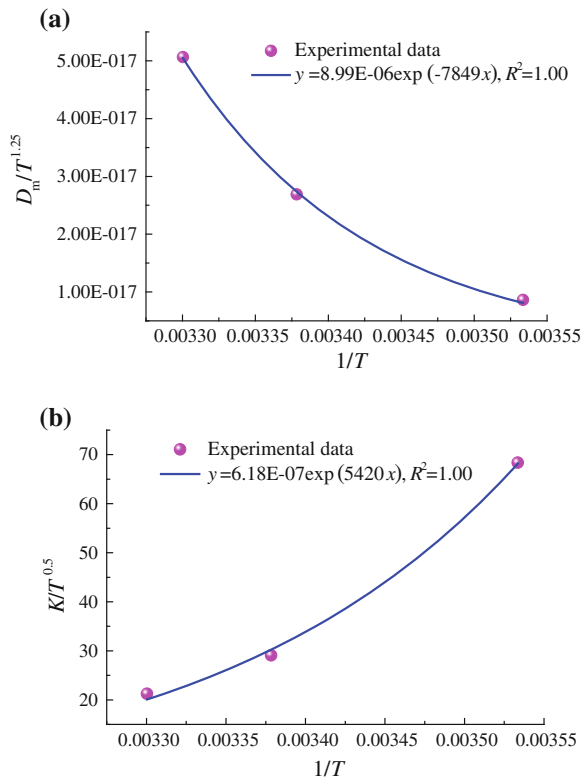
Fig. 44.2 Temperature effects on the emission parameters of the formaldehyde LIFE reference

(a)

(b)
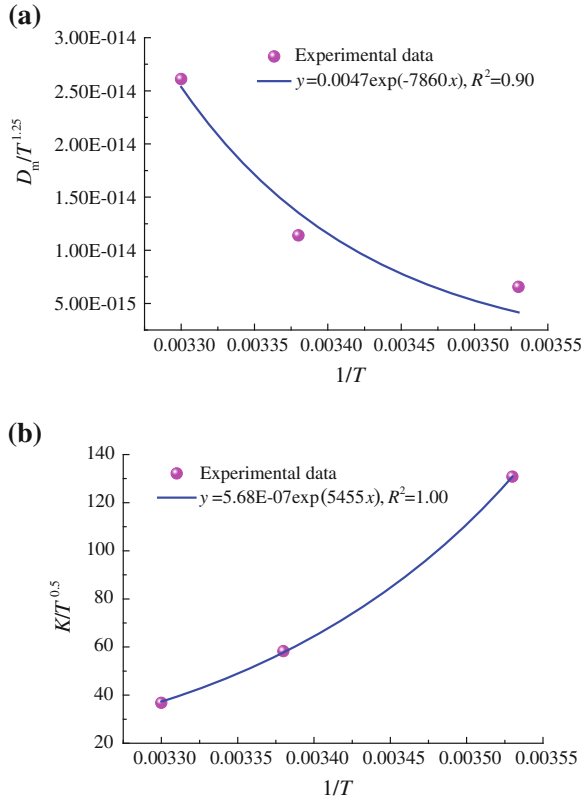
Table 44.1 Correlations of temperature and the emission parameters of PMP and LIFE references

Materials	Correlations
Toluene PMP	$\frac{D_m}{T^{1.25}} = 8.99 \times 10^{-6} \exp\left(-\frac{7849}{T}\right)$
	$\frac{K}{T^{0.5}} = 6.18 \times 10^{-7} \exp\left(\frac{5420}{T}\right)$
Formaldehyde LIFE	$\frac{D_m}{T^{1.25}} = 0.0047 \exp\left(-\frac{7860}{T}\right)$
	$\frac{K}{T^{0.5}} = 5.68 \times 10^{-7} \exp\left(\frac{5455}{T}\right)$

coefficient of formaldehyde in the PDMS film, D_m, and the material/gas partition coefficient, K) were measured at the temperature of 10, 23, and 30 °C. D_m was found to be 7.61×10^{-12}, 1.40×10^{-11}, and 3.30×10^{-11} m²/s, while K was found to be 2,200, 1,000, and 640 at 10, 23, and 30 °C, respectively.

The measured data of PMP and LIFE references were fitted to Eqs. (44.1) and (44.2) to determine the coefficient of A and B for the two references. The least square method was used, and the residual square numbers were required to be higher than 0.81 to be sure the fitted data matched the measured data.

44.3 Results and Discussion

When temperature increases, the diffusion coefficients of both PMP and LIFE references increase and the partition coefficients decrease. The temperature effects on the diffusion coefficient and partition coefficient of the toluene PMP reference are shown in Fig. 44.1a and b. The experimental data are fitted to Eqs. (44.1) and (44.2). The residual square numbers of the two fittings are both higher than 0.99. The temperature effects on the diffusion coefficient and partition coefficient of the formaldehyde LIFE reference are shown in Fig. 44.2a and b. The experimental data are fitted to Eqs. (44.1) and (44.2). The residual square numbers of the two fittings are both higher than 0.90. The correlations of temperature and the emission parameters of PMP and LIFE references are listed in Table 44.1, respectively.

44.4 Conclusions

The results of the fittings validated that the experimental correlations of temperature effects on the emission parameters of building materials can also be useful for the PMP and LIFE VOCs/formaldehyde reference. The determination of the equations makes a useful approach for the prediction of the VOCs/formaldehyde reference's emission under different temperature environments.

References

1. IARC (2004) IARC classifies formaldehyde as carcinogenic to humans. International Agency for Research on Cancer, Lyon
2. Zhang YP, Luo XX, Wang XK et al (2007) Influence of temperature on formaldehyde emission parameters of dry building materials. Atmos Environ 41:3203–3216
3. Deng QQ, Yang XD, Zhang JS (2009) Study on a new correlation between diffusion coefficient and temperature in porous building materials. Atmos Environ 43:2080–2083
4. ASTM D6670 (2007) Standard practice for full-scale chamber determination of volatile organic emissions from indoor materials/products
5. Cox SS, Liu Z, Little JC et al (2010) Diffusion-controlled reference material for VOC emissions testing: proof of concept. Indoor Air 20:424–433
6. Howard-Reed C, Liu Z, Benning J et al (2011) Diffusion-controlled reference material for volatile organic compound emissions testing: pilot inter-laboratory study. Build Environ 46:1504–1511
7. Wei WJ, Xiong JY, Zhang YP et al (2012) A standard reference for chamber testing of material VOC emissions: design principle and performance. Atmos Environ 47:381–388

8. Wei WJ, Greer S, Howard-Reed C et al (2012) Emissions from a LIFE reference: small chamber tests and factorial studies. Build Environ 57:282–289
9. Wei WJ, Howard-Reed C, Persily AK et al (2013) Standard formaldehyde source for chamber testing of material emissions: model development, experimental evaluation and impacts of environmental factors. Environmental Science and Technology (submitted)
10. Little JC, Liu Z, Howard-Reed C et al (2012) Diffusion-controlled reference material for VOC emissions testing: the effect of temperature and humidity. In: Proceedings of healthy buildings 10E.1, Brisbane
11. Little JC, Hodgson AT, Gadgil AJ (1994) Modeling emissions of volatile organic-compounds from new carpets. Atmos Environ 28:227–234

Chapter 45
The Humidification Capacity and Thermal Comfort of the Heating Room in Winter

Hao Zhang, Jinjing Zhao, Xueting Liu, Jiguang Zhang and Huajun Tang

Abstract This paper briefly describes the lower relative humidity of the heating room in winter in northern China than in southern China and discusses the relationship between the indoor relative humidity and the thermal comfort. Meanwhile, the required humidification of indoor air is calculated in this paper when it reaches to the indoor comfort zone, and the curve of the relative humidity is drawn with humidification changing. This paper also introduces the common household humidifiers and selection principles and gives the way how to control the indoor relative humidity. Furthermore, it shows how to calculate the humidification of indoor air for the comfortable design condition with heating technology. Consequently, several conclusions are reached.

H. Zhang (✉) · X. Liu
Key Laboratory of Renewable Energy Utilization Technologies in Buildings,
Ministry of Education, Shandong Jianzhu University,
Jinan 250101, China
e-mail: qdzhanghao@126.com

H. Zhang · X. Liu
Shandong Key Laboratory of Building Energy-saving Technique,
Shandong Jianzhu University,
Jinan 250101, China

H. Zhang · X. Liu · H. Tang
School of Thermal Energy Engineering, Shandong Jianzhu University, Jinan 250101, China

J. Zhao
School of Foreign Languages, Shandong Jianzhu University, Jinan 250101, China

J. Zhang
School of Environmental and Municipal Engineering, Qingdao Technological University,
Qingdao 266033, China

H. Zhang · J. Zhao · X. Liu · J. Zhang · H. Tang
Department of Thermal Engineering, University of Science and Technology Beijing,
Beijing 100083, China

45.1 Air Relative Humidity and Thermal Comfort

When air relative humidity is between 50 and 60 %, it is the most favorable for human health; humans also have the strongest resistance to disease under the condition like this. Meanwhile, the people will feel comfortable; their skin looks plump, shiny, and elastic. Quietly lower air relative humidity is disadvantageous to human health because dry air easily dries the water, which not only makes the human mucous membranes and mouth dry but also induces colds, bronchitis, asthma, and other illnesses. Researches indicate that the considerably low relative humidity will not only make flu virus and highly pathogenic Gram-negative bacteria reproduce faster, but also become epidemic with the diffusion of dust, which causes the increasing incidence of various epidemics. Similarly, higher air relative humidity is also harmful for human health. According to tests, on the one hand, air relative humidity greater than 80 % will make the human uncomfortable, slouchy, and droopy and even cause the change of some behavior. Besides, it will cause stomach problems, rashes, rheumatoid arthritis, and other diseases. On the other hand, it is easy to make clothes, food, and utensils get moldy, deteriorated, and even rotten. In winter, in most of the northern regions, the outdoor relative humidity as well as the air temperature is generally low, about 15–35 %. Most of the family houses have heating facilities, but generally they do not attach importance to humidification. Because the air relative humidity of indoor micro-environment is lower than that of the outdoor, the people feel very uncomfortable. In addition, people spend much time in the room in winter so that the people especially the elderly, infants, and persons with respiratory diseases need to add moisture into the room to ensure that they can more comfortably withstand the cold and dry winter [1].

45.2 The Calculation of Humidifying Capacity of Heating Room in Winter (Indoor Moisture Load)

The main factors affecting humidification of the heating room in winter are the humidity difference with the influence of natural ventilation of indoor air (including the cold wind penetrating through windows and doors and that through the open doors), moisture dissipating capacity of the people, and moisture transfer of the maintenance structures. Taking a three-bedroom apartment in Jinan City as an example the paper shows how to calculate the required amount of humidification of the apartment.

In Jinan, outdoor meteorological parameters include temperature -7 °C, relative humidity 54 %, and moisture content of air 1.21 g/kg. In comparison, indoor parameters include temperature 18 °C, comfortable relative humidity 50 %, and moisture content 6.5 g/kg.

45.2.1 The Amount of Natural Ventilation of the Indoor Air

The amount of ventilation indoor air in heating room includes the amount of the cold wind penetrating through windows and doors and the amount of cold air intrusive through the open door. The three-bedroom apartment on the ground floor in the eastern region of Jinan City is regarded as the subject of calculation. For one thing, the size of the sliding aluminum windows is 1.8 × 1.15 m and the total length of the openable lacuna of each window is 8.4 m. Moreover, there are two outer windows to the south, the same to the north. For another, the size of the double door (the inner door is made of wood, and the outer door is made of steel) is 0.9 × 1.9 m (Fig. 45.1), and the total length of the openable lacuna of the door is 5.6 m. At last, the building faces west whose area is about 70 m².

45.2.1.1 Volume Flow of Cold Air Penetrating Through Doors and Windows

Using the gap method to calculate the amount of cold air penetrating through the doors and windows, volume flow of the cold air penetrating is shown in formula (45.1) [3]:

$$V_s = \sum lLm \qquad (45.1)$$

V_s Volume flow of the cold air penetrating, m³/h
l The gap length of the doors and windows of the room in some direction, m

Fig. 45.1 Diagrammatic sketch of cold intrusion of the room door
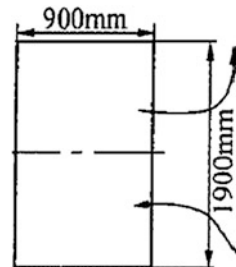
L Reference volume flow of the cold air penetrating through the gap of the
     windows and doors, m³/(m h)
m Comprehensive correction coefficient of volume flow of the cold air
     penetrating through the gap of doors and windows.

   The correction coefficient of the cold air orientation in Jinan is as follows: south
$m = 0.55$, north $m = 0.45$ [4]; for the room with two outer opposite walls, the most
negative wall (face south) is taken as the standard to calculate the volume flow of
the cold air penetrating. In Jinan, the volume flow of the cold air penetrating
through the gap of sliding aluminum windows is $L = 1.12$ m³/(m h) [4]. The total
gap length of the two external windows toward the south: $l = 8.4 \times 2 = 16.8$ m
and the total volume flow of cold air penetrating: $V_s = 1.12 \times 16.8 \times$
$0.55 = 1.35$ m³/h.

45.2.1.2 Volumes Flow of the Cold Air Intrusive Through
the Room Door

Take the door which opens for a while for consideration. Because of that there is
no better method to calculate the volume flow of the cold air intrusive when the
external door opens in multi-storey civil building at present, the calculating
method of natural ventilation is used in this paper [4], making use of the hot press
produced by the room to calculate the volume flow of the cold air intrusive when
the room door opens (the impact of the cold air intrusive on the cold air penetrating
is ignored). The size of the entrance doors of the room and the calculation of the
cold air is shown in Fig. 45.1.

$$V_j = A \sqrt{\frac{2g \times (\rho_w - \rho_n)h}{\rho_w \xi}} \tag{45.2}$$

V_j Volume flow of the inlet air, kg/s;
A The area of the air intake vents and air exhaust vents, 0.855 m²;
ρ_w, ρ_n The density of the air of the stair hall and the room, 1.268 kg/m³ and
     1.208 kg/m³ respectively;
h The distance from the interface to the center of the air intake vents and air
     exhaust vents, 0.475 m;
ξ Local resistance coefficient of the air intake vents and air exhaust vents,
     1.56;
g Acceleration of gravity, 0.98 m/s².

$$V_j = 0.855 \times \sqrt{\frac{2 \times 0.98 \times 0.475 \times (1.268 - 1.208)}{1.268 \times 1.56}} = 0.4544 \, (\text{m}^3/\text{s})$$

Similarly, the volume flow of exhausted air is $V_p = 0.4655\,(\mathrm{m^3/s})$. Because opening the door will cause the increase in the volume flow of cold air penetrating, the larger of the V_j and V_p is chosen. Assuming that the door opens for 60 s per hour on average during the day, the volume flow of the cold air hourly is about:

$$V_w = V_p \times 60 = 0.4655 \times 60 = 27.93\,\mathrm{m^3/h} \qquad (45.3)$$

The total volume flow of the indoor air per hour on average during the day:

$$V = V_s + V_w = 10.35 + 27.93 = 38.28\,(\mathrm{m^3/h}) \qquad (45.4)$$

The total volume flow of the indoor air per hour on average when the door closes at night is calculated as follows:

$$V = V_s = 10.35\,(\mathrm{m^3/h}) \qquad (45.5)$$

45.2.2 The Humidification of the Heating Room in Winter

The required humidification of indoor air when it reaches to the indoor comfortable zone is as follows:

$$\Delta d = V\rho_n(d_n - d_w) \qquad (45.6)$$

Δd Humidification, $\mathrm{g/m^3}$
ρ_n The density of the indoor air, $1.208\,\mathrm{kg/m^3}$
d_n The moisture content of indoor air, $6.5\,\mathrm{g/kg}$
d_w The moisture content of outdoor air, $1.21\,\mathrm{g/kg}$.

We can calculate the required humidification of indoor air in the daytime, which is 244.62 g/h and 66.14 g/h at night. The change of the relative humidity with the humidification changing in heating room is shown in Fig. 45.2 of which moisture content curve is applied to the environment temperature at 18 °C and the curve of humidification is drawn by proportional.

The moisture will be evaporated from the people staying in the room. The moisture on average evaporated from each one is 35 g/h under the indoor temperature of 18 °C so that the humidification of the room should be properly deducted. However, the question could not be considered when the humidifier is chosen, making the efficiency of the humidifier surplus. Furthermore, when the pressure of vapor inside the indoor air is greater than the outdoor, the vapor inside the indoor air will be transferred to the outside through the maintenance structure. For the wall built with heavy mortar clay bricks, when vapor permeability coefficient $\mu = 1.05 \times 10^{-4}\,(\mathrm{m\,h\,P_a})$, the thickness of the wall is 0.24 m and the pressure of vapor inside the indoor air $P_1 = 860\,\mathrm{P_a}$, the pressure of vapor inside

Fig. 45.2 The relative humidity with the humidification in heating room
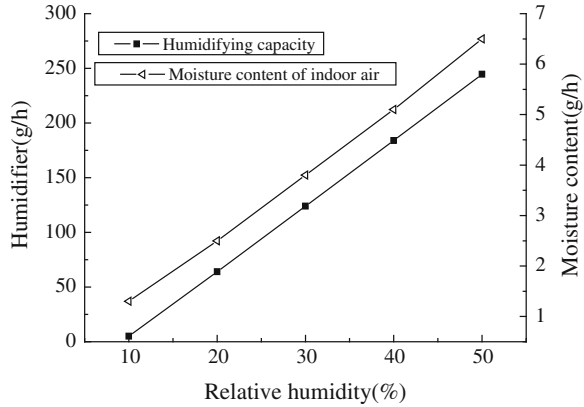
the outdoor air $P_2 = 150\,P_a$, the height of room $h = 2.7$ m, circumference of the outer wall $c = 25$ m, the amount of moisture transferred through the maintenance structure is as follows:

$$\Delta d = \frac{\mu}{\delta} hc(P_1 - P_2) = \frac{1.05 \times 10^{-4}}{0.24} \times 27 \times 25 \times (860 - 150) = 20.97\,\text{g/h}$$

(45.7)

In summary, if we consider occasionally opening windows and the moisture dissipating capacity of the people are, the required humidification of the three-bedroom apartment during the day is about 200 g/h:

$$\Delta d = V\rho_n(d_n - d_w)$$

(45.8)

45.3 Humidifier

Nowadays, there are four household humidifiers on the market. They are ultrasonic humidifier, electric heating humidifier, clean humidifier, and siphonal humidifier. Their working principle and features are as follows:

The ultrasonic humidifier: The ultrasonic humidifier uses high-frequency oscillatory to separate the water from its molecular state to produce fog particles. Therefore, the mist is spread into the air evenly for the purpose of humidification by wind-driven device. Its biggest advantage is, apart from moistening the air, that negative oxygen ions can be produced which could fresh the air, improve health, and change heat generated by heating system in winter, making the indoor environment more comfortable. Meanwhile, it has many other characteristics, such as high wet strength, low power consumption, low noise, and long life. In addition, it has lots of functions, including medical atomization, beautifying life, and cleaning jewelry. However, such products have certain requirements on water quality.

If hard water is used, "white powder" phenomenon may be emerged. As a result, we had better use softened water (such as distilled water). To solve the "white powder" issue, there has been a new humidifier with a water softener on the market currently.

The electric heating humidifier: The electric heating humidifier is a purely functional product whose principle is that heating element is used to heat the water to the boiling point so that steam is produced and released into air to humidify. Because of the thermal evaporation, water impurities are deposited in the bottom and they cannot be evaporated into the air with vapor. As a result, the "white powder" phenomenon is avoided effectively. Its drawbacks are high power consumption, single function, and scaling on the humidifier easily.

The clean humidifier: Clean humidifying and siphonal humidifying technology are the new high-tech in the area of humidification at present. Selective volatilization technique in molecular level used the special filter to filter dust in the air and to absorb impurities in the water aiming at humidifying through micro-heating The water molecules splashed from the humidifier into the air are very pure without "white powder" phenomenon, but it is quite strict with the water quality. Pure water must be used; otherwise, the life of the filter will be shortened and the quality of the added moisture will be poor.

The siphonal humidifier: Selective volatilization technique in molecular level makes the water volatilize directly by the PTC materials, without vapor in the working process. Because the air in the cycle goes through the antibacterial filter, the humidifier could also clean indoor air. The humidifier is very noisy while the performance is good. Moreover, before the siphonal humidifier is saved because of the change of the season, its evaporator used for filtering should be taken out for drought.

In addition, there are new products on the market. For example, the air purifier is combined with the humidifier on the market, used for humidifying and filtering the air at the same time and releasing negative oxygen ions to achieve the combination of humidifying and purifying.

45.4 Conclusion

1. The relative humidity of the heating room is generally low in winter in northern China, so the humidifier or other appropriate measures must be used to improve the thermal comfort of indoor environment.
2. The temperature and the humidity of outdoor air have great influences on the humidifying capacity of heating room. For "a set of three" in Jinan, the appropriate humidification of the heating room is about 200 g/h.
3. The quality of local water should be considered for the choice of the humidifier equipment. We take the product with automatic humidity control into account in order to preset humidity depending on demands. As a result, the space need to be humidified is under the state of the constant relative humidity.

References

1. Zhao R (2003) Air condition. China Architecture & Building Press, Beijing
2. Geng S (2005) Calculation of moisture load in underground structure. Heating, Vent Air Condition 32(6):70–71
3. Sun M (2005) Analysis on humidifying heating system. China Acad J Electr Publishing House 4:85–87

Chapter 46
Field Study on Thermal Environment and Thermal Comfort at Rural Houses in Severe Cold Areas

Zhaojun Wang, Xiaohui Sheng, Jing Ren and Dongdong Xie

Abstract In order to investigate indoor thermal environment and thermal comfort at rural houses, a field study was carried out at 10 rural houses in 2 villages near Harbin from December 2012 to January 2013. The environmental parameters and the subjects' thermal sensation were collected simultaneously. The results showed that the indoor air temperature ranged from 9.0 to 21.8 °C, with an average of 16.6 °C. The operative temperature varied within the range of 10.5–22.7 °C, averaging 18.1 °C. The average relative humidity was 40.4 %. The mean air velocity was 0.08 m/s. The mean surface temperature of Chinese Kang was 35.1 °C. The mean surface temperature of exterior window was 9.5 °C. The neutral operative temperature was 18.5 °C. The lower limit of the accepted operative temperature by 80 % of the peasants was 10.6 °C, much lower than the specified heating temperature for urban residential buildings, because the peasants wore more clothes than residents in the urban. The mean clothing insulation was 1.47clo. 92.5 % of the subjects felt the thermal environment acceptable, and 92.5 % of the subjects felt the humidity of the environment acceptable. Regulating the Kang and the separated heating equipments were the main measures taken by the occupants to improve the indoor environment.

Keywords Thermal environment · Thermal comfort · Rural houses · Field study

46.1 Introduction

In recent years, many field studies have been conducted on indoor thermal environment and thermal comfort. However, most studies focused on urban residential buildings, a few on rural houses. Researches showed [1] that human past

Z. Wang (✉) · X. Sheng · J. Ren · D. Xie
School of Municipal and Environmental Engineering, Harbin Institute of Technology,
Harbin 150090, China
e-mail: wzjw02@yahoo.com.cn

living environment, climate conditions, and cultural background had significant influences on their expectations of the indoor thermal environment, which would in turn affect the human adaptability to the thermal environment. Compared with the city residents, both the living habits and economic level of people living in rural areas are different. Therefore, it is necessary to study on indoor thermal environment and thermal comfort at rural houses in China. Zhang et al. conducted a field study on thermal environment and thermal comfort at rural houses in a hot summer and cold winter area [2]. Zhu et al. carried out an investigation on indoor thermal comfort at rural houses around Beijing during heating period [3]. Jin et al. mainly focused on the indoor thermal environment at rural houses in severe cold areas, instead of human thermal comfort [4]. Wang et al. conducted some field studies on thermal comfort in Harbin residential buildings [5–7]. For further study, we launched an investigation on the indoor thermal environment and thermal comfort at 10 rural houses in 2 villages near Harbin during December 2012 to January 2013.

46.2 Method

46.2.1 Subjects

Ten rural houses in 2 villages near Harbin were chosen for this study. A total of 40 valid subjective questionnaires were provided by 40 respondents, of whom 17 were females. The subjects were all local peasants who had lived in the suburb of Harbin for a long time, which indicated that they had fully adapted to the cold and dry climate of the severe cold area.

46.2.2 Indoor Environmental Parameters

The test instruments include a temperature and humidity data collector (HT-II), a blackball temperature recording instrument (HWZY-1), a hot-wire anemometer (Testo425) and an infrared thermometer (Testo830-T1). The temperature and humidity data collector is used to measure air temperature and relative humidity simultaneously. The accuracy of air temperature measurement is within 0.5 °C and its measurement accuracy of relative humidity is ± 3 %. The accuracy of the blackball temperature recording instrument is within ± 0.4 °C. The air velocity can be measured by hot-wire anemometer with an accuracy of $\pm(0.03$ m/s $+ 5$ % measured value) in the measurement range of 0–20.0 m/s. The infrared thermometer is used to measure the surface temperature of the external window and Chinese Kang (built of stone or brick) with an accuracy of ± 1.5 °C.

Bedroom and living room were selected as testing zone. As the residents usually sit or lie down in the room, the air temperature, relative humidity, blackball temperature, and air velocity were measured at a height of 0.6 m above the floor, and then, the mean radiant temperature was derived by calculation. The surface temperatures of the exterior window and the Chinese Kang were measured on the center points.

Table 46.1 provides statistical summaries of the indoor for the rural houses in winter. The indoor air temperature fell within the 9.0–21.8 °C interval, with an average of 16.6 °C. The blackball temperature varied within the range of 10.7–23.1 °C, averaging 18.5 °C. The operative temperature varied within the 10.5–22.7 °C range, with a mean of 18.1 °C. The mean surface temperature of exterior window was 9.5 °C. The mean surface temperature of Kang was 35.1 °C. The relative humidity fell within the range of 26.0–57.4 %, with a mean of 40.4 %. And the relative humidity was in the thermal comfort zone. The mean air velocity was 0.08 m/s, which was similar with the air velocity in Harbin residential buildings [5]. The mean clothing insulation was 1.47clo, ranging from 0.93clo to 2.11clo.

46.2.3 Subjective Questionnaires

The subjective questionnaires were collected simultaneously with the measurement of the indoor parameters. The questionnaires included: (1) Background survey, such as gender, age, etc. (2) The clothing and activities of the subjects. (3) Thermal sensation, which used the ASHRAE seven-point scale: −3 cold, −2 cool, −1 slightly cool, 0 neutral, +1 slightly warm, +2 warm, +3 hot. (4) Thermal expectation: −1 cooler, 0 no change, +1 warmer. (5) Thermal acceptability, evaluating the environment acceptable or unacceptable directly. (6) The measures of improving the indoor thermal environment, such as regulating the Kang, regulating their own separated heating equipment, opening the windows, changing clothes, changing activity level, etc.

Table 46.1 Indoor environmental parameters and clothing insulations in winter

	Average	Maximum	Minimum	Standard deviation
Air temperature/°C	16.6	21.8	9.0	3.4
Relative humidity/%	40.4	57.4	26.0	9.4
Air velocity/m/s	0.08	0.18	0.04	0.03
Blackball temperature/°C	18.5	23.1	10.7	3.5
Mean radiant temperature/°C	19.6	26.1	12.0	3.8
Operative temperature/°C	18.1	22.7	10.5	3.3
Surface temperature of Kang/°C	35.1	46.0	16.5	7.7
Surface temperature of exterior window/°C	9.5	16.0	−2.0	4.7
Mean clothing insulation/clo	1.47	2.11	0.93	0.33

46.3 Results and Analyses

46.3.1 Thermal Neutral Temperature and Ranges of Acceptable Temperature

The operative temperature was used to evaluate the indoor thermal environment, and the temperature–frequency method was applied. The linear regression equation between mean thermal sensation vote and indoor operation temperature is as follows:

$$\text{MTS} = 0.094t_o - 1.742 \tag{46.1}$$

where t_o is the indoor operative temperature, °C; MTS is the mean thermal sensation vote.

The correlation coefficient $R = 0.581$. Let MTS $= 0$, we get the thermal neutral temperature of 18.5 °C. The slope of the MTS-on-operative temperature was quite small, which indicates the sensitivities of the subjects to temperature changes. If the indoor operative temperature changes 1 °C, the thermal sensation will only change about 0.094.

Let MTS $= -0.75$, we obtain the lower limit of the accepted operative temperature by 80 % of the respondents of 10.6 °C, which was much lower than that specified heating temperature for urban residential building. So it is necessary to further research the thermal environment at rural houses.

46.3.2 Thermal Acceptability and Thermal Expectation

The subjects were asked if they accepted the thermal environment they were exposed to. The results show that 95 % of the subjects marked acceptable.

Figure 46.1 shows the distribution of thermal expectation votes. The thermal expectation vote used Preference scale: −1 (colder), 0 (no change), +1 (warmer). In this study, 60 % of the subjects wanted "no change", 37.5 % requested "warmer", and only 2.5 % requested "colder".

46.3.3 Improvement Measures of Indoor Thermal Environment

Figure 46.2 gives the distribution of measures taken by the occupants to improve the indoor environment. The measures were as the follows: regulating the Kang, regulating their own separated heating equipment, opening or closing the door and window, changing clothes, adjusting activity levels and so on.

Fig. 46.1 Distribution
of thermal expectation votes
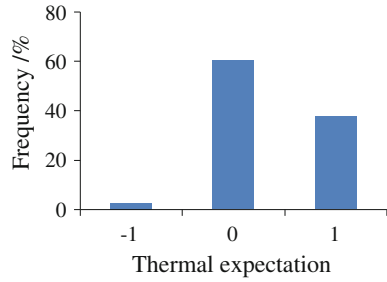
Fig. 46.2 Distribution of
measures to improve the
indoor environment
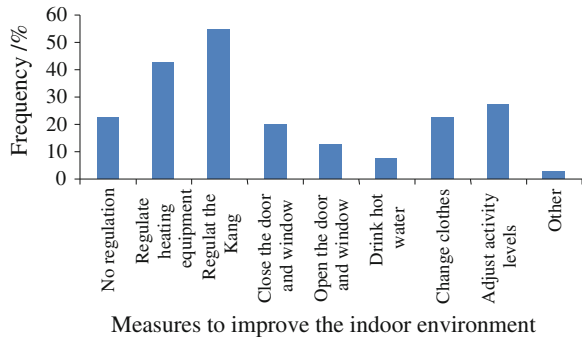
Fifty-five percent of the peasants adjusted indoor temperature by regulating the power of Kang, 42.5 % regulated their own separated heating equipment, and 20 % closed the door and window. 22.5 % of the occupants improved their comforts by putting on more clothes and 27.5 % by more activities. It is found that regulating the Kang and their own separated heating equipment were the main processes used by the occupants to improve the indoor environment.

46.4 Discussions

Wang et al. [5, 6] conducted a field study in 66 apartments in Harbin from 2000 to 2001 in winter. They have derived a linear regression equation between mean thermal sensation votes and indoor operative temperature as follows:

$$MTS = 0.302t_o - 6.506 \qquad (46.2)$$

The correlation coefficient $R = 0.872$. The neutral temperature is 21.5 °C. Compared the two Eqs. (1) and (2), it is found that the neutral operative temperature of their urban samples was 3 °C higher than that of our suburb samples. The peasants were less sensitive to temperature changes.

The mean clothing insulation was 1.47clo at rural houses, larger than those of the urban residential buildings of 1.37clo [5]. The lower neutral temperature and the lower limit of the accepted operative temperature of 10.6 °C may be explained by the higher metabolic rate and larger clothing insulation of people at rural houses.

46.5 Conclusions

Based on the above study at rural houses around Harbin, we got the following conclusions:

1. The mean indoor air temperature was 16.6 °C. The average operative temperature was 18.1 °C. The average RH was 40.4 %. The mean air velocity was 0.08 m/s.
2. The neutral temperature was 18.5 °C. The lower limit of the operative temperature accepted by 80 % of the peasants was 10.6 °C.
3. Ninety-five percent of subjects voted the thermal environment acceptable. The indoor relative humidity fell in the range of thermal comfort. The mean air velocity was similar with the air velocity in Harbin residential buildings.
4. The mean clothing insulation was 1.47clo, more than the occupants in Harbin residential buildings.
5. Regulating the Kang and their own separated heating equipment were the main measures taken by the occupants to improve the indoor environment at rural houses.

References

1. Dear RJ, Brager GS (2004) Developing an adaptive model of thermal comfort and preference. ASHRAE Trans 104(1):145–167
2. Han J, Zhang GQ, Zhou J (2009) Research on the rural residential thermal environment and thermal comfort in hot summer and cold winter climate zone. J Hunan Univ 36(6):13–17 (in Chinese)
3. Huang L, Zhu YX, Ouyang Q et al (2011) Indoor thermal comfort in rural houses around Beijing in heating season. HVAC 41(6):83–85, 115 (in Chinese)
4. Jin H, Zhao H, Wang XP (2006) Research on the indoor thermal comfort environment of rural housing in winter in super-cold region. J Harbin Inst Technol 38(12):2108–2111 (in Chinese)
5. Wang ZJ, Wang G, Lian LM (2003) A field study of the thermal environment in residential buildings in Harbin. ASHRAE Trans 109(2):350–355

6. Wang ZJ (2006) A field study of the thermal comfort in residential buildings in Harbin. Build Environ 41(8):1034–1039
7. Wang ZJ, Zhang L, Zhao JN et al (2011) Thermal responses to different residential environments in Harbin. Build Environ 46(11):2170–2178

Chapter 47
Numerical Study of the Effect of Bake-Out on the Formaldehyde Migration in a Floor Heating System

Xiaozhong Shen and Zhenqian Chen

Abstract To comply with concentration requirements in previously constructed homes, many people are conducting bake-out in buildings prior to occupancy. The material temperature is considered a major factor that determines the effect of the bake-out. To confirm the effect of the bake-out, an improved model of the coupled heat and formaldehyde migration process is developed and analyzed to investigate the transport features in under floor heating system. Based on the theory of non-equilibrium thermodynamics and molecular kinetics, the mechanisms of the heat and mass transfer in dry porous building materials are discussed. The coupled heat and formaldehyde migration process in a floorboard is simulated under nonisothermal conditions of the temperature. Numerical results show that the effect of under floor heating becomes more and more important with the increasing of the temperature of the bottom layer, and the emission of formaldehyde from the board increases with the increasing of bake-out frequency. The longer the time of ventilation is in bake-out, the smaller the concentration remained in the chamber is. The removal efficiency of formaldehyde from building materials with a under board heating process within the ventilation period is prominent, but the energy consumed under such a mode is unsatisfied.

Keywords Formaldehyde migration · Porous building material · Bake-out · Heat and mass transfer

X. Shen
Department of Electric Engineering, Wuxi Institute of Commerce, Wuxi, China

Z. Chen (✉)
School of Energy and Environment, Southeast University, Nanjing, China
e-mail: zqchen@seu.edu.cn

47.1 Introduction

Recently, an increasing attention to reveal the transport features of formaldehyde in building materials has been paid by IAQ (Indoor Air Quality) researchers (Yang and Chen [1], [2–5]. Formaldehyde is one of the main VOCs emitted from wood-based building materials, including medium density board, particle board and wood-based floorboards. It is well known that formaldehyde is irritant, neurotoxic and carcinogenic. Large-scale concern is intrigued due to a particular damage of formaldehyde pollution. The main characteristics of the interior formaldehyde pollution are widely ranged, longly exposed, serious immunotoxic or indicative of sick building syndrome (SBS) [6]. Criteria for the limitation and regulation of formaldehyde emissions from wood-based materials were established in 1981 in Germany and Denmark [7, 8].

To comply with concentration requirements in previously constructed homes, many people are conducting bake-out in buildings prior to occupancy. The theoretical concept of the bake-out is to remove VOCs out of the material into the indoor air by raising the temperature [9]. However, the effect of bake-out on the migration process of VOCs, including formaldehyde, is investigated mainly by experiments. The elevated temperature accelerates the diffusion of formaldehyde in the material, resulting in lowering the equilibrium partition coefficient, thereby allowing formaldehyde content to rapidly reduce [10], [11]. Follin [12] also concluded that the bake-out successfully reduced the VOC emissions of 2-ethylhexanol from the concrete surface by 13 % of the initial level. However, contradictory evidence exists regarding the effectiveness of the bake-out. According to the study by Hicks et al. [13], which was performed in a hospital with an air heating system, there was no clear reduction of VOCs from the bake-out. Offerman et al. [14] reported that the VOC concentration immediately reduced after the bake-out in an office building with air heating system but subsequently rebounded to the level before the bake-out. Recently, Kang et al. [15] investigated the effect of bake-out on reducing indoor VOCS concentrations in a residential housing unit with a radiant floor heating system. In Germany and the United States, large-scale test chambers were used for the evaluation of formaldehyde emissions [8].

Due to a lack of accurate description of the coupled heat and formaldehyde migration process, the bake-out characteristics of the heat and mass transfer in dry porous building materials has not been fully revealed in floor heating systems. In this study, an improved model of the coupled heat and formaldehyde migration process is developed and analyzed to investigate the transport features in floorboards. Based on the theory of nonequilibrium thermodynamics and molecular kinetics, the mechanisms of the heat and mass transfer in dry porous building materials are discussed. The coupled heat and formaldehyde migration process in a floorboard is simulated under bake-out conditions of the temperature.

47.2 Model Development

According to the chamber experiments and simulation and the analytical solution carried out by Xu and Zhang [4], VOCs emitted out of the surface layer of a wood-based board with a VOC-impermeable bottom layer. In these tests, the side edges of each sample were sealed with aluminum foil to make the mass diffusion in the material to be approximately one-dimensional. By using a water bath, the chamber and air temperature were maintained at the desired temperature. The mix between the formaldehyde and air was promoted by a fan in the top of the chamber. A schematic shown of an idealized slab placed in such a simplified environmental chamber is showed in Fig. 47.1. In order to simulate the effect of temperature on the formaldehyde diffusive transport, the temperature of the bottom layer is regulated by a constant temperature bath which varied from 15 to 65 °C in the model.

47.2.1 Flux of Thermodynamics

47.2.1.1 Mass Migration

As porous building materials are micro-porous medium, the effective diffusion coefficient De can be written as [16]:

$$D_e = \frac{D_{atm}D_{kn}}{D_{atm} + D_{kn}} \tag{47.1}$$

where general molecular diffusion coefficient D_{atm} and Knudsen diffusion coefficient D_{kn} are:

$$D_{atm} = 4.942 \times 10^{-4} \varepsilon T^{1.5} / (Pf_0) \tag{47.2}$$

$$D_{kn} = \frac{8\varepsilon^2}{3f_0 s_g} \left(\frac{2R_V T}{\pi M_V}\right)^{0.5} \tag{47.3}$$

Fig. 47.1 Schematic shown of a simplified environmental chamber
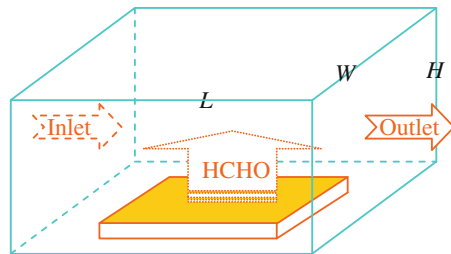
Under nonisothermal conditions, the migration flux of the air and formaldehyde is:

$$\overrightarrow{J}_a = \rho_a \overrightarrow{u}_a - D_{ea} \nabla \rho_a \tag{47.4}$$

$$\overrightarrow{J}_V = \rho_V \overrightarrow{u}_v - D_{eV} \nabla \rho_V \tag{47.5}$$

In dried porous building materials, the mass flux of the air $\overrightarrow{J}_a = 0$. The convection velocity of air is the same as that of formaldehyde vapor ($\overrightarrow{u}_a = \overrightarrow{u}_v$). So Eq. [13] is expressed in the following:

$$\overrightarrow{J}_V = \rho_V \left(\frac{D_{ea}}{\rho_a} \nabla \rho_a - \frac{D_{eV}}{\rho_V} \nabla \rho_V \right) \tag{47.6}$$

We assume that the air and formaldehyde comply with the ideal gas state law in dry porous building materials. Therefore,

$$\overrightarrow{J}_V = -\lambda_p \nabla P_V - \lambda_p^{11} \nabla T \tag{47.7}$$

where the infiltration coefficient λ_p and thermal infiltration coefficient λ_p^{11} are:

$$\lambda_p = \frac{\rho_V}{T} \left(\frac{D_{ea}}{\rho_a R_a} + \frac{D_{eV}}{\rho_V R_V} \right) \tag{47.8}$$

$$\lambda_p^{11} = \frac{\rho_V}{T^2} \left(\frac{D_{ea}(P - P_V)}{\rho_a R_a} - \frac{D_{eV} P_V}{\rho_V R_V} \right) \tag{47.9}$$

47.2.1.2 Heat Migration

The heat flux is consisted of heat conduction heat flux ($\overrightarrow{J}_{qd}$) and convection heat flux ($\overrightarrow{J}_{qc}$) caused by infiltration fluid flow. So, the total heat flux $\overrightarrow{J}_q$ is:

$$\overrightarrow{J}_q = \overrightarrow{J}_{qd} + \overrightarrow{J}_{qc} = -(1 - \varepsilon)\lambda_s \nabla T + \varepsilon(\overrightarrow{J}_V h_V + \overrightarrow{J}_a h_a) \tag{47.10}$$

where λ_s is the effective thermal conductivity of the solid matrix. The enthalpies of the formaldehyde h_V and air h_a are described as:

$$h_V = C_{PV} T \tag{47.11}$$

$$h_a = C_{Pa} T \tag{47.12}$$

So the heat flux can be expressed in the following:

$$\overrightarrow{J}_q = -\lambda_p^1 \nabla P_V - \lambda \nabla T \tag{47.13}$$

where the migration coefficient λ_p^1 and apparent thermal conductivity λ are described as:

$$\lambda_p^1 = C_{PV}\rho_V(\frac{D_{ea}}{\rho_a R_a} + \frac{D_{eV}}{\rho_V R_V}) \tag{47.14}$$

$$\lambda = (1 - \varepsilon)\lambda_s + \frac{\varepsilon C_{PV}\rho_V}{T}(\frac{D_{ea}(P - P_V)}{\rho_a R_a} - \frac{D_{eV}P_V}{\rho_V R_V}) \tag{47.15}$$

Apparent thermal conductivity depends not only on the thermal conductivity of each phase, but also on the structure property of the solid grids, forms, and states of each phase in the porous media.

47.2.2 Conservation Equations

Using the approach in which the macroscopic conservation equations are obtained by averaging the equations over a representative volume, the microscopic mass and energy conservation equations are as follows:

$$\varepsilon\frac{\partial\rho_V}{\partial t} + \nabla(\overrightarrow{J}_V) = 0 \tag{47.16}$$

$$\frac{\partial[(1 - \varepsilon)\rho_s C_{Ps}T + \varepsilon\rho_V C_{PV}T + \varepsilon\rho_a C_{Pa}T]}{\partial t} + \nabla(\overrightarrow{J}_q) = 0 \tag{47.17}$$

By combining Eq. (47.7), Eq. (47.16) can be rewritten as:

$$\varepsilon\frac{\partial\rho_V}{\partial t} = \frac{\partial}{\partial z}\left[\lambda_p\frac{\partial P_V}{\partial z}\right] + \frac{\partial}{\partial z}\left[\lambda_p^{11}\frac{\partial T}{\partial z}\right] \tag{47.18}$$

By combining Eq. (47.13), Eq. (47.17) can be rewritten as:

$$[(1 - \varepsilon)\rho_s C_{Ps} + \varepsilon\rho_V C_{PV} + \varepsilon\rho_a C_{Pa}]\frac{\partial T}{\partial t} = \frac{\partial}{\partial z}\left(\lambda_p^1\frac{\partial P_V}{\partial z}\right) + \frac{\partial}{\partial z}\left(\lambda\frac{\partial T}{\partial z}\right) \tag{47.19}$$

The initial and boundary conditions can be obtained by analyzing the heat and mass migration on the surface:

$$T_{t=0} = T_0 \tag{47.20a}$$

$$P_{V,t=0} = P_{V0} \tag{47.20b}$$

$$T_{z=0} = T_1 \tag{47.21a}$$

$$\partial P_V/\partial z|_{Z=0} = 0 \tag{47.21b}$$

$$\left(\lambda_p \frac{\partial P_V}{\partial z} + \lambda_p^{11} \frac{\partial T}{\partial z}\right)\bigg|_{z=L} = \alpha_m(\rho_{VS} - \rho_{V\infty}) \tag{47.21c}$$

$$\left(\lambda_p^1 \frac{\partial P_V}{\partial z} + \lambda \frac{\partial T}{\partial z}\right)\bigg|_{z=L} = \alpha(T_S - T_\infty) \tag{47.21d}$$

47.2.3 Parameters

47.2.3.1 Convection Heat Transfer Coefficient and Mass Transfer Coefficient

According to [16], upon a porous material surface, the convection heat transfer coefficient α is obtained from the following equations:

$$\mathrm{Nu} = 0.0131 \mathrm{Re}^{0.9} \mathrm{Pr}^{0.33} \tag{47.22}$$

The mass transfer coefficient $\alpha m = 0.00117$ m/s is an experimental result. Similar values are also used by Xu and Zhang [4].

47.2.3.2 Formaldehyde Concentration in the Chamber

According to Clapeyron's equation for ideal gas, the molar concentration of formaldehyde CV can be written as:

$$C_V = \rho_V/M_V = P_V/(R_0 T) \tag{47.23}$$

When the partial pressure of formaldehyde is low, the Langmuir's equation can be simplified to Henry's law. In fact, the equation used in our formaldehyde emission modeling of dry building materials, CV = KCs, is a different expression of Henry's law. K is the partition coefficient. Based on the Langmuir's equation and experimental analysis, the correlation of K and T of the particle board is given as [17]:

$$K = 0.00013\, T^{0.5} \exp\left(4722/T\right) \tag{47.24}$$

The following equation is needed to combine Eqs. (47.17–47.19) to obtain the formaldehyde concentration in the chamber:

$$\frac{\mathrm{d}C_\infty}{\mathrm{d}t} = \frac{A}{V} m(t) as - \frac{Q}{V} C_\infty \tag{47.25}$$

The formaldehyde emission rate m(t) can be expressed as:

$$m(t) = -\left(\frac{\lambda_p}{\varepsilon} \frac{\partial P_V}{\partial z} + \frac{\lambda_p^{11}}{\varepsilon} \frac{\partial T}{\partial z} \right)\Bigg|_{z=L} \tag{47.26}$$

Based on the parameter expressions, numerical simulation is carried out for one-dimensional heat and formaldehyde migration of an ordinary particle board by using a finite difference method.

47.3 Results and Discussion

To illustrate the effect of bake-out on the formaldehyde migration in a floor heating system, seven typical cases were designed in our simulation as shown in Table 47.1.

47.3.1 Concentration in a Baked-Out Chamber

Figure 47.2 shows the comparison of the formaldehyde concentration in a bake-out chamber with the different temperature of the bottom layer. The temperature of the bottom layer of the board is regulated at 25 °C (case 1) and 45 °C (case 2), respectively, under baked process, while the temperature of the air keeps 25 °C under ventilation process. For clarity, the trends within earlier 120 h are enlarged in Fig. 47.2a-a. As shown in Fig. 47.2, the trends of the formaldehyde concentration in the chamber are similar with the experimental results [15]. In all cases, the formaldehyde concentration in the chamber decreases along with the time, while the formaldehyde concentration in the airtight chamber reaches the peak level more quickly under the non-isothermal condition than that under the isothermal condition. Within the earlier several days as shown in Fig. 47.2a-a, the difference between the isothermal and nonisothermal cases is not so clear. After the bake-out

Table 47.1 Case parameters for simulation

Case number	Under floor heating	Time for heating (h)	Temperature of the bottom layer (°C)	Time for ventilation (h)	Temperature of the air when ventilation (°C)
1	No heating		25	25	12
2	Heating	12	45	12	25
3	Heating	12	35	12	25
4	Heating	24	35	24	25
5	Heating	18	35	6	25
6	Heating	6	35	18	25
7	Heating	12	45	12	45
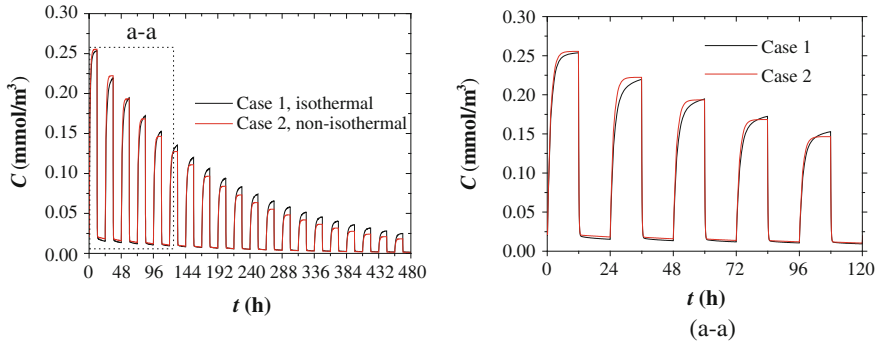
Fig. 47.2 Comparison of the concentration in a bake-out chamber under isothermal and non-isothermal condition

arrived at 120 h, the concentration level of the nonisothermal case is obviously smaller than that of the isothermal case. With the increasing of the time of the formaldehyde diffusion, the difference between isothermal and nonisothermal cases becomes more and more obviously. This phenomenon implies that the effect of under floor heating becomes more and more important, and the method of remove formaldehyde from building materials by under floor heating is feasible.

47.3.2 Sensitivity Analysis

Figure 47.3a illustrates the comparison of the concentration in the chamber under varied heating time and varied bake-out period. The bake-out frequency in case 4 is 2 times than that in case 3. Figure 47.3a shows that with the increasing of bake-out frequency, the emission of formaldehyde from the board increases, and the formaldehyde concentration remained in the chamber decreases after 2 days. As shown in Fig. 47.3b, the longer the time of ventilation is, the smaller the
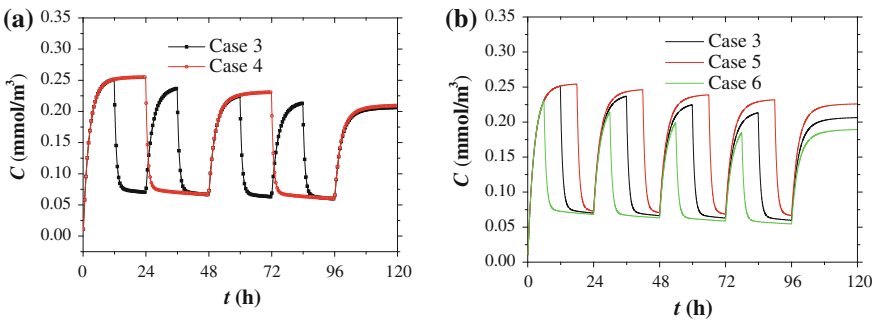
Fig. 47.3 Comparison of the concentration in a bake-out chamber, **a** under varied heating frequency with constant heating time, **b** under varied heating time with constant period

concentration remained in the chamber is. Comparing with case 3, the bake-out frequency is the same in case 5 and case 6, while the heating time is 1.5 times in case 5 and 0.5 times in case 6. In other words, case 5 has the shortest time of ventilation while case 6 has the longest time of ventilation in Fig. 47.3b.

47.4 Conclusions

To comply with concentration requirements in previously constructed homes, many people are conducting bake-out in buildings prior to occupancy. The material temperature is considered a major factor that determines the effect of the bake-out. Except that some experimental studies have conducted within the past decade, all of the previous researchers have suggested that further studies are required. To confirm the effect of the bake-out, an improved model of the coupled heat and formaldehyde migration process is developed and analyzed to investigate the transport features in under floor heating system. Based on the theory of non-equilibrium thermodynamics and molecular kinetics, the mechanisms of the heat and mass transfer in dry porous building materials are discussed. The coupled heat and formaldehyde migration process in a floorboard is simulated under noniso-thermal conditions of the temperature. Numerical results show that the effect of under floor heating becomes more and more important with the increasing of the temperature of the bottom layer, and the emission of formaldehyde from the board increases with the increasing of bake-out frequency. The longer the time of ventilation is in bake-out, the smaller the concentration remained in the chamber is. The removal efficiency of formaldehyde from building materials with a under board heating process within the ventilation period is prominent, but the energy consumed under such a mode is unsatisfied.

References

1. Yang X, Chen Q (2001) A coupled airflow and source/sink model for simulating indoor VOCs exposures. Indoor Air 11:257–269
2. Deng BQ, Kim CN (2004) An analytical model for VOC emission from dry building materials. Atmos Environ 38(8):1173–1180
3. Haghighat F, Lee CS, Ghaly WS (2002) Measurement of diffusion coefficients of VOCs for building materials: review and development of a calculation procedure. Indoor Air 12:81–91
4. Xu Y, Zhang YP (2003) An improved mass transfer based model for analyzing VOC emissions from building materials. Atmos Environ 37:2497–2505
5. Zhang LZ, Niu JL (2003) Effects of substrate parameters on the emissions of volatile organic compounds from wet coating materials. Build Environ 38:939–946
6. Molhave L (1989) The sick buildings and other buildings with indoor climate problems. Environment 15:65–74

7. Que ZL, Furuno T, Katoh S et al (2007) Evaluation of three test methods in determination of formaldehyde emission from particle board bonded with different mole ratio in the urea-formaldehyde resin. Build Environ 42:1242–1249

8. Zhang JS (2005) Combined heat, air, moisture, and pollutants transport in building environmental systems. JSME Int J (B) 48(2):182–190

9. Girman JR, Alevantis LE, Kulasingam GC et al (1989) The bake-out of an office building: a case study. Environ Int 15:449–453

10. Wiglusz R, Sitko E, Nikel G et al (2002) The effect of temperature on the emission of formaldehyde and volatile organic compounds (VOCs) from laminate flooring-case study. Build Environ 37:41–44

11. Kim S, Kim HJ (2005) Comparison of formaldehyde emission from building finishing materials at various temperatures in under heating system; ONDOL. Indoor Air 15:317–325

12. Follin T (1997) Airing out pollutions. In: Proceedings of healthy building/IAQ 3, 353–356

13. Hicks J, Worl K, Hall K (1990) Building bake-out during commissioning. In: Proceedings of Indoor Air 90, Toronto, 5th international conference on indoor air quality and climate 3, 413–418

14. Offerman FJ, Loiselle SA, Ander GD, Lau H (1993) Indoor contaminant emission rates before and after a building bake-out. In: Proceedings of the ASHRAE conference IAQ93, Philadelphia, pp 157–163

15. Kang DH, Choi DH, Lee SM (2010) Effect of bake-out on reducing VOC emissions and concentrations in a residential housing unit with a radiant floor heating system. Build Environ 45:1816–1825

16. Shen XZ, Chen ZQ (2010) Coupled heat and formaldehyde migration in dry porous building materials. Build Environ 45:1470–1476

17. Zhang YP, Luo XX, Wang XK, Qian K, Zhao RY (2007) Influence of temperature on formaldehyde emission parameters of dry building materials. Atmos Environ 41:3203–3216

Chapter 48
Evaluation of Four Office Buildings' Indoor Air Quality Using the Decibel Concept in Guilin

Zhiping Zhou and Rong Wang

Abstract In order to find out indoor air quality (IAQ) condition at the Guilin public building, four office buildings' IAQ had been investigated with the carry-home fast inspect instrument from November 2010 to September 2011 in Lingui New District. Based on the research data, IAQ in four public buildings in Guilin was evaluated using the decibel concept index method. The results show that SBS happens in three of the buildings. The main pollutants indoor are PM_{10} and HCHO. Due to the decibel concept, index method requires few assessment indexes; it is easy to operate; however, there will be a large deviation if some unmeasured parameter value is over proof. Regarding CO_2, TVOC, and HCHO as chemical pollutant, evaluation index representatives are suitable to estimate IAQ when considering the condition of China. Comparatively, the composite index method may sometimes underestimate it.

Keywords Office building · IAQ · The decibel concept index · Logarithm assessment · Composite index method

48.1 Introduction

With the improvement of people's living standards, indoor air quality (IAQ) has been paid more and more attention. The majority of people spend more than 80 % of the time living and working in indoor area; IAQ directly affects the health of the people. In 1989, Denmark Professor P. O. Fanger proposed "quality reflects the requirement". The Chartered Institute of Building Services Engineers (CIBSE) believe that if there exists any smell, less than 50 % occupants can perceive it, less

Z. Zhou (✉) · R. Wang
School of Architecture & Transportation Engineering,
Guilin University of Electronic Technology, Guilin, China
e-mail: zzpn98@163.com

than 20 % of occupants feel uncomfortable, less than 10 % of occupants feel mucosa irritate, and less than 5 % of occupants feel restless in less than 2 % of the time, then the IAQ can be considered as acceptable [1]. ASHRAE Standard 62-1989 "Ventilation for Acceptable Indoor Air Quality" defines acceptable IAQ as "no contaminants in air reach the harmful concentrations limit determined by cognizant authorities and with which a substantial majority (80 % or more) of the people exposed in this circumstance do not feel dissatisfaction". The meaning of the definition of IAQ mainly includes two aspects: subjective evaluation and objective evaluation. Recently, there has no unified standard been established in China; the subjective evaluation method, the objective evaluation method, and the general evaluation method are the most commonly used ways to estimate indoor air quality. At present, there are many scholars who put forward the gray theory evaluation method and application of the decibel concept evaluation method (decibel index method). The DB index method is not widely used in China. The method was first proposed by the Czech University of Prague Jokl [2] in 2000. In 2002, Chinese scholars Liu and Shen [3] put forward a new method of indoor chemical pollutants evaluation method based on CO_2 and HCHO, and the principle of the method is just the same as the M. V. Jokl principle. Besides, few decibel indexes were used in our country. In order to find out IAQ condition at the Guilin public building, four office buildings had been investigated for their IAQ. According to the reach data, IAQ was evaluated using the decibel concept index and compared with the result given out by popularly used evaluation method of the indoor air quality, and the feasibility of this evaluation method was found out in China.

48.2 Data Detection

Four comprehensive office buildings' IAQ had been measured from November 2010 to September 2011 in Lingui New District. Four office buildings are located in Lingui New District. The building A is a 21-m^2, 4/6-layer, cement-floor middle school office, and its height is 3 m. There is an air conditioner, a ceiling fan, and 7 computers in the room, the ceiling fans and 5–7 computers normally run, air conditioner occasionally runs at the same time, no indoor combustion equipment is in the room, and outdoor belongs to campus roads. The building B is a 2-floor, 98-m^2 independent office building; there are isolated air-conditioning system, one computer, one printer, and one copy machine in the room. There are some company's products and no indoor combustion equipment in the room. Outdoor parking lot is downstairs. The building C and D are different offices within the same office, 25 m^2, 33/48 layer, their heights are 3 m, central air conditioning is operating normally, no combustion equipment and toilet, around which belong to office. There are four pots of green plants and some company products in the building D's room. According to the "civil engineering indoor environmental pollution control standard" [4] and "IAQ standards" [5] provisions, combined with the practical condition of the building and the resources of the laboratory,

Table 48.1 IAQ sampling value in four office buildings and related IAQ standards

Parameters	Unit	Building A	Building B	Building C	Building D
Temperature	°C	28	29.5	23.5	23
Relative humidity	%	78	68	62	75
CO	mg/m^3	2.375	1.5	0	0
CO$_2$	ppm	477	1,096	782	731
O$_3$	mg/m^3	0.086	0.107	0.128	0.128
HCHO	ppb	90	140	60	180
PM$_{10}$	mg/m^3	0.221	0.464	0.171	0.237
TVOC	μg/m^3	433	430	445	360

selected temperature, relative humidity, atmospheric pressure, carbon monoxide, carbon dioxide, ozone, formaldehyde, respirable particulate matter (PM$_{10}$), and volatile organic compound parameters as detection parameters, used portable instrument as testing instrument. Specific data are shown in Table 48.1.

48.3 Data Evaluation

48.3.1 DB Index Method

Czech University of Prague Jokl M. V according to the Yaglou theory and the Weber/Fechner theorem using the decibel concept to IAQ evaluation method defined the $L_{\text{odour(CO}_2)}$ and $L_{\text{odour (TVOC)}}$ as CO$_2$ and TVOC evaluation indexes. It makes CO$_2$, TVOC as the main indoor pollutants objects in evaluation method. Domestic scholars Liu Yufeng, Shen Jinming put forward a new method of indoor chemical pollutants evaluation method based on CO$_2$ and HCHO, and the principle of the method proposed by the Jokl M. V principle. Considering the two evaluation methods, the concentration of CO$_2$, TVOC, and HCHO are used to evaluate air quality in the office building as the evaluation of the indoor pollutants. The definition of the three indicators are as follows:

$$L_{\text{odour(CO}_2)} = 90 \log \frac{C_{\text{CO}_2}}{485} \text{ (dCd)} \tag{48.1}$$

$$L_{\text{odour (TVOC)}} = 50 \log \frac{C_{\text{TVOC}}}{50} \text{ (dTv)} \tag{48.2}$$

$$L_{\text{odour(HCHO)}} = 67 \log \frac{C_{\text{HCHO}}}{50} \text{ (dFm)} \tag{48.3}$$

Table 48.2 Various limits and ranges for CO_2 and TVOC concentrations (unadapted persons)

CO_2		TVOC		Evaluation level	Notes
C_{CO_2}/ppm	$L_{odour(CO_2)}$/dCd	C_{TVOC}/µg/m^3	$L_{odour(TVOC)}$/dTv		
485–1,015	0–29	50–200	0–30	I	Optimal range
485–615	0–9	50–85	0–12		Asthm. optimal range
616–1,015	10–29	86–200	13–30		Asthm. admissible range
1,016–1,570	30–46	201–360	31–43	II	Admissible range
1,571–5,000	47–91	361–3,000	44–89	III	Long-term tolerable (SBS) range
5,001–15,000	92–134	3,001–25,000	90–135	IV	Short-term tolerable range
≥15,001	≥135	≥25,001	≥136	V	Intolerable range

where 485 (ppm), 50 (µg/m^3), and 50 (ppb) are severally the threshold concentration values of CO_2, TVOC, and HCHO; C_{CO_2} (ppm), C_{TVOC} (µg/m^3), and C_{HCHO} (ppb) are severally measured concentrations of CO_2, TVOC, and HCHO; and 90, 50, and 67 are coefficients of proportionalities.

On the psycho-physical scale according to Yaglou, the weakest odor that can be detected by the human smell sensors is equal to 1 and corresponds to the lower limit of percentage dissatisfaction (PD) of 5.8 % and is equivalent to a CO_2 threshold concentration of 485 ppm–0 dB (odor CO_2)–0dCd (decicarbdiox), and a TVOC threshold concentration of 50 µg/m^3–0 dB (odor TVOC)–0dTv (decitvoc), and a HCHO threshold concentration of 50 ppb–0 dB(odor HCHO)–0dFm (decihcho). The upper limit is determined by the initial value of toxicity CO_2: 15,000 ppm–134 dCd and TVOC: 25,000 µg/m^3–135 dTv, and HCHO: 5,000 ppb–134 dFm.

The logarithmic evaluation indicators and evaluation levels of CO_2 and TVOC are presented in Table 48.2. The logarithm evaluation of HCHO is presented in Table 48.3.

Generally, most irritant gases' stimulation show an additive effect. It is reasonable to assume that stimulation of CO_2 as the representative of the human body odor and stimulation of TVOC and HCHO as organic compounds on the human body exhibit additive. At least, to understand the common stimulus resulting in increased level of symptoms or dissatisfied feelings rate is no problem. Because people feel the amount proportional to the logarithm of the stimulus, adding the logarithmic evaluation of CO_2, TVOC, and HCHO together as an evaluation level of indoor chemical pollution indicators is reasonable, namely:

Table 48.3 Various limits for HCHO concentrations

HCHO(ppb)	≤50	100	200	400	1,000	1,500	2,000	2,500	5,000
$L_{odour(HCHO)}$(dFm)	0	20	40	60	87	99	107	114	134

Table 48.4 Measured CO_2, TVOC and HCHO levels in various locations (unadapted persons)

Building	C_{CO_2}/ ppm	$L_{odour(CO_2)}$/ dCd	C_{TVOC}/mg/ m^3	$L_{odour(TVOC)}$/ dTv	C_{HCHO}/ ppb	$L_{odour(HCHO)}$/ dFm	$\sum L$
A	477	0	433	46.88	90	12.76	59.64
B	1,096	31.87	430	46.72	140	22.36	100.95
C	782	18.67	445	47.47	60	3.96	70.1
D	731	16.04	360	42.87	180	27.82	86.73

$$\sum L = L_{odour(CO_2)} + L_{odour(TVOC)} + L_{odour(HCHO)} \qquad (48.4)$$

According to Eqs. (48.1–48.4) calculations, the logarithmic evaluation of CO_2, TVOC, and HCHO is shown in Table 48.4.

48.3.2 The Comprehensive Evaluation Index of IAQ

In order to verify the DB index evaluation method in IAQ evaluation of reliability, now the IAQ of four buildings was evaluated by commonly comprehensive evaluation index method with reference to environmental quality grading standards, the evaluation grades, and comments are showed in Table 48.5 and the evaluation results are shown in Table 48.6.

48.4 Evaluation of the Results and Analysis

Based on the comparison, the evaluation of logarithmic values of CO_2, TVOC, and HCHO, in Table 48.4, TVOC impact on IAQ is the largest, followed by HCHO. However, HCHO concentration beyond the limit of the standard when TVOC concentration is within the limits. Is it concerned with testing instruments or is the given formula coefficient too big? Further research is needed.

Seen from the calculation results of the Table 48.4, for building A, when the concentration of CO_2 is below a predetermined threshold, logarithmic evaluation index is 0 and the impact of the chemical contaminants HCHO and TVOC will be highlighted. The concentration of TVOC is similar to the buildings A and B, but the CO_2 concentration is different; the total logarithmic value is difference of nearly double between them.

From the comparison of the evaluation of CO_2, TVOC, and HCHO in Table 48.4, for unadapted, the sum index of IAQ logarithmic ($\sum L$) of four office buildings in descending order are as follows: building B > D > C > A. It shows IAQ of building A is the best, followed by building C and D, building B is the worst. But for the single logarithm index, besides building D is less than 43, to allow the scope, four buildings' TVOC logarithm index is greater than 44, belong to the IAQ grade III, for the long-term bear (SBS) range.

Table 48.5 Indoor air quality grade and rating standard

The synthesis Index	IAQ grade	Grade evaluation	Characters
≤0.49	I	Cleanly	It is fit for living in mankind
0.50–0.99	II	No pollution	The elemental pollutant in each environment does all not go beyond the limit, mankind live normal
1.00–1.49	III	Light pollution	There is a factor going beyond limit in environment pollutant at least, in addition to the allergy, cannot take place the acute chronic poisoned generally
1.50–1.99	IV	Moderate pollution	There are 23 factors going beyond limit in environment pollutant generally, the crowd health victimizes obviously, the allergy victimizes more seriously
≥2.00	V	Heavy pollution	There are 3–4 factors going beyond limit in environment pollutant generally, the crowd health victimizes serious, the allergy may die

According to maximum index value analysis in Table 48.6, main indoor air pollutants are PM_{10} and HCHO. The comprehensive index of IAQ of four office buildings in descending order are as follows: building B > D > A > C. It shows IAQ of building C is the best, followed by building A and D, building B is the worst. For building B and D, the results of the two evaluation methods are very consistent, but the sequencing results are opposite in Table 48.4 for building A and C.

If the indoor pollutants concentration is not exceed the standard, the DB index method is feasible. But once the individual chemical pollutant exceeds the standard, the evaluation method is very safe.

For example buildings A and C, from the aspect of over proof rate, test results of HCHO and PM_{10} are over proof in building A, test results of PM_{10} is over proof in building C without considering respirable PM_{10} effect, and the concentration of PM_{10} exceeds the standard, so the sort result is not reliable. It should adopt air quality comprehensive index sort, namely building B > D > A > C.

Table 48.6 IAQ evaluation value in four office buildings

Building	CO	CO_2	O_3	HCHO	PM_{10}	TVOC	Maximum value of index	The synthesis index of air quality	Air quality grade and evaluation
A	0.238	0.477	0.535	1.206	1.473	0.721	1.473	1.069	III/moderate pollution
B	0.15	1.096	0.668	1.877	3.093	0.717	3.093	1.98	IV/moderate pollution
C	0	0.782	0.802	0.804	1.14	0.742	1.14	0.901	II/light pollution
D	0	0.731	0.802	2.413	1.58	0.6	2.413	1.57	IV/moderate pollution

Compared with the comprehensive index method, the DB index method has few assessment indices, easy to test, low cost, but the evaluation index is essential to choose.

In accordance with M. V. Jokl, CO_2 and TVOC are selected as the evaluation index; using the DB index method, logarithmic index of 4 buildings is sorted by size: building $B > C > D > A$, and the analysis result showed big difference. Such as building A, the concentration of CO_2 is lower than the standard limit value, the logarithmic index is 0, and the concentration of TVOC is equal to the building B, but the result shows that the worst air quality is in building B, the best is in building A, exaggerate the contribution of CO_2 to indoor air pollution. For CO_2 and TVOC concentration meet the requirement of the standard in building A, C and D, without considering the effects of over proof HCHO and PM_{10} in indoor air, we can draw the actual opposite conclusion. Apparently in China to select only the CO_2, TVOC for evaluation indices is unreasonable.

If according to Liu Yufeng, Shen Jin Ming proposed the CO_2 and HCHO as evaluation indices, logarithmic index of 4 buildings is sorted by size: building $B > D > C > A$; it is consistent with the paper, but still does not match with the actual. The main reason is to ignore the effect of PM_{10}.

DB index method in IAQ evaluation application is simple but there are still many deficiencies. It can not simply be applied to all occasions. In the case that indoor pollutant constituents are undefined, the proposal remains to evaluate the air quality by comprehensive index method. It is suggested to use CO_2, TVOC and HCHO as evaluation indices.

IAQ grade is sometimes inconsistent with rating comment in comprehensive index method, as building A and C shown in Table 48.6.

48.5 Conclusion

According to the DB index method, three buildings IAQ belong to the scope of SBS. It shows the office building IAQ is not optimistic. From the comprehensive index method, we can see that PM_{10} and HCHO are main pollutants of indoor air.

The DB index method has few assessment indices and is easy to evaluate. CO_2, TVOC, and HCHO concentrations are suitable to use as chemical pollutant evaluation index in China.

If any unevaluated parameters are over proof, evaluation results of the DB index method will have greater deviation; the application of comprehensive index method is more reasonable and more safety.

The comprehensive index method sometimes makes evaluation results smaller.

References

1. Wang ZJ, Zhao JN, Liu J (2006) Indoor air environment. Chemical Industry Press, Beijing, pp 112–115
2. Jokl MV (2000) Evaluation of indoor air quality using the decibel concept based on carbon dioxide and TVOC. Build Environ 35(8):677–697
3. Liu YF, Shen JM (2002) New methods for assessing indoor compound contaminants. Build Sci 18(6):53–56, 52
4. GB50325-2010 (2011) Civil engineering indoor environmental pollution control standard. China Planning Press, Beijing
5. GB/T 18883-2002 (2003) Indoor air quality standard. China Standard Press, Beijing

Chapter 49
Research on Natural Ventilation Technology of Traditional Dwelling House in the Southern Area of Anhui Province

Zhijia Huang and Wei Qian

Abstract The traditional dwelling house is taken as the object to identify the main architectural elements which affect natural ventilation in the southern area of Anhui province. Based on CFD method, the traditional dwelling house in southern area of Anhui province was simulated under different size and shape of courtyard, and also the effect of interior lighting is conducted by using Ecotect. The results show that the best size of courtyard has a nice natural ventilation and interior lighting with the length of distance between the midline of the two windows of bedrooms and the width of the yard. The average wind speed reaches 0.1 m/s and average age of air is 340 s in living room and bedroom, and lighting coefficient of living room and bedroom is 5 %.

Keywords Traditional dwelling house · Southern area of Anhui province · Natural ventilation · Interior lighting · Courtyard

49.1 Introduction

Chinese traditional dwelling house, which has been taken as a rich cultural heritage of domestic architecture culture, containing much eco-technology and experience [1–5], reflects the ideology product of adaptation to the local climate and other natural conditions. Therefore, it is very necessary to restudy Chinese traditional dwelling house. Huizhou traditional dwelling house located in the southern area of Anhui province whose formation is inextricably linked with

Z. Huang (✉) · W. Qian
School of Civil Engineering and Architecture, Anhui University
of Technology, Maanshan, 243002 Anhui, China
e-mail: hzj@ahut.edu.cn

the history and culture of Huizhou also has its own distinctive local characteristics. Huizhou ancients are famous for business; in order to achieve the purpose of fire security, tall and thick external wall which has less number of windows or a small window is designed. Thus, indoor natural ventilation and lighting is completely dependent on the courtyard. The courtyard is the most positive; the most active elements of architectural space play an important role in indoor air flow. The test of interior environment of Huizhou traditional dwelling house of Hongcun village in mild season has been performed by Xiaoyang [6]. Field study of thermal environment in Wannan traditional dwelling house in the summer also has been carried out by Song [7] in Tsinghua University. He points out that the courtyard is important in improving indoor air quality. On the basis of the previous studies, the traditional dwelling house is simulated using Airpak to identify the main architectural elements which affect natural ventilation in the southern area of Anhui province, and also the effect of interior lighting is studied using Ecotect in this paper.

49.2 Simulation Program

49.2.1 Simulation Object

The courtyard style is used to the layout of traditional dwelling house in the southern area of Anhui province, as shown in Fig. 49.1. The most common layout of the traditional dwelling house is traditional San He Yuan, as shown in Fig. 49.1(a), which also is the most economical one. The traditional Sanhe yuan is taken as the object in this paper. The traditional Sanhe yuan has two floors with one door on the external wall, courtyard in the center of the house; the first floor is the living room; the left and the right of living room is bedroom; tall and thick external wall which has less number of windows or a small window is designed to achieve the purpose of fire security. The length of traditional Sanhe yuan is 10 m and the width is 9 m. The first floor is 3 m high and the second is 4.5 m high. Based on above information, building model is done in Airpak and Ecotect.

49.2.2 Simulation Program

The traditional dwelling house is simulated using Airpak to identify the main architectural elements which affect natural ventilation in the southern area of Anhui province, and also the effect of inner daylight is studied by Ecotect in this paper, and simulation programs are shown in Table 49.1.
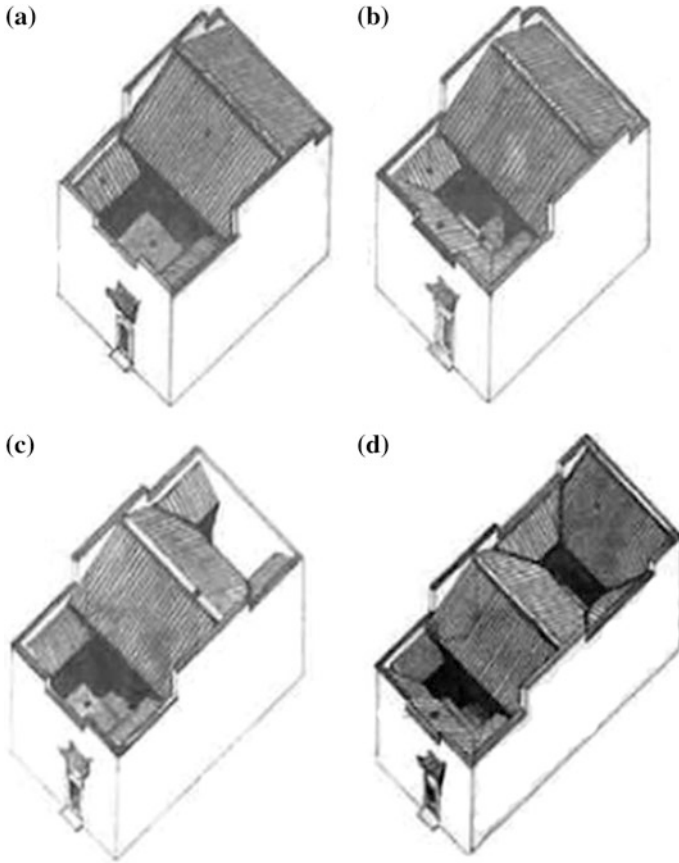
Fig. 49.1 The common layout of the traditional dwelling house (a) San He Yuan, (b) Si He Yuan, (c) San He Yuan with two yards, (d) Si He Yuan with two yards

Table 49.1 Simulation program

Case	length × width (m)
Case 1	6.5 × 3
Case 2	3 × 3
Case 3	9 × 3
Case 4	6.5 × 1.5

49.2.3 Mathematical Models

The processes of the fluid flow and heat transfer comply with the three basic laws of physics, namely the conservation of mass, conservation of momentum, and the conservation of energy. From the viewpoint of the numerical heat transfer, the

mathematical expressions of the law of conservations can be expressed as the following general form:

$$\frac{\partial(\rho\phi)}{\partial t} + \text{div}\left(\rho \vec{U} \phi\right) = \text{div}\left(\Gamma_{\phi}\text{grad}\phi\right) + S \qquad (49.1)$$

where ϕ which is a common variable can represent a solution variables such as u, v, w, T. Γ_{ϕ} is a generalized diffusion coefficient, S is a generalized source. In this paper, in order to simplify the problem, the following assumptions are made: indoor air is an incompressible Newtonian fluid of constant material properties; to account for turbulence, the model is an indoor zero equation; the model is solved when mass residuals are reduced to less than 10^{-5} and velocity residuals to 10^{-4}.

49.2.4 Boundary Conditions

On the basis of the previous studies [2] about heat and wind environment of the traditional dwelling house in the southern area of Anhui province, the inlet velocity of the courtyard is set 0.5 m/s; outlet boundary condition set free export. In Ecotect, cloudy model is used; critical illumination value is set 4,500 lx.

49.3 Results Analysis

49.3.1 Distribution of Wind Speed

Distribution of wind speed at the height of 1.5 m under different size of courtyard is shown in Fig. 49.2. The figure shows that the effect of natural ventilation of the yard is better than that of the living room and bedroom. In case 2, there are large no wind area in living room and bedroom although its yard has a nice natural ventilation. In living room and bedroom, wind speed is below 0.07 m/s in most of the area. The same condition is in case 4. Compared to case 2, the effect of natural ventilation has improved in living room and bedroom in case 1. Air flows through the hall and outside window into the living room and bedroom, where the average wind speed reaches 0.1 m/s. Compared to case 1, the effect of natural ventilation has not much improved.

49.3.2 Distribution of Age of Air

Distribution of age of air at the height of 1.5 m under different size of courtyard is shown in Fig. 49.3. The average age of air is 340 s in living room and bedroom in case 1, and reaches 600 s at the corner of the living room.
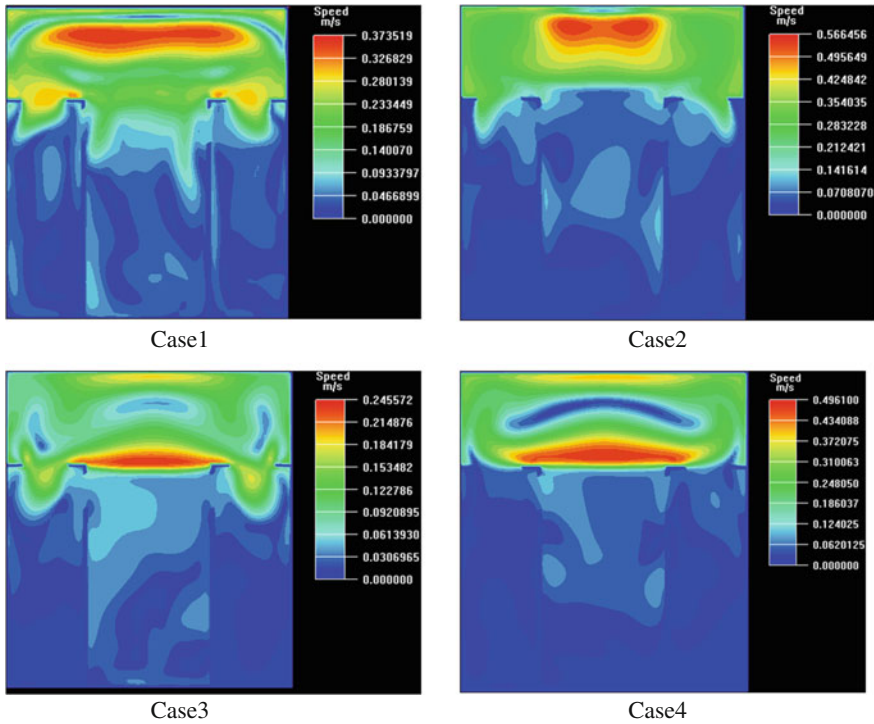
Fig. 49.2 Distribution of wind speed at the height of 1.5 m of different cases

The average age of air is 260 s in living room and bedroom in case 2, which has a better overall age of air. Under case 3, the average age of air is too large and reaches 1,700 s at the corner of the bedroom. Under case 4, the average age of air has not improved in bedroom.

49.3.3 Distribution of Lighting Coefficient

Distribution of lighting coefficient at the height of 0.8 m under different size of courtyard is shown in Fig. 49.4. Courtyard plays an important role in indoor air flow because of the tall and thick external wall which has less number of windows or a small window. As is shown in Fig. 49.4, lighting coefficient of living room and bedroom is below 8 %. Compared to case 2 and case 3, two bedrooms have a nice lighting effect in case 1 and case 3. The lighting effect is very nice in case 1 which is of great significance for indoor lighting. Under case 3, although it has a nice effect of lighting, it will gain much heat in summer.
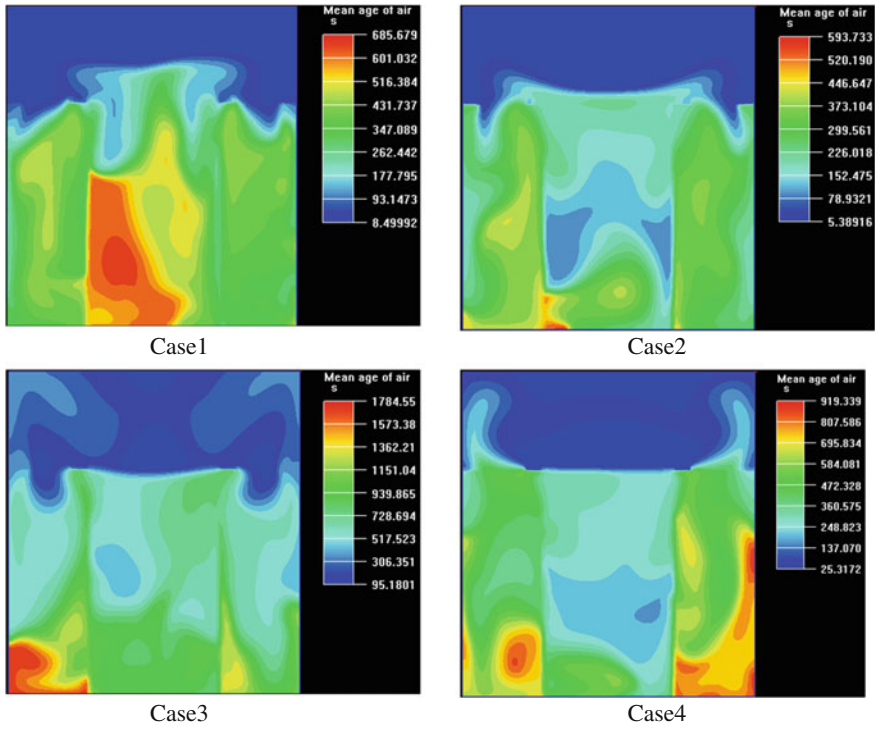
Fig. 49.3 Distribution of age of air at the height of 1.5 m of different cases

49.3.4 Effect of Natural Ventilation Under Case 1

The effect of natural ventilation under case 1 is shown in Fig. 49.5. Under case 1, the traditional dwelling house has a nice natural ventilation and daylight with the length of distance between the midline of the two windows of bedrooms and the width of the yard. As is shown in Fig. 49.5, the effect of natural ventilation of the first floor is better than that of the second floor. The average wind speed of second floor reaches 0.6 m/s and average age of air is nearly about 100 s. Although it has a nice effect of natural ventilation in second floor, it will gain much heat in summer. Therefore it is unsuitable to live in the second floor.
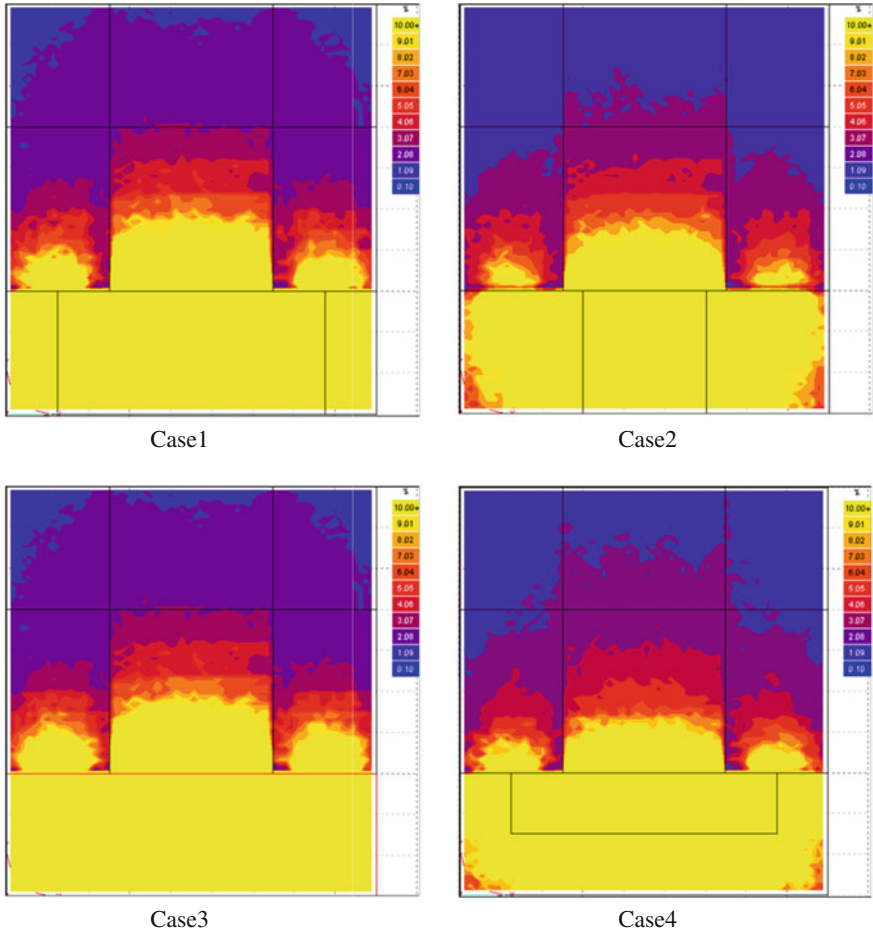
Fig. 49.4 Distribution of lighting coefficient at the height of 0.8 m of different cases
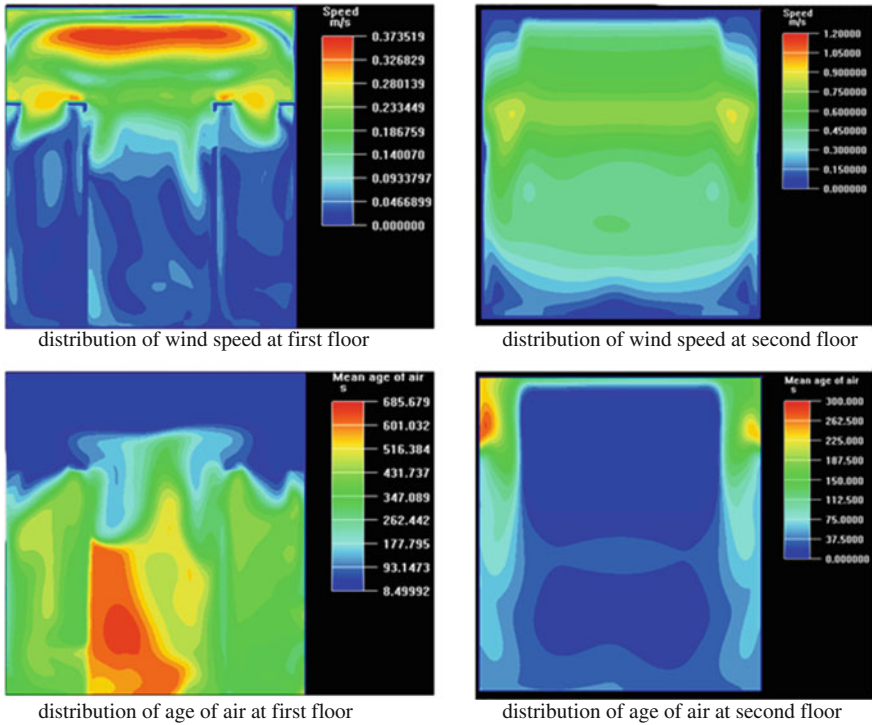
distribution of wind speed at first floor

distribution of wind speed at second floor

distribution of age of air at first floor

distribution of age of air at second floor

Fig. 49.5 Effect of natural ventilation under case 1

49.4 Conclusion

1. Indoor natural ventilation and lighting is completely dependent on the courtyard, which plays an important role in indoor air flow because of tall and thick external wall which has less number of windows or a small window. The best size of courtyard has a nice natural ventilation and daylight with the length of distance between the midline of the two windows of bedrooms and the width of the yard. The average wind speed reaches 0.1 m/s, the average age of air is 340 s in living room and bedroom, lighting coefficient of living room and bedroom is about 5 %.
2. The effect of natural ventilation of the second floor is better than that of the first floor since the second floor is near the courtyard. The average wind speed of second floor reaches 0.6 m/s, average age of air is nearly about 100 s. But in summer, it will gain much heat. Therefore it is unsuitable to live in the second floor.

References

1. Jiaping ZQZWL (2005) Ecological building experiences in Chinese traditional dwellings. New Archit 4:7–9
2. Song L, Lin B, Zhu Y (2003) Simulation of the summer indoor thermal condition of a traditional Chinese residential building in Anhui. Tsinghua Univ 43(6):30
3. Guohua T (1996) The thermal, light and sound environment of Xiguan buildings at Guangzhou. South Archit 1:54–57
4. Guohua T (2005) "Xia Changshi's Sunshade" and Lingnan architecture heatproofness. New Archit 6:6
5. Lin B, Wang P, Zhao B (2002) Numerical simulation study of wind environment of traditional Sihe yuan. Archit Technol (5):74–78
6. Xiaoyang C (2009) Interior environment of Huizhou traditional dwelling house of Hongcun village in mild season. Archi J 2:68–70
7. Lin B, Tan G, Wang P et al (2002) Field study of the thermal environment in Wannan traditional residential buildings in the summer. J Tsinghua Univ 42(8):1071–1074

Chapter 50
Self-Reported Situations of Residential Heating and Ventilation Methods Among Shanghai Young Families

Wei Liu, Chen Huang, Yu Hu, Zhijun Zou and Li Shen

Abstract Based on 15,266 questionnaires which were filled out by parents of preschool children, this study investigated the distribution of heating and ventilation equipments and the habit of natural ventilation among young families in Shanghai. The mean age ± standard deviation (SD) of child's mothers is 32.6 ± 3.8 years. The usage rates of coal stove, district heating, or individual heating are smaller than 0.5 %, floor heating 1.3 %, electric room heater 20.7 %, and others 2.0 %. The most common equipment for heating in winter is air conditioner (77.6 %). But 12.4 % of the families still have no residential heating. The usage rate of exhaust fan in kitchen and in bathroom is 16.1 and 78.6 %, respectively. Most of (86.2 %) the families have smoking exhaust ventilator in kitchen. In addition, 44.0, 62.0, 45.3, and 17.5 % of the families frequently open the windows in spring, summer, autumn, and winter, respectively. The usage rates of those equipments and the habit in natural ventilation are significantly associated with the location of residences. Generally, more urban residents frequently open windows than suburban and rural residents. Our results indicate that more urbanization, more new-fashioned air-handled equipments are used in Shanghai families.

W. Liu · C. Huang (✉) · Y. Hu · Z. Zou · L. Shen
School of Environment and Architecture, University of Shanghai
for Science and Technology, Shanghai, China
e-mail: huangc@usst.edu.cn; hcyhyywj@163.com

50.1 Introduction

With the rapid development of economy and technology in China, more and more equipments for ventilation and heating in different styles have been used in the residence [1–9]. From 1991 to 2005, the annual output of household air conditioner in China has increased 14-fold [1]. In 2002, a questionnaire study, which conducted in a Shanghai residential community, found that 45.5 and 95.2 % of the families have had two air conditioners and at least one such device, respectively [2]. Another questionnaire study in 2003 found that the usage rate of air conditioner in Shanghai is up to 98 % [3]. Yoshino found that most of Shanghai residents use individual space heating in winter for residential heating [4]. In 2006, a survey in Shanghai has revealed that the families in the new residential community which was built in 2000s used more mechanical equipments for household heating or cooling than those families in the old community which was built in 1980s, and the usage rates of these equipments have strong association with families' annual household income [5]. These surveys have partly showed the situations of Shanghai residential heating, ventilation, and air-conditioning in different years.

However, the sample sizes in these surveys were relatively small; thus, the results may not be able to represent the overall situations of Shanghai city. In addition, the development of Shanghai economy is so rapid that the situations of heating and ventilation in Shanghai residences perhaps have largely changed. Based on a large-scale questionnaire study, the present study aims at investigating the usage rates of different equipments for residential heating and ventilations in young families with different building style and age and shows the young residents' habit in natural ventilation of child's room in different districts.

50.2 Materials and Methods

From October 2010, a national survey, which was named China, Children, Homes, Health (CCHH), has conducted in ten cities of China independently. Shanghai is one of these cities. The present study is based on the nested questions for residential heating and ventilation in the phase one of this survey in Shanghai.

50.2.1 CCHH Study in Shanghai—Phase One

The CCHH study concluded a cross-sectional study (questionnaire) and a nested case–control study. From April 2011 to April 2012, the cross-sectional study (phase one) in Shanghai has accomplished in three urban districts (Hongkou, Zhabei, and Jingan) and two suburban districts (Banshan and Fengxian). Totally, 17898 parents or guardians of 1–8-year-old children from 72 kindergartens in

these districts have been surveyed. Distributions of questionnaires were conducted in two ways: One is by sending and recovering on-site with the teachers–parents meeting and another is by posting to the teachers of the kindergarten who distributed the questionnaires with papery explanation and guidance to the children's parents or guardians, and then, the teachers recovered and posted the filled questionnaires to us. The cross-sectional study was supported by the Shanghai Municipal Bureau of Education and ethically approved by the ethical committee of School of Public Health, Fudan University in Shanghai.

50.2.2 Statistical Analysis

All specific analyses in the present study were restricted in those individuals with complete data on the variables. Pearson's chi-square (χ^2) test (2-sided) was used to reveal the significance of difference in the usage rates between different groups. A P-value < 0.05 indicated statistically significant. SPSS version 17.0 (SPSS Ltd., Chicago, Illinois, USA) was used to input and analyze the data.

50.3 Results and Discussion

In the survey, 15,266 questionnaires (85.3 %) were effectively filled out. All of these questionnaires were selected to be analyzed in the present study. Children's mean age $\pm$ standard deviation (SD) is 4.9 ± 1.0 years old (range 1–8 years old) and the mean age $\pm$ SD of children's mothers is 32.6 ± 3.8 years old (range 21–52 years old). 68.5 % ($n = 10,259$), 27.0 % ($n = 4,034$), and 4.5 % ($n = 674$) of the families are from urban, suburban, and rural areas, respectively.

Totally, 96 % of Shanghai young families have air conditioner. The results in Table 50.1 indicate that more urbanization, more new-fashioned air-handled equipments would be used in household. The usage rates of these equipments in urban area are significantly higher than those in suburb and rural areas.

Among Shanghai young families, there are several heating methods (Table 50.2). Most of the usage rates of these equipments in different areas have

Table 50.1 The percentage of different air-conditioning equipments among Shanghai young families

Equipments	Total (%)	Percentage			P-value
		Urban area	Suburb	Rural area	
Air conditioner	96.0	96.6	96.1	85.3	<0.001
Air humidifier	16.7	19.5	10.9	5.9	<0.001
Air ionizer	1.5	1.8	0.8	0.8	<0.001
Air cleaner	8.0	9.9	3.8	1.7	<0.001

Table 50.2 The percentage of different household heating methods among Shanghai young families

Heating method	Total (%)	Percentage			P-value
		Urban area	Suburb	Rural area	
Air conditioner	77.6	82.9	69.6	46.1	<0.001
Electric room heater	20.7	21.8	17.7	19.5	<0.001
Floor heating	1.3	1.7	0.5	0.6	<0.001
District heating	0.2	0.2	0.1	0.5	0.249
Individual heating	0.2	0.3	0.2	0.3	0.911
Coal stove	0.2	0.2	0.1	0.3	0.653
Others	2.0	1.3	3.3	6.2	<0.001
$\geq$ 2 methods	14.1	15.7	11.4	8.3	<0.001
No heating	12.4	7.8	20.3	35.2	<0.001

significant differences. The main household heating methods are air conditioner (77.6 %) and electric room heater (20.7 %). Relatively, other heating methods have small usage rates. Urban families significantly use more such devices than suburban families. However, 35.2 % of rural residences and 20.3 % of suburban residences still have no heating, which are significantly higher than urban residences (7.8 %). The usage rate of different heating methods in the dwellings with different building styles and ages are shown in Table 50.3. Using air conditioner for heating is the most common in the multi-family dwelling (81.6 %), followed by electric room heater. The families (6.9 %), who lived in the villa, obviously used more floor heating than others.

The usage rates of different heating methods in the dwellings with different building ages are shown in Table 50.4. Most of the usage rates of these equipments in the dwellings with different building ages have significant differences. Following the building age decrease, the usage rate of electric room heater has

Table 50.3 The distribution of heating methods among the dwellings with different building styles

Percentage Heating method	Single-family dwelling (n = 3370)	Multi-family dwelling (n = 10131)	Villa (n = 175)	Others (n = 1198)	P-value
Air conditioner	72.1	81.3	74.7	62.4	<0.001
Electric room heater	21.0	20.5	16.1	21.1	0.429
Floor heating	0.7	1.5	6.9	0.7	<0.001
District heating	0.1	0.2	1.1	0.3	0.020
Individual heating	0.1	0.3	1.1	0.1	0.032
Coal stove	0.3	0.1	0.0	0.5	0.001
Others	2.9	1.5	2.9	4.3	<0.001
$\geq$2 methods	12.8	15.0	15.5	10.3	<0.001
No heating	15.7	10.3	12.6	21.1	<0.001

Table 50.4 The distribution of heating methods among the dwellings with different building ages

Percentage Heating method	Before 1980 (n = 1673)	1980–1990 (n = 2355)	1991–2000 (n = 5191)	2001–2005 (n = 4622)	2006–Now[a] (n = 2293)	P-value
Air conditioner	72.6	75.3	78.4	82.3	76.2	<0.001
Electric room heater	23.5	21.4	21.3	20.6	16.5	<0.001
Floor heating	0.5	0.1	0.8	1.8	3.4	<0.001
District heating	0.1	0.0	0.1	0.2	0.6	0.001
Individual heating	0.1	0.2	0.2	0.3	0.6	0.532
Coal stove	0.5	0.1	0.2	0.0	0.2	0.001
Others	2.4	2.1	2.0	1.9	1.7	0.626
≥2 methods	13.2	13.5	14.7	15.9	11.9	<0.001
No heating	13.9	14.6	12.2	9.3	13.4	<0.001

[a] It means that the time is during the survey (from April 2011 to April 2012)

Table 50.5 The distribution of household ventilation methods among the Shanghai young families[a]

Percentage	Kitchen		Bathroom		
	Smoke exhaust ventilator	Exhaust fan	Exhaust fan	Bathroom air is exhausted[b]	
				to outside	to inside
Total	86.2	16.1	78.6	84.0	16.0
Area					
Urban area	89.5	16.6	82.7	85.0	15.0
Suburb	84.8	14.2	74.0	82.5	17.5
Rural area	44.8	19.1	42.9	76.3	23.7
Building style					
Single-family dwelling	74.3	19.7	68.7	83.6	16.4
Multi-family dwelling	94.3	14.1	84.8	84.3	15.7
Villa	87.9	19.7	73.1	90.5	9.5
others	49.0	22.9	53.2	79.8	20.2
Building age					
Before 1980	55.6	21.0	56.4	82.5	17.5
1980–1990	84.3	16.4	69.6	76.9	23.1
1991–2000	93.0	14.5	82.0	78.2	21.8
2001–2005	93.4	14.7	87.3	91.0	9.0
2006–Now[c]	85.8	16.6	81.8	91.0	9.0

[a] All of the *P*-values in Pearson's chi-square ($\chi 2$) test are <0.001
[b] The direction of bathroom air is exhausted to, outside, or inside of the residence
[c] It means that the time is during the survey (from April 2011 to April 2012)

downward tendency from before 1980 (23.5 %) to 2006–now (16.5 %). However, from 1980 to present, the usage rates of floor heating and district heating have significantly upward tendency among Shanghai young families.

Furthermore, the usage rates of different ventilation in the kitchen and bathroom are shown in Table 50.5. Most of the residences in Shanghai (86.2 %) have smoke exhaust ventilator and exhaust fan in the bathroom (78.6 %). Urban residents used more of these equipments than suburban and rural residents. Among those residences with exhaust fan in the bathroom, most of the bathroom air is exhausted to outside of the residence (84.0 %).

Moreover, we found that 44.0, 62.0, 45.3, and 17.5 % of the families frequently open the windows in spring, summer, autumn, and winter, respectively. The mothers' frequencies in opening the windows of child's room for natural ventilation in different areas and seasons are shown in Table 50.6. Most of Shanghai young residents have awareness in exchanging the air of child's room by opening the windows (sometimes or frequently). Expect for the summer, urban residences open the windows more frequently and have stronger willingness in opening the windows (sometimes and frequently) than suburban and rural residences.

Table 50.6 The distribution of parents' frequency in opening the window of child's room[a]

Percentage	Spring			Summer			Autumn			Winter		
	UA	SA	RA	UA	SA	RA	UA	SA	RA	UA	SA	RA
Never	9.8	14.6	15.5	9.3	6.1	4.8	9.3	12.6	12.6	32.9	42.9	41.3
Sometimes	40.7	53.7	54.2	31.5	25.8	29.4	41.3	51.9	50.5	47.5	44.2	47.9
Frequently	49.5	31.6	30.3	59.2	68.0	65.8	49.4	35.4	36.9	19.6	12.9	10.8

[a] *UA* stands for urban area, *SA* for suburban area, *RA* for rural area

The usage rate of air conditioner in our survey (Table 50.1) is slightly lower than 98.0 % in the previous questionnaire [2–4]. These previous questionnaire studies were conducted in a residential community [2] or other specific places [3, 4] with small sample sizes. Thus, the usage rates in these studies maybe cannot stand for the actual situations of the whole Shanghai city. But our survey involved five districts (3 urban districts and 2 suburban districts) and up to 15,266 families. The results probably represent the current situations of household heating and ventilation method among Shanghai young families. In the present study, we found that air conditioners are the most popular methods for heating in Shanghai young families, followed by the electric room heater (Tables 50.2, 50.3, 50.4). Those results are consistent with other studies [2–5]. We also found that the some families use air conditioners for cooling in summer but not for heating in winter.

Furthermore, urban residences use more equipment for heating than suburban and rural residences. The usage rates of floor heating and district heating have upward tendency from 1980 to present (Table 50.4) although the usage rates of these methods are still very low. Those results indicate that with the development of economy and technology, more equipments for improving the indoor comfort and more advanced methods for heating would be used in the ordinary families [1]. We also found urban families open the windows less frequently and have weaker willingness in opening the windows in total (sometimes and frequently) than suburban and rural residences in summer. It perhaps related to that urban families use more air conditioners or other devices for cooling in the residence than suburban and rural residences, and perhaps they want to keep the indoor comfort or save energy in summer. But it is still need to be further confirmed.

Although our survey has large sample size, the investigated families have certain specificities that they have at least one preschool child. Some parents also perhaps cannot exactly distinguish the heating methods. Thus, the results may have little deviation with the actual situations of the overall Shanghai city.

50.4 Conclusions

Air conditioners are the most popular equipments for heating in Shanghai (77.6 %), followed by the electric room heater (20.7 %). But the usage rates of floor heating and district heating have upward tendency from 1980 to 2011. Urban

families used more electric room heater and air conditioner or floor heating for heating and used more smoking exhaust ventilator in kitchen or exhaust fan in bathroom than suburban and rural families. The demand in the quantity and style of these household ventilation and air-conditioning equipments perhaps would be stronger with the rapid urbanization in Shanghai, China.

References

1. Zhou Q, Ji ZL (2007) The actuality and developing trend of appliance air-conditioner. (Chinese) Shanxi Archit 33(3):159–160
2. Zhong T, Long WD (2003) The survey on room air conditioner in Shanghai and the calculation of energy consumption in summer. (Chinese) Build Energy Environ 3:22–24
3. Shi RH, Li ZH, Yoshino H (2005) An investigation and analysis on indoor thermal environment of urban residential buildings in Shanghai. (Chinese) Energy Technol 26(1):27–30
4. Yoshino H, Yoshino Y, Zhang QY et al (2006) Indoor thermal environment and energy saving for urban residential buildings in China. Energy Build 38:1308–1319
5. Sun J, Li ZH, Wu X et al (2009) Survey and analysis of energy consumption of two residence community founded in different ages in Shanghai. (Chinese) Refrig Air Conditioning Electr Power Mach 1:85–89
6. Wang XL, Yu H, Dong Q (2007) Investigation and analysis of energy consumption of residential buildings in Shanghai Songjiang District. (Chinese) Build Energ Effi 35(197):53–55
7. Zhong YJ, Du JY, Zhang XM et al (2002) Primary analysis on residential heating requirement in the region of Jiang Zhe Hu in new time. (Chinese) Energy Eng 5:12–14
8. Wang EC, Tan HW (2004) Application study on floor heating system with air source heat pump in Shanghai area. (Chinese) Build Energy Environ 23(6):25–29
9. Feng XP, Zou Y, Long WD (2005) Analysis on air-conditioner development and influenced factors in residential buildings. (Chinese) Energy Conserv Technol 23(133):437–440

Chapter 51
Angle Factor Calculation for the Thermal Radiation Environment of the Human Body

Yan Wang, Xi Meng, Lili Zhang, Yulan Liu and Enshen Long

Abstract The angle factor of the human body is an important parameter of thermal exchanges. The purpose of this paper is to explain the indoor thermal radiation environment of the human body in detail. Starting with a simplified analytical model, an angle factor calculation between a human body and its surroundings is executed. Firstly, a simplified expression of the angle factor between the human body and the surrounding area is conducted. Secondly, the angle factor of variation with body position in the room is shown in detail, using the model testified before. The calculated results revealed that no matter where the human body position was, the angle factor between a human body and the ground surface was much higher than any other surface in the room with $L \times W \times H$ (6 × 4 × 3 m). Thirdly, the angle factor between the human body and each surface of a room is calculated by the simplified analytical expression. A relationship between the angle factor and room dimension is analyzed. At last, the fitted equations between the angle factor and room dimensions were built separately. The fitted equations are convenient with an acceptability of precision, which can reduce the complex calculation of angle factor.

Keywords Radiation environment · Human comfort · Angle factor

Y. Wang · E. Long (✉)
Institute for Disaster Management and Reconstruction,
Sichuan University, Chengdu 610065, China
e-mail: Longes2@163.com

X. Meng · L. Zhang · Y. Liu · E. Long
College of Architecture and Environment, Sichuan University,
Chengdu 610065, China

51.1 Introduction

Since the mean radiant temperature has a considerable influence on man's heat loss and thus on his state of comfort, its calculation is important in the detailed thermal analysis of a room [1, 2]. The mean radiant temperature is easy to define but quite complicated to calculate or measure in practice [3]. In calculating the mean radiant temperature, it is necessary to know the angle factors between the person and the different surfaces [4–6]. Up to now, however, data for angle factors between persons and typical surfaces have been inadequate. It has therefore been necessary to use rough approximations, e.g., by calculating the mean radiant temperature as the mean temperature of all the surface areas $A_1, A_2 \ldots A_N$ in the enclosure [7]. Although this method has been widely used in practical engineering, it is of highly questionable accuracy and can under many conditions lead to serious errors and directly misleading results. In order to be able to use the more exact radiant temperature, it is necessary to know the angle factors between the human body and typical surrounding surfaces.

For the typical room geometry structure, angle factor between the rectangles has analytical solution [3, 8–15], but the angle factor between a person and rectangle has no accurate analytical solution. The main reason is that the human body surface is irregular, and the location is of uncertainty, etc., which made it impossible to get the analytical answer. Usually, it is by giving each part of the enclosure a certain proportion [8]. For the conventional air-conditioning construction environment of the human body thermal comfort analysis, the impact is not notable, but to radiation cooling air-conditioning system or natural ventilation buildings, there will be obvious error. Accurately solving the angle factor between the human body and surrounding surface is an important premise of the analysis of thermal comfort.

51.2 Methods

51.2.1 Angle Factor Between Differential Area Element and Vertical and Horizontal Rectangles

The enclosure surfaces, which are found most often in a normal room, are rectangular in form (walls, floors, ceilings, windows, heating and cooling panels, etc.), and it is therefore the angle factors between a person and vertical and horizontal rectangles, which are of primary interest in the calculation of mean radiant temperature and radiant exchange between a person and his practical surroundings. The angle factors between differential area element and vertical and horizontal rectangles located anywhere in the plane (see Fig. 51.1) can be calculated by formulas (51.1) and (51.2).

For the differential area element is parallel to rectangle (see Fig. 51.1):

Fig. 51.1 Element parallel/
perpendicular to rectangle
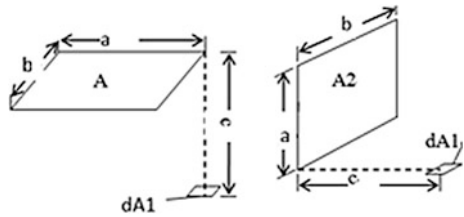
$$F_{dA_1-A_2} = \frac{1}{2\pi} \left(\frac{x}{\sqrt{1+x^2}} \tan^{-1} \frac{y}{\sqrt{1+x^2}} + \frac{y}{\sqrt{1+y^2}} \tan^{-1} \frac{x}{\sqrt{1+y^2}} \right) \quad (51.1)$$

where $x = a/c$, $y = b/c$.

For the differential area element is perpendicular to rectangle (see Fig. 51.1):

$$F_{dA_1-A_2} = \frac{1}{2\pi} \left(\tan^{-1} \frac{1}{y} - \frac{y}{\sqrt{x^2+y^2}} \tan^{-1} \frac{1}{\sqrt{x^2+y^2}} \right) \quad (51.2)$$

where $x = a/c$, $y = b/c$.

Besides, the angle factor between the differential area element and a horizontal rectangle like Fig. 51.2 can be calculated by simple angle factor algebra:

$$X_{dA_1-A_2} = \sum_{i=1}^{4} X_{dA_1-A_{2i}} \quad (51.3)$$

51.2.2 Angle Factor Between Person and Enclosure

The surface of the human body is irregular, which makes it impossible to calculate the angle factor between person and enclosure from the definition. In order to

Fig. 51.2 Angle factor
algebra
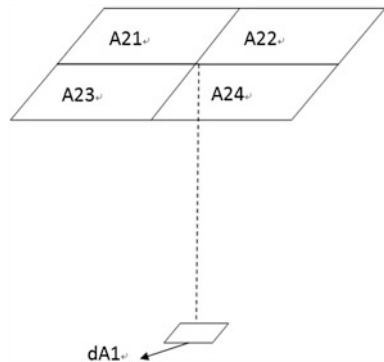
calculate the angle factor between a person and the enclosure by using the analytic method, the person is simplified to a rectangular hexahedron. The angle factor between the human body surface and the enclosure is equal to the mean angle factor between the differential area element of human body surface and the enclosure; taking the ceiling as an example, the angle factor $F_{A_{cl}-C}$ between the person and the ceiling can be calculated by the following expression:

$$F_{A_{cl}-C} = \int_{A_{cl}} F_{dA_{cl}-C} dA_{cl} \bigg/ \int_{A_{cl}} dA_{cl} \qquad (51.4)$$

A_{cl} is the clothing person area, it can be determined by:

$$A_{cl} = f_{cl} A_D \qquad (51.5)$$

where A_D is the nude person area, it is calculated as follows [16]:

$$A_D = 0.202 W^{0.425} H^{0.725} \qquad (51.6)$$

where W is the weight (kg), and H is the height (m) of the subject.

Moreover, the clothing area factor f_{cl} can be calculated as the relation between the A_{cl} values for clothed and nude subjects. The surface area factor of complete sets of clothing can get through the literature. If there is not appropriate reference data, the McCullough and Jones proposed estimation formula can be used to estimate [17]:

$$f_{cl} = 1 + 0.3 I_{cl} \qquad (51.7)$$

where I_{cl} is the clothing thermal resistance, $m^2 \cdot °C/W$ [13].

In Eq. 51.4, the product of surface area and angle factor is often called direct exchange area (direct interchange area) in the application of radiation heat transfer model [13], which is equivalent to radiant heat resistance of the network inverse [1].

51.2.3 The Semi-Analytic Method

When the subject size is far less than the room size, the angle factors between differential area elements of subject and rectangle can be seen to have the same value. The human body was compared simply to a hexahedron, with certain length, width, and height. So, the angle factor between the rectangle center and enclosure can be instead of the angle factor between the rectangle enclosures. This can be greatly simplified the integral calculation process. And it is called to be the semi-analytic method.

Fig. 51.3 A typical space
showing the position of the
person schematic diagram
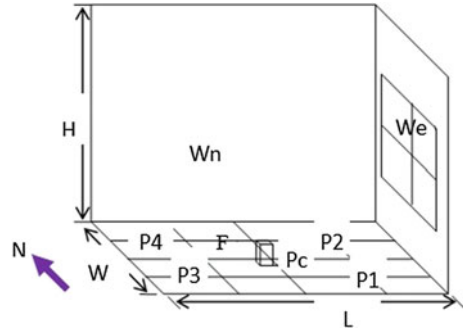
51.3 Calculation Model

The angle factors between a person and the room will be studied. The location of
the person in the room is known, and the room size is also known, see Fig. 51.3
where L is the length of the room, W is the width of the room, and H is the height
of the room. Wn is the north wall and We the East wall. C is the ceiling and F the
floor. P1–4 is instead of 4 different locations of the person. Pc is instead of the
center place.

To calculate the angle factor, the size of the person needs to know. The person
is simplified to a hexahedron, so the area of the hexahedron has to be equal to the
clothed human surface area. A person, whose height is 1.78 m and weight is 65 kg,
wears 0.5 clo clothes and is sitting in the room. Through Eqs. 51.4–51.7, the A_{clo}
will be 2.08 m^2 when the person size can be expressed with $l \times w \times h$, the l is 3
times w. We mainly study the seated person in this paper, so the $h = 1.2$ m, and it
can deduce $w = 0.2$ m, $l = 0.6$ m. This will be applied in this study.

51.4 Results and Discussion

51.4.1 The Influences of Person Location on Angle Factor

The angle factors for five different locations of the person have been calculated.
The person is in a room with $L \times W \times H$ (6 × 4 × 3 m). The five different
locations can be seen in Fig. 51.3. The calculation results are given in Table 51.1.
As a check on the calculations, the sum of all the angle factors between the person
and the surrounding surfaces should equal unity.

Table 51.1 shows that the angle factor for different positions is different. Taking
the floor rectangle as an example, the person in the center has greater angle factor
than the other four positions. While the person is in the same position, the angle
factor between the person and the floor is greater than other enclosure surfaces.
Due to the anterior–posterior symmetry of the person, there is the same angle

Table 51.1 Angle factors for person in different locations

Position	Ceiling	Floor	Wall-e	Wall-w	Wall-n	Wall-s
Pc	0.112	0.286	0.076	0.076	0.225	0.225
P1	0.097	0.250	0.154	0.040	0.140	0.319
P2	0.097	0.250	0.154	0.040	0.319	0.140
P3	0.097	0.250	0.040	0.154	0.140	0.319
P4	0.097	0.250	0.040	0.154	0.319	0.140
Mean	0.100	0.257	0.093	0.093	0.229	0.229

factor for the north wall and south wall when the person is in the center. There is also the same angle factor for the east wall and the west wall. In this case, the largest angle factor is 0.319, which is between the person and the south wall surface, and the smallest is 0.04, when the person is in positions P3 and P4.

51.4.2 The Influences of the Room Dimensions on Angle Factor

Not only the angle factor is in relation to the person position, but the angle factor is also in relation to the dimensions of the room. The different dimensions of the room have been studied. The calculation data are shown in Table 51.2. Three cases have been studied to find the rule. The angle factor between the person and enclosure with different dimensions has been calculated separately. The calculation results are given in Fig. 51.4.

From Fig. 51.4 case 1, it can be found that the angle factor between the person and ceiling surface, ground surface and north wall surfaces is increased while the length (L) of the room increases, but the angle factor for the east wall is decreased. As the L size increases, the east wall is farther and farther away from the human body, and the angle factor between the human body and the east wall becomes more and more smaller. In other words, the radiation heat transfer between the person and the east wall is less, and to the other enclosures, the radiation heat transfer is more. From Fig 51.4 case 2, when the width size is varied, the angle factor for all the enclosure is increased, except for the north wall. However, Fig. 51.4 case 3, when the room height (H) size increases, the angle factor for the ground surfaces is increased significantly, but the angle factor for the ceiling

Table 51.2 The room dimensions data of the three cases

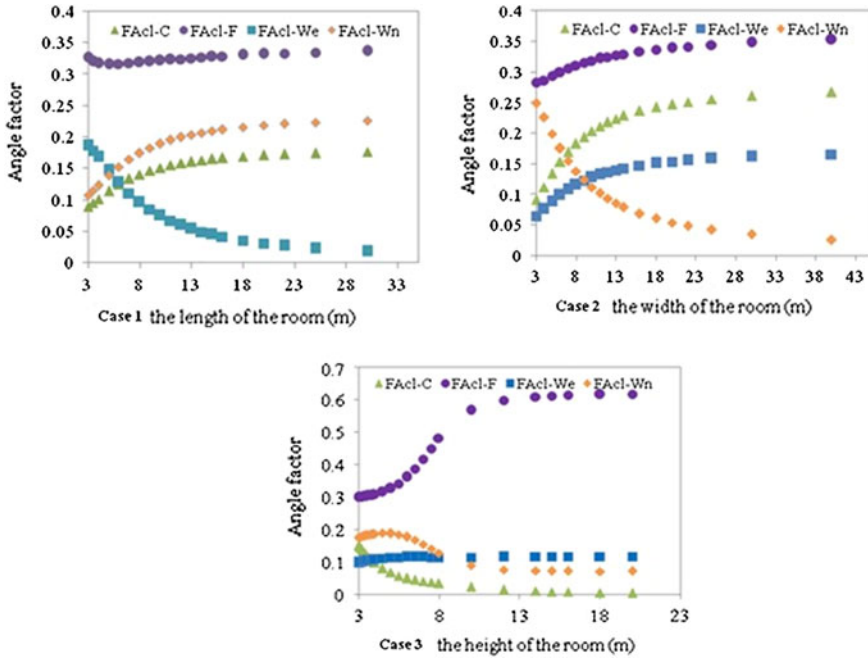| Cases	L (m)	W (m)	H (m)
Case 1	(3–35)	8	4
Case 2	6	(3–35)	3
Case 3	6	6	(3–20)

Fig. 51.4 Mean value of angle factor between a seated person and the enclosure (walls, ceiling, and floor) with the room dimensions variations

surfaces is decreased. The angle factor for the walls is increased slightly first and then reduced. These variations would influence the radiation heat exchange.

51.4.3 The Relationship Between the Angle Factor and the Room Dimensions

The calculation of the angle factor between the person and the enclosure is complicated. And the calculations have been performed by a digital computer using the necessary programmers, according to the formula derived earlier. In order to form a simple and easy method to use the angle factor results, the fitted equations between the angle factor and room dimensions will be built separately.

We assume that the angle factors have a relationship with the room dimensions as follows:

$$F_{\text{Acl}-R} = \alpha \cdot H^{m1} W^{m2} L^{m3} \tag{51.8}$$

where $F_{A_{cl}-R}$ is the angle factor between the person and certain room surface, α is the influence coefficient, and $m1$, $m2$, and $m3$ are the respectively corresponding variable indexes.

Room size (L, W, H) is changed between 3 and 10 m. Each of the parameters is selected eight grades and introduced the front semi-analytical method to calculate. Forming the construct sample, the fitting formulas are as follows:

$$F_{A_{cl}-C} = 0.091H^{-1.483}W^{0.719}L^{0.455} \quad R^2 = 0.988 \tag{51.9}$$

$$F_{A_{cl}-F} = 0.1971H^{0.029}W^{0.041}L^{0.252} \quad R^2 = 0.877 \tag{51.10}$$

$$F_{A_{cl}-We} = 0.132H^{0.295}W^{0.523}L^{-0.894} \quad R^2 = 0.931 \tag{51.11}$$

$$F_{A_{cl}-Wn} = 0.227H^{0.054}W^{0.318}L^{-0.496} \quad R^2 = 0.937 \tag{51.12}$$

The equations can be applied in the condition of L 3–10 m, W 3–10 m, and H 2.5–10 m. Only if the room dimensions were known could the angle factor be calculated immediately, regardless of the complex calculation of former methods.

51.5 Conclusions

Radiation heat transfer is an important part of the human body heat balance. To solve the radiation heat transfer, the mean radiant temperature is vital. This paper focuses on analyzing the calculation method for angle factor between the person and the enclosure. According to the common room model, the semi-analytic method was introduced to calculate the angle factor between the person and enclosure. The study shows that no matter where the human body position was, the angle factor between the person and the ground surface is much higher than any other surface in the room with $L \times W \times H$ (6 × 4 × 3 m). What's more, the angle factor between the human body placed in the center of the room and the enclosure has also been calculated, and a relationship between the angle factor and room dimension is analyzed. Lastly, the fitted equations between the angle factor and room dimensions were built separately. In a word, the shape factor can be calculated at once, when the room dimensions were known. The calculation results would be useful in engineering application. Though the human body has been simplified to a hexahedron shape to use the analytical method in this paper, the precise of the angle factor is acceptable.

References

1. Oppenheim A (1956) Radiation analysis by the network method. Trans ASME 78(4):725–735
2. Kurazumi Y, Tsuchikawa T, Ishii J et al (2008) Radiative and convective heat transfer coefficients of the human body in natural convection. Build Environ 43(12):2142–2153
3. Sparrow EM, Cess RD (1978) Radiation heat transfer Series in Thermal and Fluids Engineering. McGraw-Hill, New York
4. Xin-ai B (2008) Calculation of radiation heat transfer angle coefficient. Infrared 29(8):30–33
5. Yufang Y (1985) The application of descriptive geometry in determination of the radiation angle factor. J Harbin Inst Technol 1:126–129
6. Yannan F (2010) Heat transfer characteristics of under floor plenum. Master thesis, Xi'an University of Architecture and Technology
7. Fanger P, Robert E (1982) Thermal comfort. Krienger Publishing Company, Malabar, FL
8. Clarke J (2001) Energy simulation in building design. Routledge, London
9. Murakami S, Kato S, Zeng J (2000) Combined simulation of airflow, radiation and moisture transport for heat release from a human body. Build Environ 35(6):489–500
10. Kalisperis LN, Steinman M, Summers LH (1991) Expanded research on human shape factors for inclined surfaces. Energy Build 17(4):283–295
11. Dozier J, Frew J (1990) Rapid calculation of terrain parameters for radiation modeling from digital elevation data. IEEE Trans Geosci Remote Sens 28(5):963–969
12. Lyons P, Arasteh D, Huizenga C (2000) Window performance for human thermal comfort. Trans Am Soc Heat Refrig Air Conditioning Eng 106(1):594–604
13. Omori T, Yamaguchi S, Taniguchi H (1998) Accurate Monte Carlo simulation of radiative heat transfer with unstructured grid systems. In: Proceedings of 11th international symposium on transport phenomena, pp 567–573
14. Howell J (1998) The Monte Carlo method in radiative heat transfer. Trans Am Soc Mech Eng J Heat Transfer 120:547–560
15. Atkins A, Wyndham C (1969) A study of temperature regulation in the human body with the aid of an analogue computer. Pflügers Archiv Eur J Physiol 307(2):104–119
16. Du Bois D, Du Bois EF (1916) Clinical calorimetry: tenth paper a formula to estimate the approximate surface area if height and weight be known. Arch Int Med 17(6–2):863
17. Mccullough EA, Jones BW, Huck J (1985) A comprehensive data base for estimating clothing insulation. ASHRAE Trans 91(2):29–47

Chapter 52
Analysis of Microbiology Test of Air-Conditioning System in Severe Cold Area

Huixing Li, Beini Li, Guohui Feng, Peng Cheng
and Chengcheng Tang

Abstract Central air-conditioning system of Liaoning Provincial Museum has been taken as the target to study microbiology contamination since it is a typical public building. Three AHUs that conduct with different functional areas were considered as testing object in the museum, including constant temperature and humidity AHU B1, B2, and B3. Using microbiological method, six levels of impingement air microorganism sampler, fluorescent optical microscope, high-pressure steam sterilization pot, thermostatic incubator, thermostatic oven, biochemical incubator, and testing instruments are selected to test dust and air, which contain microbial organisms in the AHUs. Results show that the average product dust of the museum is 12.36 g/m^2; the dust contains bacterial concentration in the microbiological is 85.2×104 cfu/m^2, the air contains bacterial concentration in the microbiological is 568.19 cfu/m^3, and the fungus concentration is 938.37 cfu/m^3; the advantage strains in microbiologic is gram-positive bacterium; advantage strains in fungus is penicillium, aspergillums, branch spore mold.

Keywords Central air-conditioning system · Air handling unit · Microbial · Pollution

52.1 Introduction

In recent years, a growing number of studies have found a central air-conditioning system to bring people comfortable temperature and humidity. But it produces, induces and aggravates the formation and development of the pollution, by causing

H. Li · B. Li · G. Feng (✉) · P. Cheng · C. Tang
School of Municipal and Environment Engineering, Shenyang Jianzhu University, Shenyang 110168, China
e-mail: fengguohui888@163.com

poor indoor air quality. It has a significant impact on human health. The air handling unit (AHU) is the source of the central air-conditioning system is one of the central air-conditioning system, hot–wet processing, and purification of air processing equipment. People call AHU the "heart" of central air-conditioning system vividly. Maintaining a clean operation of the AHUs is the inevitable choice to avoid microbial contamination of central air-conditioning.

52.2 Test Object

52.2.1 Climate Situation

Detection object is located in Shenyang, Liaoning Province. It is located in the south of northeast China. It belongs to the cold region in winter. Temperature is very low and against microbial survival. In summer, high temperature rainy conditions provide essential temperature and humidity environment, which make microbe easy to survive.

52.2.2 Construction Situation

The museum is the predecessor of the northeast museums, which is the first museum after the founding of New China. The museum exhibition floor covers an area of 25,000 m^2, a total height of 24.8 m. It has 12 exhibition rooms. Cultural relics used glass closed exhibition rooms. Exhibition rooms, calligraphy and painting display area are using two different sets of air-conditioning system to control the indoor environment. Exhibition rooms use the central air-conditioning systems with constant air volume and single duct to control indoor thermal environment. The air-conditioning systems work from 8:00 to 16:00. Painting and calligraphy display area use constant temperature and humidity air-conditioning control system to control the temperature and humidity. This system works the whole day (24 h). And other cultural relics are placed closed glass room without air-conditioning equipment (Figs. 52.1, 52.2, 52.3, 52.4).

52.3 Detection Methods

52.3.1 Dust and Air Test Method

Dust was collected by wiping method. Before sampling, the materials used were dried in the constant temperature at 105 °C. After 2 h, the dryer was cooled for

Fig. 52.1 Museum building

Fig. 52.2 Constant temperature and humidity system unit B1

Fig. 52.3 Unit B2

Fig. 52.4 Unit B3

4 h. The bag was sealed and made good number, with electronic balance weighing the initial weight.

In the AHU 50 cm^2 sampling area is selected. All remaining dust on the surface of the area is removed for sample. After sampling, dust samples are sealed for storage and then sent to the laboratory for testing.

In previous research, air sampling using impact method has been studied [1]. Air impact method is to make the air which contains bacteria air flow through the sampler and hit the AGAR surface. According to the training count and sample quantity, the total number of bacteria in air is calculated. The bacteria capture rate is higher in this method. The results relative natural sedimentation method is more accurate. In particular, the bacteria and fungi medium was poured into a diameter of 90 mm sterile glass plate. The plates are well marked in the impactor. The impactor and the air inlet are connected with the rubber hose. We wear masks to prevent from bacterial contamination. In order to keep the accuracy of the colony count, we take sample before opening the cover of the impactor. The working personnel should be 2 m away from the sampling point and avoid walking. The sample time were set for ten minutes. The samples are taken into the sample plates later. Then we cover the lid, complete the marks and put the samples back to the laboratory for training and counting (Fig. 52.5).

Main instruments and equipment include: FA—type 1 six levels of impingement air microorganism sampler, super clean bench, fluorescent optical microscope analysis, high-pressure steam sterilization pot, thermostatic oven, electric constant temperature incubator, biochemical incubator, etc.

52.3.2 Point Layout

On the basis of AHU in microbial contamination test content, AHU internal microbial pollution source, composition, etc., we put the sampling point in fresh air handling units, to detect the air microorganism concentration. Later, internal growth of microorganism concentration of the air handling unit are detected.

52.4 Testing Results and the Analysis

In this paper, requirements of the air conditioning system can be seen in Table 52.1, which are in accordance with the health requirements in the standard of public place with centralized air ventilation system.

Fig. 52.5 Staff at the scene for sampling

According to the test results in Table 52.2, we find that the product dust at control points are not more than that in the national standards (product dust acuities and g/m^2). Table 52.3 shows the test results of the bacteria concentration in the AHUs. The results showed that all the bacteria concentration control points are no more than the national standard (or less gasoloid density was exceed 100 cfu/cm^2). Microbial concentration in dust reached the peak in B2 unit and it is close to the national standard of the upper limit value.

Table 52.4 shows the results of the gram staining for three units, which gives the final summary. The test data for every measuring point is the average value of three tests. It can be seen from the table that three units of bacteria strains are gram-positive bacteria. Table 52.5 shows bacterial classification and identification results in summary. The results showed three units of coccus that are advantage strains.

Figure 52.6 shows bacterial distribution. The chart indicates that air bacterial particles are mainly distributed in the stage 1–stage 4 (size greater than 2.1 μm). Stage 5 (particle size is within 1.1–2.1 μm) occupies more than 90 % of the total grain number and two stages content of stage (0.65–1.1 μm) are less than 10 %. Grain

Table 52.1 Air-conditioning system health requirements [2]

	Item	Demand
The surface of the equipment health requirements	Product dust	≤20 g/m^2
	Total bacterial count	≤100 cfu/cm^2
	Total fungi count	≤100 cfu/cm^2
Air supply sanitary requirements	Total bacterial count	≤500 cfu/m^3
	Total fungi count	≤500 cfu/m^3

Table 52.2 Test results of dust in each sampling point (g/m^2)

		B1	B2	B3
	First	9.03	13.84	12.21
Point A	Second	9.49	14.57	12.95
	Third	10.11	15.68	13.39
	First	10.62	16.54	14.03
Point B	Second	11.16	17.46	14.62
	Third	11.70	18.38	15.21

Table 52.3 Test results of dust contain microbial concentration ($\times 10^4$ cfu/m^2)

		Bacterial concentration			Fungi concentration		
		B1	B2	B3	B1	B2	B3
	First	70.2	81.9	75.9	70.6	81.9	87.6
Point A	Second	71.7	83.7	77.4	72.5	84.7	88.5
	Third	73.8	85.2	80.1	74.1	86.4	91.2
	First	75.3	87.3	81.9	75.6	87.6	92.7
Point B	Second	77.4	88.5	84.0	76.5	88.2	93.5
	Third	79.2	90.3	86.1	80.1	91.1	95.3

Table 52.4 Gram staining results of AHU bacteria particle (%)

	Bacteria in the dust particles			Bacteria in the air particles		
	G+	G−	Rests	G+	G−	Rests
B1 Point A	58.37	38.77	2.86	51.44	45.23	3.33
B1 Point B	55.81	41.48	2.71	51.02	45.92	3.06
B2 Point A	56.43	40.80	2.77	53.67	42.63	3.70
B2 Point B	59.05	38.12	2.82	52.28	45.38	2.34
B3 Point A	58.67	38.45	2.88	53.92	43.10	2.98
B3 Point B	56.29	40.78	2.93	52.53	44.85	2.62

Table 52.5 Identification results of AHU contain bacteria (%)

	Bacteria in the dust particles			Bacteria in the air particles		
	Coccus	Bacillus	Rests	Coccus	Bacillus	Rests
B1 Point A	55.81	40.09	4.10	51.90	44.11	3.99
B1 Point B	54.24	41.81	3.96	51.17	44.80	4.03
B2 Point A	55.40	40.76	3.85	52.49	43.22	4.29
B2 Point B	54.56	41.71	3.74	52.82	42.63	4.55
B3 Point A	56.72	39.66	3.63	53.14	42.05	4.81
B3 Point B	56.88	39.61	3.52	53.47	41.46	5.07
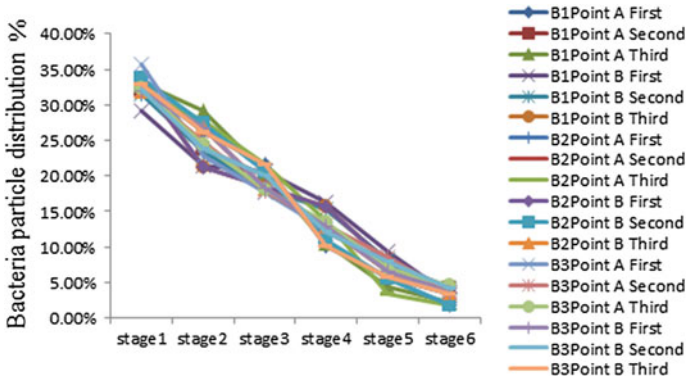
Fig. 52.6 Distribution of AHU bacteria particle
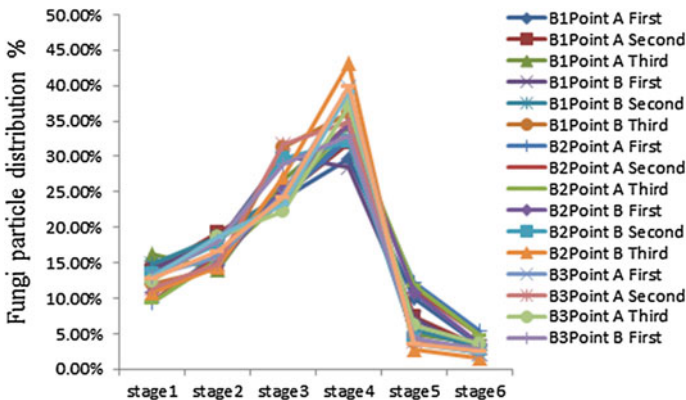
Fig. 52.7 Distribution of AHU air contains fungus particle in museum

number percentage from stage 1 to stage 6 gradually reduces and it is related to the aerosol particle size. More nutrients, make it the more suitable for microbial survival.

Fig. 52.7 shows that, fungi particle distribution is an unimodal type function, the number of fungal particles from stage 1 to stage 4 increases gradually and stage 4 reaches the peak. The content of stage 5 and stage 6 is stable and very low. The test results are shown as below: Cladosporium are mainly distributed in the stage 3–stage 5; Penicillium and Aspergillus are mainly distributed in stage 4 and stage 5; Chain lattice mold is mainly distributed in stage 1–stage 2; No spore fungus genera are distributed at various levels.

Table 52.6 shows three testing results for dust and fungi particle identification for AHU. The results showed that: the dust of the AHU contains fungi branch

Table 52.6 Identification results of AHU dust and air contain fungi (%)

		Penicillium	Aspergillums	Branch spore mold	Chain case mold	No Alternaria	Rests
Dust							
B1 Point A		45.03	22.05	21.12	5.90	3.73	2.17
B1 Point B		46.32	21.75	20.70	5.26	3.51	2.46
B2 Point A		45.87	21.94	20.51	5.41	3.99	2.28
B2 Point B		46.38	21.70	20.45	5.49	3.74	2.24
B3 Point A		45.96	21.72	20.71	5.05	3.54	3.03
B3 Point B		45.93	21.78	20.47	5.77	3.41	2.62
	B1 Point A	26.22	17.68	43.90	5.49	3.66	3.05
	B1 Point B	25.78	17.07	44.60	5.23	3.48	3.83
	B2 Point A	25.14	17.80	44.92	5.37	3.67	3.11
	B2 Point B	25.62	16.67	45.02	4.98	3.23	4.48
	B3 Point A	25.89	16.75	45.18	4.57	3.55	4.06
	B3 Point B	26.34	17.14	44.50	4.86	3.07	4.09

spore mold genera and Penicillium is for dominant fungi genera; The results also showed that AHU air contains middle mildew fungi genera and Aspergillus is advantage bacterium.

52.5 Conclusion

With the development of society, the air-conditioning system is widely used. People are enjoying their lives, and at the same time, the air-conditioning system affects people's health with microbial pollution. According to the analysis, the museum's AHUs are contaminated in different degrees. We find that the average product dust of the museum is 12.36 g/m^2; the dust contains bacteria concentration in the microbiological is 85.2×104 cfu/m^2, the fungus concentration is 91.2×104 cfu/m^2, the air contains bacteria concentration in the microbiological is 568.19 cfu/m^3, the fungus concentration is 938.37 cfu/m^3; the advantage strains in microbiology is gram-positive bacterium, coccus, advantage strains in fungi are Penicillium, Aspergillus, branch spore mold. The test results provide reference for the operation of the air-conditioning system in museum.

References

1. Nanqi R, Fang M et al (2002) Microbiology of environmental engineering. Harbin Institute of Technology Press, Harbin
2. The ministry of health of the People's Republic of China (2006) Public centralized air ventilation system health standards. Beijing. Issued by the ministry of health supervision, No. 58

Chapter 53
Numerical Study of Coagulation and Sedimentation of Indoor Suspended Particles

Jun Huang and Zhenqian Chen

Abstract For suspended particles coming from the outdoor environment system, Brownian coagulation is the main reason that causes the sedimentation of the indoor particles. In this paper, we first gave particles a reasonable lognormal size distribution, using the moment method, and predicted the change of particle-size distribution (PSD) in the diffusion settlement process. The results showed that with the motion of fluid, diffusion and coagulation happened to the particle simultaneously, and the volume of the particles was continuously increasing, while particle concentration decreasing. In the interface between the dynamic fluid and static fluid, the diameter of the particles reached the maximum.

Keywords Suspended particle · Sedimentation · Coagulation · Moment method

53.1 Introduction

Particulate behaviors in a dispersed system, such as nucleation, coagulation, condensation, sedimentation, and surface reaction, are important elements of many natural phenomena [1–3]. As a variety of physical and chemical effect are detected in the formation and growth of particles in an indoor system, it is necessary to study these reaction mechanism simultaneously in order to predict the properties of particles, and a method that is capable of capturing thermodynamic and chemical microscopic behaviors between particles and the fluid is required. The moment method depends on the description of aerosol evolution by the moments of the

J. Huang (✉) · Z. Chen
School of Energy and Environment, Southeast University, Nanjing 210096, China
e-mail: 568850230@qq.com

Z. Chen
e-mail: zqchen@seu.edu.cn

particle-size distribution (PSD) function [1]. The accuracy of this approach is based on the exactness of the presumed distribution function [4]. In 2003, a direct numerical simulation (DNS) of particle coagulation in a temporal mixing layer was performed by Settumba and Garrick [5]. In 2006, a CFD method is introduced by Brown et al. to study the nucleation, coagulation, evaporation, and condensation of poly-disperse particles in turbulent flows with strong mass and energy coupling between the phases [6].

In this work, a numerical simulation of particle coagulation in indoor space is performed using the moment method. The first three moments of the PSD are required. Simulations are performed for progress in different time, and PSD is obtained.

53.2 Sumerical Method

53.2.1 Hydrodynamic Field

The fluid is an incompressible viscous fluid under consideration. The primary transport variables of the hydrodynamic field are governed by conservation equations of mass and momentum:

$$\frac{\partial u_i}{\partial x_i} = 0 \tag{53.1}$$

$$\frac{\partial u_i}{\partial t} + u_j \frac{\partial u_i}{\partial x_j} = -\frac{1}{\rho}\frac{\partial p}{\partial x_i} + v\frac{\partial^2 u_i}{\partial x_j \partial x_j} \tag{53.2}$$

where v is the kinetic viscosity, and ρ is the fluid density. In the present study, the volume ratio of particle to fluid is far less than 1; therefore, the effects of particles on the fluid flow are neglected.

53.2.2 Particle Field

The transport of particles dispersed throughout the fluid is governed by the general dynamic equation (GDE). The general dynamic equation for particles undergoing Brownian coagulation is as follows [1]:

$$\frac{\partial n}{\partial t} + u_j \frac{\partial n}{\partial x_j} = \frac{\partial}{\partial x_j}\left(D\frac{\partial n}{\partial x_j}\right) + \frac{1}{2}\int_0^v \beta(v-\bar{v})n(v-\bar{v},x,t)n(\bar{v},x,t)d\bar{v}$$

$$- n(v,x,t)\int_0^\infty \beta(v,\ \bar{v})n(\bar{v},x,t)d\bar{v}$$

(53.3)

where $n = n(v,x,t)$ is the PSD function, and u_j is the flow velocity. The first term on the left-hand side represents the time rate of change of particle concentration, and the second term accounts for the fluid transport. The first term on the right-hand side represents the diffusion of particles throughout the fluid, which is the coefficient of diffusivity. The second and third terms on the right-hand side represent the gain and loss of particles during Brownian coagulation. The second term on the right-hand side represents the production rate of particles of volume v by collision of particles of volumes $v - \bar{v}$ and v. The third term on the right-hand side gives the disappearance rate of particles having volume by collisions with particles of all sizes. In both two terms, β is the collision coefficient which is dependent on particle size.

A moment method is adopted to facilitate the solution of the GDE by obtaining the first N_M moments of the PSD function, M_k, 1,2,…, N_M. The kth moment of the particle distribution is defined as follows:

$$M_k = \int_0^\infty v^k n(v,x,t)dv$$

(53.4)

where v is the particle volume, and $n(v,x,t)$ is the PSD function. The transport equation for M_k is obtained by multiplying v^k on both sides of the GDE and integrating over the range of v [7]. The governing equation for the kth moment in a coagulation process is expressed as follows:

$$\frac{\partial M_k}{\partial t} + \frac{\partial u_j M_k}{\partial x_j} = \frac{\partial}{\partial x_j}\left(\kappa\frac{\partial M_{k-2/3}}{\partial x_j}\right) + \overset{\bullet}{\omega}_{M_k}$$

(53.5)

where $\kappa = Dv^{2/3}$ and D is given by

$$D = \frac{(3/4\pi)^{1/3}k_B T}{v^{2/3}\rho\bar{c}(1 + \pi\alpha/8)}$$

(53.6)

where $\bar{c}$ is the mean thermal speed, α is the accommodation coefficient, T is the fluid temperature, and k_B is Boltzmann's constant [8]. The source term, $\overset{\bullet}{\omega}_{M_k}$, comes from the integration of coagulation terms in Eq. (53.3) and is expressed as follows:

$$\overset{\bullet}{\omega}_{M_k} = A_1 B_k(M_{k/2+2/3}M_{k/2-1/2} + 2M_{k/2+1/3}M_{k/2-1/6} + M_{k/2+1/6}M_{k/2})$$

(53.7)

where

$$A_1 = \left(\frac{3}{4\pi}\right)^{1/6} (\frac{6k_BT}{\rho_p})^{1/2} \tag{53.8}$$

is the size-independent coefficient of the particle collision frequency function, and ρ_p is the particle density. When a lognormal distribution function with a standard deviation σ_g is assumed, B_k is expressed as follows:

$$B_0 = 0.633 + 0.092\sigma_g^2 - 0.022\sigma_g^3 \tag{53.9}$$

$$B_1 = 0 \tag{53.10}$$

$$B_2 = 0.39 + 0.5\sigma_g - 0.214\sigma_g^2 + 0.029\sigma_g^3 \tag{53.11}$$

For 0, 1, and 2, the zeroth moment M_0 corresponds to the total particle number concentration, the first moment M_1 is proportional to the total particle mass, and the second moment M_2 is proportional to the total light scattered. To close this equation, an assumption of PSD is required. In this work, a lognormal distribution function is used:

$$n(v, x, t) = \frac{N}{3 \ln \sigma_g \sqrt{2\pi}} \exp\left(-\frac{\ln^2\left(\frac{v}{v_g}\right)}{18 \ln^2 \sigma_g}\right) \frac{1}{v} \tag{53.12}$$

where N is the total particle number concentration, v_g is the geometric mean particle volume, and σ_g is the geometric standard deviation of the PSD [9]. v_g and v_g can be expressed as functions of the first three moments:

$$v_g = \frac{M_1^2}{M_0^{3/2} M_2^{1/2}} \tag{53.13}$$

$$\ln^2 \sigma_g = \frac{1}{9}\ln(\frac{M_0 M_2}{M_1^2}) \tag{53.14}$$

The fractional moments appearing in Eq. (53.5) are given by

$$M_k = M_0 v_g^k \exp\left(\frac{9}{2}k^2 \ln^2 \sigma_g\right) \tag{53.15}$$

53.3 Numerical Specifications

As illustrated in Fig. 53.1, the flow under consideration is a two-dimensional flow in confined space. The space coordinate is $x = (x, y)$, where x corresponds to the stream-wise direction and y the cross-stream direction. The area is free of particles
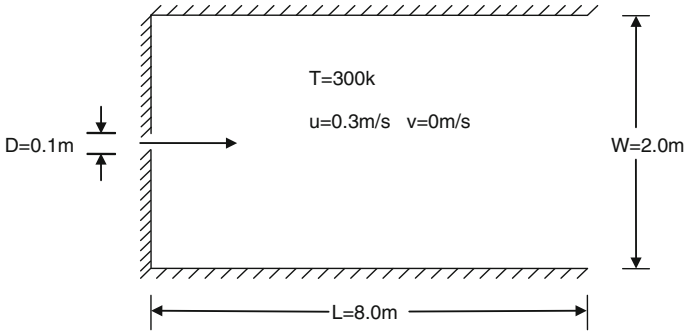
Fig. 53.1 Flow configuration

at the initial time $(t = 0)$. The incident flow is air with a uniform velocity $u = 0.3$ m/s and $v = 0$ m/s at a temperature of $T = 300$ K. Small particles (in order to be universal, here take for TiO_2, particle density 4,000 kg/m^{-3}) come from the jet whose uniform diameter for 10 nm with reference number intensity 10^{15} particles per m^3. The computation grid is comprised of 320×80 grid points for nozzle distance of 0.1 m. The computational size in the x direction is 8.0 m, while the y direction is 2.0 m. The zero gradient boundary conditions are applied to the wall boundaries. The implicit difference scheme in time and the second-order Crank–Nicolson scheme are employed to solve moment equations. In the initialization simulation, the variables for all moments are initialized by zero except in the jet where the moments are given by $M_0 = 1 \times 10^{15}$, $M_1 = 5.24 \times 10^{-10}$, and $M_2 = 2.74 \times 10^{-33}$. The RNG turbulence model is used in the transient process. Correlatively, the time step and its convergence error are 0.01 s and 10^{-5}, respectively.

53.4 Results and Discussions

53.4.1 Evolution of Moments

Figures 53.2 and 53.3 are contour map of moment variable M_0 and M_1 in different time. The results show that with the motion of fluid, particles diffused and coagulated simultaneously, and particle size was increasing continuously but particle concentration reducing. When the coagulation develops enough, the vortices generate in the downstream and finally induce secondary vortices emergence in the flow regions. This process reduplicates periodically. Coherent structures can be discovered by vorticity in the figure below. Near central axis along the y direction, unite volume number concentration of maximum value appeared. In general, coagulation is a process in which particles collide with one another and adhere to

Fig. 53.2 Contour of M_0 at different time (from *top* to *bottom* in turn to 10, 30, and 50 s)

5.0E+13 3.0E+14 5.5E+14 8.0E+14
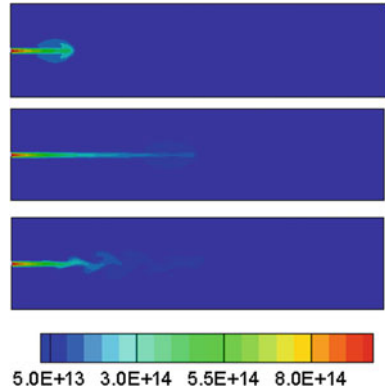
Fig. 53.3 Contour of M_1 at different time (from *top* to *bottom* in turn to 10, 30, and 50 s)

5.0E-11 2.0E-10 3.5E-10 5.0E-10
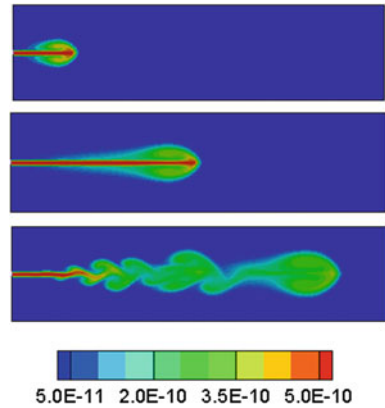
form larger particles, so the final result is a continuous decrease in number concentration and an increase in particle size.

53.4.2 Mean Particle Size

Growth of particle sizes is represented by the geometric mean particle diameter $d_{\mathrm{mean}} = \sqrt[3]{\frac{6M_1}{\pi M_0}}$. The evolution of d_{mean} along center axis in x direction is shown in Fig. 53.4. It is seen that the variance of d_{mean} exhibits the same trend for the different propagation time. The mean particle diameter is largest in the stagnation point and then decrease in the downstream. This is because particles have more residence time to coagulate, and thus, particle number decreases obviously. Correspondingly, particles have the more chances to collide and adhere to form larger ones as time flies.

Fig. 53.4 Stream-wise variation of the geometric mean particle diameter d_{mean}
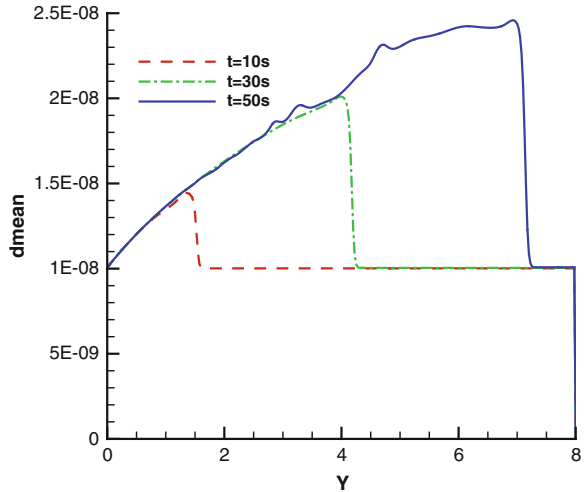
53.4.3 Geometric Standard Deviation

The evolution of geometric standard deviation σ_g in the stream-wise direction is shown in Fig. 53.5. From the figure, a self-preserving size distribution is attained regardless of the time. This self-preserving form may be approximated by a log-normal distribution with a geometric standard deviation in the range $1.07 \leq \sigma_g \leq 1.63$. Before the extreme point, the geometric standard deviation increases significantly due to strong particle collision and then decreases drastically under the corporate influence of large coherent structures and particle coagulation. It can be said that the value of σ_g is larger, the greater difference of particle size.

Fig. 53.5 Stream-wise variation of the geometric standard deviation
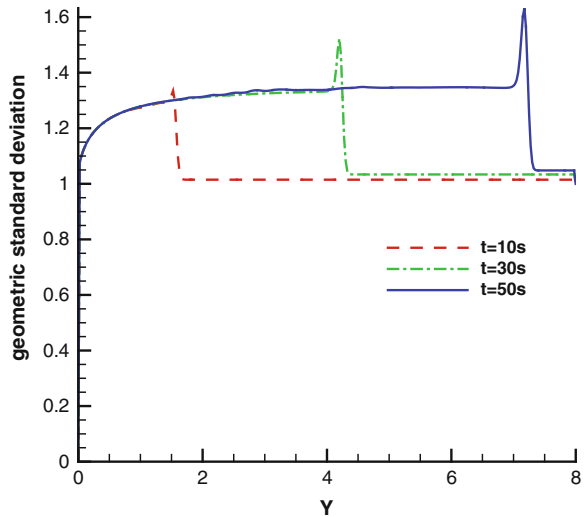
53.5 Conclusions

The motion of particle aerosol and the accompanying physical and chemical phenomena are of great importance in research. The moment method is an approximate method in solving the general dynamic equation. On solving this system of equations, the number concentration, mean volume, and volume standard deviation of particles are obtained, and the spatial distribution of particles is depicted. Results reveal the effects of diffusion and coagulation on particle distribution qualitatively. This work provides a framework for further studies on the scalar transport in indoor environment.

Results show with coagulation, and it occurs with a continuous decrease in number concentration and an increase in particle size repeatedly. Vorticity has a pronounced dilution effect on the particle intensity, dimensions, and distributions. The standard deviation in the particle increases until it reaches that of the self-preserving distribution. The value of geometric standard deviation is larger, the greater difference of particle size. The maximum value of mean particle diameter always occurs near the interface between the dynamic particle stream and static air flow.

References

1. Friedlander SK (2000) Smoke, dust and haze: fundamentals of aerosol behavior. Wiley, New York
2. Sun L, Lin J, Bao F (2006) Numerical simulation on the deposition of nanoparticles under laminar conditions. J Hydrodyn Ser B 18(6):676–680
3. Xiong H, Chen L, Lin J (2006) Smoothed particle hydrodynamics modeling of free surface flow. J Hydrodyn Ser B 18(3 Suppl):443–445
4. Barrett JC, Jheeta SJ (1996) Improving the accuracy of the moments method for solving the aerosol general dynamic equation. J Aerosol Sci 27(8):1135–1142
5. Settumba N, Garrick SC (2003) Direct numerical simulation of nano-particle coagulation in a temporal mixing layer via a moment method. J Aerosol Sci 34(2):149–167
6. Brown DP, Kauppinen EI, Jokiniemi JK et al (2006) A method of moments based CFD model for polydisperse aerosol flows with strong interphase mass and heat transfer. Comput Fluids 35(7):762–780
7. Pratsinis SE (1988) Simultaneous nucleation, condensation and coagulation in aerosol reactors. J Colloid Interface Sci 124(2):416–427
8. Suh MS, Zachariah MR, Girshick SL (2002) Numerical modeling of silicon oxide particle formation and transport in a one-dimensional low-pressure chemical vapor deposition reactor. J Aerosol Sci 33(6):943–959
9. Smith EJ, Jordan LM (1964) Mathematical and graphical interpretation of the log-normal law for particle size distribution analysis. J Colloid Sci 19(3):549–559

Chapter 54
The Platform Piston Wind Velocity Variation Analysis with Different Conditions

Lihui Wang, Rui Chen, Xiaoming Du and Jie Song

Abstract In a subway environment control system without screen doors, the tunnel piston wind enters the platform with the train and significantly affects the platform's thermal environment. The piston wind distributed on the platform here is defined as the platform piston wind. In this case, the diffusion regularity of platform piston wind is regarded as a wall jet along the platform's length and width, and its origin is a piston wind jet at the tunnel exit. According to classical wall jet theory, the jet can be approximately divided into initial and main sections in the development process. This study is based on the mathematical theory model. The model divided the platform piston wind velocity distribution into the initial section and the main section. This platform piston wind mathematical theory model is solved with time circle and along the vertical wall directions. The various conditions include changing the tunnel cross sections, train cross sections, the maximum train velocities. It is concluded that the cross-sectional ratio and maximum train velocities are the main factors on this velocities distribution. The building up and solution of this platform piston wind mathematical model serve as an important reference for the optimal design of practical thermal environments in engineering.

Keywords Platform piston wind · Velocity · Mathematical theory model · Numerical simulation

L. Wang (✉) · R. Chen · X. Du
School of Environment and Architectures, University of Shanghai for Science and Technology, Shanghai 200086, China
e-mail: 66amy99@126.com

J. Song
Shanghai Shentong Rail Transit Research Consulting Co. ltd, Shanghai 201103, China

54.1 Introduction

Piston wind occurs in tunnels as a result of subway travel. Its fundamental cause lies in the differential pressure found before and after a train traveling through the tunnel and has been observed for many years. Saiben [1] derived a one-dimensional, incompressible, and unsteady equation to describe the flow field of an operating train. More recent studies focused on the velocity, temperature, and pressure characteristics of subway tunnel thermal environments. Kim and Kim [2] investigated tunnel pressure and air velocity variations over time by conducting both experimental and three-dimensional numerical analyses, and the predicted numerical model results matched the experimental data well. To further optimize tunnel ventilation, Huang [3] presented the velocity, pressure, and flow characteristics of piston wind ducts and identified optimum vent locations.

In a subway environment control system without screen doors, the tunnel piston wind enters the platform with the train and significantly affects the platform's thermal environment. The piston wind distributed on the platform in this case is defined as the platform piston wind. To analyze the velocity and temperature variation of this platform piston wind, Wang and Wu [4] used multiple points to simultaneously and dynamically field test a variety of typical platform cross sections during the train's arrival and departure. Yuan and You [5] studied the three-dimensional transient turbulence flow characteristics on the platform using CFD simulation. Wang et al. [6] discussed the coupled airflow of the platform piston wind and wall jet using field measurements. Meanwhile, the junction area between the tunnel and the platform can be regarded as the entrance site of the platform piston wind. Shen et al. [7] measured entrance velocity variation characteristics. This paper introduces the wall jet theory according to the geometrical structure's relative position between the subway platform, the tunnel and the limit of one side of the platform to describe the platform piston wind. The source of this wall jet is the intermittent unsteady jet located at the tunnel exit. After giving the mathematical theory model, the variation characteristics of the platform piston wind under different conditions are analyzed here with theoretical calculation.

54.2 Mathematical Theory Model

In this case, the diffusion regularity of platform piston wind is regarded as a wall jet along the platform's length and width, and its origin is a piston wind jet at the tunnel exit. According to classical wall jet theory, the jet can be approximately divided into initial and main sections in the development process. In the initial section, the upper boundary of the initial section's jet sends the surrounding fluid toward the platform center after ejecting from the tunnel exit. A free shear zone is formed with the jet mixing and continuous development. Near the tunnel wall of the platform area, the lower boundary is affected by the resistance of the solid wall,

creating a boundary layer. Between the free shear zone and the boundary layer, the potential flow core area lies in the center in the initial section. In the main section, the jet can be divided into two areas by the maximum velocity of the platform cross section: The upper part is the free shear zone, and the lower part is the boundary layer close to the tunnel wall of the platform area. Based on the mathematical theory modeling, the formulas in the initial section and main section are obtained as follows:

$$u = \frac{5.18 u_0 \eta^{1/7} \left(1 - \frac{2}{\sqrt{\pi}} \int_0^{0.68\eta} e^{-\eta^2} d\eta \right)}{\sqrt{x/b_0}} \tag{54.1}$$

$$u = u_0 \left(\frac{y \mathrm{Re}^{0.2}}{0.376x}\right)^{1/7} \tag{54.2}$$

$$u = u_0 \left[1 - \left(\frac{y + x\tan(5^\circ) - b_0}{x\tan(5^\circ) + x\tan(10^\circ)}\right)^{1.5}\right]^2 \tag{54.3}$$

where b_0 is the tunnel width in m, u_0 is the piston wind velocity at the tunnel exit in m/s, x is the axis in the direction of the train operation, y is the axis perpendicular to the wall, and u_m is the maximum velocity in the cross section in m/s. The distance between the wall and u_m is the boundary layer thickness δ in m. $\eta = y/b$.

When the platform piston wind position L > 12.3 b$_0$, the velocity adheres to the basic rules of the main section and can be expressed with formula (54.1). When the platform piston wind position L $\leq 12.3b_0$, it belongs to the initial section. The boundary layer velocity adheres to formula (54.2) as soon as y $\leq \delta$, and the potential flow core speed u is equal to u$_0$ if b$_0$-xtan(5°) $\geq$ y$\geq\delta$. Formula (54.3) describes the free shear zone velocity characteristics if b$_0$ + xtan(10°) $\geq$ y$\geq$b$_0$-xtan(5°).

When u0 is equivalent to the piston wind velocity at the tunnel exit, it is intermittent and unsteady and its basic calculation formula [8] is as follows:

$$u_0 = \frac{-2AC + 2ACe^{t\sqrt{B^2 \pm 4AC}}}{C\left(B + \sqrt{B^2 \pm 4AC}\right) - C\left(B - \sqrt{B^2 \pm 4AC}\right)e^{t\sqrt{B^2 \pm 4AC}}} \tag{54.4}$$

In this expression, the values for *A*, *B*, and *C* are related to the train operation times and behavior, including the train speed, blockage area ratio between the tunnel and train section, and the surface friction coefficient of the train and tunnel.

54.3 Solution to the Velocity Theoretical Analytical Expression

54.3.1 Solution for the Cyclic Dynamic Velocity at Typical Points

The solutions to the analytical expressions given above are relatively complicated. VBA programming combined with Excel software is adopted to solve the analytical formulas for the initial and main sections of the model. The basic parameters for the theoretical solution process are given in Table 54.1.

Based on the parameters in Table 54.1, the length of the initial section is calculated to be 28 m, so the X-coordinates of the selected typical points are 17.5 and 60 m in the initial segment and the main section, respectively. As for the cross section, where $X = 17.5$ m in the initial section, the distances to the wall from the boundary layer end, the potential flow core area end, and the free shear zone end are 0.27, 2.67, and 7.28 m, respectively. Thus, the two typical points are selected at $(X = 17.5$ m, $Y = 2.4$ m) in the potential flow core area (point 1) and $(X = 17.5$ m, $Y = 6.0$ m) in the free shear zone (point 2). Similarly, the characteristic distance to the wall from the ends of the boundary layer and shear zone are 0.72 m and 6.18 m, respectively, in the main section where $Y = 60$ m. Therefore, typical points are selected at $(X = 60$ m, $Y = 0.7$ m) and $(X = 60$ m, $Y = 6.0$ m) in the boundary layer (point 3) and the free shear zone (point 4), respectively. Using these formulas, the cyclic dynamic velocity variation characteristics of the four points are obtained over the entire train operation from the tunnel to the platform, as shown in Figs. 54.1 and 54.2.

As shown in Figs. 54.1 and 54.2, the velocity tendency of the platform varies over time is a manner similar to that of the tunnel exit, increasing first, and then maintaining a plateau before reducing gradually at the end. In Fig. 54.1, point 1 is

Table 54.1 Basic dimensions of the train, tunnel, and platform

Category	Dimension
Cross-sectional area of the train (m × m)	3 × 3.3
Train length (m)	120
Friction coefficient of the train surface	0.045
Cross-sectional area of the tunnel (m × m)	4.4 × 5.3
Tunnel length (m)	1600
Friction coefficient of the tunnel surface	0.055
Train acceleration (m/s^2)	0.7
Maximum train velocity (m/s)	24
Uniform velocity time length of the train (s)	36
Train deceleration (m/s^2)	−0.65
Dimensions of the platform (length (m) × width (m) × height (m))	86 × 12 × 4

Fig. 54.1 Cyclic velocity variations of the points in the initial section and tunnel exit
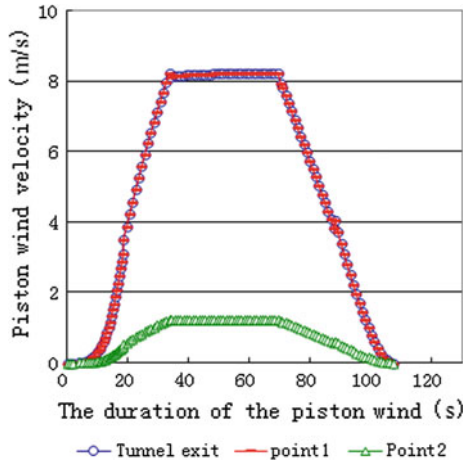
Fig. 54.2 Cyclic velocity variations of the points in the main section and tunnel exit
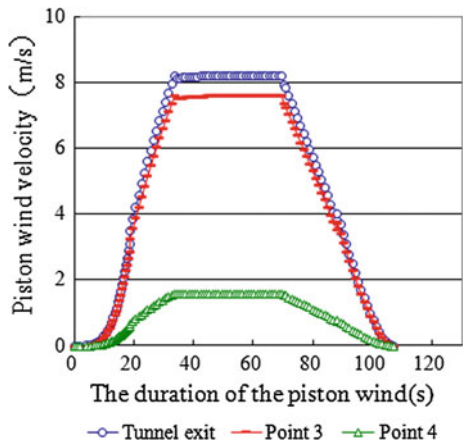
located in the potential flow core area of the initial wall jet section. Its velocity is near that of the piston wind at the tunnel exit. However, point 2 is located in the free shear zone of the initial section, and its velocity is much smaller than that at point 1. Points 3 and 4 are located in the boundary layer and the free shear zone of the main section, respectively, as shown in Fig. 54.2, and the velocity of point 4 is much less than that of point 3. The velocities of both points are less than that of the tunnel exit at the same time.

54.3.2 Solution for the Cross-Sectional Velocity Distribution at Typical Time Values

Figures 54.1 and 54.2 indicate that the platform piston wind velocity varies little in the X-direction and greatly in the Y-direction. Therefore, a typical time value when the maximum velocity of the platform piston wind is 8 m/s is selected to analyze the piston wind distribution in the Y-direction. The cross-sectional velocity distributions of the platform piston wind in the initial segment (where $X = 17.5$ m) and in the main section (where $X = 60$ m) are shown in Figs. 54.3 and 54.4, respectively.

Figures 54.3 and 54.4 show that the velocity distributions in the Y-direction are significantly different between the initial and main sections of the platform piston wind wall jet at a moment of influence by the piston wind. In the initial section, the following regions appear in turn as the distance to the wall increases in the Y-direction: the boundary layer (a–b in Fig. 54.3), the potential flow core area (b–c in Fig. 54.3), and the free shear zone (c–d in Fig. 54.3). Meanwhile, the boundary layer (a–b in Fig. 54.4) and the free shear zone (b–c in Fig. 54.4) emerge successively in the main section. This behavior agrees with classical wall jet theory. The width of the platform's rail line area is commonly 4–5 m, so the platform, to which passengers are always confined, is located within the free shear zone of the initial or main section.

54.4 Validation of the Theoretical Model with Field Measurements

A subway station on Shanghai's Line 2 is field tested for two days to validate the theoretical mathematical model. The corresponding field-test program was described in paper [5]. According to the theoretical calculation, the cutoff point for the initial section and the main section for the platform piston wind are 46.74 m from the tunnel exit. As shown in Fig. 54.5, two points in the initial section and

Fig. 54.3 Cross-sectional velocity in the Y-direction in the initial section
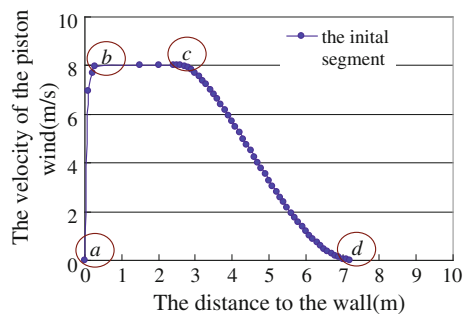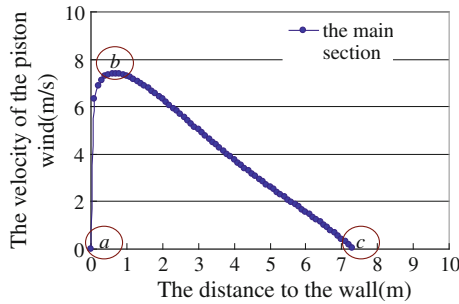
Fig. 54.4 Cross-sectional velocity in the Y-direction in the main section
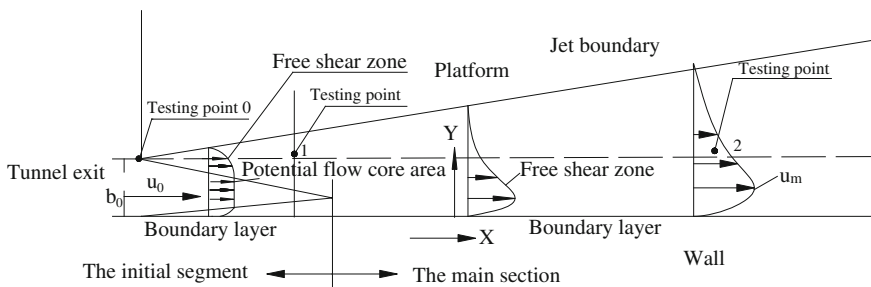
Fig. 54.5 Schematic of the platform piston wind wall jet and the field-test points

main section of the platform piston wind are chosen as test points, respectively, and the three-dimensional coordinates of which are shown in Table 54.2.

The field measurement data and calculated values for the two points in the initial section and main section are shown in Figs. 54.6 and 54.7 with the standard deviations of 0.326 and 0.347, respectively. It is indicated that the calculated results and field-test data are in good agreement. It can be concluded that the free shear zone mathematical models of the platform piston wind in the initial and main sections are both validated by the field measurements.

54.5 The Affecting Factors Analysis on the Platform Piston Wind

It is well known that the train velocity and cross-sectional ratio of tunnel and train have an obvious affect on the tunnel piston wind. With the single-factor analysis method, here the piston wind velocity and duration time variation characteristics are studies with different tunnel cross section, train cross section and train velocity, respectively. In this case, the typical point 2 in the initial section and point 4 in the main section are selected.

Table 54.2 Coordinates of each testing point

		X (m)	Y (m)	Z (m)
At the tunnel exit	Point 0	0	3.8	1.6
In the initial section	Point 1	16.8	4.6	1.6
In the main section	Point 2	69	4.6	1.6

Fig. 54.6 Calculated results and field-test data for Point *M* in the initial section
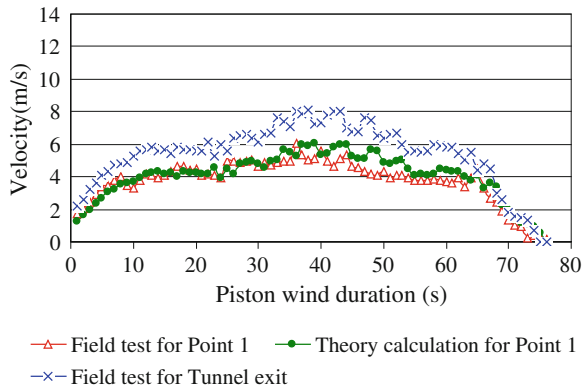
54.5.1 Different Tunnel Cross-Sectional Area

Keeping the other parameters stable, the tunnel cross section is taken as 3.6×4.5 m, 4.0×4.9 m, 4.4×5.3 m, 4.8×5.7 m, and 5.2×6.1 m, separately. Figures 54.8 and 54.9 give the cyclic dynamic piston wind velocity variations of typical point 2 and point 4.

Fig. 54.7 Calculation results and field-test data for Point *N* in the main section
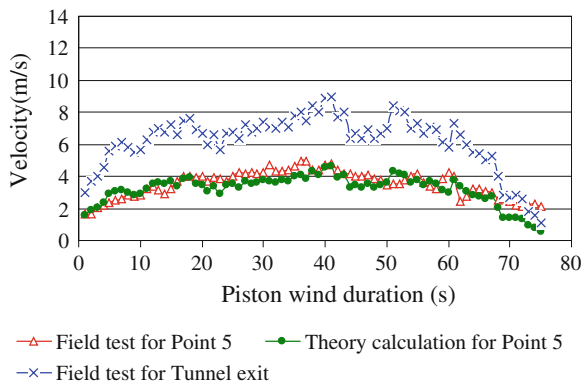
Fig. 54.8 Platform piston wind circled velocity variation with different tunnel cross sections in point 2

tunnel corss-section 3.6×4.5   tunnel corss-section 4.0×4.9
tunnel corss-section 4.4×5.3   tunnel corss-section 4.8×5.7
tunnel corss-section 5.2×6.1
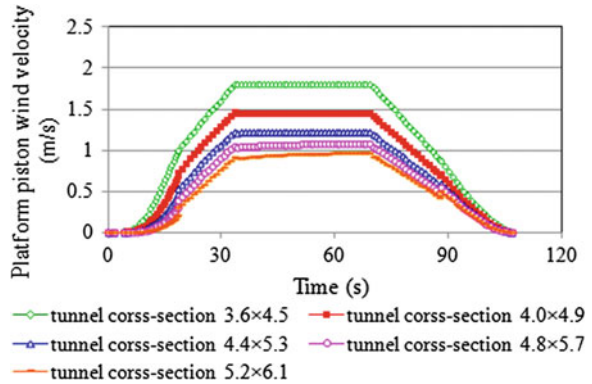
Fig. 54.9 Platform piston wind circled velocity variation with different tunnel cross sections in point 4

tunnel corss-section 3.6×4.5   tunnel corss-section 4.0×4.9
tunnel corss-section 4.4×5.3   tunnel corss-section 4.8×5.7
tunnel corss-section 5.2×6.1
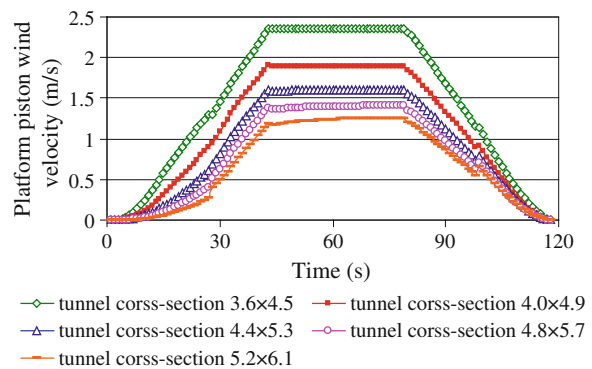
54.5.2 Different Train Cross-Sectional Area

While other parameters are kept uniform, the train cross sections are selected as 2.4 × 2.7 m, 2.7 × 3.0 m, 3.0 × 3.3 m, 3.3 × 3.6 m, and 3.6 × 3.9 m, respectively. The piston wind velocities in point 2 and point 4 are shown in Figs. 54.10 and 54.11.

54.5.3 Different Maximum Train Velocity

With other parameters unchangeable, the maximum train velocity is taken as 18, 20, 24, and 28 m/s, separately. The platform piston wind variation characteristics of point 2 and point 4 are demonstrated in Figs. 54.12 and 54.13.

As shown in above pictures, the maximum velocity and the duration of the platform piston wind are influenced by tunnel cross-sectional area, train cross-sectional area, and train maximum velocity in different degrees.

Fig. 54.10 Platform piston wind circled velocity variation with different train cross sections in point 2
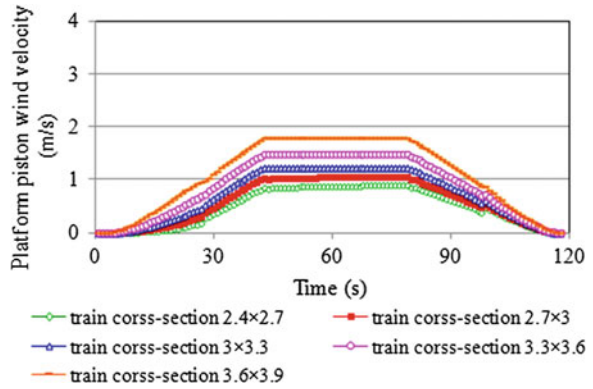
Fig. 54.11 Platform piston wind circled velocity variation with different train cross sections in point 4
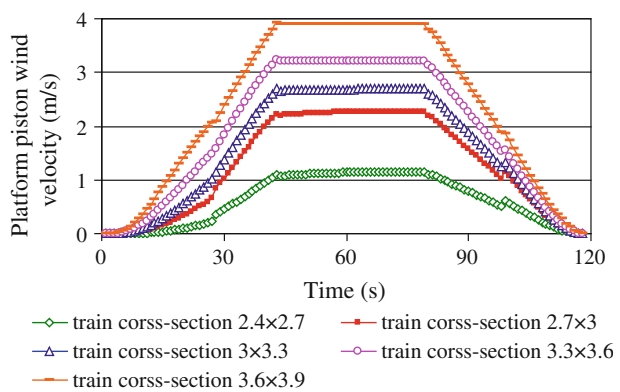
Fig. 54.12 Platform piston wind circled velocity variation with train maximum velocities in point 2
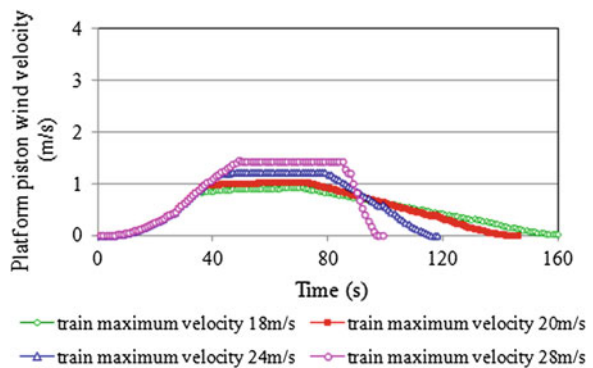
Fig. 54.13 Platform piston wind circled velocity variation with train maximum velocities in point 4
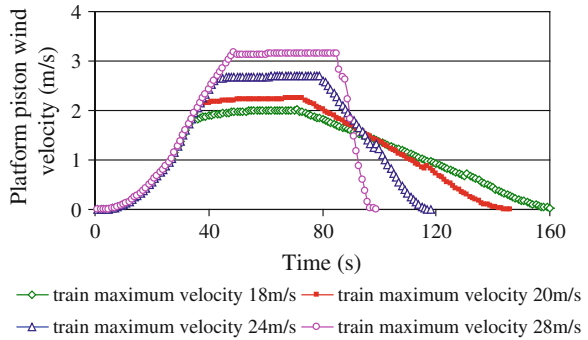
(1) Figures 54.8, 54.9, 54.10 and 54.11, the maximum velocities of the platform piston wind in the initial and main section increase with tunnel cross-sectional area reducing and train cross section increasing, namely which increase with the blockage ratio of the cross-sectional areas between tunnel and train. However, the duration of the platform piston wind does not change with tunnel cross-sectional area and train cross-sectional area.

As illustrated on the pictures from 5.1 to 5.2, the maximum velocity of the initial and main section approximately increases 50 % as the tunnel cross-sectional area reducing from 5.2×6.1 m to 3.6×4.5 m (which reduces about 49 %). As shown in Figs. 54.10 and 54.11, the maximum velocity of the initial and main section increases about 55.6 % and 69.2 %, respectively as the train cross section increasing from 2.4×2.7 m to 3.6×3.9 m (which increases about 54 %).

So, the blockage ratio of the cross-sectional areas between tunnel and train has a significant effect on the maximum velocity of the platform piston wind in the initial and main section.

(2) Based on the single-factor analysis shown in Figs. 54.12 and 54.13, with train speed increasing, the maximum velocity of the platform piston wind in the initial and main section increases, while the duration of the platform piston wind reduces.

Further analysis, when the train maximum velocity increases about 36 %, the maximum velocity of the piston wind in both initial section and main section increase about 40 % and 38 %, respectively, while the duration of the piston wind reduces about 38 %, mainly reflected in the velocity decay process. This main reason lies in that the train deceleration increases with the train speed increasing under the same train and tunnel length conditions, so the time of the piston wind velocity decay decreases.

(3) Compared the above theoretical results in the initial section so that in the main section, it can be seen that the platform piston wind velocity in the initial section is much greater than that in the main section under different affecting conditions. This is because the piston wind in the Y-direction in initial section is not widely expanded, while it expands more sufficiently in the main section.

54.6 Conclusions

With typical wall theory, the mathematical theory model of the platform piston wind has been created. Through Excel software, the expressions are solved in the initial section and main section separately. Along the direction vertical to the wall, the initial section is composed of three parts and the main section consists of two parts, which has been validated by the field measurement. With single-factor experiment, it could be seen that the cross-sectional ratio of the tunnel and train and the maximum train velocity have an obvious impact on the platform piston wind velocities and duration period.

References

1. Saiben M (1971) Fluid mechanics of train-tunnel systems in unsteady motion. AIAA J 9:1538–1545
2. Kim JY, Kim KY (2007) Experimental and numerical analyses of train induced unsteady tunnel flow in subway. Tunn Undergr Space Technol 22:166–172
3. Huang YD (2012) A numerical analysis of the ventilation performance for different ventilation strategies in a subway tunnel. J Hydrodyn 24:193–201
4. Wang LH, Wu XP (2007) The effect on the subway system from the piston action wind. Chin J Undergr Space Eng 3:161–166
5. Yuan FD, You SJ (2007) CFD simulation and optimization of the ventilation for subway side-platform. Tunn Undergr Space Technol 22:474–482
6. Wang LH, Li Z, et al (2011) A measurement analysis of subway thermal environment characteristics of the coupling airflow between air-conditioning air supply and piston wind. J Chongqing Univ 34:116–121
7. Shen X, Wu XP, Dong ZhZh (2005) Character testing of piston wind in a underground railway tunnel. HV&AC 35:103–106
8. Shen X (2001) Underground railroad piston wind characteristics. Master dissertation in Tongji University

Chapter 55
Research on Fungal Microorganisms Growth Under Various Thermal Conditions

Yang Lv, Bailin Fu, Wenjie Yuan, An Xie and Jinmu Huang

Abstract Indoor air quality has a great impact on our health, and there are many reasons contributing to the pollution of indoor air. At present, people have widely concerned about air-conditioning system, which is regarded as potential microbial pollution sources. The study is about separation and identification of fungal microorganisms on the surface of the central air-conditioning system filters, and then doing research on the colonies and mycelium grown and reproduce regular of fungal microorganisms in different thermal environment, which aim to lay the groundwork of effective air microbial contamination solved by thermal methods. This study has shown that *Penicillium spp* and Cladosporium spp are dominant fungi, and the number of CFUs is 600 and 140 cfu/cm^2, respectively. No matter constant or variable temperature conditions, the reproduce rate of *Penicillium* is faster than *A. glaucus* and the relationship between colony diameter and time is liner relation. Through these constant and variable experiments, it is found that variable temperature does obvious restrain on *Penicillium spp*, while *A. glaucus* has the same tendency.

Keywords Fungi growth · Thermal response · Measurement · Temperature control technology

Y. Lv (✉) · B. Fu · A. Xie · J. Huang
Lab of Building Environment and New Energy Resource, School of Civil Engineering,
Dalian University of Technology, Dalian, China
e-mail: lvyang20022002@yahoo.com.cn

W. Yuan
School of Life Science and Biotechnology, Dalian University of Technology, Dalian, China

55.1 Introduction

At present, the indoor air pollution caused by air-conditioning system becomes worse, especially does harm to people who expose in indoor environment. Therefore, the health status of air-conditioning system attracts people's attention. There are many places could propagate microorganism easily in the air-conditioning system which is regarded as primary pollution source. Research shows that the air-conditioning filter accumulates a lot of dust, as well as some places provide high humidity or even ponding environment, such as bibulous material in equipment and humidifier, cooling coil and condensate plate. However, this environment often comes to be propagating places of bacteria and fungi [1–3]. Moreover, fungi account for a high proportion of existed microorganisms in the air-conditioning system. Lu et al. from Harbin Industrial University tested central air-conditioning system of two buildings in the northern Harbin city and then indicated that the number of fungi is 4.7 times than that of bacteria [4]. Li et al. from Xi'an University of Architecture and Technology measured the air-conditioning system of Shaanxi History Museum and indicated that the fungal concentration is 1.60–128.06 times than the bacterial concentration in the all working parts of air supply section [5].

The influence of the fungi microorganism is also particularly serious in the aspect of human health hazard. The research by the French National Health and Medical Research Institute shows that the indoor fungal harm to patients with severe asthma is as twice as that of other allergic materials [6]. People predispose to dermatophytosis, dermatitis, psoriasis, eczema, and other diseases [7]. Somers et al. found that the rat inhaling polluted fungal particles had a genetic mutation [8]. Besides, the hazard is worse than other microorganisms decided by physiological characteristics. Firstly, fungus has a wide growing temperature range. Secondly, fungal spore can be dormant in low-temperature environment, but quickly grow when temperature back to suitable range. Furthermore, fungal spore spreads easily, especially after the operation of air-conditioning system, as a consequence of fungal spore spreading in indoor environment and contributing to biological pollution [9].

So, it is extremely important to do research on growth characteristic of fungi microorganism in air-conditioning system and then find appropriate control methods based on the above reasons. The study obtains the dominant fungi on the filter surface in air-conditioning system by actual measurement of fungi microorganism in air-conditioning system of building in reality and then analyzes the hyphal growth responses of fungi microorganism in different thermal environments by study on the environmental thermal response. The overarching objective is to lay the foundation of solving microbial pollution problems in air by using thermal methods.

55.2 Isolation and Identification of Dominant Fungi

55.2.1 Actual Measurement Instruments and Materials

Sterile non-woven gauze, distilled water, Czapek's medium, autoclave, constant temperature incubator, shaking incubator with two-way regulation of temperature functions, microscope, TR-72i thermal recording instrument were used.

55.2.2 Sampling and Counting of Fungi

The actual measured object was a central air-conditioning system of one gymnasium and 5×5 cm area on the filter of this air-condition system was chosen. Dabbed with sterile non-woven gauze and collected all dust on the area. The non-woven was put into sterile water using aseptic technique and fully mixed to make sure that organic substance on the non-woven was soluble in sterile water well, and then, the stock solution was prepared. After then, prepared solution of original concentration, 10 times diluted concentration and 100 times diluted concentration, respectively; 1 ml solution was dropped from each of three different concentrations on agar plates and observed the number of colonies, which was counted of average of parallel sample colonies. After calculating, two dominant fungi were found. The number of colonies of Fungus 1 and Fungus 2 was 600 and 140 cfu/cm^2, respectively.

55.2.3 Identification of the Dominant Fungi

According to morphology, color and other physiological and biochemistrical characteristics, and structures of hypha and spore at the same time, the fungi were identified. The features of Fungus 1 (Fig. 55.1) were septate and coenocytic hypha, conidiophores with fastigiated branch, which looked like elliptic and had no partition. The features of Fungus 2 (Fig. 55.2) had green fluey colony, white hypha, and steadily specific color and hypha had septate and coenocytic. Combined with Fungal Identification Manual [10], Fungus 1 was preliminarily judged as *Penicillium spp,* and Fungus 2 was Cladosporium spp.
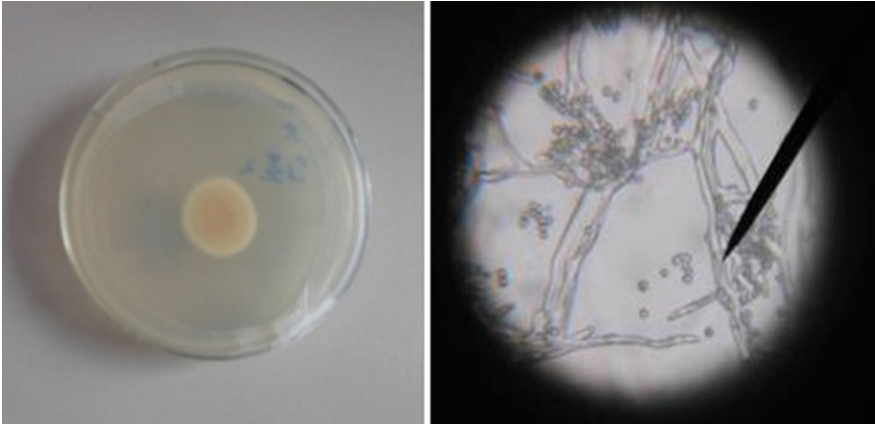
Fig. 55.1 Colony and hypha of Fungus 1
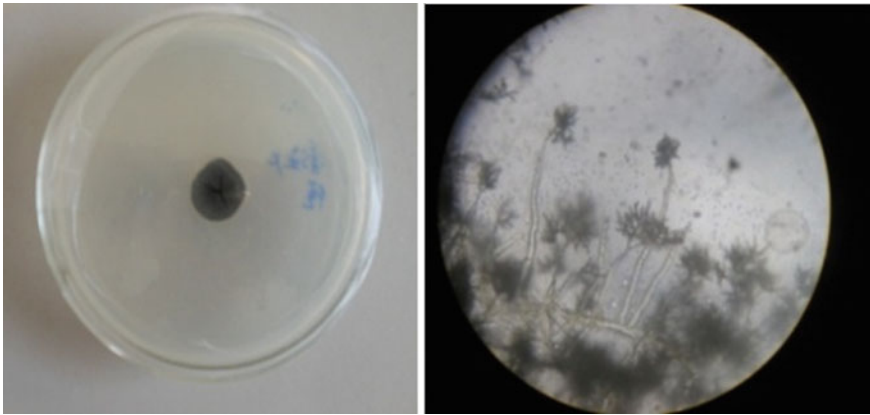
Fig. 55.2 Colony and hypha of Fungus 2

55.3 Temperature Experimental Study

55.3.1 Experimental Program

In order for study on the regulation of growth of fungi microorganism in the air-conditioning system at different temperature, the research carried on two groups of experiments, which was formed of constant temperature cultivation and variable temperature cultivation. The environmental temperature of constant one was set at 25 °C and the environmental temperature of variable one was set at the range of 22 and 28 °C, which was swapped once between 22 and 28 °C every 12 h (shown in

Fig. 55.3 Experimental program of the variable temperature cultivation
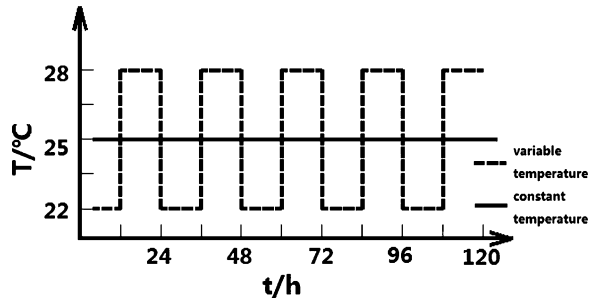
Fig. 55.3, where *T* is the control temperature and *t* is time). The diameter of the colony was monitored every 12 h during the incubation period for a week. The relative humidity was executed a special control and assumed to be maintained at constant concentration.

55.3.2 Result of Temperature Experiment

Figures 55.4 and 55.5 show growth changes of dominant fungi at the constant temperature of 25 °C and the fungi grew as time went on whatever way cultivated, and colonies were continuously scaled up on agar plates but with different rates and morphology.

Figure 55.6 shows growth curve of two fungi at the constant temperature of 25 °C. From this figure, it was known that both two fungi could grow well in the environment of constant temperature and the relationship between fungal diameter and time was similar to linear relation, where the vertical and horizontal axis in the figure stand for diameter of fungal colony and time, respectively. Neither two fungi turned into steady period before cultivation finished and the growth rate of *Penicillium spp* was faster than that of *A. glaucus*.

Figure 55.7 shows growth curve of two dominant fungi in the air-conditioning system at the variable temperature ranging from 22 to 28 °C. From this figure, it was known that the situation of fungi that stepped from slow growth to no longer growth happened to *Penicillium spp* early (the diameter of colony did not change after 5-day cultivation), and the tendency of no longer growth appeared on *A. glaucus* after 8-day cultivation.

Compared the growth situation of *Penicillium spp* in different temperature environments, Fig. 55.8 indicated that *Penicillium spp* grew quickly in constant temperature environment. But it was restrained obviously after 4 days in the variable environments, and its colonies did not scaled up any more. So, means of variable temperature conduct can control fungal growth.

Then compare the growth situation of *A. glaucus* in different temperature environments. Figure 55.9 indicated that the growth rate of *A. glaucus* in the
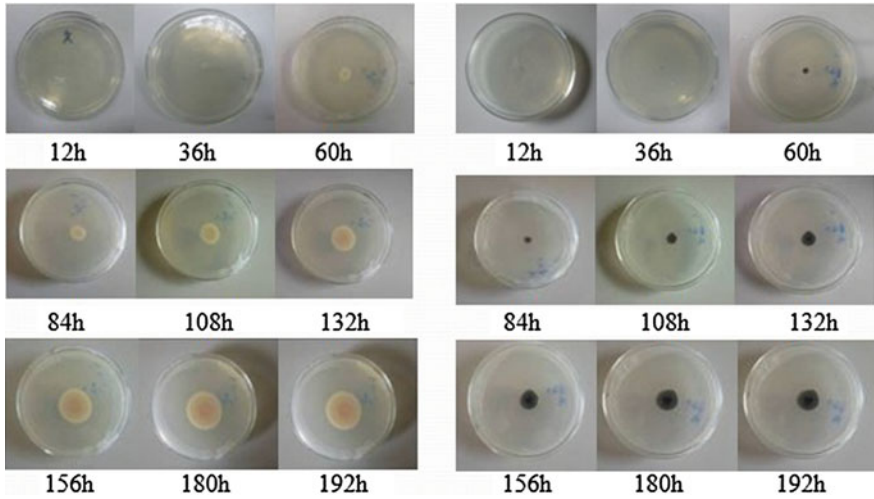
Fig. 55.4 Time series of two fungal colonies at constant temperature of 25 °C
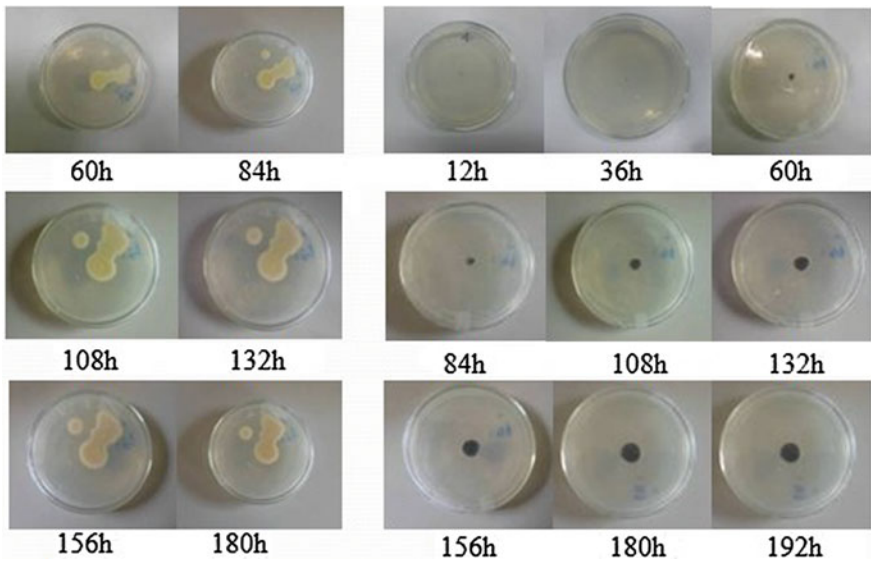
Fig. 55.5 Time series of two fungal colonies at variable temperature ranging from 22 to 28 °C

constant temperature environment was faster than that of variable one. In the variable temperature environment, there was a restrained tendency on the growth of *A. glaucus* after 3 and 8 days, respectively.
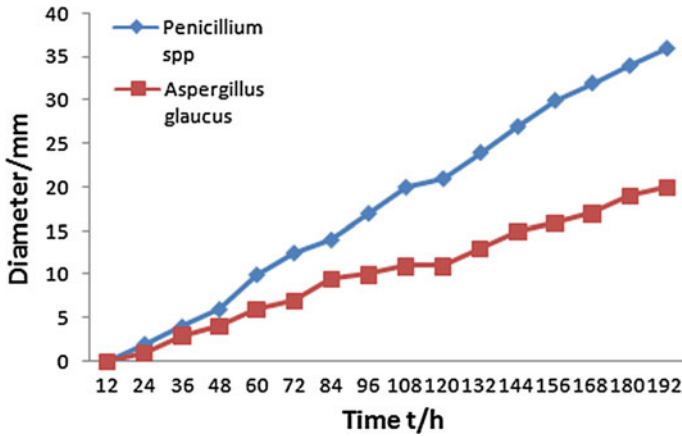
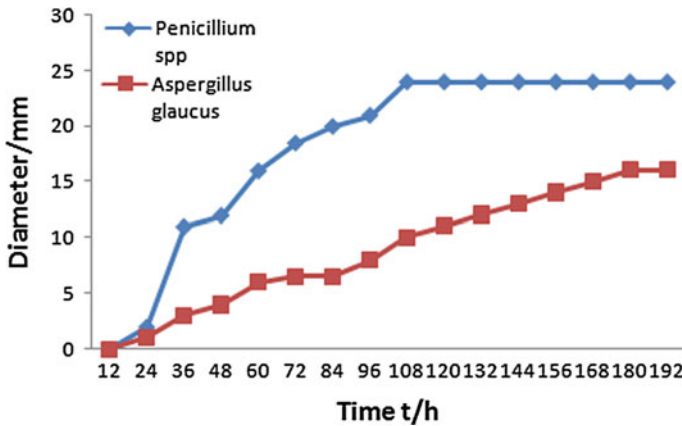**Fig. 55.6** Growth curve of two fungi at constant temperature of 25 °C

Fig. 55.7 Growth curve of two fungi at variable temperature ranging from 22 to 28 °C

55.4 Analysis and Discussion

55.4.1 Analysis of Different Fungi in Same Temperature Environment

From the above experimental results, it was shown that both fungi propagated at certain rates at constant temperature of 25 °C, steady period still did not appear after a week, and the relationship between diameter of colony and time was linear. So, steady temperature was beneficial to fungal growth. In variable temperature environment, the growth stability of fungal colony was worse than that of constant temperature of 25 °C for whatever fungus. The growth rate also reduced, and
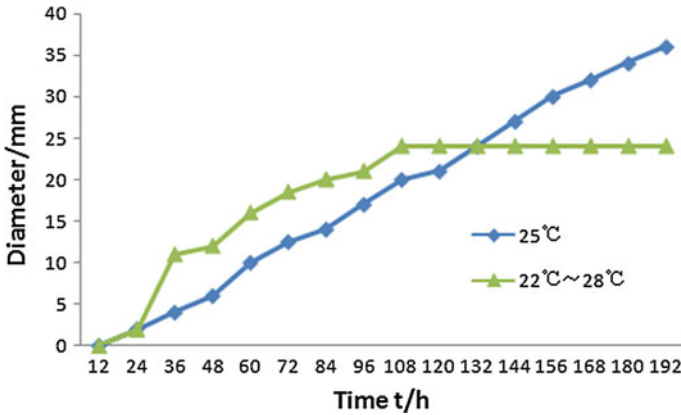
Fig. 55.8 Growth curve of *Penicillium spp* in two environments
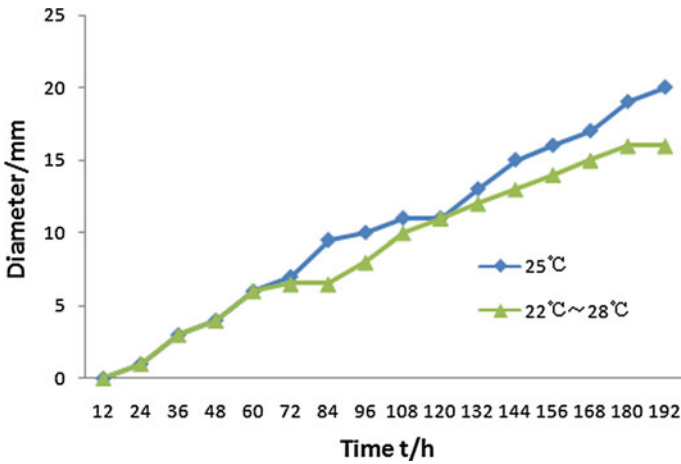
Fig. 55.9 Growth curve of Cladosporium spp in two environments

colony formation was restrained. In addition, the colony of *Penicillium spp* was spread easily in variable temperature environment. This phenomenon was submitted that it perhaps relate to variable temperature.

55.4.2 Analysis of Same Fungi in Different Temperature Environment

The analysis of same fungi in different temperature environment indicated that variable temperature does obvious restrain on *Penicillium spp* and *A. glaucus* had the same tendency.

Table 55.1 Change of two fungal diameter in different environment

Environment	Fungus	24 h	48 h	72 h	96 h	120 h	144 h	168 h	192 h
Constant temperature	*Penicillium spp*	2	6	12.5	17	21	27	32	36
	Cladosporium spp	3	6	9.5	11	13	16	19	21
Variable temperature	*Penicillium spp*	2	12	18.5	21	24	24	24	24
	Cladosporium spp	1	4	6.5	8	11	13	15	16

Unit in the table: mm

55.4.3 Analysis of Diameter Change of Penicillium spp and Cladosporium spp

Table 55.1 compared the growth rates of *Penicillium spp* and *A. glaucus* in different environments. From Table 55.1, it was known that the diameter of *Penicillium spp* could reach 36 and 24 mm, while *A. glaucus* could reach 21 and 16 mm after 192 h both in constant and in variable temperature, respectively. So, no matter what environment, the growth rate of *Penicillium spp* was faster than that of *A. glaucus,* and this fact cannot be changed by temperature control. But for one fungus, no matter *Penicillium spp* or *A. glaucus*, the growth rates of fungi in variable temperature environment were slower than that in constant temperature environment. So, the fungal colony growth could be controlled by changing temperature.

55.5 Conclusions

The study reached the following conclusions by isolating, identifying, and doing environmental thermal response of fungal microorganisms in central air-conditioning system.

1. *Penicillium spp* and *A. glaucus* were the dominant fungi among all fungal microorganisms in air-conditioning system. The number of colonies was 600 and 140 cfu/cm^2, respectively.
2. No matter constant or variable temperature conditions, the growth rate of *Penicillium spp* was faster than that of *A. glaucus,* and this fact cannot be changed by temperature control.
3. Through the research of constant and variable temperature, it was found that no matter *Penicillium spp* or *A. glaucus*, the growth rates of fungi in variable temperature environment were slower than that in constant temperature environment, and variable temperature does obvious restrain on *Penicillium spp* and *A. glaucus* had the same tendency.

References

 1. Bluyssen PM, Cox C, Seppanen O et al (2003) Why, when, how do HVAC-systems pollute the indoor environment and what to do about it? Environ 38(2):209–225
 2. Hou J (2009) Field and analysis for microbial contamination and characteristics of ventilated systems in air conditioning. Master thesis, Xi An University of Architecture and Technology, Xi An, China (In Chinese)
 3. Chen F, Zhao B, Yang X (2009) Investigation and review of microbial pollution in air conditioning systems of public buildings. Heating ventilating and air conditioning (39):50–56 (In Chinese)
 4. Lu Z, Jang J, Cao D et al (2007) Testing and analysis for microbes and particles in central air conditioning systems of public buildings. J Heating ventilating and air conditioning 37:103–107 (In Chinese)
 5. Li A, Yao L, Hou J (2010) Field test and analysis of microbial contamination in central air conditioning systems. Heating ventilating and air conditioning 40:121–125 (In Chinese)
 6. Zhang J, Guo X (2005) Living environment and health. Chemical Industry Press, Beijing (In Chinese)
 7. Zhao A, Guo Y, Pan X (2009) Research advance in indoor microbial contamination and health impact. J Environ Health (26):82–84 (In Chinese)
 8. Somers CM, McCarry BE, Malek F et al (2004) Reduction of particulate air pollution lowers the risk of heritable mutations in mice. Science 304:1008–1010
 9. Gorny RL, Reponen T, Willeke K et al (2002) Fungal fragments as indoor air biocontaminants. Appl Environ Microbial (68):3522
10. Wei J (1979) Fungal identification manual. Shanghai Science and Technology Press, Shanghai (In Chinese)

Chapter 56
Study on Indoor Air Quality of Ceiling Radiant Cooling Panel System Integrated with Displacement Ventilation

Jing Du and Nianping Li

Abstract Compared with variable air volume (VAV) system, the ceiling radiant cooling panel (CRCP) system integrated with displacement ventilation (DV) has better thermal comfort and excellent energy-saving potential. As a result, CRCP/DV has been paid more attention and used widely in advanced buildings in recent years. However, the indoor air quality (IAQ) under the above-mentioned system still needs to be tested. Firstly, this article studies two zones stratified by ventilation system in a room. Between the two zones is a transitional area called as stratified boundary which divides a room into two spaces with totally different air quality. It is analyzed that there are three important factors that decide the height of the stratified boundary. Secondly, the paper uses an office room as an example studied numerically. To simulate this room, a numerical model using finite volume method for CRCP/DV is created based on computational fluid dynamics (CFD). The objective of this model is to research contaminant removal efficiency of active contaminants (as indicated by CO_2) concentration and passive contaminants (as indicated by VOCs) concentration under CRCP/DV. As a consequence, it is found that contaminant removal efficiency of active contaminants performs well while that of passive contaminants is poor. At last, this paper analyzes the cause and proposes an optimal control strategy to improve IAQ. This research can provide guidance for the buildings with CRCP/DV demanding high IAQ.

Keywords CRCP system · DV · IAQ · Numerical simulation

J. Du · N. Li (✉)
College of Civil Engineering, Hunan University, Changsha 410082, China
e-mail: linianping@126.com

56.1 Introduction

Ceiling radiant cooling panel system integrated with displacement ventilation (CRCP/DV) is one of the HVAC systems that attract attention for its excellent energy-saving potential while providing better thermal comfort. In this system, DV supplies fresh air with low velocity to remove all the latent heat load and part of sensible heat load, while CRCP system applies radiation mainly to eliminate the rest of sensible heat load [1–3]. In this way, it can increase supply water temperature of CRCP system and then improve the COP of chiller, while it reduces the energy consumption of fan. Therefore, the energy consumption of operating CPCR/DV accounts for 57.7 % of that of conventional system according to the research of Boulder.Colorado [4]. On the other hand, the heat loss through radiation of human body takes 45 % of the total heat loss in the comfortable condition and it is the main heat loss method of human body [5, 6]. Consequently, people can gain more thermal comfort because of the CRCP system removing heat from the heat sources directly by radiation and indirectly by convection.

Although it is recognized that DV has good indoor air quality (IAQ), what is it like combined with CRCP system? Few people have taken further consideration into it, and the IAQ under such system still needs to be tested. This article employs an office room as an example to simulate its IAQ based on computational fluid dynamics (CFD). The result shows that contaminant removal efficiency of active contaminants performs well, while contaminant removal efficiency of passive contaminants is poor. To improve the IAQ, this paper proposes an optimal control strategy.

56.2 Indoor Air Quality Parameters

Along with the improvement in our living standards, the amounts of the sources and categories of indoor air contaminant are becoming more and more. There are many kinds of contaminant influencing human health such as CO_2, volatile organic compounds (VOCs), particulate matter (PM), and radon. Building decoration materials and furniture are the main sources of pollution in a room. Moreover, it is worth mentioning that humanity itself is the major sources of CO_2. The environmental parameter that indicates IAQ is contaminant concentration in the occupied zone (0–1.1 m), especially in the breathing zone (0.9–1.2 m) [7]. The contaminant concentration and distribution not only depend on spatial distribution of the contaminant sources, but also on the airflow pattern which is decided by what kind of ventilation pattern it is [6].

56.2.1 IAQ Index

The air quality for a certain location in a room can be determined by the contaminant removal efficiency that is also called dimensionless concentration or contamination degree,

$$\mu = \frac{C_i - C_s}{C_e - C_s} \tag{56.1}$$

where C_i is the local contaminant concentration, C_s is the contaminant concentration in the supply air, and C_e is the contaminant concentration in the exhaust air [8].

For the ideal mixing ventilation (MV), contaminant degree is equal to 1.0 because the exhaust contaminant concentration is close to the local concentration [2]. Nevertheless, DV can provide more better contaminant removal efficiency compared with the MV. As a result, for the same supply flow velocity and temperature, the DV has higher contaminant removal efficiency and the contaminant degree is lower than 1.0 under DV system.

56.2.2 The Indoor Airflow Stratification

The indoor airflow stratification on the vertical surface creates a high ventilation effectiveness for DV without CRCP. This stratification is characterized by the following two zones in a room. The first one is a lower zone with stratified airflow pattern and clean air; the second one is an upper zone with hybrid airflow pattern and polluted air [9, 10].

Between the two zones is a transitional area called as stratified boundary which divides a room into two spaces with totally different air quality. With well-designed CRCP/DV, the stratified boundary is higher so that polluted air cannot approach the breathing zone.

56.2.3 Stratified Boundary

If stratified boundary is below the top surface of the occupied zone, or even lower than the top surface of the breathing zone, human beings will breathe badly polluted air and then get ill as time passes. Therefore, to deeply analyze the factors that affect the height of stratified boundary is of great importance.

There are three effects influencing the height of the stratified boundary and air quality in the occupied zone in a room under CRCP/DV. As shown in the Fig. 56.1:
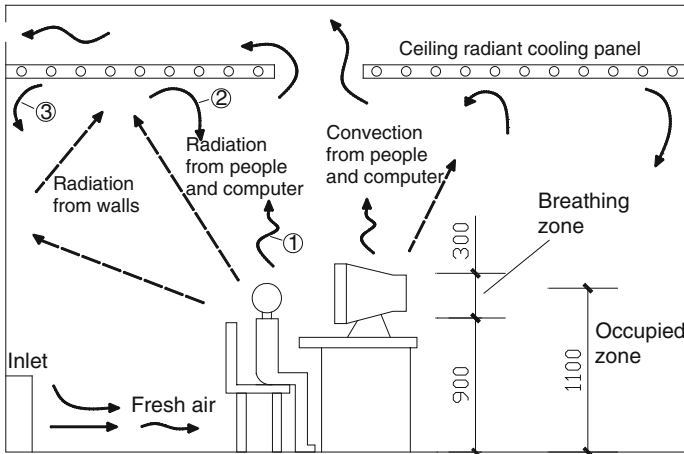
Fig. 56.1 CRCP system dedicated DV

1. Upward heat flux caused by heat sources.
2. Downward convection under cooling radiant ceiling panel.
3. Downward convection from cold walls.

The downward convection from CRCP might move the stratified boundary with CRCP/DV into the occupied zone compared with the height of the stratified boundary layer with only DV. Furthermore, the downward convection from cold walls caused by CRCP's cooling radiant effect has the same impact on the stratified boundary. However, when heat sources exist in a room, they will have reverse effects on stratified boundary. The heat flux from heat sources might have remarkable improvement in upward convection which is primary near the occupants even with the strong downward air motion from the cold panels.

56.3 Numerical Simulation

Numerical simulation is becoming more and more popular as its accuracy improves and computing speed increases. One of the reasons for computer modeling's wide application in research of HVAC's system mainly lies in the relatively low cost. Another advantage over experiment is that numerical simulation can easily change the boundary conditions to research different experimental situations. Therefore, this article will adopt numerical simulation to study the concentration distribution and contaminant removal efficiency of active contaminant (as indicated by CO_2) concentration and passive contaminant (as indicated by VOCs) concentration under CRCP/DV.

(a)

(b)
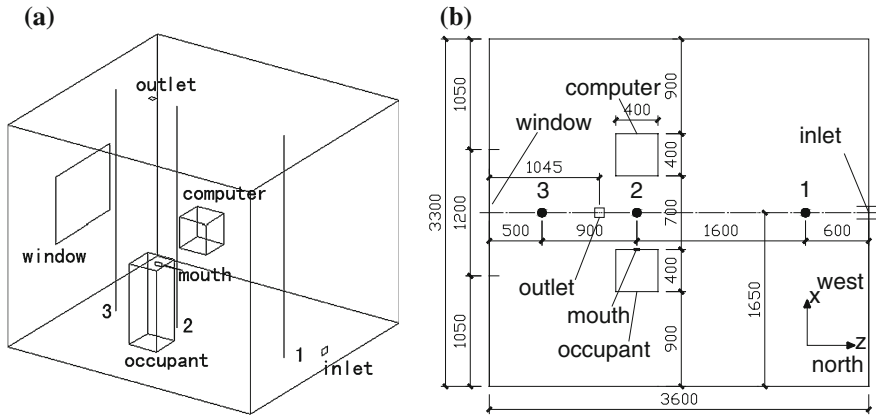
Fig. 56.2 The layout of the room: **a** perspective view and **b** plane view

56.3.1 Physical Model

In this study, the physical model is based on an office room, which is located in Hunan University, Changsha, China. The structure and layout of the room are shown in Fig. 56.2.

The whole ceiling is simplified as CRCP whose temperature is set to 18 °C above dew-point temperature in a room. The floor is spread out a carpet seen as VOC source where the simulation uses formaldehyde representing VOCs. There is a person and a computer in the room, which are the heat sources. For convenience sake, we use a 400 × 400 × 1,100 mm cuboid as the person and a 400 × 400 × 400 mm cube as the computer. Each person is also regarded as active contaminant CO_2 source whose mouth is simplified as a 50 × 50 mm outlet. The south wall of this room is outdoor wall and it is opened a 900 × 1,200 mm window. The simulation takes the bottom supply and upper return mode as its airflow pattern. The supply air opening (120 × 80 mm) is set on the north wall, and return air opening (90 × 90 mm) is set on the roof. To satisfy human being's minimal theoretical air requirements and health demands, every person's fresh air rate is set to 40 m³/man-h, so the total supply air volume is 40 m³/h.

56.3.2 Meshing

The three-dimensional heat transfer in the ceiling is complicated and asymmetrical, so this article ignores the heat transfer process and sees the ceiling as a symmetrical surface heat source in the numerical simulation. Considering the accuracy and operation speed of the calculation, each edge of the room is divided into twenty parts. For some places whose concentration gradient is great, this paper adopts part grid refinement technology.

56.3.3 Governing Equations and Boundary Conditions

Differential equation describing indoor air motion and heat transfer contains continuity equation, momentum equation, energy equation, gas composition equation which can be normalized as follows:

$$\frac{\partial(\rho\phi)}{\partial t} + \frac{\partial(\rho u\phi)}{\partial x} + \frac{\partial(\rho v\phi)}{\partial y} + \frac{\partial(\rho w\phi)}{\partial z} = \frac{\partial}{\partial x}\left(\Gamma\frac{\partial\phi}{\partial x}\right) + \frac{\partial}{\partial y}\left(\Gamma\frac{\partial\phi}{\partial y}\right) + \frac{\partial}{\partial z}\left(\Gamma\frac{\partial\phi}{\partial z}\right) + S$$

(56.2)

where ϕ is a dependent variable, which represents 1, u_i, T, k, ε, m, corresponding to continuity equation, component velocity, energy equation, turbulence kinetic energy equation, turbulent kinetic energy dissipation rate equation, and gas composition equation separately. Γ is diffusion coefficient, and S is generalized source item [6, 11].

In order to simplify the model, the following assumptions are applied:

1. For convenience of calculations, the person and computer are regarded as plane heat sources.
2. There is no heat transfer process in the interior wall and floor which is set as adiabatic boundary.
3. The air of the room is incompressible.

The inlet on the northern wall is set as velocity inlet whose temperature is 21 °C and velocity is 2 m/s. The contaminant carbon dioxide is 0.03 % of supply air. The temperature of people's breathing out air is 36.5 °C, and velocity is set to 1 m/s. The CO_2 accounts for 4 % of exhalation.

56.3.4 The Results of Numerical Simulation

In the post-processing course, the contaminant concentration distribution in the occupied zone is mainly what this paper studies. Therefore, in order to research numerical results easily, we choose three representational positions whose locations are shown in the Fig. 56.2 to analyze the change in contaminant removal efficiency of CO_2 and formaldehyde along with the increase in the height of the room.

From the results shown in Figs. 56.3, 56.4, and 56.5, we can see that the contaminant removal efficiency of CO_2 has a similar profile at different positions and the concentration is higher along with the increase in the height of the room. However, the formaldehyde distribution is different from that of CO_2 and it is random. Even in some locations, the removal efficiency μ is far higher than 1.0 under CRCP/DV and it provides worse quality air than the mixing system.
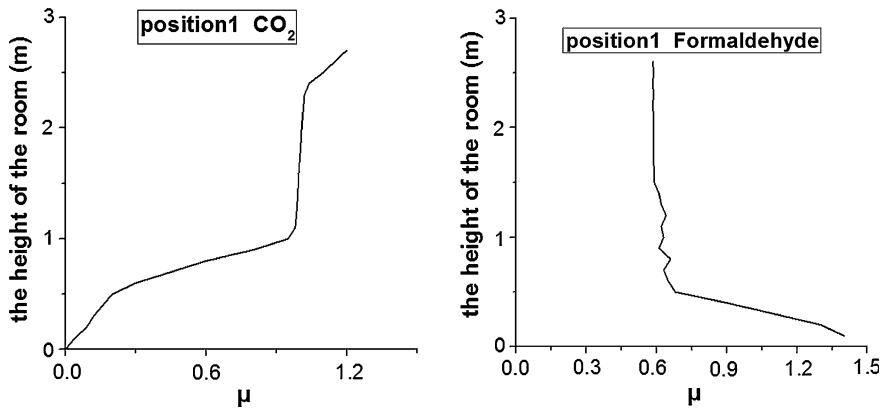
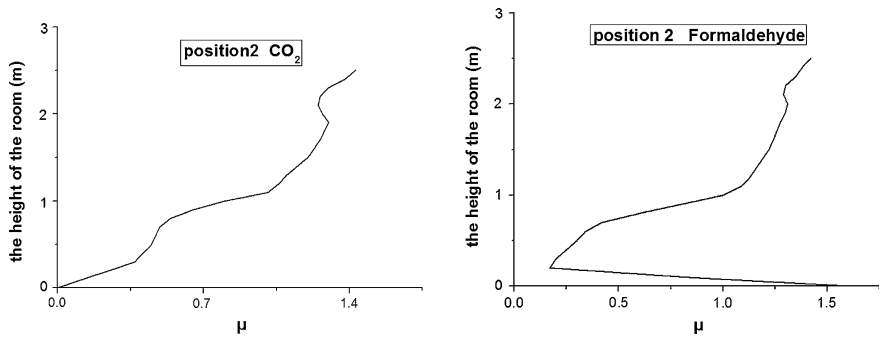**Fig. 56.3** The contaminant removal efficiency of CO_2 and formaldehyde in the Position 1

Fig. 56.4 The contaminant removal efficiency of CO_2 and formaldehyde in the Position 2
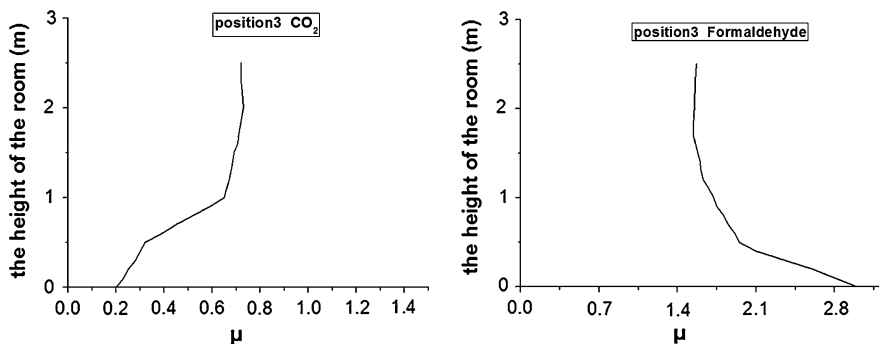

Fig. 56.5 The contaminant removal efficiency of CO_2 and formaldehyde in the Position 3

Therefore, we can conclude that contaminant removal efficiency of CO_2 is better than that of formaldehyde for CRCP integrated with DV.

Because we are short of experiment condition and high-precision measuring equipment, this paper does not have measured data. However, the results of Position 1, Position 2, and Position 3 are similar separately to simulation results of Position 1, Position 5, and Position 3 in Reference [6] whose boundary conditions are also similar to that of this paper. Thus, it can verify the correctness of the simulation method and the accuracy of the simulation results in this article.

56.4 The Analysis of Numerical Simulation Results and Optimal Strategy

The difference in removal efficiency between active contaminant and passive contaminant is that active source is associated with heat source. Because the temperature of CO_2 from people is higher than that of VOCs from carpet, the probability of CO_2 having upward convection motion is higher. As a result, thermal plume effect is significant for IAQ under CRCP/DV. The thermal plumes from the person bring CO_2 to the upper zone and prevent the mixture of contaminants with the clean air in the breathing zone, while passive contaminants can mix with the clean air and reduce the IAQ in the occupied zone.

In order to improve the IAQ, this article is committed to optimize the airflow pattern to decrease the passive contaminant concentration. If another return air opening is set on the opposite wall of inlet, it will form a convection zone on the floor, which prevents the pollutant generated by carpet from entering into the breathing zone. Otherwise, appropriate supply air velocity can avoid the short circuit and optimize airflow pattern.

56.5 Conclusions

1. A room is divided into two spaces with totally different air quality by stratified boundary: The first one is a lower zone with stratified airflow pattern and clean air; the second one is an upper zone with hybrid airflow pattern and polluted air under CRCP/DV.
2. There are three factors influencing the height of the stratified boundary including upward heat flux caused by heat sources, downward convection under cooling radiant ceiling panel, and downward convection from cold walls.
3. Through the numerical simulation, we can conclude that the contaminant removal efficiency of active contaminant is better than that of passive contaminant. It is because that the thermal plumes from the person bring CO_2 to the upper zone and prevent the mixture of contaminants with the clean air in the

breathing zone, while passive contaminants can mix with the clean air and reduce the IAQ in the occupied zone.

4. Changing the airflow pattern is efficient to decrease the passive contaminant concentration. Another return air opening set on the opposite wall will form a convection zone on the floor, which prevents the pollutant generated by carpet from entering into the breathing zone. This research can provide guidance for the buildings with CRCP/DV demanding high IAQ.

References

1. Kruhne H (1993) Effect of cooled ceilings in rooms with displacement ventilation on the air quality. Proc Indoor Air 93(5):395–400
2. Behne M (1999) Indoor air quality in rooms with cooled ceilings: Mixing ventilation or rather displacement ventilation. Energy Build 30:155–166
3. Niu J, Kooi JVD (1994) Indoor climate in rooms with cooled ceiling systems. Build Environ 29(3):283–290
4. Boulder.Colorado. Radiant Cooling Design Brief. www.energydesignresources.com. 2005-03-27
5. Wang Z (2004) Radiant cooling and radiant heating in low-temperature condition IMI. China Machine Press, Beijing
6. Xu L, Weng P (2005) Numerical research development of indoor air pattern and air quality. Shanghai Electr Power Coll J 9:286–230
7. Standard 62-1989. Ventilation for acceptable indoor air quality
8. Yang S, Srebric J (2000) Modeling performance of different ventilation system on VOC removal in a full-scale room. Proceedings of CLIMA, vol 2001
9. Fitzner K (1996) Displacement ventilation and cooled ceilings, results of laboratory tests and practical installations. Proc Indoor Air 96(1):41–50
10. Blay D (1996) Convective phenomena involved in a displacement ventilation system. Indoor Air 96
11. Li N (1997) Numerical prediction and evaluation methodology of indoor air quality. Dust Removal by Ventilation 16(1):10–13

Chapter 57
Influence of Indoor Air Environment on Human Dynamic Thermal Comfort

Xin Yi, Bingkun Xu and Xiaoping Feng

Abstract In terms of human body comfort and energy efficiency in buildings, it is significantly important to do the research on indoor air environment and human body dynamic thermal comfort. This article firstly analyzes their relationship between objective and subjective aspects of the air atmosphere. Secondly, according to thermal equilibrium and the main thermal comfort index, the influence factors of thermal comfort are described, which involve indoor temperature, air humidity, air distribution, the mean radiant temperature on the different surfaces, IAQ, etc. At last, a security, economics, reasonable, and health air processing scheme is put forward.

57.1 Introduction

As mechanization of society develops and industrialization boosts, people spend more than 80 % of the total life time indoors. Indoor air environment is closely related to human health increasingly, because indoor air environment exerts a direct impact on people's health, work efficiency, and human thermal creative.

X. Yi (✉)
School of Environmental and Municipal Engineering, Xi'an University of Architecture and Technology, Xi'an, Shaanxi, China
e-mail: yixin05@163.com

X. Yi · B. Xu
School of Energy and Resource, Xi'an University of Science and Technology, Xi'an, Shaanxi, China

X. Feng
School of Environment and Civil Engineering, Jiangnan University, Wuxi, Jiangsu, China

Unhealthy buildings have been associated with the high prevalence of several symptoms: headaches, dry eyes or throat, itchy or watery eyes, sneezing, blocked and stuffy nose, runny nose, and dry or irritated skin [1, 2]. At the same time, indoor air environment often changes due to the weather, that is, the indoor thermal parameters are not constants. Thus, researches on indoor air environment and human body dynamic thermal comfort are of particular importance. In this paper, the effects of indoor air environment on human thermal comfort are briefly analyzed.

57.2 The Relationship Between Indoor Air Environment and Human Thermal Comfort

Indoor air atmosphere has certain influence on human health and comfort. Thermal comfort is defined as "the condition of the mind which satisfaction is expressed with the thermal environment" [3]. Bodies thermal comfort is not only related to the objective scale of air environment, but it involves a series of physiological and psychological feelings, namely the subjective scale. The objective scale includes air temperature, humidity, velocity, air quality, inner surface temperature of building envelope, and body's temperature. However, the subjective scale consists of two parts. On the one hand, the human senses of environmental factors are included. On the other hand, it is the environmental influence on health. According to the indoor environmental conditions, the thermal balance equation is shown in Eq. (57.1):

$$M = E_{\mathrm{RE}} + E_{\mathrm{SW}} + E_c + E_R + W \tag{57.1}$$

where M is metabolic rate of human body (w/m^2); E_{RE} is the rate of evaporative heat loss from respiration (w/m^2); E_{SW} and E_c are total evaporative heat loss from the skin and the quantity of heat convection between human body and air environment, respectively (w/m^2); E_R shows the quantity of radiation between human body and surface (w/m^2); W reveals rate of mechanical work accomplished (w/m^2).

57.3 Influence Factors of Thermal Comfort

57.3.1 Distribution of Indoor Temperature

Under the stable thermal environmental conditions, the metabolism of body is produced by breathing, sweat evaporation, convection with ambient air, and various surface radiation indoors. It is known that temperature is one of the most sensitive parameters for human thermal comfort. So feelings reacting to the body

reflectivity vasomotor adjustment are attributed to a slight amount of thermal stimulation. If the indoor temperature distribution changes non-uniformly, it is bounded to destroy the human body normal heat equilibrium. If the ambient temperature increases, convection and radiation will be reduced with the increase in human body's perspiration and heat dissipating capacity inversely, which leads to the rise in the temperature and generating heat. Oppositely, it results in the drop of the body temperature and feeling cold. Overheating or excessively cool situations not only affect the human comfort, health, and work efficiency, but it even seriously does harm to human life. In particular, the influence of vertical temperature distribution on the human body is obvious. When the temperature of upper working areas is higher than that of lower, number of people who feel uncomfortable goes up. Compared with the thermal comfort of floor heating and ceiling heating, thermal comfort of that is excellent, resulting from the fact that the temperature of lower areas is much higher than the upper ones [4].

As can be analyzed in the test results [5], human beings feel significantly comfortable when the temperature of ankle is 2–3 °C higher than that of head. It reveals that comfortable temperature indoors in winter should be controlled below 23 °C and the temperature in summer is up to 27 °C. At the same time, the most suitable working temperature of the human body is 27 °C. Therefore, in the HVAC design, we should determine the temperature of air supply and airflow on the basis of human dynamic thermal comfort.

57.3.2 Indoor Air Humidity

Air humidity affects the human's feelings of cold and hot. The higher the relative humidity is, the less is the heat loss through sweat evaporation and skin evaporation. If indoor air humidity increases at high temperature, the feeling of hot will also increase. In converse, feeling of cold is intensified at low temperature. As researches show, people feel happy and comfortable when they breathe moderate humidity and cool air. On the contrary, it leads them to feeling the air not fresh and discomfort.

What the high enthalpy value means is that the cooling capacity of air is low. As a consequence, the effect of the respiratory tract is insufficient especially convection and evaporative cooling. Undoubtedly, the lack of cooling is closely related to the air quality [6]. An appropriate temperature and humidity can reduce "sick building syndrome" from happening. So it is beneficial to both thermal comfort control and energy saving under the least enthalpy estimation in air-conditioning systems. The residual of the least enthalpy difference in the current space state is the symbol of energy consumption in the air-conditioning system [7].

So we should use the effective temperature to determine a reasonable air supply state point. At the same time, we select appropriate temperature and humidity of the low enthalpy value in accordance with human body comfort.

57.3.3 Room Flow Distribution

The air velocity is one of the important factors that affect human thermal comfort. A reasonable indoor air distribution can not only create a good indoor environment to meet the needs of thermal comfort, but also it can save energy and improve the economic operation of air-conditioning systems. The air velocity range of indoor comfort provokes a problem that each HAVC professional designer is concerned about, but has not yet been resolved. The key is how to accurately quantify airflow fluctuation influence on the human comfort. Therefore, research on the relationship between the air flow and human thermal comfort mainly contains the following aspects.

1. Put forward the reasonable and accurate evaluation of the air flow in the room, which tell the difference between the mean velocity, wave frequency, and intensity.
2. The air velocity is selected based on the methods of room air flow evaluation. Especially, we should decide the evaluation index of the effect of the airflow fluctuations on the human comfort. In addition, experiments are made based on the evaluation index.
3. According to the effects of the wave intensity and frequency on human comfort, the evaluation indexes of indoor environment are determined on the basis of the mean velocity and air temperature.
4. According to the relationship between flow fluctuation and human thermal comfort, the periodic scanning-type air supply terminal devices are employed. Thus, the way of supplying air enters a new stage.

Hence, we base on the human thermal comfort when the air-conditioning system is designed. Many measures are taken into consideration. (1) Determining a reasonable air supply state point and selecting the best combination of temperature and humidity to achieve the low enthalpy. (2) Making airflow pulsation frequency, velocity, wave be similar to natural wind and realizing the personalized ventilation.

57.3.4 The Mean Surface Radiant Temperature

The mean radiant temperature is a significant factor [8]. The human body radiation intensity is determined by the indoor different surfaces' temperature. It affects the human thermal comfort level. The radiant heat transfer between human and the surrounding surfaces may be given as follows [9]:

$$Q = 3.96 \times 10^{-8} f_{cl} \left[(273 + t_{cl})^4 - (273 + \bar{t}_r)^4 \right] \tag{57.2}$$

where f_{cl} is dressing area coefficient; t_{cl} is clothing thermal resistance($m^2 \bullet K/w$); $\bar{t}_r$ is the mean surface radiant temperature (°C). The higher $\bar{t}_r$ is, the more the human thermal sensation increases from Eq. (57.2). On the contrary, the body feels cold.

Therefore, in order to insure the human thermal comfort, we should choose the reasonable heat transfer coefficient of the building materials and avoid producing indoor partial heat or cold source.

57.3.5 Indoor Air Quality

Nowadays, high-rise buildings have been built rapidly as well as the promotion of people's material and cultural living standards. High-grade decorations are put into practice in the residential and office buildings. As a result, air-conditioning is widely used to solve indoor environmental problems. But it consumes a large number of negative ions, so that negative ion concentration fell down. Therefore, the harmful gas concentration increases to some extent. Consequently, people get "sick building syndrome" due to deterioration of the indoor air quality [10]. Negative air ion can make the person comfortable and improve health conditions. It is an important index of fresh air. The relationship between various environmental distributions of negative ion and human health is shown in Table 57.1 [5].

It is shown in the research that indoor air quality is judged by both objective and subjective scale. There is no doubt that it makes indoor air quality evaluation more comprehensive and authenticity. Now the main ways to improve indoor air quality are as follows: (1) improving the indoor negative ion content; (2) controlling indoor pollution sources effectively; (3) enhancing fresh air effect; (4) improving HVAC system.

Table 57.1 Relationship between the content of distribution of negative ion and health

Name of space	Ion content(ions/mL)	Related to the human health
Forest, waterfall	100,000–500,000	Natural healing ability
Mountain, sea	50,000–100,000	Bactericidal effect and reduce the spread of the disease
Suburban, field	5,000–50,000	Enhance human immunity and antibacterial ability
Park	1,000–2,000	Maintain basic health needs
Street green area	100–200	Induce physiological disorder limit
Residential closed area	40–50	Induce physiological disorder, such as headache, insomnia
Air-conditioning room	After a long time 0.25 (no fresh air)	Cause "Air-conditioning disease"

57.3.6 Other Factors

Human thermal comfort is associated with the subjective factors, such as human activities, costume, health conditions, sensitive degree. The feelings of diverse bodies on the heat capacity seem different. It must be pointed out that the feelings of the thermal comfort are of great difference even in the same air-conditioning room. Therefore, considering the different environment, evaluation index of the thermal comfort should be adjusted constantly to obtain the best human thermal comfort.

57.4 Conclusions

As the economy develops and the living standards improve rapidly, strengthening self-health consciousness is considered an important factor in lives. People pay more attention to the indoor thermal comfort and air quality. So the "people-oriented" purposes should be followed in HVAC design. According to the subjective elements ranging from different groups, effect factors of human dynamic thermal comfort are analyzed with the help of evaluation index of the thermal comfort. To summarize, the responding measures should be taken as follows. (1) determining a reasonable air supply rate and improve the effect of outdoor air; (2) organizing a appropriate and effective air distribution with periodic scanning-type air supply terminal devices; and (3) deciding a reasonable air supply state point. At last, a save, economics, reasonable, and healthy air processing scheme is put forward to improve indoor air quality and reduce energy consumption. Meanwhile, we ensure human body health and improve work efficiency.

References

1. Daisey JM, Angell WJ, Apte MG (2003) Indoor air quality, ventilation and health symptoms in school and analysis of existing information. Indoor Air 13:53–64
2. Kavgic M, Mumovic D, Stevanovic Z, Young A (2008) Analysis of thermal comfort and indoor air quality in a mechanically ventilated theatre. Energy Build 40:1334–1343
3. ASHRAE Handbook—fundamentals (1993) Physiological principles and thermal comfort. In: ASHRAE, Atlanta Chapter 8
4. Fang Lv (2000) Thermal comfort and building energy saving. Dissertation for the Master Degree, Tianjin University, Tianjin

 5. Zhou Z et al (2002) Inspection and control of indoor pollution. Chemical Industry Press, Beijing
 6. Jin Z et al (2001) Built environment. China Architecture and Building Press, Beijing
 7. Chu CM, Jong TL (2008) Enthalpy estimation for thermal comfort and energy saving in air conditioning system. Energy Convers Manag 49:1620–1628
 8. Atmaca I, Kaynakli O, Yigit A (2007) Effects of radiant temperature on thermal comfort. Build Environ 42:3210–3220
 9. Zhao R et al (1998) Air conditioning. China Architecture and Building Press, Beijing
10. Yang R et al (2002) Indoor air environment with comfort and health. Refrig Air Conditioning Electr Power Mach 2:46–49

Chapter 58
Experiment and Numerical Simulation on Natural Ventilation for Transportation Tunnel with Shafts Under Traffic Jam

Yan Tong, Linlin Liu and Ronghua Su

Abstract Based on the current researches on the natural ventilated urban transportation tunnel with shafts, fluid flowing characteristics under traffic jam were analyzed and problems were pointed out. According to similarity laws, a small-scale model tunnel was set up including vehicle heat sources. Air velocities were tested out functioned only by thermal pressure. A three-dimensional unsteady flow numerical model was chosen. Temperature and velocity field were simulated with Fluent software. Its velocities of three identical positions were verified by that of experiments. Further sensitivity analyses including vehicle speed, shaft number, and buried section length show that under traffic jam, thermal pressure is a main factor which influences its inside flow field while not traffic wind pressure; air velocities are non-uniform inside a buried section, and the flow field of its midst is influenced little by shaft number for it being far away from adjacent shafts; increasing length of a buried section contributes to its increased air velocities.

Keywords Tunnel · Natural ventilation · Shafts · Traffic jam · Thermal pressure

58.1 Introduction

Urban transportation tunnel is shallowly buried under the ground, and shaft groups are built on its top with its height being 6 m or less dividing the tunnel into several buried sections. Pure natural ventilation is taken. Such tunnel has come out in

Y. Tong (✉)
Department of HVAC, Nanjing University of Technology Nanjing, Nanjing, China
e-mail: njtongyan@njut.edu.cn

Y. Tong · L. Liu · R. Su
College of Urban Construction and Safety Engineering, Nanjing University of Technology, Nanjing, 210009 Jiangsu Province, China

China with its length reaching up to 1,410 m conflicting with the current code *Specifications for Design of Ventilation and Lighting of Highway Tunnel* (JTJ026.1-1999): for one-way traffic tunnel, when L (tunnel length, km) $\times$ N (traffic volume, cars/h) $\geq 2 \times 10^3$, mechanical ventilation should be adopted. Modic [1] found that for an unidirectional natural ventilated tunnel, when N $\leq$ 750 cars/h.lane and vt (vehicle speed) $\geq$ 30 km/h, L is allowed to be 3,000 m, but it referred to the tunnel without shafts. Pimolsiri [2] studied on natural ventilation of a high-rise residential building and found that shafts play a role of strengthening natural ventilation. *Natural Ventilation Design of Urban Transportation Tunnel With Shafts* (DGJ32/TJ102-2010) Jiangsu, China, has been implemented [3–7]; however, the local administrative department and fire protection institutions still give much attention and concern about it. In DGJ32/TJ102-2010, when traffic jam, the flow field inside is treated to be uniform, and an one-dimensional steady thermal pressure equation is chosen [3]. But in practice, weak piston effect may have an effect on the inside flow field and vary at different buried sections [7]. In this study, model experiment and CFD simulation [8] were both carried out to study coupling of wind and thermal pressure under traffic jam [9].

58.2 Thermal Pressure Model Experiment

Under natural ventilation, thermal pressure equation is as follows

$$gh(\rho_w - \rho_n) = \sum \zeta \cdot \frac{v^2}{2} \rho \qquad (58.1)$$

Here, g is acceleration of gravity, h is height difference between top and bottom of a shaft, ρ is air density, w denotes outside and n for inside, $\sum \zeta$ are coefficients of local energy loss, and v is air velocity. Also, the ideal gas state equation is as follows:

$$\frac{\rho_w - \rho_n}{\rho} = \frac{T_w - T_n}{T} \qquad (58.2)$$

Then, Eq. (58.1) can be expressed as follows:

$$gh\Delta T = \sum \zeta \cdot \frac{v^2}{2} T \qquad (58.3)$$

By definition: $C_g = g_m/g_p$, $C_1 = h_m/h_p$, $C_{\Delta T} = \Delta T_m/\Delta T_p$, $C_{\sum \zeta} = \sum \zeta_m/\sum \zeta_p$, $C_v = v_m/v_p$, $C_T = T_m/T_p$, in which subscript "m" means model and "P" means prototype, and then, Eq. (58.3) is rewritten as follows:

$$C_g C_l C_{\Delta T} = C_{\sum \zeta} \cdot C_v^2 C_T/2 \qquad (58.4)$$

Fig. 58.1 Internal scene for a natural ventilated road tunnel with shafts

**Fig. 58.2** Schematic plan of the model tunnel
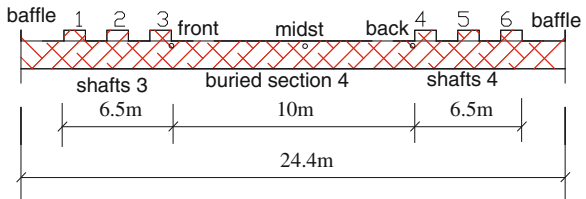
When two types are dynamically similar, we can suppose that $C_g = 1$, $C_T = 1$, $C_{\Delta T} = 1$, $C_{\sum \zeta} = 1$, then $C_v = C_1^{1/2}$. Non-dimensional relation of heat release rate $C_Q = C_{\Delta T} C_v C_1^2 = C_1^{5/2}$ which can be also obtained based on Ar [10].

The prototype is a one-way three-lane urban transportation tunnel, being 1,410 m long, 12 m wide, and 5 m high. Each shaft is 12 m long, 3 m wide, and 4 m high. Every three shaft constitutes a shaft group, as shown in Fig. 58.1. There are a total of 4 groups, so the tunnel is divided into 5 buried sections. All vehicles move at a same speed. Each vehicle is 2.4 m (length) $\times$ 1.4 m (width) $\times$ 1.5 m (height). Under traffic jam, there has 1,800 cars/h.lane, 254 cars/lane (according to NL/vt), 0.007 m^3/100 km for fuel consumption, 0.725 kg/m^3 for gasoline density, 4,4000 kJ/kg for heat of combustion, so the whole vehicle heat release rate is 4,722.8 kW and its rate per meter is 3.35 KW [3].

Transparent plastic board was chose, and the reduced scale 1:10 [7] was adopted. The length of the model should be 141 m, but an experiment field longer than 141 m could not be found out. Considering the fourth buried section which is far away from two exits, ambient air would have little influence on its flow field through exits, so the fourth buried section model was built including its nearest two shaft groups. Its two side openings were closed by baffles, as shown from Fig. 58.2.

In experiments, vehicles were motionless, but heat was still released. For the 24.4 m model, its heat release rate was 2.58 kW based on $C_Q = C_1^{5/2}$ mentioned above. 172 incandescent lamps (each 15 W) were evenly placed on the model ground so as to replace vehicles' heat releasing. Ambient pressure was 1 atm, and ambient temperature was about 15 °C. Tested points were, respectively, at the

**Fig. 58.3** Averaged air velocities tested on three positions
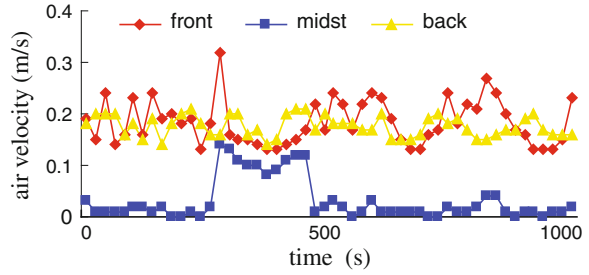
front, midst, and back sections, as shown in Figs. 58.2, and 58.3 wind speed probes were uniformly arranged on each section, all being 0.125 m under the ceiling [11]. Air velocities at front, midst, and back positions have been averaged and depicted in Fig. 58.3. Its fluctuation was partly caused by backflow through shafts. Air velocity at the midst was the lowest because it was more far away from shafts where buoyance effect is less evident, and then, heat would gather here causing higher temperature.

58.3 Numerical Modeling

58.3.1 Description of the CFD Model

The airflow, temperature, and spices concentration transport can be described by the unsteady time-averaged Navier–Stokes equations [12]. For the scaled-down model, a standard k-ε two equations and simple algorithm were used. All vehicles were equally spacing and moved unidirectionally on three lanes. Each car was 0.24 m (length) × 0.14 m (width) × 0.15 m (height). There are 44 cars on each lane corresponding to that of the 244 m prototype. Simulating a moving car using the moving boundary technique in the CFD model for such a space is almost impractical [13]. The CFD model simulated these cars as "still" objects with momentum and heat source characteristics [14]. Unstructured grids were adapted to the main body, while structured grids were to shafts. Grid refinement was used around cars, as shown in Fig. 58.4. The total number of grids was 86,382. Pressure inlet boundary was applied to the inlet, and outlet boundaries were used for the outlet and all shaft tops where first-order gradients of all quantities were zero. Heat release from lighting and walls was ignored.

Fig. 58.4 Schematic plan of grids in tunnel
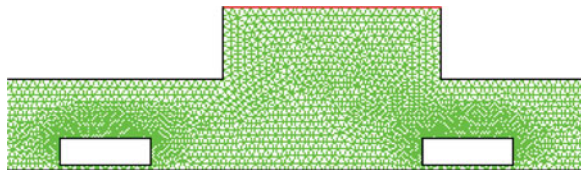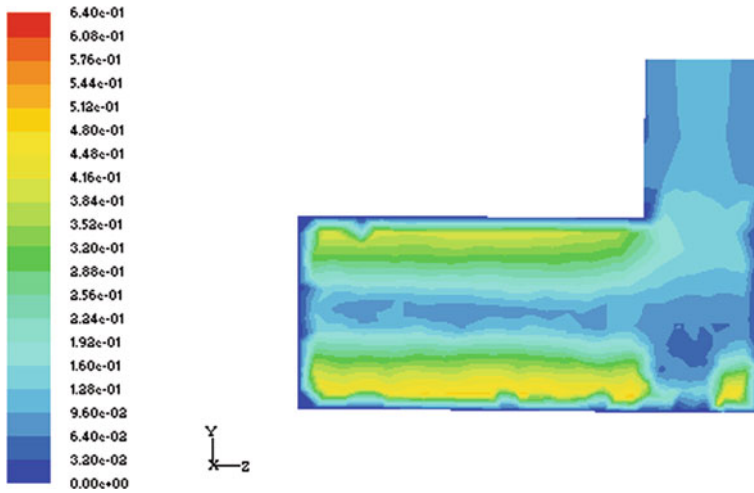
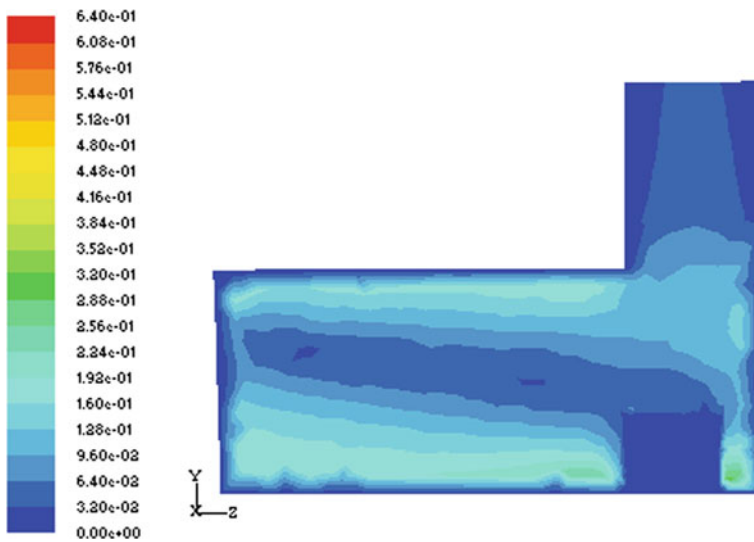**Fig. 58.5** Contours of air velocity around Shaft 1 in the model ($vt = 0$)

Fig. 58.6 Contours of air velocity around Shaft 6 in the model ($vt = 0$)

58.3.2 Validation

When $vt = 0$ km/h, only thermal pressure effect exists in the tunnel. Air velocity contours around Shaft 1 and Shaft 6 were shown, respectively, in Figs. 58.5 and 58.6. It was obvious that air flow is driven out of shaft tops; much heat is released by vehicles which contribute to its high air velocity around the ground; hot air rise

upward and attach with the ceiling, then flow along the ceiling. Air velocities at the front, midst, and back are, respectively, 0.1, 0.3, and 0.2 m/s, and these results are compared well with that from experiments. Differences exist because the air flow in experiment varied with the outside wind and it was not in simulation. In all, the simulation has been validated.

58.4 Results and Analysis

58.4.1 Vehicle Speed

For $vt = 10$ km/h, traffic wind pressure and thermal pressure both exist in the tunnel. Flow field around a moving vehicle is shown in Fig. 58.7. Comparisons between three air velocities at the front, midst, and back were conducted on different vehicle speeds: $vt = 10$ for simulation and $vt = 0$ for experiment (Fig. 58.3), as shown in Fig. 58.8. It shows that two results are roughly same, so thermal pressure is a main factor which influences the flow field inside the tunnel, while not traffic wind.

Fig. 58.7 Vectors of air velocity around a moving vehicle ($vt = 10$)
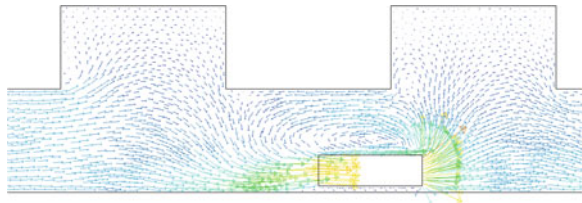
Fig. 58.8 Air velocities for different vehicle speeds
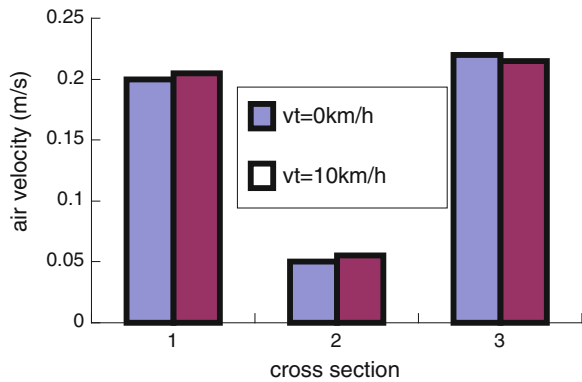
Fig. 58.9 Air velocities for different shaft numbers
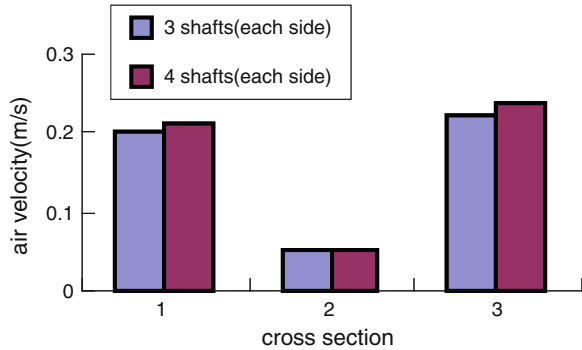
58.4.2 Shaft Number

In this section, a 100 m buried section with 4 shafts at each side was studied when the boundary condition vt was set as 10km/h. Comparisons of air velocities at the front, midst, and back were conducted for differen shaft number: 4 for simulation and 3 for experiment (Fig. 58.3), as shown in Fig. 58.9. It shows that the lowest velocities are both at the midst and they are fairly same, so the air flow at the midst is rarely influenced by shaft number. The front and back velocities with 4 shafts are larger than that with 3 shafts.

58.4.3 Length of Buried Section

For a 150 m buried section with 3 shafts at each side and $vt = 10$ km/h, its averaged velocities at the front, midst, and back were obtained which were compared to that of Fig. 58.3, as shown in Fig. 58.10. It is obvious that velocity at any position increases with the increase in the section length. It can be explained that there are more cars in a longer section with much heat release rates, so thermal effect becomes strong.

Fig. 58.10 Air velocities for different length of buried section
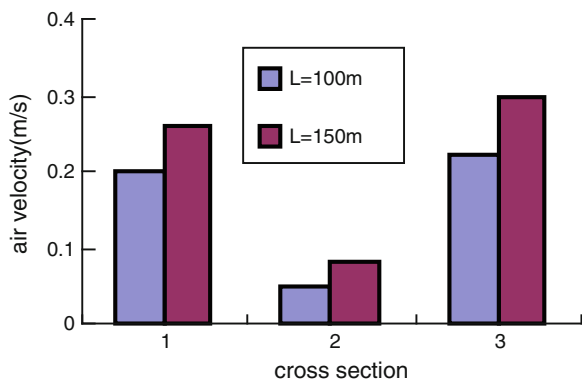
58.5 Conclusions

A small-scale 1:10 model was built. Heat release rates from still cars were replaced by incandescent lamps. Three air velocities in the model were tested. The standard k-ε two equations were used in simulation, and the car movement was defined by User_Defined_Function (UDF). From comparisons of simulation and experiment, the validity of the CFD model is confirmed. Further studies found that traffic jam thermal pressure is a main factor and piston wind effect can be ignored. Air flow of the midst is influenced little by adjacent shafts with the lowest air velocity and badly by shaft number. All air velocities inside the tunnel increase with increasing length of buried section, showing its increasing thermal effect.

References

1. Modic J (2003) Air velocity and concentration of noxious substance in a naturally ventilated tunnel. Tunn Undergr Space Technol 18:405–410
2. Prajongsan P, Sharples S (2012) Enhancing natural ventilation, thermal comfort and energy savings in high-rise residential buildings in Bangkok through the use of ventilation shafts. Build Environ 50:104–113
3. Zhong X, Zeng Z (2006) Distribution of harmful gas concentration in highway tunnel with natural ventilation. J Railway Eng Soc 12(9):44–49 (in chinese)
4. Wang Y, Jiang J, Zhu D (2009) Diesel oil pool fire characteristic under natural ventilation conditions in tunnels with roof openings. J Hazard Mater 166:469–477
5. Yan T et al (2009) Full scale experimental study on smoke flow in nature ventilation road tunnel fires with shafts. Tunn Undergr Space Technol 24:627–633
6. Mao J, Huang Y, Zhu P et al (2008) Experiment of city tunnel model with natural ventilation in case of fire. J PLA Univ Sci Technol 9(4):357–362 (in chinese)
7. Yan T (2010) Theoretical and experimental studies on natural ventilation and smoke exhaust for city road tunnels with shafts. Southeast University, Nanjing (in chinese)
8. Chen Q (2009) Ventilation performance prediction for buildings: a method overview and recent applications. Build Environ 4:848–858
9. Yi W, Liu J, Xiao Y (2006) Coupling numerical method on thermal environment of naturally ventilated buildings. Acta Energiae Solaris Sinica 27(1):67–72 (in chinese)
10. Li A, Li X, Ma Q et al (2010) Comparison of air distribution in two reduced scale models for large workplace of hydropower station. HV&AC 40(3):98–102, 72 (in chinese)
11. Zhu P, Mei J, Tu J et al (2012) Research on natural ventilation in city tunnel by model experiment at the status of block. Fluid Mach 40(3):60–63 (in chinese)
12. Zhai Z et al (2007) Evaluation of various turbulence models in predicting airflow and turbulence in enclosed environments by CFD: part1—summary of prevalent turbulence models. HVAC&R Res 13(6):871–886
13. Zhai Z, Chen Q, Scanlon PW (2002) Design of a ventilation system for an indoor auto racing complex. ASHRAE Trans 108(1):989–998
14. Hu D et al (2012) Numerical Study of Piston Wind Effect in a Subway Station with screen doors and by-pass tunnels. In: Boulder: The Second International Conference on Building Energy and Environment. U.S.2012,8

Chapter 59
Experimental Study on Impact of Ventilated Double-Skin Facade on the Indoor Thermal Environment in Winter

Hua Yang, Xiyang Feng, Guoqiang Xia and Qianzhao Wan

Abstract An actual office building with ventilated double-skin facade (VDSF) in cold region has been studied for researching the influence of VDSF as envelope to the indoor thermal environment in winter. Setting up an experimental system to test some factors which effected the indoor thermal environment, such as the solar radiation intensity in winter, outdoor temperature, application of VDSF or not, the airflow window of internal facade in opening and closing mode. The research provided a reasonable way of using VDSF in winter.

Keywords Cold region · Ventilated double-skin facade (VDSF) · Indoor thermal environment

59.1 Introduction

Due to pursuing the aesthetics of building appearance, single-skin facade is widely used in office buildings in China. As a result of poor heat insulation, air condition should be opened to adjust thermal comfort, which leads to the building in a high energy consumption. In recent years, studies have indicated that air conditioning system used in buildings with fully closed building facade extremely did harm to people's health and consequently influenced people's comfort and working productivity [1, 2]. The need to avoid high energy consumption and inadequate ventilation problem has caused the appearance of ventilated double-skin facade (VDSF) [3]. VDSF can achieve passive heating in winter and intensify ventilation in summer. Therefore, building energy consumption can be reduced apart from aesthetic consideration [4–6].

H. Yang (✉) · X. Feng · G. Xia · Q. Wan
School of Energy and Environmental Engineering,
Hebei University of Technology, Tianjin, China
e-mail: y8h8@163.com

Yong Ding et al. present that application of DSF is obviously effective for reducing heat loss during wintertime and reducing heat gain during summertime. However, this is based on rational design, such as width of air cavities, size of inlet and outlet airflow windows, and building orientation, which is coupled with CFD simulation of thermal environment inside DSF air cavities so that the rational DSF parameters of building structure can be determined [7].

The effect of using VDSF to improve the indoor thermal environment is strongly associated with the reasonable ways of using it. The study on the law of VDSF on indoor thermal environment in different seasons is of great significance. But in our country, there are fewer field tests focusing on the VDSF in cold region, and therefore, a pyrology field test made in an office building in cold region is introduced in this paper. Setting up a experimental system to test some factors which effected the indoor thermal environment, such as the solar radiation intensity in winter, outdoor temperature, application of VDSF or not, the airflow window of internal facade in opening and closing mode. The research provided a reasonable way of using VDSF in winter.

59.2 Experimental Setups

59.2.1 Introduction of the Building

In this paper, the performance of ventilated double-skin facade applied to a building located in a university of cold region (Tianjin) of China is tested. There are four floors that compose the building. The height of the first floor is 4.2 m, and the height from the second floor to the forth floor is 3.6 m, respectively. The VDSF of which the inner skin adopts double glazing glass and the external skin adopts single coated glass is installed in the south, as shown in Fig. 59.1. The width of the air cavity of DSF is 800 mm. The air cavity is through the whole DSF that covers from the first floor to the forth floor, which is called integrated ventilated DSF. There is no sun-shading device, and the air cavity is separated by perforated strainer, as shown in Fig. 59.2.

Fig. 59.1 The experimental building

59.2.2 Experimental Rooms

The testing rooms chosen for the experimentation were the east room in the third floor without VDSF (Room A), the east room in the third floor with VDSF (Room B), and the room in the west with VDSF (Room C), as shown in Fig. 59.3. During the test, no one was allowed to enter the testing room and no air conditioning system or lighting equipment can be turned on. Polystyrene board was used for the floors in need of segregation.

59.2.3 Experimental Modes

The outdoor temperature was based on the average temperature per hour collected by the weather station. The intensity of solar radiation was collected by TRM-ZS2 automatic weather station. The testing time was 32 days, since December 20, 2011, to January 20, 2012. Through setting up an experimental system, the influence of potential factors which might affect the indoor thermal environment is explored, such as the solar radiation intensity in winter, outdoor temperature, application of VDSF or not, opening and closing mode of airflow window of internal facade.

Fig. 59.3 Schematic diagram of room location of third floor

59.3 Experimental Results and Discussion

59.3.1 Effects of Solar Radiation Intensity and Outdoor Temperature

Room B was chosen as the experimental room, and the airflow windows of both internal and external facades were in closing mode. The data of two typical contrary days during the test period were selected to analyze. Temperature variations of the facade in vertical direction of 0.3, 1.8, and 3.3 m in overcast weather and sunny weather are shown in Fig. 59.4.

As can be seen from Fig. 59.4, temperature trends of the facade were roughly the same in the two days, which both increase as the height increases in vertical direction. The temperature variation was relatively gentle in overcast weather, while the peak temperature of the facade appeared at around 13:00 in sunny weather. The average outdoor temperature difference of the two days was 2.68 °C, and the solar radiation intensity difference was 190.69 w/m^2. But the temperatures
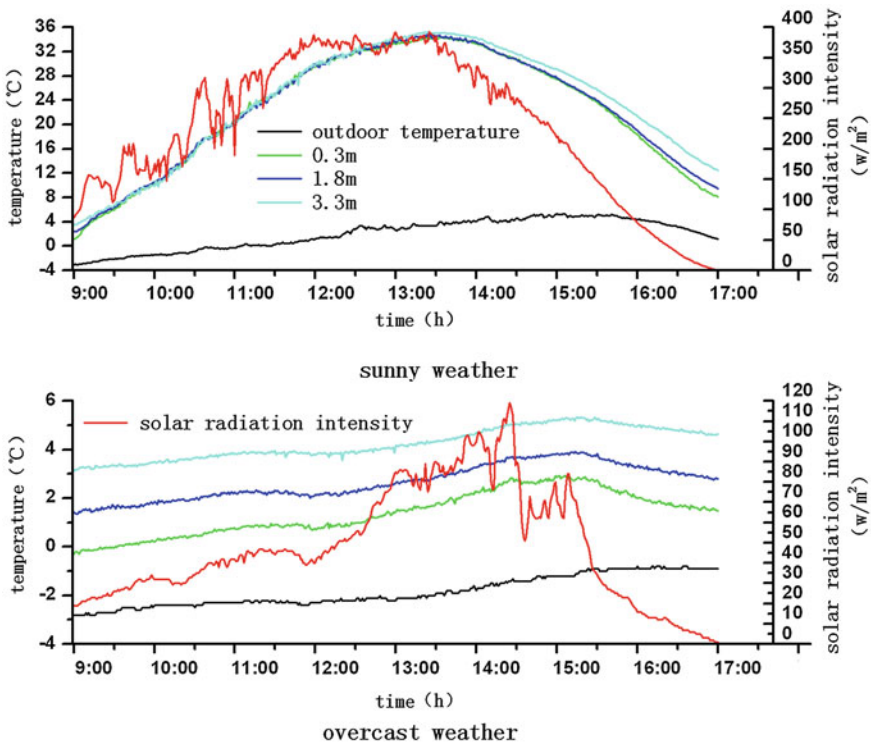
Fig. 59.4 Temperature distribution of facade with overcast weather or sunny weather

of the air in the facade were quite different, the average temperature difference was 20.07 °C, and the maximum temperature difference can reach 32.08 °C.

In winter, what dominantly caused temperature changes inside the VDSF was the solar radiation intensity rather than the outdoor temperature.

59.3.2 Effects of VDSF

Rooms A and B were chosen as the experimental rooms, and the airflow windows of both internal and external facades were in closing mode. The data of two typical contrary days during the test period were selected to analyze. Temperature variations of the facade in vertical direction of 0.2 and 1.7 m when there is VDSF or not in the two days are shown in Fig. 59.5.

As can be seen from Fig. 59.5, in winter of the cold region, whether there is VDSF in the building, temperature trend of the room was gentle. When the solar radiation intensity was strong (in sunny weather), the indoor temperatures of the room with VDSF and the one without VDSF increase as the height increases, and the peak temperature of the one with VDSF appeared at around 12:00, which was roughly identical to the time when the peak of the solar radiation appeared. All these have proved the effect of the solar radiation on indoor temperature. When the solar radiation intensity was strong(in sunny weather), the average indoor temperature in the room with VDSF was higher than that in the room without VDSF, and the temperature difference was 0.28 °C at the vertical height of 0.2 m and 1.42 °C at 1.7 m. However, when the solar radiation intensity was poor (in overcast weather), the average indoor temperature in the room with VDSF was
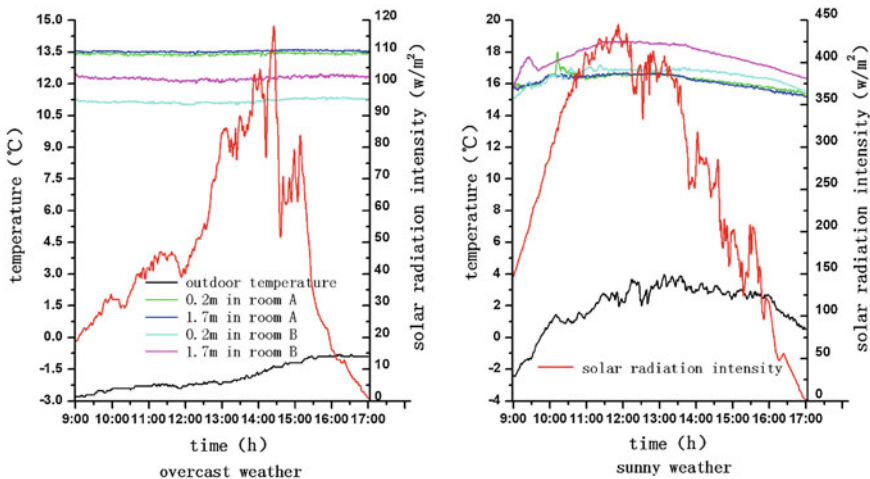

Fig. 59.5 Indoor temperature with when there is VDSF or not

lower than that in the room without VDSF, and the temperature difference was −2.23 °C at the vertical height of 0.2 m and −1.27 °C at 1.7 m.

Ventilated double-skin facade (VDSF), as an emerging external structure for protection of buildings in cold regions, was greatly affected by the solar radiation intensity. In the daytime of a winter with strong solar radiation, the interlayer of VDSF was like a warm house that can preserve heat so the purpose for improving indoor thermal environment was achieved.

59.3.3 Effects of the Airflow Window of Internal Facade in Opening and Closing Mode

Experimental rooms include Room B and C, and only the airflow window of internal facade of room C was open. The data in January 9, 2012, were selected for analysis.

59.3.3.1 Effects of the Airflow Window of Internal Facade Opening and Closing Mode on the Temperature inside the Facade

The temperature changes in the vertical direction at 0.8 and 2.8 m were shown in Fig. 59.6.

From Fig. 59.6, we can know that whether the vents of the VDSF were open or close, the temperature of facade always increased along with the increase in height. The trend was basically the same, i.e., in the morning, the temperature increased gradually until 12:00 or so to reach the peak and reduced gradually in the afternoon. We also can find it easily that in most of the daytime, when the airflow window of internal facade was close, the temperature in the 0.8 m-high places of the facade was higher than that when it was open, but the situation in the 2.8 m-high places of the facade was opposite.

59.3.3.2 Effects of the Airflow Window of Internal Facade in Opening and Closing Mode on the Indoor Temperature

The changes in the indoor temperature were shown in Fig. 59.7. The temperature value shown in the figure was measured at 0.2 and 1.7 m on the vertical direction which was the temperature measuring points. It was the average value hourly measured according to the figure of the temperature measuring points.

We can clearly see from the Fig. 59.7. The inner temperature change was relatively flat in the room where the airflow window of internal facade was close. However, the indoor temperature changed obviously with the intensity of solar radiation in the room where the airflow window of internal facade was open. The
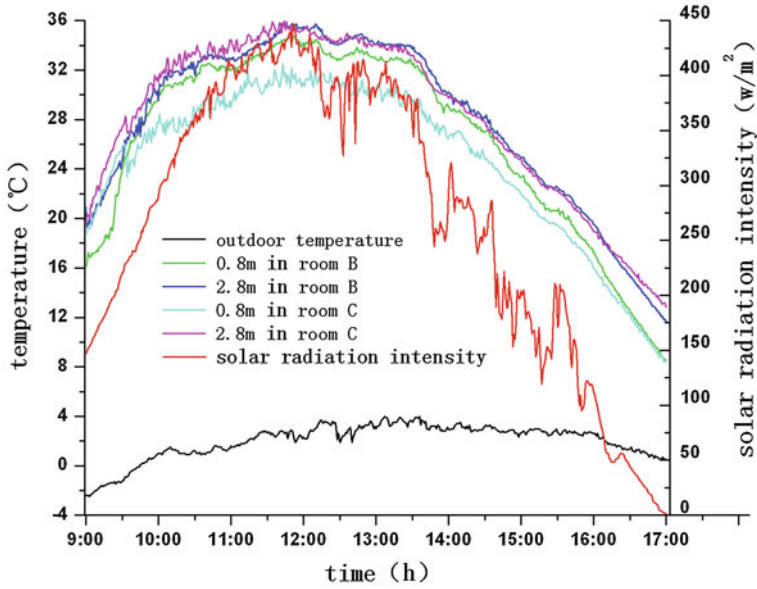
Fig. 59.6 Temperature of the cavity in vertical direction whether airflow window of internal facade opened or not
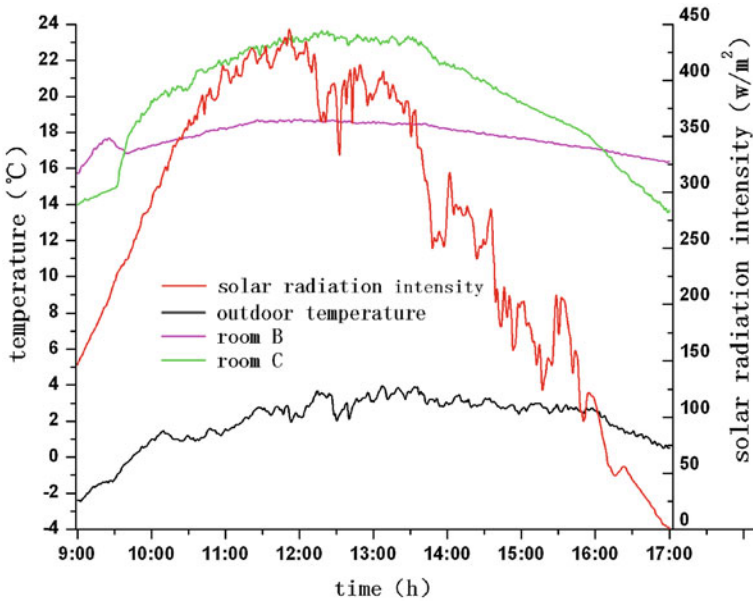

Fig. 59.7 Indoor temperatures when air vent is opened or not

temperature in the two test rooms was significantly higher than the outdoor temperature. In the room, of which the air vent was open, the highest temperature was 20.1 °C, and in the other room, of which the air vent was close, the highest temperature was 17.8 °C.

The air inside the VDSF, in the daytime of winter, generates so-called greenhouse effect due to solar radiation, and the heated air stays there. So opening the airflow window for heat exchange within the air within VDSF of high temperature and room air can improve the indoor temperature.

59.4 Conclusions

This paper, through setting up an experimental system, explores the influence of potential factors which might affect the indoor thermal environment, such as the solar radiation intensity in winter, outdoor temperature, application of VDSF or not, opening and closing mode of airflow window of internal facade. The research provided a reasonable way of using VDSF in winter and came to the conclusions as follows:

1. In winter, what dominantly caused temperature changes inside the VDSF was the solar radiation intensity rather than the outdoor temperature. Besides, the trend of inside temperature changes was consistent with that of solar radiation intensity, the temperature going up along with the intensifying radiation.
2. In the daytime of a winter with strong solar radiation, VDSF can preserve heat so the purpose for improving indoor thermal environment was achieved. However, when the solar radiation was poor, the indoor temperature of the building with VDSF would become lower than that of traditional buildings, which revealed the deficiency of the former.
3. The reasonable way of applying the VDSF in cold region was to open the airflow window for heat exchange within the air within VDSF of high temperature and room air, so as to improve the indoor temperature and reduce load of indoor heat and consumption of heating energy.

References

1. Zhu Y (2005) Building environment, China Building Industry Press, China
2. Seppanen O (2005) A model to estimate the cost-effectiveness of improving office work through indoor environmental control. In: ASHRAE 2005 annual meeting, 111(2):663–672
3. Yilmaz Z, Cetintas F (2005) Double skin facade's effects on heat losses of office buildings in Istanbul. Energ Build 37(7):691–697
4. Gratia E, Herde A (2004) Optimal operation of a south double-skin facade. Energ Build 36(1):41–60

5. Manz H, Frank T (2005) Thermal simulation of buildings with double-skin facade. Energ Build 37(11):1114–1121
6. Ding Y (2007) A experimental analysis of ventilation effects of double-skin facade in Chongqing of China. In: HVAC, 37(8):42–45
7. Wan Qianzhao (2012) Study on impact of ventilated double-skin facade on the indoor thermal environment in different seasons. Hebei University of Technology, Tianjin

Chapter 60
Mesoscopic Simulation of VOCs' Migration in Porous Building Materials with Different Spatial Scale

Qiang Ma and Zhenqian Chen

Abstract Volatile organic compounds (VOCs) emission from building materials are the main pollution sources of indoor air quality (IAQ). The migration characteristics of VOCs in porous building materials are important to control VOCs concentration level in indoor environment. In this study, we examined VOCs desorbed from matrix of building material and diffused in pore of porous building material using lattice Boltzmann method (LBM) with different spatial scale. In pore scale of porous building materials, the LBM model of gas diffusion was developed, which is based on the theory of binary mixtures proposed by Luo Lishi. The quartet structure generation set (QSGS) proposed by Wang moran is used to construct the random porous building material. The unsteady binary gas diffusion with third boundary condition in channel was simulated with this model. The results of simulation were compared with analytical solution. The effective mass diffusion coefficient of gas diffusion through random porous media was calculated in this chapter. The comparison of effective mass diffusion coefficient shows that the numerical simulation results agree with the traditional empirical model, so reliability of this model was verified. Based on the assumption of Henry law, an approach for disposing boundary conditions of adsorbed gas was proposed. The process of VOC emitted from porous media was investigated with different partition coefficient. It is concluded that transient concentration in porous media of VOC will be increased with the increase in partition coefficient. In representative elementary volume (REV) scale, the VOC emission rate of porous building material to static chamber was simulated by LBM in static chamber. VOC

Q. Ma
Key Laboratory of Energy Thermal Conversion and Control of Ministry of Education,
Southeast University, Nanjing 210096, China
e-mail: maqiang19860525@126.com

Z. Chen (✉)
Key Laboratory of Energy Thermal Conversion and Control of Ministry of Education,
IIUSE, School of Energy and Environment, Southeast University, Nanjing 210096,
China
e-mail: zqchen@seu.edu.cn

concentration of static chamber in emission process agrees with analytical method very well.

60.1 Introduction

Humans will stay in indoor environment for more than 70 % of their life, so humans' health and quality of life will be determined by indoor air quality (IAQ) obviously [1, 2]. With the development of the construction and decoration materials processing technology, volatile organic compounds (VOCs) in building materials which when emitted to indoor environment may cause discomfort to our body and affect people's living quality and work efficiency greatly. Some of volatile organic compounds, such as benzene, tetrachlorethylene, trichloroethane, trichlorethylene, formaldehyde, and so on, have been proved to be carcinogens or suspected carcinogens; therefore, indoor environmental pollution caused by VOCs has become an important issue in relation to human health, and have been more and more concerned by scholars from domestic and foreign in recent years.

According to emission characteristics of VOC in building materials, building materials are divided into moist building materials (such as paints, varnishes, wood adhesives) and dry building materials (such as carpet, flooring, PVC board, MDF). For dry building materials, the emission characteristics of VOC depend on porosity and pore structure of building plates, which is a major pollution source affecting IAQ, in that VOCs emitted from dry plate have slow attenuation concentration with time and long duration.

Based on kinetic theory of gas molecules, the lattice Boltzmann (LB) equation can be used to obtain continuum flow quantities from simple and local update rules based on particle interactions. The simplicity of formulation and its versatility explain the rapid expansion of the LB method to applications in complex and multi-scale flows [3]. In this chapter, emission process of VOCs is explored from different spatial scales. In pore scale, we have simulated VOC desorption from porous media and diffusion in pore through LBM derived from binary mixture diffusion theory. The effect of structural parameters on migration characteristic of VOC was investigated. In representative elementary volume (REV) scale, we have examined VOCs emitted from porous building materials in a static chamber. The feasibility of LBM in the prediction of VOC emission rate was discussed.

60.2 Simulation in Pore Scale

60.2.1 Numerical Model

According to the kinetic equations for a binary system, the lattice Boltzmann equation can be constructed as fellows [4]:

$$f_\alpha^\sigma(\mathbf{x}_i + \mathbf{e}_\alpha \delta_t, t + \delta_t) - f_\alpha^\sigma(\mathbf{x}_i, t) = J_\alpha^{\sigma\sigma} + J_\alpha^{\sigma\varsigma} \tag{60.1}$$

The right side of the equation is the self-collision term and cross-collision term, which are obtained as:

$$J_\alpha^{\sigma\sigma} = -\frac{1}{\tau_\sigma}\left[f_\alpha^\sigma - f_\alpha^{\sigma(0)}\right] \tag{60.2}$$

$$J_\alpha^{\sigma\varsigma} = -\frac{1}{\tau_{\sigma\varsigma}}\frac{\rho_\varsigma}{\rho}\frac{f^{\sigma(\mathrm{eq})}}{R_\sigma T}(\mathbf{e}_\alpha^\sigma - \mathbf{u})\cdot(\mathbf{u}_\sigma - \mathbf{u}_\varsigma) \tag{60.3}$$

where f_α^σ is the equilibrium distribution function and $\mathbf{e}_\alpha^\sigma$ is lattice velocity of species σ, which is despond on numerical model selected such as D2Q9 or D3Q19. If $m_\sigma = m_\varsigma$ is assumed, the lattice velocity are identical for different species.

Based on Chapman-Enskog expansion, we can obtain the macroscale advection–diffusion equation for an isothermal mixture:

$$\partial_t \rho_\sigma + \mathbf{u}\cdot\nabla\rho_\sigma = \nabla\cdot D_{\sigma\varsigma}\frac{m_\sigma m_\varsigma n^2}{\rho}\left[\nabla\left(\frac{n_\sigma}{n}\right) + \frac{n_\sigma n_\varsigma}{n\rho}(m_\varsigma - m_\sigma)\nabla\ln p\right] \tag{60.4}$$

where the diffusion coefficient is defined as:

$$D_{\sigma\varsigma} = \frac{\rho p}{n^2 m_\sigma m_\varsigma}\left(\tau_{\sigma\varsigma} - \frac{1}{2}\right)\delta_t \tag{60.5}$$

60.2.2 Results and Discussion

In this chapter, we can consider that species σ as VOCs and species ς as air which is considered to be stationary when VOC diffuses in porous media. Because the density of air is much larger than the density of VOCs, we can obtain that $n \approx n_\varsigma, \mathbf{u} \approx 0$, and pressure is approximately a constant. Mass diffusion equation can be obtained:

$$\partial_t C_\sigma = \nabla\cdot D_{\sigma\varsigma}\nabla C_\sigma \tag{60.6}$$

where C_σ is the concentration of VOC.

The transient concentration of VOCs was calculated by LBM for unsteady diffusion of binary gas in 2D channel, and these results were compared with

analytical solution to examine the validity of the numerical model. The boundaries of 2D channel are set to non-permeable boundary, except for outlet, which is considered as the third boundary condition, and the convective mass transfer coefficient is h. When Fo = 0, the VOCs and air have all uniform density in 2D channel. Where Fo is dimensionless time and Bi is Biot number, which are defined as:

$$F_0 = \frac{D_{\sigma\zeta}\tau^2}{L^2}, \mathrm{Bi} = \frac{hL}{D_{\sigma\zeta}}, \Theta = \frac{C_\sigma - C_\sigma^e}{C_\sigma^0 - C_\sigma^e} \tag{60.7}$$

Figure 60.1 shows the transient concentration of VOCs with different position in 2D channel (x/L), where x-axis is dimensionless time (Fo number) and y-axis is dimensionless concentration of VOCs, and the concentration distribution of VOCs along L direction was calculated at different Fo numbers through LBM simulation as Fo increases when Bi number is 10. Our results show the concentration distribution predicted by LBM simulation confirms analytical solution of Eq. (60.6), so reliability of the calculated results is confirmed.

Quartet structure generation set (QSGS) is a novel method which can generate random porous media based on the random growth theory [5]. As theory research, the random porous media which are considered as porous building materials are constructed through the statistical structural parameters such as the core distribution probability (Cd), the porosity (ε), and the directional growth probability (D_i).

For diffusion process in porous media, the effective mass diffusion coefficient is key parameter. We simulate the D_e of random porous media with different porosity. According to Fick law, the effective mass diffusion coefficient can be calculated as [6]:

Fig. 60.1 Transient concentration of VOCs with different Fo numbers
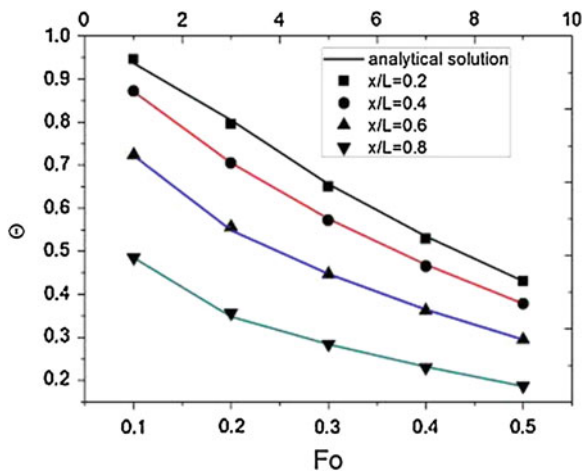
$$D_e = -\frac{\int A j_\sigma \frac{\tau_{\sigma\zeta} - 0.5}{\tau_{\sigma\zeta}} dA}{A\left(\frac{dC_\sigma}{dz}\right)} \tag{60.8}$$

where the A is cross-sectional area which is perpendicular to the diffusion direction.

Figure 60.2 shows the calculated results of effective mass diffusion coefficient by LBM. Comparing with Maxwell equation and empirical equation, the correctness of the LBM simulation to predict effective diffusion coefficient is proved. The Maxwell equation [7] and empirical equation [8] can be obtained as follows:

$$\frac{D_e}{D_0} = \frac{2D_0 + D_I - 2(1 - \varepsilon)(D_0 - D_I)}{2D_0 + D_I + (1 - \varepsilon)(D_0 - D_I)} \tag{60.9}$$

$$\frac{D_e}{D_0} = \frac{\varepsilon}{\tau_f} \tag{60.10}$$

where D_0, D_I are diffusivity in pore and solid matrix, respectively, τ_f is tortuosity of porous media.

If VOC of gas phase and adsorption phase follow Henry law in pore of porous building materials, conservation relationship is obtained on gas–solid interface:

$$(1 + K)\partial_t \rho C_g = D_{\sigma\varsigma}\nabla^2 \rho C_g \tag{60.11}$$

where C_g is the VOCs concentration of gas phase on gas–solid interfaces. The desorption process VOCs from matrix of porous building materials has great effect on VOC emission characteristics. Fig. 60.3 shows the dimensionless transient concentration (Θ) of gas phase in porous media with different partition coefficient when $\varepsilon = 0.6$. It is obvious that Θ rises with the partition coefficient's rise. The reason may be that VOCs of adsorption phase increase as K rises, so total

Fig. 60.2 The effective mass diffusion coefficient with different porosity
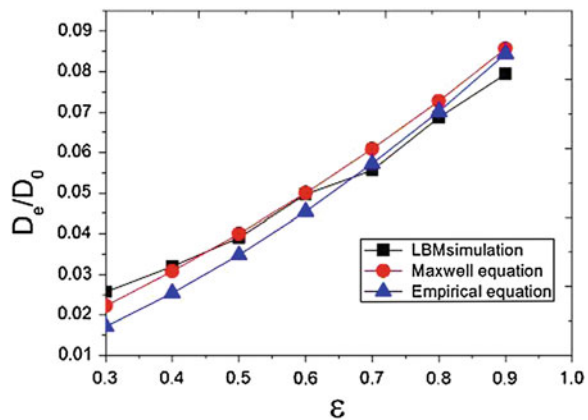
adsorption capacity which can be diffuse from porous media rises, the diffusion process tends to slow at the same effective mass diffusion coefficient.

60.3 Simulation in REV Scale

60.3.1 VOCs Emission in Static Chamber

In the order to research emission characteristic of VOCs, we can assume that a defined volume of building material samples is set into a static chamber in the order to test key parameters.

In the order to establish the mathematical model of VOC diffusion in static chamber, some assumptions are proposed: (1) VOCs mix uniformly in static chamber; (2) the concentration of VOCs is zero at initial time; and (3) the gradient of VOC concentration is zero at the bottom of building materials.

The diffusion equation is described by Eq. (60.6). The emission rate of surface of building materials is defined as:

$$R = -D_e \frac{dC_m}{dx}_{x=L} \tag{60.12}$$

Numerical model of REV scale with LBM is similar to the method which has been proposed above, but the diffusion coefficient is equal to effective mass diffusion coefficient of porous building materials.

Fig. 60.3 VOC concentration with different partition coefficient
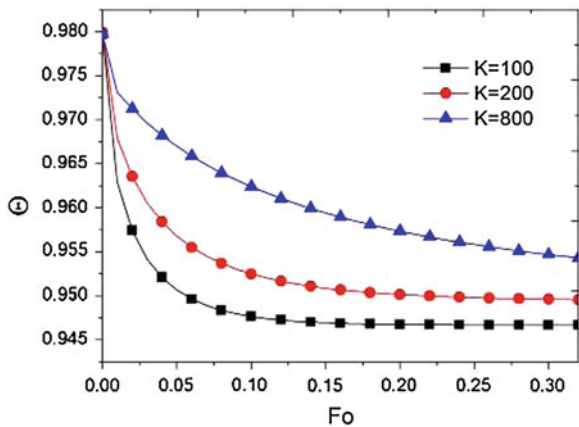
Fig. 60.4 Contrast of LBM and analytical solution for transient concentration in static chamber
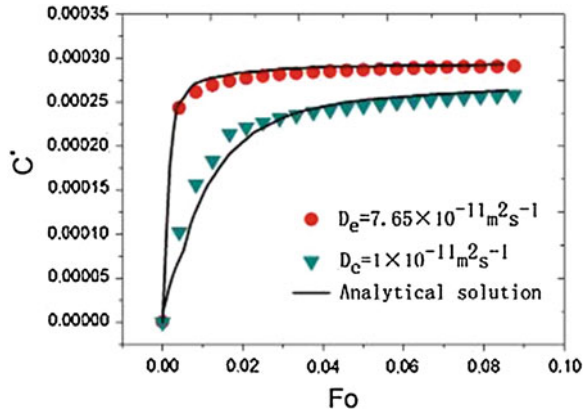
60.3.2 Results and Discussion

These parameters which are used by numerical simulation are selected from Yang's experiment data [9]. The dimensionless concentration of VOCs in static chamber can be compared with analytical solution solved by Xiong JY [10] (see Fig. 60.4). The curve of transient concentration with different effective mass diffusion coefficient can be observed. The VOC diffusion rate significantly slows as effective mass diffusion coefficient decreases. The numerical results are consistent with the analytical results, so LBM can simulate the diffusion process of the porous building materials within the VOC on REV scale.

As shown in Fig. 60.5, adsorption capacity of building materials for VOC is enhanced as partition coefficient increases, so VOC emission from building materials is difficult at higher partition coefficient; therefore, concentration in static chamber has lower equilibrium concentration.

Fig. 60.5 The effect of partition coefficient on transient concentration of VOCs
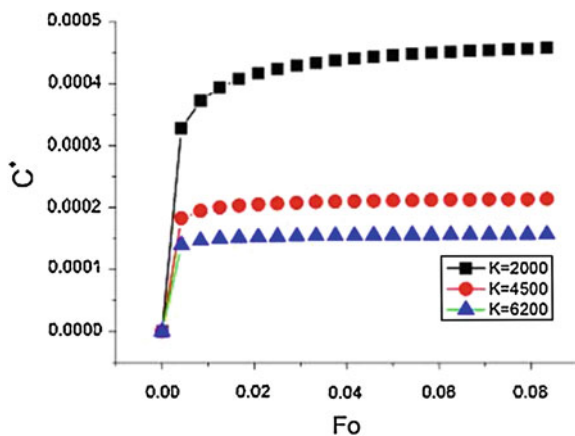
60.4 Conclusions

The migration processes of VOC in porous building materials were analyzed with pore scale and REV scale through lattice Boltzmann method. Feasibility of mesoscopic simulation was proved by comparing with analytic solution. The effective mass diffusion coefficient was predicted with different porosity successfully. The emission characteristics of VOC with different partition coefficient were presented in pore scale and REV scale. The effect of partition coefficient on emission characteristics of porous building materials was obtained with different spatial scale. A useful method to research migration process of VOCs in porous building materials was proposed in our chapter.

References

1. Jones AP (1999) Indoor air quality and health. Atmos Environ 33(28):4535–4564
2. Kim YM, Harrad S, Harrison RM (2001) Concentrations and sources of VOCs in urban domestic and public microenvironments.ENVIRON SCI TECHNOL 35:997–1004
3. Cyrus K, RC Jonathan A (2010) Lattice-Boltzmann method for complex flows. Annu Rev Fluid Mech 42:439–472
4. Luo LS, Girimaji SS (2003) Theory of the lattice Boltzmann method: two-fluid model for binary mixtures. Phys Rev E 67:036302
5. Wang MR, Pan N, Wang JK et al (2007) Esoscopic simulations of phase distribution effects on the effective thermal conductivity of micro granular porous media. J Colloid Interf Sci 311:562–570
6. Jeong N, Choi DH, Lin CL (2008) Estimation of thermal and mass diffusivity in a porous medium of complex structure using a lattice Boltzmann method. Int J Heat Mass Transfer 51:3913–3923
7. Xuan YM, Zhao K, Li Q (2010) Investigation on mass diffusion process in porous media based on Lattice Boltzmann method. Heat Mass Transfer 46:1039–1051
8. Mcduff RE, Ellis RA (1979) Determining diffusion coefficients in marine sediments; a laboratory study of the validity of resistivity techniques. Am J Sci 279:666–675
9. Yang X, Chen Q, Zhang JS et al (2001) Numerical simulation of VOC emissions from dry materials. Build Environ 36(10):1099–1107
10. Xiong JY (2010) VOC emission characteristics from building materials: measurement. Micro-mesocosmic interpretation and simulation, Beijing

Chapter 61
Numerical Simulation of Indoor Gas Chemical Reaction Under Multiple Ventilation Patterns

Jun Wang and Enshen Long

Abstract As chemical reaction can significantly alter concentrations of indoor pollutants and reaction products often are more irritating than their precursors, indoor gas chemical reaction is one significant factor affecting air quality and occupants' health and comfort. Meanwhile, reaction level and product quantity depend on reactants concentration and residence time, impacted by ventilation patterns. For air environment of office room, influence of different factors on indoor gas chemical reaction under four kinds of ventilation patterns were analyzed with CFD, including air exchange rate, supplied air velocity, and ozone concentration of supplied air. One kind of typical reaction between ozone and terpene, including d-limonene and alpha-terpinene, was chosen for analysis. Distribution characteristics of reactants and products concentration are given, and variations of their mean concentration in respiratory region with impacting factors are provided and compared.

Keywords Indoor air quality · Gas chemical reaction · Ventilation pattern · CFD

61.1 Introduction

Outdoor air pollution and ventilation system pollution are two important factors influencing the supplied air quality, e.g., containing high ozone concentration. Rise of indoor ozone (O_3) concentration can induce gas chemical reactions, which may significantly alter components and concentrations of indoor pollutants, namely

J. Wang (✉) · E. Long
College of Architecture and Environment, Sichuan University, 610065 Chengdu, China
e-mail: wangjunhvac@163.com

E. Long
e-mail: Longes2@163.com

secondary pollution occurring. Meanwhile, reaction products are often more irritating than their precursors, so indoor gas chemical reaction is one significant factor affecting air quality and occupants' health and comfort [1, 2]. For depicting indoor gas chemical reaction and predicting concentrations of reactants and products, some previous studies have provided models and methods [3–10], mainly including general chemical reaction model put forward by Nazaroff and adopted pseudo steady state approximation (PSSA) [3]; Weschler established single-zone mass balance model based on fully mixed assumption and analyzed indoor single molecule and bimolecular reactions [9]. In addition, Rai built one CFD model and predicted O_3 concentration distribution in aircraft cabin [10]. However, the impact characteristics of ventilation patterns, air exchange rates, and O_3 concentration of supplied air on indoor gas chemical reaction need to be determined, which is the purpose of present study.

61.2 Model and Methods

For typical indoor environment, one office room with length of 10 m and width of 5 m and height of 3 m is selected as the object, shown in Fig. 61.1. Displacement ventilation and mixing ventilation are applied in this room, including top inlet and top outlet (TITO: AC), top inlet and bottom outlet (TIBO: AD), bottom inlet and top outlet (BITO: DA), and bottom inlet and ceiling outlet (BICO: DB). Its ventilation process is assumed to be steady. All walls are well insulated and indoor air temperature is kept at 25 °C and relative humidity is equal to 50 %. One kind of representative indoor chemical reaction between ozone and terpene, including d-limonene and alpha-terpinene, is chosen for analysis. Meanwhile, according to purpose of this study, hypothetical gas-phase products may be assumed to be produced, although a number of products generate in this kind of chemical reaction.

The ozone derives from supplied air of ventilation, and the terpene is introduced as a source all along the floor, as might be the case after a cleaning situation. The ozone concentration of supplied air is chosen as 20, 40, and 60 ppb,

Fig. 61.1 Geometric model used as analysis object
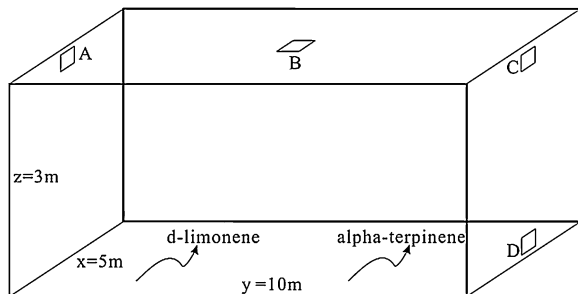
respectively. Emission strength of d-limonene and alpha-terpinene sources was 30 and 40 ppb/h, correspondingly. Reaction rates are 0.0184 ppb^{-1}h^{-1} for ozone and d-limonene and 0.756 ppb^{-1}h^{-1} for ozone and alpha-terpinene. Diffusion coefficients of ozone and products are 1.82×10^{-5} m^{2}s^{-1} and 6×10^{-6} m^{2}s^{-1}, respectively. Moreover, those of d-limonene and alpha-terpinene are both equal to 6.2×10^{-6} m^{2}s^{-1}. In addition, three different air exchange rates are considered, containing 0.5 h^{-1}, 1.0 h^{-1}, and 2.0 h^{-1}.

For modeling turbulence, the renormalization group (RNG) K–ε turbulence model combined with standard wall functions is applied. The standard scheme is used for discretization of pressure and the QUICK scheme for those of momentum, turbulence, energy, and species. Meanwhile, the SIMPLE algorithm for pressure–velocity coupling is chosen.

61.3 Results and Discussion

61.3.1 Influence of Ventilation Patterns

For the condition that air exchange rate is 1.0 h^{-1}, supplied air velocities are 1.1 m/s for mixing ventilation and 0.2 m/s for displacement ventilation, and ozone concentration of supplied air is 40 ppb, Figs. 61.2 and 61.3 give concentration distributions of reactants and products at the surface of x = 2.5 m under four kinds of ventilation patterns, respectively. Product 1 is produced from reaction between ozone and d-limonene, and product 2 is the result of reaction between ozone and alpha-terpinene.

It can be found that ozone concentration decreases along with flow path, but decline of d-limonene and alpha-terpinene concentrations occur at its opposite
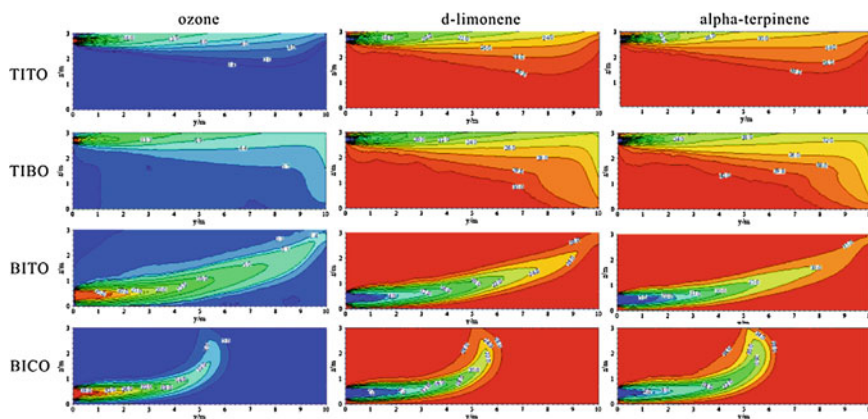

Fig. 61.2 Reactants concentration distributions under *four* kinds of ventilation patterns (ppb)
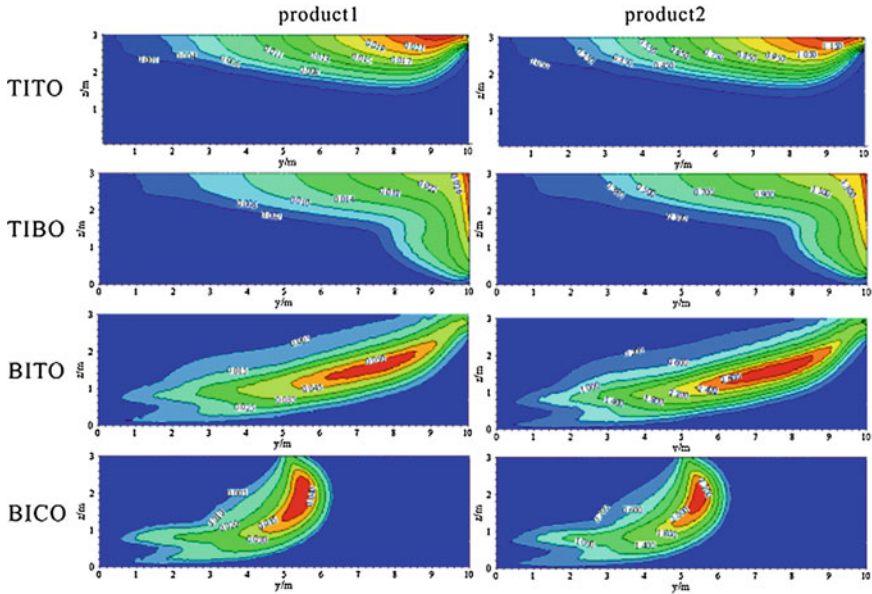
Fig. 61.3 Products concentration distributions under *four* kinds of ventilation patterns (ppb)

direction, as a result of chemical reaction, dilution, and displacement effect of ventilation. Meanwhile, high ozone concentration appears in the upper region of the room for mixing ventilation (TITO and TIBO), but ozone concentration is lower in this region than that in respiratory region under displacement ventilation (BITO and BICO).

For d-limonene and alpha-terpinene, their concentration distributions present opposite characteristics. On the other hand, product concentrations rise along with flow path and become high in the upper region of the room under mixing ventilation. As to displacement ventilation, both the upper region of the room and respiratory region present high ozone concentration. In addition, the maximum concentration of ozone rises in the middle of this room for displacement ventilation.

61.3.2 Influence of Air Exchange Rates

When ozone concentration of supplied air is 40 ppb and supplied air velocities are 1.1 m/s for mixing ventilation and 0.2 m/s for displacement ventilation, Fig. 61.4 shows mean concentration variation of reactants and products with air exchange rate of z = 1.5 m at the surface for four kinds of ventilation patterns.

The results indicate that rise of air exchange rate makes mean concentrations of ozone, product 1, and product 2 to increase and mean concentrations of d-limonene
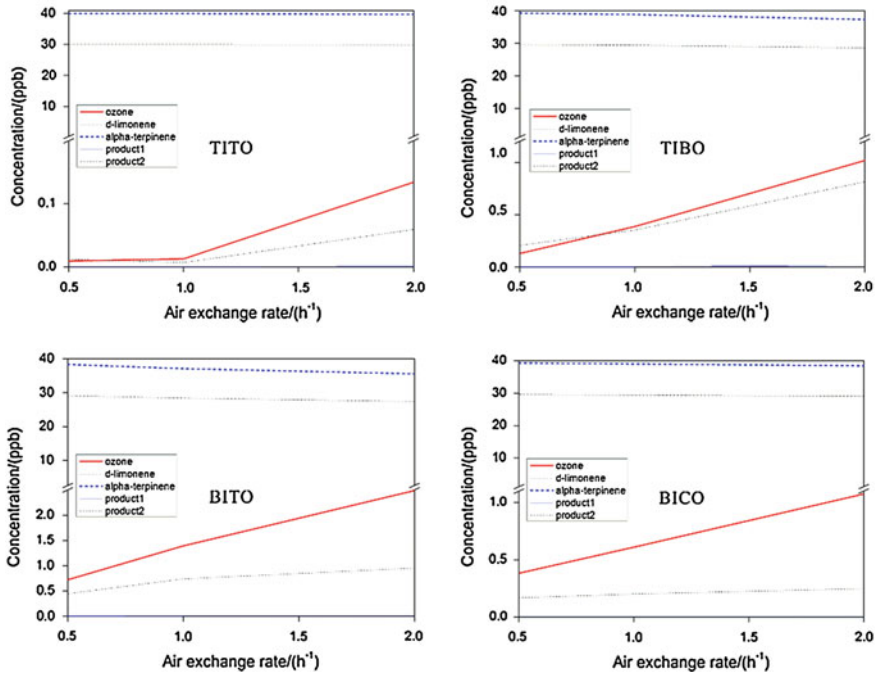
Fig. 61.4 Variation of reactants and products mean concentrations with air change rate

and alpha-terpinene to decrease. Meanwhile, in accordance with the rising degree from high to low for ozone concentration, the ventilation modes are BITO, BICO, TIBO, and TITO, respectively. As to product 1 and 2 concentrations, the sequence is BITO, TIBO, BICO, and TITO for meeting the above requirement. In addition, in the light of the descending degree from high to low for d-limonene and alpha-terpinene concentrations, the ventilation patterns are BITO, TIBO, BICO, and TITO, correspondingly. Therefore, indoor gas chemical reaction in respiratory region (z = 1.5 m) may be enhanced obviously under BITO and TIBO with increase in air exchange rate, as a result of ozone quantity growing up in unit time, although residence time of reactants and products declines.

61.3.3 Influence of Supplied Air Velocity

As air exchange rate is 1.0 h^{-1} and ozone concentration of supplied air is 60 ppb, Fig. 61.5 presents concentration variation of reactants and products with supplied air velocity at the surface of z = 1.5 m under four kinds of ventilation patterns.

It can be seen that ozone mean concentration rises and mean concentrations of d-limonene and alpha-terpinene descend, when supplied air velocity increases.
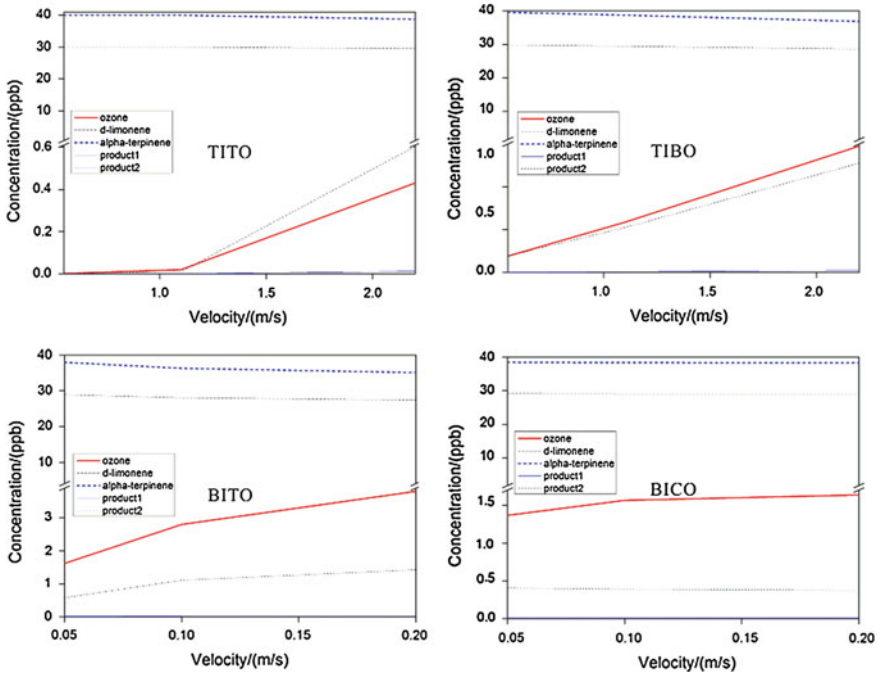
Fig. 61.5 Variation of reactants and products mean concentrations with supplied air velocity

Meanwhile, product 1 and 2 mean concentrations also go up except the case in the ventilation pattern of BICO for rising of supplied air velocity. On the other hand, as to ozone mean concentration, the sequence of ventilation modes for increasing level from high to low is BITO, BICO, TIBO, and TITO. But for product 1 and 2 mean concentrations, the sequence is BITO, TIBO, and TITO. In addition, the sequence for decreasing level of d-limonene and alpha-terpinene mean concentrations from high to low is BITO, TIBO, BICO, and TITO. Actually, rise of supplied air velocity may lead air turbulence to be strengthened in respiratory region and induce obvious gas chemical reaction, especially for BITO.

61.3.4 Influence of Ozone Concentration in Supplied Air

When air exchange rate is 1.0 h^{-1} and supplied air velocities are 1.1 m/s for mixing ventilation and 0.2 m/s for displacement ventilation, Fig. 61.6 gives concentration variation of reactants and products with ozone concentration of supplied air at the surface of z = 1.5 m for four kinds of ventilation patterns.

The results show that, as ozone concentration of supplied air rises, ozone, product 1, and 2 mean concentrations increase and mean concentrations of
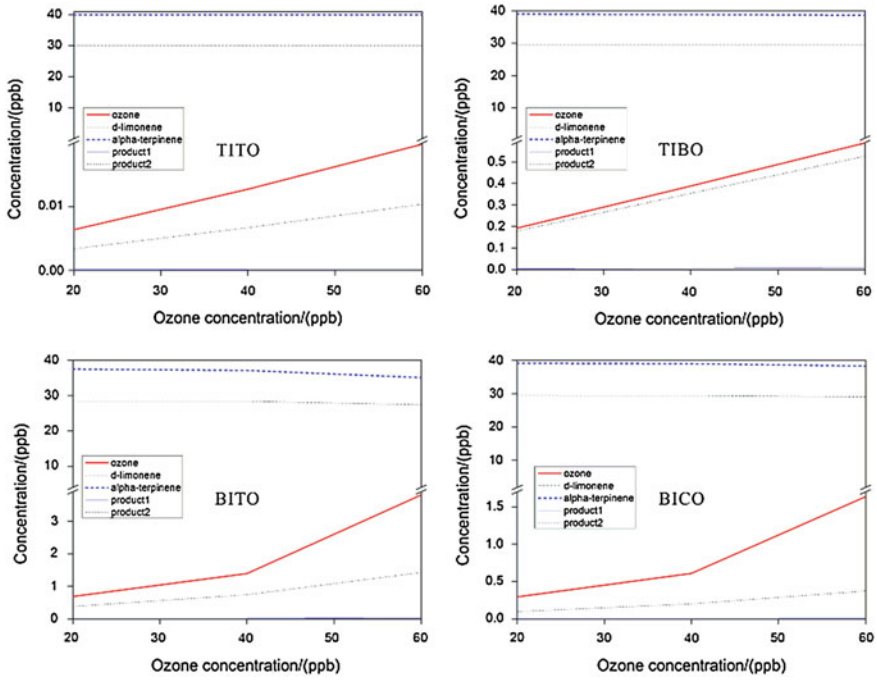
Fig. 61.6 Variation of reactants and products mean concentrations with ozone concentration of supplied air

d-limonene and alpha-terpinene decrease. Meanwhile, both for increasing level of ozone mean concentration from high to low and for decreasing level of d-limonene and alpha-terpinene mean concentrations from high to low, the sequence of ventilation patterns is BITO, BICO, TIBO, and TITO. In addition, as to increasing level of product 1 and 2 mean concentrations from high to low, the sequence is BITO, TIBO, BICO, and TITO. Therefore, rise of ozone concentration in supplied air may induce more strong gas chemical reaction and produce obvious impact on BITO.

61.4 Conclusions

As to air environment of office room, influence of different factors on indoor gas chemical reaction under four kinds of ventilation patterns was analyzed with CFD. For the same air exchange rate, supplied air velocity and ozone concentration of supplied air, more obvious gas chemical reaction occurs in respiratory region under displacement ventilation, especially at BITO. Meanwhile, increase in air exchange rate, supplied air velocity, and ozone concentration in supplied air may

produce the strongest and the lightest influence on gas chemical reaction of respiratory region under BITO and TITO, respectively. The results of this study provide some guides for ventilation system design, running, and optimization.

References

1. Cross CE, Valacchi G, Schock B (2002) Environmental oxidant pollutant effects on biologic systems: a focus on micronutrient antioxidant oxidant interactions. Am J Resp Crit Care 166 S:44–50
2. Valacchi G, Fortino V, Bocci V (2005) The dual action of ozone on the skin. Brit J Dermatol 153:1096–1100
3. Nazaroff WW, Cass GR (1986) Mathematical modeling of chemically reactive pollutants in indoor air. Environ Sci Technol 20:924–934
4. Cano-Ruiz JA, Kong D, Balas RB, Nazaroff WW (1993) Removal of reactive gases at indoor surface: combining mass transport and surface kinetics. Atmos Environ 27A:2039–2050
5. Morrison GC, Nazaroff WW (2002) The rate of ozone uptake on carpet: mathematical modeling. Atmos Environ 36:1749–1756
6. Sorensen DN, Weschler CJ (2002) Modeling-gas phase reactions in indoor environments using computational fluid dynamics. Atmos Environ 36:9–18
7. Nicola C (2007) A new detailed chemical model for indoor air pollution. Atmos Environ 41:1164–1179
8. Wang J, Zhang X (2012) A new scale for representing the level of reaction in indoor air as affected by ventilation and source. HVAC & R Res 18(4):681–691
9. Weschler CJ, Shields HC (2000) The influence of ventilation on reactions among indoor pollutants: modeling and experimental observations. Indoor Air 20:92–100
10. Rai AC, Chen QY (2012) Simulation of ozone distribution in an aircraft cabin using computational fluid dynamics. Atmos Environ 54:348–357

Part II
Climate and Outdoor Environment

Chapter 62
Mitigation of Urban Heat Development by Cool Island Effect of Green Space and Water Body

Chundie Li and Chuck Wah Yu

Abstract In order to understand how green space and water body could mitigate urban heat island, a study was carried out to quantitatively evaluate the influence of park/garden and lake characteristics on surrounding air temperatures. Five thousand one hundred and eighty-five air temperature data of the surrounding areas of 6 parks and 3 lakes in Chongqing were collected during the daytime. The data were analyzed using regression analysis of the park and lake characteristics such as area, landscape shape index (LSI), green ratio, altitude, distance to lake body, and canopy comprehensive temperature (CCT). The findings were as follows: (1) the cool island effect of parks with a maximum of 3.6 °C was greater than that of lake with maximum of 2.9 °C, (2) key factors influencing thermal environment of park and lake were respectively due to the park area and CCT, (3) the less LSI or the rounder the shape of the parks and lakes were, the better the improvement effects of parks and lakes on the thermal environment of the surrounding environment, and (4) the statistic model of parks and lakes could effectively predict the cool island intensity (CII) of parks and surrounding air temperature of lakes (SAT) in Chongqing, the R^2 was 0.787 and 0.721, respectively.

C. Li (✉)
Key Laboratory of the Three Gorges Reservoir Region's Eco-Environment,
Ministry of Education, Chongqing University, Chongqing 400045, China
e-mail: lcdshiwo@126.com

C. W. Yu
International Society of the Built Environment (ISBE),
Milton Keynes, MK7 8HQ, UK

62.1 Introduction

The rapid urbanization of Chongqing has brought with it an environmental impact due to pollution effects of anthropological emissions mostly in the urban cities under the urban canopy, and this has led the urban heat island (UHI) [1]. Chongqing is situated within the hot summer and cold winter zone, and residents in this region of China would require HVAC system to alleviate thermal comfort conditions [2]. The UHI effect would be particularly acute due to the wide spread use of HVAC air conditioners in the densely urbanized districts of the city, as well as due to the increasing industrial developments and the massive rise in volume of automobile traffic leading to the UHI effect and other pollution effects [3–5]. Thus, to mitigate UHI effects is an essential approach to improve human habitat condition.

The main methods to mitigate UHI effect are as follows: provision of green spaces, water bodies and utilization of direct shading in urban environments, and use of evapotranspiration and evaporation of plants in green roofs and green spaces to cool and humidify the thermal environment [6–9]. Remotely sensed observations have confirmed that vegetation body can have a cooling effect on urban environment [10]. Li [11], utilizing remote sensing technology to discover the effective range of mitigation of UHI effect by water. In the experimental aspect, Shuko and Takeshi [12] measured the cooling effect of a pool with an area of $127,000 \text{ m}^2$ under water storage condition; their findings had illustrated that the cooling effect could extend to several hundred meters of downwind, producing a temperature difference of 3 °C between water surface and the streets. Chang [13] found the cool island effect in 61 parks in Taiwan, and the large parks were usually cooler than the smaller parks. The findings of remote sensing monitoring and experiments reported by previous researches have proved the existence of cool island effect of green spaces and water body. However, there is a lack of comparative analysis study between green space and water body such as a lake in the urban environment to understand the differences in their ways to mitigate UHI effects. Therefore, actual measurements on Park Cool Island (PCI) and intensity of parks and lakes were conducted, and the particular factors were discussed in order to resolve the issues concerning the mitigation effects. This paper reports the following analyses: (1) Comparative analysis of the daily cool island intensity (CII) variation between park and lake, (2) analysis of the leading factors which could influence the surrounding air temperature; and (3) analysis to establish park CII and surrounding air temperature (SAT) prediction models. The findings of this study would be of benefit to planning of urban cities in mountainous areas which should incorporate park and water bodies to improve the pleasantness of urban environments.

62.2 Methods

62.2.1 Study Site and Data

The complex canopy structure and special climate in Chongqing are due to the existence of two rivers (Yangtze River and Jialing River) and the surrounding mountains. Land use in Chongqing is heterogeneous, with a complex assemblage of business districts, densely populated residential areas, vegetated spaces, and water bodies. Chongqing is situated in a region characterized by the wet, cold winter, stifling hot summer, and minor daily temperature range. In summer, there are 15–25 days with temperature above 35 °C, and the extreme temperature in the hottest month can reach 44 °C. UHI effect can aggravate torridness. The peak value of actual measurement about UHI intensity in the summer of 2007 was reported to reach 4.2 °C [14], so the purpose of this paper was to evaluate the PCI effect on the urban environment in the summer of Chongqing.

To evaluate how park and water body characteristics can affect the air temperature, the following locations were selected for the study:

- six parks located in the city center without large area of water body, with a size ranging from 1.2–45 ha;
- three lakes located in the city center without large area of green space, with a size ranging from 0.88–6.96 ha.

The observations were carried out in calm days during the period of July to August in the summer of 2009 and 2010. Measurements were conducted 5 times a day, namely every 2 h from 9:00 to 17:00. Six stationary observation points were set up in each park. Measurement of the temperature outside each park was based on mobile observation by walking 500 m along the normal direction of the park. Measurement of the air temperature surrounding the lake body and temperature of the canopy was also based on mobile observation by walking 1,000 m along the normal under direction of wind flow of the lake. All the observation points were set 1.5 m above the ground. Three thousand and ten data of 6 parks and 2175 data of 3 lakes were recorded, respectively, at every 10 s during the measurement periods.

62.2.2 Definition of CII, LSI, and CCT

This chapter introduced CII to describe the mitigation effects of park green spaces and lake bodies have on UHI. Usually, CII is determined by measurement of air temperature of a park or a lake and compared with the surrounding urban areas [15]. Because the measurements methods of a lake and a park were different in this chapter, the definition of CII for the lake and park would be different.

The definition of Park CII is the difference in the average temperature value between the mobile observations (about 500 m) outside the park and stationary observations inside the park.

The definition of Lake CII is the temperature difference between the lake side and the surrounding areas, 1,000 m from the lake.

$$CII = T_0 - T_i \tag{62.1}$$

where T_0 is the average temperature of urban surroundings about 500 m from the park, or the air temperature of 1,000 m away from the lake, which include thermal information on roads, buildings, and other spaces. T_i is the average temperature inside the park including thermal information of trees, open clay ground, etc. or the air temperature of the lake side.

The land shape index (LSI) and canopy comprehensive temperature (CCT) at a certain investigation (T_S) as the influencing factors of CII are defined, respectively, as:

$$LSI = \frac{P_t}{2\sqrt{\pi \times A}} \tag{62.2}$$

where P_t is the total perimeter around a park/lake, and A is the area of the park/lake. LSI of a round-shaped park or a lake would be 1. Figure 62.1 shows the shapes of parks/lakes and their LSI values ranging from 1.24 to 2.56.

$$T_s = \sum_{i=1}^{n} x_i T_i \tag{62.3}$$

where x_i is the proportion of a certain canopy in 15 m radius range, and T_i is the surface temperature of a certain canopy.
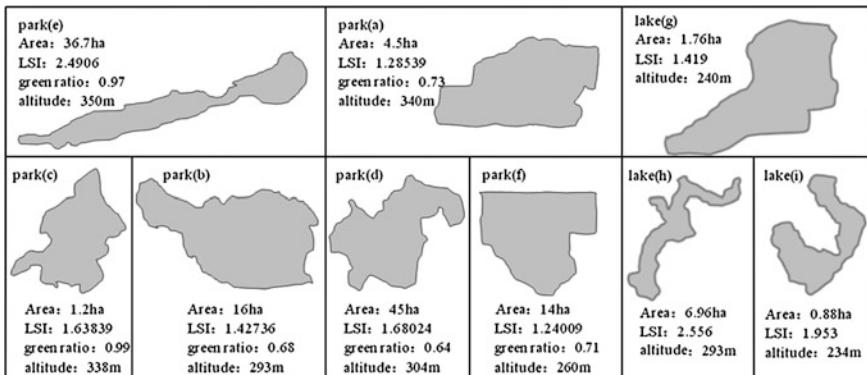

Fig. 62.1 The LSI, area, and altitude values of different parks and lakes

62.2.3 Data Analysis

All the data analyses, graphical displays, ANOVA, t-tests, and correlations were calculated by SPSS. To analyze the factors affecting CII in summer, the following analytical methods were used:

1. The CII was calculated for each park and lake in every time interval to uncover daily variation of the CII.
2. Multivariate regression utilizing stepwise method was conducted to evaluate the roles of the characteristics (LSI, green ratio, area, altitude) of the parks which were affecting the park CII and the characteristics (LSI, area, distance from the measure point to lake, T_S) of the lakes that were affecting the surrounding temperature of the lakes, T_A.
3. Two new linear statistical models were developed to predict CII of parks and T_A of lakes in Chongqing, based on multivariate regression, and then the linear model was validated by the leave-one-out method.

62.3 Results and Discussion

62.3.1 Daily Variation of CII

From Fig. 62.2, the cool island effect was observed to exist in each park and lake at each moment, the temperature in the parks and lakes was 1 °C lower than that of the surrounding air temperatures, which meant that the green spaces and lakes could effectively lower the ambient air temperatures of the built environment. However, the mechanisms were different: the vegetation would cool the air temperature by physical shading and evapotranspiration, while the water bodies cool the air temperature by absorbing heat from evaporation. The daily variation of CII in each park and lake has a distinct differentiation, and the fluctuation of CII of the parks was greater than that of the water bodies. The maximum temperature difference in the park would be 3.8 °C, while that around the lake would be 2.4 °C. This was because the specific heat of water was larger than that of the other types of canopies, leading to a slower temperature rise and temperature fall of the lakes due to the water.

The time-based variation of different lakes CII tend to be the same, while that of different parks tend to be different, because the parks could easily be influenced by other factors such as anthropogenic heat and physiological phenomenon of vegetation. In (a), (b) parks, and (g) lakes, the maximum value of CII was 1.65, 1.34, and 1.3 °C, respectively, at 17:00. This was due to the high traffic heat emission obtained during mobile observations at T_0 point during the rush hour of 17:00. Parks are the best places for morning exercises, so there were a high number of people at 9:00, which therefore had lead to an increase in the anthropogenic heat

Fig. 62.2 The cool island intensity of park and lake
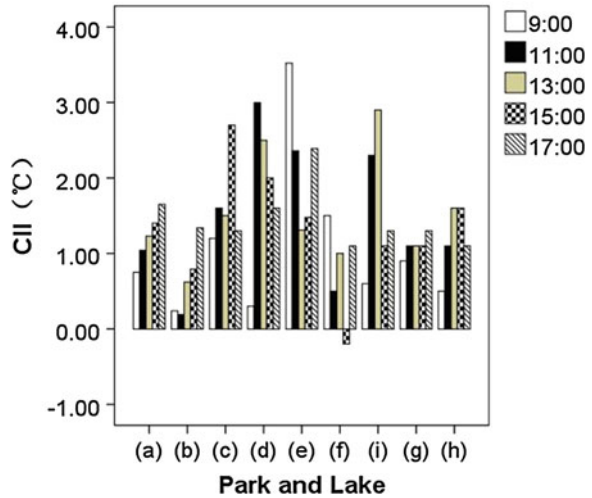
emission. Hence, the average park CII value was just 0.9 °C at 9:00, which was the minimum value. At that time, average lake CII was 0.67 °C, which was the lowest of the day. This was because at that time the solar radiation was weak for the water to absorb, so the cooling effect was not obvious. The average PCI intensity value at 13:00 was 1.36 °C, which was the second smallest value besides the value at 9:00; however, at this time, the cooling effect of the lakes was the most obvious and CII was the highest at 1.87 °C. This was because at this time the solar altitude was the highest and the solar radiation was at the maximum. Also, at this time, in order to prevent too fast evapotranspiration, vegetation would close the stomata, leading to less latent exchange which has therefore lessen the capability of cooling the surrounding air temperature—the phenomenon was called photosynthesis midday depression. However, at this time, the water evaporation was at the fastest rate, thus leading to most latent exchange with most heat being taken from air.

62.3.2 Predicting Park CII and SAT by Linear Regression Model

In Fig. 62.2, the fluctuation of the park CII at different times was shown to be greater than that of lake CII.

In order to understand how park and lake characteristics could influence surrounding air temperature, the different measurement methods and characteristics of the green spaces and lakes, LSI, green ratio, and area, were chosen for multiple regression analysis of park CII. In addition, Chongqing is a typical mountain city with different altitude of each park, so the altitude was considered as an essential park characteristic factor in the regression analysis of LSI. The distance from the

Table 62.1 Multivariate linear regression result of park

Independent variables	9:00		11:00		13:00		15:00		17:00	
	Std. coefficient	Sig.	Std. coefficient	Sig.	Std. coefficient	Sig.	Std. coefficient	Sig.	Std. coefficient	Sig.
LSI	−0.171	0.000[a]	−0.594	0.000[a]	−0.581	0.000[a]	−0.471	0.000[a]	–	–
Green ratio	0.368	0.000[a]	0.536	0.000[a]	0.491	0.000[a]	0.417	0.000[a]	0.100	0.000[a]
Area	0.360	0.000[a]	0.746	0.000[a]	0.658	0.000[a]	0.499	0.000[a]	0.390	0.000[a]
altitude	0.137	0.000[a]	0.524	0.000[a]	0.401	0.000[a]	0.360	0.000[a]	0.295	0.000[a]
R2	0.673		0.750		0.514		0.498		0.335	

[a] are significant variable with $p < 0.05$

lake, T_s, and area were chosen for multiple regression analysis of surrounding air temperatures of the lakes. Because the SATs showed very little differences between the altitudes of each lake, this factor was not considered in the analyses.

Table 62.1 indicates the multiple linear regression results of park CII and park characteristics. The coefficient of determination (R^2) for multiple linear regression models was as follows: 0.673, 0.750, 0.514, 0.498, and 0.335 at 9:00, 11:00, 13:00, 15:00, and 17:00, respectively, for the following four factors: LSI, green ratio, area, and altitude. Therefore, the PCI effect was most effective before 15:00. R^2 at 17:00 was at a minimum because of the increase of anthropogenic heat. The standardized coefficients of multiple linear regressions are useful indicators for indentifying which independent variables could make a greater contribution to the dependent variables. Park CII and green ratio, area, and altitude are positively correlated; therefore, the higher the green ratio was, the larger was the area; higher the altitude was, the more distinct the park CII would be. However, Park CII and LSI presented negative correlations, and these have illustrated that the cool island effect would be more evident when the shape of park is more round.

Because the daily variation of lake CII was stable and the independent variable of regression analysis included time-varying parameter (T_s), this paper took surrounding air temperature of daily measurement point as dependent variable to evaluate multiple linear regression using LSI, distance from the lake, T_s, and area as variable characteristics. The regression showed that R^2 was 0.700, meaning these four factors can explain the surrounding air temperatures of the lake. The standardized coefficients shown in Table 62.2 have indicated that T_s as the key influencing factor of the surrounding air temperatures of the lakes with a max Std. coefficient of 0.672, and these were shown to be positively related, which means that the higher T_s was, the higher surrounding air temperature was, so improving the canopy characteristic would be an effective way to cool the air. Distance to the lakes and LSI was positively related to surrounding air temperatures but with a low Std. coefficient of 0.154 and 0.175, respectively, which means that the closer to the lake and rounder the lake shape was, the lower the surrounding air temperature would be. According to the regression analyses of the influencing factors of parks and lakes, statistic models were established to predict the mitigation effect of parks or lakes on the daily urban thermal environment (temperature) under similar conditions. The linear model of daily park CII is defined as

Table 62.2 The multivariate linear regression result of lake

Independent variables	Unstandardized coefficients		Standardized coefficients	t	Sig.
	B	Std. Error			
(Constant)	18.129	0.752		24.103	00.000[a]
Area	0.115	0.000	00.165	40.511	00.000[a]
distance from the lake	0.003	0.001	00.154	40.669	00.000[a]
T_S	0.300	0.016	00.672	19.039	00.000[a]
LSI	1.394	0.266	00.175	50.242	00.000[a]

[a] are significant variable with $p < 0.05$

Fig. 62.3 The observed
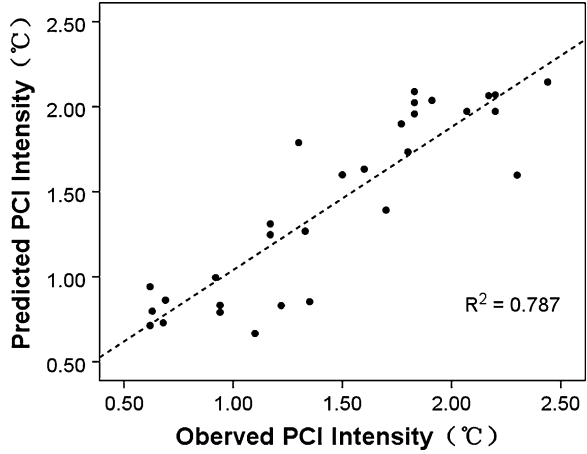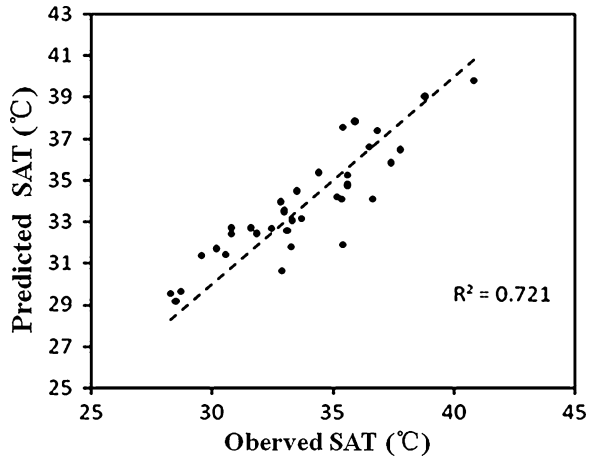and predicted park CII by
Linear model

Fig. 62.4 The observed
and predicted lake CII by
Linear model

$$PCI = -2.741 - 2.368L + 0.069A + 7.326G + 0.003H + \varepsilon \qquad (62.4)$$

where PCI is the intensity of park cooling island (°C); L is LSI of the park; A is the area of the park (ha); G is the green ratio (%); H is the altitude (m); ε is the random error, and $\varepsilon \sim N(0, \delta)$. The linear model of daily SAT is defined as

$$T_A = 18.129 + 0.300T_S + 1.394LSI + 0.003D + 0.115A + \varepsilon \qquad (62.5)$$

In the equation, T_A is the SAT, T_s is the average temperature of canopy (°C), LSI is the shape index of the lake, D is the distance from the lake (m), A is the area of the lake (ha), ε is the random error, $\varepsilon \sim N(0, \delta)$.

Considering the limited number of park samples, leave-one-out cross-validation method was used to validate park CII and SAT. This method would use a part of data (30 data of park, 36 data of lake) which was not taken part in the regression operation

of the actual measurement to validate the regression results. Figures 62.3 and 62.4 shows that the observed value and predicted value were distinctively positively related. R^2 was 0.787 and 0.721, respectively, giving linear models which would be the appropriate way to forecast the park CII and SAT in Chongqing.

62.4 Conclusions

By taking green spaces and water bodies as key factors for mitigation of UHI effects, this paper has carried out analyses of the factors of 6 parks and 3 lakes in Chongqing, and the findings are as follows:

1. The CII of the parks was more obvious than that of lakes, and the maximum CII of the parks was 3.6 °C, while that of lakes was 2.9 °C.
2. Due to the specific physiological phenomenon of vegetation and artificial influences, the daily variation of CII of the parks were greater than that of lakes, the maximum temperature difference of parks was 3.8 °C, while that of water bodies (lakes) was 2.4 °C.
3. The regression analyses showed that area, shape, green ratio, and altitude of parks could have a significant influence on the CII of parks, while the area, shapes, CCT, and distances from the lakes have a significant influence on the surrounding air temperatures at measurement points.
4. Park areas and CCT are positive related and could pose key influence on the thermal environment of parks and lakes, respectively, meaning that the larger the park area is, the more obvious the CII would be; while the higher the surface temperature of the canopy is, the higher the surrounding air temperature of lake would be. The lesser the LSI of the parks and lakes is (or the rounder the shape is), the more obvious the cooling effect would be.
5. The statistic models of the parks and lakes could effectively predict the CII of the parks in Chongqing and the air temperatures surrounding the lakes, with R^2 of 0.787 and 0.721, respectively, for the parks and lakes. The models could be utilized in the planning and design of parks and lakes in Chongqing with the purpose of mitigating UHI.

References

1. Li CF, Yin JY, Zhao JJ (2010) Study on the relationships between ground bright temperature and land-use types of city based on landsat image. Int J Environ Sci Dev 1(3):268–272
2. Li BZ, Yu W, Liu M, Li N (2011) Climatic strategies of indoor thermal environment for residential buildings in yangtze river region. China. Indoor and Built Environ 20(1):101–111
3. He Z, Gao Y, Bai Y, Yang S (2010) Monitoring and simulating urban heat island phenomenon during unusual high temperature and drought period in 2006 summer in Chongqing, China. In: Proceeding WMSVM'10, Proceedings of the 2010, 15–16 May, second international conference on modeling, simulation and visualization methods, Sanya, pp 70–73

4. Zhang JF, Deng W (2010) Industrial structure change and its eco-environmental influence since the establishment of municipality in Chongqing, China. International conference on ecological informatics and ecosystem conservation (ISEIS 2010), Beijing, 27–29 August 2010. Procedia environment sciences Vol 2: pp 517–526
5. Zhao W (2009) Changes in temperature in the Chongqing one-hour economic circle region and their heat-island effect. J Southwest Univ (Nat Sci Edn) 31(9):124–130 (in Chinese)
6. Lu J, Li C, Yu C, Jin M, Dong S (2012) Regression analysis of the relationship between Urban heat Island effect and urban canopy characteristics in a mountainous city. Chongqing. Indoor and Built Environ 21(6):821–836
7. Chen Y, Wong NH (2006) Thermal benefits of city parks. Energ Build 38:105–120
8. Argiro D, Marialena N (2003) Vegetation in the urban environment: microclimatic analysis and benefits. Energ Build 1:69–76
9. Su CX, Hu YQ (1987) Microclimate characteristics and "cool island effect" of Hexi area. Atmospheric Sci 12:4–11 (in Chinese)
10. Weng Q, Lu D, Schubring J (2004) Estimation of land surface temperature—vegetation abundance relationship for urban heat island studies. Remote Sens Environ 89:467–474
11. Li DH, Ai L, Li X (2008) Urban water body alleviating heat island effect based on RS and GIS: a case study of Dongguan. Tropical Geography 9:28–32 (in Chinese)
12. Shuko H, Takeshi O (2010) Seasonal variations in the cooling effect of urban green areas on surrounding urban areas. Urban Forestry and Urban Greening 9:15–24
13. Chang C-R, Li M-H, Chang SD (2007) A preliminary study on the local cool-island intensity of Taipei city parks. Landscape and Urban Planning 80:386–395
14. Dong S-W (2007) Research on the heat effect of underlying surfaces and the urban heat island effect using mobile measurement in Chongqing city. PhD dissertation, Chongqing University: faculty of urban construction and environmental engineering (in Chinese)
15. Chen Y, Wong NH (2006) Thermal benefits of city parks. Energ Build 38:105–120

Chapter 63
A Mathematic Model for Calculating Urban Heat Island Intensity Using Mobile Survey Data

Zhihao Wang and Jun Lu

Abstract Mobile survey is one of the significant and frequently used methods in the field measurement of urban heat island (UHI). In order to solve the synchronously modifying problem of calculating the UHI intensity and overcome the deficiency of mobile survey data, a mathematic model was proposed by designing a round-trip mobile survey route and analyzing the method of calculating UHI intensity in detail. This model can be used for calculating the heat island intensity at any time during the survey period. Associated with a mobile survey test of UHI carried out in Chongqing, the parameters of the mathematic model are explained, and the results are analyzed in this paper. The results indicate that this mathematic model can effectively solve the synchronously modifying problem generated during the process of calculating UHI intensity using mobile survey data.

Keywords Mobile survey · Urban heat island · Mathematic model

63.1 Background

"Urban heat island," (UHI) a term first coined in the 1940s [1], refers to the atmospheric warmth of a city compared to its countryside. Heat islands occur in almost all urban areas, large or small, with warm or cold climates. The UHI is

Z. Wang (✉)
Faculty of Civil Engineering and Architecture, Kunming
University of Science and Technology,
Kunming 650500, China
e-mail: wangzhihao84@163.com

J. Lu
Key Laboratory of the Three Gorges Reservoir Region's Eco-Environment,
Ministry of Education, Chongqing University,
Chongqing 400045, China
e-mail: lujun66@vip.sina.com

induced by two of the most serious environmental issues: population growth and climate change. This partly explains why the worldwide stock of heat island studies has grown so remarkably in recent decades. From Tokyo to London, Ottawa to Beijing, cities of every cultural and physical description have focused the heat island investigation.

Heat islands in hot climates or seasons can increase the discomfort level, raise the threat of heat stress and mortality, and increase the energy demand and cost. A lot of researches and practices have been carried out by means of meteorological study, remote sensing images, modeling and simulating, as well as thermal land-scape analysis [2, 3]. Currently, most of the field measurements of UHI are using urban–rural dichotomy to calculate the heat island intensities. For cities with adequate meteorological stations and abundant data, UHI intensities can be calculated easily through urban–rural dichotomy. However, the minimum time resolution of UHI intensity obtained through this method is one hour. Time modification and interpolation are needed in order to get a higher time resolution of UHI intensity. Besides, this method is not applicable for towns or areas which have rapid economic development and urbanization progress but without any meteorological stations. As a result, new methods are under urgent requirement.

Mobile survey is one of the significant and frequently used methods in the field measurement of UHI. To investigate the UHI characteristic in Tokyo, Shuji [4] conducted moving observations of the horizontal distribution of air temperature from electric trains of the transportation network. In addition, Unger et al. [5] in Hungary, Kuttler et al. [6] in Germany, Wong and Chen [7] in Singapore employed moving observation method in the urban thermal environment investigations. Tso [8] summarized state of the art of UHI studies in Singapore, in which moving observation method was also included. However, data processing was not mentioned in any of the published researches. There are also practices [9, 10] of moving observations conducted in the UHI studies in China, but a few mathematic models for calculating UHI intensity using moving observation data were proposed.

63.2 Mathematic Model

63.2.1 Method Description

The traverse route of mobile survey usually begins at one place and finishes at the other. Sometimes, the traverse route is closed. The investigators start the mobile survey at certain time (e.g., 14:00) and then conduct another survey at other time (e.g., 20:00), beginning at the same place and following the same direction. The mobile survey method has been discussed a lot, but the key issue to use mobile survey method is to process the asynchronous data obtained from the survey. If the actual change rate of the air temperature observed from each sample site along the
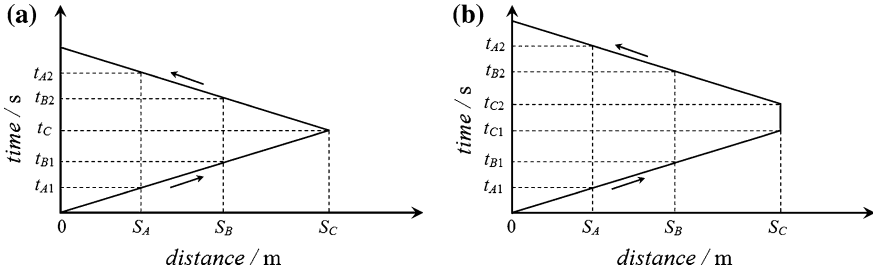
Fig. 63.1 Relation between distances away from starting point and survey time

traverse route can be calculated easily, the synchronously modifying problem can be solved.

Imagining there is a certain mobile survey experiment, which is conducted for investigating the UHI intensity with round-trip survey along a predesigned route. Under ideal condition, when the mobile survey car moves ahead at a uniform speed, the distance away from the starting point varies with the survey time (Fig. 63.1a). In Fig. 63.1a, S_A, S_B, and S_C present the distances from the starting point to the survey points A, B, and C on the route, respectively.

If the change rate of air temperature is assumed identical at each survey point during the survey period, it can be calculated with any two air temperatures at certain place on the route. However, it is obvious that change rate of air temperature at survey point C cannot be calculated with only one value as shown in Fig. 63.1a. It is easy to handle this problem if the survey car stays for a period of time at survey point C (knee point), just as shown in Fig. 63.1b.

Therefore, the change rate of air temperature at survey point A can be expressed as follows:

$$\varepsilon = \frac{|T_{A2} - T_{A1}|}{t_{A2} - t_{A1}} \tag{63.1}$$

where T_{A1} is the air temperature of survey point A at the first time t_{A1} that the mobile survey sensor passes survey point A in the outbound survey; T_{A2} is the air temperature of survey point A at the second time t_{A2}, $t_{A2} > t_{A1}$. Here, survey point A is taken for example to calculate the change rate of air temperature, and the calculations for the survey points B and C are analogy.

63.2.2 Establishment of the Model

As the change rate of air temperature at each survey point is assumed identical during the whole survey period and the rate could be calculated using Eq. 63.1, therefore, for any chosen reference time t_i during the survey period, modified temperature T_i of any survey point along the traverse route could be obtained.

Fig. 63.2 Time intervals of round-trip mobile survey
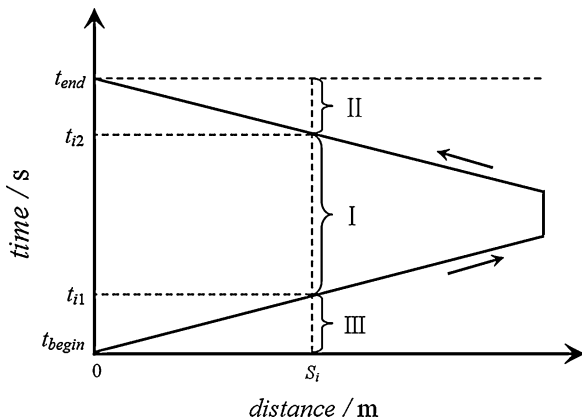
In Fig. 63.2, i is any one of all the survey points along the route, t_{i1} is the first time when mobile survey sensor passes survey point i in the outbound survey, t_{i2} is the second time when mobile survey sensor passes survey point i in the inbound survey ($t_{i1} < t_{i2}$), and T_{i1} and T_{i2} are separately the corresponding recorded air temperature at time t_{i1} and t_{i2}. When calculating the modified air temperature at any time during the survey time period is needed, two aspects should be considered. One is to confirm which time interval does the chosen reference time t_i belong to before calculating, and the other one is to judge whether mobile survey is in a temperature-rise period or temperature-fall period. The whole mobile survey period is divided into three intervals (I, II, III) so that the modified temperature T_i of any survey point along the traverse route at t_i could be calculated using equations in Table 63.1.

In Table 63.1, $\varepsilon = -\varepsilon'$, so the equations for calculating the modified temperature T_i keep the same in both the temperature-rise and temperature-fall periods, regardless of the background air temperature conditions.

With the air temperature obtained at rural places, the UHI intensity of any survey point along the traverse route at the chosen reference time t_i could be calculated using urban–rural dichotomy method (Eq. 63.2).

Table 63.1 Equations for calculating the modified temperature

Time intervals	Temperature-rise period $\left(T_{i1} < T_{i2}, \varepsilon = \frac{T_{i2} - T_{i1}}{t_{i2} - t_{i1}}\right)$	Temperature-fall period $\left(T_{i1} > T_{i2}, \varepsilon' = \frac{T_{i1} - T_{i2}}{t_{i2} - t_{i1}}\right)$
I $t_1 < t_i < t_2$	$T_i = T_{i1} + \varepsilon(t_i - t_{i1})$ $= T_{i2} - \varepsilon(t_{i2} - t_i)$	$T_i = T_{i1} - \varepsilon'(t_i - t_{i1})$ $= T_{i2} + \varepsilon'(t_{i2} - t_i)$
II $t_1 < t_2 < t_i$	$T_i = T_{i1} + \varepsilon(t_i - t_{i1})$ $= T_{i2} + \varepsilon(t_i - t_{i2})$	$T_i = T_{i1} - \varepsilon'(t_i - t_{i1})$ $= T_{i2} - \varepsilon'(t_i - t_{i2})$
III $t_i < t_1 < t_2$	$T_i = T_{i1} - \varepsilon(t_{i1} - t_i)$ $= T_{i2} - \varepsilon(t_{i2} - t_i)$	$T_i = T_{i1} + \varepsilon'(t_{i1} - t_i)$ $= T_{i2} + \varepsilon'(t_{i2} - t_i)$

$$\Delta T = T_i - T_{ri} \tag{63.2}$$

where T_{ri} is the rural air temperature at the chosen reference time t_i.

Additionally, the average UHI intensity of mobile survey area at the same chosen reference time could also be calculated by averaging the air temperatures observed from all the sample survey points along the traverse route, which can be shown in Eq. 63.3:

$$\Delta T_{average} = \frac{1}{m} \sum_{i=1}^{m} T_i - \frac{1}{n} \sum_{i=1}^{n} T_{ri} \tag{63.3}$$

where m is the number of sample points along the traverse route and n is the number of sample survey sites at the rural places.

Equation 63.2 is the mathematic model for calculating the UHI intensity of single sample survey point, and Eq. 63.3 is the mathematic model for calculating the average UHI intensity of the whole mobile survey areas. Both of them are also the processes for correcting all recorded air temperature data to be synchronous.

63.3 Application of the Model

63.3.1 Field Measurement

A round-trip mobile survey was designed and carried out on 15th of August 2008 to verify the feasibility and practicability of this method. The duration time of the outbound survey was from 20:09:25 to 20:53:00 p.m., and the duration time of inbound survey was from 20:54:00 to 21:34:50. The outbound mobile survey route is shown in Fig. 63.3. The mobile survey car began from the starting point and travelled southeastward heading to Hualong Road, then travelled northward and turned left to the Dajian Road, Huayu Road, and Jinqiao Road, and then headed southward to Hualong Road and Huafu Road and reached Tiaodeng Town. The car travelled on Tianxi Road for the last section of the route and reached the ending point. The inbound survey was backtracked from ending point to the starting point.

The measuring and testing instruments include automatic temperature and humidity data loggers (HIOKI 3641) and a GPS data logger (GlobalSat DG-100). The automatic temperature and humidity data loggers were made in Japan with the inaccuracy of 0.5 °C (0.0–35.0 °C). The GPS data logger was made in Taiwan with SiRF star III wafer. The activation time of all the instruments was set to be coincident with the observation time, and the record intervals were 5 s. Mobile survey car kept nearly an even speed at 40 km per hour.

A large amount of air temperature data were obtained owing to the short time interval. In order to calculate the actual change rate of air temperature at any survey point along the route, it is primary to determine the spatial position, the time, and the corresponding air temperature of the survey point for both the

Fig. 63.3 Outbound mobile
survey route
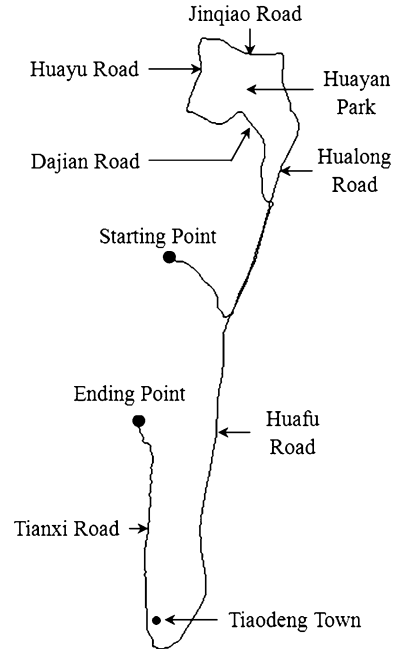
outbound and inbound surveys. The authors realize that it will be a huge time-consuming work to determine the temperature difference between the inbound time and outbound time at each sample survey point even with the help of Google Earth software. Hence, only parts of the survey points were selected at certain distances where the traverse route changes direction. At last, 29 survey points were selected and the corresponding time and air temperature values at these survey points were also found out. The spatial location of selected survey points was shown in Fig. 63.4. The red points were selected for the outbound survey and the black ones presented the inbound survey.

It can be seen from Fig. 63.4 that the 29 selected survey points can be representative of air temperature characteristic within the mobile survey areas, and the distance from outbound survey point to inbound survey point is shortly indeed, the maximum distances of which is nearly the width of the road where the points located.

63.3.2 Results and Analysis

The relationship between the distances of selected survey points away from the starting point and the corresponding survey time is shown in Fig. 63.5. The actual change rate of air temperature at selected survey points is shown in Fig. 63.6.

Fig. 63.4 Spatial location of selected survey points
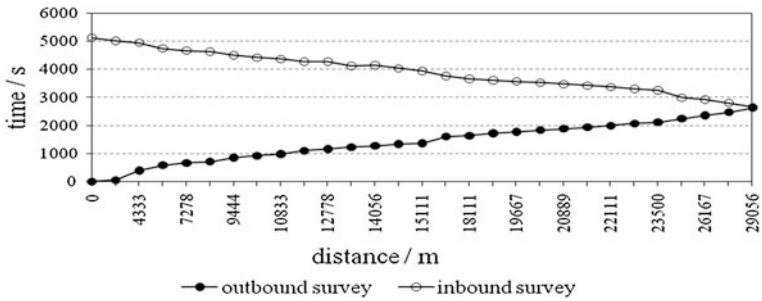
Fig. 63.5 Relationship between the distance of selected survey points away from the starting point and the corresponding survey time

It can be seen that the Fig. 63.5 presents a little different shape from the Fig. 63.1. The reason is that the experimental round-trip mobile survey was influenced by the real-time traffic under actual conditions. So, the curves in Fig. 63.5 did not appear straight lines like those in Fig. 63.1, but the slope of the curves only changed slightly.
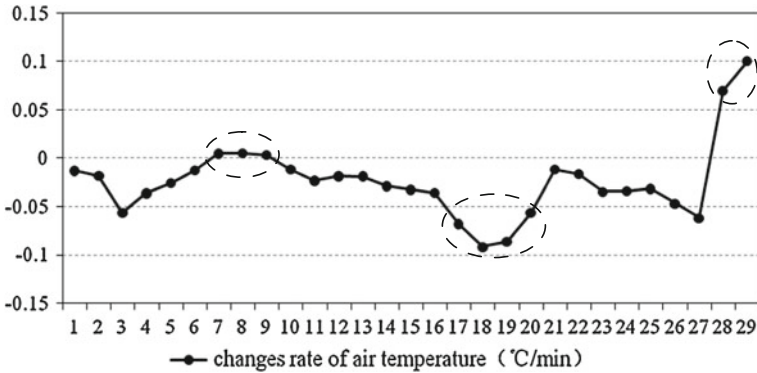
Fig. 63.6 Change rate of the air temperatures of selected survey points

In Fig. 63.6, positive values represent that the air temperatures are raising and the negative values represent the air temperatures are falling. It can be found in Fig. 63.6 that the change rate of air temperature at most selected survey points fluctuated within ± 0.05 °C/min, which reflect the actual conditions. It is worthwhile to note that the variations in the air temperatures appeared abnormal in three places (marked with dotted-line circles): The first is the air temperature increased at survey points 7–9, the second is the air temperature dropped as high as $0.06 \sim 0.09$ °C/min at survey points 17–20, and the third is the abnormal air temperature increase at survey points 28–29.

Survey points 7–9 were on the Huayu Road, which is at the left side of Huayan Park. Huayu Road is the main road of Huayan new city, and the traffic was heavy. Therefore, the human activities near these three points are intensive. A large amount of anthropogenic heat will be released, which is the mainly reason causing the higher air temperature rise at the survey points 7–9. Survey points 17–20 were located in the Jiulong industrial zones at the southern section of Huafu Road, and construction lands are the main landscapes. The heat absorbed in the soil during the day time releases quickly as the large sky view-factors. Therefore, air temperature at the survey points 17–20 dropped a lot. Although the survey points 28–29 were in a village landscape and had less anthropogenic heat released, the survey points were sheltered by tall trees; hence, the heat is released much slowly. These induced the air temperature rising at the survey points 28–29.

After calculating the change rate of air temperatures at the selected survey points, combined with the temperature data recorded at a rural place, an average UHI intensity of the mobile survey areas could be obtained. The main purpose of this study is to validate the mathematic model.

63.4 Discussion

The mathematic model proposed in this study is based on the traditional urban–rural dichotomy. The model looks simple, but the formulas for calculating the modified temperature of any survey point along the traverse route at referred time can be effectively applied in the investigation of UHI. The hypothesis for conducting the round-trip mobile survey and calculating the modified temperature is the change rate of air temperature at each survey point which is postulated identical during the survey period. As the reasonableness of the hypothesis is the premise to use this method, the relatively short survey time has restricted the areas of round-trip mobile survey. Therefore, this method is only adequate for UHI investigation within a small scale.

63.5 Conclusion and Implications

A mathematic model was proposed by designing a round-trip mobile survey route and analyzing the method of calculating the modified air temperature of any survey point along the traverse route at a reference time in detail, which can be used for calculating the UHI intensity at any time during the survey period. The change rate of air temperature at the most selected survey points fluctuated within ± 0.05 °C/min. The released anthropogenic heat, sky view-factor, and landscapes are the important factors influencing the air temperatures and the UHI. Round-trip mobile survey and the mathematic model proposed in this study provide another way to solve the synchronous modifying problem in the process of calculating UHI intensity by employing the mobile survey data. This mobile survey method might be a good way to investigate the PM 2.5 and other atmospheric pollutants if the deficiency of mobile survey data could be overcome effectively.

References

1. Balchin WGV, Pye N (1947) A micro-climatological investigation of bath and the surrounding district. Quart J Roy Meteor Soc 73:297–323
2. Oke TR (1982) The energetic basis of the urban heat island. Q J R Meteorol Soc 108:1–24
3. Parham AM, Fariborz H (2010) Approaches to study urban heat island—abilities and limitations. Build Environ 45:2192–2201
4. Shuji Y (1996) Detailed structure of heat island phenomena from moving observations from electric tram-cars in metropolitan Tokyo. Atmos Environ 30:429–435
5. Unger J, Sumeghy Z, Zoboki J (2001) Temperature cross section features in an urban area. Atmos Res 58:117–127
6. Kuttler W, Andreas B, Frank R (1996) Study of the thermal structure of a town in a narrow valley. Atmos Environ 30:365–378

7. Wong NH, Chen Y (2005) Study of green areas and urban heat island in a tropical city. Habitat Int 29:547–558
8. Tso CP (1996) A survey of urban heat island studies in two tropical cities. Atmos Environ 30:507–519
9. Liu JP, Lin XD, Liu YF, Sun ZY (2007) Survey on winter urban heat island in Xi'an. Acta Energiae Solaris Sinica 28:912–917
10. Wang ZH, Lu J, Yang K (2012) Study on heat island effect of Huayan new city in Chongqing in summer. Acta Energiae Solaris Sinica 33:953–957

Chapter 64
Effect of the Fence of Urban Residence Communities on the Diffusion of Ground Pollutants

Yi Huang, Qibin He, Huiyuan Shen and Yanhua Liu

Abstract Ground pollutants such as SO_2, CO, and other gaseous pollutants generated by the traffic always harm the environment of urban residence communities. Fences or enclosures are common for residence communities in China for security reasons, while they really hinder the wind flow and the pollutant diffusion. In this paper, the computational fluid dynamic (CFD) method has been used to simulate how the fence affects the diffusion of the traffic pollutants around a building. The k-ε equation is used to simulate the diffusion of the CO. The results show that (1) the fences hinder the diffusion of the CO on the horizontal direction, but they promote the diffusion in the vertical direction. (2) The higher the fence, the more the CO concentration between the fence and the building. (3) When a ground pollutant source is on the leeward side of a building, it poses the greatest threat to the air quality around the building. It has the least threat when it is set on both sides of the building in wind direction.

Keywords Fence · Traffic · Environment · K-ε model · Diffusion of pollutant

64.1 Introduction

Cars have been popular in cities with the improvement of people's life. Then, the exhaust gas produced by the cars has been one of the main pollutant resources. The pollutants such as CO, SO_2, and some hydrocarbons are greatly hazardous to

Y. Huang · H. Shen · Y. Liu (✉)
Department of Building Environment and Services Engineering, School of Human Settlements and Civil Engineering, Xi'an Jiaotong University, Xi'an, China
e-mail: yhliu@mail.xjtu.edu.cn

Q. He
Shenzhen Institute of Building Research, 29#, three Road, Meiao, Shangmeilin, Shenzhen, China

the residential air environment and the people's health. They even cause cancer. CO, which is one of the typical traffic pollutants in exhaust gas, reaches 70 % of the traffic pollutants [1]. The diffusion of the exhaust from vehicles among the buildings has been studied by many researchers, but the influence of fence, a common safety facility, is often ignored and seldom studied on the diffusion of exhaust gases.

The computational fluid dynamic (CFD) method has been used widely with the development of computer technology. It can be used to calculate various flow fields conveniently, quickly, and with low cost of money. The Reynolds time-averaged simulation methods (RANS) are popular methods to simulate turbulent flow. The k-ε model in RANS is often used to simulate the turbulent flow. Similar models include the standard k-ε model, the RNG k-ε model, and the realizable k-ε model. Huang et al. [2] simulated the air movement and pollutants diffusion in street canyon with seven different models (the standard k-ε model, the RNG k-ε model, the realizable k-ε model, the standard k-ω model, the SST k-ω model, the RSM model, and the Spalart–Allmaras model, etc.). The results showed that the prediction with the standard k-ε model is the best. The following one is that with the RNG k-ε model and the realizable k-ε model. Since the influence of fences of buildings has not been paid close attention and CO is a common ground pollutant, how the fence affects the diffusion of CO around a building has been studied in this paper using the k-ε model.

64.2 Computational Domain and the Method

64.2.1 Computational Domain

Figure 64.1 shows the modeled case used in the study. A $20 \times 10 \times 10\,\mathrm{m}^3$ building is in the middle of a quadrate fence. The length of the fence is 26 m, the width of the fence is 16 m, and its thickness is 0.2 m. It is 1.7, 2, and 2.3 m high, respectively. The computational domain is set as a $80 \times 70 \times 70\ \mathrm{m}^3$ cuboid. The traffic pollutants' source is considered as a point source. The height of the source is 0.4 m. The density of CO at the source is given 166 mg/(m$^3\cdot$s) according to reference 3.

64.2.2 Mesh Generation

The more the mesh density, the higher the calculation accuracy while the longer the time it takes. The less the mesh density, the less the time it takes while the lower the calculation accuracy. To ensure the less calculation time and the higher calculation accuracy, some local mesh refinement and density of mesh transition region are made. The size of the mesh near the pollutant source is 0.2. The size of

Fig. 64.1 The layout in the vertical view
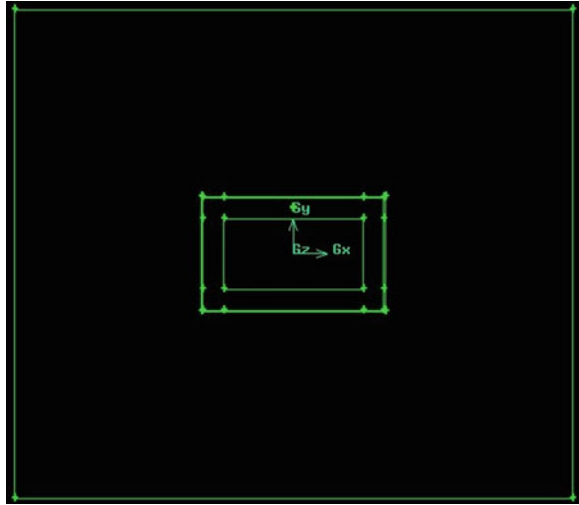
the meshes in the transition region is 1. And the size of the meshes in the exterior zone is 2.

64.2.3 Governing Equations and Turbulence Model

To calculate the diffusion of CO in turbulent flow, the k-ε equation and the component transport equation are necessary. For steady turbulent flow, the equations containing the continuity equation, energy equation, and the standard k-ε equations are used below. Since it is not good enough for the calculation near the wall, the wall function method is used for good calculation accuracy.

1. Continuity equation

$$\frac{\partial}{\partial X_i}(\rho U_i U_i) = -\frac{\partial}{\partial X_i}\left[(\mu_l + \mu_i)\left(\frac{\partial \mu_i}{\partial X_j} + \frac{\partial \mu_j}{\partial X_i}\right)\right] + \beta(T_0 - T)\rho g \quad i,j = 1,2,3$$

(64.1)

2. Energy equation

$$\frac{\partial}{\partial X_i}(\rho U_i T) = -\frac{\partial}{\partial X_i}\left[\left(\frac{\mu_l}{\text{Pr}} + \frac{\mu_t}{\sigma_T}\right)\frac{\partial T}{\partial X_i}\right] + \frac{q}{Cp} \quad i = 1,2,3 \qquad (64.2)$$

3. Turbulent kinetic energy equation

$$\frac{\partial}{\partial X_i}(\rho U_i k) = -\frac{\partial}{\partial X_i}\left(\frac{\mu_l}{\sigma_k}\frac{\partial k}{\partial X_i}\right) + \mu_l\left(\frac{\partial U_i}{\partial X_j} + \frac{\partial U_j}{\partial X_i}\right)\frac{\partial U_i}{\partial X_j} - \rho\varepsilon + \beta g\frac{\mu_t \partial T}{\text{Pr}\,\partial X_i} \quad i,j = 1,2,3$$

(64.3)

where Cp is air specific heat at constant pressure; g is acceleration of gravity; k is fluid turbulent kinetic energy; p is time average pressure; q is heating source intensity; Pr is pr number when turbulence flow developed fully; T is fluid temperature. T_0 is reference temperature; U_i is velocity component (i = 1, 2, 3 means x-axis, y-axis, and z-axis); μ_i is laminar flow viscosity coefficient and μ_t is turbulence flow viscosity coefficient; ρ is the density of fluid; β is coefficient of fluid cubic expansion.

In the k-ε equations, the turbulence energy 'k' is '$G_k - \rho\varepsilon + G_B$' and the energy dissipation rate 'ε' is '$c_1\rho\frac{\varepsilon}{k}(G_k + G_B) - c_2\rho\frac{\varepsilon^2}{k}$' where

$$G_k = \mu_t\left\{2\left[\left(\frac{\partial U}{\partial x}\right)^2 + \left(\frac{\partial V}{\partial y}\right)^2 + \left(\frac{\partial W}{\partial z}\right)^2\right] + \left(\frac{\partial U}{\partial z} + \frac{\partial V}{\partial x} + \frac{\partial W}{\partial y}\right)^2\right\} \quad (64.4)$$

$$G_B = \beta g\frac{\mu_t}{\sigma_T}\frac{\partial T}{\partial z} \quad (64.5)$$

The component transport equation is as follows:

$$\frac{\partial C}{\partial t} + u_j\frac{\partial C}{\partial u_j} = \frac{1}{\rho}\left[\left(\rho D + \frac{\mu_t}{\text{Sc}_t}\right)\frac{\partial C}{\partial x_j}\right] + S_t \quad (64.6)$$

where D is the pollutant diffusion coefficient in air, m^2/s; u_j is velocity, m/s; x_j is coordinate, m; t is time, s; μ_t is turbulent kinetic, $N{\cdot}S/m^2$; Sc_t is turbulent Schmidt number; C is the pollutant concentration, kg/m^3; the pollutant diffusion coefficient $D_t = D + \mu_t/(\rho \cdot Sc_t)$; the pollutant source strength $S_t = 166$ ($mg/m^3{\cdot}s$).

64.2.4 Boundary Conditions

(1) The velocity boundary condition of the air inlet is given, the velocity in vertical direction increases according the followed equation [3]:

$$\frac{U(z)}{U_{\text{ref}}} = \left(\frac{z}{z_{\text{ref}}}\right)^{\alpha} \qquad (64.7)$$

where α is equal to 0.2, corresponding to urban exposure; $U_{\text{ref}}(1.2\,z\,\text{gm}^{-1})$ is the wind velocity at reference height $z_{\text{ref}} = 0.4$ m (full scale: 70 m); and z is the height above the ground.a

(2) At the side and top outlet, symmetry boundary conditions are given.
(3) In outlet or on the cross-section at $x = 40$, outflow $= 1$.
(4) On the floor, the faces of the fences, and the building, wall boundaries are given.

64.3 Results and Discussion

64.3.1 The Effect of Fence

It is shown in Fig. 64.2 that CO diffuses symmetrically around the pollutant source for the symmetrical geometrical structures of the buildings and fence. Since the direction of gas flow near the boundary of the inlet is the same, the flow field is symmetrical in x-axis direction which is shown in Fig. 64.3.

It is shown in the Fig. 64.4 that CO diffuses strongly along the minus x-axis direction in both cases against wind. This is because the building hinders the movement of gas flow around the building. A backflow or a vortex is generated between wall and the building. The fence hinders the diffusion of the gas flow at the horizontal direction, but it enhances the diffusion in the vertical direction.

It is shown in Fig. 64.5 that the gas flowing around the vortex center moves in circle between the fence and the building. Since the flow is blocked by the fence, it
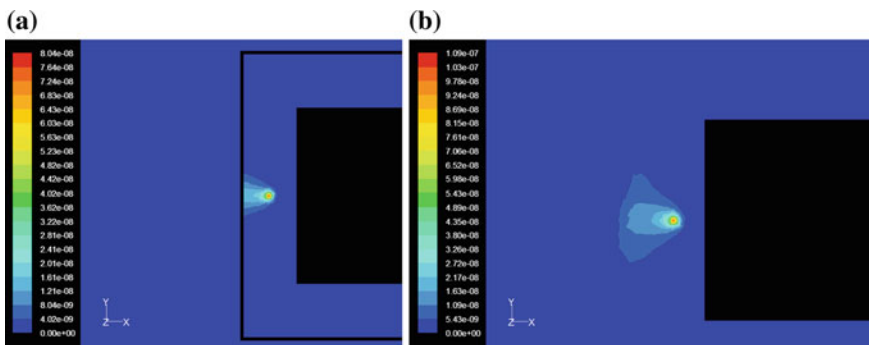
Fig. 64.2 Contour of CO mass fraction at $z = 0.4$, **a** with 2-meter-high fence, **b** without fence
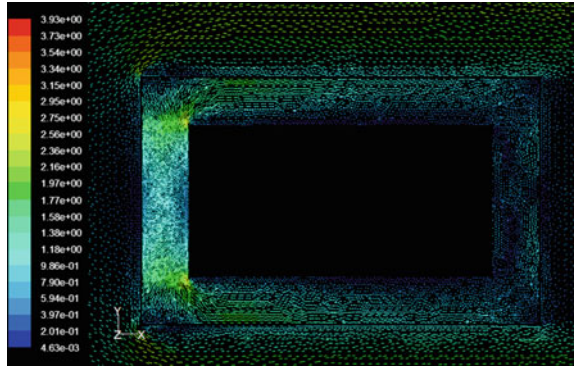
Fig. 64.3 The velocity at $z = 0.4$ m without fences
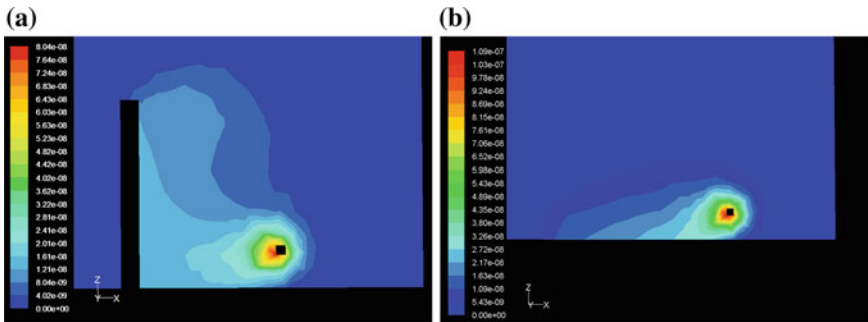
Fig. 64.4 CO distribution at $y = 0$, **a** with a 2-meter-high fence, **b** without any fence

leads to an irregular movement of the flow and a strong vertical diffusion of pollutant. When there is no fence around the building, the gas flow around the vortex center moves like an irregular ellipse and the pollutant in gas flow diffuses along the minus x-axis direction.

64.3.2 Effects of Fence Height on the Diffusion of CO

The pollutants diffuse in x-axis direction and vertical direction. It is shown in Fig. 64.6 that the influence region of the pollutant between the fence and the building is greater with a higher fence. Figure 64.7 shows the velocity distribution with the three fence heights. It can be seen that the eddy appearance for the three cases is the same, but the size of them is different. It is probably the reason why the height of fence affects the diffusion of pollutants.
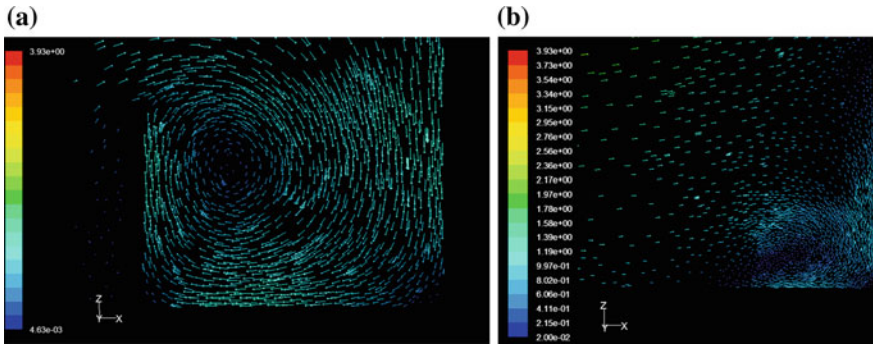
Fig. 64.5 Velocity vector at $y = 0$ and with pollutant source in the upstream of the building, **a** with a 2-meter-high fence, **b** without any fence
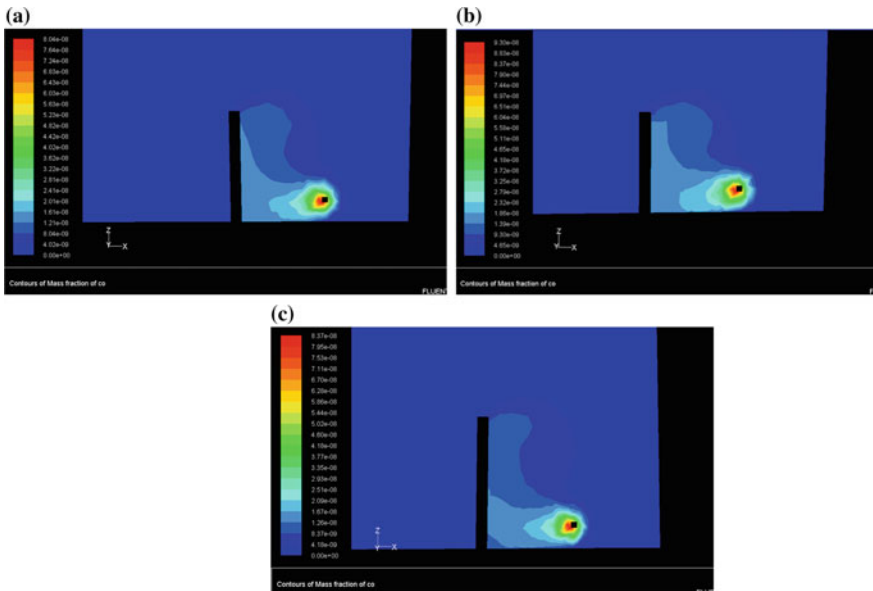
Fig. 64.6 CO distribution at $y = 0$ **a** with a 2-meter-high fence, **b** with a 1.7-meter-high fence, and **c** with a 2.3-meter-high fence
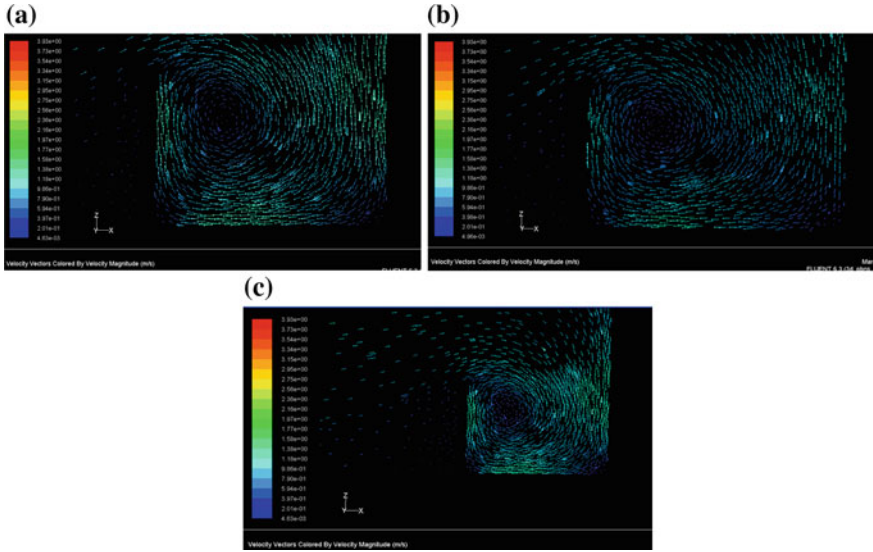
Fig. 64.7 The velocity vector distribution at $y = 0$ **a** $Z = 2$, **b** $Z = 1.7$, and **c** $Z = 2.3$ m

64.3.3 The Effect of the Pollutant Source Position

It is shown in Fig. 64.8 that CO diffuses toward the fence when the pollutant source is set in the upstream of the building. It influences little on the building. It is shown in Fig. 64.8c that CO diffuses toward the building when the pollutant source is in the leeward side of the building. And it causes the most serious pollutant of the building. It is shown in Figs. 64.8b and 64.9 that CO diffuses between the fence and the building with the pollutant source in the middle area along the buildings in the x-axis direction. In addition, the concentration of CO reduces gradually when it diffuses from the pollutant source to the ground along the positive x-axis direction. The harmful effect of the CO diffusion on the building environment is the least when the pollutant source is in the upstream of the building.

(a)   **(b)**

(c)
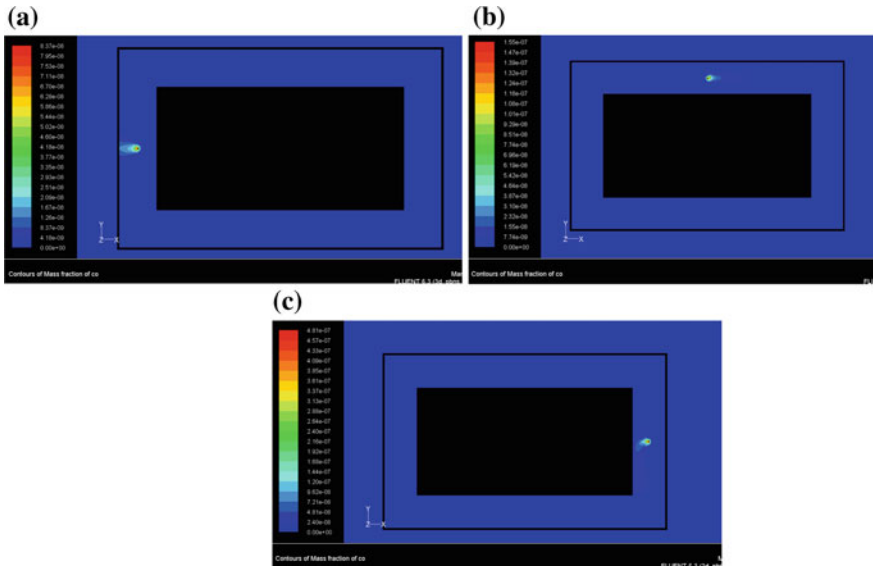
Fig. 64.8 CO diffusion when a pollutant source is located at different places, **a** CO source is at $x = -11.5$, $y = 0$, $z = 0.4$, **b** CO source is at $x = 0$, $y = 6.5$, $z = 0.4$, and **c** CO source is at $x = 11.5$, $y = 0$, $z = 0.4$

Fig. 64.9 The contour of mass fraction of CO the cross-section at $y = 0$ m with pollutant source at the point (0, 6.5, 0.4)
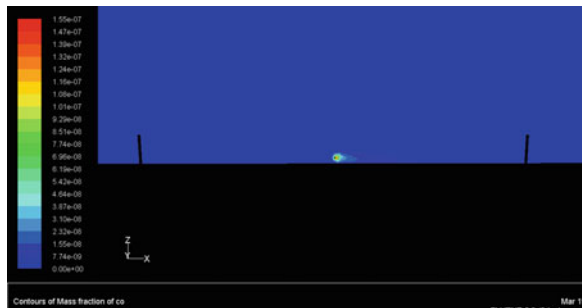
64.4 Conclusion

Fluent software is used in this paper to simulate the effect of the fence for urban residence communities on the diffusion of traffic pollutant source. The diffusion of CO, a typical traffic pollutant, is calculated in the simulation and the k-ε model with RANS used in the calculation.

The results show that (1) the fences hinder the diffusion of the CO on the horizontal direction, but they promote the diffusion in the vertical direction. (2) The higher the fence, the more the CO concentration between the fence and the building. (3) When a ground pollutant source is on the leeward side of a building,

it poses the greatest threat to the air quality around the building. It has the least threat when it is set on both sides of the building in wind direction.

References

1. Sun J, Dai Y (2012) Forecast and assessment on exhaust gases pollutants of basement parking. Environ Prot Sci 38(3):99–101
2. Huang Y, Wang S, Jin X, Sun Y, Jin M (2008) A comparative study of various turbulence models for simulating pollutant dispersion within an urban street canyon. The study and possess on hydrodynamics. Special A 2:189–195
3. Gousseau P, Blocken B, Stathopoulos , van Heijst GJF (2011) CFD simulation of near-field pollutant dispersion on a high-resolution grid: a case study by LES and RANS for a building group in downtown Montreal. Atmos Environ 47:428–438

Chapter 65
Research on the Vertical Distribution of Air-Conditioning Load in a Thousand-Meter Scale Megatall Building

Junliang Cao, Jing Liu, Chunliang Zhang and Xiaoxin Man

Abstract This paper analyzes the impact of height on the air-conditioning (A/C) load for a hypothetical thousand-meter scale megatall building in Beijing by both the energy simulation software TRNSYS16 (Transient System Simulation Program) and the mesoscale meteorological model WRFV3.4.1 (Weather Research and Forecasting Model). We assumed that the building would be an office building according to the investigation on the use of the supertalls and megatalls that had been constructed. We modified the database of TRNSYS16 according to the result from WRF based on the vertical distribution of the atmospheric parameters used in the calculation of building A/C load and calculated the A/C load of each room at different heights. The result shows that the A/C load gradually decreased with the increase in the height. The room A/C load at the height of 1000 m above the ground was 30 % less than that close to the ground.

Keywords Megatall · Mesoscale meteorological model · Air-conditioning load

65.1 Introduction

The tall building room of the past decades has been unprecedented in that it has taken place across virtually the entire globe simultaneously. By the end of 2012, the statistic shows that 58 of 100 tallest buildings in the world have been completed in the past seven years. According to Council on Tall Buildings and Urban

J. Cao · J. Liu
School of Municipal and Environmental Engineering, Harbin Institute of Technology, Harbin 150090, China

J. Cao · J. Liu (✉) · C. Zhang · X. Man
State Key Laboratory of Urban Water Resource and Environment, Harbin Institute of Technology, Harbin 150090, China
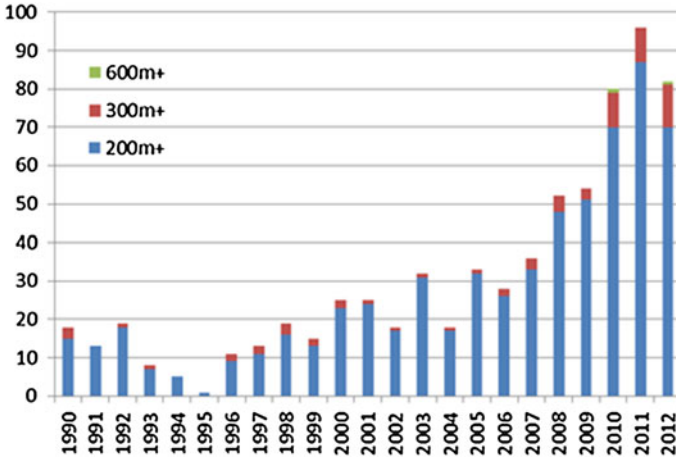e-mail: liujinghit0@163.com

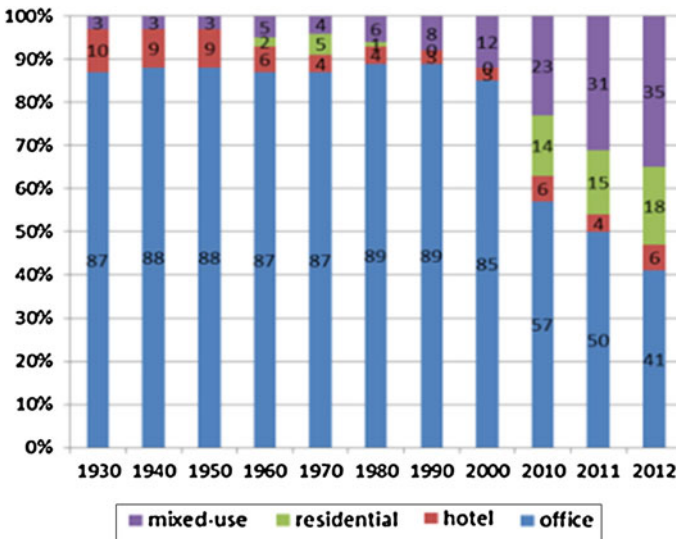**Fig. 65.1** Number of tall buildings

Fig. 65.2 Use of tall buildings

Habitat (CTBUH), the supertall is defined as a building over 300 m and the megatall as a building over 600 m. As the graph shows (see Fig. 65.1) the total number of buildings over 200 m in existence globally. It is more than double level in the last ten years. The function of the tallest building has been changing, but the office buildings are still in a large proportion (see Fig. 65.2) [1]. With the increase in the number and the height, the cooling load calculation of the tall buildings has brought the designers new problems. The heights of megatalls have gone far

beyond the ordinary buildings, and the parameter of the design code could not meet the needs of the megatallls yet. In this study, we used the mesoscale meteorological model WRFV3.4.1 to simulate the air relative humidity and temperature values along the vertical direction in Beijing, which was widely used in meteorology; then, we got the variation of the parameters along the vertical direction and calculated the air-conditioning load of rooms at different heights in a hypothetical thousand-meter scale megatall building in Beijing by the software of TRNSYS16.

65.2 Method of Research

65.2.1 Combination of WRF and TRNSYS

WRF model is a numerical weather prediction (NWP) and atmospheric simulation system designed for both research and operational applications. The development of WRF has been a multi-agency effort to build a next-generation mesoscale forecast model and data assimilation system to advance the understanding and prediction of mesoscale weather and accelerate the transfer of research advances into operations. WRF reflects flexible, state of the art, portable code that is efficient in computing environments ranging from massively parallel supercomputers to laptops. It is suitable for a broad span of applications across scales ranging from large eddy to global simulations [2].

We simulated the distribution of the air temperature and relative humidity with by WRF and got the variation of the parameters along the vertical direction. According to the previous results, we modified the weather database of TRNSYS16 with the height. Finally, the cooling load was calculated with the modified parameters. Figure 65.3 shows the concise information of this research.

65.2.2 Calculation Conditions

65.2.2.1 Atmospheric Conditions

In our study, the model was designed as follows: We used WRFV3.4.1 and made the simulation area quadruple nested with 37 levels in vertical direction (default levels). The simulation domains are shown in Fig. 65.4. The WRF model is built over a parent domain (1) with 120 km of spatial resolution, covering all of Beijing area. The first nested domain (2), with a spatial resolution of 70 km, comprises the main city center of Beijing. The second domain (3) has a spatial resolution of 3.7 km. The innermost domain (4) has a spatial resolution of 0.4 km, and it is focused on the chosen area to simulate. All domains are centered in a point with

Fig. 65.3 Concise
information of research
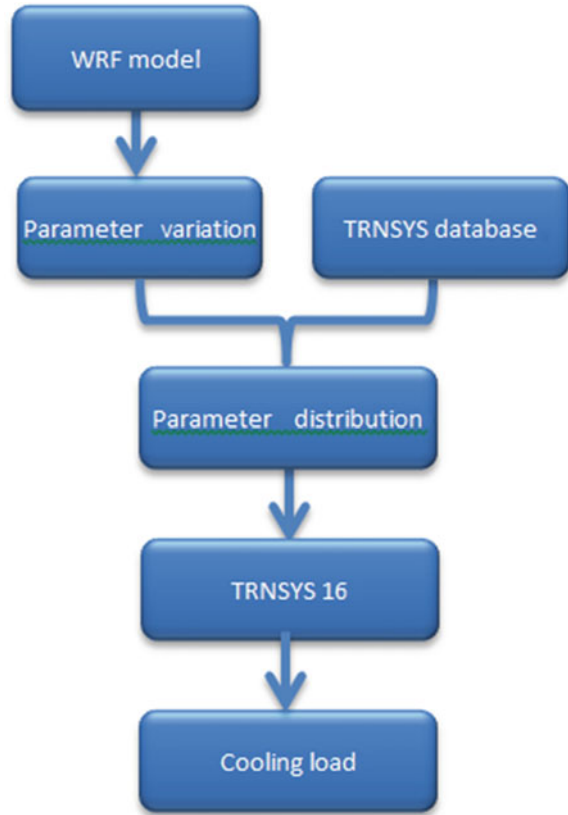
the coordinates: latitude $= 39°54'20''$, longitude $= 116°25'29''$, and they interact
with each other through a two-way nesting strategy [3].

65.2.2.2 Building Model

There is no such a standard building that can represent all the actual situations. In
this study, we selected a normal rectangle office building model in Beijing that has
normal typical floor (see Fig. 65.5), which is consisted of office rooms with the
same area. We calculated the cooling loads of the rooms of each orientation by the
software of TRNSYS16 with the design conditions that the office hours are from
8:00 to 18:00 and one computer is for each person. The building envelope
parameters and calculation conditions are shown in Table 65.1 [4].

Fig. 65.4 Domains of
simulation
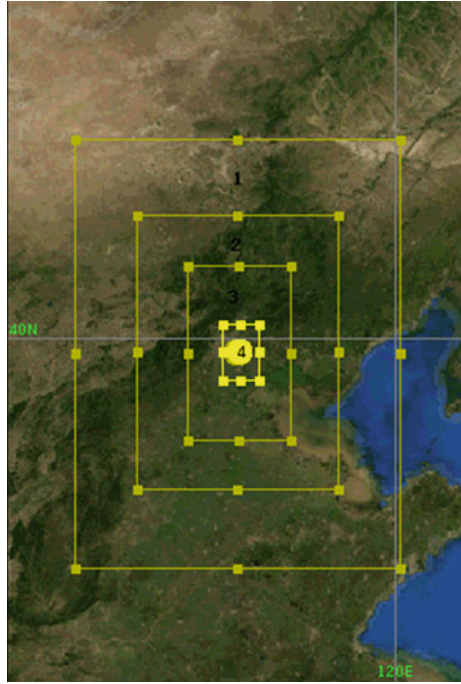
Fig. 65.5 Model for
simulation
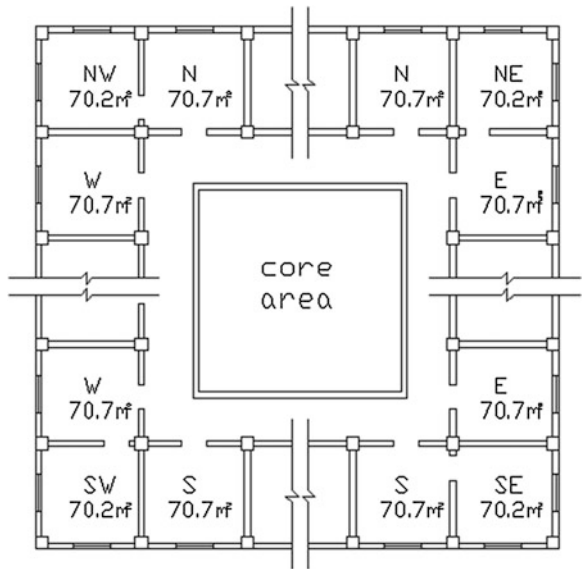
Table 65.1 Parameters of the load calculation

Parameter	Value
Heat transfer coefficient of exterior wall	0.6 W/(m^2 K)
Window/wall ratio	0.4
Heat transfer coefficient of exterior window	2.7 W/(m^2 K)
Effective area/total area of window	0.85
Shading coefficient of exterior window	0.86
Tn (design temperature)	25 °C
ψn (design relative humidity)	60 %
Occupant density	4 m^2/person
Equipment power	56 w/m^2
Lights	12 w/m^2
Air change of ventilation	2.2/h
Activity	Very light

65.3 Results and Analysis

65.3.1 Atmospheric Parameters Calculated by WRF

We simulated the origin meteorology data from 1 July to 7 July 2012 by WRFV3.4.1 and extracted the relative humidity and temperature of the air that range from 0 to 1,800 m above the ground. The average temperature of each hour in the simulation period variations is shown in Fig. 65.6.

The temperature decreases with the increase in the height in July. As the height increases beyond 500 m above the ground, the temperature begins to be lower than 25 °C all day long. The temperature close to the ground is in relatively large fluctuations with the time, and the daytime temperature is significantly higher than the night temperature. Daytime maximum temperature appears around 14:00, up to 30 °C, the lowest temperatures appears around 4:00, up to 22 °C. With the
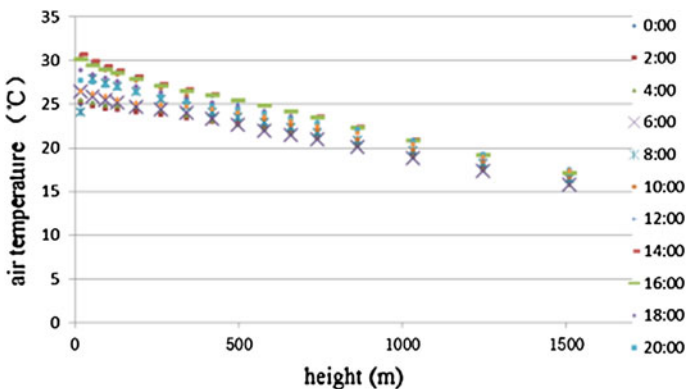
Fig. 65.6 Variation of temperature

increase in the height, the air absorbs less radiation of the ground and gradually decreases in temperature, resulting that the air temperature becomes lower with the time; at the height of 1,800 m, the fluctuation of the air temperature with time is relatively small. In order to illustrate the air temperature with height variation better, we defined the temperature gap θ:

$$\theta = T_b - T_x \qquad (65.1)$$

T_x The air temperature at the height of x meters above the ground (°C);
T_b The air temperature at the bottom of atmosphere (°C).

The variation of temperature gap θ with the height is shown in Fig. 65.7, and the fluctuations of θ with time are relatively small compared to the previous. From the diagram, the formula of the air temperature gap is as follows:

$$T_x = T_b - 0.0073x - 0.2713 \left(R^2 = 0.998\right) \qquad (65.2)$$

x The height of room above the ground (m).

By this formula, we calculated the outdoor temperature of the megatall building according to the data which is provided by TRNSYS16. Another parameter that determines the cooling load of a room is the air relative humidity. We got the variation of this parameter along the vertical direction as well as the air temperature. The average air relative humidity in the simulation period variations is shown in Fig. 65.8.
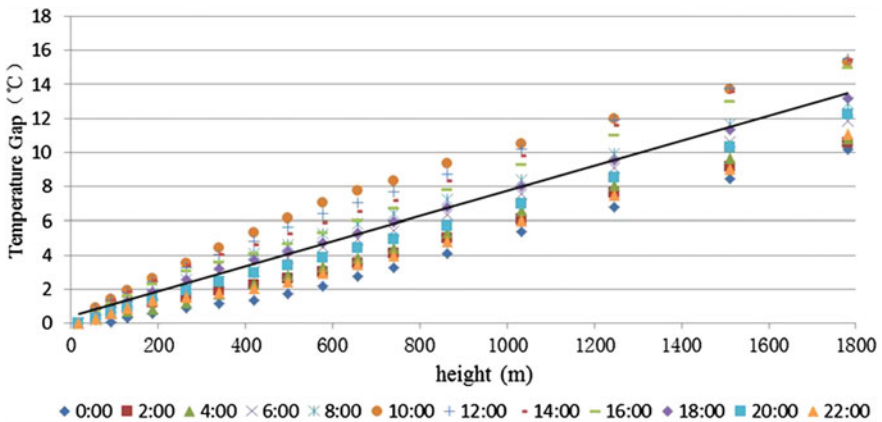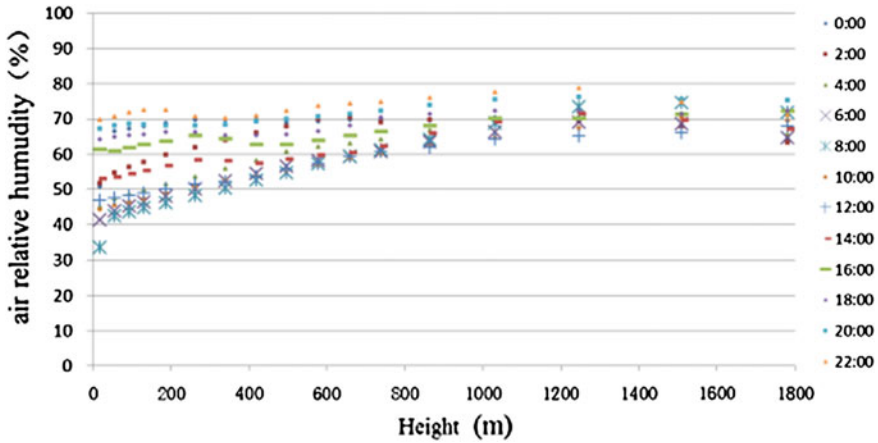

Fig. 65.7 Variation of temperature gap

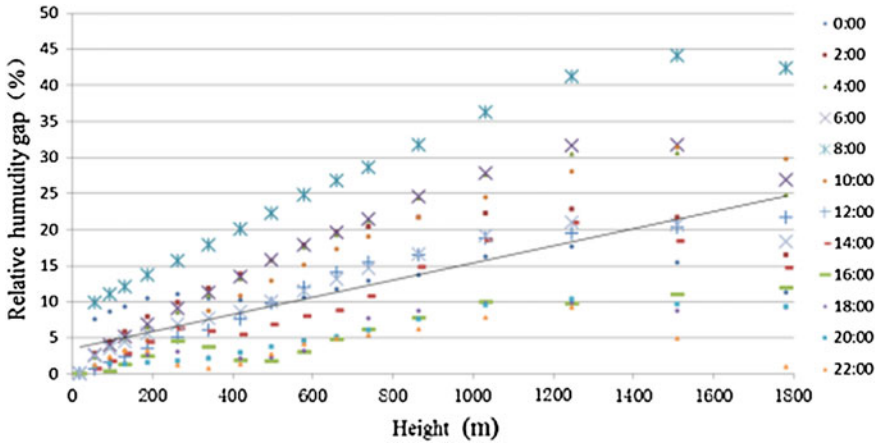**Fig. 65.8** Variation of relative humidity in July

Fig. 65.9 Variation of relative humidity gap

The air relative humidity increases with the height elevated. In the lower position, the relative humidity range variation with time is relatively large. As the height increasing, the radiation effects from the ground gradually reduced, coupled with the influence of air temperature decreasing, the relative humidity of the air changes with time and gradually weaken. We defined air relative humidity gap as follows:

$$\varphi = \varphi_b - \varphi_x \tag{65.3}$$

φ_x The air relative humidity at the height of x meters above the ground (%);
φ_b The air relative humidity at the bottom of atmosphere (%).
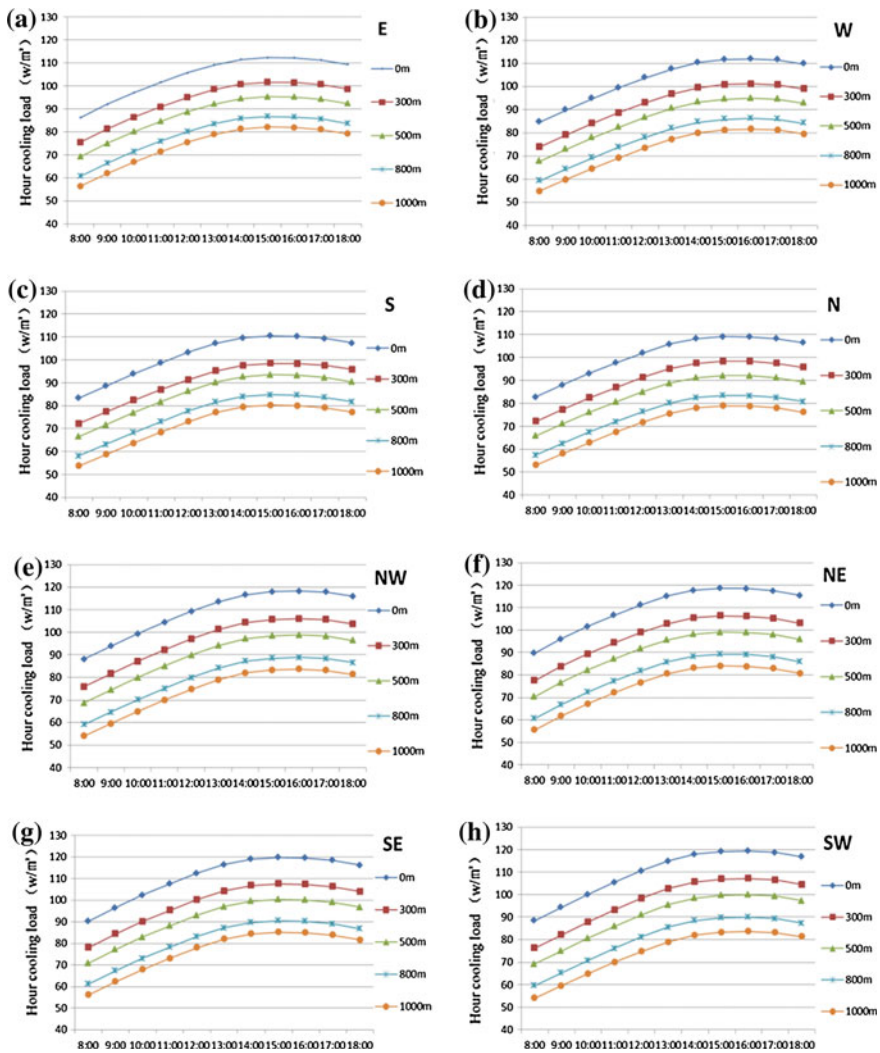
Fig. 65.10 Variation of hourly cooling load with height. **a** E. **b** W. **c** S. **d** N. **e** NW. **f** NE. **g** SE. **h** SW

The variations of the air relative humidity gap are shown in Fig. 65.9. The formula of air relative humidity gap is as follows:

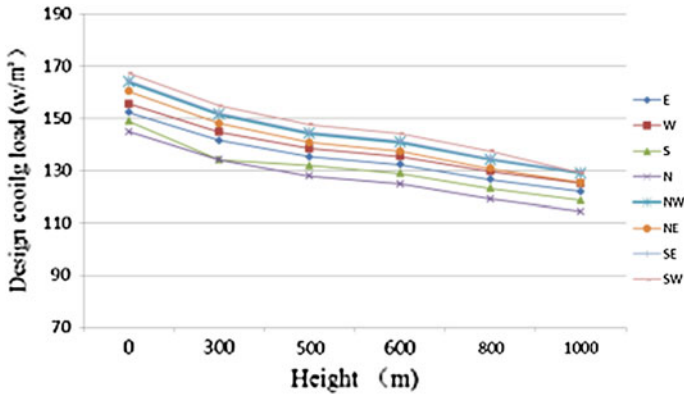$$\varphi_x = \varphi_b - 0.0118x - 3.5506 \ (R^2 = 0.897)$$ (65.4)

Fig. 65.11 Variation of design cooling load with height

65.3.2 Cooling Load Calculation

By the formulas above, the air parameters of TRNSYS16 had been modified. In this study, we calculated the A/C loads of the rooms above the ground 0, 300, 500, 800, and 1,000 m from 1 July to 31 July. The average hourly cooling loads of this period are shown in Fig. 65.10.

The hourly cooling loads of different orientations gradually decrease with the increase in the height. We define the maximum hourly cooling load in the calculation period as the design cooling load. Figure 65.11 shows the relationship between the design cooling load and the height. We notice that the design cooling load decreases more sharply with the increase in the height where the room is lower than 500 m. The ground radiation plays an important role in air temperature at a lower position. As the height increases, this impact becomes weaker. At the same time, the design cooling load is relatively light where the room is over 500 m, and the design cooling load is 30 % less where the room is at the height of 1,000 m than that close to the ground. As the height increases, especially a thousand-meter scale megatall building, the A/C loads of the rooms have changed a lot. If the designers follow the traditional design code to calculate the load, this would not only lead to inaccurate load calculation and energy wasting, but also would make the comfort greatly reduced. To solve this problem, we suggest developing more reasonable specific design code to adapt to characteristics of various megatall buildings.

References

1. Wood A, Johnson T, Li GQ (2012) Multi-disciplinary paper on tall buildings and sustainable cities. Council on Tall buildings and Urban Habitat
2. WRF ARW Version 3 Modeling System User's Guide (2012) USA, National Center for Atmospheric Research
3. David C, Alfred R, Moncho G, Carlos S (2012) A sensitivity study of the WRF model in wind simulation for an area of high wind energy. Environ Model Softw 33:23–24
4. Pan YG (2006) Design cooling load and cooling consumption in office buildings in Beijing area. Heating ventilating and air conditioning. HAVC 36(1):35

Chapter 66
Application and Numerical Investigation of Novel Dust-Controlling Equipments of Main Fan Diffuser in Industry Square of Coal Mine

Shiqiang Chen, Haiqiao Wang and Yiqun Li

Abstract Based on parameters of main fan diffuser in such a coal mine, the paper set forward two novel types of dust-controlling equipment, and the physical models of two equipments are constructed. Kinetic and dynamic fields of two-phase flow in two equipments are numerically calculated, and the both coefficients of performance are comparatively analyzed. The results are shown as follows: (1) in the condition of non-dust-controlling equipment, the dust pollutes the industry square of the coal mine; (2) the two novel dust-controlling equipments can decrease the quantity of escaping dust; (3) the efficiency of dust controlling of equipment of closed-baffles diffuser is higher than that of the non-baffle diffuser; (4) the energy consumed of equipment of enclosed-baffles diffuser is lower than that of non-baffle diffuser. According to technique and engineering, the reformation application is dust-controlling equipment of non-baffle, the data are shown that the novel equipment can control partly the dust escaping, and the dust pollution can be relieved in the industry square of coal mine.

Keywords Dust-controlling equipment · Coal dust pollution · Industry square · Numerical calculation · Reformation application

66.1 Introduction

Always researchers have paid almost all attention on control and treatment of coal dust in underground working places. The theories and techniques of control coal dust in ground places are inadequately discussed and researched. However, the coal dust escaped from main fan diffuser of coal mine is main pollution source of

S. Chen (✉) · H. Wang · Y. Li
School of Mining and Safety Engineering, Hunan University of Science and Technology, Xiangtan 411201 Hunan, China
e-mail: zunyichsq@163.com

decreased environment quality of industry square [1–6]. For improving environment quality of coal mine ground, researches of techniques and equipments of main fan diffuser are important practical and environmental benefits [7–9].

66.2 Physics Models

The physics model of main fan diffuser of coal mine is originated from Xingdong Mine in Xingtai, Hebei Province, P.R. of China. The sizes of physics model are shown in Figs. 66.1 and 66.2. In the running time, one fan runs, and other fan is spare. So, one diffuser outflows, and other diffuser is spare. Therefore, the section area of main fan diffuser is $5.5 \times 3.2 \text{ m} = 17.6 \text{ m}^2$.

Through field investigation, coal dusts that escaped from main fan diffuser and discharged into air environment are large quantity and broad particle size distribution. And the largest diameter is more than 5×10^{-3} m. These coal particles carried by air flow of main fan diffuser, are diffused with exhaust air, and then slowly are settled to ground by gravity. The settled coal particles directly polluted industry square of Xingdong Mine. For the improvement of environment quality of industry square, decreased quantity of coal particles of directly discharged into air environment is effective approach of treating coal dust. And in order to resistance of control equipment little affected on mine system as possible, it is necessary that the energy consumed of equipment is deceased to such a limit. From the above, in application of inertia separation and gravity sedimentation, two types of control coal dust of main fan diffuser of coal mine are designed. And the physics models are shown in Figs. 66.3 and 66.4.

Fig. 66.1 Photograph of air shaft outlet of coal mine before reformation
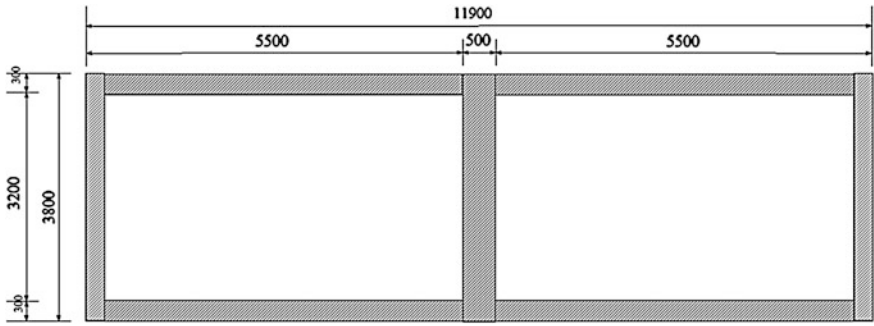
Fig. 66.2 *Top view* drawing of air shaft outlet of coal mine before reformation
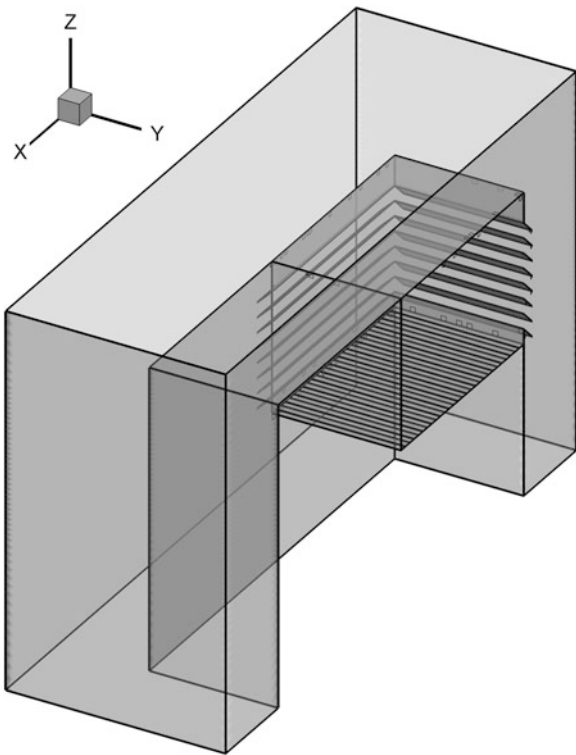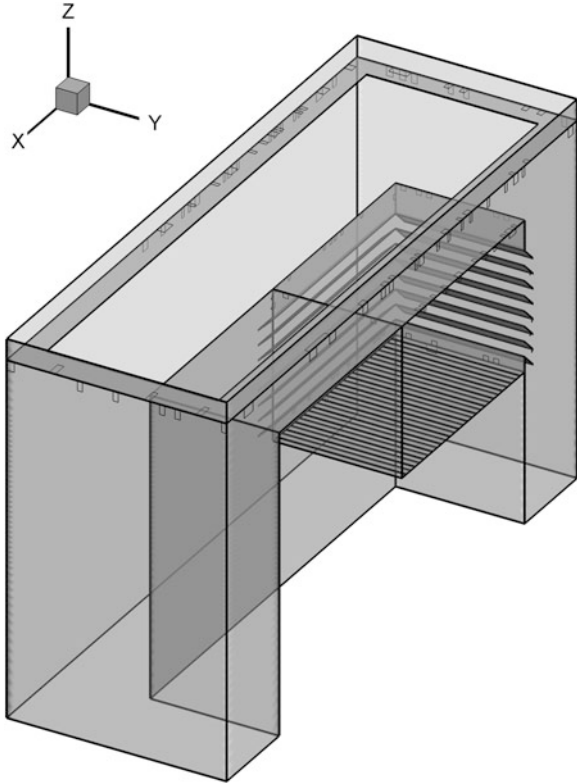
Fig. 66.3 Main fan diffuser of non-baffle

66.3 Numerical Simulation and Results Analysis

66.3.1 Numerical Simulation and Results Analysis of Air Phrase in Equipment

Two physics models of dust-controlling equipment are constructed and meshed by virtue of Gambit3.23. In application of FLUENT6.3 software package, turbulent model is realizable k-epsilon, and coupling algorithm is SIMPLE, and difference scheme is first upwind [10–14]. And the initial values of inlet velocity condition of air phrase are in sequence of 8 and 10 m/s. Numerical simulations of two types of dust-controlling equipment are investigated by FLUENT6.3. On the basis of the above, numerical calculations of non-baffle and closed baffles, and the static pressure distributions, velocity distributions and streamline distributions are analyzed. The results are shown in Figs. 66.5, 66.6, 66.7, 66.8, 66.9, 66.10, 66.11, 66.12, 66.13 and 66.14.

In Figs. 66.5 and 66.6, static pressure distribution of dust-controlling equipment of non-baffle main fan diffuser of coal mine has 5 characteristics. (1) In the diffuser
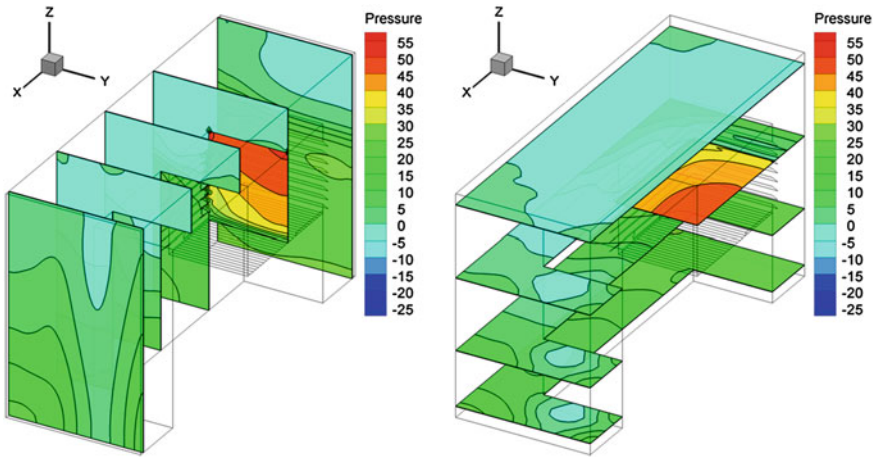
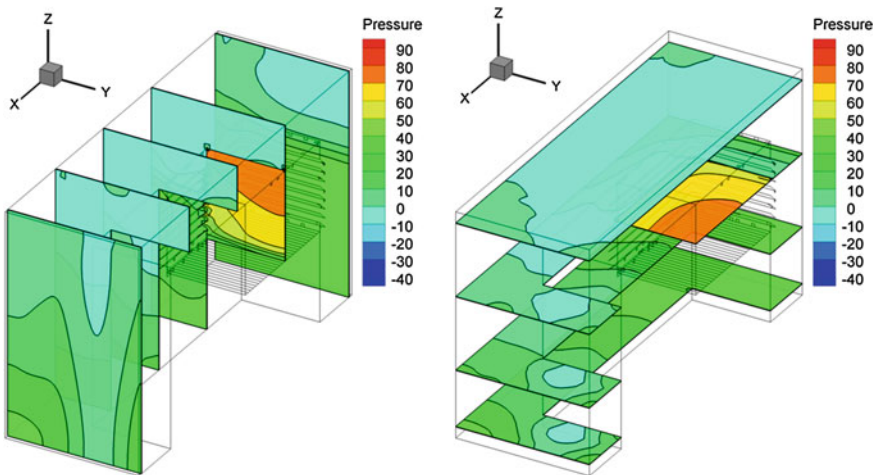**Fig. 66.5** Slice graph of static pressure distribution of main fan diffuser of non-baffle (v = 8 m/s)

Fig. 66.6 Slice graph of static pressure distribution of main fan diffuser of non-baffle (v = 10 m/s)

of main fan, the down zone is low, and the up zone is high. (2) In the diffuser of main fan, the zone near to guide vanes is low, and the zone far from guide vanes is high. (3) In cavity zone from diffuser outlet to main fan diffuser, the static pressure in zone near to diffuser outlet is high, and the static pressure in zone far from diffuser outlet is low. (4) In this cavity zone of dust-controlling equipment, the up is low, and the down is high. (5) In this cavity zone of dust-controlling equipment, the central is low, the corner is high. Through synthetic analysis of Figs. 66.5 and
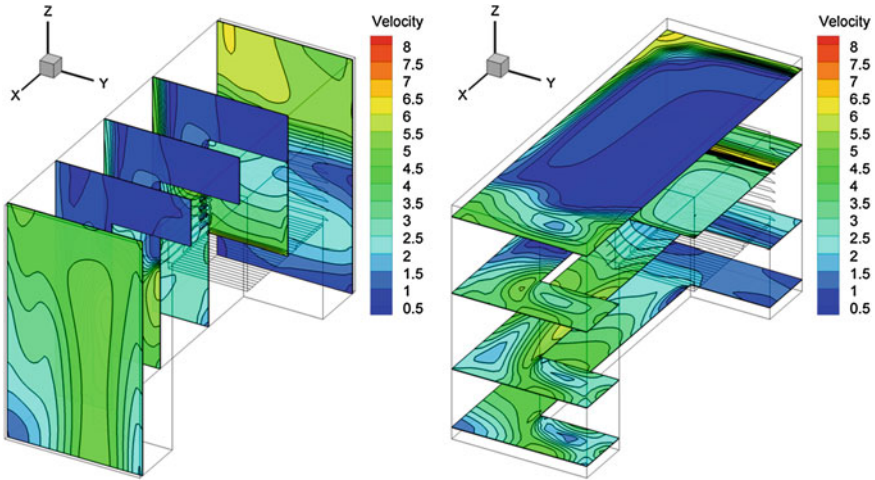
Fig. 66.7 Slice graph of velocity distribution of main fan diffuser of non-baffle (v = 8 m/s)
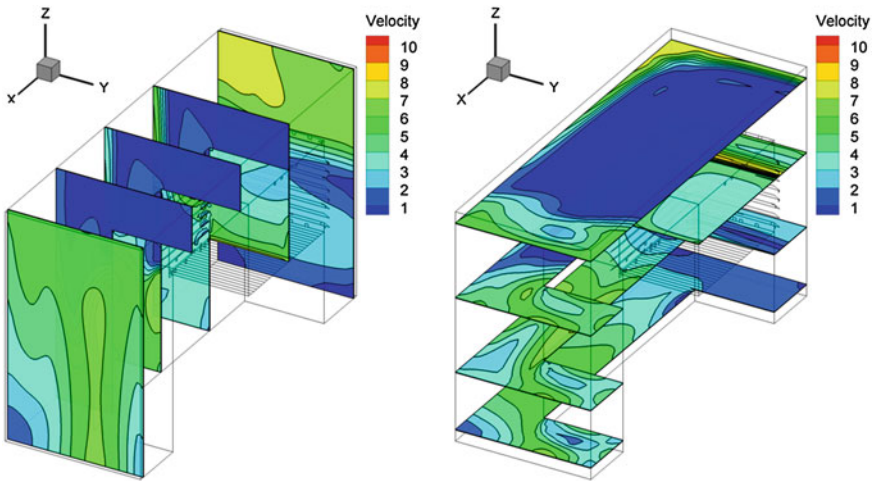

Fig. 66.8 Slice graph of velocity distribution of main fan diffuser of non-baffle (v = 10 m/s)

66.6, the static pressure distributions of numerical simulation cases of boundary condition of 8 m/s and boundary condition of 10 m/s are similar.

In Figs. 66.7 and 66.8, velocity distribution of dust-controlling equipment of non-baffle main fan diffuser of coal mine has 4 characteristics. (1) In the diffuser of main fan, the down zone is high, and the up zone is low. (2) In the diffuser of main fan, the zone near to guide vanes is high, and the zone far from guide vanes is low. (3) In cavity zone from diffuser outlet to main fan diffuser, the zone near to diffuser outlet is high, and the zone far from diffuser outlet is low. (4) In this cavity zone,
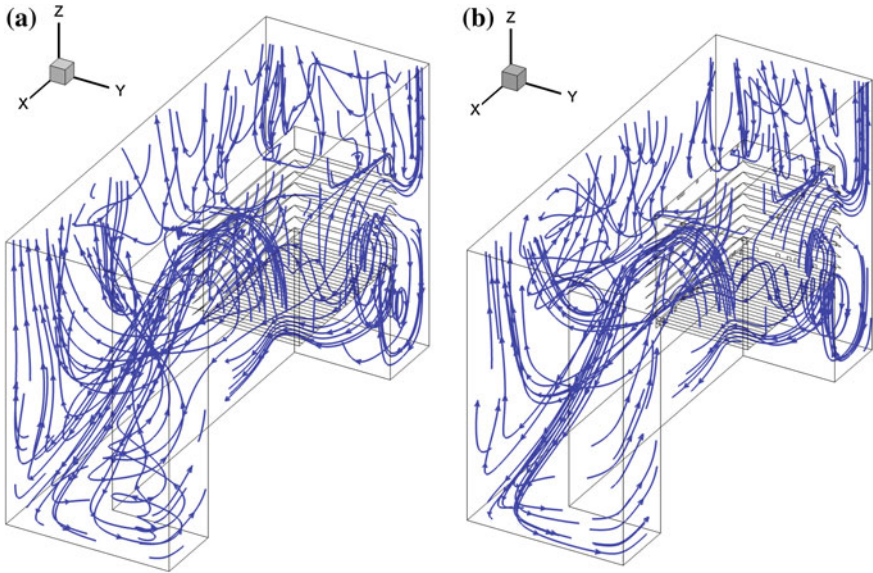
Fig. 66.9 Spatial streamline graph of main fan diffuser of non-baffle, (**a**) v = 8 m/s, (**b**) v = 10 m/s

Fig. 66.10 Slice graph of static pressure distribution of main fan diffuser of closed baffles (v = 8 m/s)

the range of low velocity zone in up the cavity zone is large, and the range of high velocity zone in the down cavity zone is small. Through synthetic analysis of Figs. 66.7 and 66.8, the two velocity distributions of numerical simulation cases of boundary condition of 8 m/s and boundary condition of 10 m/s are similar.

Fig. 66.11 Slice graph of static pressure distribution of main fan diffuser of closed baffles (v = 10 m/s)
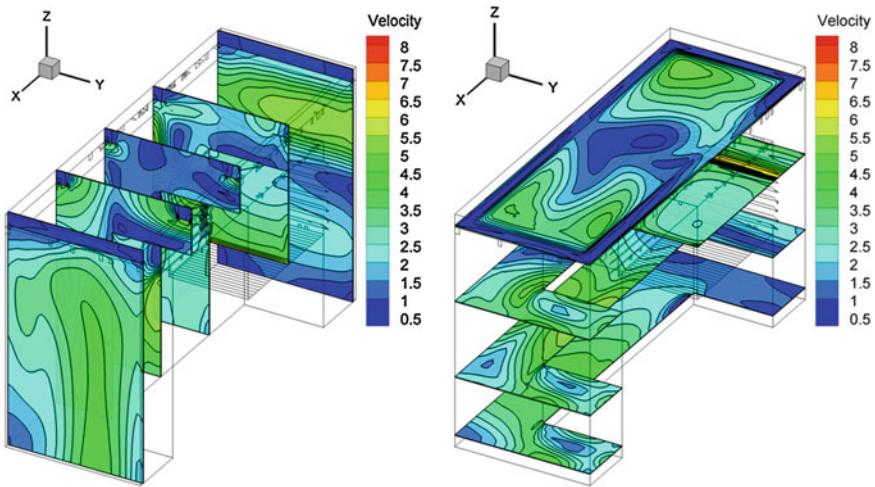
Fig. 66.12 Slice graph of velocity distribution of main fan diffuser of closed baffles (v = 8 m/s)

In Fig. 66.9a and b, spatial streamline distribution of dust-controlling equipment of non-baffle main fan diffuser of coal mine has 4 characteristics. (1) In whole zone of the dust-controlling equipment, outflow zones are several. (2) Guide vanes have obvious effects of flow interference, and flow around is realized. (3) In whole zone, there consist in distinct vortexes of flow around, and the effects of flow around are strong. (4) In whole zone, there are partitions of flow around, and there

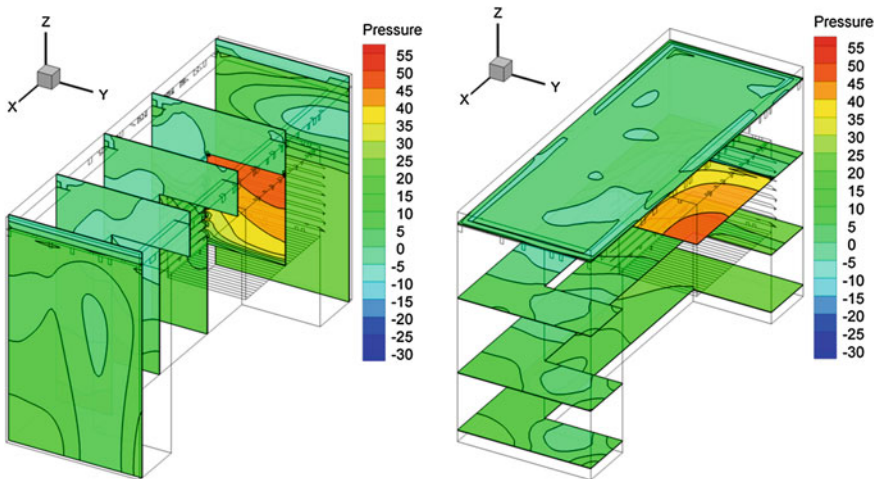**Fig. 66.13** Slice graph of velocity distribution of main fan diffuser of closed baffles (v = 10 m/s)

Fig. 66.14 Spatial streamline graph of main fan diffuser of closed baffles, (**a**) v = 8 m/s (**b**) v = 10 m/s

consist in 3 large size partitions of flow around. Through synthetic analysis of Fig. 66.9, the two spatial streamline distributions of numerical simulation cases of boundary condition of 8 m/s and boundary condition of 10 m/s are similar.
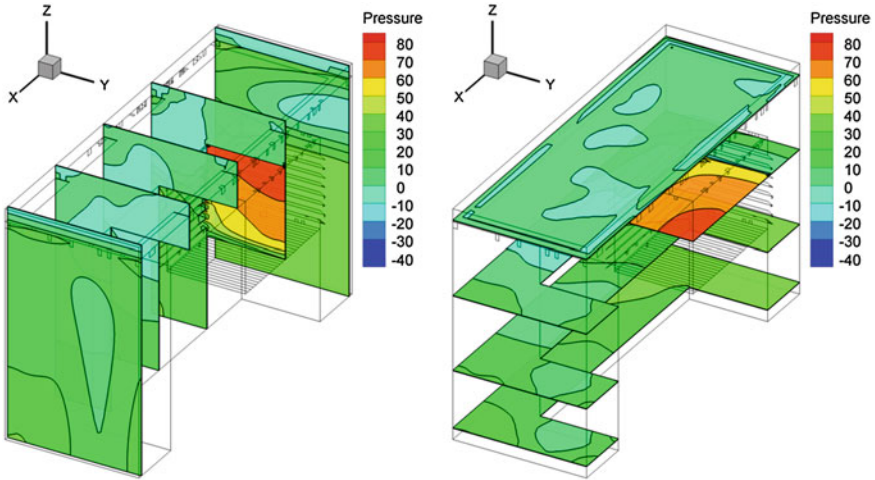
In Figs. 66.10 and 66.11, static pressure distribution of dust-controlling equipment of closed baffles main fan diffuser of coal mine has 5 characteristics. (1) In the diffuser of main fan, the down zone is low, and the up zone is high. (2) In the diffuser of main fan, the zone near to guide vanes is low, and the zone far from guide vanes is high. (3) In cavity zone from diffuser outlet to main fan diffuser, the static pressure in zone near to diffuser outlet is high, and the static pressure in zone far from diffuser outlet is low. (4) In this cavity zone of dust-controlling equipment, the up is low, the down is high. (5) In this cavity zone of dust-controlling equipment, the central is low, and the corner is high. Through synthetic analysis of Figs. 66.10 and 66.11, the static pressure distributions of numerical simulation cases of boundary condition of 8 m/s and boundary condition of 10 m/s are similar.

In Figs. 66.12 and 66.13, velocity distribution of dust-controlling equipment of closed baffles main fan diffuser of coal mine has 4 characteristics. (1) In the diffuser of main fan, the down zone is high, and the up zone is low. (2) In the diffuser of main fan, the zone near to guide vanes is high, and the zone far from guide vanes is low. (3) In cavity zone from diffuser outlet to main fan diffuser, the zone near to diffuser outlet is high, and the zone far from diffuser outlet is low. (4) In this cavity zone, the range of low velocity zone in up the cavity zone is small, and the range of high velocity zone in the down cavity zone is large. Through synthetic analysis of Figs. 66.12 and 66.13, the two velocity distributions of numerical simulation cases of boundary condition of 8 m/s and boundary condition of 10 m/s are similar. In Fig. 66.14, see (a) and (b), spatial streamline distribution of dust-controlling equipment of closed baffles main fan diffuser of coal mine has 4 characteristics. (1) In whole zone of the dust-controlling equipment, outflow zones are several. (2) Guide vanes have obvious effects of flow interference, and flow around is realized. (3) In whole zone, there consist in distinct vortexes of flow around, and the effects of flow around are strong. (4) In whole zone, there are pa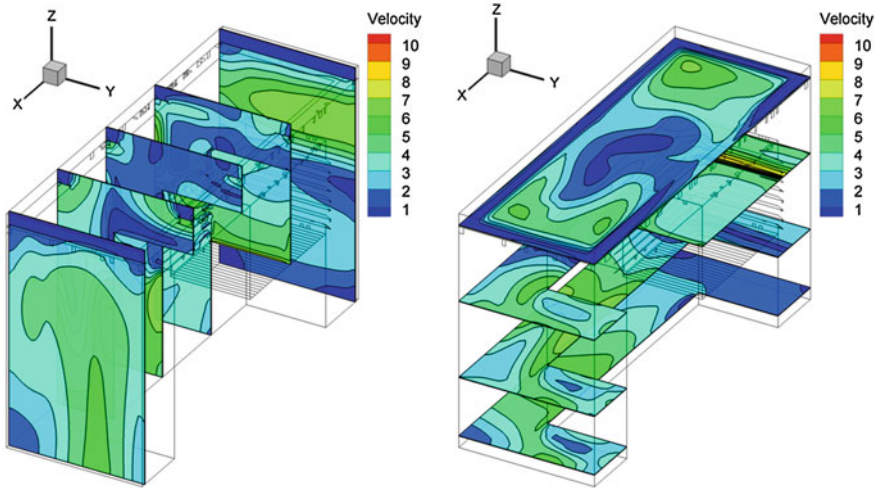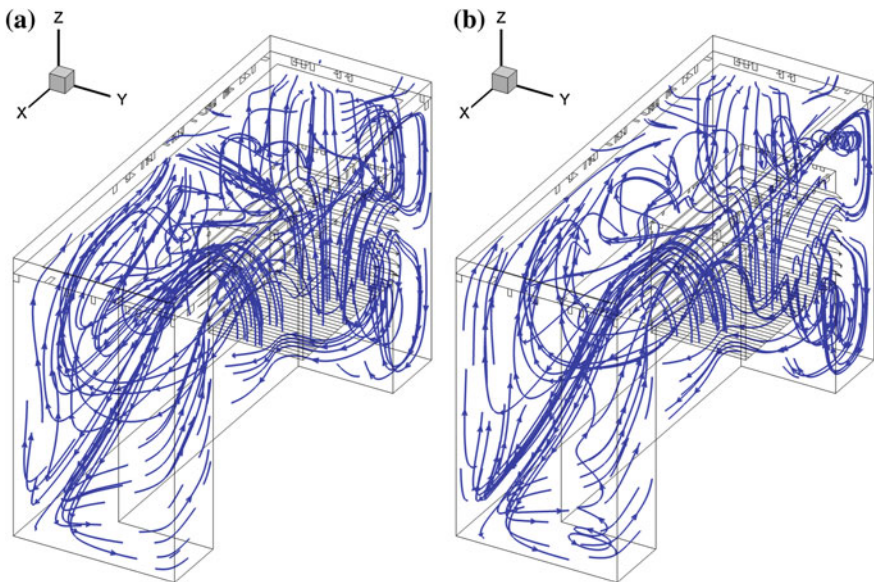rtitions of flow around, and there consist in 6 large size partitions of flow around. Through synthetic analysis of Fig. 66.14, the two spatial streamline distributions of numerical simulation cases of boundary condition of 8 m/s and boundary condition of 10 m/s are similar.

Through synthetic analysis of Figs. 66.5, 66.6, 66.10, and 66.11, the results are shown. (1) In the outlet section, the area of low pressure of non-baffle is larger than closed baffles. (2) In diffuser, the area of high pressure of non-baffle is larger than closed baffles. Through synthetic analysis of Figs. 66.7, 66.8, 66.12 and 66.13, the results are shown. (1) In the outlet section, the area of low velocity of non-baffle is larger than closed baffles. (2) In the outlet section, there consist in the central the zones of low velocity of non-baffle, and the corners and boundary zones are as far as closed baffles. (3) In diffuser, the area of high velocity of non-baffle is smaller than closed baffles. Through synthetic analysis of Figs. 66.9 and 66.14, the results are shown. (1) There consist in 3 large size partitions of flow around in non-baffle and 6 large size partitions of flow around in closed baffles. (2) There do not consist in flow around in non-baffle, and there consist in flow around in corners and boundary zones of closed baffles.

66.3.2 Numerical Simulation and Energy-Consumed Analysis of Air Phrase in Equipments

For research of energy consumed of two types of dust-controlling equipment, by method of area-weighted average, inlet pressure values, and outlet pressure values of two equipments are analyzed, and the results are shown in Tables 66.1 and 66.2.

From Tables 66.1 and 66.2, it is shown that total pressure values and static pressures values of two equipments are approached in inlet and outlet, and the resistance values are, respectively, 68.32 and 64.84 Pa; furthermore, the value of non-baffle is higher 3.48 than that of closed baffle. So, the difference of energy-consumed values of two equipments is little. Furthermore, the effects of two equipments on mine ventilation system are similar.

66.3.3 Numerical Simulation of Coal Particle and Analysis of Dust-Controlling Effect

In numerical simulation investigations of control equipments by FLUENT6.3, the boundary conditions are as follows: (1) While the initial values of inlet velocity of air phrase is 10 m/s, the initial values of inlet velocity of discrete phase is 8 m/s, and the weight of discrete phase is 42.56 g/s. (2) While the initial values of inlet velocity of air phrase is 8 m/s, the initial values of inlet velocity of discrete phase is 6 m/s, and the weight of discrete phase is 42.56 g/s. (3) The discrete phase is the group of coal particle and in accords with the distribution of Rosin–Rammler; its particle diameters are 6 sizes; the largest diameter is 0.12 mm, the smallest diameter is 0.02 mm, and the average diameter is 0.079 mm; the coefficient of diffusion is 3.676. (4) By 500 times of iteration of

Table 66.1 Between inlet pressure and outlet pressure of fan diffuser of non-baffle

Inlet velocity (m/s)	Average value of total pressure (Pa)		Average value of dynamic pressure (Pa)		Average value of static pressure (Pa)	
	Inlet	Outlet	Inlet	Outlet	Inlet	Outlet
8	46.41	2.73	29.06	2.59	18.35	0.11
10	72.60	4.28	45.34	4.28	28.80	0.17

Table 66.2 Between inlet pressure and outlet pressure of main fan diffuser of closed baffles

Inlet velocity (m/s)	Average value of total pressure (Pa)		Average value of dynamic pressure (Pa)		Average value of static pressure (Pa)	
	Inlet	Outlet	Inlet	Outlet	Inlet	Outlet
8	44.82	3.18	29.06	3.32	16.76	0.06
10	69.77	4.93	45.33	5.01	25.97	0.09

Table 66.3 Dust-controlling coefficient of two types of main fan diffuser (v = 8 m/s)

Items	%			
	<100um	100um	120um	Total efficiency
Non-baffle	18.00	31.22	44.66	18.86
Closed baffles	24.46	41.20	54.87	28.35

Table 66.4 Dust-controlling coefficient of two types of main fan diffuser (v = 10 m/s)

Items	%			
	<100um	100um	120um	Total efficiency
Non-baffle	17.42	28.27	39.31	18.13
Closed baffles	22.33	35.56	47.00	23.13

the air phrase coupled with one time of discrete phase, the coupled calculation of air-discrete phrase is simulated. (5) By this way, numerical simulations of two types of dust-controlling equipment are investigated. The results of numerical simulation are shown in Tables 66.3 and 66.4.

In the Tables 66.2 and 66.3, as inlet velocity of air phrase adds and the velocity of coal particle increases, the probability of coal particle escaped from control equipment comes to higher, and the efficient of dust-controlling decreases. As far as two types of dust-controlling equipment, the main fan diffuser of non-baffle is lower than the main fan diffuser of closed baffles, and the efficiencies of dust-controlling are little related with the inlet velocity. From the above, it is shown that the key of dust-controlling efficient of equipment is structure feature.

66.4 Application of Main Fan Diffuser of Non-baffle

Through the above analysis, the results are shown. (1) As far as flowing distri-bution, the closed-baffles diffuser is better than non-baffle. (2) As far as energy consumed, the closed-baffles diffuser is lower than non-baffle, but the difference value is only 3.48 Pa. (3) As far as dust-controlling coefficient of total dust, in condition of 8 m/s of inlet velocity, the difference value of both is 9.48 and the value is 5.00 in 10 m/s of inlet velocity. Although the coefficient of performance of closed-baffles diffuser is higher than non-baffle diffuser, the construction of closed-baffles diffuser is more complex than that of non-baffle diffuser. Therefore, the reformation of fan diffuser is the application of non-baffle diffuser. The finished construction of non-baffle diffuser is shown in Fig. 66.15. Before reformation, the dust pollution is shown in Fig. 66.16, and the effective of controlling dust is shown in Fig. 66.17.

Fig. 66.15 The photograph of reformed fan diffuser in Xingdong Mine

Fig. 66.16 The photograph of dust pollution in interest-station of diffuser and industry square

Fig. 66.17 The photograph of controlling dust effective in corners of non-baffle equipment

66.5 Conclusions

1. The application of dust-controlling equipment of main fan diffuser of coal mine is an effective way of the treatment of coal dust pollution in industry square.
2. The adding of flow around measurements of main fan diffuser can increase the probability of inertia separation of coal dust and increase the probability of gravity sediment of coal dust.
3. The comprehensive consideration of techniques and engineering and the application of main fan diffuser of non-baffle are feasible. And the effective of controlling dust is basically acceptable.

References

1. Trenczek S (2000) Air pollution as a result of dust emission by coal mines. Mechanizacja i Automatyzacja Gornictwa 354:65–71
2. Ghose MK, Majee SR (2007) Characteristics of hazardous airborne dust around an Indian surface coal mining area. Environ Monit Assess. doi:10.1007/s10661-006-9448-6
3. Armbruster L (2003) 50 years coal research: dust control. Gluckauf 139(10):546–551
4. Mvssa (2002) Recent advances in dust control technology on South African underground coal mines. J Mine Vent Soc S Afr 55(4):138–144
5. Naidoo RN, Robins TG, Seixas N (2005) Differential respirable dust related lung function effects between current and former South African coal miners. Int Arch Occup Environ Health. doi:10.1007/s00420-005-0602-1
6. Trubitsyn A (2005) Coal cutting process and dust control. Russ Min 2:21–22
7. Qian MG, Xu JL, Miao XX (2003) Green technique in coal mining. J China Univ Min Technol 32(4):343–348
8. Qian MG, Xu JL, Miao XX (2007) Green mining of coal resources harmonizing with environment. J China Coal Soc 32(1):1–7
9. Miao XX, Qian MG (2009) Research on green mining of coal resources in China: current status and future prospects. J Min Saf Eng 26(1):1–14
10. Patankar SV, Spalding DB (1972) A calculation procedure for heat, mass and momentum transfer in three-dimensional parabolic flows. Int J Heat Mass Transf 2(15):1787–1806
11. Yakhot V, Orszag SA (1986) Renormalization group analysis of turbulence. J Sci Comput 1(1):39–51
12. Shih TH, Liou WW, Shabbir A (1995) A new k-ε eddy viscosity model for high Reynolds number turbulent flows model development and validation. Comput Fluids 24(3):227–238
13. Baron PA, Willeke K (2005) Aerosol measurement: principles, techniques, and applications. Wiley, New York
14. Anderson JD (2007) Computational fluid dynamics: the basics with applications. China Machine Press, Beijing

Chapter 67
The Influence of the High-Rise Buildings on Local Thermal Environment in Severe Cold Region

Jing Ao, Jing Liu, Shengjun Liu, Zhiqing Zhao and Biao Li

Abstract The aim of this study was to understand the influence of the architectural morphology on thermal environment of an urban residential district in severe cold region by taking a typical urban residential district in severe cold region as research object. The numerical simulation was carried out to study the buildings' impact on the local thermal environment under the different height in the center area and evaluate the contribution of wind speed and temperature to microclimatic effect based on the joint action of the wind velocity, temperature, and solar radiation in this residential district, and find the varied rules of the wind velocity and temperature by the change in the center regional buildings' height. In addition, the outdoor personnel comfort in this residential district was analyzed by the principle of estimation on aeolian environment. The results can provide theoretical reference for the buildings' planning and prediction of thermal environment in the severe cold area and has proved the feasibility of buildings' planning based on the microclimatic effects.

Keywords CFD · Severe cold region · Thermal environment · Principle of estimation on Aeolian environment

J. Ao · J. Liu (✉)
School of Municipal and Environmental Engineering, Harbin Institute of Technology, Harbin 150090, China
e-mail: liujinghit0@163.com

J. Liu · S. Liu · Z. Zhao · B. Li
State Key Laboratory of Urban Water Resource and Environment, Harbin Institute of Technology, Harbin 150090, China

67.1 Introduction

Under the rapid development of China's urbanization and the living standard, urban architecture should meet the indoor comfortable requirements and the outdoor requirements. Therefore, it is pivotal for urban architecture in the rational design of thermal environment. Unreasonable planning could have adverse impact on building regional microclimate, for example, unreasonable distance between residential buildings may cause the roadway wind effect, which would have an impact on neighboring constructions and pedestrian comfort in the streets [1]. Specially, in severe cold region, the excessive wind differential pressure around buildings could increase the cold air infiltration effect and heating load in winter, and cause more heat loss eventually. After a snow in winter, streets are easy to form a snowdrift and affect the pedestrian safety. Few people conduct the wind environment's research currently at urban residential district in severe cold region in winter. So, it is necessary to make up for the study on thermal environment at urban residential district in severe cold region in winter.

67.2 Physics Problems and Turbulence Model

### 67.2.1 The Description of Physics Problems

A residential district of Yichun City, Heilongjiang Province, is selected as the research object, its most frequent wind direction is northwest, its average temperature is −20 °C, and the relative humidity is 40 % in winter. Physical model is shown in Fig. 67.1. This paper analyzes the effect of the variable height of buildings based on the actual planning program in the center area on the thermal environment in residential district by changing the height of buildings No.1–14 (6, 9, 12, 15, 18 floors).

In this paper, the physical model is built by a tetrahedral mesh after the grid independence test; considering the computer's hardware, the mesh generation method is unstructured hybrid grid generation method [2] and finally the grid numbers are 2.21 million, shown as Fig. 67.1. Choosing the computational domain [3], the length of the computational domain is 10 times that of the highest building to the inflow direction and 18 times that of the outflow direction. The width is respectively 5 times and 9 times that of the highest building to the vertical flow direction; the height is 2.7 times.

67.2.2 Turbulence Model

Considering actual situation, this paper takes the Spalart–Allmaras one-equation turbulence model [4].

Fig. 67.1 1 The physical
model and unstructured
hybrid grid
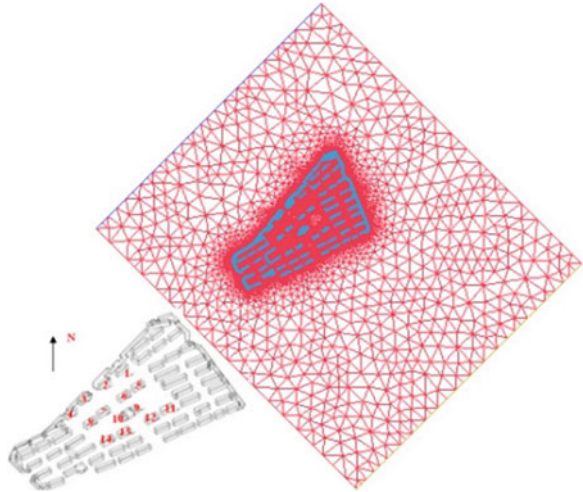
67.3 Research Methods and Settings

67.3.1 Research Methods

This paper takes a residential district in YiChun City as example to carry out the numerical simulation of the thermal environment and considers the effect of variable buildings on thermal environment in winter and the land surface and roof snowdrift. The DO Radiation Model and Solar Ray Tracing in Solar Load are used to calculate the temperature field in the residential district.

67.3.2 Boundary Conditions Settings

1. Inlet and outlet boundary condition

Inlet is set to the velocity entrance. According to the local weather date, the average wind velocity is 4.0 m/s in winter. Inlet velocity uses the exponential distribution function. Because the wind velocity was recorded at 10 m height in local weather station, the wind velocity function is chosen from the ASHRAE handbook along the height change [5]. In the paper, according to the terrain in computational domain in the ASHRAE handbook [5], the function of the wind velocity is obtained at the height of h, $V_h = 1.477 \times h^{0.22}$. The outlet is set to free outflow boundary.

2. Wall surface boundary condition

Top and both side surface boundary conditions are set to symmetry boundary. Buildings and bottom boundary conditions are set to no-slip wall boundary.

3. Solar radiation calculation conditions

Choosing sunny coefficient as 0.8, BC type is set to opaque. The absorptivity and reflectivity are set because the land and buildings' surfaces have been covered by snow in severe cold region. In this paper, the emissivity in building surface is 0.97, the direct visible absorptivity is 0.28, and the direct IR absorptivity is 0.97 [6].

67.4 Results and Analysis

67.4.1 Wind Velocity Analysis and Comfort Evaluation

Figure 67.2 shows the wind velocity of 6 floors, 9 floors, 12 floors, 15 floors and 18 floors at the height of 1.5 m. Figure 67.2 shows the layout of No 2, 3, 6, and 7 buildings form a significant roadway wind effects. Due to the effect of the positive pressure in windward side and negative pressure in crosswind surface, the angle district airflow effect [7] was formed in the corner of the windward side of the building, such as in No 1, 5, 8, 11, and 12 buildings. And the wake region and airflow stagnation zone was formed in the leeward side of the building and the corner and concave corner of the construction phase of the compact layout, such as in the right bottom construction area. With the increasing floors of the center region buildings, the air velocity around the variable high-rise buildings gradually increased and so are the roadway wind effect and the angle district airflow effect.

In this paper, the "Principle of Estimation on Aeolian environment" [8] has been taken to evaluate the wind environment comfort.

A large number of measured data show that wind velocity approximately obeys the two-parameter Weibull function distribution [9]. The probability function of the wind velocity more than v_0 is

$$P(v > v_0) = \exp\left[-\left(\frac{v_0}{C}\right)^K\right] \tag{67.1}$$

where v is wind velocity, m/s; C, Weibull distribution scale parameter; and K, Weibull distribution shape parameter. Parameters C and K are drawn according to the average wind velocity $\tilde{v}$ and standard deviation S_v [10]. Combining the local weather station data, in Yichun city, $K = 1.29$, $C = 2.13$.

Use Eq. (67.1) and the "Principle of Estimation on Aeolian environment" to evaluate the urban wind environment by the suburban weather station data,
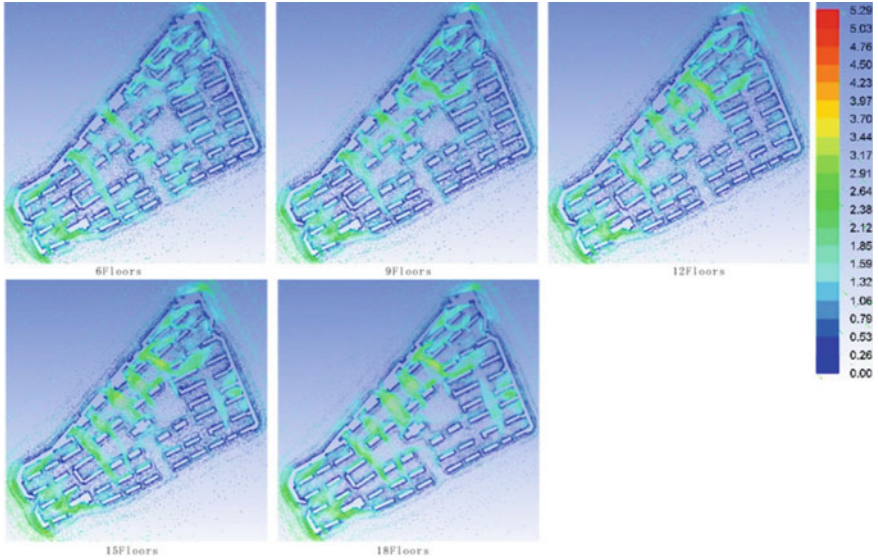
Fig. 67.2 The wind velocity of 6 floors, 9 floors, 12 floors, 15 floors, and 18 floors at the height 1.5 m

considering the conversion between the average height of the staff activities 1.5 m in urban and 10 m height in suburban, the conversion process is

1. The local wind speed is converted to the inflow wind velocity at the same height 1.5 m in urban residential district, and conversion ratio R_{max} is the max wind velocity in simulation to the inflow wind velocity v_h at the same height 1.5 m,

$$R_{max} = \frac{v_s}{v_h} \tag{67.2}$$

where v_s is the max wind velocity in simulation, *m/s*.

2. Considering the conversion between urban and the suburban, turning inflow wind velocity in urban residential district into the wind velocity in suburban at the same height 1.5 m, the conversion ratio a is,

$$a = \frac{V_h}{V_{hmet}} = 0.46h^{0.12} \tag{67.3}$$

where: V_h is the wind velocity at h height in urban, *m/s*; V_{hmet} is the wind velocity at h height in suburban, *m/s*.

3. (3)Convert the wind velocity at 1.5 m to the wind velocity V_0 at 10 m in suburban, the ratio b is,

$$b = \frac{V_{met1.5}}{V_{met10}} = 0.8272 \tag{67.4}$$

where $V_{met1.5}$ is the wind velocity at 1.5 m in suburban, m/s; and V_{met10} is the wind velocity at 10 m in suburban, m/s.

In winter in the Yichun city, the effect of wind velocity on pedestrian comfort in case of rapid walking and short standing and sit in outdoor is evaluated from the "Principle of Estimation on Aeolian environment"; when the local wind velocity reaches 6 degrees(wind velocity over 10.8 m/s), the principle of estimation on aeolian environment is not tolerable. By the Eq. (67.1), (67.2), (67.3), and (67.4), the probability of the wind velocity over 6 degrees° is calculated in residential district, shown in Table 67.1.

In evaluation criteria, a wind event lasts 1.7–2.5 h, if chosen 2 h, the number of occurrences per week should be

$$n_{week} = P(v > v_0) \times 7(d) \times 24(h/d) \div 2(h) \tag{67.5}$$

By the Eq. (67.5), the number of occurrences per week over 6 degrees in different floors in the residential district is shown in Table 67.1.

By the Table 67.1, in 6, 9, 12, 15, and 18 floors, the frequency are 0.09, 0.21, 0.25, 0.27, and 0.28. It meets the principle of estimation on aeolian environment. However, with the increase in the floors, the frequency increases, and the comfort is terrible. So increasing the buildings' height results in the wind velocity increase in some areas in the district and affects the people's comfort.

67.4.2 Temperature Analysis

Figure 67.3 shows the temperature of 6 floors, 9 floors, 12 floors, 15 floors, and 18 floors at 1.5 m. It shows that the temperature distribution is lower in the center and higher in a round, and has the coincident trend in different floors. Because of the

Table 67.1 The probability and frequency over 6 degrees in different floors in the residential district (a = 48.29 %, b = 82.72 %)

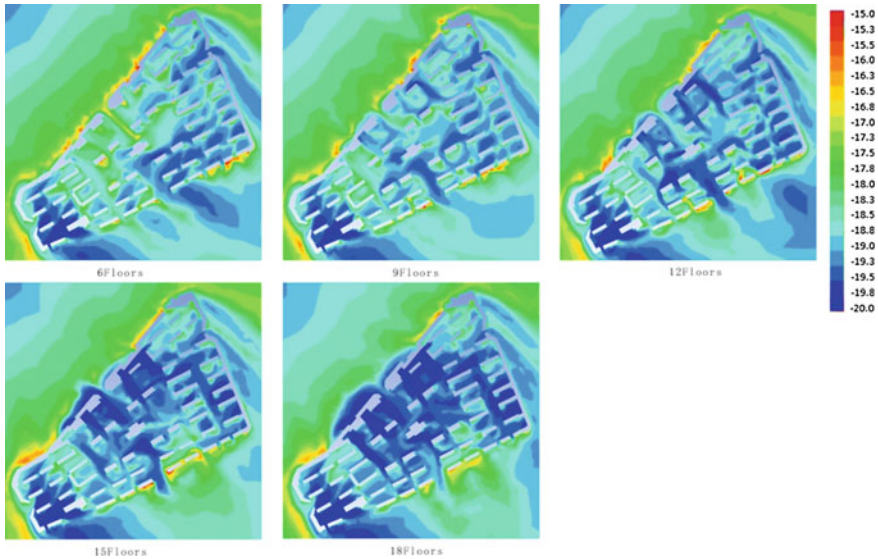| Floors	V_s,m/s	R_{max}	p. %	n/week
6	4.61	2.85	0.11	0.09
9	5.11	3.16	0.25	0.21
12	5.21	3.23	0.29	0.25
15	5.28	3.27	0.32	0.27
18	5.29	3.28	0.33	0.28

Fig. 67.3 The temperature of 6 floors, 9 floors, 12 floors, 15 floors, and 18 floors at the height 1.5 m

effect of solar radiation which is mainly from the southwest direction at the winter solstice, the temperature in the south part is slightly higher than the north part almost 1 °C. The external wall temperature is relevant to the height at the first row of buildings in the direction of inflow velocity. The incoming flow is heated by the influence of solar radiation. When the height is low, such as 6 floors, and 9 floors, the wind velocity and airflow speed are so slow that the heat gathered makes the temperature increase in this region. On the other hand, when the height is high, such as 12 floors, 15 floors, and 18 floors, the wind velocity and airflow speed are faster and accelerate heat away quickly; in the end, temperature in this region becomes low. When the distance between the buildings is too small in internal region, due to the occlusion influence of the front row buildings, the back row buildings are covered by the shadow area of the front row buildings, and the temperature is much lower in this region. In summary, the temperature field distribution is formed by the common action of the solar radiation, building height, building orientation, building layout, and the airflow organization.

67.5 Conclusion

In this paper, by changing the height of the buildings in the center area , its effect on the thermal environment was analyzed and the comfort with the wind velocity was evaluated. The results show that, with the rising of the height in center

buildings, the roadway wind effect and the angle district airflow effect that formed around the high-rise buildings are strengthened, and the accelerated wind velocity makes the environment uncomfortable in some area. Meanwhile, the temperature field's variation is effected by change in the wind speed in some area, and the temperature field trend is lower in the center and higher in a round, and the standard effective temperature and comfort are also reduced. The micro-climate will affect the building planning and design and should attract more attention of the designer in severe cold region.

References

 1. Binrong G, Guoxin M (1995) Building design and wind environment. Arch J (H):44–48
 2. Marcum DL, Gaither JA (1999) Mixed element type unstructured grid generation for viscous flow applications [R]. AIAA 99–3252
 3. Yang J, Guangbei T, Yi C et al. (2004) Natural ventilation of highrise residential buildings with sky garden. Heating Ventilating Air Conditioning 34(3):1–5
 4. Spalart P, Allmaras SA (1992) One-equation turbulence model for aerodynamic flows. AIAA 92–0439
 5. ASHRAE Handbook Fundamentals (2009) American society of heating, refrigerating and air-conditioning engineers, Inc., 1791 Tullie Circle, N. E, Atalanta, GA 30329
 6. Zhang J, Fang X, Zhang H, Yang W, Zhu C (1997) A model to predict the radiative temperature of the snow surface. J Inf Millimeter Waves 16(3):206–210
 7. Dexin He etc. (2006) Wind engineering and industrial aerodynamics. vol. 1 National Defence Industry Press, Beijing pp 404–405
 8. Jiang Y, Jianguo S, Boyin Z (2006) An evaluation on wind environment around skyscrapers. Acta Scientiarum Naturalium Universitatis Pekinensis 42(1):68–73
 9. Ding M, Wu W, Wu H, Mao M, Zhang Y (2008) Research on forecasting of probabilistic distribution parameters of wind speed and its application. Power Syst Technol 32(14):10–14
10. Weiming X, Xinglin Z, Xinhong K (2007) Comparison for three methods to calculate Weibull distribution parameters of wind speed. Jiangxi Electric Power 31(1):1–3

Chapter 68
A Review of Carbon Accounting Models for Urban Building Sector

Zhiyong Ren and Xiangli Li

Abstract Global warming caused by greenhouse gas (GHG) emission has become a common concern in the international community. Building sector is one of the major areas to produce GHG emissions. There are a lot of carbon emission researches by the domestic and overseas scholars, although the international standards for carbon accounting have not been established in the building sector. In this paper, we first introduce the major modeling techniques for estimating the national or urban building energy consumption in brief. And then give an overview of urban building energy consumption and carbon emissions accounting models based on these methods, particularly describe the scale and the scope applied in the accounting, the relationships between the models, the evaluation and analysis of the existing models focused on their purposes, strengths, and shortcomings. Finally, the main part of this paper puts forward an elementary conceives to establishing a more smaller scale of carbon accounting model used the life cycle assessment (LCA) theory aim at regional building energy system. And we wish the carbon accounting model can guide the design of new regional building energy system and the retrofit of existing regional building energy system.

Keywords Building sector · Carbon accounting models · District building energy system · LCA

68.1 Introduction

Greenhouse gas emission causing global warming has become a heated topic in the international community. And it is widely recognized that the climate change is a

Z. Ren (✉) · X. Li
Institute of Building Environment and Equipment Engineering,
Dalian University of Technology, Dalian 116024, China
e-mail: renzydlut@163.com

Table 68.1 Energy consumption ratio of different countries

Country	Energy consumption ratio (%)		
	Industry	Building	Transportation
USA (2007)	32.2	39.5	28.3
EU (2006)	27.5	41.1	31.4
Japan (2007)	45.6	31.2	23.2
Chin (2007)	58.3	24.5	17.2

(data source from statistical yearbook of China, the world bank, DOE, EU)

severe threat with a forecast that the average temperatures in global surface will increase between 1.1 and 6.4 °C by the end of this century [1].

Energy-related CO_2 emission is one of the largest drivers contributed to global warming because of the accelerating atmosphere radiation and thus needs to be taken into high priority for mitigating GHG emission. Cities with its aggregation of economic activities and associated energy use are the main contributors of energy consumption CO_2 emissions and may be critical for CO_2 mitigation and adaptation to climate change.

Building sector energy consumption is the majority in the whole national or urban energy consumption, Table 68.1. Especially, developed countries that service more developed the building department energy consumption of carbon emissions will reach more than 50 %. Developing countries, such as China, those are in the middle of industrialization, industrial consumption dominant. But the promotion of the proportion the carbon emissions from country building sector taken up is an inevitable trend along with the adjustment of the economic structure and the quality of people life improving.

In China, buildings have become an increasingly important energy-demand sector accounting for nearly one-fourth of total primary energy consumption and are very likely to increase to 35 % by 2030, whereby 25 % of GHG emission are being produced in the building sector [2]. And according to the IEA's report (IEA 2010), CO_2 emissions of the building sector, including indirect emissions from the use of electricity, account for almost 30 % of global CO_2 emissions. Accordingly, the global warming and the increased GHG emissions have been the biggest interest in the building sector.

68.2 Overview of Modeling Techniques

Generally speaking, there are two fundamental classes of modeling methods used to predict and analyze various aspects of the overall building stock energy use and associated CO_2 emissions: the top-down and bottom-up approaches. Top-down methods focus on the interaction between the energy sector and the economy at large and rely on aggregate economic behavior to predict future changes in energy and CO_2 emissions. The method of IPCC Guideline for National GHG Emission
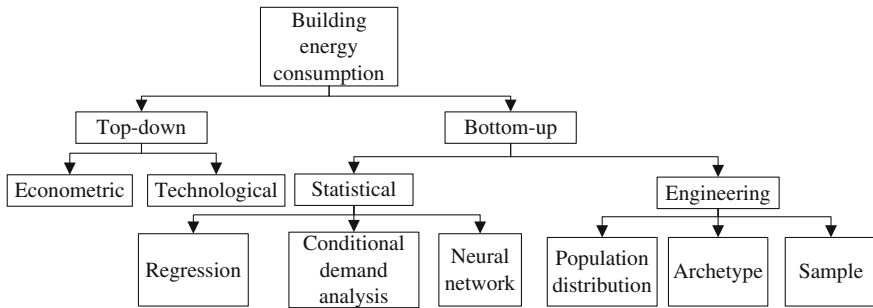
Fig. 68.1 Top-down and bottom-up modeling techniques for estimating the nation or urban building energy consumption

Inventory is a main representative of this approach [3]. Bottom-up methods are built up from data on a hierarchy of disaggregated components that are then combined according to some estimate for their individual impact on energy usage, for instance in the United Kingdom, the contribution from Victorian terrace housing might be weighted according to their prevalence in the stock. This implies that they may be useful for estimating how various individual energy deficiency measures impact on CO_2 emission reduction, such as by replacing one type of heating systems with another. Often these models are seen as a way to identify the most cost-effective options to achieve given carbon reduction targets based on the best available technologies and processes [4].

Groupings of top-down and bottom-up techniques for modeling building energy consumption are shown in Fig. 68.1 [5]. The terminology is with reference to the hierarchal position of data input as compared to the housing sector as a whole. Top-down models utilize the estimate of total building sector energy consumption and other pertinent variables to attribute the energy consumption to characteristics of the entire housing sector. In contrast, bottom-up models calculate the energy consumption of individual or groups of houses and then extrapolate these results to represent the region or nation.

68.3 Carbon Accounting Models in Different Scales

Building energy using carbon accounting models may focus on a thermal zone, building, neighborhood, city, state or province, region, or nation. The level of detail of input parameters is a function of data availability, model focus and purpose, and assumptions. Increased detail allows for a more comprehensive investigation of particulars, although accurate assumptions may significantly ease the modeling process and provide suitable results.
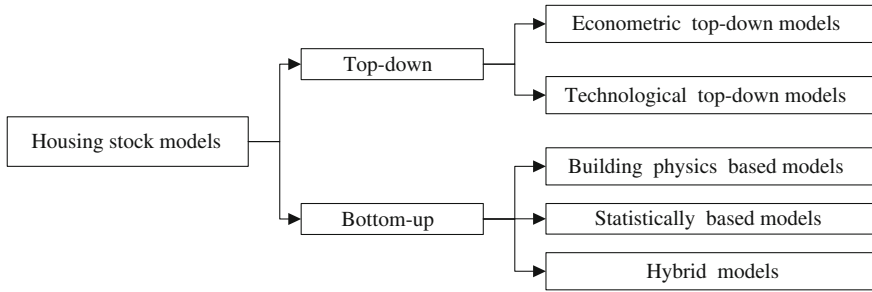
Fig. 68.2 The classification of housing stock energy consumption carbon emissions models

68.3.1 Nation and Urban Level

Urban is a basic but important unit to perform energy and environmental strategies on carbon emission reduction, and it is necessary to consider how to control carbon emission at urban level. And there is a growing interest in reducing energy consumption and the associated GHG emissions in every sector of the economy. It can be easily calculated, and the forecast building energy consumes carbon emissions to establish energy consumption carbon emissions model, and on this basis, more reasonable policy of carbon emission reduction is formulated.

There are two energy consumption carbon emissions models according different modeling methods: Top-down model and bottom-up model [6]. The detailed classification of housing stock energy consumption carbon emissions models are shown in Fig. 68.2.

68.3.1.1 Top-Down Models

Top-down models mainly apply to carbon accounting in nation level, and it could be broadly categorized as econometric and technological top-down models [7].The econometric top-down models are primarily based on energy use in relationship to variables, such as income, fuel prices, and gross domestic product to express the connection between the energy sector and economic output. They can also include general climatic conditions, such as population-weighted temperature, for a nation. As such, the econometric top-down models often lack details on current and future technological options as they rather place the emphasis on the macroeconomic trends and relationships observed in the past, rather than on the individual physical factors in buildings that can influence energy demand [8]. More importantly, the reliance on past energy–economy interactions might also not be appropriate when dealing with climate change issues where environmental, social, and economic conditions might be entirely different to those previously experienced. They have no inherent capability to model discontinuous changes in technology. The

technological top-down models include a range of other factors that influence energy use (i.e., saturation effects, technological progress, and structural change); however, they are not described explicitly within the models [9].

68.3.1.2   Bottom-Up Models

Bottom-up building physics stock models are used to explicitly determine and quantify the impact of different combinations of technological measures on delivered energy use and CO_2 emissions and therefore represent an important tool for policy-makers. And the models work at a disaggregated level and thus need extensive databases of empirical data to support the description of each component [10]. Contingent upon the type of data input and structure, statistical and building physics-based methods represent two distinct approaches applied in the bottom-up models to determine the energy consumption of specified end-uses [5]. Currently, there are many bottom-up building physics stock models, most for residential building. The residential sector is a substantial consumer of energy in every country, and therefore, a focus for energy consumption efforts. The Huang and Brodick model [11] for the US building stock is not based on dwellings per set, but on the aggregated cooling and heating loads attributable to different building envelope components in the stock, such as windows, roofs, walls, internal processes, and space conditioning systems. The LEAP model [12] in South Korea was established to assess the potentials of energy saving and GHG emission mitigation offered by implementation of residential building energy efficiency. The current and future energy demand and CO_2 emission in residential buildings was estimated using energy/environment model called "Long-range Energy Alternative Planning System" from 2007 to 2030. In China, to assess the energy demand and environment effect for household sector, a bottom-up LEAP Henan model was developed to simulate three different scenarios from 2005 to 2030 [13]. Kavgic [6] compare five building physics-based bottom-up models focusing on the same building stock—UK case study to critically analyze the existing bottom-up building physics-based residential energy models focusing on their purposes, strengths, and shortcomings, and identify the next generation of coupled energy–health bottom-up building stock models. In the United Kingdom, the development is relatively perfect; especially the residential buildings have been set up and updated a lot of energy consumption and carbon emissions prediction model. Such as BREHOMES (1997) [14], UK Domestic Carbon Model (UKDCM 2007) [15], the DECard model(2007) [16], the Energy and Environment Prediction model (EEP 2007) [17], the Community Domestic Energy Model (CDEM 2010) [18], the Johnston model [19], modified to varying degrees. They generally have the ability to estimate the baseline energy consumption of the existing housing stock and predict the future energy demand, energy saving and CO_2 emission reduction for a variety of scenarios.

There are a lot of different limitations on the models. The most important shortcoming of all these models is their lack of transparency and quantification of

inherent uncertainties. The lack of publicly available detailed data on the models' inputs and outputs, as well as underlying algorithms renders any attempt to reproduce their outcomes problematic. In addition, the relative importance of input parameter variations on the predicted demand outputs needs to be quantified as a matter of course.

68.3.2 Regional Level

In this paper, "regional" is refers to the community, neighborhood and a piece of development zones, which covers an area in a few km^2, and the building area less than one million m^2. At this level, the energy system satisfies the needs of "built environment (BE)" basically. In China, heating and hot water consumption occupies two-thirds of energy demand in buildings. The energy-related CO_2 emission coming from district heating in China is equivalent to the total emission of Poland [20]. Region building energy systems lack scientific carbon accounting methods and carbon emissions quantitative index, the traditional simple statistical method only considered the "quantity" of energy consumption is difficult to accurately evaluate energy system carbon emissions. So far, there are more than 3,000 CDM projects in the global, but the energy conservation of the building only six small projects [21]. So we put forward a regional building energy system carbon emissions model in order to solve these problems.

68.3.2.1 The Determination of GHG Emissions Source

In this paper, we divided a regional building energy system carbon footprint accounting boundary using the life cycle assessment (LCA) theory. According to the basic idea of process analysis divided the life-cycle of the regional building energy system into physicochemical phase, operation and dismantle disposal stage three phases. Every phase will produce carbon emissions, including the direct emissions in operating phase and the indirect emissions form equipment production, process, transport, installation, etc. The determination of GHG emissions source of regional building energy system life cycle are shown in Fig. 68.3

68.3.2.2 Mathematical Model

From the view of the whole life cycle, building energy system carbon footprint can use the following formula:

$$W = \sum_{i=1}^{4} W_i \tag{68.1}$$

Physicochemical phase		Operation phase	Dismantle and disposal phase
Equipment materials manufacturing phase	Construction phase		
GHG emissions			
GHG emissions from system equipment and materials Production, manufacture, process	GHG emissions from system equipment materials transportation and the installation construction machines	GHG emissions from system operation process of the energy consumption and equipment maintenance	GHG emissions from System dismantled machines, equipment recovery, waste processing

Fig. 68.3 Carbon emissions of regional building energy system life-cycle

In the formula, W is the total carbon emission of building energy system whole life cycle, W_1 is material equipment manufacturing phase carbon emission of building energy system, W_2 is construction phase carbon emission of building energy system, W_3 is operation phase carbon emission of building energy system, W_4 is demolition and disposal phase carbon emission of building energy system.

68.4 Conclusions

Many ways have been used to make sure building energy consumes emissions currently, include macroscopic model, direct measurement, calculation and estimation. The understanding of the accuracy, the value and the applicability is also increasing for every kind of the method with the passage of time and the promotion of experience. The current statistics system needs to be more explicit to satisfy the calculation requirement of carbon emissions from energy consumption. But there are a number of different limitations associated with the current models. The most important shortcoming of all these models is their lack of transparency and quantification of inherent uncertainties. The lack of publicly available detailed data on the models' inputs and outputs, as well as underlying algorithms render any attempt to reproduce their outcomes problematic.

And we find that the research of building energy consumption carbon accounting focuses on the big energy system at state and urban scale, lack of research for small scale regional building energy system at present. So we use the LCA theory put forward an elementary conceive to establish a small scale of carbon accounting model aiming at urban region building energy system and wishes the model can improve the new energy and renewable energy technology and other low carbon technology's application and development in building sector, get through guide the design of new and the retrofit of existing regional building energy system

References

1. IPCC, Climate Change (2007) Synthesis Report, http://www.ipcc.ch/
2. Li J (2008) Towards a low-carbon future in China's building sector—a review of energy and climate models forecast. Energy Policy 36:1736–1747
3. Liu Z, Geng Y, Xue B, Xi F, Jiao J (2011) A calculation method of CO2 emission from urban energy consumption. Resources Sci 1007–7588, 07-1325-06
4. Rivers N, Jaccard M (2005) Combining top-down and bottom-up approaches to energy–economy modelling using discrete choice methods. Energy J 26(11):83–106
5. Swan LG, Ugursal VI (2009) Modelling of end-use energy consumption in the residential sector: a review of modelling techniques. Renew Sustain Energy Rev 13:1819–1835
6. Kavgic M, Mavrogianni A, Mumovic D, Summerfield A, Stevanovic Z, Djurovic-Petrovic M (2010) A review of bottom-up building stock models for energy consumption in the residential sector. Build Environ 45:1683–1697
7. Böhringer C, Rutherford TF (2008) Combining bottom-up and top-down. Energy Econ 30:574–596
8. MIT (1997) Energy technology availability: review of longer term scenarios for development and deployment of climate-friendly technologies. Cambridge, Massachusetts, USA: Massachusetts Institute of Technology Energy Laboratory
9. Johnston D (2003) A physically based energy and carbon dioxide emission model of the UK housing stock. Ph.D. thesis. Leeds Metropolitan University, UK
10. Shorrock LD, Dunster JE (1997) The physically-based model BREHOMES and its use in deriving scenarios for the energy use and carbon dioxide emissions of the UK housing stock. Energy Policy 25(12):1027–1037
11. Huang YJ, Brodrick J (2000) A bottom-up engineering estimate of the aggregate heating and cooling loads of the entire building stock. In: Proceedings of the 2000 ACEEE summer study on energy efficiency in buildings, Pacific Grove, 20th–25th Aug 2000
12. Jeong YS, Kim KW, Yu KH (2012) Assessment of CO2 emissions and reduction potential in residential buildings in South Korea. Second Int Conf Build Energ Environ
13. Shuguang TI, Yun W, Guangyin XU (2010) Energy and environment scenario analysis for resident sector based on LEAP. J Henan Agric Univ 1000–2340, 02-0229-04
14. Natarajan S, Livermore GJ (2007) Predicting future UK housing stock and carbon emissions. Energy Policy 35(1):5719–5727
15. Natarajan S, Livermore GJ (2007) Domestic futures-which way to a low-carbon housing stock? Energy Policy 35(11):5728–5736
16. Firth SK, Lomas KJ, Wright AJ (2010) Targeting household energy-efficiency measures using sensitivity analysis. Build Res Inf 38(1):25
17. Jones P, Patterson J, Lannon S (2007) Modelling the built environment at an urban scale-energy and health impacts in relation to housing. Landscape Urban Plann 83:39–49
18. Firth SK, Lomas KJ, Wright AJ (2010) Targeting household energy-efficiency measures using sensitivity analysis. Build Res Inf 38(1):25–41
19. Johnston D, Lowe R, Bell M (2005) An exploration of the technical feasibility of achieving CO2 emission reductions in excess of 60 % within the UK housing stock by the year 2050. Energy Policy 33(13):1643–1659
20. The World Bank (2001) China: Opportunities to Improve Energy Efficiency in Buildings. The World Bank, Washington, DC
21. WeiDing L, Bai W, Liang H, Fan R (2009) Energy system in low-carbon city. Heating Vent Air Conditioning 3(8):79–84

Chapter 69
Wind Around Tall Building: A Comparison Between RANS and LES

Huiyuan Shen, Qibin He, Yi Huang and Yanhua Liu

Abstract With the expansion of city, more and more tall buildings arise. It is very important to understand the wind field around buildings for creating safe and comfortable wind environment. At present, three kinds of methods can be used to obtain the wind field information around tall buildings. They are wind tunnel experiment, wind field measurement, and numerical simulation. Numerical simulation is the cheapest way, in which Reynolds averaged Navier–Stokes equations and large eddy simulation approaches are commonly used to simulate turbulent flow. To ensure the accuracy and reliability of the two approaches, the solution validation studies are needed. In this paper, Shear Stress Transport (SST) $k - \omega$ model has been used in solving Reynolds averaged Navier–Stokes equations (RANS) and kinetic-energy transport subgrid model has been employed in large eddy simulation (LES) in the simulation of the flow field around a square column. Comparing the numerical results with experimental data, the characteristics of the two models are revealed and their reliability is analyzed. The results show that both kinetic-energy transport model in LES and SST $k - \omega$ model in RANS can be used to simulate the field around building but the results are different. With kinetic-energy transport model in LES, the vortex generation and a group of high vertex zones are observed.

Keywords Wind field · Tall building · Large eddy simulation (LES) · Reynolds averaged N–S (RANS) · Turbulence

H. Shen · Y. Huang · Y. Liu (✉)
Department of Building Environment and Services Engineering,
School of Human Settlements and Civil Engineering, Xi'an Jiaotong University,
Xi'an, China
e-mail: yhliu@mail.xjtu.edu.cn

Q. He
Shenzhen Institute of Building Research, 29#, three Road, Meiao, Shangmeilin,
Shenzhen, China

69.1 Introduction

With the increasing number of tall buildings in Chinese city, the wind phenomenon has been desired to be effectively predicted. Numerical simulation is one of the most effective methods for predicting the flow field around buildings. Shear stress transport (SST) $k - \omega$ model is usually used to provide closure in simulation of the wind field around buildings [1, 2]. As we know, large eddy simulation (LES) now is successful in predicting turbulent flow [3, 4]. The fluid flow surrounding building is often in high Reynolds number. So it is possible to simulate the field characteristics around buildings with LES. The characteristics of SST $k - \omega$ model for RANS and kinetic-energy transport subgrid model for LES in the flow filed simulation around a square column were compared with experimental data in this paper. With the above two models, the wind around a single building was analyzed.

69.2 Rans Model

69.2.1 Governing Equations

In RANS, the instantaneous space–time variable may be written as

$$\phi(x, t) = \overline{\phi}(x, t) + \phi'(x, t) \tag{69.2.1}$$

where $\overline{\phi}(x, t)$ is the Reynolds-averaged component which represents the mean scalar component and $\phi'(x, t)$ is the fluctuating component.

And the incompressible mass and momentum equations in a Cartesian coordinate frame are:

$$\frac{\partial \overline{u}_i}{\partial x_i} = 0 \tag{69.2.2}$$

$$\frac{\partial}{\partial t}(\rho \overline{u}_i) + \frac{\partial}{\partial x_j}(\rho \overline{u}_i \overline{u}_j) = \frac{\partial^2 \sigma_{ij}}{\partial x_j^2} - \frac{\partial p}{\partial x_i} - \frac{\partial}{\partial x_j}(\rho \tau_{ij}) \tag{69.2.3}$$

where ρ is the density which is constant for incompressible fluid, μ is the molecular dynamic viscosity, u_i is the velocity in i-direction, the momentum flux is $\tau_{ij} = \overline{u_i' u_j'}$, and τ_{ij} needs to be modeled, σ_{ij} is the stress tensor based on molecular dynamic viscosity:

$$\sigma_{ij} = \left[\mu \left(\frac{\partial \overline{u}_i}{\partial x_j} + \frac{\partial \overline{u}_j}{\partial x_i} \right) \right] - \frac{2}{3} \mu \frac{\partial \overline{u}_l}{\partial x_l} \delta_{ij} \tag{69.2.4}$$

where δ_{ij} is Kronecker tensor.

69.2.2 Shear Stress Transport $k - \omega$ model

The equations for turbulence kinetic energy (k) and specific dissipation rate (ω) for the SST $k - \omega$ model are written as follows [5]:

$$\frac{\partial}{\partial t}(\rho k) + \frac{\partial}{\partial x_j}(\rho \bar{u}_j k) = \frac{\partial}{\partial x_j}\left[\rho(v + \sigma_k v_T)\frac{\partial k}{\partial x_j}\right] - \rho \beta^* k\omega + \rho P_k \qquad (69.2.5)$$

$$\frac{\partial}{\partial t}(\rho\omega) + \frac{\partial}{\partial x_j}(\rho \bar{u}_j \omega) = \frac{\partial}{\partial x_j}\left[\rho(v + \sigma_\omega v_T)\frac{\partial \omega}{\partial x_j}\right] + 2\rho(1 - F_1)\sigma_{\omega 2}\frac{1}{\omega}\frac{\partial k}{\partial x_j}\frac{\partial \omega}{\partial x_j} - \beta\omega^2$$
$$+ \alpha S^2$$

$$(69.2.6)$$

where $v_T = \frac{a_1 k}{\max(a_1 \omega, SF_2)}$, $F_1 = \tanh\left\{\left\{\min\left[\max(\frac{\sqrt{k}}{\beta^* \omega y}, \frac{500v}{y^2 \omega}), \frac{4\sigma_{\omega 2}k}{CD_{k\omega}y^2}\right]\right\}^4\right\}$, $F_1 = \tanh\left[\max(\frac{\sqrt{k}}{\beta^* \omega y}, \frac{500v}{y^2 \omega})\right]^2$, $P_k = \min(\tau_{ij}\frac{\partial \bar{u}_i}{\partial x_j}, 10\beta^* k\omega)$, $CD_{k\omega} = \max(2\rho\sigma_{\omega 2}\frac{1}{\omega}\frac{\partial k}{\partial x_i}\frac{\partial \omega}{\partial x_i}, 10^{-10})$, $\phi = \phi_1 F_1 + \phi_2(1 - F_1)$, $\alpha_1 = \frac{5}{9}$, $\alpha_2 = 0.44$, $\beta_1 = \frac{3}{40}$, $\beta_2 = 0.0828$, $\beta^* = \frac{9}{100}$, $\sigma_{k1} = 0.85$, $\sigma_{k2} = 1$, $\sigma_{\omega 1} = 0.5$ and $\sigma_{\omega 2} = 0.856$.

69.3 LES Model

69.3.1 Governing Equations

In LES, the Navier–Stokes equations are spatially filtered. The filtering is represented mathematically in physical space as a convolution product:

$$\overline{\phi}(x, t) = \int_{-\infty}^{+\infty} \phi(\xi, t)G(x - \xi)d\xi \qquad (69.3.1)$$

where $\overline{\phi}(x, t)$ is the resolved part of an arbitrary space–time variable while the convolution kernel $G(x - \xi)$ is used as the characteristic of the filter, generally named the filtering function. Since the finite volume method was considered in this paper, box filter was used.

The instantaneous space–time variable may be written as

$$\phi(x, t) = \overline{\phi}(x, t) + \phi'(x, t) \qquad (69.3.2)$$

where $\overline{\phi}(x, t)$ is the box-averaged filtered component which represents the resolved spatial variable and $\phi'(x, t)$ is the box-averaged SGS component which represents the unresolved spatial variable at length smaller than the filter width Δ.

The box-filtered incompressible mass, momentum and energy conservation equations in a Cartesian coordinate frame are:

$$\frac{\partial \bar{u}_i}{\partial x_i} = 0 \tag{69.3.3}$$

$$\frac{\partial}{\partial t}(\rho \bar{u}_i) + \frac{\partial}{\partial x_j}(\rho \bar{u}_i \bar{u}_j) = \frac{\partial}{\partial x_j}(\mu \frac{\partial \sigma_{ij}}{\partial x_j}) - \frac{\partial p}{\partial x_i} - \frac{\partial}{\partial x_j}(\rho \tau_{ij}) \tag{69.3.4}$$

where ρ is the density which is constant for incompressible fluid, μ is the molecular dynamic viscosity, u_i is the velocity in the i-direction. In Eq. (69.3.4), σ_{ij} is the stress tensor based on molecular dynamic viscosity,

$$\sigma_{ij} = \left[\mu \left(\frac{\partial \overline{u_i}}{\partial x_j} + \frac{\partial \overline{u_j}}{\partial x_i} \right) \right] - \frac{2}{3} \mu \frac{\partial \overline{u_l}}{\partial x_l} \delta_{ij} \tag{69.3.5}$$

And τ_{ij} represents the sub-grid momentum flux, $\tau_{ij} = \overline{u_i u_j} - \bar{u}_i \bar{u}_j$, representing the unknown SGS correlations when the box filtering operation is applied to the governing equations.

69.3.2 LES Kinetic-Energy Transport SGS Model

In kinetic-energy transport SGS model, τ_{ij} is expressed as [6]:

$$\tau_{ij} = -2C_\tau \overline{\Delta} k_{\text{sgs}}^{1/2} \overline{S}_{ij} + \frac{2}{3} \delta_{ij} k_{\text{sgs}} \tag{69.3.6}$$

where k_{sgs} is SGS kinetic energy and $k_{\text{sgs}} = \frac{1}{2}(\overline{u_i u_i} - \overline{u_i u_i})$. Furthermore, k_{sgs} satisfies the following equation:

$$\frac{\partial}{\partial t}(\rho k_{\text{sgs}}) + \frac{\partial}{\partial x_j}(\bar{u}_j k_{\text{sgs}}) = \frac{\partial}{\partial x_j}\left(\frac{\mu_t}{\sigma_k}\frac{\partial}{\partial x_j}k_{\text{sgs}}\right) - \tau_{ij}\frac{\partial \bar{u}_i}{\partial x_j} - C_\varepsilon \frac{k_{\text{sgs}}^{3/2}}{\Delta_f} \tag{69.3.7}$$

where σ_k is typically 1.0.

More details of C_ε and C_τ in kinetic-energy transport SGS model can be seen in literature [6].

69.4 The Validation of the Two Models

The SST $k - \omega$ model and LES kinetic-energy transport subgrid model are validated using the experimental data in literature [7].

The computational domain is shown in Fig. 69.1 where $W = 15d$ and $L = 26d$. In the study, X-direction is the flow direction, Y-direction is the span direction. The inlet of the domain is at x $= -10.5d$ meeting the velocity inlet boundary condition: $u = U$, $v = 0$ and the flow turbulent intensity is 3 %. The outlet is at $x = 15.5d$ meeting the pressure outlet boundary condition, the gauge pressure
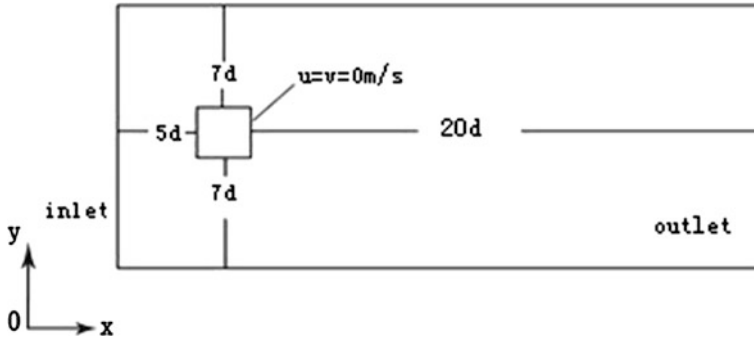
Fig. 69.1 Simulation domain

equals to zero. The boundary condition on the square column surface meets the no-slip boundary condition, i.e. $u = 0$, $v = 0$, and $d = 10$ m. ANSYS Fluent 14.5 was used to simulate the flow field.

For dimensionless, $\bar{U}/U_0$ where $\bar{U}$ is the local time averaged velocity and U_0 is the bulk velocity, x/d and y/d where d is the diameter of the square column are used.

Figures 69.2, 69.3 and 69.4 show the dimensionless velocity profiles where $y = 0$, $x = -4.125d$ and $x = -3.875d$, respectively, obtained with the SST $k - \omega$ model and kinetic-energy transport SGS model. The experimental data are also given for comparison.

It can be seen that a great discrepancy exists between numerical values obtained using the SST $k - \omega$ model and the kinetic-energy transport SGS model at $y = 0$ (Fig. 69.2). For example, the SST $k - \omega$ model velocity profile in x direction is much lower than experimental measurements and too steep in a wide range under $x = 0$, but closer near the point $x = 0.5d$. The result from kinetic-energy transport SGS model profile shows the similar trend with experimental data, and they are closer in the range under $x = -d$, but deviate up the range.

Figure 69.3 shows the dimensionless time averaged velocity profile where $x = -4.125d$. It is very clear that near 0.8d, the velocity field obtained using the SST $k - \omega$ model is more consistent with the experimental data. However, the results from the kinetic-energy transport SGS model is better than that from SST $k - \omega$ model near $x = 0$ or $x = 1.45d$.

Figure 69.4 shows the dimensionless time averaged velocity profile where $x = -3.875d$. Although near 0.9d, the velocity field obtained using the SST $k - \omega$ model is more consistent with the experimental data, as a whole view, the kinetic-energy transport SGS model is a better model than the SST $k - \omega$ model near $x = 0$ or $x = 1.45d$ in forecasting velocity field.
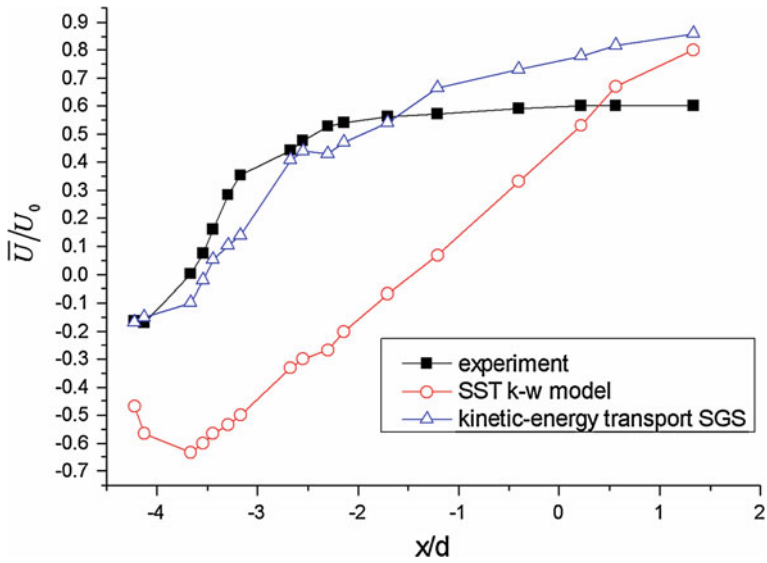
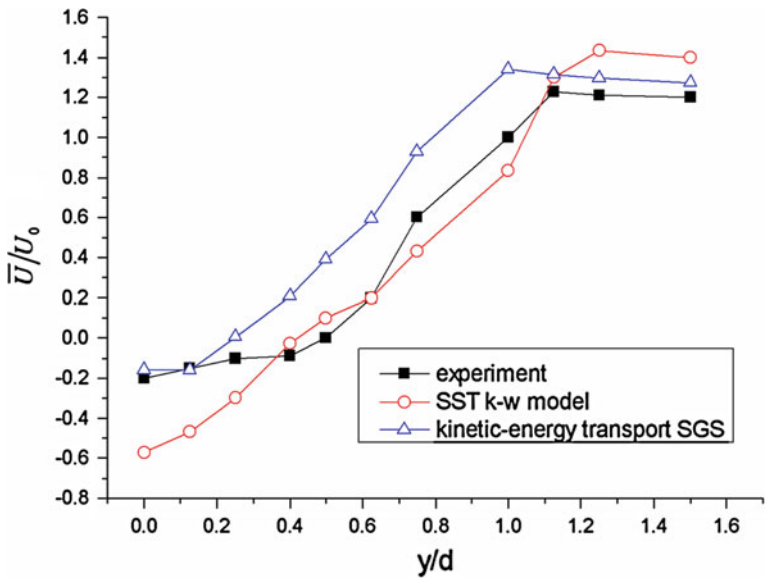**Fig. 69.2** Dimensionless velocity data sampling for time statistics at $y = 0$

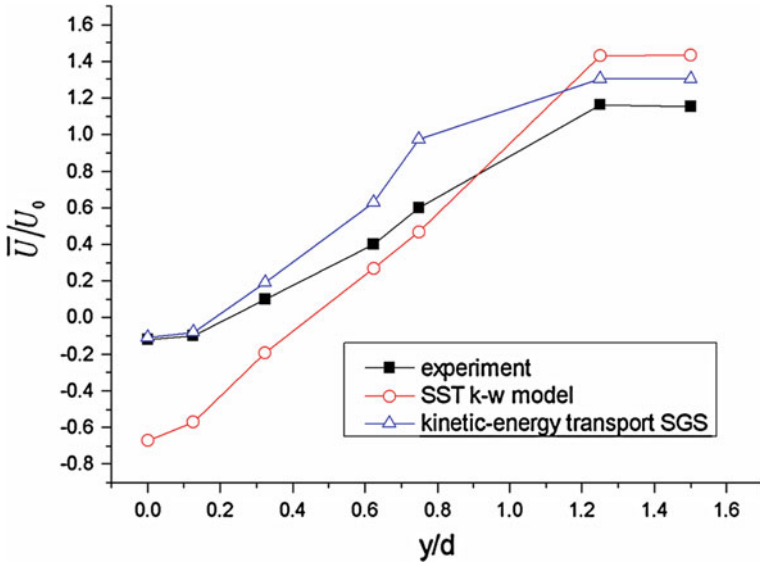**Fig. 69.3** Dimensionless velocity data sampling for time statistics at $x = -4.125d$

Fig. 69.4 Dimensionless velocity data sampling for time statistics at $x = -3.875d$

69.5 Application of Kinetic-Energy Transport SGS Model

Figure 69.5 shows the local velocity distribution in detail near an imaginary building using the kinetic-energy transport SGS model and SST $k - \omega$ model. The Reynolds number is 21400. A group of vortex cores only can be seen clearly at one side of the building in the velocity distribution profile from the kinetic-energy transport SGS model (Fig. 69.5a). Nothing is there in Fig. 69.5b obtained with the RANS. In Fig. 69.5b, the dual-line-vortex wake approximating to Karman Vortex Street is observed by SST $k - \omega$ model.

Figure 69.6 shows the detailed turbulence intensity distribution from the kinetic-energy transport SGS model and SST $k - \omega$ mode near the building. A
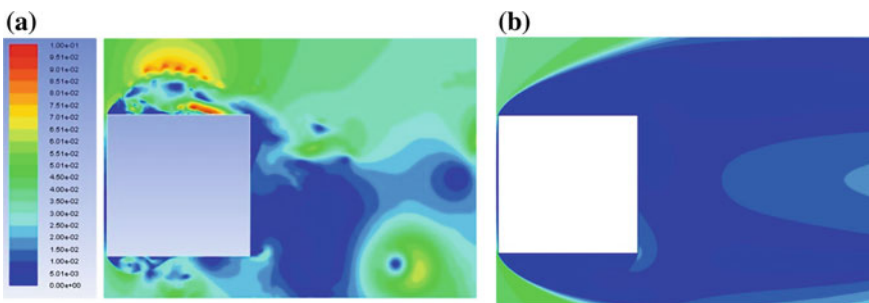

Fig. 69.5 Detailed velocity distribution around virtual building (**a**) SGS model. **b** SST $k - \omega$
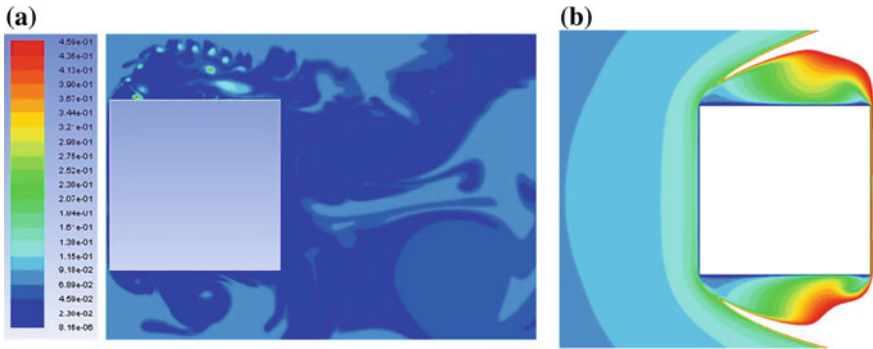
Fig. 69.6 Detailed turbulence intensity distribution around virtual building (**a**) SGS model. **b** SST $k - \omega$

group of high turbulence intensity zones can be seen clearly at the side of the building from the kinetic-energy transport SGS model (Fig. 69.6a); however, it cannot be seen in Fig. 69.6b from SST $k - \omega$ mode. In Fig. 69.6b, there are two symmetric higher turbulence intensity zones.

69.6 Conclusion

The characteristics of SST $k - \omega$ model for RANS and kinetic-energy transport subgrid model for LES in the flow filed simulation around a square column were compared. The results show the kinetic-energy transport model is more accurate than the SST $k - \omega$ model in the simulation of transient wind field around tall building. The vortex generation and a group of high turbulent intensity zones are observed by kinetic-Energy Transport model. However, the dual-line-vortex wake approximating to Karman Vortex Street and two symmetric higher turbulence intensity zones are observed by SST $k - \omega$ model.

References

1. Yuan C, Ng E (2012) Building porosity for better urban ventilation in high-density cities—a computational parametric study. Build Environ 50:176–189
2. Ramponi R, Blocken B (2012) CFD simulation of cross-ventilation for a generic isolated building: Impact of computational parameters. Build Environ 53:34–38
3. Jiang G, Yoshie R, Shirasawa T, Jin X (2012) Inflow turbulence generation for large eddy simulation in nonisothermal boundary layers. J Wind Eng Ind Aerodyn 104:369–378

4. Nozu T, Tamura T (2012) LES of turbulent wind and gas dispersion in a city. J Wind Eng Ind Aerodyn 104:492–499
5. Menter FR (1994) Two-equation eddy-viscosity turbulence models for engineering applications. AIAA J 32(8):1598–1605
6. Kim WW, Menon S (1997) Application of the localized dynamic subgrid-scale model to turbulent wall-bounded flows. AIAA, Aerospace Sciences Meeting & Exhibit, 35th, Reno, NV, Jan. 6–9
7. Chen X, Zhou X, Li H, Zhu Y (2008) The unsteady numerical simulation of flow around building. Build Energy Environ 27(1):1–7

Chapter 70
Approach to Choose Proper Passive Design Strategies for Residential Buildings

Maohui Luo, Borong Lin and Bin Cao

Abstract The climates differ greatly in China, ranging from severe cold to hot. This significantly influences building design strategies used to achieve indoor thermal comfort. To choose proper passive strategies for different climate zones in the early design stage, bioclimatic chart method has been used during the past decades. However, limited efforts have been conducted to test this method. This paper focuses on developing an approach to choose suitable passive strategies by combining building simulation tools and thermal comfort theories together. To achieve this purpose, hourly simulation program was used to obtain indoor thermal environment based on building description and outdoor weather condition. Adaptive thermal comfort model was used to determine whether indoor thermal environment was comfortable.

70.1 Introduction

Providing comfortable indoor environment is one of the primary objectives of building. Numerous studies have been done to research occupant's thermal comfort in different climates around the world. Several significant theories have been widely recognized, such as the "PMV" and "PPD" model proposed by Fanger [1], the ASHRAE comfort standard [2], and adaptive model proposed by De Dear and Brager [3]. However, how to use these theories to guide building design still needs further research.

M. Luo (✉) · B. Lin · B. Cao
Department of Building Science, Tsinghua University, Beijing 100084, China
e-mail: luo_mao_hui@163.com

During the past decades, efforts have been paid to develop a systematic approach to adapt human comfort requirements and outdoor climate conditions in the early building design stage [4]. These attempts aimed at choosing suitable design strategies based on climate feature. Olgyay's bioclimatic chart [5] was first proposed in 1950s to incorporate the outdoor climate into building design. In his chart, Olgyay located human comfort zone on a psychometric chart to facilitate the analysis of climate characteristics. As the concept of Olgyay's chart was based on outdoor climatic data, it was not appropriate to analyze the requirement of indoor thermal environment. To overcome the disadvantages of Olgyay's chart, Givoni developed his bioclimatic charts aimed at predicting the indoor conditions according to the outdoor climatic environment in 1979 [6]. In Givoni's chart, the effect of each passive strategy was determined and the specific boundary for each technique was presented. Proper passive strategies could be determined by plotting temperature amplitude and vapor pressure on psychometric chart. The strategies included evaporative cooling, thermal mass, natural ventilation cooling, passive heating, and Givoni's bioclimatic charts have been widely referenced by many studies and some researchers even attempted to develop computerized program to further Givoni's bioclimatic chart analysis. In China, limited works have been done in the field of bioclimatic design strategies' analysis, except recent efforts by Yang et al. [7, 8]. These researches mainly tried to apply Givoni's bioclimatic method in China and develop boundaries of passive strategies on psychometric chart under various weather conditions.

However, although computer simulation method is becoming more accessible, limited efforts have been conducted to test the boundaries of passive design strategies on Givoni's bioclimatic chart [9]. This study mainly focused on developing passive strategy zones on psychometric chart by combining simulation method and thermal comfort theories together. Differences between the results from Givoni's bioclimatic chart and the simulation approach were analyzed.

70.2 Methodology

This study consists of two stages: The first simulation process involved obtaining indoor thermal condition based on building descriptions and outdoor weather condition and the Design Builder simulation program, which was a comprehensive user interface of EnergyPlus dynamic thermal simulation engine, which was used as simulation tool. The second stage analyzed the results of building simulation in Microsoft Excel program.

As this paper mainly focused on the method of developing boundaries of different passive strategies on psychometric chart, only residential buildings and one representative city were taken into consideration.

70.2.1 Simulation Tool

The first part of Fig. 70.1 describes the simulation process, and it mainly consisted of 4 steps: Firstly, a three-story residential building input file that compliant with national design standard for energy efficiency of residential buildings' code was used as basic case. The second part of Fig. 70.1 displays the architecture rendering of prototype model in Design Builder program. And Table 70.1 provides a brief description of the base case. Secondly, typical meteorological year (TMY) weather data of selected city were prepared. In the third stage, the basic building model with four different passive strategies, namely ventilation, shading, passive solar, and insulation, was simulated, respectively. Table 70.2 lists the description of these strategies. Finally, the input files were generated to run the simulation program.

70.2.2 Analyzing Tool

The process to display outcomes includes two main tasks: (1) extracting the simulation results and (2) projecting the simulation results on the psychometric chart.

The hourly reported weather data obtained from EnergyPlus simulation program were used in this study. Several Excel spreadsheets were developed to identify, extract, and rearrange the data into an appropriate format. The thermal
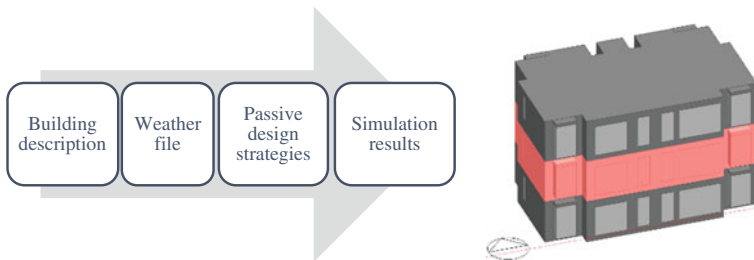

Fig. 70.1 Flowchart of simulation process and the prototype model of the building model

Table 70.1 The building components information

Envelop	Value and type	Description in input file
House	15 × 8 × 3.2 m	3 occupants
Window	U = 2.5 W/(K·m^2)	Double plane, 30 % of external wall area
Wall	U = 0.92 W/(K·m^2)	Brickwork, polystyrene, concrete, gypsum plaster
Floor	U = 1.69 W/(K·m^2)	Concrete, plaster
Roof	U = 0.74 W/(K·m^2)	Asphalt, foam phenol, concrete, and plasterboard

Table 70.2 The passive strategies information

Strategies	Types	Description in input file
Ventilation	Natural ventilation	Ventilation is on when $T_{in} > T_{out}$ and $T_{in} > 24$ °C
Shading	Outside shading	Shading is on when $T_{in} > 25$ °C
Passive solar	–	Shading is off when $T_{in} < 22$ °C
Insulation	–	–

Note T_{in} and T_{out} represent indoor air temperature and outdoor air temperature, respectively

data used in the analysis process include the following: dry-bulb temperature, humidity ratio, and solar radiation. Additionally, tools were developed to find the density dots of outdoor conditions, which represent the frequencies of the occurrence of outdoor conditions when indoor thermal comfort was achieved. In this way, outdoor climate conditions were plotted on the psychometric chart combined with ASHRAE comfort zone.

70.3 Results and Discussion

70.3.1 Impact of Thermal Comfort Evaluation Criterions

Different thermal comfort evaluation criterions can significantly affect evaluation results of indoor thermal environment. As aforementioned, ASHARE comfort standard and adaptive thermal comfort model are two different comfort evaluation criterions. Which one should be applied in selecting passive design strategies for residential buildings?

Figure 70.2 presents field-measured indoor air temperature (T_{in}) of a typical residential building in Shanghai. The T_{in} fluctuated between 18 and 25 °C in April, and most occupancies felt comfortable. However, great different indoor thermal environment evaluation results could be resulted by different evaluation criterions. Figure 70.3 describes percentage of indoor thermal comfortable hours in five residential houses with two evaluation criterions. Over 90 % of the time in April could be comfortable under the judgement of thermal adaptive model, which was closer to the actual sensation of households. However, the percentage of comfortable hours would decrease to around 35 % when ASHRAE comfort standard was used.

Fig. 70.2 Indoor air temperature of a residential building located in Shanghai
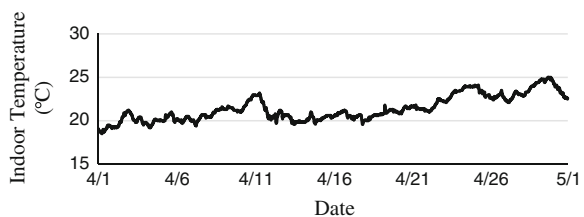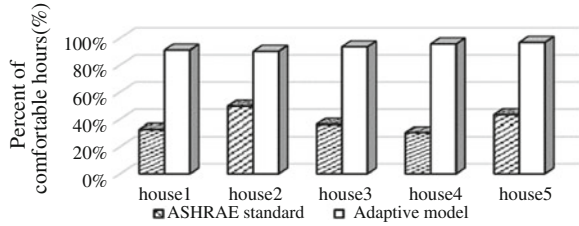
Fig. 70.3 Percentage of comfortable hours with different comfort evaluation criterions

As the primary objective of passive design strategies is to provide comfortable indoor environment, the definition of "comfort" greatly depends on actual sensation of households. This study did not focus on thermal comfort evaluation criterion discussion, and the adaptive thermal comfort model proposed in [10] was used.

70.3.2 Simulation Results' Validation

Although computer building simulation is becoming more accessible, it is still important to validate the accuracy of simulation results. In this study, the simulation results were compared to field-measured data in Shanghai residential buildings. Figure 70.4 shows the monthly percentage of comfortable hours obtained from three different methods. It can be seen that the simulation results were quite close to the field investigation results, while the results obtained from bioclimatic chart were significantly different from field investigation results. Additionally, Fig. 70.4 also reveals that Givoni's bioclimatic method may underestimate the role played by building envelops in maintaining indoor thermal comfort.

70.3.3 Boundaries of Passive Strategies on Psychometric Chart

This section consists of two stages: (1) Displaying boundaries of passive strategies on psychometric chart and (2) comparing the new boundaries and Givoni's bioclimatic chart.

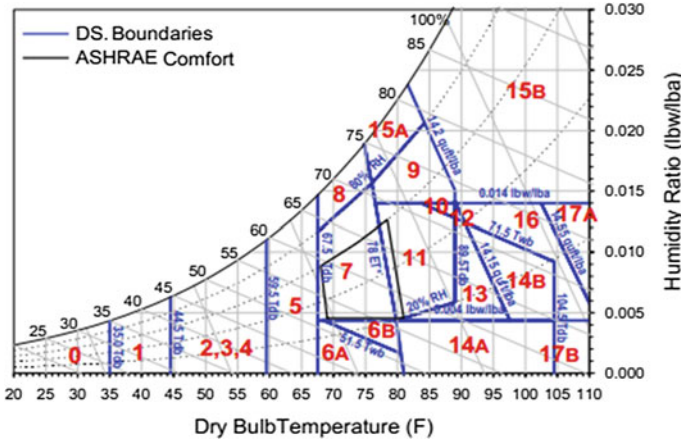**Fig. 70.4** Simulation result validation
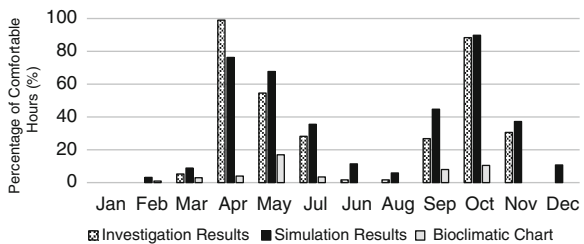
Fig. 70.5 Givoni–Milne strategies' boundaries [6]

To present boundaries of passive strategies on psychometric chart, Microsoft Excel program was used to rearrange annual outdoor weather conditions and project density data dots of outdoor weather conditions onto psychometric chart. In the second stage, comparison between present study and Givoni's bioclimatic method was conducted.

Figure 70.5 describes the boundaries of passive design strategies on Givoni's bioclimatic chart. These strategies include the following: passive solar, internal gains, dehumidification, ventilation, evaporative cooling, high thermal mass. Figure 70.6 displays the TMY weather data of Shanghai, and the following figures present boundaries of selected passive strategies based on simulation results.

Figure 70.7 indicates that not only outdoor weather condition located in comfort zone could result in comfortable indoor thermal environment. Owing to the thermal performance of building envelops, it could still maintain indoor environment comfortable, while the outdoor climate was slightly outside of
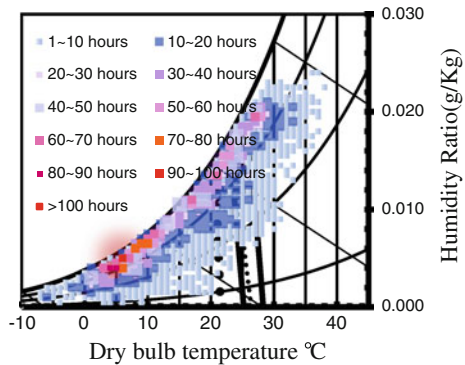
Fig. 70.6 Shanghai weather data
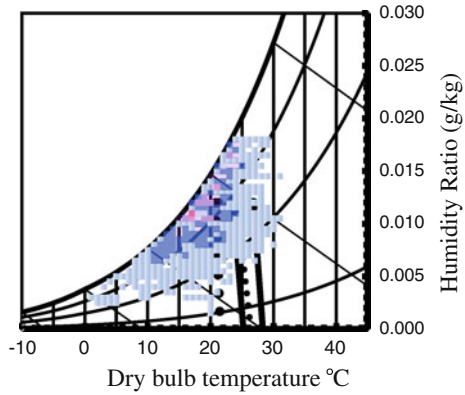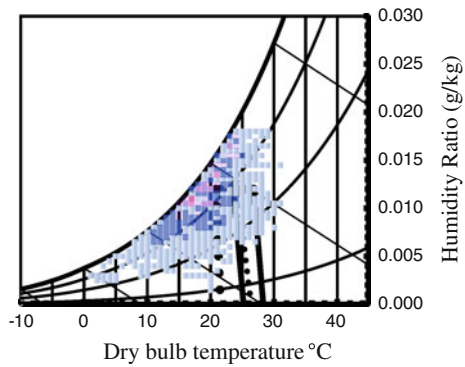
Fig. 70.7 Boundary of basic model

Fig. 70.8 Boundary of insulation

comfort zone. However, in Givoni's bioclimatic chart shown in Fig. 70.5, only outdoor climate located in comfort zone would be considered as comfortable. This resulted in Givoni's bioclimatic chart method underestimating the percentage of comfortable hours. Also, it could explain why Givoni's bioclimatic chart method led to the lowest percentage of comfortable hours as shown in Fig. 70.4.

As Givoni's method did not pay enough attention on the effect of building itself, some strategies associated with thermal performance of building envelops could not be well expressed on the chart. Figure 70.9 indicates that when outdoor temperature was relatively high, appropriate shading could maintain the indoor temperature within comfort range. However, Givoni's bioclimatic chart did not describe the effect of shading, although there were 21 zones on the chart (Figs. 70.8, 70.10, 70.11).

In the aspect of ventilation and passive solar strategies, the boundaries obtained from simulation results were quite similar to those from Givoni's method. However, in future study, more attention should be paid on specific value of comfortable hours. For instance, on Givoni's chart, all outdoor weather condition fell in the ventilation region would be considered as comfortable. But, simulation results

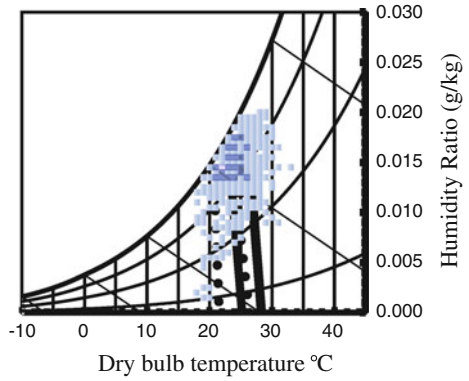**Fig. 70.9** Boundary of shading

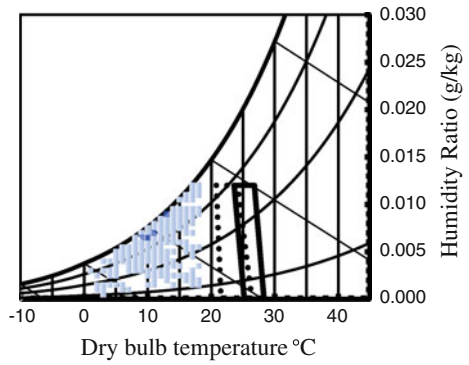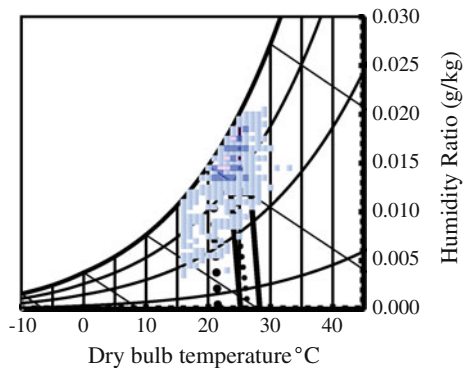
Fig. 70.10 Boundary of passive solar

Fig. 70.11 Boundary of ventilation

showed that because of thermal performance of building envelops, some outdoor weather data in this region could also result in appreciate indoor environment even without ventilation. This revealed that the effect of some passive strategies may be overestimated in Givoni's method.

70.4 Conclusion

This study proposed an approach to develop boundaries of passive strategies on psychometric chart by combining simulation tools and thermal comfort theories together. The result of proposed method was validated by field-measured data, and it was accurate enough.

The comparison between simulation method and Givoni's bioclimatic chart was conducted. The results indicated that Givoni's bioclimatic chart neglected thermal performance of building envelop. Therefore, some passive strategies could not be well described on the chart, while some of others might be overestimated.

References

1. Fanger PO (1982) Thermal comfort. Robert E Krieger Publishing Company, Malabar
2. ASHRAE (2005) ASHRAE standard 55, thermal environmental conditions for human occupancy. American Society of Heating, Refrigerating and Air-Conditioning Engineers
3. De Dear R, Brager GS (2001) The adaptive model of thermal comfort and energy conservation in the built environment. Int J Biometeorol 45:100–108
4. Zuhairy AA, Sayigh AAM (1993) The development of the bioclimatic concept in building design. Renew Energy 3:521–533
5. Olgyay V (1963) Design with Climate: bioclimatic approach to architectural regionalism. Princeton University Press, Princeton
6. Givonin B (1976) Man, climate and architecture. Applied Science Publishers Ltd, London
7. Yang L (2003) Climatic analysis and architectural design strategies for bio-climatic design. Xi'an University of Architecture and Technology. (In Chinese)
8. Lam JC, Yang L (2006) Development of passive design zones in China using bioclimatic approach. Energy Convers Manage 47:746–762
9. Visitsak S (2007) An evaluation of the bioclimatic chart for choosing design strategies for a thermostatically-controlled residence in selected climates. PhD paper of Texas A&M University
10. Cao B (2012) Research on the impacts of climate and built environment on human thermal adaption. Tsinghua University. (In Chinese)

Chapter 71
Investigation and Analysis on Air Quality Around a Power Plant in Xi'an

Xiaojing Meng, Yi Wang, Hai Wang and Jingtao Lai

Abstract The effect of power plant on air quality is a focused issue. The intention of this paper is to survey the air quality around a power plant in Xi'an. The concentration of pollutants in non-heating season and heating season has been tested, and the concentration of pollutants in different time of a day has been tested. In non-heating season, the concentrations of sulfur dioxide and nitrogen oxide at each test point meet the national standard of daily average concentration. The distance of maximum concentration of pollutants is 2 km to the leeward. The concentration of particular matter at six test points exceeded the national standard of daily average concentration. In heating season, the concentrations of sulfur dioxide, nitrogen oxide, and particulate matter at each test point meet the national standard of daily average concentration. Compare the results of non-heating season and heating season, the concentrations of particular matter are higher in non-heating season. The road dust and the sand soil dust have an important effect on the concentrations of particular matter.

Keywords Power plant · Pollutant · Air quality · National standard

X. Meng · Y. Wang (✉) · H. Wang · J. Lai
School of Environmental and Municipal Engineering, Xi'an University
of Architecture and Technology, Xi'an 710055 Shaanxi, China
e-mail: wangyi@xauat.edu.cn

X. Meng
e-mail: mengxj@mail.ustc.edu.cn

X. Meng
College of Materials and Mineral Resources, Xi'an University
of Architecture and Technology, Xi'an 710055 Shaanxi, China

71.1 Introduction

In recent years, large fog–haze weather has happened many times in China. Air quality has become a popular topic recently. The air quality reflects the degree of air pollution, and it is judged according to the level of air pollutant concentration. The major pollutants of power plant are sulfur dioxide, nitrogen oxide, and particulate matter, which affect the human health, vegetation ecology, and visibility [1]. Numerous investigations have been made on the air quality of the environment; especially, the air quality was great attention in Beijing [2–5]. Zhu [6] analyzed and studied the main pollution compounds and their seasonal dynamic and spatial distribution on the basis of the air-monitoring data of Harbin. Fand [7] studied the relationship between the inorganic components in TSP and their pollution sources in four typical cities in Jilin Province. But there are few studies on the air quality around a power plant.

At present, power plants are built in the suburbs. But as the city construction and development, the suburban areas will be the further developed. The research on environment around a power plant is limited. The major pollutants of power plant are sulfur dioxide (SO_2), nitrogen oxide (NO_X), and particulate matter (PM_{10}). The intention of this paper is to survey the air quality around a power plant in Xi'an. The concentration of pollutants in non-heating season and heating season has been tested.

71.2 Test

The major pollutants of sulfur dioxide (SO_2), nitrogen oxide (NO_X), and particulate matter (PM_{10}) are tested around a power plant in Xi'an. The concentration of pollutants in non-heating season and heating season has been tested. The test time of non-heating and heating is October and December 2011, respectively.

The test equipment of SO_2 and NO_X is used Handpump LP-1200. The lower limit of test of SO_2 and NO_X is 0.13 and 0.08 mg/m^3, respectively. Although the lower limit of test is high, both the lower limit of test of SO_2 and the lower limit of test of NO_X are lower than the national standards of ambient air quality for daily average. The test equipment of PM_{10} used dust detector, and the test equipment of wind speed and environment temperature used Swema 3000.

Prevailing direction of the wind in the power plant location is northeast, but the wind direction is not stable. The arrangement of test points uses the concentric circles' method, which can achieve the test requirement and reduce the actual test. Because of some hindering factors in the actual test, some theoretical points are no way to test and use the equivalence of the practical points to replace the theoretical points. In non-heating season, thirteen test points are arrangement (Fig. 71.1). Due to the test points in heating season, six test points are arrangement (Fig. 71.2). Each grid of the side length is 1 km.
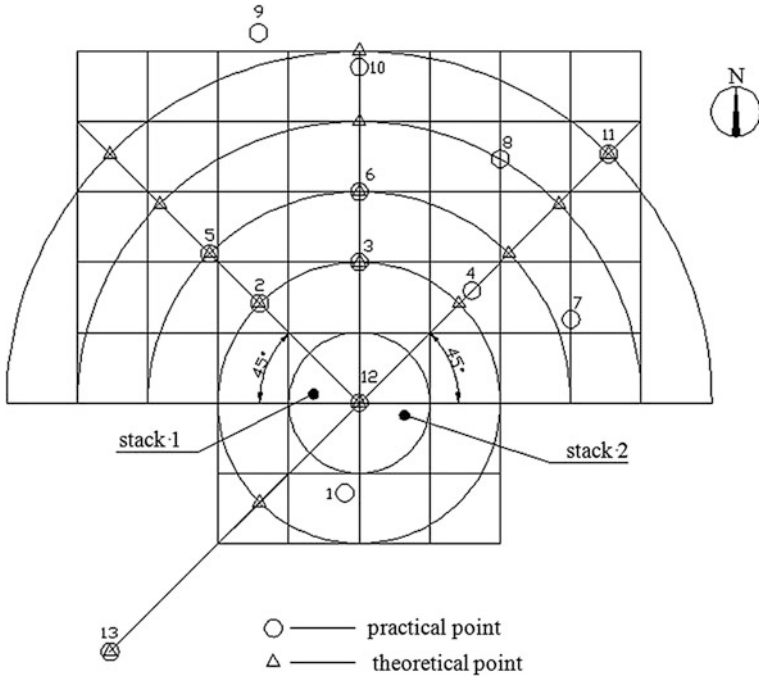
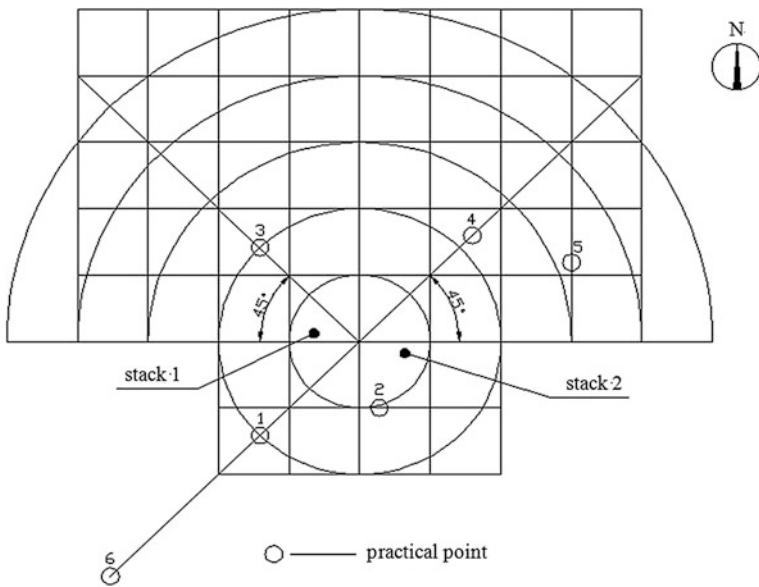**Fig. 71.1** The layout drawing of test point in non-heating season

Fig. 71.2 The layout drawing of test point in heating season

71.3 Results and Discussion

71.3.1 Test Results in Non-heating Season

In non-heating season, the test time is October 2011 and thirteen test points are arrangement. The average atmospheric temperature is 12 °C, and the wind direction is northeast.

The test results show that in non-heating season, the concentration of SO_2 at each test point is lower than the lower limit of test (0.13 mg/m^3), and the national standard of daily average concentration is 0.15 mg/m^3. The test results also show that the concentration of NO_X at each test point is lower than the lower limit of test (0.08 mg/m^3), and the national standard of daily average concentration is 0.10 mg/m3. So in non-heating season, the concentrations of SO_2 and NO_X at each test point meet the national standard of daily average concentration. In non-heating season, the concentration of PM_{10} at each test point is shown in Fig. 71.3.

Figure 71.3 shows that the maximum concentration of PM_{10} occurs at test point 1, i.e., two kilometers to the leeward. The concentration of PM_{10} at six test points (test points 1, 6, 8, 11, 12, and 13) exceeded the national standard of daily average concentration. That is because the test points 1, 12, and 13 are downwind of the power plant. And the passing vehicles have a great influence on the test results, which make the concentration of PM_{10} at each test point higher than the actual concentration.

71.3.2 Test Results in Heating Season

In heating season, the test time is December 2011 and six test points are arrangement. The average atmospheric temperature is 6 °C, and the wind direction is northeast.
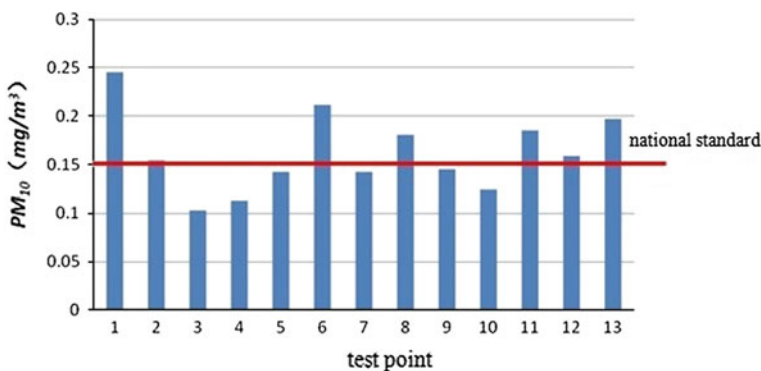

Fig. 71.3 The concentration of PM_{10} at each test point in non-heating season
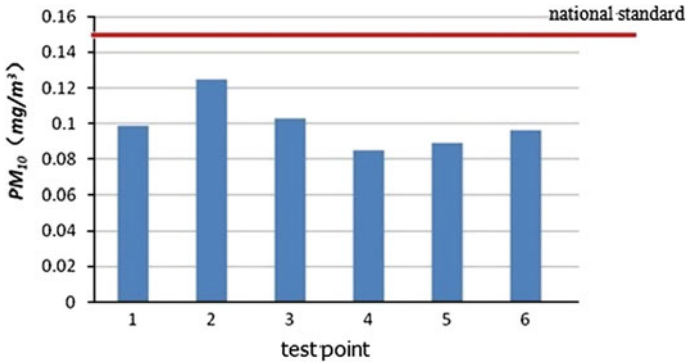
Fig. 71.4 The concentration of PM_{10} at each test point in heating season

The test results show that in heating season, the concentration of SO_2 at each test point is lower than the lower limit of test (0.13 mg/m^3), and the national standard of daily average concentration is 0.15 mg/m^3. The test results also show that the concentration of NO_X at each test point is lower than the lower limit of test (0.08 mg/m^3), and the national standard of daily average concentration is 0.10 mg/m^3. So in heating season, the concentrations of SO_2 and NO_X at each test point meet the national standard of daily average concentration. In heating season, the concentration of PM_{10} at each test point is shown in Fig. 71.4.
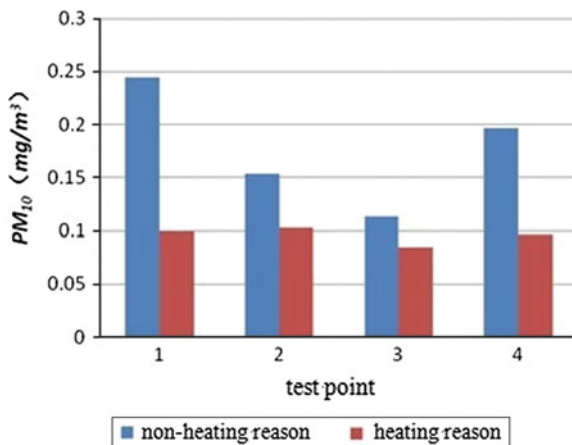
Figure 71.4 shows that in heating season, the concentration of PM_{10} at each test point is lower than the national standard of daily average concentration (0.15 mg/m3). So in heating season, the concentrations of PM_{10} at each test point also meet the national standard of daily average concentration.

71.3.3 Comparison Between Non-heating Season and Heating Season

There are 4 common points in non-heating season and heating season, namely the test point 1 in non-heating season corresponds to the test point 1 in heating season, the test point 2 in non-heating season corresponds to the test point 3 in heating season, the test point 4 in non-heating season corresponds to the test point 4 in heating season, and the test point 13 in non-heating season corresponds to the test point 6 in heating season. New corresponding points 1, 2, 3, 4, and the results are shown in Fig. 71.5.

Figure 71.5 shows that the concentration of PM_{10} in non-heating season is higher, mainly due to the impact of meteorological factors such as wind speed and wind direction, as well as road dust and soil wind dust, while the test in heating season tries to avoid the impact of the passing vehicles and the two test averaging

Fig. 71.5 The concentration of PM_{10} in non-heating season and heating season

method to minimize the impact of the chance factors. So in non-heating season and heating season, road dust and soil wind dust have an important impact on the atmospheric pollutants PM_{10}.

71.4 Conclusions

The concentration of pollutants in non-heating season and heating season has been tested around a power plant in Xi'an. The concentrations of SO_2 and NO_X at each test point in non-heating season and heating season meet the national standard of daily average concentration. In non-heating season, the concentration of PM_{10} is higher than that in heating season and six test points exceeded the national standard of daily average concentration; the season is the impact of meteorological factors such as wind speed and wind direction, as well as road dust and soil wind dust. In heating season, the concentrations of PM_{10} at each test point meet the national standard of daily average concentration.

References

1. Hao J (1989) Air pollution control engineering. Higher Education Press, Beijing
2. Hao J, Wu Y, Fu L et al (2001) Motor vehicle source contributions to air pollutants in Beijing. Environ Sci 22(5):1–6
3. Zhang J, Miao H, Ouyang Z et al (2006) Ambient air quality trends and driving factor analysis since 1980s in Beijing. Acta Scientiae Circumstantiae 26(11):1886–1892

4. Zhao X, Xu Z, Wang X et al (2010) Analysis of Beijing cars with license plates allowed on the streets on air quality impact. J Safety Environ 10(4):82–87
5. Xu Y, Cheng S, Chen D et al (2007) Effect of road dust on air quality in Beijing. J Safety Environ 7(1):53–56
6. Zhu N, An G, Yu G et al (2002) The primary analysis of atmospherical environment in Harbin. J Northeast Forest Univ 30(3):123–126
7. Fang C, Lv L, Zhong Y et al (2007) The source analysis of the components in total suspended particulates in ambient air of typical cities in Jilin province. J Jilin Univ 37(5):988–992

Chapter 72
New Models for Separating Hourly Diffuse and Direct Components of Global Solar Radiation

Wanxiang Yao, Zhengrong Li, Yuan Lu, Fujian Jiang and Cui Li

Abstract Due to the lack of domestic hourly solar radiation measured data, models which are used to separate hourly diffuse and direct components of global solar radiation on horizontal surface are always referencing foreign models. However, because of different geographical factors (such as latitude and longitude) and meteorological conditions (such as atmospheric transparency, temperature, and humidity), it is difficult to have broad application. This study uses hourly solar radiation measured data from Shanghai to evaluate and compare models in the published literature which were used to separate hourly diffuse and direct components of global solar radiation on horizontal surface, and several relatively accurate available models are chosen. Then, new improved models are consequently proposed and compared with these existing models for calculating hourly diffuse solar radiation based on statistical parametric analysis, residual histogram analysis, and fitted curve analysis. It is found that these new improved models are in better agreement with the measured data, and they are more suitable for calculating diffuse and direct solar radiation under complicated weather conditions.

Keywords Solar radiation · Clearness index · Diffuse fraction · New models

Nomenclature

H_0 Hourly extraterrestrial global solar radiation on a horizontal surface (kJ/m^2)
H Hourly global solar radiation on a horizontal surface (kJ/m^2)
H_d Hourly diffuse solar radiation on a horizontal surface (kJ/m^2)
H_b Hourly beam solar radiation on a horizontal surface (kJ/m^2)
H_{bc} Hourly beam solar radiation on a horizontal surface under clear-sky conditions (kJ/m^2)

W. Yao · Z. Li (✉) · Y. Lu · F. Jiang · C. Li
College of Mechanical and Energy Engineering, Tongji University, 200092 Shanghai, China
e-mail: lizhengrong@tongji.edu.cn

K_T Daily clearness index (dimensionless)
K_t Hourly clearness index (H/H_0)(dimensionless)
K_{t+1} Hourly clearness index at hour h + 1(dimensionless)
K_{t-1} Hourly clearness index at hour h-1(dimensionless)
K_d Hourly diffuse solar radiation fraction (H_d/H)(dimensionless)
K_b Hourly beam solar radiation fraction (H_b/H)(dimensionless)
ΔK_b Hourly direct beam atmospheric transmittance changes (dimensionless)
K_{nc} Hourly direct beam atmospheric transmittance under clear-sky conditions
           $(H_{bc}/(H_0/\sin h))$(dimensionless)
ϕ Latitude of site (degrees)
H   Solar altitude (degrees)
K_1 Intermediate variable (dimensionless)
K_2 Intermediate variable (dimensionless)
m   Air mass (dimensionless)
t   Ambient temperature (°)
φ Relative humidity (%)
S_0 Apparent solar time (h)
ψ Persistence index (dimensionless)

72.1 Introduction

Knowledge of the solar radiation incident at a specific location is necessary for the design and assessment of solar energy conversion systems [1]. Solar system and building design as well as thermal performance analysis require irradiation values on inclined surfaces. However, for most areas, these data are not available and must be estimated generally through models that use input of daily and hourly global irradiation data on the horizontal surface [2]. Our stations always measure only global radiation and for which an estimated model of diffuse radiation is desired. Even when data on both global and diffuse radiation are available, it is often necessary to compile long, unbroken sequences of data to estimate missing values of diffuse radiation [3].

Most existed works on diffuse irradiation have been based on data from North American, Canadian, Australian, or North European stations as well as from Liu and Jordan [4]. After that, a lot of models have been proposed to establish a relationship between diffuse and total global horizontal irradiation. Orgill and Hollands [5] analyzed the hourly diffuse radiation and recommended an equation to determine hourly ratio of diffuse to total radiation received on horizontal surfaces. Collares-Pereira and Rabl [6] proposed a new correlation for the daily total ratio of diffuse over hemispherical insolation, which agreed with results reported in India, Israel, and Canada which included the shade-ring correction. This model suggested that latitude independence was a good approximation, and it implied

that the diffuse component was significantly larger than that predicted by the original formulas of Liu and Jordan. Erbs et al. [7] used a new database (from four US weather stations) composed with hourly direct, normal radiation and global radiation to develop an estimated model of the diffuse fraction of hourly, daily, and monthly average global radiation. Spencer [3] compared four models of estimating hourly diffuse irradiation from global radiation and then suggested a new method for deriving suitable values of the constants for places situated between 20° and 45° Reindl et al. [8] studied the influence of climatic and geometric variables on the hourly diffuse fraction and concluded that the diffuse correlations are season and location dependent. Chandrasekaran and Kumar [1] used five-year data of hourly global and diffuse radiation on a horizontal surface at a tropical location (Madras, India) to establish the relationship between the hourly diffuse fraction and hourly clearness index. Lam and Li model [9] analyzed the data for diffuse, global horizontal radiation measured at the City University of Hong Kong for the period 1991–1994 and proposed a hybrid correlation model for the prediction of hourly direct and diffuse components from the global solar radiation for Hong Kong. Boland et al. [10] developed two models: one model used hourly data from a weather station setup at Deakin University, Geelong. Another model was developed for 15-min data values. These two models show that apparent solar time is a better predictor than solar altitude. Miguel et al. [2] examined the performance of daily and hourly diffuse horizontal solar irradiation models and correlations using an assembled data set of multivariate meteorological time series from countries in the North Mediterranean Belt area. Oliveira et al. [11] developed correlation models to estimate hourly, daily, and monthly values of diffuse solar radiation on horizontal surfaces using global and diffuse solar radiation data measured from May 1994 to June 1999 in São Paulo City, Brazil. Karatasou et al. [12] presented an analysis of hourly diffuse radiation on a horizontal surface. Soares et al. [13] applied a perceptron neural network technique to estimate hourly values of the diffuse solar radiation at the surface in São Paulo City, Brazil, using as input the global solar radiation and other meteorological parameters measured from 1998 to 2001. Boland et al. [14] used the logistic function instead of piecewise linear or simple nonlinear functions to estimate hourly diffuse solar radiation.

We choose some models from the literature. The criteria for selection in this study are as follows: (1) full availability of algorithms and numerical coefficients, (2) use of input data either generally available or obtainable from available model cascades, and (3) the results reported by the original literature as well as those published in reviews were considered [2]. This paper presents a comparison of these 19 models of estimating hourly diffuse from global solar radiation using data from Shanghai. For comparative analysis, models are divided into five groups according to the performance characteristics. After analyzing the existing models, five new improved correlations are proposed and compared with these existing models.

72.2 Data and Methodology

72.2.1 Meteorological Data Collection

The data of hourly diffuse, direct, and global solar radiation on a horizontal surface were measured by Tongji University (31°17′N, 121°31′E) from July 2012 to November 2012.

In order to investigate the relationship between hourly diffuse and global radiation, we have to control the quality of records. The quality control procedures used are based on Miguel et al. (2001) [2] and referred to the physical and climatic extremes found in our measured data. About three percent of the data are discarded which have incomplete or unreasonable records. Application of above criteria does not have any significant effect on our results. The final data set contains 1,155 pairs of data points.

72.2.2 Statistical Analysis Methods

In the literature, there are several statistical test methods used to statistically evaluate the performance of the solar radiation models. Among those, the coefficient of correlation (R), the relative standard error (RSE), the mean bias error (MBE), the root mean square error (RMSE), Nash–Sutcliffe Equation (NSE), and the t-statistic (t-stat) are the most commonly used methods to compare the results statistically [2, 11–13, 15].

72.3 Performance Results and Discussion

These models are evaluated by three indexes: statistical parametric, fitted curve, and residual histogram.

72.3.1 Statistical Parametric Analysis

For the five groups of models studied, the following statistical parameters are obtained from the evaluation of the values presented in Table 72.1:

The measured data are compared with the values calculated from the correlations tabulated in Table 72.1 which shows the following results:

Table 72.1 The R, MBE, RMSE, NSE, and t-stat values of the models

Models	R	MBE	RMSE	NSE	t-stat
Orgill and Hollands model [5]	0.917	0.091	0.164	0.722	22.706
Spencer model [3]	0.913	0.190	0.232	0.440	47.898
Reindl et al. model 1 [8]	0.916	0.094	0.170	0.701	22.427
Louche et al. model [17]	0.911	0.122	0.192	0.620	28.186
Oliveira et al. model [11]	0.861	0.077	0.185	0.645	15.488
Soares et al. model [13]	0.877	0.122	0.198	0.593	26.383
Collares-Pereira and Rabl model [6]	0.792	0.020	0.191	0.623	3.658
Erbs et al. model [7]	0.916	0.088	0.169	0.704	20.730
Hawlader model [18]	0.906	0.122	0.180	0.665	31.330
Chandrasekaran and Kumar model [1]	0.912	0.081	0.161	0.731	19.658
CLIMED hourly model [2]	0.915	0.088	0.165	0.718	21.277
Karatasou et al. model [12]	0.896	0.117	0.183	0.654	28.353
Boland et al. model 1 [10]	0.920	0.097	0.168	0.707	24.132
Boland et al. model 2 [14]	0.921	0.103	0.176	0.679	24.527
Skartveit and Olseth Model [19]	0.558	0.090	0.292	0.116	10.976
DISC model [20]	0.642	0.087	0.432	0.939	6.980
Reindl et al. model 2 [8]	0.894	0.063	0.161	0.730	14.478
Reindl et al. model 3 [8]	0.881	0.076	0.174	0.687	16.595
Boland-Ridley-Lauret (BRL) model [21]	0.926	0.099	0.172	0.693	24.048

(a) Among Group I (piecewise linear models), coefficient of correlation (R) of these models are greater than or equal to 0.913. Reindl et al. model 1 gives the best results of t-stat value, while Orgill and Hollands model gives the best results of R, MBE, RMSE, and NSE. So in this group, Orgill and Hollands model is the most accurate model, and the optimal statistical parameters of this model are as follows: $R = 0.917$, MBE $= -0.091$, RMSE $= 0.164$, and t-stat $= 22.427$.

(b) Among Group II (polynomial models), coefficient of correlation (R) of these models are greater than or equal to 0.861. Louche et al. model gives the best results of R, while Oliveira et al. model gives the best results of MBE, RMSE, NSE, and t-stat. So in this group, Oliveira et al. model is the most accurate model, and the optimal statistical parameters of this model are as follows: $R = 0.911$, RSE $= -0.077$, MBE $= 0.185$, RMSE $= 0.645$, and t-stat $= 15.488$.

(c) Among Group III (piecewise polynomial models), coefficient of correlation (R) of most models are greater than or equal to 0.896 except Karatasou et al. model equal to 0.792. Collares-Pereira and Rabl model gives the best results of RSE and t-stat, while Erbs et al. model gives the best results of R and MBE. So in this group, Erbs et al. model is the most accurate model, and the optimal statistical parameters of this model are as follows: $R = 0.916$, RSE $= -0.020$, MBE $= 0.169$, RMSE $= 0.731$, and t-stat $= 3.658$.

(d) Among Group IV (nonlinear models), coefficient of correlation (R) of models are greater than or equal to 0.920. Boland et al. model 2 gives the best results of R, while Boland et al. model 1 gives the best results of RSE, MSE, RMSE, and

t-stat. So in this group, Boland et al. model 1 are the most accurate models, and the optimal statistical parameters of these models are as follows: $R = 0.921$, RSE $= -0.097$, MBE $= 0.168$, RMSE $= 0.707$, and t-stat $= 24.132$.

(e) Among Group V (multi-parameters models), coefficient of correlation (R) of most models are greater than or equal to 0.881 except Skartveit and Olseth Model and DISC model. Reindl et al. model 2 gives the best results of MBE and RMSE. However, Boland-Ridley-Lauret (BRL) model gives the best results of R. So in this group, BRL model is the most accurate model, and the optimal statistical parameters of these models are as follows: $R = 0.926$, RSE $= -0.090$, MBE $= 0.161$, RMSE $= 0.730$, and t-stat $= 6.980$.

From the above analysis, it can be concluded that Orgill and Hollands model, Oliveira et al. model, Erbs et al. model, Boland et al. model 1, and BRL model are more accurate than other models in each group, and BRL model is the most accurate one.

72.3.2 Residual Histogram Analysis

Graphical residual analysis of typical models (residuals are estimations of experimental error obtained by subtracting the observed hourly diffuse solar fraction from the estimated one) for the horizontal surface is shown in Fig. 72.1.

The residual distribution of hourly diffuse solar fraction shows four tendencies, wide and left-skewed, wide and centered, concentrated and left-skewed, and concentrated and centered. Most of them are concentrated and left-skewed, only Collares-Pereira and Rabl model is concentrated and centered.

The above histograms show that the values of residuals of Orgill and Hollands model, Reindl et al. model 1, Spencer model, Oliveira et al. model, Chandrasekaran and Kumar model, CLIMED hourly model, Collares-Pereira and Rabl model, Erbs et al. model, Boland et al. model 1, BRL model, Reindl et al. model 2, and Reindl et al. model 3 exhibit generally small difference and are very close to zero. The average errors of these models are from -0.099 to 0.020. This suggests that these models' estimation of irradiation agree well with measured data [16]. On the contrary, the values of residuals for DISC model and Skartveit and Olseth Model exhibit generally large differences and are far away from zero, and these models are therefore not recommended.

72.3.3 Fitted Curve Analysis

The correlation between diffuse fraction and clearness index is displayed via $K_t–K_d$ scatter diagrams. The scatter diagrams of hourly values of $K_t–K_d$ are based
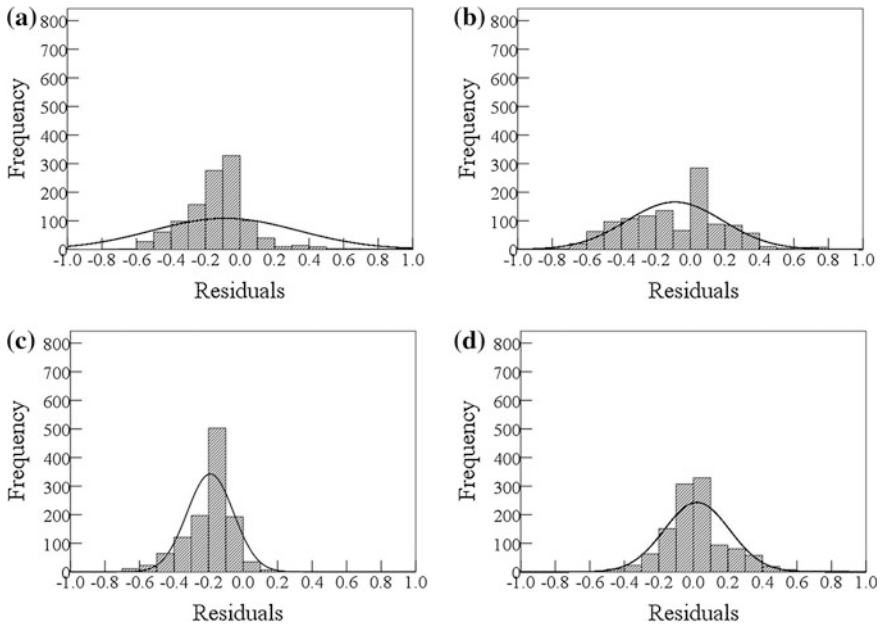
Fig. 72.1 Frequency of the residuals of the hourly diffuse solar fraction on a horizontal surface, calculated by models using the experimental data (**a**) wide and left-skewed (DISC model), (**b**) wide and centered (Skartveit and Olseth Model), (**c**) concentrated and left-skewed (Soares et al. model), and (**d**) concentrated and centered (Collares-Pereira and Rabl model)

on 1,155 pairs of points. The K_t–K_d diagrams displayed in Fig. 72.2 show 4 group correlations between diffuse fraction and clearness index in Shanghai.

It can be seen from Fig. 72.2 that the main differences among these models are the following two aspects. One is whether hourly diffuse solar fraction is close to 1 when clearness index is close to 0. Another one is what value hourly diffuse solar fraction is equal to when clearness index is greater than 0.75. The hourly diffuse solar fraction of most models is close to 1 when clearness index is close to 0 except for Spencer model ($K_d = 0.85$ when $K_t = 0$), Soares et al. model ($K_d = 0.9$ when $K_t = 0$), and Hawlader model ($K_d = 0.915$ when $K_t = 0$), and this is supported by the observed data shown in black square scatters in Fig. 72.2. However, hourly diffuse solar fraction is diverged when clearness index is greater than 0.75. It could hardly draw a conclusion from Fig. 72.2 that hourly diffuse solar fraction value is more accurate, because of deficient observed data in this interval.
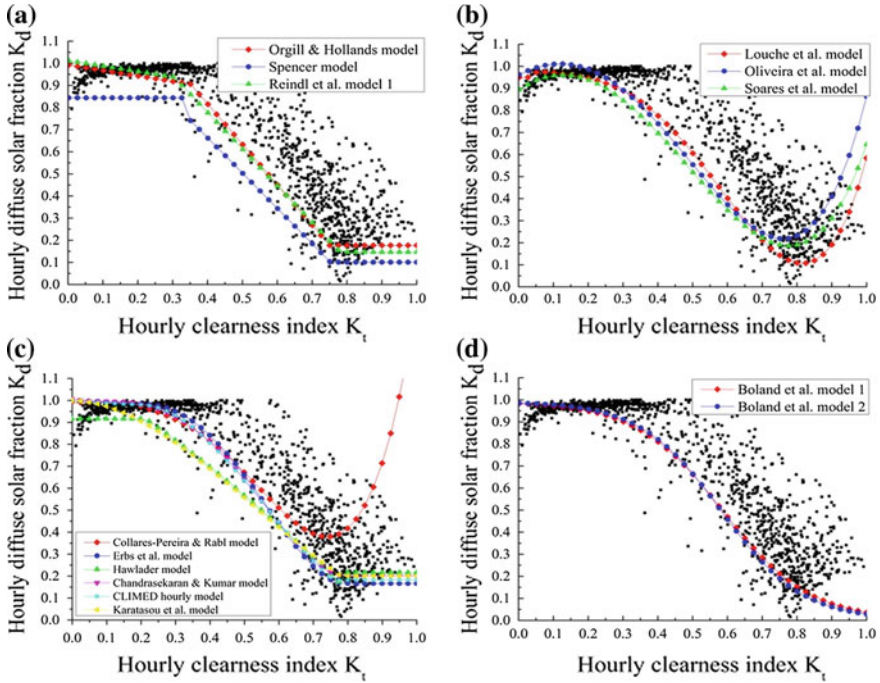
Fig. 72.2 Correlation of hourly diffuse solar fraction with clearness index. (**a**) Group I (piecewise linear models), (**b**) Group II (polynomial models), (**c**) Group III (piecewise polynomial models), and (**d**) Group IV (nonlinear models)

72.4 Improved Hourly Diffuse Solar Fraction Model

Five new improved correlations are proposed based on hourly diffuse, direct, and global solar radiation data from June 2012 to November 2012.

(1) Hourly measured data fitting model 1(HMDF model 1)

$$K_d = 0.9381 + 0.1481\, K_t, 0 \leq K_t \leq 0.3 \tag{72.1}$$

$$K_d = 1.5197 - 1.534 K_t, 0.3 < K_t \leq 0.8 \tag{72.2}$$

$$K_d = 0.27, K_t > 0.8 \tag{72.3}$$

(2) Hourly measured data fitting model 2(HMDF model 2)

$$K_d = 0.8142 + 2.0792 K_t - 6.1439 K_t^2 + 3.4707 K_t^3 \tag{72.4}$$

(3) Hourly measured data fitting model 3(HMDF model 3)

$$K_d = 0.8775 + 1.3991\,K_t - 4.9285\,K_t^2, K_t \leq 0.2 \tag{72.5}$$

$$K_d = 1.1209 - 2.1699K_t + 11.06K_t^2 - 22.355K_t^3 + 12.863K_t^4, K_t > 0.2 \tag{72.6}$$

(4) Hourly measured data fitting model 4(HMDF model 4)

$$K_d = 0.2421 + \frac{0.7202}{1 + e^{(K_t - 0.6203)/0.0749}} \tag{72.7}$$

(5) Hourly measured data fitting model 5(HMDF model 5)

$$K_d = 1/\left[\begin{array}{c} 1 + \exp(-2.1839 - 20.745K_t + 58.29927K_t^2 - 36.6937K_t^3 - 0.97868S_0 \\ + 1.52939S_0^2 - 0.00701h + 1.14911K_T + 0.006486\psi) \end{array} \right] \tag{72.8}$$

72.5 Comparison and Verification of Models

Five more accurate models in the literature and 5 measured data fitting models are compared using solar radiation data measured in 2012 December, and the results are shown in Table 72.2.

According to Table 3, it can be seen that the hourly measured data fitting model (HMDF model 1 ∼ 5) is more consistent with the measured values than models in the literature of each group, and model 5 is the most accurate ($R = 0.935$). So, they are more suitable for calculating diffuse and direct solar radiation under complicated weather conditions in Shanghai.

Table 72.2 The R, MBE, RMSE, NSE, and t-stat values of the models

Models	R	MBE	RMSE	NSE	t-stat
Orgill and Hollands model	0.906	−0.064	0.135	0.743	9.995
HMDF model 1	0.924	−0.011	0.103	0.850	1.984
Oliveira et al. model	0.884	−0.141	0.204	0.410	17.851
HMDF model 2	0.924	−0.013	0.102	0.854	2.349
Erbs et al. model	0.916	−0.119	0.182	0.533	16.200
HMDF model 3	0.928	−0.006	0.099	0.861	1.072
Boland et al. model 1	0.919	−0.114	0.168	0.603	17.233
HMDF model 4	0.925	−0.004	0.101	0.854	0.663
Boland-Ridley-Lauret (BRL) model	0.926	−0.125	0.180	0.542	18.130
HMDF model 5	0.935	0.026	0.098	0.863	5.055

72.6 Conclusions

Measurements of global and diffuse solar radiations at the Earth's surface in Shanghai (31°24′N, 121°29′E) between July 2012 and December 2012 are used to develop models to estimate the diffuse solar radiation from values of global solar radiation. Comparison of these models based on the correlation between the hourly diffuse solar fraction and clearness index can come to the following conclusions:

(1) From statistical parametric analysis, the most accurate models in the previous literature are as follows: Orgill and Hollands model, Oliveira et al. model, Erbs et al. model, Boland et al. model 1, and BRL model are the most accurate models.
(2) Residual histogram analysis found that the residuals of Orgill and Hollands model, Reindl et al. model 1, Spencer model, Oliveira et al. model, Chandrasekaran and Kumar model, CLIMED hourly model, Collares-Pereira and Rabl model, Erbs et al. model, Boland et al. model 1, BRL model, Reindl et al. model 2, and Reindl et al. model 3 are very close to zero, and these models' estimation of hourly diffuse radiation on a horizontal surface are fitted well with measured data. On the contrary, the residuals of DISC model and Skartveit and Olseth Model are far away from zero, and these models are therefore not recommended.
(3) From fitted curve analysis, the hourly diffuse solar fraction of most models is close to 1 when clearness index is close to 0 except for Spencer model, Soares et al. model, and Hawlader model, and this is supported by the observed data shown in black square scatters in Fig. 72.2. However, hourly diffuse solar fraction is diverged when clearness index is greater than 0.75.
(4) Measured data fitting model (HMDF model 1 ∼ 5) is more consistent with the measured values than models in the literature of each group, and model 5 is the most accurate. So, they are more suitable for calculating diffuse and direct solar radiation under complicated weather conditions in Shanghai.

References

1. Chandrasekaran J, Kumar S (1994) Hourly diffuse fraction correlation at a tropical location. Sol Energy 53:505–510
2. de Miguel A, Bilbao J, Aguiar R, Kambezidis H, Negro E (2001) Diffuse solar irradiation model evaluation in the North Mediterranean Belt area. Sol Energy 70:143–153
3. Spencer JW (1982) A comparison of methods for estimating hourly diffuse solar radiation from global solar radiation. Sol Energy 29:19–32

4. Liu BYH, Jordan RC (1960) The interrelationship and characteristic distribution of direct, diffuse and total solar radiation. Sol Energy 4:1–19
5. Orgill JF, Hollands KGT (1977) Correlation equation for hourly diffuse radiation on a horizontal surface. Sol Energy 19:357–359
6. Collares-Pereira M, Rabl A (1979) The average distribution of solar radiation-correlations between diffuse and hemispherical and between daily and hourly insolation values. Sol Energy 22:155–164
7. Erbs DG, Klein SA, Duffie JA (1982) Estimation of the diffuse radiation fraction for hourly, daily and monthly-average global radiation. Sol Energy 28:293–302
8. Reindl DT, Beckman WA, Duffie JA (1990) Diffuse fraction correlations. Sol Energy 45:1–7
9. Lam JC, Li DHW (1996) Correlation between global solar radiation and its direct and diffuse components. Build Environ 31:527–535
10. Boland J, Scott L, Luther M (2001) Modelling the diffuse fraction of global solar radiation on a horizontal surface. Environmetrics 12:103–116
11. Oliveira AP, Escobedo JF, Machado AJ, Soares J (2002) Correlation models of diffuse solar-radiation applied to the city of São Paulo, Brazil. Appl Energy 71:59–73
12. Karatasou S, Santamouris M, Geros V (2003) Analysis of experimental data on diffuse solar radiation in Athens, Greece, for building applications. Int J Sustain Energy 23:1–11
13. Soares J, Oliveira AP, Božnar MZ, Mlakar P, Escobedo JF, Machado AJ (2004) Modeling hourly diffuse solar-radiation in the city of São Paulo using a neural-network technique. Appl Energy 79:201–214
14. Boland J, Ridley B, Brown B (2008) Models of diffuse solar radiation. Renewable Energy 33:575–584
15. Ulgen K, Hepbasli A (2002) Comparison of solar radiation correlations for İzmir, Turkey. Int J Energy Res 26:413–430
16. Noorian AM, Moradi I, Kamali GA (2008) Evaluation of 12 models to estimate hourly diffuse irradiation on inclined surfaces. Renewable Energy 33:1406–1412
17. Louche A, Notton G, Poggi P, Simonnot G (1991) Correlations for direct normal and global horizontal irradiation on a French Mediterranean site. Sol Energy 46:261–266
18. Hawlader MNA (1984) Diffuse, global and extra-terrestrial solar radiation for Singapore. Int J Ambient Energy 5:31–38
19. Skartveit A, Olseth JA (1987) A model for the diffuse fraction of hourly global radiation. Sol Energy 38:271–274
20. Maxwell EL (1987) Quasi-physical model for converting hourly global horizontal to direct normal insolation, in, United States
21. Lauret P, Boland J, Riley B (2010) Derivation of a solar diffuse fraction model in a Bayesian framework. Case Studies in Business, Industry and Government Statistics 3

Erratum to: Influence of Scattering Pattern on the Insulation Performance of VIP Filler Materials

Bongsu Choi, Jongmin Kim and Tae-Ho Song

Erratum to:
Chapter 4 in: A. Li et al. (eds.), *Proceedings of the 8th International Symposium on Heating, Ventilation and Air Conditioning*, **DOI 10.1007/978-3-642-39584-0_4**

The chapter is retracted because the findings have previously been published elsewhere (i.e. redundant publication).

B. Choi · J. Kim · T.-H. Song (✉)
School of Mechanical, Aerospace and Systems Engineering, Korea Advanced
Institute of Science and Technology, Daejeon, Korea
e-mail: thsong@kaist.ac.kr